The Metamorphic Histories of some Proterozoic Granulites from East Antarctica

Ian Christopher William Fitzsimons

A thesis submitted for the degree of Doctor of Philosophy

University of Edinburgh
1991

Except where indicated otherwise, this thesis is entirely my own work.

ABSTRACT

The Proterozoic Complex of East Antarctica is an extensive metamorphic terrain, which comprises various outcrop areas preserving granulite-facies mineral assemblages ascribed to a 1000 Ma metamorphic event. This study has focused on two areas of this terrain: the Brattstrand Bluffs coastline of Prydz Bay, Princess Elizabeth Land, and the Nemesis Glacier region in the northern Prince Charles Mountains of Mac.Robertson Land. Both areas are composed of granulite-facies gneisses and migmatites of igneous and sedimentary origin, with a complex history of deformation, anatexis and intrusion at high grade. The structure of both areas is dominated by a flat-lying, layer-parallel, foliation. This foliation is locally overprinted by folds and shear zones which are flat-lying in the Brattstrand Bluffs coastline, but upright in the Nemesis Glacier region.

Pressure-temperature (*P-T*) estimates were derived through application of suitable barometers and thermometers to selected specimens of garnet-orthopyroxene-plagioclase-quartz gneiss from both areas. A spread of temperature data from garnet-orthopyroxene thermometers, and pressure data from a barometer based on the solubility of alumina in coexisting garnet and orthopyroxene, are attributed to a variable extent of retrograde Fe-Mg exchange. *P-T* estimates were corrected for this exchange by using the Fe-Mg distribution coefficient required to bring the pressures derived from the exchange-sensitive barometer into agreement with pressures derived from garnet-orthopyroxene-plagioclase-quartz barometers, which are relatively insensitive to Fe-Mg exchange. Corrected peak *P-T* estimates are *c.* 6.0 kbar and 860°C for the Brattstrand Bluffs coastline and *c.* 6.5 kbar and 800°C for the Nemesis Glacier region. Zonation trends in garnet, orthopyroxene and plagioclase from the two areas are consistent with a retrograde *P-T* path gradient of *c.* 17 bar / °C in the Brattstrand Bluffs coastline, and *c.* 6 bar / °C in the Nemesis Glacier region.

Well-layered and migmatitic metapelites in the Brattstrand Bluffs coastline exhibit abundant field evidence for the generation and extraction of leucocratic melts at the metamorphic peak, and metapelite mineral assemblages imply low values of a_{H2O} (less than 0.2). Textural studies indicate that H_2O was partitioned into the silicate melt phase as melting progressed, and that the final stages of melting proceeded through incongruent reactions such as

biotite + sillimanite + quartz = garnet + cordierite + K-feldspar + melt,

which require fluid absence. Mineral assemblage development subsequent to the melting, for example spinel-cordierite symplectites after garnet and sillimanite, indicates decompression from pressures over 5 kbar to *c.* 3 kbar. Integration of microtextures with the structural history indicates that some of this decompression

was synchronous with localized development of flat-lying folds and shear fabrics. This combination of decompression and sub-horizontal shearing is attributed to progressive extension after the metamorphic peak. Hydrous fluids were released by the melts as they crystallized, and were transported along the shear zones, thus preserving anhydrous assemblages in most of the rocks.

Calc-silicate boudins in the Nemesis Glacier region are interlayered on a scale of 0.5 m with orthopyroxene-bearing gneisses, and exhibit spectacular reaction textures including garnet and garnet-quartz coronas between wollastonite and scapolite, calcite-quartz intergrowths after wollastonite, and calcite-plagioclase symplectites after scapolite. Calculated T-a_{CO2} grids indicate that these textures reflect cooling from *c.* 800°C to *c.* 700°C at 6.5 to 7 kbar, and importantly do not require H_2O infiltration as implied by previous studies of similar textures based upon an erroneous grid. Phase relationships also show that a_{CO2} values in the calc-silicates were low (0.3 to 0.5). In contrast, the enclosing orthopyroxene-bearing gneisses indicate low values of a_{H2O} (0.1 to 0.5). Assuming that no other volatile species are present in significant amounts, these low activities of H_2O and CO_2 preclude the presence of a pervasive syn-metamorphic volatile fluid phase.

The P-T evolution of the Brattstrand Bluffs coastline is believed to indicate extensional collapse of overthickened crust following continental collision. The attainment of high temperatures at relatively low pressures is speculatively ascribed to convective thinning of the mantle lithosphere, which increases heat flow. Convective thinning also promotes extensional collapse and hence accounts for the lack of an early high-pressure history before decompression in the Brattstrand Bluffs coastline, which has previously been used as evidence against a collisional model for other parts of Prydz Bay. The Brattstrand Bluffs coastline is interpreted as the centre of the former collisional zone, whereas the Nemesis Glacier region is ascribed a position towards the edge of the orogen, which was still thickening at the thermal peak to produce upright structures. The amount of thickening was less than in the Brattstrand Bluffs coastline, and the area did not undergo extensional collapse, but rather followed a near-isobaric cooling path.

ACKNOWLEDGEMENTS

Simon Harley has provided invaluable help, advice and encouragement throughout the past four years, and I would like to thank him for giving me the opportunity to work on an interesting topic in such an exciting location. I am very grateful for the time, effort and interest he has put into my work, and I feel fortunate to have had him as a supervisor.

Other staff members at Edinburgh are thanked for their interest and help, particularly Ben Harte, who acquired the position of second supervisor at rather a late stage and provided much-appreciated critical comments on part of this thesis. I have benefited from discussions in the UK and Australia on many aspects of my work with many other people including Lance Black, Ian Buick, Bas Hensen, Roger Powell, Mike Sandiford, Volker Schenk, John Sheraton, Nick Stephenson, Bob Tingey, John Valley, Dave Waters and Chris Wilson, and I would like to thank Tim Holland for letting me attend an informal course on thermodynamics in Cambridge which reminded me how much I have forgotten since I was an undergraduate. Bob Tingey also kindly lent aerial photographs of my field area in Prydz Bay. Steve Batty, Damian Carrington, Stuart Kearns, Gordon Watt and Dave Whitmarsh are thanked for proof reading the contents of this thesis carefully and promptly.

Norman Charnley introduced me to the electron microprobe at Oxford, and Peter Hill and Stuart Kearns have provided further guidance and help at Edinburgh. Diana Baty and Yvonne Cooper gave help with the photographic aspects of my work, and I would like to thank the numerous people at Oxford and Edinburgh who have provided me with countless rock thin sections.

I am indebted to the Director and staff of the Australian Antarctic Division, who gave the logistic support for my fieldwork. I would like to thank Captain Ewald Brune, and his officers and crew, for many enjoyable weeks on board the MV Icebird. Martin Betts and Rod Ledingham ensured that my two field seasons ran smoothly, aided by all the support staff at Law and Dovers Bases. Peter Arthur, Mike Hennessy, Richard Priddy, Alan Rooke and Alan White provided company in the field, and discussions with other geologists including Claude Delor, Richard Flint, Peter Kinny, Yoichi Motoyoshi, Neils Munksgaard, Geoff Nichols and Doug Thost were very helpful. The success of my season in the northern Prince Charles Mountains was partly due to Dick Smith and Giles Kershaw, who agreed to fly the field personnel from Mawson to Dovers Base. Despite bad weather, Giles, who was widely regarded as one of the most experienced and talented polar pilots, landed us at Dovers some two weeks before we could have otherwise expected. We were all shocked and saddened to hear of his death in an accident the following season.

The Station Leaders, and other personnel at Mawson and Davis, are thanked for their hospitality, as is Jim Burgess for his assistance at Law Base. The members of the Chinese National Antarctic Research Expedition and the 34th Soviet Antarctic Expedition made my time in the Larsemann Hills particularly enjoyable, and are also thanked for providing transport back to Davis Station. The help and good humour of all the members of the 1987/88 and 1988/89 Australian National Antarctic Research Expeditions is greatly appreciated, particularly the company of Doug Thost for much of the two field seasons.

Professor David Green and other members of the Geology Department, University of Tasmania, are thanked for their hospitality and support in Hobart, particularly Nic and Kate Odling, Mike and Sabine Seitz, and Ian Buick, who provided accommodation during my regular visits. The task of rock shipment back to the UK was made a lot easier thanks to the help given by Peter Cornish. Accommodation in Canberra was provided by Jim Burgess, and in Sydney by Doug Thost and Bas Hensen, and transport to and from Melbourne airport was provided on more than one occasion by Peter Mantel.

I received financial support in the form of a research studentship from the Natural Environment Research Council, who also subsidised a visit to the Australian Geological Convention at Hobart in 1990. Additional funding was provided by the Chevron Fund of St Edmund Hall, Oxford, and a grant to Simon Harley and David Green from the Antarctic Science Advisory Committee.

Finally, and most importantly, I must thank all my friends in Oxford, Edinburgh, Australia and elsewhere, and of course my family, for their support, encouragement and company during the last four years, which have been at times the most hectic, uncomfortable, and frustrating of my life, and also by far the most rewarding and enjoyable.

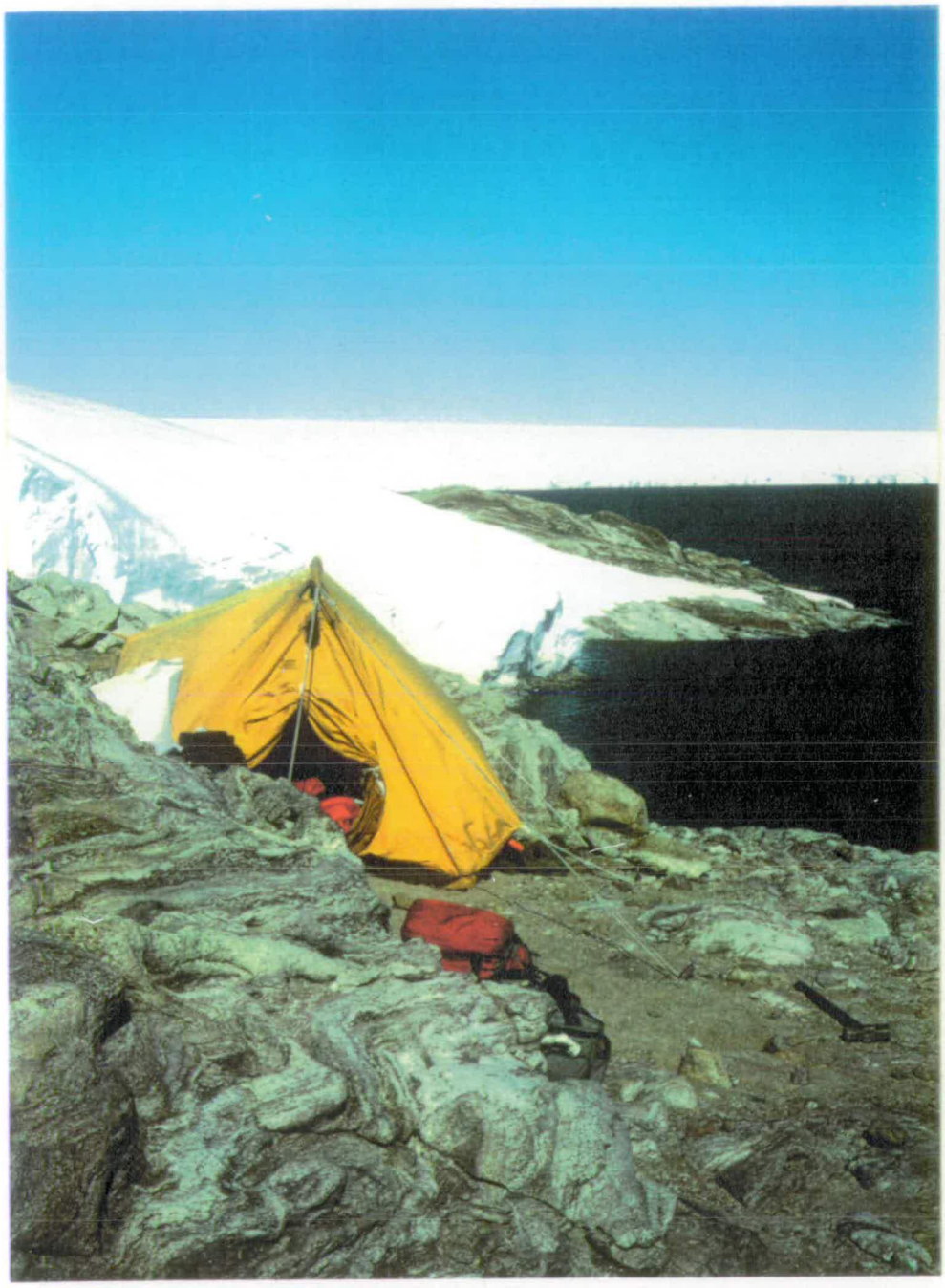

Proterozoic gneisses at Prydz Bay, on the edge of the Antarctic continent; looking southwest from Chaos Glacier, towards Ranvik Glacier and the plateau.

TABLE OF CONTENTS

List of Figures.

Chapter 1

Chapter 2

Chapter 3

Chapter 4

Chapter 5

Chapter 6

Chapter 7

Chapter 8

List of Plates.

(F refers to field photographs and TS to microphotographs of thin sections)

Chapter 3

Chapter 4

List of Tables.

Chapter 1

Chapter 2

Chapter 3

Chapter 4

Chapter 5

Chapter 6

Chapter 7

List of symbols and abbreviations

Minerals (after Kretz, 1983)

An	anorthite	Grs	grossularite	Prh	prehnite
Ap	apatite	Grt	garnet	Qtz	quartz
Bt	biotite	Hbl	hornblende	Rt	rutile
Cal	calcite	Ilm	ilmenite	Scp	scapolite
Chl	chlorite	Kfs	K-feldspar	Sil	sillimanite
Crd	cordierite	Mag	magnetite	Spl	spinel
Cpx	clinopyroxene	Ol	olivine	Spr	sapphirine
Czo	clinozoisite	Opx	orthopyroxene	Tr	tremolite
Ep	epidote	Phl	phlogopite	Wo	wollastonite
Gr	graphite	Pl	plagioclase	Zm	zircon
Additional phases:		L	silicate melt	V	volatile fluid

Mineral components (after Kretz, 1983; except for symbols marked with an asterisk)

ab	albite	gah*	gahnite	or	orthoclase
adr	andradite	gal*	galaxite	ppn*	pyrophanite
alm	almandine	gek*	geikielite	prp	pyrope
an	anorthite	grs	grossularite	usp	ulvöspinel
ann	annite	hc	hercynite	spl	spinel
chr	chromite	hem	hematite	sps	spessartine
en	enstatite	ilm	ilmenite	uvr*	uvarovite
fs	ferrosilite	mag	magnetite		

Miscellaneous symbols for mineral sites and composition

M1 and M2 refer to the two non-tetrahedral cation sites in orthopyroxene.
iv and vi refer to tetrahedral and octahedral sites in pyroxene and biotite.
EqAn is the 'equivalent anorthite content' of scapolite.

Chemical elements

Standard symbols are used for chemical elements and compounds (e.g. Mg, H_2O etc.).

Phases, components and variance

For a given chemical system, P, F, and C are the number of phases, the number of degrees of freedom or variance, and the minimum number of components needed to represent all the phases.

Chemical systems

KASH	K_2O-Al_2O_3-SiO_2-H_2O
NASH	Na_2O-Al_2O_3-SiO_2-H_2O
KNASH	K_2O-Na_2O-Al_2O_3-SiO_2-H_2O
CKNASH	CaO-K_2O-Na_2O-Al_2O_3-SiO_2-H_2O
FAS	FeO-Al_2O_3-SiO_2
FMAS	FeO-MgO-Al_2O_3-SiO_2
KFASH	K_2O-FeO-Al_2O_3-SiO_2-H_2O
KMASH	K_2O-MgO-Al_2O_3-SiO_2-H_2O
KFMASH	K_2O-FeO-MgO-Al_2O_3-SiO_2-H_2O
K(F/M)ASH	K_2O-(FeO or MgO)-Al_2O_3-SiO_2-H_2O
NKFMASH	Na_2O-K_2O-FeO-MgO-Al_2O_3-SiO_2-H_2O
CNKFMASH	CaO-Na_2O-K_2O-FeO-MgO-Al_2O_3-SiO_2-H_2O
FMASO	FeO-MgO-Al_2O_3-SiO_2-O_2 or FeO-MgO-Al_2O_3-SiO_2-Fe_2O_3
FMASTO	FeO-MgO-Al_2O_3-SiO_2-TiO_2-O_2 or FeO-MgO-Al_2O_3-SiO_2-TiO_2-Fe_2O_3
KFMASHTO	K_2O-FeO-MgO-Al_2O_3-SiO_2-H_2O-TiO_2-O_2 or K_2O-FeO-MgO-Al_2O_3-SiO_2-H_2O-TiO_2-Fe_2O_3
CASV	CaO-Al_2O_3-SiO_2-CO_2

Reactions and assemblages

(i, j...) is the univariant or multivariant assemblage (or reaction line or band) with the phases i, j etc. absent.

[i, j...] is the invariant assemblage (or invariant point) with the phases i, j etc. absent.

Thermodynamic symbols

R is the universal gas constant (equal to 8.314 J K^{-1} mol^{-1} or 1.987 cal K^{-1} mol^{-1}).

P and T are pressure and temperature.

$G_{i,P,T}$ is the Gibbs free energy of phase i at P and T.

$H_{i,P,T}$, is the enthalpy of phase i at P and T.

$S_{i,P,T}$ is the entropy of phase i at P and T.

$V_{i,P,T}$ is the volume of phase i at P and T.

$G^\circ_{i,P,T}$, $H^\circ_{i,P,T}$, $S^\circ_{i,P,T}$, $V^\circ_{i,P,T}$ are values of G, H, S, V for pure i at P and T.

$\Delta G_{P,T}$, $\Delta H_{P,T}$, $\Delta S_{P,T}$, $\Delta V_{P,T}$ are changes in G, H, S, V for a reaction at P and T.

$\Delta G^\circ_{P,T}$, $\Delta H^\circ_{P,T}$, $\Delta S^\circ_{P,T}$, $\Delta V^\circ_{P,T}$ are changes in G°, H°, S°, V° for a reaction at P and T.

n_i is the number of moles of component i.

$\mu_{i,P,T}$ is the chemical potential of component i at P and T.

$\mu^\circ_{i,P,T}$ is the standard chemical potential for pure i.

$a_{i,P,T}$ and $f_{i,P,T}$ are the activity and fugacity of component i at P and T.

$\gamma_{i,P,T}^{A}$ and X_i^A are the activity coefficient and mole fraction of component i in phase A. (X_i^A is also used to refer to the mole fraction of i in site A of a given phase).

K is the equilibrium constant for a reaction.

K_γ and K_X are those parts of K relating to γ and X terms such that $K = K_\gamma K_X$.

K_D is the distribution coefficient of two cations between two phases.

G_{ij}^{ex}, H_{ij}^{ex}, S_{ij}^{ex}, V_{ij}^{ex} are the excess G, H, S and V derived by mixing species i and j.

W_{ij} is the interaction parameter for species i and j (sometimes split into W^H, W^S, W^V).

N.b. Superscripts and subscripts in the above symbols are often omitted (e.g. X_{grs}^{Grt} may be written as X_{grs}).

Symbols in diffusion equations

C_i^A is the concentration of component i in phase A.

J_i^A is the flux of component i through phase A.

D_i^A is the diffusivity (or diffusion coefficient) of component i through phase A.

D_T is the diffusivity for a given component and phase at temperature T.

D_o is diffusivity for a given component and phase at infinite temperature.

E_a is the activation energy for diffusion.

T_c is the closure temperature for diffusion.

t is time.

a and A are parameters determined by the grain size and the diffusion geometry.

Mathematical symbols

ln and log (or $\log_{10}$) are natural logarithm and logarithm to the base 10.

exp is exponential.

Σ is sum of.

σ is the standard deviation.

dx/dy is the differential coefficient of x with respect to y.

$\int f(x)\,dx$ is the intregral of f(x).

$\partial f(x,y)/\partial x$ is the partial derivative of f(x,y) with respect to x.

Electron-probe microanalysis

T_b and T_p are background and peak X-ray count times for each element in seconds.
R_b and R_p are background and peak X-Ray count rates in counts per second.
m is the counts above background per second per wt% element in a standard material.

Miscellaneous

D_i refers to a deformational event.
S_i, L_i and F_i refer to planar fabrics, linear fabrics and folds associated with D_i.
C refers to a planar shear fabric which locally transposes an S fabric.
N, S, E, W, are north, south, east and west.
Mt is Mount.
R5.1, R5.2 etc. denote reactions used in Chapter 5.
A1, A2 etc.denote various prograde wollastonite-scapolite assemblages in Chapter 7.
FMQ refers to the fayalite-magnetite-quartz buffer of f_{O2}.

AFM, SFM, and VFM refer to projections onto the Al_2O_3-FeO-MgO, SiO_2-FeO-MgO and H_2O-FeO-MgO planes, from quartz, K-feldspar and H_2O, sillimanite, K-feldspar and H_2O, and quartz, sillimanite and K-feldspar respectively.

$\delta^{13}C$ (per mil) = 10^3 $[(^{13}C/^{12}C)_x - (^{13}C/^{12}C)_{std}] / (^{13}C/^{12}C)_{std}$,
where x is the unknown specimen and std is the standard material (PDB for carbon).

Units

length: μm, mm, m and km are micrometre, millimetre, metre and kilometre.
pressure: kbar is kilobar.
temperature: °C and K are degrees celsius and Kelvin.
time: Ma is 10^6 years.
energy: cal, J and kJ are calorie, joule and kilojoule.
quantity: mol and wt% are mole and weight per cent.
miscellaneous: kV is kilovolt, nA is nanoampere.

Part One

Introduction

1. Introduction and thesis outline

1.1 INTRODUCTION

1.1.1 Granulites and the granulite facies

The term 'granulite' was first used to describe high-grade, quartzofeldspathic rocks with distinctive textures from the Saxon Granulitgebirge of eastern Germany. Modern usage of the term stems from the facies concept of metamorphism as developed by Eskola, and encompasses rocks of a variety of textures and compositions which have equilibrated at high temperatures. Eskola (1939, pp. 360-363) defined the 'granulite facies' on the basis of ideal, anhydrous assemblages that form by dehydration of micas and amphiboles at high grades of regional metamorphism. Eskola (1952) considered a granulite to be any rock with a granulite-facies assemblage, but other workers have proposed additional chemical and textural constraints on the use of the term (e.g. Behr *et al.*, 1971; Mehnert, 1972; Winkler & Sen, 1973). It is now accepted that 'granulite' can be used as a general term to refer to a rock of undefined composition and fabric which has equilibrated under granulite-facies conditions, but usage of the term for specific lithologies is commonly limited to mafic and felsic compositions.

Granulites comprise a varied suite of rocks including mafic and felsic orthogneiss, and paragneiss derived from quartzitic, pelitic and calcareous precursors. All are typified by anhydrous or near-anhydrous assemblages. Workers in the Adirondack Mountains (Fyfe *et al.*, 1958; Buddington, 1963; de Waard, 1965*a*, *b*) defined the boundary between the granulite and amphibolite facies as the appearance of orthopyroxene at the expense of hornblende and biotite in rocks of appropriate composition, in particular the orthopyroxene isograd in basic rocks which marks the development of a plagioclase-clinopyroxene-orthopyroxene-hornblende assemblage. The continued stability of hornblende above the orthopyroxene isograd led to division of the granulite facies into a hornblende-granulite subfacies, in which hornblende is still present, and a pyroxene-granulite subfacies with no remaining hornblende (Fyfe *et al.*, 1958). A further subdivision for basic assemblages was defined using the replacement of plagioclase-orthopyroxene assemblages by clinopyroxene-garnet-quartz at high pressure (de Waard, 1965*a*). The latter reaction was also used by Green and Ringwood (1967) in their subdivision of granulites, which has been

adopted by many workers. They used assemblage changes observed experimentally for basaltic compositions to define low-, intermediate- and high-pressure granulites.

(i) Low-pressure basic granulites are characterized by olivine-plagioclase-clinopyroxene assemblages in silica-deficient rocks, and orthopyroxene-clinopyroxene-plagioclase in silica-saturated rocks.

(ii) Intermediate-pressure basic granulites are characterized by continued stability of orthopyroxene-clinopyroxene-plagioclase in silica-saturated rocks, but incompatibility of olivine and plagioclase in silica-deficient rocks.

(iii) High-pressure basic granulites are characterized by the association garnet-clinopyroxene-quartz and incompatibility of orthopyroxene and plagioclase in silica-saturated rocks.

The granulite facies in felsic lithologies is similarly characterized by stability of orthopyroxene with respect to hornblende and biotite. The amphibolite to granulite transition in pelitic rocks is associated with replacement of muscovite and biotite by anhydrous phases such as sillimanite, K-feldspar, garnet and cordierite (Heier, 1960; Binns, 1964). This process begins at lower grade than the appearance of orthopyroxene in basic lithologies, and sillimanite and K-feldpsar in the absence of muscovite is a typical metapelitic assemblage at both granulite and upper-amphibolite grade. Granulite-facies calcareous and calc-silicate lithologies are typified by phases such as calcite, diopside, scapolite, wollastonite and grossularite.

1.1.2 Age and setting of granulite-facies metamorphism

Granulites were once considered unique to deeply-eroded areas of ancient continental shields. It is now recognized that granulite metamorphism was not confined to any particular stage of earth history, but associated with deep-crustal processes throughout continental evolution (Windley, 1981; Harley, 1989). An outcrop bias towards Precambrian granulites reflects both the high proportion of continental crust formed in Precambrian times (see Fig. 1.1), and the difficulties involved in exhumation of extensive granulite terrains from their place of origin to the surface of the earth over a geologically-short timescale. Granulites have a widespread distribution (see Fig. 1.1) and occur in a variety of settings (see Tables 1.1 and 1.2).

(i) Extensive areas of crystalline basement are exposed in Precambrian continental shields, and represent the largest exposures of granulite-facies rocks. Examples include most of the classic terrains discussed in the literature (e.g. southern India, Greenland, the Lewisian of northwest Scotland; see Table 1.1). These ancient continental nuclei comprise several basement terrains of differing ages and metamorphic grade, and older terrains are commonly reworked by subsequent events. Two types of terrain can be distinguished: massive terrains which

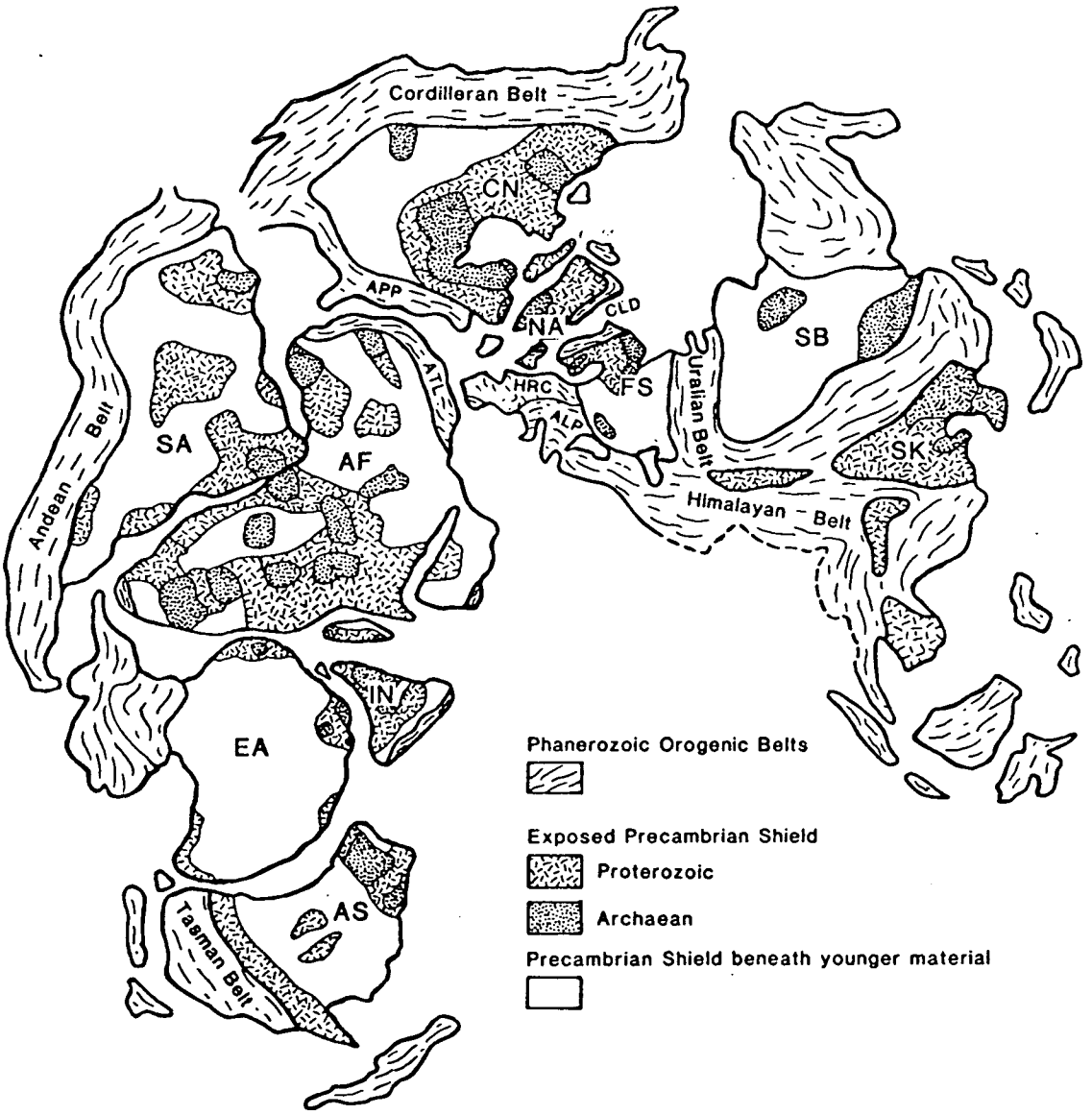

Fig. 1.1 A Permian pre-drift reconstruction of the continents showing the extent of exposed and unexposed Precambrian shield material and the Phanerozoic mobile belts. The shields comprise both Archaean and Proterozoic terrains, which are themselves composite and made up of terrains of different ages, many of which are high-grade, granulite-facies terrains. Granulites also occur as tectonic units within the Phanerozoic mobile belts, but these are both less common and less extensive than the shield granulites. The Precambrian shields are labelled as follows: CN is the Canadian, NA the North Atlantic, FS the Fenno-Scandian, SB the Siberian, SK the Sino-Korean, SA the South American, AF the African, IN the Indian, EA the East Antarctic and AS the Australian. ALP is the Alpine Belt, ATL the Atlas Belt, APP the Appalachians, CLD the Caledonides and HRC the Hercynian Belt.

Table 1.1 Examples of granulite terrains within continental shields. A and P refer to age (Archaean and Proterozoic), ITD and IBC refer to initial retrograde pressure-temperature paths (isothermal decompression and isobaric cooling).

Canadian Shield			
English River (Ontario)	A	-	Perkins & Chipera, 1985
Grenville Province	P	ITD	Currie & Gittins, 1988; Grant, 1989
		IBC	Arima *et al.*, 1986; Anovitz & Essene, 1990
Adirondacks (NE USA)	P	IBC	Bohlen *et al.*, 1985
Nain Complex (Labrador)	P	IBC	Berg, 1977*a,b*
North Atlantic Shield			
West Greenland	A	IBC	Bridgwater *et al.*, 1973; Wells, 1979
Scourian (Scotland)	A	ITD	Barnicoat, 1983; Sills & Rollinson, 1987
Fenno-Scandian Shield			
Finnish Lapland	P	-	Eskola, 1952; Raith & Raase, 1986
Uusimaa (Finland)	P	-	Schreurs & Westra, 1986
Bamble (SE Norway)	P	IBC	Touret, 1971*a,b*; Visser & Senior, 1990
Rogaland (SW Norway)	P	-	Kars *et al.*, 1980
Siberian Shield			
Aldan Block	A	ITD	Perchuk *et al.*, 1985
Yenisey Range	A	IBC	Perchuk *et al.*; 1989
Sino-Korean Shield			
Qianxi Group (China)	A	-	Sills *et al.*, 1987
South American Shield			
Jequié Complex (Brazil)	P	ITD	Sighinolfi *et al.*, 1981; Barbosa, 1990
African Shield			
Kasai Craton (Zaire)	A	ITD	Bingen *et al.*, 1988
Labwor Hills (Uganda)	P	IBC	Nixon *et al.*, 1973; Sandiford *et al.*, 1987
Limpopo Belt (S Africa)	A	ITD	Droop, 1989; Rollinson, 1989
Namaqualand (S Africa)	P	IBC	Clifford *et al.*, 1975; Waters, 1989
Zambezi Belt (Zimbabwe)	P	ITD	Treloar *et al.*, 1990
Madagascar	P	IBC	Sacchi *et al.*, 1984; Nicollet, 1990
Furua Complex (Tanzania)	P	IBC	Coolen, 1980
Iforas Unit (Mali)	P	ITD	Boullier & Barbey, 1988
Indian Shield			
Karnataka (S India)	A	-	Janardhan *et al.*, 1982; Stähle *et al.*, 1987
Madras (SE India)	A	-	Subramaniam, 1959; Bhattacharya & Sen, 1986
Kerala Khondalite Belt	P	ITD	Chacko *et al.*, 1987; Santosh, 1987
Paderu (E Ghats)	P?	ITD	Lal *et al.*, 1987
Highland Series (Sri Lanka)	P	ITD	Cooray, 1962; Sandiford *et al.*, 1988
		IBC	R. Schumacher *et al.*, 1990
East Antarctic Shield			
Napier Complex	A	IBC	Sheraton *et al.*, 1987; Harley & Black, 1987
Rayner Complex	P	ITD	Sheraton *et al.*, 1987; Black *et al.*, 1987
Molodezhnaya	P	ITD	Grew, 1981
Mawson Coast	P	ITD	Clarke *et al.*, 1989
Vestfold Hills	A	-	Collerson *et al.*, 1983; Collerson & Sheraton, 1986*a*
Larsemann Hills	P	ITD	Stüwe & Powell, 1989*a,b*
Rauer Group	P	ITD	Harley, 1987*a*, 1988; Harley & Fitzsimons, 1991
Australian Shield			
Yilgarn Block	A	IBC	Myers, 1988; Muhling, 1990
Arunta Block	P	IBC	Warren, 1983*a,b*; Warren & Hensen, 1989
Musgrave Block	P	ITD	Collerson *et al.*, 1972; Maboko *et al.*, 1989
Broken Hill (NSW)	P	IBC	Binns, 1964; Phillips, 1980; Phillips & Wall, 1981

equilibrated entirely within the granulite facies, and transitional terrains which preserve a prograde metamorphic field gradient from amphibolite to granulite-facies conditions (e.g. the Adirondacks, Broken Hill, southern India, southeast Norway). The latter should be distinguished from a retrograde transition to amphibolite assemblages, which is common in reworked granulite terrains (e.g. the Lewisian, western Greenland).

(ii) Tectonic blocks and slices of granulite are exposed in Phanerozoic fold and mountain belts (e.g. the Hercynian belt, the Himalayas; see Table 1.2). These granulites may either be relics of an early tectonic episode caught up in and partially overprinted by a later, unrelated event (e.g. Hercynian granulites in the Pyrenees), or a product of a single orogenic event (e.g. the Gruf Complex of the Alps).

(iii) Granulites also occur as xenoliths entrained in basaltic and kimberlitic magmas. These have been reviewed by Griffin and O'Reilly (1987).

Table 1.2 Examples of granulites within Phanerozoic mobile belts.

Appalachian Belt		
Blue Ridge Province (USA)	-	Absher & McSween, 1985; McLellan *et al.*, 1989
Caledonian Belt		
Western Gneisses (Norway)	ITD	Johansson & Möller, 1986
Dalradian (Scotland)	-	Baker & Droop, 1983
Hercynian Granulites (divided into two groups after Pin & Vielzeuf, 1983; Vielzeuf & Pin, 1989)		
Group 1 (tectonic units of Hercynian granulite emplaced during the Hercynian event)		
Central Iberian Zone	ITD	Gil Ibarguchi & Martinez, 1982
Granulitgebirge (E Germany)	ITD	Grew, 1986
Moldanubian Zone (Austria)	ITD	Scharbert & Kurat, 1974; Petrakakis, 1986
Group 2 (tectonic units of Hercynian granulite emplaced during the Alpine event)		
Northern Pyrenees	-	Vielzeuf & Komprobst, 1984
Ivrea Zone (Alps)	IBC	Zingg, 1983; Sills, 1984
Calabria (S Italy)	ITD	Schenk, 1984, 1989
Alpine Belt		
Gruf Complex (Alps)	ITD	Droop & Bucher-Nurminen, 1984
Himalayas		
Kohistan (NW Pakistan)	-	Jan & Howie, 1981; Bard, 1983
Cordilleran Belt		
British Columbia	ITD	Hollister & Crawford, 1986; Selverstone & Chamberlain, 1990
Tasman Belt		
Fiordland (New Zealand)	ITD	McCulloch *et al.*, 1987; Bradshaw, 1989

1.1.3 The origins of granulites

It has been recognized for some time that subjecting a typical hydrous amphibolite to the pressures and temperatures of the lower crust does not produce a granulite. There are two major problems to be overcome.

(i) Granulite-facies assemblages equilibrate over a wide range of conditions (Harley, 1989), with pressures between 3 and 12 kbar and temperatures from 700 to over

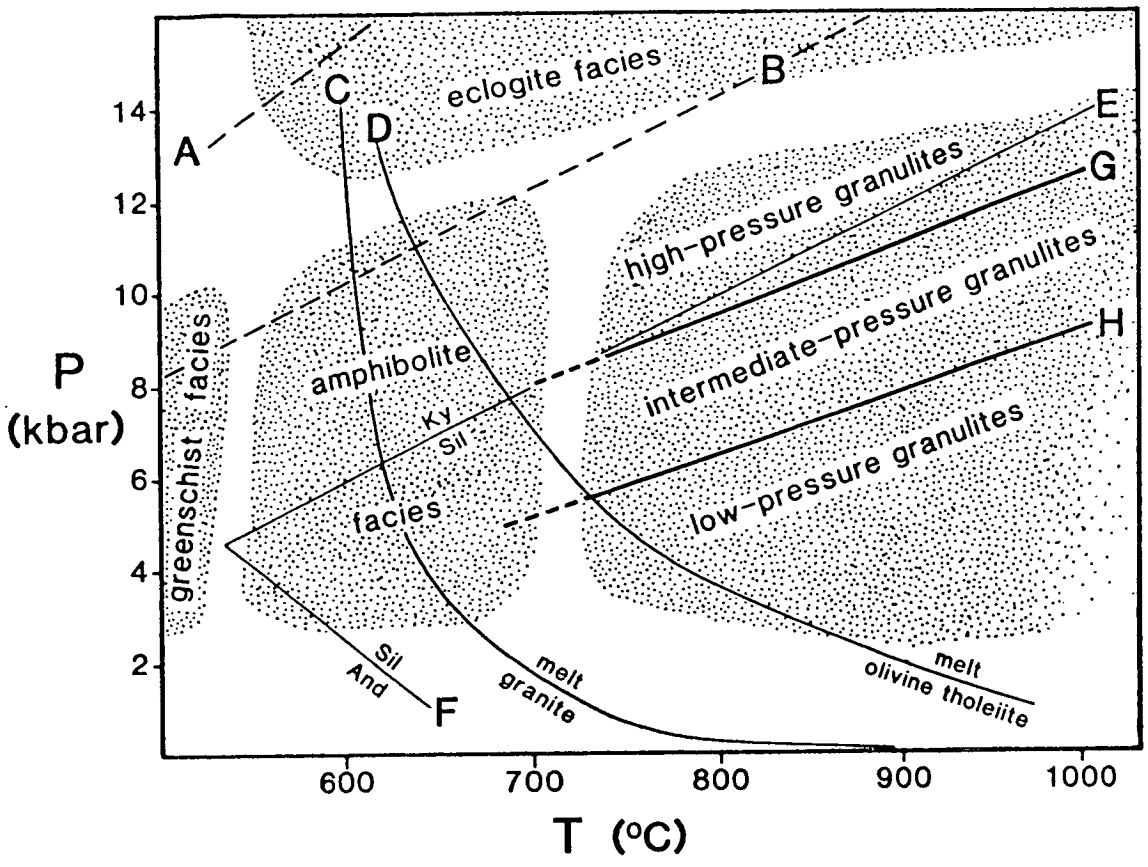

Fig. 1.2 The pressure-temperature conditions of granulite stability. The *P-T* fields of the metamorphic facies are taken from Yardley (1989, p. 50), but note that they are transitional. The dashed lines A and B represent a steady-state geotherm for stable continental shields (Chapman, 1986) and an average geotherm for recently-active terrains (Sclater *et al.*, 1980) respectively. Curves C and D are water saturated solidi for granite (Huang & Wyllie, 1973) and olivine tholeiite (Yoder & Tilley, 1962). Lines E (Holdaway, 1971) and F (curve b of Salje, 1986) depict aluminosilicate phase relationships and lines G and H are the positions of the reactions in basaltic compositions determined by Green and Ringwood (1967) and used to divide the granulite-facies. Note that granulite-facies assemblages are stable at temperatures above the continental geotherms and the granite and basalt solidi.

1000°C. However, these conditions are more extreme than those normally present in the continental crust, and hence stabilization of granulite-facies mineral assemblages requires a thermal perturbation of the continental geothermal gradient (see Fig. 1.2). Various tectonic mechanisms have been proposed to account for this thermal anomaly including crustal thickening by continental collision (England & Thompson, 1984), magmatic accretion into and under the continental crust (Wells, 1980) and extension of normal-thickness crust (Sandiford & Powell, 1986*a*). Evidence for more than one tectonic process in granulite formation is provided by the range of different retrograde pressure-temperature paths shown by granulite terrains, varying from near-isothermal decompression to near-isobaric cooling (Harley, 1989; see Table 1.1).

(ii) Most hydrous lithologies melt before the stability field of granulite assemblages is attained (see Fig. 1.2), and some mechanism is required to extract or dilute the water in order to stabilize granulite assemblages with respect to a melt. Hence the transition from amphibolite to granulite facies is related to a decrease in water activity (a_{H2O}), as well as an increase in temperature (e.g. Phillips, 1980). A number of geochemical processes have been invoked to account for the dehydration of granulite precursors, including partition of H_2O into hygroscopic silicate melts produced by some combination of anatexis and magmatism (Fyfe, 1973), and dilution with pervasive, mantle-derived, carbonic fluids[1] (Newton *et al.*, 1980).

Studies of granulites from all the settings discussed in Section 1.1.2 have been used to identify the tectonic and geochemical processes responsible for granulite stabilization. Lower-crustal xenoliths provide a wide sample of granulites, both in terms of areal and temporal extent, but provide no information on many of the mesoscopic and regional complexities preserved in surface granulite terrains. This thesis is a study of the Proterozoic Complex of East Antarctica, a high-grade shield terrain comprising granulite-facies gneiss and migmatite with subordinate younger intrusive rocks, which preserve evidence of high-grade metamorphic and deformational processes on all scales from microscopic to regional.

1.2 AN OUTLINE OF THE THESIS

1.2.1 Aims of the study

The primary purpose of this study was to investigate the geological, structural and metamorphic history of part of the Proterozoic Complex of East Antarctica, and to identify the processes responsible for granulite formation in this high-grade terrain. The chosen terrain has many features in common with other granulite occurrences, and hence the observations and conclusions of this study also have general implications for granulite metamorphism.

1.2.2 Methods employed

Investigation was focused upon two areas within the Proterozoic Complex: the Brattstrand Bluffs coastline of Prydz Bay, Princess Elizabeth Land and the Nemesis Glacier region in the northern Prince Charles Mountains of Mac.Robertson Land. Fieldwork in these two areas was performed during two consecutive austral summers,

---

1 The term fluid is used throughout this thesis to denote a supercritical fluid phase composed of one or more volatile components such as H_2O and CO_2. The term vapour is used in much of the literature for the same purpose. Silicate fluid (i.e. melt) phases are referred to as melts to avoid confusion.

as part of the 1987/1988 and 1988/1989 Australian National Antarctic Research Expeditions. The first season involved 30 days of fieldwork in the Brattstrand Bluffs coastline during January and February 1988. The second season consisted of 41 days fieldwork in the Nemesis Glacier region, between November 1988 and January 1989, and a further five days of fieldwork in the Brattstrand Bluffs coastline in March 1989. All fieldwork was supported by the Australian Antarctic Division. The geographical location of these areas is discussed and illustrated in Chapter 2, and further details of the localities visited are given in Chapters 3 and 4, and Appendix 1.

Fieldwork in both areas involved specimen collection, measurement of structural data and geological mapping, but the scale and detail of operation differed in the two areas. The geology and structure of the Brattstrand Bluffs coastline was mapped on a scale of 1:15,000, with the aid of air photographs to this scale published by the Australian Surveying and Land Information Group. Reconnaissance mapping in the Nemesis Glacier region was performed over a much larger area, and in less detail, since rugged topography and variable exposure made it difficult to trace lithological units for any great distance. Mapping in the Nemesis Glacier region was aided by air photographs at a scale of 1:50,000 and topographic maps at a scale of 1:100,000, both published by the Australian Surveying and Land Information Group, and topographic maps at scales of 1:200,000 and 1:100,000 published by the Chief Director of Geodesy and Cartography to the Soviet Ministry. Access to outcrop in both areas was by foot from a number of selected camp-sites, which were accessed by helicopter from the base camp. In addition, four-wheel drive all-terrain vehicles were available for part of the season in the Nemesis Glacier region, which extended the daily working radius to 20 kilometres or more.

In total, some 350 specimens were collected from each field area (see Appendix 2). Preliminary hand-specimen and thin-section petrography were used to identify mineral assemblages and correlate microstructure with the outcrop-scale structural scheme developed in the field. Detailed thin-section petrography was concentrated on semi-pelite specimens from both areas, metapelite specimens from the Brattstrand Bluffs coastline, and calc-silicate specimens from the Nemesis Glacier region, which were identified as the most promising lithologies for petrological study. Carefully-selected specimens of these three lithologies were analysed using electron-microprobe facilities at the Universities of Oxford and Edinburgh. The analytical and petrographic data were then combined to determine the pressure-temperature-fluid regime during peak metamorphism and retrograde evolution in the two areas, using theoretical assemblage constraints and published geothermometers and geobarometers.

1.2.3 Layout of the thesis

The thesis is divided into four parts, which discuss in turn the background to the thesis, field and petrographic relationships in the study areas, the results of a detailed petrological study of selected lithologies, and the implications of field and petrological data on granulite metamorphism in the chosen terrain and in general. Superposed onto this four-fold division of background, observation, theory and interpretation, is a further two-fold division reflecting the two field areas.

Part One is an introduction comprising Chapters 1 and 2. This chapter introduces granulite-facies metamorphism, and outlines the scope and layout of the thesis. Chapter 2 is a summary of previous geological investigation in East Antarctica between longitudes 50 and 80°E, and provides a broad geological setting to this study.

Part Two comprises Chapters 3 and 4, which detail the geological, structural and petrographic features of the Brattstrand Bluffs coastline and the Nemesis Glacier region respectively. These chapters combine the field and petrographic observations to provide relative chronologies for the geological and deformational events identified in the two areas.

Part Three uses selected lithologies to determine the pressure-temperature conditions and fluid regime associated with the Proterozoic metamorphic event in the two areas, and comprises Chapters 5 to 7. Chapter 5 is a detailed geo-thermobarometric study of garnet-orthopyroxene-plagioclase-quartz assemblages, which crop out in both study areas and for which a number of mineral thermometers and barometers are available. The chapter evaluates the peak conditions of metamorphism in both areas and constrains the retrograde evolution using compositional zonation profiles in garnet, orthopyroxene and plagioclase. It also critically assesses the reliability of various well-known thermobarometric calibrations, and considers the effect of disequilibrium on pressure-temperature estimates. Chapter 6 discusses the peak and retrograde pressure-temperature evolution and syn-metamorphic fluid regime in the Brattstrand Bluffs coastline, using theoretical constraints imposed by mineral assemblages and reaction textures in metapelitic migmatite. Chapter 7 does likewise for the Nemesis Glacier region using mineral assemblages and reaction textures in calc-silicate lithologies.

Part Four comprises one chapter, Chapter 8, which integrates field observation with petrological theory and thermobarometric calculation to establish geological histories for the two areas, and discusses the processes responsible for granulite development in the Proterozoic Complex. This final chapter also indicates the applicability of the results to other granulite terrains, and suggests further lines of research identified during this study.

1.2.4 Terminology

The precise definitions of certain terms in this thesis have been matters of intense debate in the past. The general approach in this thesis is to use descriptive terms which imply as little about process as possible. 'Granulite' is used as an all-embracing term for any rock with a granulite-facies assemblage, as suggested by Eskola (see Section 1.1.1). Most of the high-grade lithologies are described either as 'gneiss' or 'migmatite', with an additional compositional qualification. 'Gneiss' is used to denote a medium- to coarse-grained rock with a pervasive fabric in hand specimen. This foliation need not include a compositional layering (commonly called 'gneissic layering', e.g. Hobbs *et al.*, 1976, p. 230; Yardley, 1989, p. 22). 'Orthogneiss' and 'paragneiss' are used to describe gneisses of inferred igneous and sedimentary parentage respectively. 'Migmatite', following the non-genetic definitions of Mehnert (1968) and Ashworth (1985), is a composite rock comprising quartzofeldspathic or feldspathic portions of plutonic appearance and portions of metamorphic appearance. The pale-coloured, quartzofeldspathic component is described as 'leucosome', and the part resembling a gneissic metamorphic rock is termed 'mesosome'. A third component, commonly dark in colour, is referred to as 'melanosome'. Melanosome generally occurs between leucosome and mesosome, and is depleted in quartzofeldspathic material compared to the mesosome.

Migmatites have been divided into a number of structural types. 'Stromatic migmatite' comprises intimately-interlayered leucosome and mesosome. The layering is generally continuous, but, unlike the regular layering of banded gneisses, it is commonly complex and may preserve discordant relationships. In migmatite with a higher proportion of leucosome, the internal structures of the mesosome are disrupted and the mesosome occurs as isolated rafts or 'schollen'. Increased disruption of the mesosome produces isolated streaks or 'schlieren', which are commonly depleted or devoid of leucosomic phases and can be considered as bodies of melanosome.

There has been much discussion of the term 'charnockite', which was first used by Holland (1893, 1900) to describe an orthopyroxene-bearing granite from Madras, India, with a dark, greasy lustre caused by colouration of quartz and feldspar. The name has since been applied to orthopyroxene-bearing quartzofeldspathic rocks from granulite terrains worldwide, including many of non-granitic composition, but the original restriction to granitic bulk compositions is now recognized and is used here. Other terms have been introduced for other compositions (e.g. Tilley, 1936; Tobi, 1971). It has been disputed whether charnockite is a high-temperature igneous rock or a rock of metamorphic origin (Howie, 1955; Subramaniam, 1959; Pichamuthu, 1960).

However, it is now recognized that both types exist, and that local evidence must be used to determine the origins of any particular example.

Structures and fabrics are labelled using the standard symbols of F, L and S to refer to folds, lineations and planar fabrics (compositional banding, foliations or shear fabrics) respectively, with an additional numeral indicating their association with a particular deformational event. The assignment of structures and fabrics to different deformational events is made principally to aid description, and is based on temporal relationships observed in the field rather than the processes responsible for their formation. It is recognized that structures attributed to the same deformational event need not have formed at the same time, and that structures attributed to different structural events may be the result of continuous deformation under an evolving stress regime.

2. Geological setting

2.1 INTRODUCTION

2.1.1 The Antarctic continent

Antarctica has an area of some 14 million km^2, but more than 98 per cent of it is covered by the ice-cap. Bedrock is exposed in the following settings:

(i) at the edge of the ice sheet as island and coastal outcrops;

(ii) inland as isolated peaks and nunataks, or extensive ranges and massifs, where bedrock topography is sufficient to extend above the ice sheet; and

(iii) in extensive 'oases' or 'dry valleys', which are permanently ice free and commonly associated with hypersaline lakes and arid weathering.

The Antarctic continent is divided both geologically and geographically into East Antarctica and West Antarctica by the Transantarctic Mountains (see Fig. 2.1), which extend for some 3500 km. East Antarctica, which lies mainly within the eastern hemisphere between longitudes 30°W and 160°E, is an ancient continental shield overlain locally by younger sedimentary lithologies. It was last affected by major deformation and metamorphism about 500 Ma ago. West Antarctica comprises several discrete continental blocks with an extensive history of tectonic activity throughout the Phanerozoic (see Fig. 2.1).

2.1.2 The East Antarctic Shield

The East Antarctic Shield is composed largely of greenschist- to granulite-facies metamorphic rocks and subordinate igneous bodies (Grew, 1982*a*, 1984; James & Tingey, 1983). It is not a single terrain, but consists of discrete parts ranging in age from over 3000 Ma to around 500 Ma. A Permo-Triassic cover sequence of continental conglomerate, sandstone, shale and coal is locally exposed. Mesozoic and Cenozoic dykes, sills and extrusive lithologies are widespread, but form only a small fraction of outcrop. This thesis is concerned with the sector between 50 and 80°E, where basement outcrop is relatively extensive (see Fig. 2.2), and some evidence of the three-dimensional outcrop pattern is preserved.

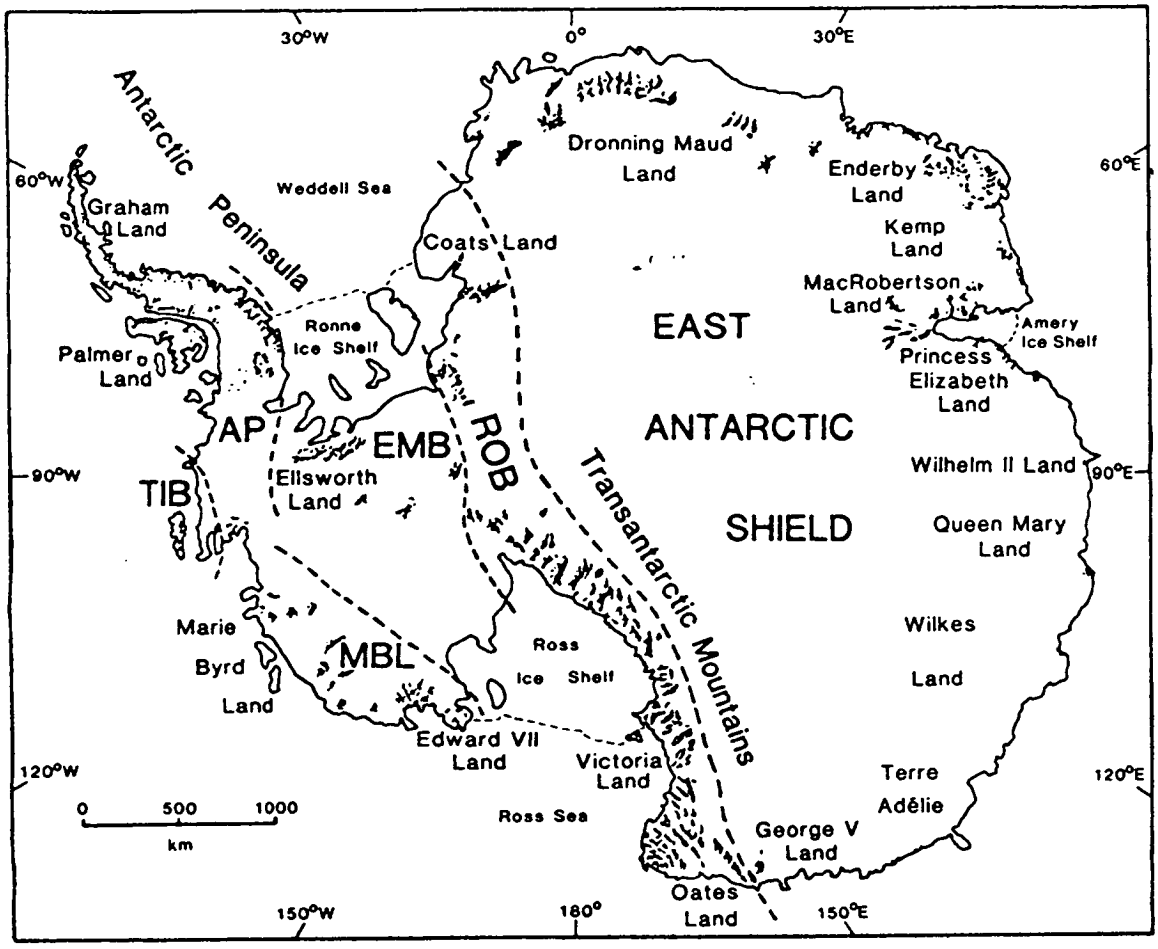

Fig. 2.1 A map of Antarctica depicting the extent of rock exposure (black areas) and the principal tectonic provinces (after Craddock, 1982; Dalziel & Elliot, 1982). The East Antarctic Shield is bounded by the Ross Orogenic Belt (ROB) extending along the Transantarctic Mountains. West Antarctica comprises at least four tectonic units: the Antarctic Peninsula (AP), the Ellsworth Mountains Block (EMB), Marie Byrd Land (MBL) and the Thurston Island - Eights Coast Block (TIB).

2.2 ANTARCTIC EXPLORATION AND GEOLOGICAL STUDY BETWEEN 50 AND 80°E

2.2.1 Exploration

The continent in this sector was first sighted in 1831 by John Biscoe, a sealing captain, who named the area Enderby Land after his employers. Peter Kemp, another sealing captain, sighted land further east in 1833, now called Kemp Land. The remainder of the coastline was unexplored until the twentieth century, although scientists on board HMS Challenger inferred the existence of a substantial continental landmass from dredgings obtained from the outer part of Prydz Bay in 1874. The British-Australian-New Zealand Antarctic Research Expedition (BANZARE) of 1929-1931, led by Sir Douglas Mawson, mapped much new territory including

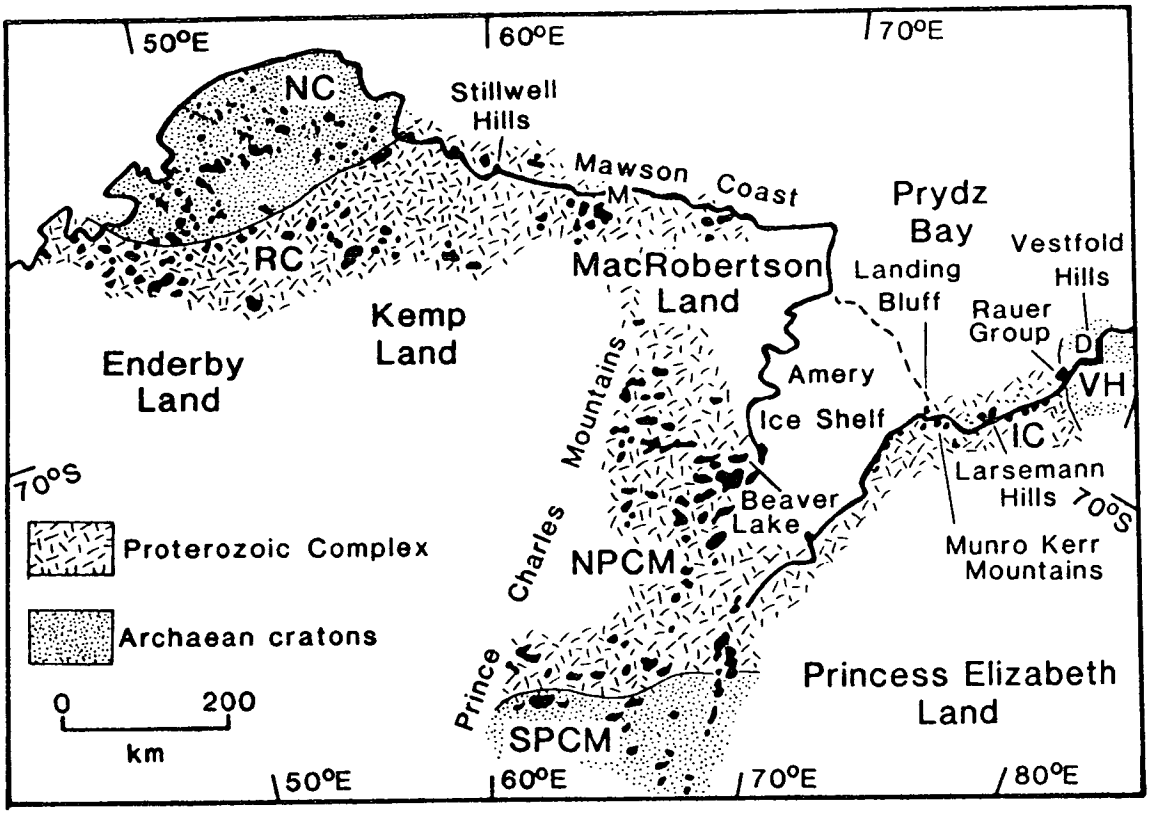

Fig. 2.2 A map of the coastal sector of Antarctica between 50 and 80°E, depicting the extent of exposure (black areas) and the inferred extent of Archaean and Proterozoic terrains. The Archaean cratons are the Napier Complex (NC), the Vestfold Hills (VH) and the southern Prince Charles Mountains (SPCM). Proterozoic outcrops include the Rayner Complex (RC), the northern Prince Charles Mountains (NPCM) and the Ingrid Christensen Coast (IC). M and D represent Mawson and Davis Stations.

Mac.Robertson Land and Princess Elizabeth Land, and laid the basis for what was later to become the Australian Antarctic Territory. Much of the Ingrid Christensen Coast in Prydz Bay was discovered and mapped by the Norwegian whalers Klarius Mikkelsen and Lars Christensen between 1935 and 1937. Most coastal outcrops had now been identified, but the existence of substantial rock outcrop inland was not realized until 1947, when a mountainous area was located by US Navy aircraft during 'Operation Highjump'. These were named the Prince Charles Mountains by an Australian party in 1954, who were the first to sight them from the ground. There is no further outcrop to the south in this sector.

2.2.2 Geological investigations

The first geological work was done by BANZARE, and consisted largely of specimen collection from isolated coastal landings and subsequent petrographic studies (e.g. Tilley, 1937*a*, *b*). Specimens were also collected by the Norwegian expeditions (Broch, 1946). There was no further geological fieldwork until the establishment of

permanent stations by the Australian National Antarctic Research Expeditions (ANARE), first at Mawson on the coast of Mac.Robertson Land in 1954, and then at Davis in the Vestfold Hills in 1957. Geologists from the Australian Bureau of Mineral Resources (BMR), based at these ANARE stations, carried out regional reconnaissance mapping in most areas of Enderby, Kemp, Mac.Robertson and Princess Elizabeth Lands (e.g. Crohn, 1959; McLeod, 1959, 1964; Ruker, 1963; McCarthy & Trail, 1964; Trail, 1964, 1970; McLeod *et al.*, 1966; Trail *et al.*, 1967). This was followed by more systematic and localized mapping by BMR geologists (e.g. Tingey, 1972, 1974, 1981, 1982; Tingey & England, 1973; Arriens, 1975). Recent ANARE geological work has involved workers of various affiliations, and concentrated on detailed aspects of the metamorphic, structural, igneous and geochronological history of the area. Soviet expeditions have been active in the area since the 1960's, particularly in Enderby Land and the Prince Charles Mountains (e.g. Ravich & Kamenev, 1975; Grikurov *et al.*, 1976). However, few of their results have been published outside the Soviet literature, and differences in nomenclature and interpretation make assimilation with other work difficult.

2.3 THE GEOLOGY OF THE EAST ANTARCTIC SHIELD BETWEEN 50 AND 80°E

2.3.1 Introduction

The East Antarctic Shield between 50 and 80°E has been divided on the basis of geological and geochronological studies into a number of distinct terrains (Grew, 1982*a*; James & Tingey, 1983; Harley & Hensen, 1990). Three Archaean cratons have been identified (see Fig. 2.2): the Napier Complex of Enderby Land, the Vestfold Hills of Princess Elizabeth Land and the southern Prince Charles Mountains of Mac.Robertson Land. These cratons are separated by a Proterozoic Complex comprising rocks of Proterozoic origin and reworked Archaean material, which preserve metamorphic assemblages attributed to a 1000 Ma event. The Proterozoic Complex can be divided into a few areas of fairly continuous outcrop: the Rayner Complex in Enderby and Kemp Lands, the Stillwell Hills and Mawson Coast of eastern Kemp Land and Mac.Robertson Land, the northern Prince Charles Mountains of Mac.Robertson Land, and the Ingrid Christensen Coast of Prydz Bay, Princess Elizabeth Land. The geological, structural, metamorphic and geochronological evolution of these areas is discussed in the following sections and summarized in Tables 2.1 to 2.7. This thesis is mainly concerned with the Proterozoic Complex, but the Archaean cratons are also described in this chapter since they preserve localized evidence of the Proterozoic event.

2.3.2 The Napier Complex

The Napier Complex is dominated by felsic to intermediate orthopyroxene-quartz-feldspar orthogneiss (Ravich & Kamenev, 1975; Sheraton *et al.*, 1980, 1987; James & Black, 1981; Black & James, 1983; Black *et al.*, 1983*a*, *b*; Sandiford & Wilson, 1983, 1984; Harley & Black, 1987). Subordinate layered paragneiss sequences were derived from various supracrustal protoliths including quartzite, pelite, ironstone and quartzofeldspathic rock. Mafic and ultramafic units occur within both the paragneiss and orthogneiss. These rocks underwent granulite-facies metamorphism at temperatures in excess of 1000°C, to produce assemblages such as sapphirine-quartz, orthopyroxene-sillimanite and osumilite-garnet in metapelitic rocks (Dallwitz, 1968; Ellis *et al.*, 1980) and inverted pigeonite lamellae in meta-ironstones (Sandiford & Powell, 1986*b*; Harley, 1987*b*). Pressures in the range of 7 to 10 kbar are inferred for this event (Ellis, 1980; Grew, 1980, Harley, 1983, 1985*a*), which was accompanied by pervasive ductile deformation (D_1; James & Black, 1981) producing tight to isoclinal, flat-lying folds and an intense axial-planar, layer-parallel foliation. A second deformational event (D_2) produced another generation of asymmetric folds, and is also considered synchronous with the high-grade conditions since it is associated with little or no change in metamorphic assemblage. The age of this high-grade tectonothermal event is constrained by a range of isotopic data, particularly a 3070 Ma Rb-Sr whole-rock isochron for syn-metamorphic orthogneiss (Sheraton & Black, 1983). Although much orthogneiss material was emplaced during the metamorphism, a significant proportion had already been resident in the crust for some time. For example, zircon grains within orthogneiss at Mt Sones preserve ages of around 3900 Ma (Black *et al.*, 1986).

The D_1-D_2 event was followed by near-isobaric cooling to 700°C at 5 to 9 kbar (Black *et al.*, 1983*a*, *b*; Harley, 1983, 1985*a*; Sandiford, 1985*a*), when the Complex was refolded about axial planes inclined at large angles to the pre-existing foliation. This deformation (D_3) caused local recrystallization and has been dated at 2450 Ma (Black *et al.*, 1983*b*). Several generations of mafic dyke were intruded during the Proterozoic, including a high-magnesium suite at around 2400 Ma, and an abundant tholeiitic suite (the Amundsen Dykes) at around 1200 Ma. Most of these dykes post-date the D_3 event and are undeformed, although they are locally affected by ductile to brittle shear zones, mylonite, and an associated metamorphic overprint. This deformation (D_4) is most apparent at the edges of the Complex. Syn-D_4 metamorphic conditions have been estimated at 700°C and 7 kbar, and were followed by near-isothermal decompression to 3-4 kbar (Black *et al.*, 1983*b*; Sandiford & Wilson, 1983; Sandiford, 1985*b*; Harley, 1985*b*). D_4 is correlated with an episode of lead loss

dated at around 1000 Ma (Grew *et al.*, 1982; Black *et al.*, 1984), and assumed to reflect development of the adjacent Proterozoic Complex. Mylonite, pseudotachylite, epidote veins and pegmatite associated with a lower-amphibolite to greenschist overprint have been dated at about 500 Ma using Rb-Sr methods (Black *et al.*, 1983*b*), and rare alkaline dykes were emplaced during the Phanerozoic (Black & James, 1983).

Table 2.1 Summary of geological features of the Napier Complex.

Event		Age
1	Orthogneiss and paragneiss protolith formation	3900-3000 Ma
2	D1 (pervasive flat-lying folds and foliation) at 1000°C, 7-10 kbar	3100 Ma
3	D2 (asymmetric folding) under continued granulite conditions	2900 Ma
4	Near-isobaric cooling	-
5	D3 (large-scale asymmetric folds) at 700°C, 5-9 kbar	2450 Ma
6	Further isobaric cooling	-
7	Intrusion of high-Mg dykes	2400 Ma
8	Intrusion of tholeiitic Amundsen Dykes	1200 Ma
9	D4 (shear zones and mylonites) at 700°C, 7 kbar	1000 Ma
10	Near-isothermal decompression to 3-4 kbar	-
11	D5 (mylonites, pseudotachylite) under amphibolite to greenschist conditions	500 Ma
12	Emplacement of alkaline dykes	Phanerozoic

2.3.3 The Vestfold Hills

The Vestfold Hills consist predominantly of granulite-facies orthogneiss and paragneiss (Oliver *et al.*, 1982; Collerson *et al.*, 1983; Collerson & Sheraton, 1986*a*). The oldest units are the mafic to ultramafic Tryne metavolcanics, the metasedimentary Chelnok supracrustals, and the tonalitic Mossel orthogneiss. These three units were metamorphosed in the granulite facies, and deformed (D_1) to produce isoclinal folds and an intense axial-planar fabric. A second deformation (D_2) folded the pre-existing units under granulite conditions, and D_1 structures were commonly transposed by an intense S_2 fabric. A suite of tonalitic and dioritic to monzonitic and granitic orthogneisses, the Crooked Lake Gneiss, exhibits a simple S_2 fabric and is interpreted as a syn-D_2 intrusion. The metamorphic conditions associated with D_2 have been estimated at 800°C and 6 to 8 kbar (Collerson & Sheraton, 1986*a*). Higher temperatures before D_2 are indicated by perthitic and pyroxene exsolution textures (Collerson & Sheraton, 1986*a*). Pre-D_2 conditions have been estimated at 900°C and 7 to 10 kbar (Harley, 1987*c*) from sapphirine-bearing assemblages occurring as boudins in the Mossel Gneiss. Collerson *et al.* (1983) derived ages of around 3000 Ma for D_1 and 2450 Ma for D_2, using Rb-Sr and Sm-Nd systems, but recent ion-probe dating of zircons (Black *et al.*, 1990) has indicated a D_1 age of 2530 Ma, and a D_2 age of 2490 Ma. Most rocks show no isotopic evidence of a long crustal history before

metamorphism (Sheraton & Collerson, 1984; Black *et al.*, 1990); however, some zircons do preserve components with ages up to 2800 Ma (Black *et al.*, 1990).

The post-D_2 structural history of the Vestfold Hills is dominated by the formation of east-west trending planar shear zones, ubiquitous pseudotachylite veins, and the emplacement of at least three generations of tholeiitic dyke at around 2400 Ma, 1800 Ma and 1400 Ma (Collerson & Sheraton, 1986*b*). The temporal relationships between these features are complex (Passchier *et al.*, 1990). Liquidus studies of the dyke swarms (Kuehner & Green, 1991) have indicated a history of near-isobaric cooling, at least until after the emplacement of a group of high-magnesium dykes at 2400 Ma, at a pressure of 7.5 kbar. However, experimental duplication of phenocryst phases in a 1380 Ma tholeiitic swarm has suggested emplacement at less than 5.5 kbar (Kuehner & Green, 1991), indicating a phase of decompression in the Early to Mid Proterozoic. Tholeiites in the southwestern part of the Vestfold Hills exhibit a metamorphic overprint, which has been correlated with the development of the adjacent Proterozoic Complex at 1000 Ma (Sheraton & Collerson, 1983). A metamorphic event at this stage has also been inferred from ductile reactivation of pseudotachylite veins (Passchier *et al.*, 1990). Later events are indicated by Rb-Sr dating of micas which yield ages of around 500 Ma (Collerson & Sheraton, 1986*a*), and the emplacement of several varieties of alkaline dyke.

Table 2.2 Summary of geological features of the Vestfold Hills.

Event		Age
1	Formation of orthogneiss and paragneiss protoliths	2800-2530 Ma
2	D1 (flat-lying isoclines and foliation) at 900°C, 7-10 kbar	2530 Ma
3	D2 (isoclinal folds) and intrusion of Crooked Lake Gneiss at 800°C, 6-8 kbar	2490 Ma
4	Near-isobaric cooling	-
5	Intrusion of high-Mg tholeiites	2400 Ma
6	Intrusion of tholeiite dykes	1800 Ma
7	Mylonite zones (D3?), uplift?	-
8	Intrusion of tholeiite dykes	1380 Ma
9	Localized metamorphic overprint and shearing (D3?)	1000 Ma
10	Mylonite formation (D3?) under greenschist conditions	500 Ma
11	Emplacement of alkaline dykes	Phanerozoic

2.3.4 The southern Prince Charles Mountains

Geological relationships in the southern Prince Charles Mountains are more complex than those discussed above, because both Archaean and Proterozoic rocks crop out together. The oldest rocks recognized in the southern Prince Charles Mountains form a massive, amphibolite-facies, granitic basement. The basement gneiss was mostly derived by partial melting of pre-existing felsic crustal rocks (Sheraton & Black,

1983; Sheraton *et al.*, 1985), and has been dated at 2800 Ma (Arriens, 1975; Tingey, 1982) using whole-rock Rb-Sr techniques.

The basement is unconformably overlain by younger metasediments of lower-amphibolite to greenschist grade. The age of the metasediments is not well established and Tingey (1982) has divided them into three series. The two older series pre-date tholeiite dyke emplacement: a white to green fuchsite-bearing quartzite series is ascribed an Archaean age on the basis of a single cross-cutting metamorphosed pegmatite with a Rb-Sr muscovite age of 2580 Ma, and a quartzite-absent series is assumed to be either of Proterozoic age or a quartzite-free facies of the Archaean sediments. Both series are intruded by pegmatites and granites which are assumed, from sparse geochronological data, to have been emplaced between 2000 and 1700 Ma. All the above units are cut by metamorphosed tholeiitic dykes, with an age constrained to lie between 2000-1700 Ma and 1000 Ma (the age of metamorphism in the northern Prince Charles Mountains where there are no undeformed tholeiite dykes). The third metasedimentary series is predominantly composed of greenschist-facies calcareous units, which are not dissected by tholeiite dykes and hence ascribed a Proterozoic age. Other workers have considered all metasediment to be of Proterozoic age (Grew, 1982*a*, *b*) on the basis of a pegmatite in the basement that appears to pre-date the quartzite and has been dated at 1000 Ma.

Ascribing metasedimentary phase assemblages to a given event is difficult since, despite the complex temporal relationships, the metamorphic grade is similar throughout the southern Prince Charles Mountains (lower amphibolite to greenschist). Tingey (1982) correlated rare, sillimanite-bearing assemblages in the pre-dyke metasediment with the poorly-defined 2000 to 1700 Ma intrusive event, but considered most assemblages in these units (e.g. kyanite-staurolite assemblages in metapelites) to be retrograde and to have developed during the 1000 Ma or 500 Ma events. Tingey (1982) correlated assemblages in the post-dyke metasediments with prograde metamorphism during the 1000 Ma event. Other workers (e.g. Grew, 1982*a*,*b*) have suggested that the majority of metasedimentary assemblages reflect the 500 Ma event. The structural history of the area is complex, and has yet to be integrated with the other geological relationships. The youngest events identified in the southern Prince Charles Mountains are the emplacement of granitic intrusions at around 500 Ma, with an associated resetting of Rb-Sr systems in biotite, and the subsequent intrusion of Phanerozoic alkaline dykes (Sheraton, 1983).

Table 2.3 Summary of geological features of the southern Prince Charles Mountains.

This history is not well established, and the table indicates the different age relationships inferred for the deposition and metamorphism of the metasediments by Tingey (1982) and Grew (1982*a*,*b*).

Event		Age
1	Orthogneiss and paragneiss protolith formation	?
2	Amphibolite metamorphism and granite emplacement	2800 Ma
3	? Deposition of older pelitic, psammitic and ferruginous sediments (Tingey)	-
4	? Pegmatite intrusion (Tingey)	2580 Ma
5	? Amphibolite metamorphism and granite emplacement (Tingey)	2000-1700 Ma
6	Intrusion of tholeiite dykes	-
7	? Deposition of younger calcareous and pelitic sediments (Tingey)	-
8	? Greenschist metamorphism (Tingey)	1000 Ma
9	? Pegmatite intrusion (Grew)	1000 Ma
10	? Deposition of all calcareous and pelitic sediments (Grew)	-
11	Emplacement of granite intrusions and greenschist metamorphism	500 Ma
12	Intrusion of alkaline dykes	Phanerozoic

2.3.5 The Rayner Complex

The Rayner Complex was originally distinguished from the adjacent Napier Complex on account of its lower grade (granulite to upper-amphibolite facies) and an absence of undeformed tholeiitic dykes (Ravich & Kamenev, 1975; Sheraton *et al*, 1980, 1987). The Napier-Rayner boundary is not exposed in Enderby Land, but is fairly sharp and possibly faulted, whereas there is a more gradual transition in western Kemp Land. Hydrous minerals (biotite and amphibole) are much more common than in the Napier Complex, and gneiss of the Rayner Complex is considerably more migmatitic. The localized occurrence of reworked Napier Complex material within the Rayner Complex is indicated by lithological similarities (Sheraton & Black, 1983), deformed mafic dykes correlated with the undeformed dykes in the Napier Complex (Sheraton *et al.*, 1980), and geochronological evidence (Black *et al.*, 1987).

The Rayner Complex is composed mainly of layered orthopyroxene-biotite-quartz-feldspar and garnet-biotite-quartz-feldspar orthogneiss. In contrast with the Napier Complex, mesoperthite is absent except as rare relict grains. Orthopyroxene-clinopyroxene-plagioclase mafic granulite and ultramafic units are widespread, and metasediments are more common than in the Napier Complex. Metapelitic assemblages include garnet-sillimanite-biotite-quartz-feldspar and garnet-cordierite-biotite-quartz-feldspar, but higher-grade assemblages considered to be Napier relics are locally preserved (e.g. Forefinger Point; Harley *et al.*, 1990). Calc-silicate units, typically diopside-plagioclase-quartz ± scapolite ± grossularite gneiss, are not common, but are much more so than in the Napier Complex. Isotopic data (Black *et al.*, 1987) indicate that reworked Archaean material occurs locally, particularly in the

Table 2.4 Summary of geological features of the Rayner Complex.

Event		Age
1	Formation and evolution of Archaean protoliths (as for the Napier Complex?)	up to 2000 Ma
2	Formation of additional continental material	2000-1800 Ma
3	Intrusion of tholeiite dykes (as for the Napier Complex?)	-
4	Further granitic crustal additions	1200-1000 Ma
5	Deposition of sediments	-
6	D1 (flat-lying mesoscopic folds) in the range 700-850°C, 5-10 kbar	1000 Ma
7	D2 (large upright folds) under continued granulite conditions	1000 Ma
8	Near-isothermal decompression	-
9	Pegmatite intrusion	770 Ma
10	D3 (shear zones and mylonites) under greenschist conditions	500 Ma

transition zone with the Napier Complex in western Kemp Land, but that most of the Complex is composed of crustal material formed at 2000 to 1800 Ma, with a relatively minor period of crustal growth at 1200 to 1000 Ma. The paragneiss precursor was deposited only shortly before the main metamorphism (*c.* 1000 Ma; see below).

The high-grade development of the Rayner Complex was associated with localized emplacement of syn-metamorphic, orthopyroxene-bearing granitic intrusions, and two deformational events (Grew, 1978; Sheraton *et al.*, 1980, 1987). The first deformation (D_1) produced mesoscopic, isoclinal and intrafolial folds with an associated axial-planar foliation. The second (D_2) produced large-scale, open to tight, upright folding about east-plunging axes, and weak axial-planar fabrics. D_2 is considered contemporaneous with the main upper-amphibolite to lower-granulite metamorphism. Estimates of the conditions of this metamorphism range between 700 and 850°C and 5 to 8 kbar (Grew, 1981; Ellis, 1983; Black *et al.*, 1987), although higher-pressure assemblages (up to 10 kbar) are preserved within the transition zone in western Kemp Land (Ellis, 1983). The age of this event was estimated at 1000 Ma by Grew (1978), using Rb-Sr dating of a syn-tectonic charnockitic gneiss. This age was confirmed by more rigorous Rb-Sr, Sm-Nd and U-Pb zircon dating of specimens collected from various Rayner localities (Black *et al.*, 1987).

The post-D_2 evolution of the Rayner Complex was characterized by cordierite-orthopyroxene symplectite around metapelitic garnet (Ellis, 1983) and orthopyroxene-plagioclase symplectite around metabasic garnet (Ellis, 1983; Sheraton *et al.*, 1987), indicating near-isothermal decompression to about 3 kbar at temperatures of 600°C (Ellis, 1983; Black *et al.*, 1987). Cross-cutting granitic veins and pegmatites have been dated at 770 Ma by Black *et al.* (1987) and at 500 Ma by Grew (1978). It is not clear whether the younger ages are reset, or indicate a second phase of granite

emplacement. A metamorphic overprint at 500 Ma is indicated by K-Ar and Rb-Sr biotite ages and lead loss from zircon and monazite in pegmatite and older gneissic units (Pieters & Wyborn, 1977; Grew, 1978; Black *et al.*, 1987). Late, upright shear zones and mylonite, commonly associated with localized greenschist retrogression (Grew, 1978; Black *et al.*, 1987), generally post-date the pegmatite and are thought to relate to the 500 Ma overprint.

2.3.6 The Stillwell Hills

The Stillwell Hills area on the eastern Kemp Land coast is dominated by orthopyroxene-clinopyroxene-plagioclase and orthopyroxene-quartz-feldspar gneisses, with subordinate layered paragneiss (Clarke, 1987). A whole-rock Rb-Sr age of 2700 Ma for an orthopyroxene-rich felsic gneiss indicates an Archaean origin for at least part of the area, but there is also Rb-Sr whole-rock evidence for a later metamorphic event, the age of which is poorly constrained (Clarke, 1987) but correlated with the 1000 Ma event. James *et al.* (1991) have identified deformed mafic dykes on Fold Island, and attribute early structures in the gneissic lithologies to Archaean events. The principal structural features of the Stillwell Hills correspond closely to those discussed below for the Mawson Coast (Clarke, 1988), with recumbent structures produced by an early deformation (D_1) locally overprinted by two stages of upright deformation (D_2 and D_3). These fabrics are cross-cut by massive biotite-garnet-quartz-feldspar pegmatites, one of which yielded a Rb-Sr biotite age of 700 Ma (Clarke, 1987). The pegmatites are deformed (D_4) by retrograde shear zones, mylonite and pseudotachylite.

2.3.7 The Mawson Coast

Granulite-facies paragneiss and charnockite intrusions crop out around Mawson Station on the coast of Mac.Robertson Land and east Kemp Land. The paragneiss comprises interlayered garnet-biotite felsic gneiss, calc-silicate, quartz-feldspar-magnetite gneiss and migmatitic garnet-sillimanite-cordierite metapelite (Trail, 1970). Early high-grade gneissic layering was folded into westward-verging recumbent isoclines during a deformation (D_1) that was also associated with an axial-planar foliation and an intense east-west trending mineral lineation (Clarke, 1988). In places the F_1 fold axes are curved and may be parallel to the lineation, which is consistent with rotation of the fold axes during progressive shear (Clarke, 1988). These flat-lying structures are locally overprinted by east-west trending, open to isoclinal folds (F_2), with moderate to steeply-dipping axial planes and a weak axial-planar fabric.

Most outcrops around Mawson consist of orthopyroxene-quartz-feldspar ± clinopyroxene ± garnet charnockite: the Mawson Charnockite. Intrusive field relationships

Table 2.5 Summary of geological features of the Mawson Coast and the Stillwell Hills.

Event		Age
1	Formation and evolution of Archaean protoliths (Stillwell Hills)	?
2	Formation of additional continental material and sediment deposition	2000-1600 Ma
3	D1 (recumbent isoclines) under low-pressure granulite conditions	*c.* 1000 Ma
4	D2 (open to isoclinal folds) under continued low-P granulite conditions	*c.* 1000 Ma
5	Emplacement of high-Ti charnockites at 6-7 kbar	985 Ma
6	Emplacement of low-Ti charnockites at 6-7 kbar	954 Ma
7	D3 (upright folds)	921 Ma
8	Near-isobaric cooling	-
9	Pegmatite intrusion (Stillwell Hills)	700 Ma
10	D4 (shear zones, pseudotachylite & mylonites) under amphibolite conditions	500 Ma

such as xenoliths of paragneiss material are preserved by this composite batholith (Crohn, 1959; Trail, 1970). Various suites are recognized and grouped into low-titanium and high-titanium categories (Young & Ellis, 1990, 1991), which are depleted and enriched in heavy rare-earth elements respectively. The charnockite was first dated by Sheraton (1982) at around 1000 Ma, an age confirmed by Black *et al.* (1987) using Rb-Sr and U-Pb systems. A recent ion-probe U-Pb study of zircons (Young & Black, 1991) yielded igneous ages of 985 Ma and 954 Ma for the high-titanium and low-titanium charnockite respectively. Charnockite intrusion post-dated early structures (F_1 and F_2) preserved in the paragneiss, but produced only very local contact effects, indicating that intrusion was synchronous with, or just post-dated, granulite-facies metamorphism. Clarke *et al.* (1989) used corona textures around spinel and ilmenite in metapelite to infer a period of near-isobaric cooling after the metamorphic peak. Phenocrysts within the charnockite of exsolved pyroxene, and antiperthite with strongly ternary bulk compositions, indicate temperatures of 950 to 1100°C, and garnet-orthopyroxene-plagioclase-quartz barometry indicates emplacement pressures of 5.5 to 7 kbar (Young & Ellis, 1991).

A third deformation (D_3) affected both the charnockite and the paragneiss (Clarke, 1988). Open to isoclinal upright folds are associated with a steep, east-dipping, axial-planar foliation, and a stretching lineation plunging steeply down dip. Feldspar megacrysts and paragneiss xenoliths within the charnockite are aligned parallel to D_3 fabrics. Zircons in a gneissic xenolith gave a U-Pb age of 921 Ma for mineral rims (Young & Black, 1991), which are correlated with D_3, whereas zircon cores in this specimen yielded ages between 2000 and 1600 Ma, implying that the paragneiss had a Proterozoic protolith. Rare shear zones, and more common mylonite and pseudotachylite, dissect all the lithologies and fabrics discussed above. These upright structures are mainly east-west trending, and the shear zones are commonly

associated with a local amphibolite-facies overprint. Clarke (1988) has correlated this deformation (D_4) with the widespread 500 Ma event.

2.3.8 The northern Prince Charles Mountains

Most work in the northern Prince Charles Mountains has been limited to reconnaissance mapping and specimen collection, and preliminary geochronology. The northern Prince Charles Mountains comprise orthogneiss and paragneiss units intruded by charnockite bodies and dolerite dykes, minor basalts and pegmatites (Crohn, 1959; McLeod, 1964; Tingey, 1972, 1982), with a fault-bounded outlier of Permo-Triassic sedimentary rocks in the Beaver Lake area. The basement gneiss decreases in grade from lower granulite in the north to upper amphibolite in the south, and is considered continuous with lower-grade amphibolite to greenschist metasediment in the southern Prince Charles Mountains. The stability of garnet-sillimanite-cordierite in metapelite, and the lack of garnet in metabasite, has been used to infer moderate metamorphic pressures for the northern Prince Charles Mountains, whereas lower-temperature metamorphism at relatively-higher pressures is indicated in the southern Prince Charles Mountains by assemblages involving kyanite, staurolite and garnet (Tingey, 1982). All these assemblages are ascribed to a Proterozoic (*c.* 1000 Ma) event on account of whole-rock Rb-Sr isochron dates which cluster around 1100 to 800 Ma (Arriens, 1975; Tingey, 1982). Initial $^{87}Sr/^{86}Sr$ ratios in the range 0.705 to 1.113 have been interpreted as evidence for both relatively juvenile crust and older material (Tingey, 1982). Charnockite and other syn-metamorphic granitic bodies have also been attributed to the 1000 Ma event.

Rb-Sr ages for biotite from the northern Prince Charles Mountains cluster around 500 Ma (Arriens, 1975; Tingey, 1982), and have been attributed to resetting of the 1000 Ma assemblages by a later event. Subsequent geological evolution is recorded by Upper Permian and Lower Triassic sedimentary rocks exposed around Beaver Lake (Crohn, 1959; Mond, 1972; Bennett & Taylor, 1972), and by basic intrusive and extrusive rocks. A selection of unmetamorphosed mafic dykes and lava flows from the northern Prince Charles Mountains were studied by Sheraton (1983), and found to range from Cambrian to Eocene in age and to be compositionally heterogeneous although generally of alkaline affinity.

The first detailed study of the area was that of McKelvey and Stephenson (1990), who described the geology and structure of the metamorphic basement and Permo-Triassic sediments in the Radok Lake area, just south of Beaver Lake. McKelvey and Stephenson (1990) identified two high-grade lithological associations; one consisting of homogeneous felsic gneiss, and the other of various layered gneisses. These rocks preserve a layer-parallel foliation (S_2), which has largely transposed earlier isoclinal

folds (F_2) and is folded into mesoscopic upright folds (F_3). The geology of this area is considered in more detail in Chapter 8, where it is integrated with the results of this study.

Table 2.6 Summary of geological features of the northern Prince Charles Mountains.

Event		Age
1	Formation of orthogneiss and paragneiss protoliths	?
2	Deformation, granulite metamorphism and charnockite emplacement	1000 Ma
3	Deformational and metamorphic overprint	500 Ma
4	Intrusion of alkaline dykes	Palaeozoic
5	Deposition of continental sandstones, shales and coal measures	Permian
6	Further alkaline igneous activity	up to Eocene

2.3.9 The Ingrid Christensen Coast

Outcrops on the Ingrid Christensen Coast of southeast Prydz Bay are distinguished from Archaean gneiss in the Vestfold Hills by the absence of undeformed tholeiite dykes (Tingey, 1981; Sheraton & Collerson, 1983). Most studies have concentrated on the two most extensive areas of outcrop, the Rauer Group immediately south of the Vestfold Hills (Harley, 1987*a*, 1988; Tait & Harley, 1988; Harley & Fitzsimons, 1991), and the Larsemann Hills further southwest (Stüwe *et al.*, 1989; Stüwe & Powell, 1989*a*,*b*).

The Rauer Group is dominated by pyroxene-bearing felsic and mafic orthogneiss, with subordinate paragneiss sequences. Four broad lithological groups have been identified (Harley, 1987*a*; Harley & Fitzsimons, 1991):

(i) composite orthogneiss comprising rafts of mafic granulite enclosed in tonalitic gneiss;

(ii) relatively-homogeneous to weakly-banded felsic to intermediate orthogneiss with a strong fabric;

(iii) layered paragneiss comprising iron-rich metapelite and semi-pelite, quartzite, leucogneiss, impure calc-silicate and rare mafic granulite; and

(iv) felsic to intermediate orthogneiss preserving simple fabrics and relict igneous features.

The mafic lithologies are commonly garnet bearing, and assemblages are indicative of the granulite facies. All of these rocks preserve reclined isoclinal folds and steeply-plunging mineral and stretching lineations attributed to syn-metamorphic deformation (D_3). Syn-D_3 metamorphic conditions have been estimated at 7 to 9 kbar and 800 to 850°C (Harley, 1988; Harley & Fitzsimons, 1991). An age of 1073 Ma from a Rauer Group orthogneiss (Tingey, 1981) has been ascribed to this event. Recent zircon work (Kinny & Black, 1990) on a syn-metamorphic leucogneiss has also identified a

Table 2.7 Summary of geological features of the Ingrid Christensen Coast.

(R) and (L) refer to deformational events in the Rauer Group (Harley, 1987*a*) and Larsemann Hills (Stüwe *et al.*, 1989) respectively.

Event		Age
1	Formation of Archaean protoliths (Rauer Group & ?Bolingen Islands)	3300-2830 Ma
2	Deformation (D1(R) & D2(R)?) and metamorphism (1000°C, 10-12 kbar)	?
3	Near-isothermal decompression to 8 kbar	-
4	Further crustal additions	1800-1600 Ma
5	? Mafic dyke intrusion	-
6	Deposition of sediments (Larsemann Hills)	-
7	D3(R)-D1(L) (reclined folds and foliation) in the range 750-850°C, 5-9 kbar	1000 Ma
8	? Mafic dyke intrusion (Rauer Group) and near-isothermal decompression	-
9	D4(R)-D2(L)-D3(L) (folds and ductile shears)	-
10	Pegmatites (Rauer Group only)	770 Ma ?
11	D5(R) (mylonites) under greenschist conditions (Rauer Group only)	500 Ma
12	Granite emplacement (Larsemann Hills & Landing Bluff)	500 Ma
13	Alkaline dyke intrusion (Rauer Group only)	Phanerozoic

Proterozoic event with dates in the range 1070 to 1030 Ma.

Earlier structures (S_1 and F_2) are present in mafic granulite and metapelite in areas of low D_3 strain, but have not been observed in the composite orthogneiss, or the felsic to intermediate orthogneiss with simple D_3 fabrics (groups (i) and (iv) above). The latter are interpreted as pre- to syn-D_3 intrusions. Some of the lithologies preserving early structures have assemblages inconsistent with syn-D_3 metamorphic conditions. In particular, garnet-orthopyroxene-sillimanite assemblages, and retrograde sapphirine and cordierite, in magnesian metapelitic rafts indicate peak conditions of 10 to 12 kbar and 1000 to 1050°C, followed by decompression to 8 kbar at temperatures greater than 800°C (Harley & Fitzsimons, 1991). Harley and Fitzsimons (1991) suggest that these conditions reflect Archaean events. The existence of Archaean material in the Rauer Group was established by Sheraton *et al.* (1984), who derived model ages for specimens of Rauer Group orthogneiss, and found that although most gave Mid Proterozoic ages (1800 to 1600 Ma), two specimens yielded ages of around 3900 Ma. Kinny and Black (1990) obtained U-Pb zircon ages of 3300 Ma and 2830 Ma for Rauer Group orthogneiss, and suggested that up to 50 per cent of the Rauer Group is composed of Archaean material.

A post-D_3 history of near-isothermal decompression to 3-5 kbar at 700°C has been documented for several lithologies in the Rauer Group (Harley, 1987*a*, 1988; Harley & Fitzsimons, 1991). Mafic dykes truncate structures attributed to D_3 (although some dykes probably pre-date D_3), but were metamorphosed under granulite conditions and deformed by folds and ductile shears (D_4). It was previously

held that all the deformed dykes were equivalent to the undeformed dykes in the Vestfold Hills and that they were hence indicators of reworked Archaean material (Sheraton & Collerson, 1983), but the latter is not the case if some of the Rauer Group dykes post-date the Proterozoic metamorphic peak. Planar pegmatite bodies post-date D_4, and are cut by mylonite zones (D_5) which are commonly associated with a greenschist-facies overprint. D_5 is correlated with a 500 Ma overprint. Rare alkaline dykes post-date all the features discussed above.

Outcrops southwest of the Rauer Group are dominated by paragneiss (Sheraton & Collerson, 1983), although orthopyroxene-bearing orthogneiss is common in the Munro Kerr Mountains. Isotopic studies have failed to identify any Archaean material in the paragneiss (Sheraton *et al.*, 1984), and are consistent with derivation of the sedimentary precursor by erosion of a Mid Proterozoic (1800 to 1600 Ma) protolith. The paragneiss comprises iron-rich garnet-sillimanite-cordierite-spinel metapelite and less-aluminous garnet-biotite and garnet-orthopyroxene gneiss (Sheraton & Collerson, 1983). These assemblages are attributed to the 1000 Ma event identified in the Rauer Group, although the only geochronological data on the paragneiss are poorly-defined Mid to Late Proterozoic ages (Sheraton *et al.*, 1984).

Detailed structural and metamorphic histories have been presented for the Larsemann Hills by Stüwe *et al.* (1989) and Stüwe and Powell (1989*a*). A pervasive foliation (S_1) was developed during peak metamorphic conditions estimated at 4.5 kbar and 750°C, which were followed by near-isothermal decompression to 3 kbar. Subsequent cooling occurred during and after the development of asymmetrical, open to isoclinal folds (F_2). Large-scale folds (F_3) determined the regional structure of the area. In contrast to the Rauer Group, no pegmatite, mylonite or alkaline dykes were identified, but an undeformed granitic body has been correlated with a similar intrusion further west at Landing Bluff, which has been dated at around 500 Ma (Tingey, 1981; Sheraton & Black, 1988). Evidence of decompression is also preserved in the Bolingen Islands, immediately west of the Larsemann Hills. Thost *et al.* (1991) have inferred two-stage decompression from two generations of symplectite around garnet in mafic gneiss. The first stage involved decompression from 10 kbar and 980°C to 8 kbar and 850°C. Other lithologies in the paragneiss-dominated Bolingen Islands indicate conditions of 6 kbar and 775°C (Thost *et al.*, 1988), which are ascribed to the Proterozoic event. The extreme conditions preserved by the mafic gneiss are attributed, in the absence of geochronological data, to an earlier, possibly Archaean, event.

2.3.10 Conclusions

It is clear from the above discussion that this sector of the East Antarctic Shield has a complex geological history, but certain events can be identified in most areas (see Table 2.8). The three Archaean terrains have different histories, but are all characterized by post-metamorphic tholeiitic dyke swarms. They are separated by an extensive Proterozoic Complex metamorphosed at around 1000 Ma and characterized by a lack of undeformed tholeiite dykes. The boundaries between the Archaean cratons and the Proterozoic Complex are commonly diffuse, with localized reworking of Archaean material during the 1000 Ma event. However, this reworking is not as simple as it may appear; for example, Archaean relics in the Rauer Group are older than any material identified in the adjacent Vestfold Block. The grade of the 1000 Ma event decreases from granulite on the coast to greenschist in the southern Prince Charles Mountains, and structural and metamorphic histories for this event vary across the Complex. Both Archaean and Proterozoic rocks were locally affected by pegmatite intrusion at 770 Ma (and/or 500 Ma), mylonite development and granite emplacement at 500 Ma, and alkaline dyke intrusion at various stages through the Phanerozoic. Further evidence of the lithological, structural and metamorphic histories of part of the Ingrid Christensen Coast and the northern Prince Charles Mountains is presented in this thesis. The evolution of the East Antarctic Shield as a whole is considered in more detail in the final chapter, which integrates the results of this study with the work outlined above.

Table 2.8 Summary of principal geological events in the East Antarctic Shield between 50 and 80°E.

	Event	Age
1	Formation of Archaean orthogneiss and paragneiss protoliths	3900-2500 Ma
2	Deformation and metamorphism (commonly multiple events)	3000-2500 Ma
3	Stabilization of Archaean cratons	-
4	Further Proterozoic crustal additions and intrusion of tholeiitic dyke swarms into both Archaean and Proterozoic material	2000-1000 Ma
5	Deposition of sediments	-
6	Widespread deformation and metamorphism of Proterozoic crustal material and emplacement of charnockite, with localized reworking of the Archaean cratons, particularly at their edges	1000 Ma
7	Pegmatite intrusion	770 Ma
8	Granite emplacement and formation of mylonite and pseudotachylite under greenschist conditions	500 Ma
9	Intrusion of alkaline dykes	Palaeozoic
10	Deposition of continental sandstones, conglomerates, shales and coal measures	Permo-Triassic
11	Further alkaline igneous activity	up to Eocene

Part Two

Field and Petrographic Relationships

3. The geology and structure of the Brattstrand Bluffs Coastline

3.1 INTRODUCTION

The Proterozoic outcrops of Ingrid Christensen Coast have been the subject of regional reconnaissance studies (Sheraton & Collerson, 1983, Sheraton *et al.*, 1984), but detailed work has been restricted to the Rauer Group and the Larsemann Hills (see Section 2.3.9). This chapter describes the field and petrographic relationships of the 70 km of coastline between the Rauer Group and the Larsemann Hills (see Fig. 3.1), referred to here as the 'Brattstrand Bluffs coastline'. This coastline comprises some 15 km^2 of island and coastal outcrop, consisting of flat or gently-undulating surfaces with steep cliffs down to sea level and excellent exposure. The following outcrop areas were visited (see Fig. 3.2): Dalkoy Island, Steinnes Peninsula, Cowell Island, Amanda Bay, Hovde Island, Brattstrand Bluffs, Chaos Glacier and the Svenner Islands. Four Svenner Islands were visited and are referred to as, from southwest to northeast, Svenner 1, 2, 3, and 4. Geological and locality maps, and a list of collected specimens are given in Appendices 1 and 2. The geology and structure of Chaos Glacier are closely related to relationships in the Rauer Group described by Harley (1987*a*) and are not discussed in this chapter.

The outcrops comprise granulite-facies gneiss and migmatite with a polyphase metamorphic and deformational history, and subordinate intrusive lithologies. Section 3.2 is a description of the field and petrographic features of the gneissic lithologies, and Section 3.3 describes the intrusive lithologies which post-date the pervasive deformational events. Section 3.4 is a description of the regional, mesoscopic and microscopic structure. Section 3.5 outlines a relative time framework for geological relationships and events described in the previous sections.

3.2 GNEISSIC LITHOLOGIES

3.2.1 Introduction

Gneissic rocks of the Brattstrand Bluffs coastline occur in two broad lithological associations:

(i) a migmatitic orthogneiss association comprising interlayered mafic and felsic gneiss, and

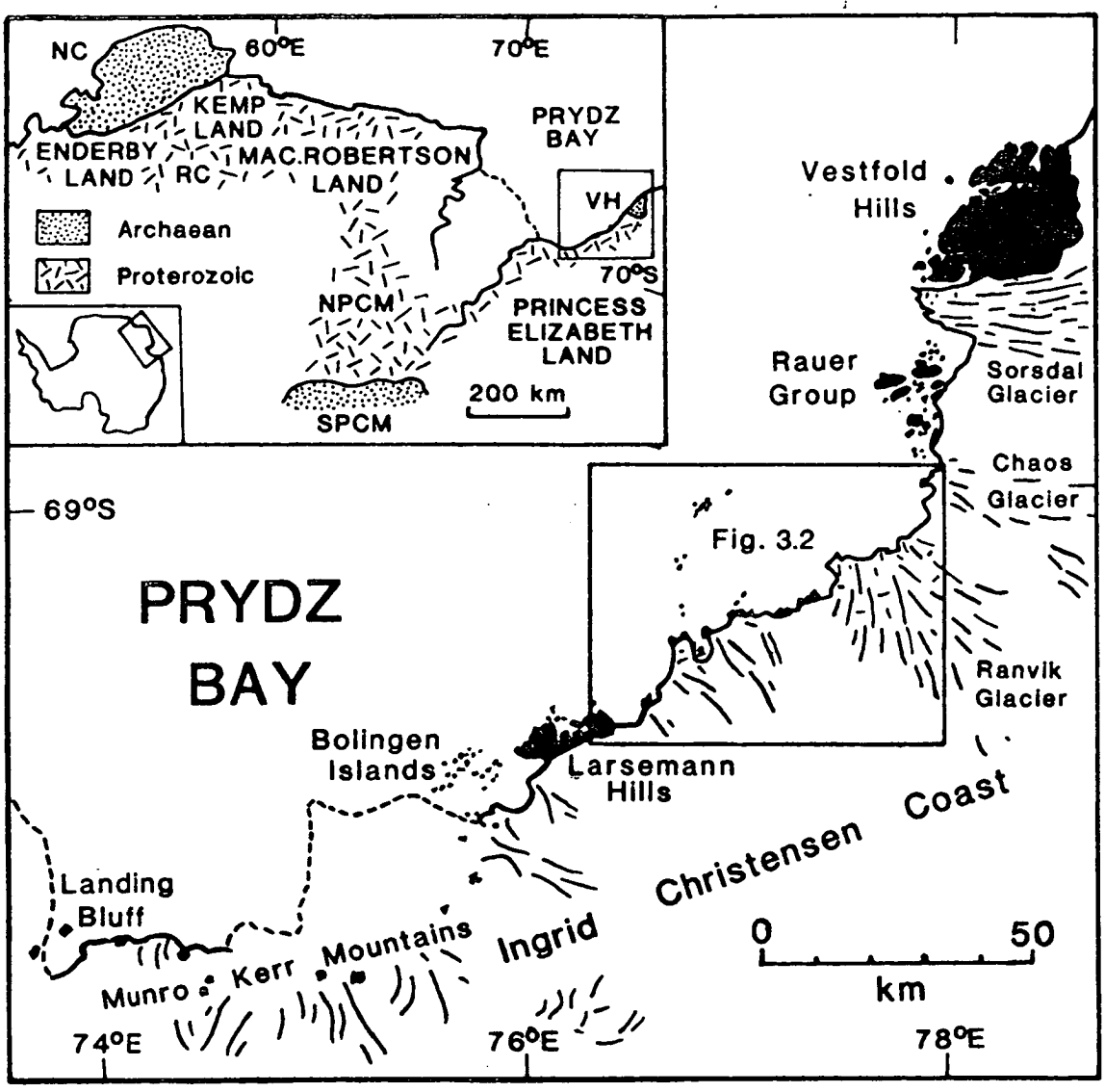

Fig. 3.1 A map of the southeast coast of Prydz Bay depicting the Archaean Vestfold Hills and the various Proterozoic outcrops further southwest. The inset shows the location of this area with respect to the Proterozoic Complex and Archaean cratons between 50° and 80°E, where NC is the Napier Complex, RC is the Rayner Complex, NPCM and SPCM are the northern and southern Prince Charles Mountains respectively, and VH are the Vestfold Hills.

(ii) a paragneiss association dominated by metapelitic migmatite and leucogneiss, interlayered with less-abundant semi-pelite, intermediate gneiss and ultramafic rock.

The spatial distribution of these two associations does not follow a simple pattern: the former crops out at the northern half of Hovde Island, and constitutes the majority of outcrop at Steinnes Peninsula; the latter occurs at Cowell Island, Svenners 2, 3 and 4, Brattstrand Bluffs, the southern half of Hovde Island and locally at Steinnes Peninsula. The contact between the two associations at Hovde Island is

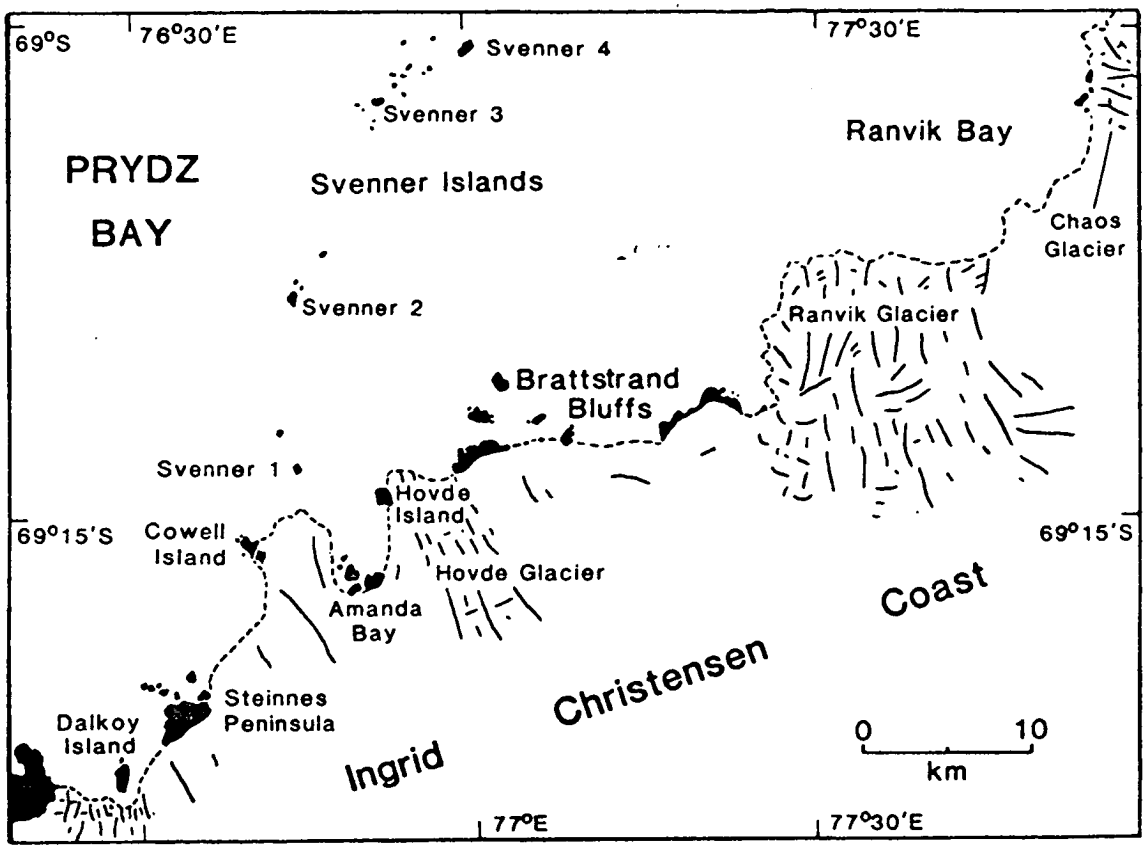

Fig. 3.2 A map of the outcrop between the Rauer Group and the Larsemann Hills, referred to here as the 'Brattstrand Bluffs coastline'.

concordant to the dominant foliation, with the paragneiss structurally below the orthogneiss. Paragneiss at Steinnes Peninsula is enclosed within, and has fabric-parallel contacts with, the orthogneiss. Svenner 1 has affinities with both associations. A summary of the lithological constitution of the two associations is given in Table 3.1. The principal gneissic lithologies that characterize these associations are described in Sections 3.2.2 to 3.2.9. Tables 3.2 to 3.6 summarize the mineralogical features of these lithologies. The metapelitic gneiss and migmatite are discussed in some detail since they exhibit complex textural relationships which are crucial to an understanding of the area. Less-rigorous descriptions are given of the other lithologies.

3.2.2 Composite orthogneiss

Migmatitic composite orthogneiss comprises layers, schollen and schlieren of dark, massive to banded, mafic granulite enclosed within or interleaved with pale-brown to yellow felsic orthogneiss (see Plate 3.1a). The mafic bodies vary in size from 50 mm across to more than 10 m, and their internal structures are commonly disrupted by felsic material. The proportion of mafic to felsic material is variable, but the mafic

Table 3.1. The lithological constitution of the Brattstrand Bluffs coastline.

Association	Lithology		Relative abundance
Orthogneiss	Composite orthogneiss	(1) mafic granulite	8%
		(2) felsic granulite	17%
		(3) coarse leucocratic veins	Less than 1%
Paragneiss	Metapelitic gneiss and migmatite		25%
	Semi-pelitic gneiss	(1) garnet-biotite	5%
		(2) garnet-orthopyroxene	2%
	Intermediate orthopyroxene gneiss		2%
	Ultramafic gneiss		Less than 1%
	Leucogneiss		10%
	Granitic orthogneiss		Less than 1%
Late intrusions	Granitic intrusive bodies (Amanda Bay granite etc.)		25%
	Pegmatites		Less than 1%
	Dalkoy Granite		2%

Relative abundances are approximate only.

component rarely exceeds 50 per cent of the total volume. Dense, purple-grey lenses of ilmenite up to 0.1 m wide occur locally within the felsic material.

The mafic bodies are hornblende-orthopyroxene-clinopyroxene-plagioclase-ilmenite granulite (see Table 3.2). Grain sizes are between 1 and 2 mm and textures are polygonal, but a banding and lineation are defined by modal variation of plagioclase and ferromagnesian minerals and a preferred orientation of individual hornblende grains (S_1 and L_1; see Section 3.4.2). Orthopyroxene is commonly poikiloblastic, and in some specimens plagioclase grains have normally-zoned rims. Biotite occurs around pyroxene as randomly-oriented laths or as less-common symplectitic intergrowths with plagioclase. Migmatitic textures are developed within the mafic granulite bodies. Coarse-grained plagioclase-orthopyroxene ± quartz leucosomes occur within mafic granulite as veins, typically between 2 and 20 mm wide, and ovoid or irregular patches up to 50 mm across (see Plate 3.1b). The leucosomes commonly contain orthopyroxene megacrysts of similar diameter to the width of the leucosomes themselves. Dark, narrow, mafic-rich melanosome is developed at the edges of the larger leucosomes. The leucosomes are commonly oriented parallel to the modal banding, but may cut across it at a considerable angle.

The mafic bodies are hosted within equigranular quartz-plagioclase-K-feldspar-orthopyroxene-biotite-ilmenite felsic gneiss (see Table 3.2). Apatite and zircon are common accessory phases. Grain sizes are between 1 and 3 mm, and a foliation and lineation are defined by quartz ribbons, biotite, and the orientation of single grains and elongate chains or clusters of pyroxene (S_3 and L_4, or locally S_4; see Sections 3.4.4 and 3.4.5). These fabrics are approximately parallel to the lithological layering

PLATE 3.1

Plate 3.1a

Composite orthogneiss at Steinnes Peninsula comprising interlayered mafic (M) and felsic (F) gneisses and a coarse-grained leucocratic layer (L). The leucocratic layer is slightly discordant to the S_3 lithological layering of mafic and felsic gneisses. The hammer is 0.3 m long.

Plate 3.1b

An orthopyroxene-bearing leucocratic vein in mafic granulite at Steinnes Peninsula. The vein is highly discordant to a weak S_1 foliation in the mafic granulite, which trends from the top to the bottom of the photograph. Pencil for scale.

Plate 3.1c

A raft of mafic granulite (M) within composite orthogneiss at Steinnes Peninsula. The raft preserves an S_1 foliation which is truncated by the S_3 foliation of the enclosing felsic gneiss (F). The lens cap is 50 mm in diameter.

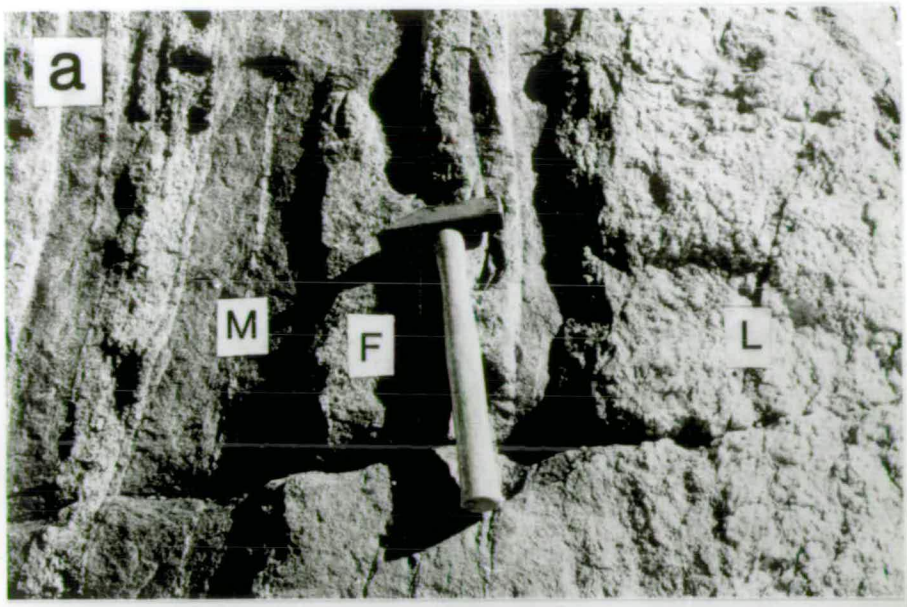
a
M
F
L

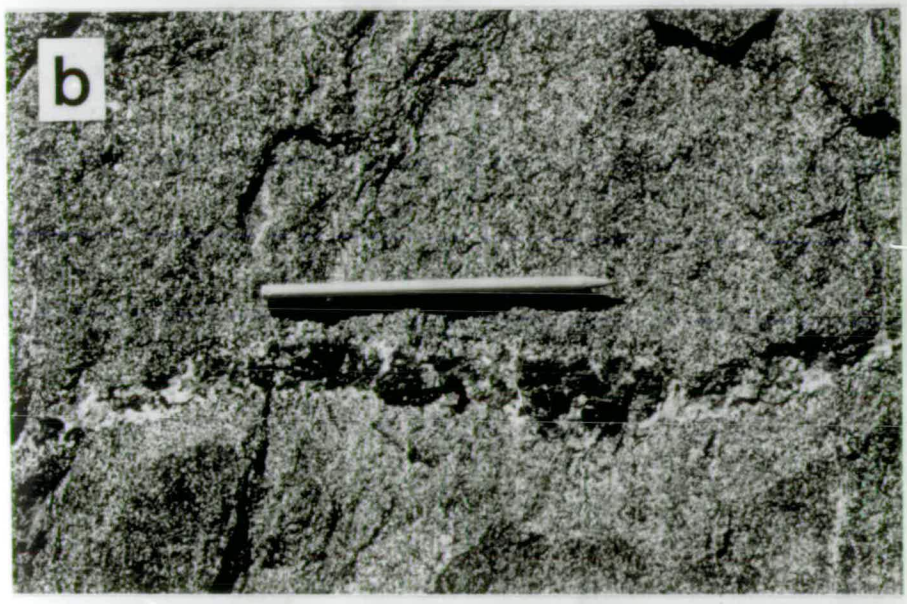
b

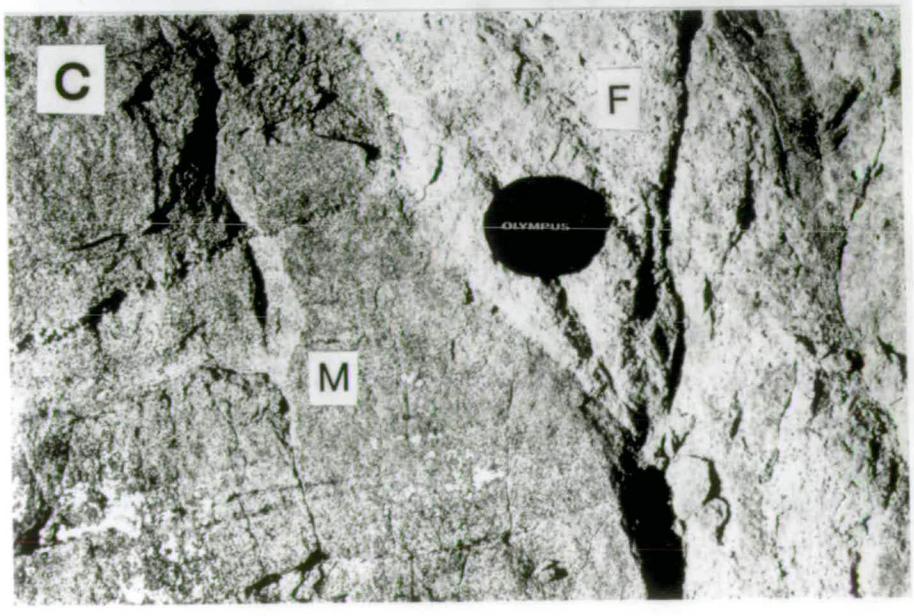
c
F
OLYMPUS
M

Table 3.2 Composite orthogneiss assemblages.

Mafic granulite assemblages (and modal abundance in per cent):	
Prograde phases	Hbl(20-30%)-Opx(10-20%)-Cpx(10-20%)-Pl(40-60%)
Retrograde phases	Bt, Bt-Pl symplectites
Accessory phases	Ilm
Felsic granulite (and modal abundance in per cent):	
Prograde phases	Qtz(20-40%)-Pl(30-45%)-Kfs(5-10%)-Opx(0-10%)-Bt(0-10%)
Retrograde phases	Bt
Accessory phases	Ilm-Ap-Zm
Leucocratic veins (and modal abundance in per cent):	
Prograde phases	Qtz(25-40%)-Pl(35-55%)-Kfs(10-20%)

of mafic and felsic gneiss, but truncate the internal tectonic fabrics and migmatitic textures of the mafic bodies (see Plate 3.1c). Microtextures are much more irregular than those of the mafic granulite. Quartz grains have lobate boundaries and plagioclase is antiperthitic. K-feldspar is only a minor phase and is microperthitic. Randomly-oriented laths of biotite are common around pyroxene grains.

Garnet is notably absent from both mafic and felsic gneiss, although it does occur locally with biotite as a selvage between the two. Elsewhere, mafic and felsic components are in direct contact. Hornblende contents in the mafic units decrease markedly towards these contacts, and an increase in grain size across the contact into felsic units is common. A third, leucocratic, component accounts for less than 10 per cent of the total volume, and consists of coarse quartz, antiperthitic plagioclase and microperthite grains up to 20 mm across. It occurs as layers and veins up to 0.3 m wide which are slightly discordant to the other components (see Plate 3.1a).

3.2.3 Metapelitic gneiss and migmatite

The paragneiss sequences are dominated by metapelite, comprising various combinations of garnet, sillimanite, cordierite, spinel, biotite, quartz, K-feldspar, and minor plagioclase and ilmenite (see Table 3.3). Accessory phases include apatite, zircon and graphite. The metapelite varies from banded gneiss, with a millimetre-scale compositional banding (S_3 or locally S_4; see Sections 3.4.4 and 3.4.5) defined by quartzofeldspathic layers and aluminous layers rich in spinel and sillimanite, to complex migmatite. The migmatite consists of variable proportions of three components (see Table 3.3):

(i) mesosome which resembles the banded gneiss and comprises quartzofeldspathic phases intimately associated with aluminous phases (i.e. quartz-present metapelitic assemblages);

(ii) melanosome which is devoid of quartz and consists predominantly of sillimanite, spinel and coarse garnet (i.e. quartz-absent metapelitic assemblages); and

Table 3.3 Metapelitic gneiss and migmatite assemblages.

Banded gneiss or mesosome assemblage (modal abundance in per cent): Grt(15-40%)-Sil(10-25%)-Crd(2-10%)-Spl(2-10%)-Bt(0-15%)-Qtz(15-25%)-Kfs(5-20%)-Pl(0-5%)
Melanosome assemblage (modal abundance in per cent): Grt(30-50%)-Sil(15-30%)-Crd(5-15%)-Spl(5-15%)-Bt(10-20%)
Leucosome assemblage (modal abundance in per cent): Qtz(20-40%)-Kfs(35-60%)-Pl(5-25%)-Grt(1-8%)-Crd(1-3%)
Accessory phases: Ilm-Ap-Zrn

(iii) leucosome which consists predominantly of coarse quartz, K-feldspar and plagioclase, with fine-grained garnet and, less commonly, cordierite.

There is a continuous textural variation between banded gneiss, stromatic migmatite comprising intimately-interlayered mesosome and leucosome, and leucosome-dominated units enclosing isolated schollen of mesosome and stromatic migmatite, or schlieren of aluminous melanosome (see Plates 3.2 and 3.3). This variation reflects an increasing segregation of mesosome into melanosome and leucosome components.

The metapelite has a complex array of microtextural features, which are discussed in three stages corresponding to the three migmatite components identified above. The microtextural evolution of these components is summarized in Table 3.4.

(i) The compositional layering observed in hand specimens of banded gneiss and stromatic migmatite (see Plates 3.2 and 3.3) is associated with a foliation defined by coarse, prismatic sillimanite, which is commonly intergrown with ilmenite (S_3; see Section 3.4.4). The sillimanite foliation anastomoses between lenses of quartz and microperthite, and wraps around irregular garnet porphyroblasts crowded with inclusions of acicular sillimanite and rounded quartz, K-feldspar and biotite (type-1 garnet; see Plate 3.4a). Sillimanite and biotite inclusions are generally oriented parallel to the external foliation, but sillimanite needles rarely trace out helicitic folds (F_3; see Section 3.4.4). Biotite does not occur in the external foliation. A second textural form of garnet (type 2), either sub-idioblastic or intergrown with quartz (see Plate 3.4b), does not contain acicular sillimanite, although it does rarely overgrow prismatic sillimanite, and never contains biotite. It occurs both within the sillimanite fabric and in the quartzofeldspathic areas. Some garnet grains are composite in nature, comprising inclusion-free domains and domains with biotite and sillimanite inclusions, but there is generally no consistent spatial relationship between the two. Sub-idioblastic cordierite commonly occurs in association with the inclusion-free garnet (see Plate 3.4c).

Xenoblastic green spinel locally overgrows the coarse sillimanite foliation, and occurs in a number of textural settings depending on the local assemblage. In

PLATE 3.2

Plate 3.2a

Schollen-type metapelitic migmatite at Brattstrand Bluffs. The raft of metapelitic mesosome preserves an S_3 foliation, and is enclosed within garnet-bearing leucosome. The lens cap is 50 mm in diameter.

Plate 3.2b

Schollen-type metapelitic migmatite at Brattstrand Bluffs. The S_3 foliation of the pelitic raft is internally disrupted, and truncated by the massive leucosome. The lens cap is 50 mm in diameter.

Plate 3.2c

Schlieren-type metapelitic migmatite at Brattstrand Bluffs. Clots of garnet-sillimanite-spinel melanosome are enclosed within massive leucosome. Pencil for scale.

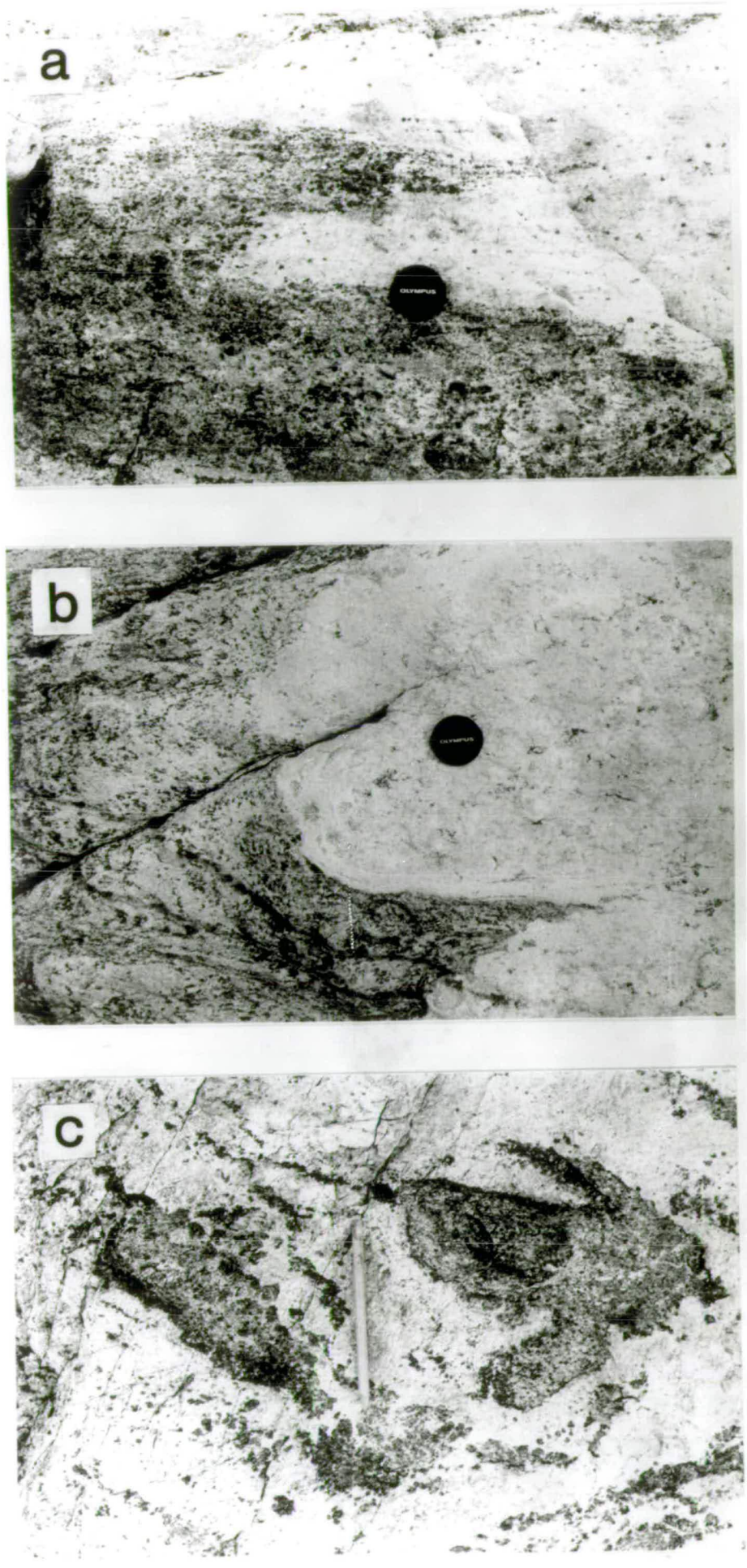
a
b
c

PLATE 3.3

Plate 3.3a

Schlieren-type metapelitic migmatite at Brattstrand Bluffs. Both the schlieren of aluminous melanosome and the garnet-bearing leucosome preserve a penetrative S_4 foliation. The lens cap is 50 mm in diameter.

Plate 3.3b

Metapelitic migmatite from Brattstrand Bluffs. Well-layered metapelitic mesosome, preserving an S_3 foliation, is cross-cut by a discordant vein leucosome. The lens cap is 50 mm in diameter.

Plate 3.3c

Interlayered metapelite and leucogneiss sheets at Brattstrand Bluffs, looking south. At the top of the photograph, the gneisses preserve an S_3 lithological layering folded by sinistral F_4 folds. At the bottom, structure is dominated by attenuated S_4 shear fabrics. The horizontal field of view is about 15 m. The leucocratic material accounts for about 25 per cent of the outcrop.

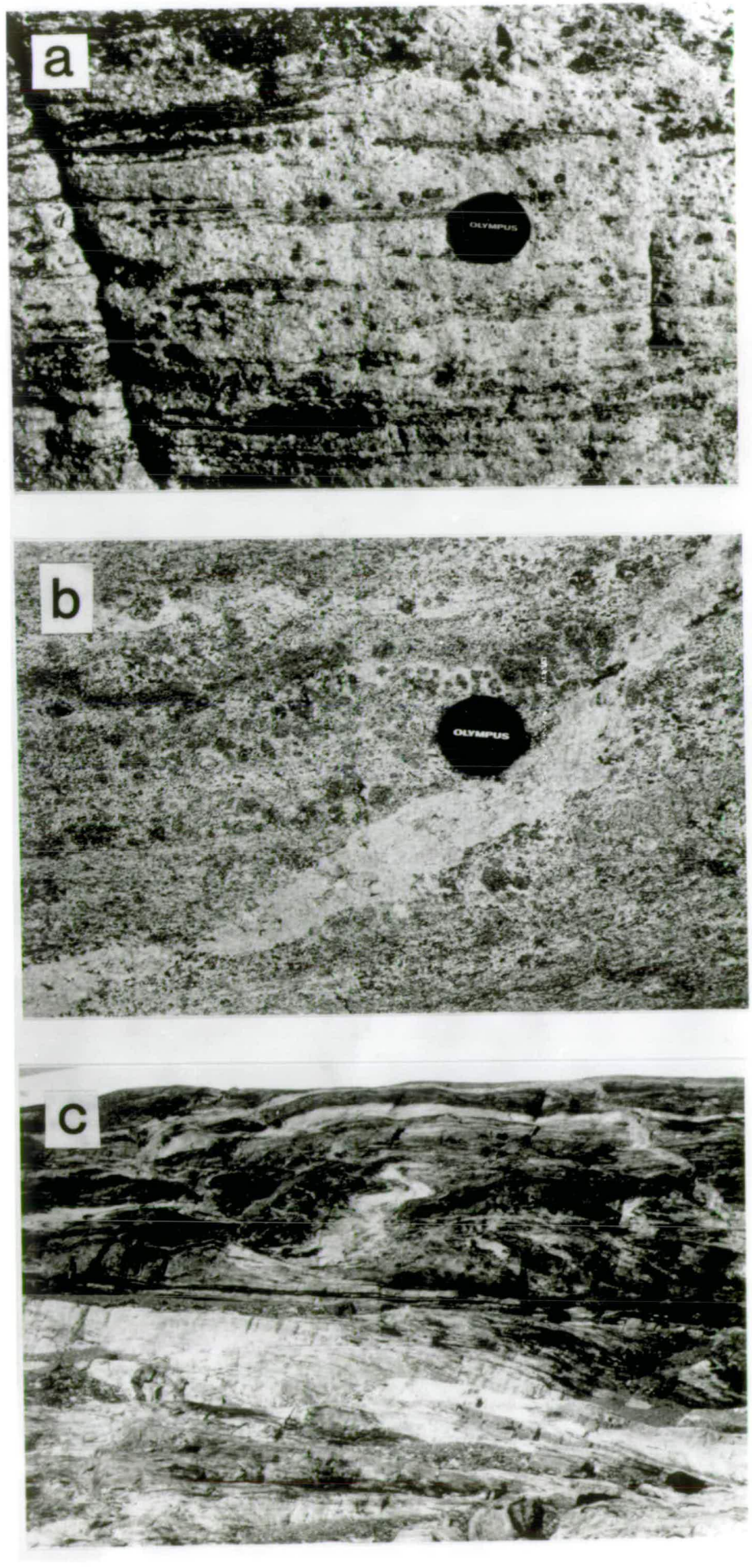
a
OLYMPUS
b
OLYMPUS
c

PLATE 3.4

Plate 3.4a

Type-1 garnet in a metapelite from Dalkoy Island, enclosing inclusions of acicular sillimanite and dark grains of rounded biotite. The sillimanite preserves helicitic F_3 structures folding an S_2 foliation. Specimen 88/14B, plane-polarized light, field of view is about 1.5 mm.

Plate 3.4b

An intergrowth of quartz and type-2 garnet in metapelitic leucosome from Cowell Island. Specimen 88/219, plane-polarized light, field of view is about 170 mm.

Plate 3.4c

Type-2 garnet and cordierite in metapelitic leucosome from Hovde Island. The cordierite preserves idioblastic grain edges adjacent to garnet. The elongate laths of opaque material are graphite. Specimen 88/190, plane-polarized light, field of view is about 14 mm.

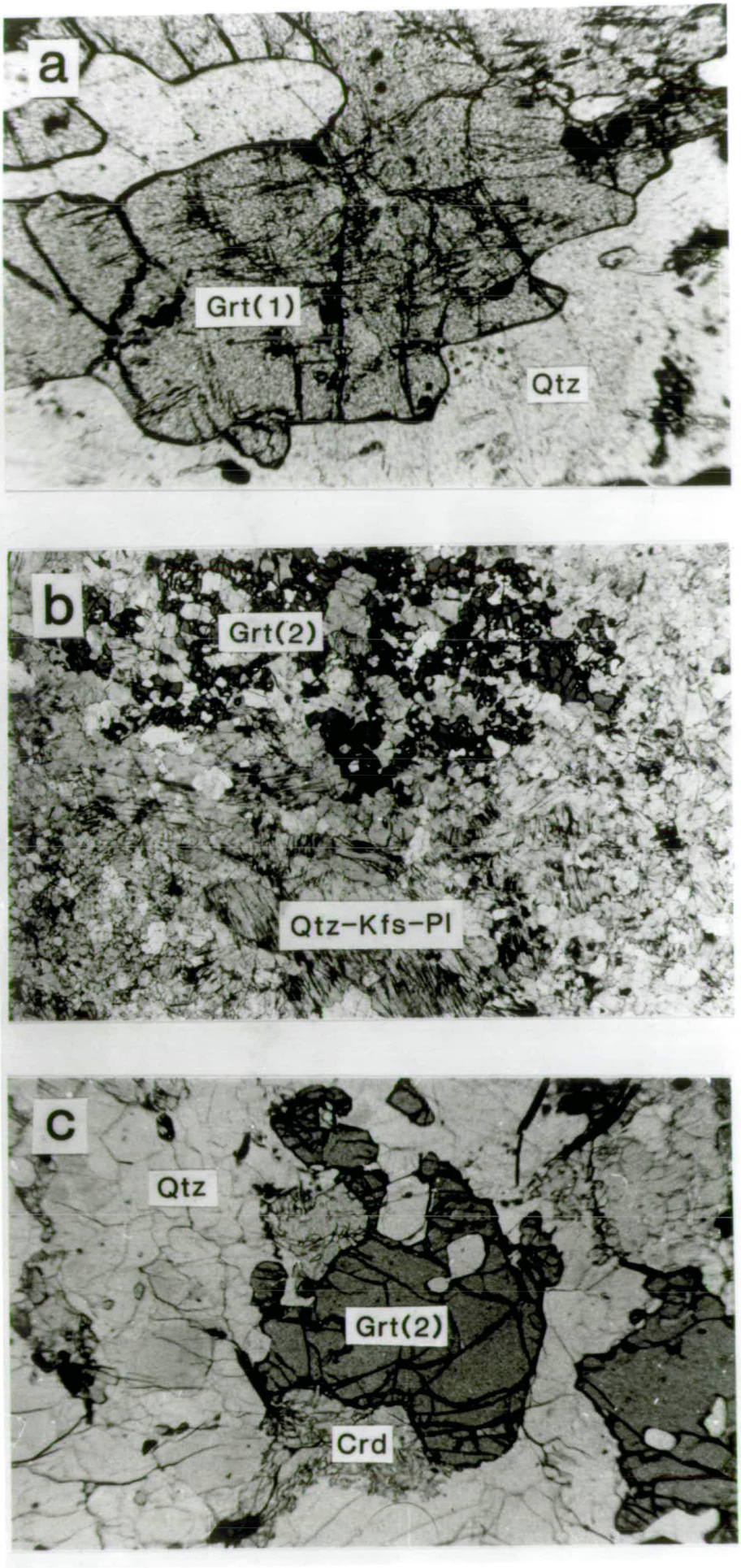
a
Grt(1)
Qtz
b
Grt(2)
Qtz-Kfs-Pl
c
Qtz
Grt(2)
Crd

quartz-absent domains it forms symplectitic intergrowths with poikiloblastic cordierite (see Plate 3.5), and in cordierite-absent domains it forms lobate intergrowths with quartz (see Plate 3.6a,b). A combination of these textures is commonly developed, comprising symplectitic cordierite, spinel and worms or ovoid blebs of quartz. All three types of texture enclose, and form adjacent to, resorbed garnet and sillimanite. The garnet associated with these textures may be the inclusion-rich or the inclusion-free variety. Rare, randomly-oriented, biotite laths and biotite-quartz symplectites occur adjacent to resorbed sillimanite and K-feldspar (see Plate 3.6c), but biotite is generally not associated with the spinel symplectites and intergrowths. Biotite is, however, common in shear zones, which locally overprint the textures described above and are characterized by a pervasive, planar fabric defined by blocky biotite laths, resorbed sillimanite prisms, elongate spinel and ilmenite (S_4; see Plate 3.7a and Section 3.4.5). This foliation is locally folded (F_5; see Plate 3.7b and Section 3.4.6). Small-scale post-S_4 coronas of cordierite, garnet, idioblastic sillimanite, biotite, or biotite and sillimanite commonly separate spinel and ilmenite from quartz (see Plate 3.8). Corona mineralogy depends on the local environment; for example, garnet rims form around spinel in areas adjacent to garnet porphyroblasts, whereas cordierite rims are common in domains away from garnet and sillimanite. Other post-deformational textures include narrow plagioclase rinds around garnet, sillimanite and spinel, particularly where adjacent to K-feldspar.

(ii) Melanosome assemblages also contain two types of garnet distinguished by their shape and inclusion content (see Plate 3.7c). Large, elongate garnet grains up to 30 mm in diameter, crowded with acicular sillimanite and small rounded biotite grains, are by far the most common, but some garnet is devoid of fine inclusions, and commonly contains coarse, isolated inclusions of biotite, spinel and rarely cordierite. No consistent spatial relationship between the two types of garnet has been identified, and both types commonly occur together as composite grains. In some grains, acicular sillimanite is confined to the edges, whereas other grains have inclusion-rich cores. Garnet also contains prismatic sillimanite, but this commonly follows narrow fractures. Garnet is wrapped by coarse, prismatic sillimanite, elongate spinel, and biotite laths, which do not define a consistent foliation, but form arcuate trails determined principally by the location of garnet porphyroblasts. Inclusions in garnet commonly preserve a foliation of more consistent orientation than external sillimanite, but sillimanite inclusions locally preserve complex helicitic trails. Spinel contains inclusions of biotite and ilmenite. Poikiloblastic cordierite locally overgrows matrix sillimanite, spinel and

PLATE 3.5

Plate 3.5a

Spinel-cordierite symplectite adjacent to resorbed sillimanite in a metapelite from Brattstrand Bluffs. There is a pleochroic halo in the cordierite between spinel and sillimanite near the top of the photograph. Specimen 88/46C, plane-polarized light, field of view is about 1.5 mm.

Plate 3.5b

Spinel-cordierite symplectite adjacent to resorbed sillimanite in a metapelite from Brattstrand Bluffs. The spinel and sillimanite are separated by cordierite, and are never in direct contact. Quartz occurs locally within the symplectite. Specimen 88/90, plane-polarized light, field of view is about 1.5 mm.

Plate 3.5c

Spinel-cordierite symplectite adjacent to, and enclosing, resorbed grains of garnet and sillimanite in a metapelite from Brattstrand Bluffs. Specimen 88/90, plane-polarized light, field of view is about 14 mm.

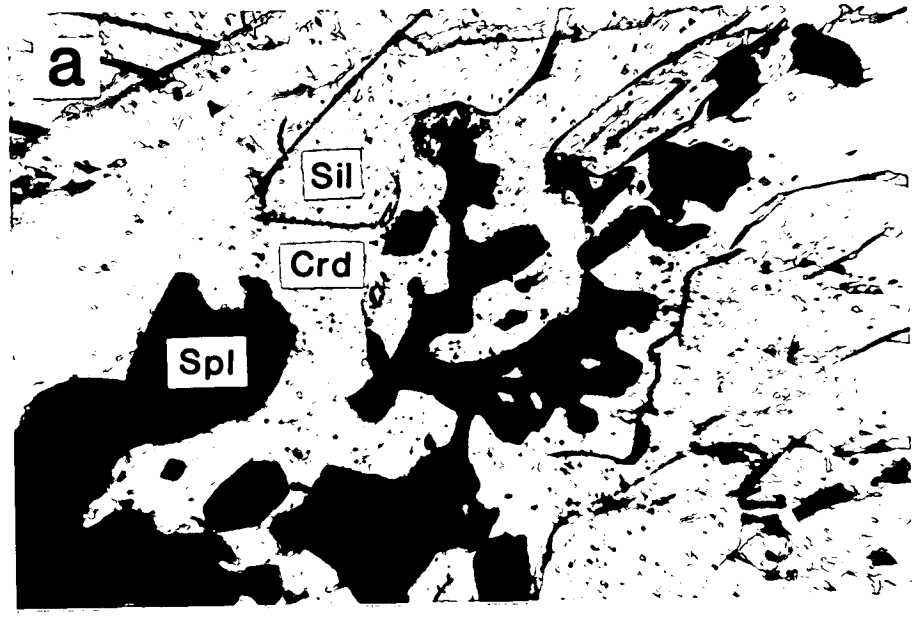
a
Sil
Crd
Spl

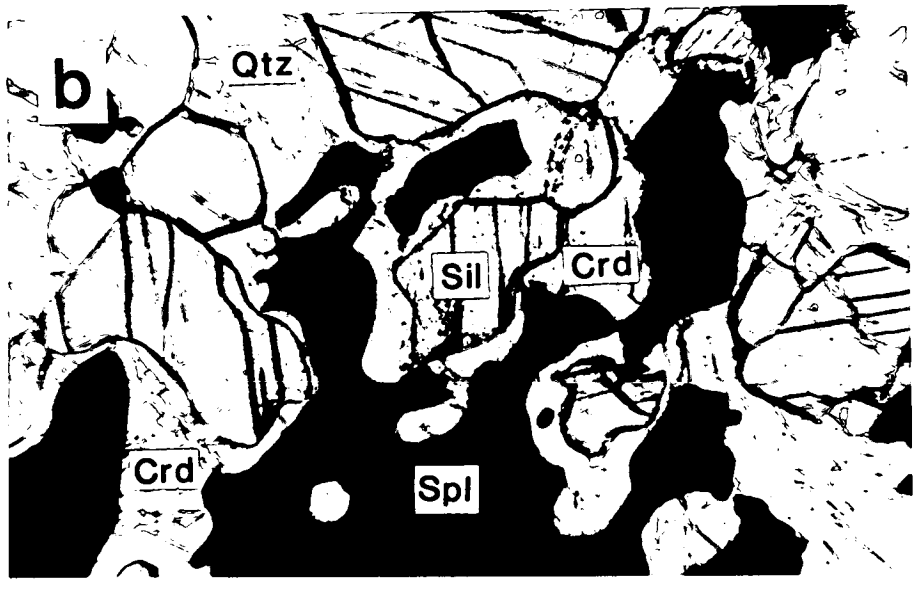
b
Qtz
Sil
Crd
Crd
Spl

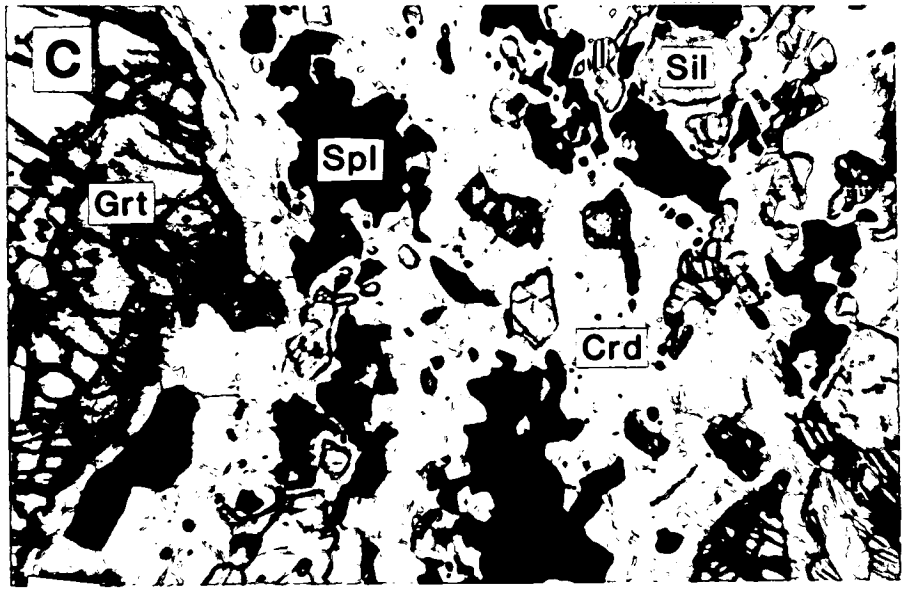
c
Sil
Spl
Grt
Crd

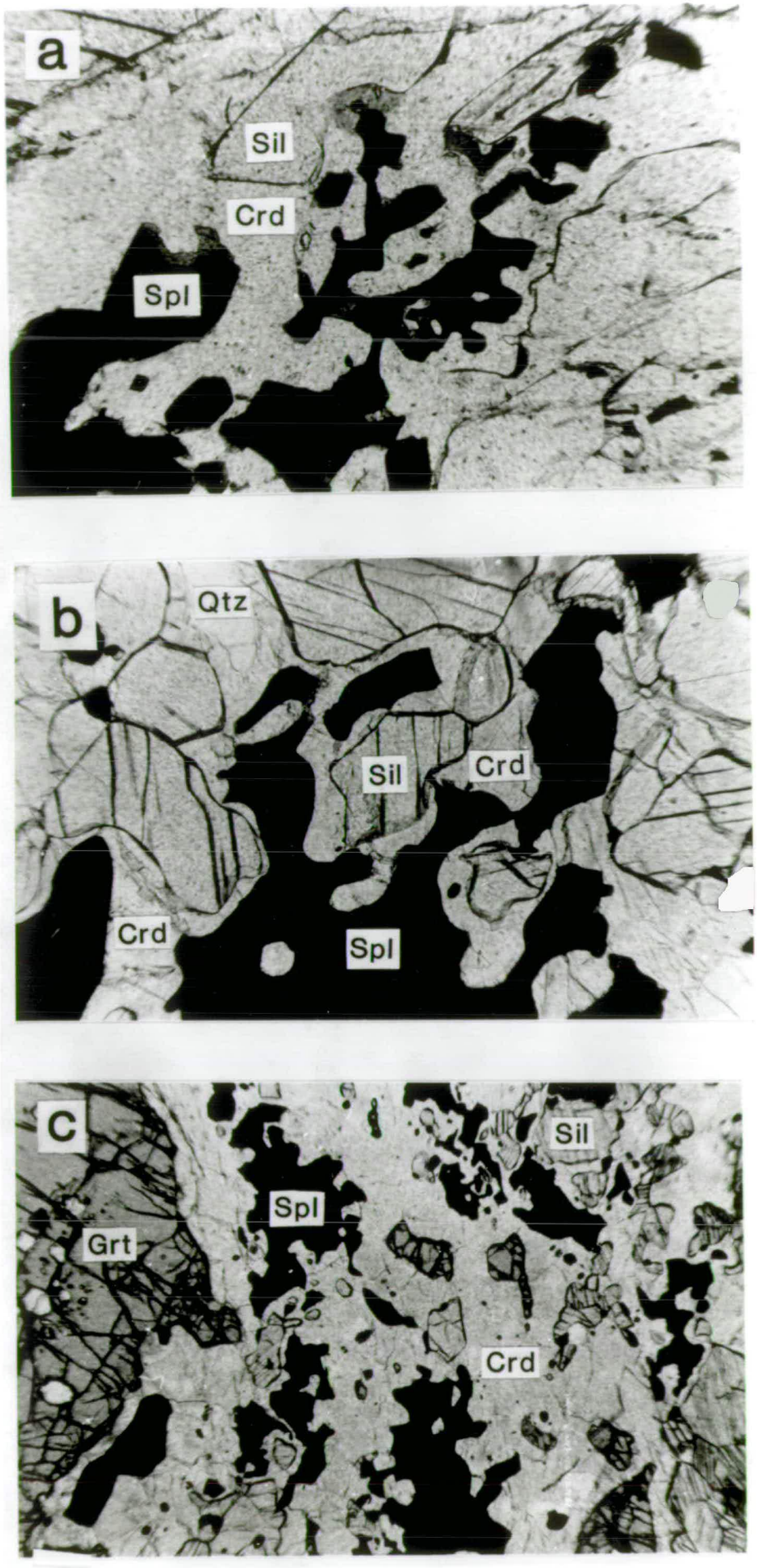
a
Sil
Crd
Spl
b
Qtz
Sil
Crd
Crd
Spl
c
Sil
Spl
Grt
Crd

PLATE 3.6

Plate 3.6a

Spinel-quartz symplectite adjacent to resorbed garnet and sillimanite in a metapelite from Brattstrand Bluffs. Specimen 88/106, plane-polarized light, field of view is about 1.5 mm.

Plate 3.6b

Spinel-quartz intergrowth in a metapelite from Brattstrand Bluffs. Specimen 88/62, plane-polarized light, field of view is about 1.5 mm.

Plate 3.6c

Biotite and biotite-quartz symplectite adjacent to resorbed sillimanite and microperthite in a metapelite from Brattstrand Bluffs. Specimen 88/51, plane-polarized light, field of view is about 1.5 mm.

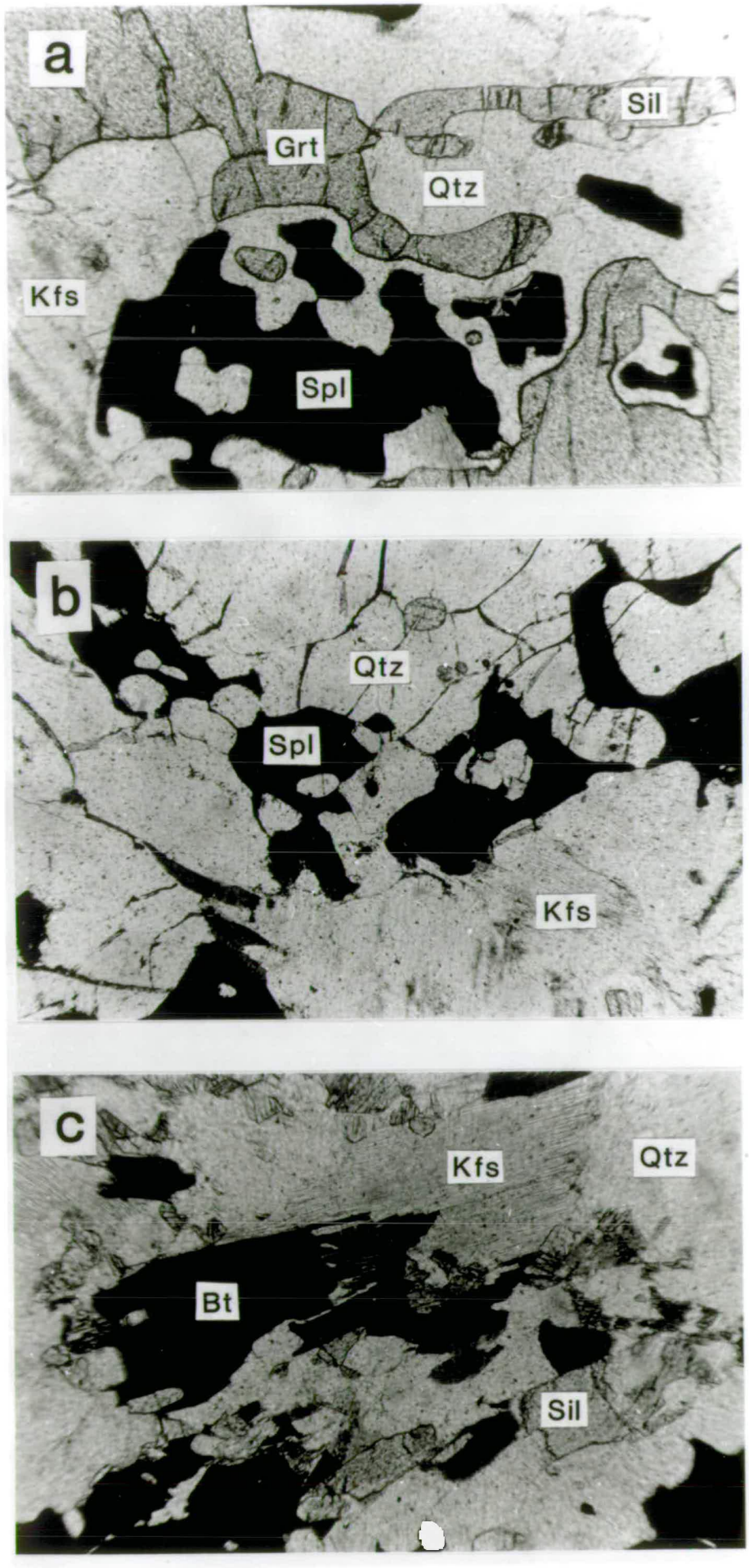
a
Sil
Grt
Qtz
Kfs
Spl
b
Qtz
Spl
Kfs
C
Kfs
Qtz
Bt
Sil

PLATE 3.7

Plate 3.7a

A metapelite from Brattstrand Bluffs with a penetrative S_4 foliation defined by biotite laths and elongate lenses of spinel-quartz intergrowth. Specimen 88/62, plane-polarized light, field of view is about 18 mm.

Plate 3.7b

A metapelite from Hovde Island preserving F_5 microfolds. The folds deform an S_4 foliation defined by sillimanite, spinel and biotite. Specimen 88/192, plane-polarized light, field of view is about 10 mm.

Plate 3.7c

Garnet-sillimanite-spinel-biotite melanosome from Brattstrand Bluffs. Garnet is present both as inclusion-rich (type 1) and inclusion-poor (type 2) varieties, which are wrapped around by an arcuate sillimanite foliation. Cordierite and cordierite-spinel symplectite are developed at the edges of the spinel grains. Specimen 88/46A, plane-polarized light, field of view is about 14 mm.

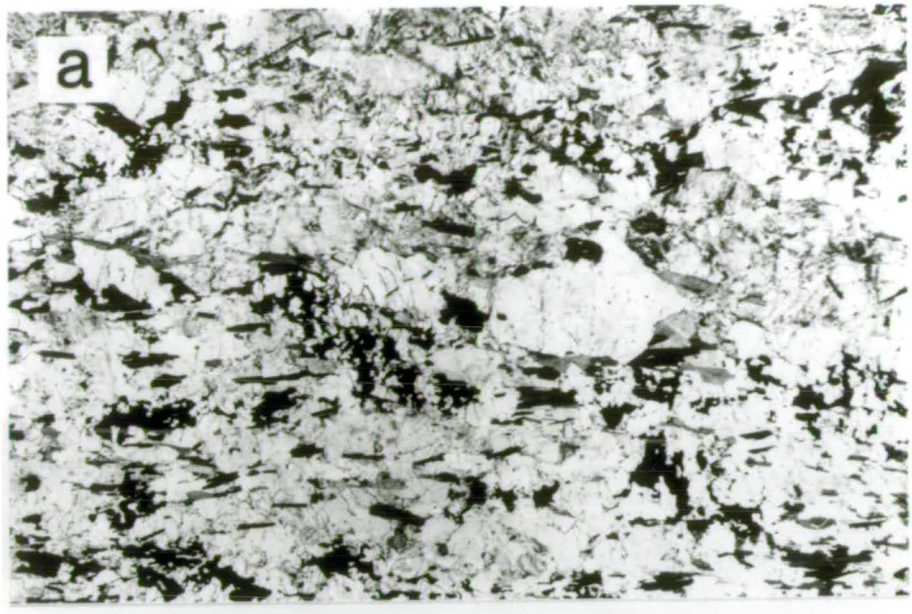
a

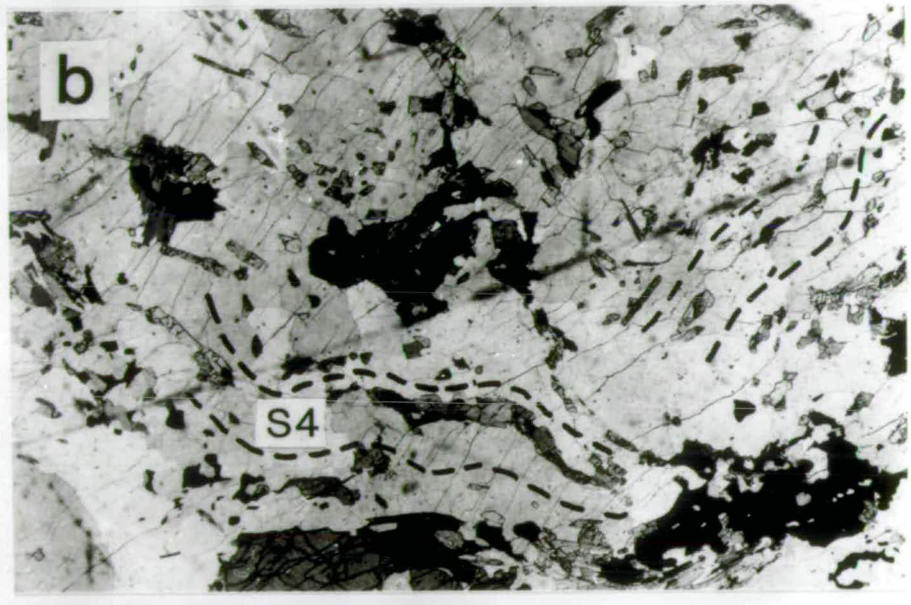
b
S4

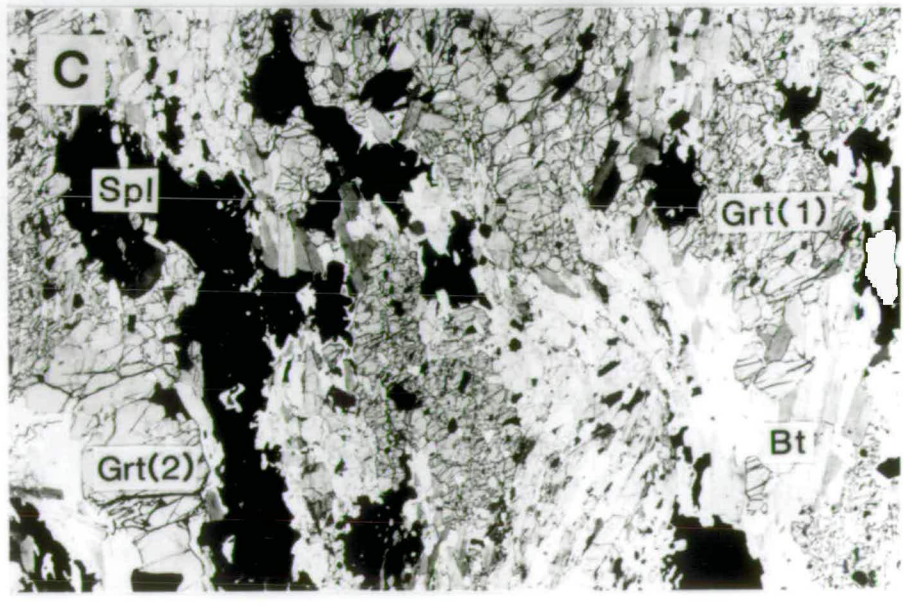
c
Spl
Grt(1)
Bt
Grt(2)

PLATE 3.8

Plate 3.8a

Spinel-quartz symplectite adjacent to resorbed sillimanite in a metapelite from Brattstrand Bluffs. The spinel and quartz are separated by a narrow corona of cordierite. Specimen 88/148, plane-polarized light, field of view is about 1.5 mm.

Plate 3.8b

A narrow corona of garnet around spinel in a metapelite from Brattstrand Bluffs. Specimen 88/51, plane-polarized light, field of view is about 1.5 mm.

Plate 3.8c

A composite corona of sillimanite and biotite around spinel and ilmenite (difficult to distinguish in a black and white photograph) in a metapelite from Hovde Island. Specimen 88/192, plane-polarized light, field of view is about 1.5 mm.

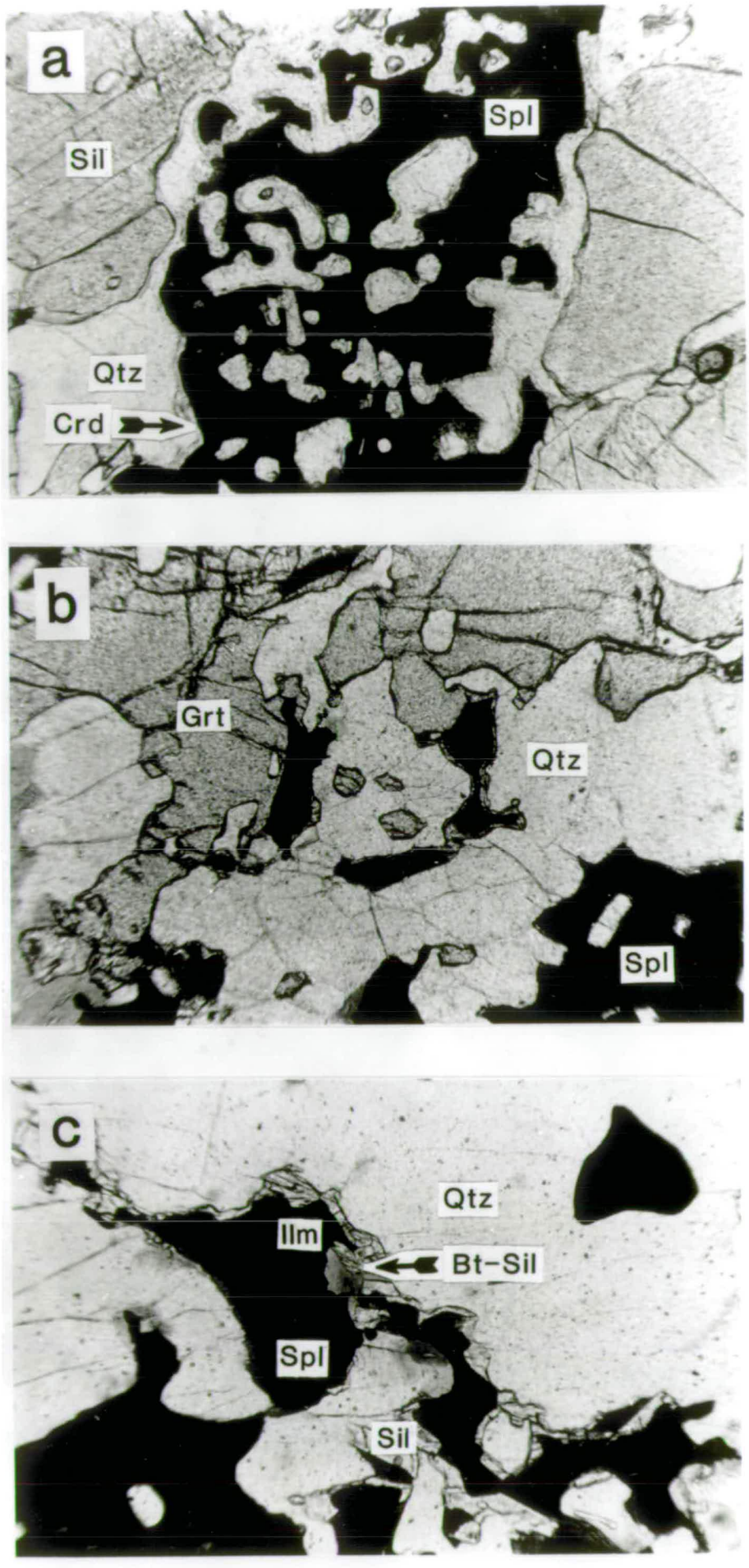
a
Spl
Sil
Qtz
Crd
b
Grt
Qtz
Spl
c
Qtz
Ilm
Bt–Sil
Spl
Sil

Table 3.4 Assemblage development in the metapelitic migmatite.

Mesosome assemblages	
Inclusion assemblage (in garnet):	Grt(1)-Bt-Sil-Qtz-Kfs
S_3 matrix assemblage:	Grt(1+2)-Crd-Sil-Qtz-Kfs
Post-S_3 spinel growth:	Spl-Crd symplectite next to resorbed Grt(1+2)-Sil
	Spl-Qtz symplectite next to resorbed Grt(1+2)-Sil
	Spl-Crd-Qtz intergrowths next to resorbed Grt(1+2)-Sil
Post-S_3 biotite growth:	Bt adjacent to resorbed Kfs-Sil, concentrated in S_4 shear zones
Post-S_4 coronas	Composite Grt, Sil or Bt coronas around Spl and Ilm
	Crd rims between Spl and Qtz
	Pl rims between Sil and Kfs and adjacent to Grt
Melanosome assemblages	
Inclusion assemblage (in garnet):	Grt(1)-Bt-Sil
S_3 matrix assemblage:	Grt(1+2)-Sil-Spl-Bt (± poikiloblastic Crd, ± Kfs)
Post-S_3 cordierite growth:	Crd-Spl symplectites next to resorbed Grt(1+2) and Sil
Leucosome assemblages	
S_3 assemblage:	Qtz-Kfs-Pl-Grt(2)-Crd

Grt(1) and Grt(2) refer to inclusion-rich and inclusion-poor textural varieties of garnet.

biotite, and commonly forms symplectitic intergrowths with spinel adjacent to resorbed sillimanite. The spinel in these symplectites is rarely in direct contact with sillimanite, but commonly separated from it by cordierite. Cordierite-spinel symplectites are also developed adjacent to garnet, and again cordierite commonly separates the symplectitic spinel from garnet. Microperthitic K-feldspar has a low modal abundance but can be identified in most specimens.

(iii) Leucosome assemblages, dominated by quartz, microperthite, and lesser amounts of antiperthitic plagioclase, are characterized by lobate grain boundaries, heterogeneous grain sizes, and myrmekitic and granophyric intergrowths (see Plate 3.9). Quartz occurs both as xenoblastic grains, 3 mm or more across, which have extensive sub-grain development, and as ovoid inclusions, less than 0.5 mm across, within feldspar. Garnet is generally free of inclusions other than quartz, and occurs as small, isolated, sub-idioblastic grains or as lobate intergrowths with quartz. Some specimens also contain cordierite, which is commonly in close spatial association with, and preserves idioblastic grain edges against, garnet. There is an inverse relationship between the grain size and modal abundance of garnet and cordierite, and the size of the leucosome. Garnet is up to 5 mm across in narrow lenses of leucosome (less than 0.2 m wide), but between 0.5 and 3 mm across, and less abundant, in extensive leucosome bodies. Similarly, cordierite is more common in narrow veins and lenses than in large areas of leucosome. Rare resorbed sillimanite grains commonly occur near to aluminous pods and

PLATE 3.9

Plate 3.9a

A leucosome from Cowell Island, showing heterogeneous grain sizes and irregular grain boundaries. Specimen 88/219, viewed under crossed polars, field of view is about 8 mm.

Plate 3.9b

A garnet-bearing leucogneiss from Hovde Island, showing irregular grain boundaries and myrmekitic intergrowths. Specimen 88/193, viewed under crossed polars, field of view is about 6 mm.

Plate 3.9c

Garnet-bearing leucogneiss from Svenner 3, showing heterogeneous grain sizes and irregular grain boundaries. Specimen 88/325, viewed under crossed polars, field of view is about 8 mm.

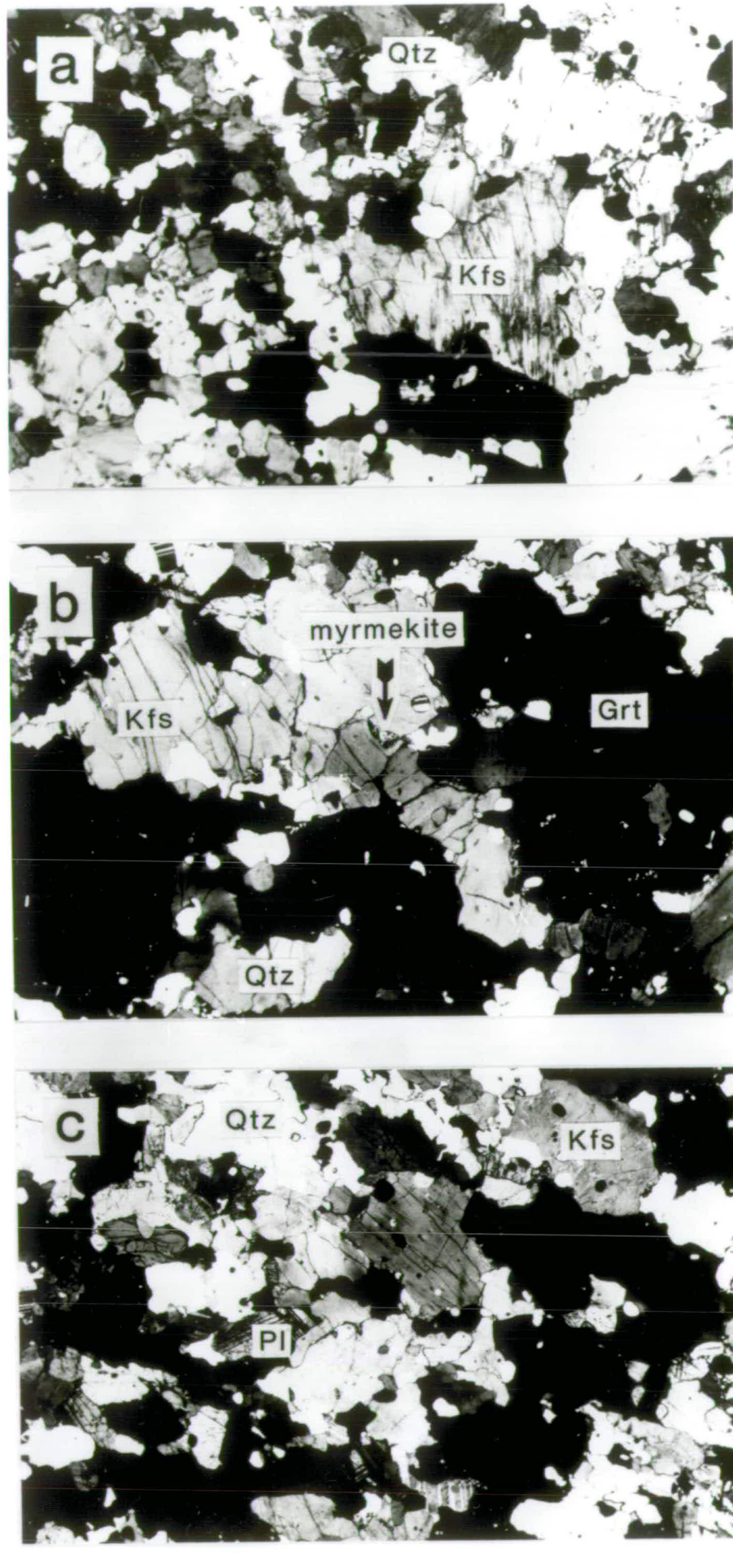
a
Qtz
Kfs
b
myrmekite
Kfs
Grt
Qtz
c
Qtz
Kfs
Pl

schlieren, and are interpreted as melanosomic grains rather than part of leucosome assemblage. Rare randomly-oriented biotite laths occur around garnet porphyroblasts, and graphite occurs as random flakes and radial clusters (see Plate 3.10a) which are much more common in the leucosome than in other migmatite components.

These complex assemblages and textures, and the constraints they impose on the metamorphic evolution of the Brattstrand Bluffs coastline, are considered further in Chapter 6.

3.2.4 Magnesian gneiss and migmatite

Cordierite-rich magnesian migmatite crops out on Svenner 3. It consists of cordierite, biotite, quartz, K-feldspar, plagioclase, magnetite, spinel and rare garnet (see Table 3.5). No sillimanite has been observed. Lenses of leucosome comprising quartz, microperthite and antiperthitic plagioclase, with grain sizes up to 4 mm, occur within biotite-rich mesosome containing relatively fine-grained quartz and feldspar. Xenoblastic cordierite and magnetite-spinel grains occur both in the leucosome and the biotite-bearing mesosome, but rare xenoblastic garnet grains occur only at the edges of the leucosome. Leucosome-dominated units comprise quartzofeldspathic material and narrow lenses and layers rich in cordierite ± magnetite ± spinel. Cordierite is xenoblastic and elongate, and contains vermicular quartz inclusions. Spinel and magnetite occur as composite grains. Quartz occurs as large irregular grains with lobate boundaries and as small ovoid grains within microperthitic K-feldspar and antiperthitic plagioclase, or at their interstices, and also forms myrmekitic intergrowths with plagioclase. Quartz-K-feldspar granophyric intergrowths are less common.

Table 3.5 Magnesian gneiss and migmatite assemblages

Banded gneiss or mesosome assemblage (modal abundance in per cent)
Crd(20-40%)-Bt(10-15%)-Qtz(20-35%)-Pl(10-20%)-Kfs(5-10%)-Mag(2-5%)-Spl(2-5%)-Grt(0-2%)
Migmatite or interlayered leucosome and melanosome (modal abundance in per cent)
Qtz(20-35%)-Pl(25-40%)-Kfs(25-35%)-Crd(5-10%)-Mag(2-5%)-Spl(0-2%)-Bt(0-2%)

3.2.5 Semi-pelitic gneiss

Narrow semi-pelitic layers and lenses up to 2 m across occur within the paragneiss sequences. Two characteristic assemblages have been identified (see Table 3.6).

(i) Garnet-biotite-plagioclase-quartz gneiss contains irregular and commonly lobate garnet porphyroblasts, which include rounded quartz, plagioclase, biotite and ilmenite, and are usually elongated parallel to a planar fabric. The planar fabric comprises a foliation defined by blocky laths of biotite wrapping around garnet,

and a compositional banding of quartz and feldspar from garnet and biotite (S_3 or locally S_4; see Sections 3.4.4 and 3.4.5). A second textural type of garnet, forming lobate intergrowths with quartz and plagioclase, generally occurs in areas depleted in biotite. Randomly-oriented biotite occurs either as very elongate grains around garnet, or as grain aggregates distributed throughout the gneiss. Accessory minerals include ilmenite, apatite and zircon. Migmatitic textures comprising a stromatic layering of garnet-biotite and quartzofeldspathic material are commonly developed.

A distinctive migmatitic texture was observed in semi-pelite at one locality in Steinnes Peninsula. Elongate, isolated blebs of leucosome, between 30 and 100 mm long and 10 and 20 mm wide, occur within a biotite-quartz-microperthite-plagioclase mesosome. Quartz and feldspar in the mesosome have a polygonal fabric with grain sizes around 0.5 mm, and a foliation is defined by preferred orientation of biotite. The elongate leucosomes are oriented parallel to the biotite foliation, but are themselves unfoliated and locally truncate the mesosome foliation. The leucosomes consist of quartz, microperthite, plagioclase and garnet, with heterogeneous grain sizes and lobate or irregular grain boundaries. Quartz and plagioclase are about 0.5 mm across, but K-feldspar grains are up to 2 mm across and garnet grains vary in diameter between 1 and 4 mm. Garnet grains are concentrated in the centres of the leucosomes, and contain rounded quartz inclusions. Garnet has lobate grain boundaries intergrown with quartz, although there is some evidence of idioblastic form (see Plate 3.10b). Narrow, randomly-oriented, elongate biotite grains occur within the leucosomes, concentrated around garnet.

(ii) Garnet-orthopyroxene-plagioclase-quartz-K-feldspar gneiss has a compositional banding and layer-parallel foliation (see Plate 3.10c) defined by chains of garnet and orthopyroxene, separated by quartz and feldspar (S_3 or locally S_4; see Sections 3.4.4 and 3.4.5). Accessory phases include ilmenite, apatite and zircon. Sub-idioblastic to rounded garnet porphyroblasts contain rounded inclusions of quartz, plagioclase, orthopyroxene, biotite and ilmenite. Sub-idioblastic orthopyroxene is aligned parallel to the foliation, and contains inclusions of garnet, biotite, quartz, plagioclase and ilmenite. Rare biotite-plagioclase or biotite-quartz symplectites are locally developed around resorbed orthopyroxene. Ilmenite is locally mantled by garnet.

3.2.6 Intermediate orthopyroxene gneiss

Narrow, well-foliated to massive, plagioclase-quartz-orthopyroxene-biotite layers and lenses, between 0.1 and 1 m across, occur within the paragneiss sequences (see Table

PLATE 3.10

Plate 3.10a

A radial cluster of graphite in metapelitic leucosome from Brattstrand Bluffs. The graphite occurs within, and along the grain boundaries of, microperthite and quartz. Specimen 88/46B, plane-polarized light, field of view is about 14 mm.

Plate 3.10b

A lobate intergrowth of garnet and quartz in a semi-pelitic migmatite from Steinnes Peninsula. The garnet is separated from the biotite-bearing mesosome by a biotite-absent anhydrous halo of quartz and feldspar. Specimen 88/34, plane-polarized light, field of view is about 14 mm.

Plate 3.10c

A garnet-orthopyroxene semi-pelite from Steinnes Peninsula. A planar S_3 fabric is defined by layers of garnet and orthopyroxene separated by quartz and feldspar. Specimen 88/38, plane-polarized light, field of view is about 10 mm.

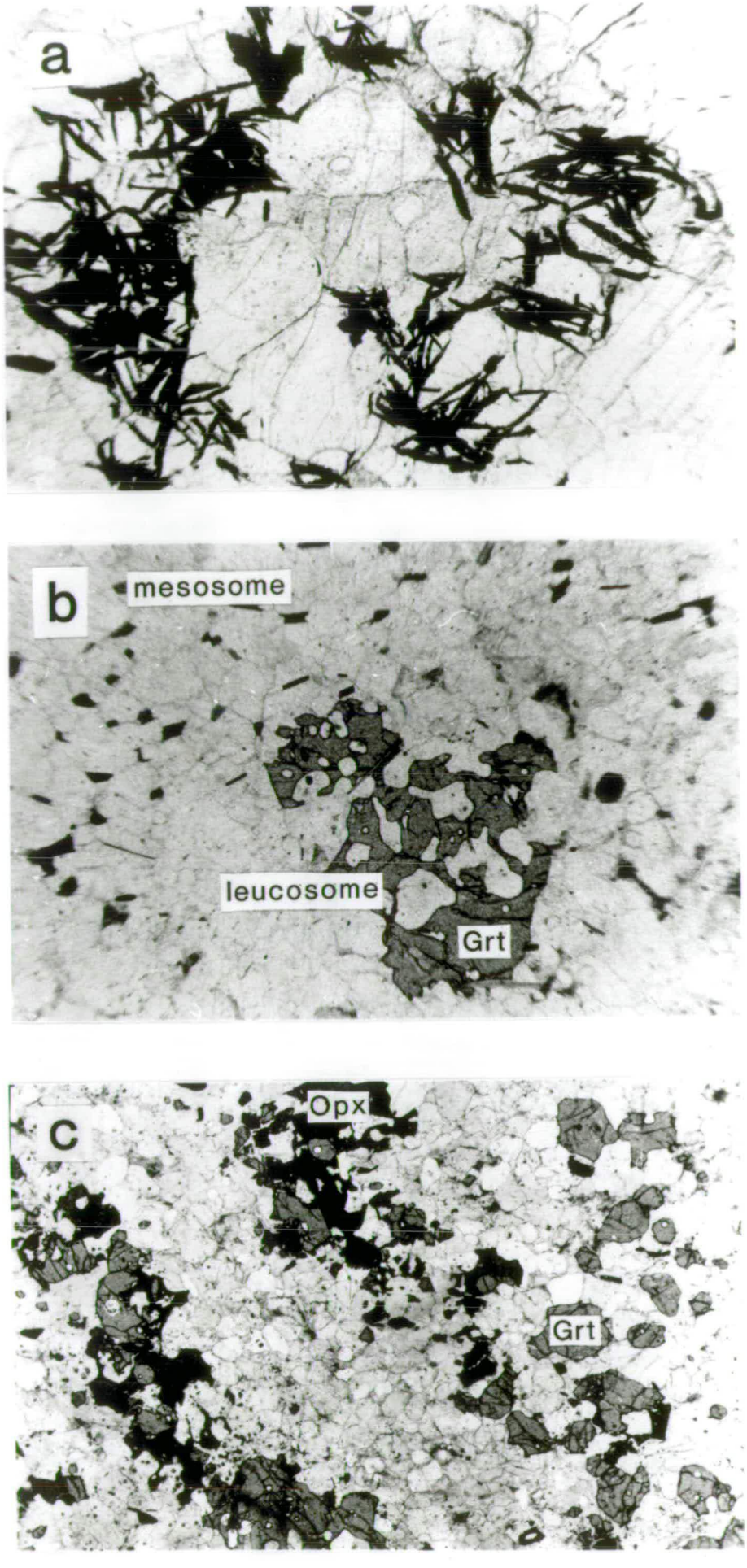
a
b
mesosome
leucosome
Grt
c
Opx
Grt

Table 3.6 Miscellaneous gneissic assemblages.

Prograde phases represent syn-S_3 assemblages, and retrograde phases are post-S_3.

Semi-pelitic gneiss assemblages (and modal abundances):		
Prograde phases	(1)	Grt(5-15%)-Bt(5-20%)-Pl(40-70%)-Qtz(10-40%)
Retrograde phases		Bt
Accessory phases		Ilm-Ap-Zrn
Prograde phases	(2)	Grt(5-10%)-Opx(5-20%)-Pl(40-60%)-Qtz(10-40%)-Kfs(0-5%)
Retrograde phases		Bt, Bt-Pl and Bt-Qtz symplectites around Opx
Accessory phases		Ilm-Ap-Zrn
Intermediate orthopyroxene gneiss assemblages (and modal abundances):		
Prograde phases		Qtz(5-15%)-Pl(40-60%)-Opx(10-30%)-Bt(5-30%)
Retrograde phases		Bt, Bt-Pl symplectites around Opx
Accessory phases		Ilm-Ap
Ultramafic assemblages (and modal abundances):		
Prograde phases		Opx-Cpx-Hbl ± Pl ± Bt ± Spl (modal abundances are variable)
Retrograde phases		none identified
Accessory phases		none identified
Leucogneiss assemblages (and modal abundances):		
Prograde phases		Qtz(20-40%)-Kfs(35-60%)-Pl(5-25%)-Grt(1-8%) ± Crd(0-3%)
Retrograde phases		Bt around Grt
Accessory phases		Gr-Zrn
Granitic orthogneiss assemblages (and modal abundances):		
Prograde phases		Qtz(20-40%)-Kfs(20-40%)-Pl(15-35%)-Bt(5-10%)-Grt(0-5%)
Retrograde phases		none identified
Accessory phases		Ilm-Ap-Zrn

3.6). Elongate grains or grain clusters of orthopyroxene are parallel to a foliation defined by short, stubby biotite laths (S_3 or locally S_4; see Sections 3.4.4 and 3.4.5). Biotite also occurs in a random orientation as isolated elongate grains, aggregates of blocky laths, and biotite-plagioclase symplectites around resorbed pyroxene. Ilmenite and apatite are common accessory minerals.

3.2.7 Ultramafic rock

Dark, podiform, ultramafic bodies, 1 to 5 m across, occur within the well-layered paragneiss sequences. They consist of various combinations of orthopyroxene, clinopyroxene and hornblende (see Table 3.6), and have a granular, polygonal fabric. Grain sizes vary between 0.5 and 3 mm. Biotite, plagioclase, ilmenite and spinel are commonly present, but have a low modal abundance.

3.2.8 Leucogneiss

White, granular, quartz-K-feldspar-plagioclase leucogneiss sheets and lenses, between 1 and 5 m wide, occur in the paragneiss association (see Plate 3.3c), and contain minor garnet and more rarely cordierite (see Table 3.6). These units are discordant but sub-parallel to the dominant compositional banding and foliation of most lithologies

(S_3; see Section 3.4.4), and are locally deformed by folds and planar fabrics attributed to a later event (D_4; see Section 3.4.5). These planar fabrics (S_4) are defined by quartz ribbons or chains of garnet. The leucogneiss sheets are of similar hand-specimen and microscopic appearance to leucosome-dominated metapelitic migmatite.

There is extensive evidence of recrystallization in the quartzofeldspathic matrix, and myrmekitic and granophyric intergrowths are common (see Plate 3.9). K-feldspar is microperthitic and plagioclase commonly antiperthitic. Garnet is inclusion free, and occurs either as lobate intergrowths with quartz or as smaller idioblastic grains. Cordierite is sub-idioblastic or xenoblastic, although idioblastic grain edges are preserved adjacent to garnet. Rare sillimanite and spinel occur as isolated, resorbed grains or grain aggregates, and the symplectite and corona textures described in Section 3.2.3 are commonly developed around these melanosome aggregates. Randomly-oriented biotite occurs as extremely elongate grains around garnet, and graphite flakes are common throughout leucogneiss units.

3.2.9 Granitic orthogneiss

A homogeneous, granitic orthogneiss body, at least 300 m in diameter, crops out at Steinnes Peninsula. Grain sizes in the centre of the body are up to 40 mm and textures are massive, but grain sizes at the edges are about 3 mm and a localized biotite foliation is developed (S_3; see Section 3.4.4). The orthogneiss consists of quartz, microperthite and plagioclase, with minor biotite (see Table 3.6). K-feldspar commonly shows simple twinning. Ilmenite, apatite and zircon are common accessory phases, and rare garnet grains are concentrated in pegmatitic veins and patches.

3.2.10 Summary and interpretation of gneissic lithologies

The gneissic lithologies have been divided into a composite orthogneiss association, and a paragneiss association comprising units of various sedimentary origins, which all pre-date the development of a pervasive foliation (S_3). Leucogneiss and granitic orthogneiss bodies are locally discordant to these lithologies, and are interpreted as syn- to post-S_3 in age. Many of these lithologies are characterized by migmatitic textures, which require further explanation. A number of different processes have been proposed to account for migmatite formation (e.g. Yardley, 1978; Ashworth, 1985; Olsen, 1985):

(i) igneous injection of felsic magma;
(ii) *in situ* anatexis and local segregation of melt;
(iii) sub-solidus differentiation by chemical or mechanical processes; and
(iv) metasomatism of various elements from an external source.

Processes (i) and (ii) occur in the presence of melt, whereas (iii) and (iv) are melt

absent. Processes (ii) and (iii) can occur within a closed system, whereas (i) and (iv) require open-system behaviour (Ashworth, 1985). It has been recognized that more than one process can operate during the formation of a migmatite (e.g. Brown, 1973), but most migmatite is regarded as primarily anatectic in origin. Various textural, mineralogical and chemical criteria have been used to indicate anatectic migmatization. A number of the textural characteristics of the various types of migmatite described in Sections 3.2.2 to 3.2.9 are indicative of the former presence of melt (Johannes & Gupta, 1982; Ashworth & McLellan, 1985; McLellan, 1988; Vernon & Collins, 1988).

(i) The discordant nature of the leucosomes in all cases implies some degree of melt intrusion rather than metamorphic differentiation.

(ii) Leucosomes within mafic granulite, semi-pelite and metapelite are unfoliated, except where overprinted by a local planar fabric (S_4; see Section 3.4.5). This implies that an origin by metamorphic differentiation during deformation is unlikely. The felsic matrix of the composite orthogneiss is foliated, but this is attributed to a penetrative deformation following migmatite formation (D_3; see Section 3.4.4).

(iii) The grain size of quartzofeldspathic phases in the leucosome is greater and more heterogeneous than in the mesosome.

(iv) Myrmekitic plagioclase-quartz intergrowths are common adjacent to K-feldspar grains, and granophyric K-feldspar-quartz intergrowths occur locally.

(v) Polygonal grain boundaries do not occur in the leucosomes, and feldspar grains are lobate and intergrown.

(vi) The sub-idioblastic (subhedral?) form and, particularly in narrow leucosomes, the coarse grain size of garnet and cordierite in the metapelitic and semi-pelitic leucosomes, and orthopyroxene in the mafic leucosomes, are indicative of growth or modification in a fluid medium.

All the migmatitic textures described in this section are interpreted as mixtures of leucocratic crystallized melt and a restitic component which has not melted. There is evidence that at least some of these melts were derived by local anatexis.

(i) Local leucosome generation is indicated by the small size and isolation of leucosomes in the semi-pelite specimen from Steinnes Peninsula and many of the leucosomes within the mafic units of the composite orthogneiss, and to a lesser extent the intimately-interlayered stromatic metapelitic migmatite.

(ii) The existence of melanosome at the edges of leucosomes within the mafic units implies a local segregation of partial melt (Johannes & Gupta, 1982).

Hence there is good evidence for a local anatectic origin for the mafic, semi-pelitic

and some of the less-advanced metapelitic migmatites, with melt migration limited to scales of a metre or less. The continuous range of metapelitic migmatite from banded gneiss to leucosome-dominated units, and the similarity between schollen, schlieren and leucosome in the leucosome-dominated units, and mesosome, melanosome and leucosome in the stromatic migmatite, implies a common origin. The disrupted metapelitic migmatite is also assumed to be of local origin, with a scale of melt migration of 10 m or less. The felsic gneiss enclosing the mafic units of the composite layered gneiss is also interpreted as recrystallized melt on the basis of field and microtextural evidence. There are no textural constraints on the origin of this melt, and in particular whether it was derived by *in situ* anatexis of mafic material similar to the mafic rafts and schlieren, but a geochemical study of similar migmatitic orthogneiss from the Rauer Group indicated that the felsic material was derived by near-closed system anatexis of the mafic granulite (Tait & Harley, 1988; Tait, 1989).

The spectrum of migmatitic textures observed in the various lithologies is a reflection of a variable degree of anatexis and segregation of the resultant melt. Isolated blebs and veins of orthopyroxene and garnet-bearing leucosome in the mafic and semi-pelitic lithologies reflect low degrees of localized partial melting and segregation (cf. Waters, 1988; Stüwe & Powell, 1989*b*). Partial melting is much more advanced in the metapelite. In the stromatic migmatite, the melt has remained in close proximity to its source rock, but the schollen- and schlieren-type migmatites reflect a greater segregation of melt from its source. The leucogneiss sheets are regarded as the ultimate end-member in this progression of increasing migmatization. However, the leucogneiss is not strictly a migmatite, since it comprises only a leucosome component. The inclusion-free garnet and rare cordierite in the leucogneiss sheets are correlated with similar type-2 garnet and cordierite in the metapelitic leucosomes and mesosomes, and are clearly related to the migmatization process. This process is considered in detail in Chapter 6. The discordant leucosome-dominated units are interpreted as recrystallized partial melts which have segregated from their pelitic source on a scale at least equivalent to the width of the leucogneiss sheets. They need not have been derived locally, but were clearly derived from very similar lithologies to the metapelite they have recrystallized within, and are thought to have migrated on scales less than 100 m. The volume of leucosome and discordant leucogneiss implies a local degree of partial melting of up to 25 per cent (see Plate 3.3c).

3.3 INTRUSIVE LITHOLOGIES

3.3.1 Introduction

A number of intrusive units truncate the gneissic fabrics of the lithologies discussed

above. They commonly preserve igneous features and are either unfoliated or preserve a weak to moderate foliation interpreted as igneous in origin. Their assemblages are summarized in Table 3.7.

3.3.2 Amanda Bay Granite and related intrusions

A pink, K-feldspar-megacrystic, quartz-K-feldspar-plagioclase-biotite-garnet granitic body of at least 3 km diameter crops out at Amanda Bay. A moderate foliation is defined by the orientation of subhedral to euhedral K-feldspar and plagioclase crystals up to 30 mm in length, and by finer-grained biotite (see Plate 3.11a). Xenoliths of metapelite, semi-pelite and felsic gneiss are common. The xenoliths vary in size from 0.1 to 10 m across, and the smaller ones are commonly rimmed by coarse grains of K-feldspar. Graded layering was identified at one locality, and consists of units, about 0.1 m thick, with a base rich in garnet, biotite and coarse K-feldspar, and a top rich in quartz and smaller grains of K-feldspar but poor in garnet and biotite (see Plate 3.11b). These units are laterally discontinuous and oblique to the K-feldspar foliation.

Grain sizes are heterogeneous, and vary between 1 and 30 mm. K-feldspar occurs as both microperthite and microcline, which commonly exhibit simple twins. Antiperthitic plagioclase is elongate parallel to its multiple twins. Quartz is anhedral, and even large grains show little evidence of recrystallization. Garnet contains inclusions of quartz, biotite and ilmenite, and occurs as lobate intergrowths with quartz or subhedral grains, which form aggregate clots and schlieren or are disseminated through the rock. Biotite is generally aligned parallel to the foliation, but also occurs as elongate randomly-oriented grains around garnet. Apatite, zircon, ilmenite and spinel are common accessory minerals. An almost identical lithology crops out as a series of dykes at Brattstrand Bluffs and the Svenner Islands (see Plate 3.11c), but has grain sizes between 0.5 and 3 mm. The dykes transect the gneissic foliations (S_3; see Section 3.4.4) and mesoscopic folds (F_4; see Section 3.4.5) of the country rocks, and contain gneissic xenoliths (see Plate 3.12a), but are themselves cut by planar pegmatite bodies. These intrusive rocks have imparted little overprint on adjacent gneisses, although aggregates of randomly-oriented biotite in metapelite and semi-pelite are common adjacent to syn-D_5 granitic intrusions. Other phases such as garnet and sillimanite are still stable within these aureoles.

3.3.3 Pegmatite

Coarse-grained, steeply-dipping, planar pegmatite bodies occur in the eastern half of the area (i.e. Brattstrand Bluffs and the Svenner Islands), and consist of quartz, K-feldspar, plagioclase, biotite and rare garnet (see Plate 3.12b). They cut across the gneissic units, granitic dykes and the Amanda Bay Granite, and trend either north-

PLATE 3.11

Plate 3.11a
The Amanda Bay Granite, with a foliation defined by coarse grains of K-feldspar. Pencil (aligned with the foliation) for scale.

Plate 3.11b
Graded layering in the Amanda Bay Granite. The layering is defined by the abundance of dark biotite and the size and abundance of blocky grains of K-feldspar, and is oblique to the foliation defined by K-feldpsar. Pencil for scale.

Plate 3.11c
A granitic dyke cross-cutting layered metapelite, semi-pelite and leucogneiss at Brattstrand Bluffs. The hammer at the centre of the photograph is 0.7 m long.

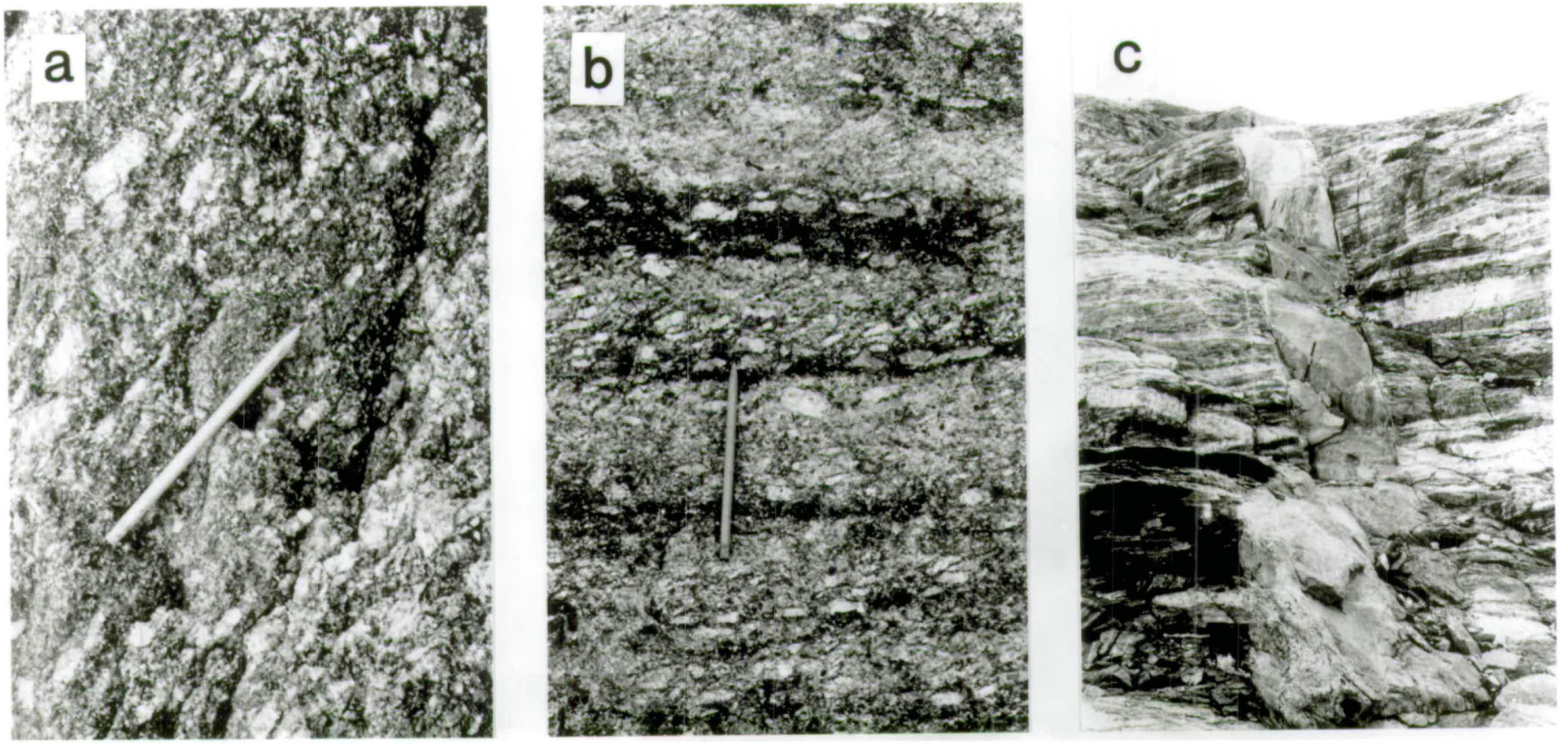
a
b
c

Table 3.7 Intrusive assemblages.

Granitic intrusive assemblages (and modal abundances):	
Prograde phases	Qtz(20-35%)-Kfs(25-45%)-Pl(15-30%)-Bt(5-15%)-Grt(5-20%)
Retrograde phases	Bt around Grt
Accessory phases	Ap-Zrn-Ilm-Spl
Pegmatite assemblages (and modal abundances):	
Prograde phases	Qtz(25-40%)-Kfs(20-35%)-Pl(25-45%)-Bt(2-8%)-Grt(0-3%)
Retrograde phases	Chl after Bt
Accessory phases	Zrn
Dalkoy Granite assemblages (and modal abundances):	
Prograde phases	Qtz(20-30%)-Pl(20-30%)-Kfs(30-40%)-Bt(10-15%)
Retrograde phases	Chl and Ep after Bt, white mica
Accessory phases	Spn-Ap-Zrn

south or east-west. Pegmatites cross-cut all pervasive fabrics, and may be related to a late flexing of earlier structures (D_6; see Section 3.4.7). They are commonly cut or offset by mylonitic shear zones (D_7; see Section 3.4.8).

3.3.4 Dalkoy Granite

A grey equigranular granite, with grain sizes between 0.5 and 2 mm, crops out at the northern end of Dalkoy Island (see Plate 3.12c). It consists of quartz, plagioclase, microcline, microperthite and biotite. Feldspar is subhedral, quartz is anhedral and generally undeformed, and a weak foliation is defined by biotite. Xenoliths are widespread, and a contact aureole is developed in gneiss up to 5 m from the granite. Coarse-grained pegmatitic segregations are common, and vary in width between 10 and 200 mm. Segregations less than 50 mm wide have a wispy morphology and no particular orientation, whereas wider ones tend to parallel one of two major joint sets. Planar zones of alteration, where chlorite and epidote occur at the expense of biotite, are oblique to the foliation. Accessory phases include sphene, apatite and zircon, and white mica is a common retrograde phase.

3.3.5 Summary and interpretation of intrusive lithologies

All the intrusive lithologies preserve evidence of their igneous origin on outcrop and microscopic scales, and none are thought to have undergone pervasive post-emplacement deformation. The Amanda Bay Granite and the Dalkoy Granite preserve weak foliations, which are interpreted as igneous in origin. Paterson *et al.* (1989) reviewed various criteria for granitic rocks that can be used to distinguish magmatic foliations from imposed tectonic foliations, and a number of these criteria are satisfied by the fabrics described above (see Sections 3.3.2 and 3.3.4).

(i) The foliation is defined by preferred orientation of K-feldspar and plagioclase

PLATE 3.12

Plate 3.12a

A layered xenolith of metapelitic gneiss within a granitic dyke at Brattstrand Bluffs. The lens cap is 50 mm in diameter.

Plate 3.12b

A garnet-bearing pegmatite cross-cutting metapelite at Brattstrand Bluffs. D_7 mylonite fabrics are developed along the edges of the pegmatite. The lens cap is 50 mm in diameter.

Plate 3.12c

The contact between massive granite (at the base of the photograph) and layered paragneiss (at the top of the photograph) at Dalkoy Island, looking south. The horizontal field of view is about 120 m.


a


b

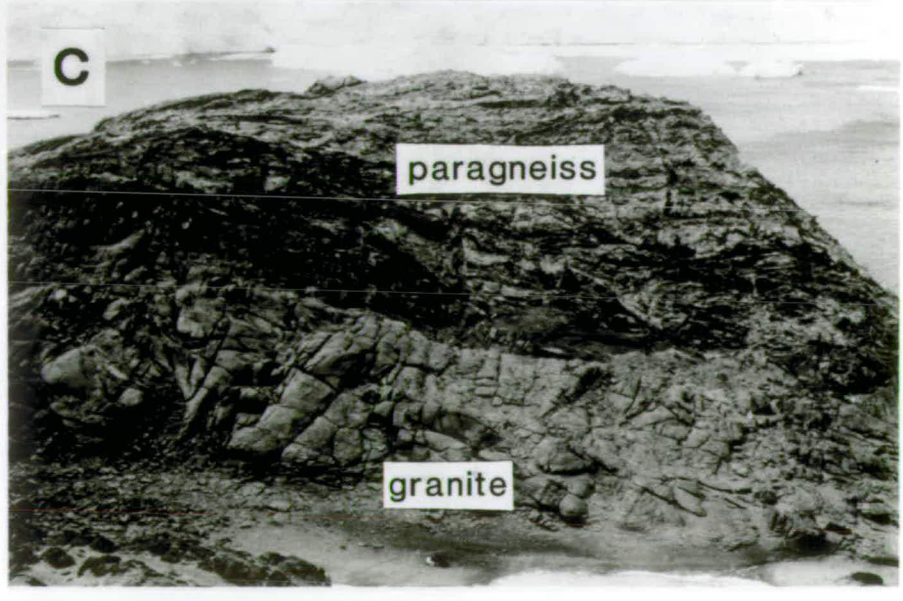
c
paragneiss
granite

crystals with euhedral to subhedral shapes, which are indicative of growth in a magmatic environment.

(ii) The aligned feldspar crystals show little or no evidence of plastic deformation or recrystallization.

(iii) K-feldspar grains commonly have simple twins, which imply an igneous origin.

(iv) Plagioclase grains are elongate parallel to the length of their multiple twins, consistent with an igneous origin.

(v) The aligned crystals are surrounded by anhedral grains or grain aggregates of quartz, which show little or no evidence of plastic deformation. This suggests that there was no deformation after quartz crystallization.

(vi) The obliquity of K-feldspar grains to graded layering in the Amanda Bay Granite is consistent with imbrication during magmatic flow.

3.4 STRUCTURE

3.4.1 Introduction

Seven phases of deformation have been identified and are labelled D_1 to D_7. These deformational episodes, and their associated fabrics and structures, are listed in Table 3.8 and discussed in more detail below. Regional structural features and trends are determined principally by D_3, D_4 and D_5, and are illustrated in Fig. 3.3. Equal-area projections of structural data are presented in Fig. 3.4.

3.4.2 The first deformation

Mafic granulite bodies in the composite orthogneiss have a planar fabric (S_1) and lineation (L_1), defined by millimetre-scale compositional banding and mineral orientation (see Section 3.2.2). These fabrics are truncated by the foliation of the enclosing felsic gneiss (S_3; see Section 3.4.3), and are the oldest fabrics preserved in the field area. The mafic bands and bodies are the only units that preserve S_1 and L_1. The extent to which S_1 and L_1 have re-equilibrated or recrystallized during later events is difficult to assess due to the apparent continued stability of syn-D_1 mineral assemblages, and the relationships between D_1 and later events cannot be assessed.

3.4.3 The second deformation

Structures attributed to D_2 are not common, but rare isoclinal fold hinges in the composite orthogneiss, and helicitic inclusion textures in metapelitic garnet grains (F_3; see Section 3.4.4), fold an earlier S_2 foliation. S_2 is defined by lithological layering of mafic and felsic material in the composite orthogneiss, and hence post-dates S_1. In the metapelite, S_2 is defined by the orientation of acicular sillimanite (see

Plate 3.4a). For simplicity, it is assumed that both these fabrics reflect the same deformational event, although comparison is made difficult by the difference in scale and lithology.

Table 3.8 Summary of the geological and structural history of the Brattstrand Bluffs coastline.

Age	Event	Structures and fabrics	Metamorphism
Archaean ?	Orthogneiss protolith formation		
	D_1	S_1 and L_1 in mafic component of orthogneiss	Granulite
	Syn- to post-D_1 partial melting	Pl-Opx-Qtz segregations in mafic gneiss parallel and discordant to S_1	Granulite
	Migmatization of orthogneiss	Felsic melt injected into and derived from mafic protolith to produce mafic schlieren and rafts in felsic gneiss	Granulite
	Erosion and deposition of paragneiss precursor		
	D_2	a) Interleaving of orthogneiss and paragneiss b) S_2 preserved in rare F_3 hinges	Upper amphibolite?
1000 Ma	D_3	a) Early F_3 isoclines preserved in orthogneiss and F_3 helicitic Sil in metapelitic Grt b) Intense flat-lying S_3 defined by Sil in metapelite, Opx-Bt in felsic orthogneiss Bt or Opx in semi-pelite and Bt-Opx in intermediate gneiss c) Partial melting of metapelite to produce migmatite and discordant leucogneiss sheets d) Intrusion of granitic orthogneiss	Granulite
	D_4	a) Early flat-lying asymmetric F_4 b) Intense flat-lying S_4/L_4 fabric defined by Bt-Sil-Spl in metapelite (no phase change from S_3 in other lithologies)	Granulite
	D_5	a) Emplacement of syn-D_5 granite pluton at Amanda Bay and related dykes b) Reorientation of earlier structures about a regional antiform plunging shallowly southwest c) Parasitic F_5 and S_{5a} and S_{5b} shears in the vicinity of Amanda Bay	Upper amphibolite?
770 Ma	D_6	a) Large-scale flexing of earlier structures b) Intrusion of upright planar pegmatite bodies	
500 Ma	D_7	a) Intrusion of granite at Dalkoy Island b) Upright mylonite zones	Greenschist

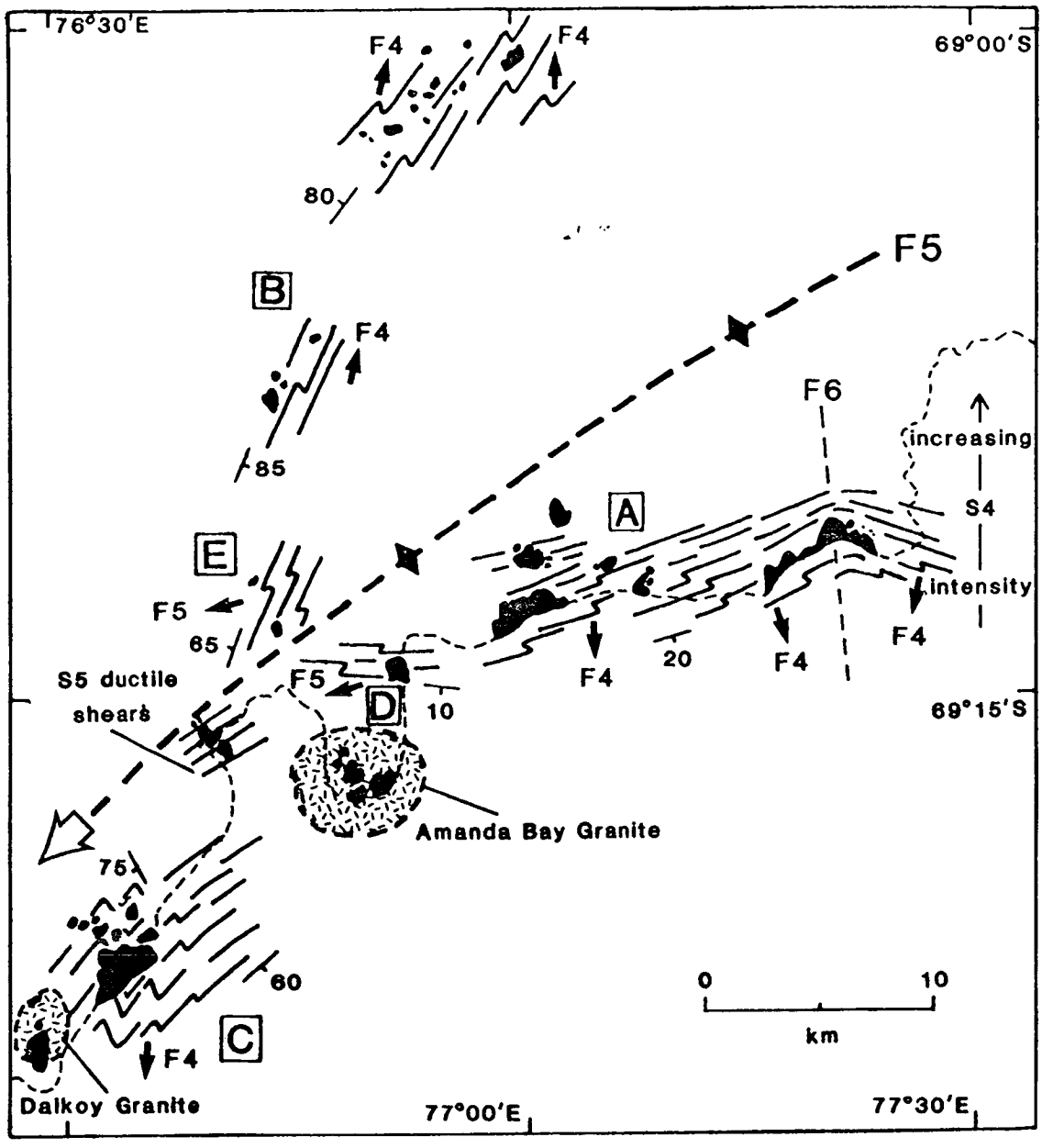

Fig. 3.3 A map of the structural trends defined by S_3, or locally S_4, in the Brattstrand Bluffs coastline. The map also indicates representative strike and dip values, the vergence and fold-axis orientation of mesoscopic F_4 and F_5 folds, and the trace of the regional F_5 antiform.

3.4.4 The third deformation

Interlayered mafic and felsic units (S_2; see Section 3.4.3) in the composite orthogneiss are folded about rare, intrafolial, isoclinal hinges, which have been ascribed to D_3. The F_3 hinges are commonly 0.1 to 10 m across, but a large refolded isocline about 100 m wide occurs at Steinnes Peninsula (see Appendix 1). These isoclines are enclosed within, and transposed by, the dominant regional foliation of the area (S_3), which appears to be axial planar to F_3 in the few localities that both can be identified and has been ascribed to a later stage of D_3. Folded inclusion trails in metapelitic

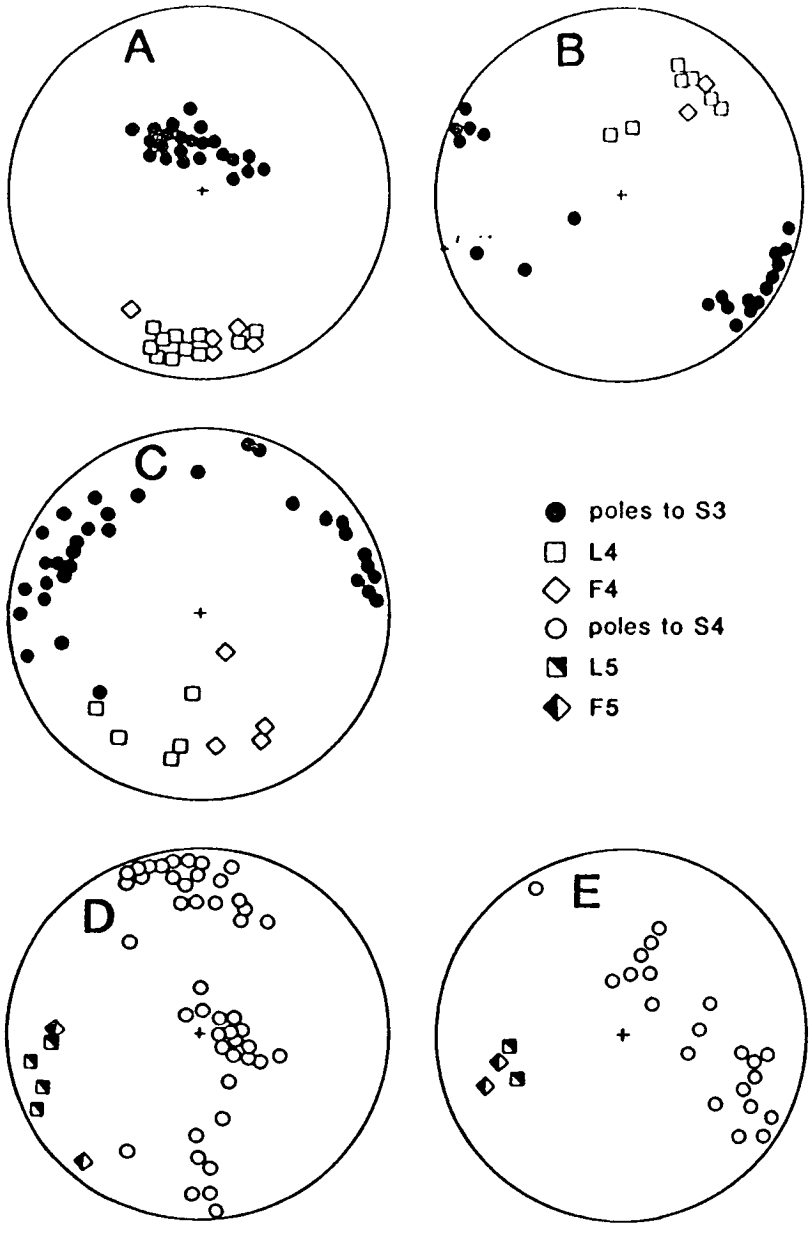

Fig. 3.4 Representative equal-area projections of lineations, fold axes and poles to foliations in the Brattstrand Bluffs coastline. Each projection corresponds to one of the areas A to E marked on Fig. 3.3.

garnet, also ascribed to F_3, are enclosed within an external S_3 foliation. Except where overprinted by localized planar and linear fabrics (S_4 and L_4; see Section 3.4.5), S_3 is the dominant fabric element in all gneissic lithologies apart from the mafic granulite, which preserves S_1 and L_1 (see Section 3.3.2). Compositional layering between units in both lithological associations is mostly parallel to S_3, which is commonly defined by preferred orientation of elongate grains and grain aggregates, as detailed in the lithological descriptions (see Section 3.2).

3.4.5 The fourth deformation

D_4 is the most pervasive folding event on outcrop scale. Metre-scale F_4 asymmetric structures fold S_3 compositional layering and foliation (see Plate 3.3c), and are commonly non-cylindrical. F_4 structures are transposed in local areas of high strain characterized by ductile shear and a penetrative planar fabric (S_4). In most lithologies, S_4 is similar to S_3 on hand-specimen and microscopic scales, but S_4 in the metapelite can be distinguished by the presence of aligned biotite grains within the foliation. These areas of high strain are developed both as narrow zones, less than 1 m wide, along the long limbs of F_4 folds (see Plate 3.13a), and as extensive zones up to 20 m wide or more (see Plate 3.13b,c). High-strain zones are separated by less-deformed zones, which preserve attenuated S_3 foliations and F_4 structures. A mineral lineation of variable intensity (L_4) is defined by sillimanite and spinel in the metapelite. L_4 is best developed in areas exhibiting the greatest attenuation of S_3 and F_4 fabrics, particularly the high-strain S_4 zones. F_4 fold axes parallel this lineation.

At Brattstrand Bluffs, S_4 dips shallowly to the south, and its intensity increases with deeper D_4 structural level (i.e. towards the north). S_4 is not developed at Steinnes Peninsula, where asymmetric F_4 folds are completely preserved. S_4 is present on Hovde Island and Svenner 1 (see Section 3.4.6), but absent from the other Svenner Islands where F_4 fold style is considerably more asymmetric than at Steinnes Peninsula. It follows that D_4 intensity is greatest in a zone at the centre of the field area, which corresponds to the core of a younger regional antiform (see Section 3.4.6 and Fig. 3.5) and hence the deepest D_4 structural levels exposed (see Fig. 3.6).

There are substantial regional differences in F_4 and S_4 orientation and sense of vergence or shear. At Steinnes Peninsula, F_4 fold vergence varies consistently from east to west, and can be related to a series of larger-scale, south-plunging, F_4 synforms and antiforms. In the Svenner Islands, F_4 has a dextral vergence and sub-vertical plunge. At Brattstrand Bluffs, F_4 has a sinistral vergence and a shallow plunge (*c.* 15°) to the south. These F_4 orientations and vergences are inconsistent with a major F_4 fold closure between the Svenner Islands and Brattstrand Bluffs, but rather imply a single sense of F_4 asymmetry over a large region which has been refolded in a later regional deformation (see Section 3.4.6 and Fig. 3.7).

3.4.6 The fifth deformation

On outcrop and microscopic scales, Svenners 2, 3 and 4 and Brattstrand Bluffs show no evidence for major post-D_4 ductile deformation. However, comparison of S_3, F_4 and L_4 orientations in each area indicates the presence of a large antiformal structure (F_5) between the Svenner Islands and Brattstrand Bluffs, plunging shallowly (*c.* 20°) to the southwest (see Fig. 3.7). Further southwest, F_5 plunge increases, causing F_4

PLATE 3.13

Plate 3.13a

Leucogneiss sheets and metapelite folded into a sinistral F_4 structure at Brattstrand Bluffs, looking south (i.e. down plunge). There is localized S_4 shearing along the sub-horizontal dextral limbs. The hammer is 0.3 m long.

Plate 3.13b

Leucocratic metapelite at Brattstrand Bluffs showing a sub-horizontal S_4 planar fabric and partly-transposed F_4 fold closures. The lens cap is 50 mm in diameter.

Plate 3.13c

Penetrative sub-horizontal S_4 shear fabric in a metapelite at Brattstrand Bluffs. The lens cap is 50 mm in diameter.

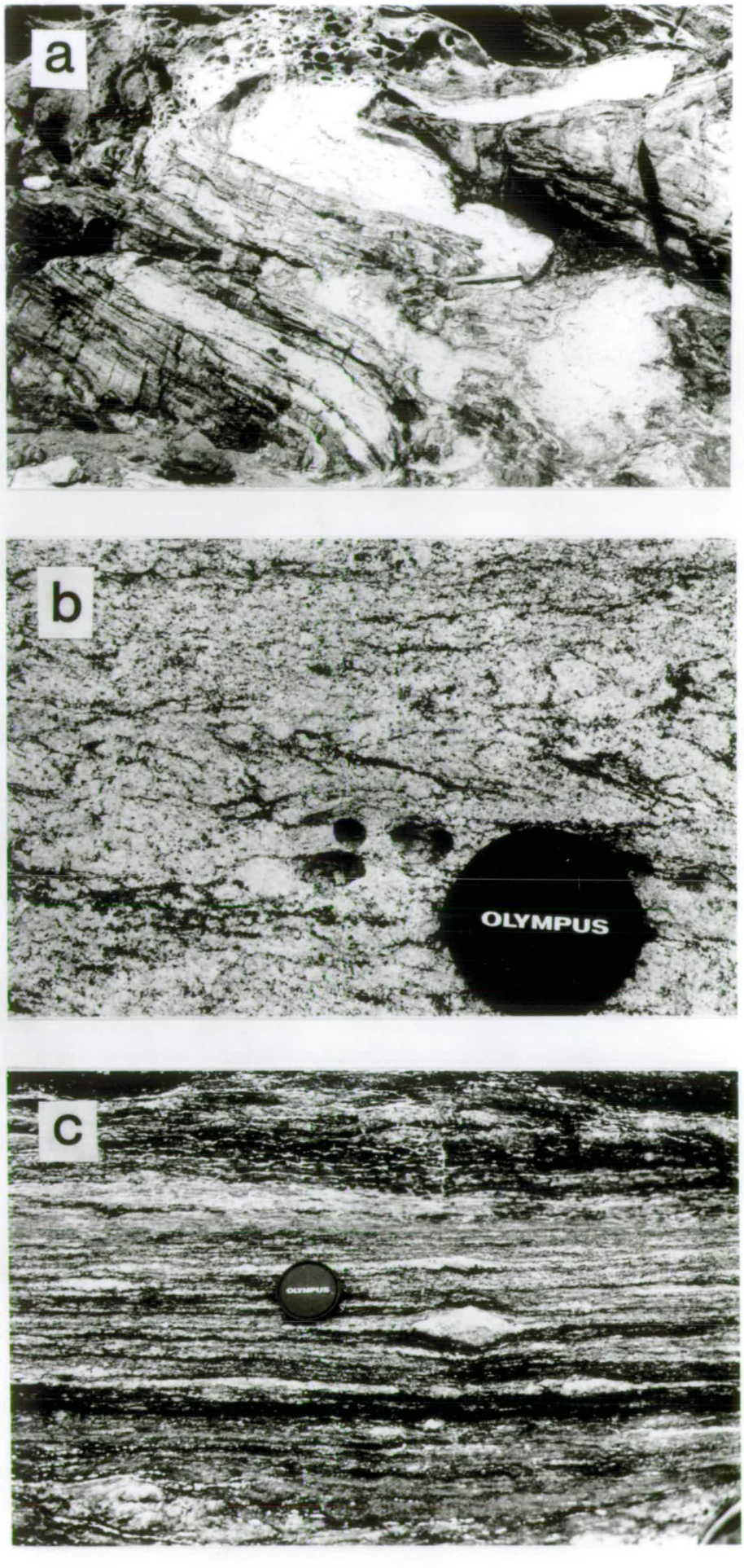
a
b
OLYMPUS
c
OLYMPUS

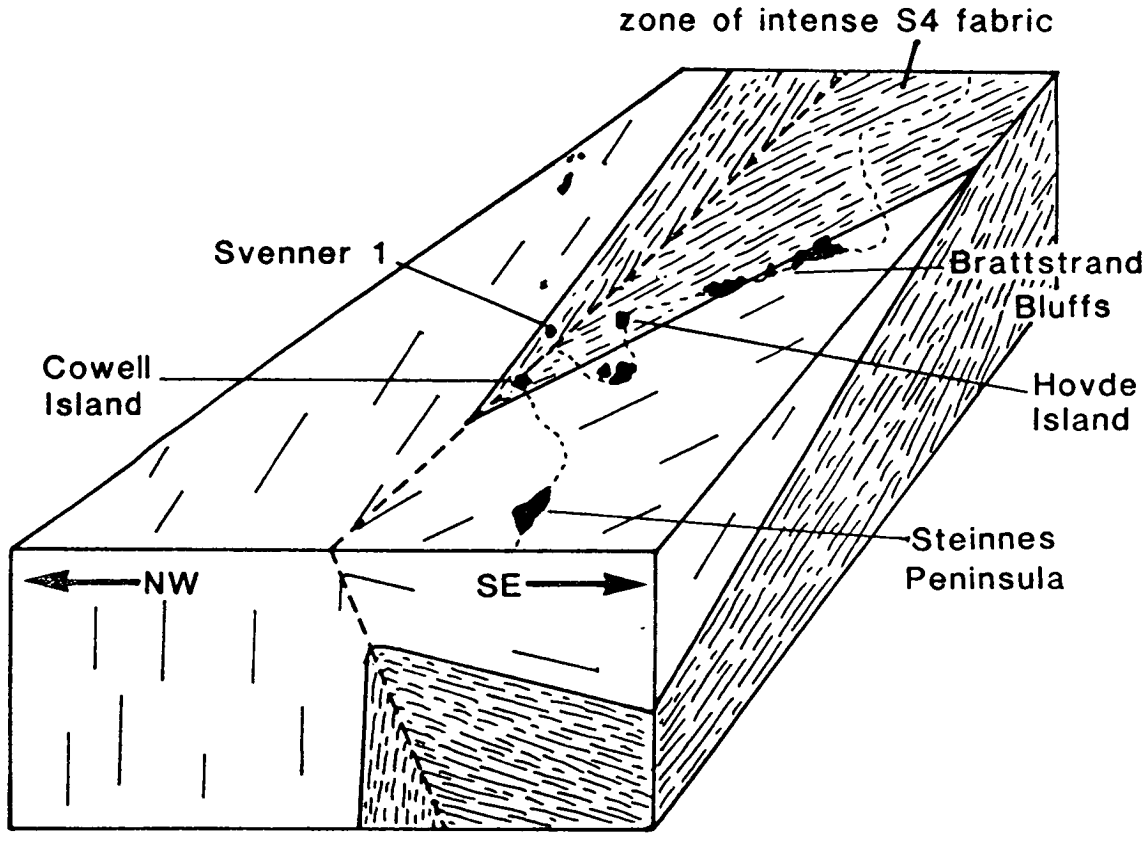

Fig. 3.5 Block diagram depicting the inferred zone of intense S_4 fabric at the F_5 antiformal core and its relationship to various geographical localities.

Fig. 3.6 Cartoon depicting the variation in intensity of D_4 structures along the Brattstrand Bluffs coastline in terms of increasing D_4 structural depth. No scale is implied.

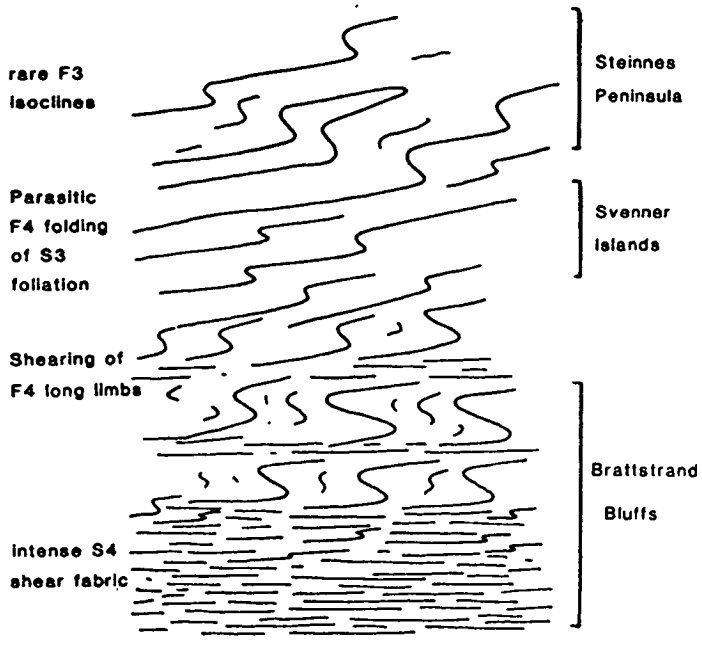

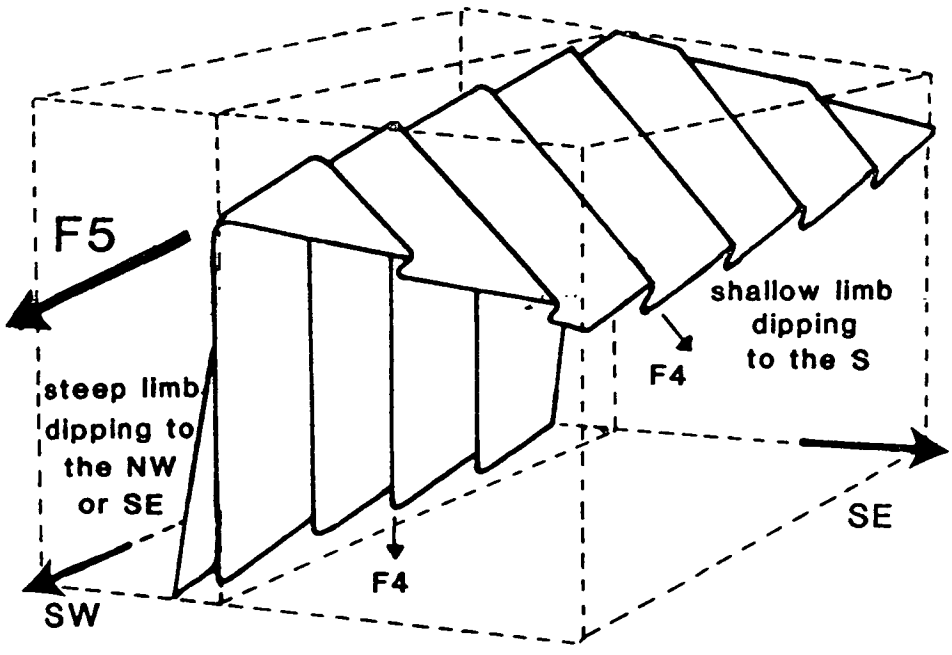

Fig. 3.7 Block diagram showing the effect of the F_5 antiform on the orientation of F_4 structures. The size of the F_4 structures has been exaggerated with respect to the F_5 antiform.

axes at Steinnes Peninsula to plunge more steeply (30-50°), and F_4 folds to be more upright, than at Brattstrand Bluffs.

D_5 structures are observed on outcrop and microscopic scale at Hovde Island, Svenner 1 and Cowell Island, and are depicted schematically in Fig. 3.8. An intense S_4 foliation at Hovde Island and Svenner 1, defined by sillimanite, spinel and biotite in metapelite, is deformed by microscopic F_5 folds (see Plate 3.7b) and by mesoscopic asymmetric F_5 folds plunging shallowly (10-40°) southwest (see Plate 3.14a). F_5 vergence is dextral on Hovde Island, but sinistral on Svenner 1. At the southern ends of both islands, the long limbs of F_5 structures are partly transposed by narrow shear zones (S_{5a}), which trend southwest and are less than 50 mm wide (narrower than S_4 shear zones). S_{5a} shears have a sinistral sense of movement on Hovde Island and a dextral sense on Svenner 1. They commonly contain garnet and sillimanite, and leucogneiss or quartz lenses. S_{5a} shears are interpreted as localized zones of high D_5 strain. Both F_5 and S_{5a} are associated with an L_5 lineation, which is approximately parallel to F_5 axes and defined by quartz ribbons and sillimanite. All the orientational and vergence relationships are consistent with these mesoscopic to microscopic fabrics and structures being parasitic to the regional southwest-plunging antiform inferred from regional variation in S_3 and F_4 orientations (see Fig. 3.8). The antiform axis lies between Hovde Island and Svenner 1. Hovde Island is on the shallow limb, southeast of the F_5 axis, but is located at or just northwest of the F_5 crest since many of the long limbs and shears dip shallowly northwest rather than south. Svenner 1 is northwest of the fold axis.

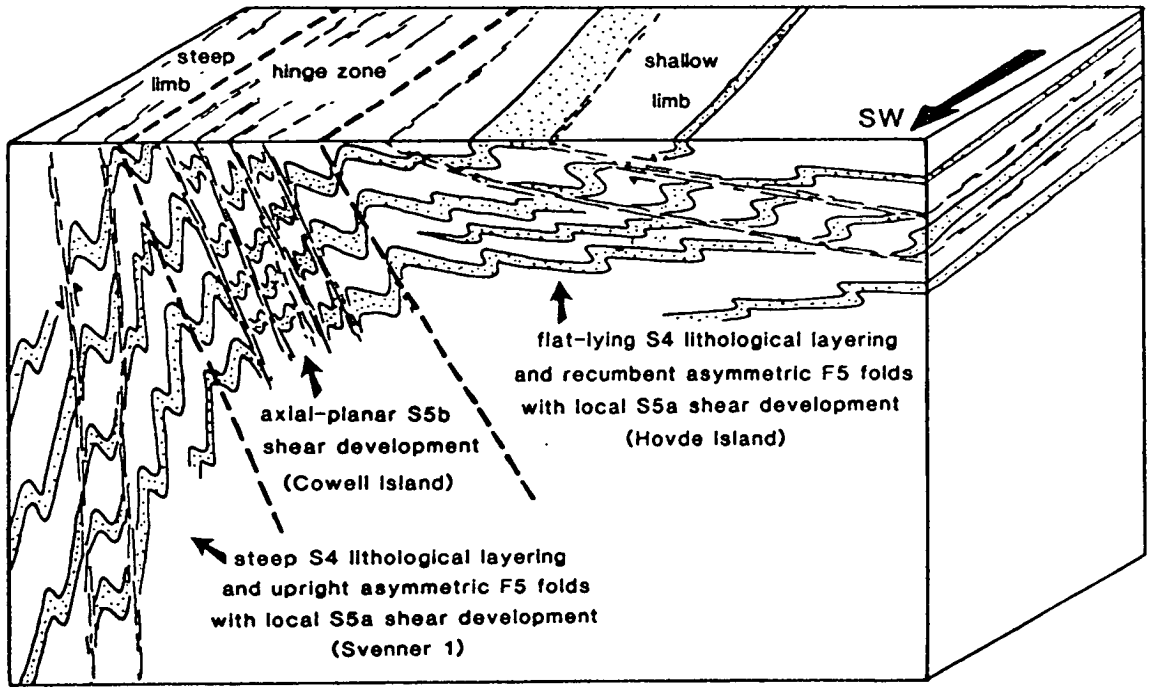

Fig. 3.8 A schematic block diagram depicting the mesoscopic D_5 structures developed on the steep limb, shallow limb and hinge zone of the regional F_5 antiform. The size of the mesoscopic structures has been exaggerated with respect to the scale of the antiform.

Cowell Island is dissected by a series of narrow, parallel, ductile S_{5b} shear zones (see Plate 3.14b), which trend southwest and dip steeply (*c.* 80°) southeast. They are of similar appearance to S_{5a} shears at Hovde Island and Svenner 1, but more closely spaced. The sense of shear changes across the island: sinistral in the southeast and northwest, but dextral in the central zone. Shear orientation is consistent with an axial-planar relationship to the regional F_5 antiform. The foliation between the shears dips steeply (60 to 85°) to the south, and is interpreted as S_4 since it is defined by sillimanite, spinel and biotite in the metapelite. F_5 parasitic folds are absent from Cowell Island, and sillimanite stretching lineations plunging moderately (20 to 45°) south or southeast are interpreted as L_4 rather than L_5 (which plunges southwest, see above). L_4 and S_4 fabrics dip more steeply at Cowell Island than L_4 and S_4 at Hovde Island, Brattstrand Bluffs or the Svenner Islands. This could reflect either regional steepening of the F_5 plunge to the west of Hovde Island, as proposed to explain L_4 orientation at Steinnes Peninsula, or smaller-scale rotation between steep-dipping S_{5b} shears. Consistent differences in strike (*c.* 40°) between S_4 foliations cut by dextral and sinistral S_{5b} shears implies about 20° of syn-D_5 rotation in a horizontal plane and a sense dependent on the sense of shearing. If this rotation is due to axial-planar shearing, with a direction of shear perpendicular to the fold axis, a greater component of rotation would be expected in the vertical plane perpendicular to the shears, since

PLATE 3.14

Plate 3.14a
Folded composite orthogneiss at Hovde Island, looking southwest (i.e. down plunge). The mafic layer is folded into a shallowly-plunging dextral F_5 structure. The lens cap is 50 mm in diameter.

Plate 3.14b
A southwest trending, sub-vertical, sinistral S_{5b} shear zone in metapelite at Cowell Island. The lens cap is 50 mm in diameter.

Plate 3.14c
A D_7 mylonitic shear zone developed in metapelite parallel to a pegmatite body at Brattstrand Bluffs. Pencil for scale.

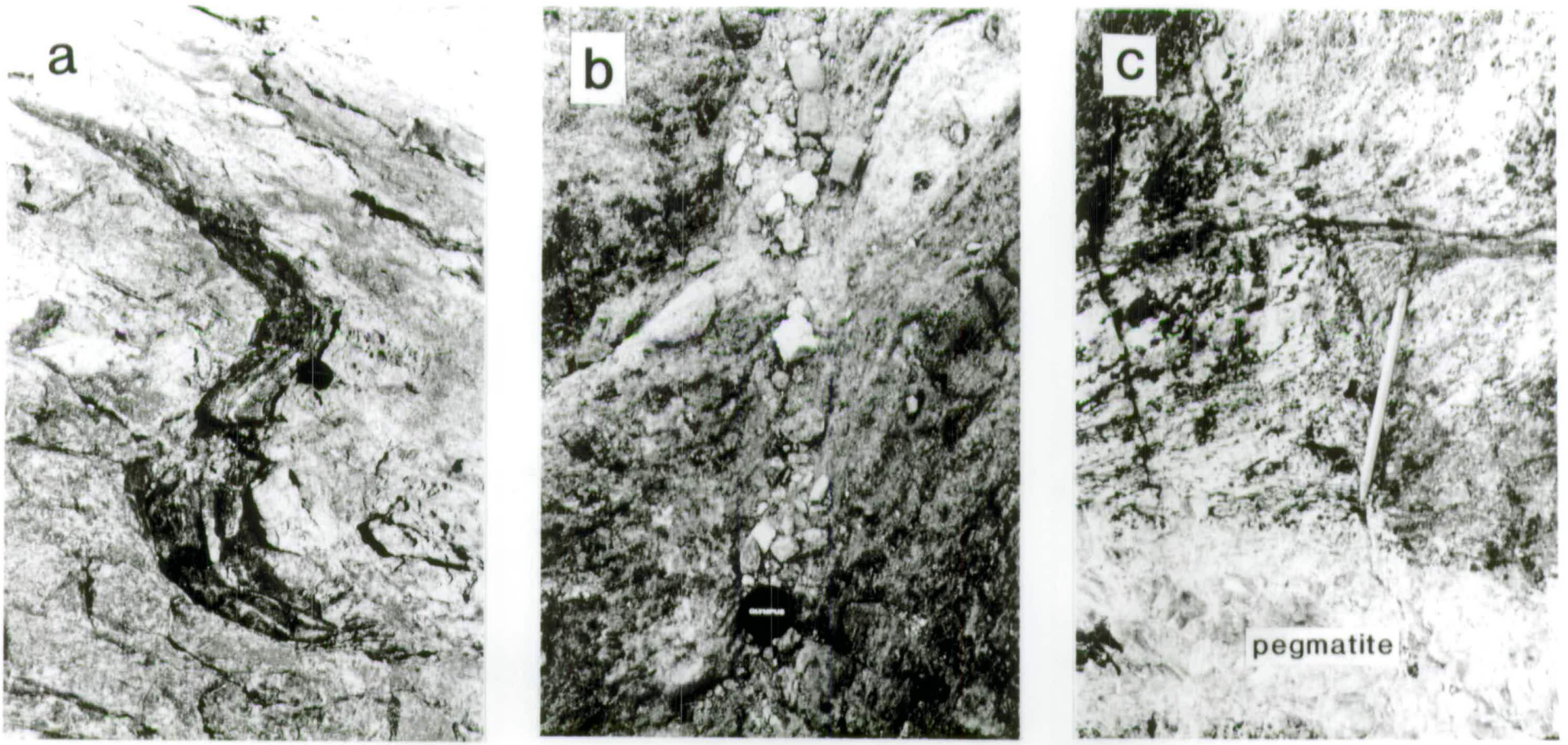
a
b
c
pegmatite

F_5 has a shallow plunge. However, no evidence has been found of a bimodal distribution of S_4 dip.

The Amanda Bay Granite has a flat-lying foliation interpreted as an igneous fabric (see Sections 3.3.2 and 3.3.5), and has not been greatly affected by sub-solidus deformation. However, related granitic dykes (see Section 3.3.2), which truncate D_3 and D_4 structures in the Svenner Islands and Brattstrand Bluffs, are locally deformed into a series of asymmetric steps. The vergence of these steps is consistent with a parasitic relationship to the F_5 antiform.

3.4.7 The sixth deformation

A flexure of S_4 foliations in eastern Brattstrand Bluffs causes a change in strike of 30 to 40° (see Fig. 3.3). This orientation change is attributed to D_6, and occurs in an area cut by numerous pegmatite bodies (see Appendix 1), which are approximately axial planar to the flexure. The relative timing of pegmatite intrusion and D_6 is not clear, but they appear to be related. A similar late-stage flexure may be responsible for the steepening of the F_5 antiform at Cowell Island and Steinnes Peninsula.

3.4.8 The seventh deformation

Narrow sub-vertical mylonite zones dissect all lithologies except the Dalkoy Granite, and are attributed to D_7. Mylonite zones are less than 1 m wide, and commonly occur within or at the edges of planar pegmatite bodies (see Plate 3.14c). Mineral assemblages on either side of these mylonites commonly exhibit a metamorphic overprint characterized by green amphibole, epidote and chlorite.

3.4.9 Summary and interpretation of structure

S_1, S_2 and F_3 are early structures, which are commonly transposed by S_3 fabrics. S_1 is only preserved in mafic granulite bodies. S_2 and F_3 are locally preserved in the orthogneiss and the metapelite. The preservation of early fabrics in the composite orthogneiss is attributed to the competence and stability of syn-D_2 orthogneiss assemblages throughout syn-D_3 metamorphism. In contrast, the paragneiss units underwent significant migmatization and metamorphic re-equilibration during D_3, decreasing the survival potential of earlier structures. S_2 and F_3 structures were only preserved in paragneiss assemblages if mantled by syn-D_3 porphyroblast growth. The limited extent of S_1, S_2 and F_3 structures precludes a detailed analysis of their origin, although some inferences can be made from a combination of structural and lithological evidence (see Section 3.5). The rest of this section is concerned with the deformation responsible for the widespread S_3 fabric, and particularly its subsequent modification by F_4 folds, localized S_4 shear fabrics, and finally regional D_5 structures

accompanied by smaller-scale structures around Amanda Bay.

D_4 structures are sub-parallel to S_3, and both are assumed to have been flat lying before the development of the regional F_5 antiform. S_3 is a homogeneous foliation, which is layer parallel to the compositional banding in most lithologies. Anatexis of the metapelite, and formation of the metapelitic migmatite and leucogneiss, occurred during and immediately after S_3 development, and reflect peak metamorphism. D_4 structures reflect progressive deformation after the metamorphic peak. Flat-lying asymmetric F_4 folds developed during non-coaxial simple bulk shear (Berthé & Brun, 1980). Cobbold and Quinquis (1980) have shown that highly non-cylindrical sheath folds develop at high strains within shear zones, and only require small perturbations of fabric to form. However, folds formed within shear zones need not have such curvilinear hinges, and Coward and Potts (1983) have shown how cylindrical asymmetric folds, with linear hinges and uniform vergence, can form at high strain in shear zones with some differential component of movement. The observed parallelism of F_4 axes with the intense L_4 stretching lineation (see Fig. 3.4) reflects rotation of the fold axes towards the direction of extension during progressive high bulk strain (Escher & Watterson, 1974; Bell, 1978).

Subsequent strain was concentrated into discrete shear zones, initially along the long limbs of F_4 folds, and then into wider zones of S_4 non-coaxial ductile shear (Ramsay & Graham, 1970) in which no S_3 or F_4 structures are preserved. The relationship between S_3 and S_4 fabrics is similar to that of the S-C structures described by Berthé *et al.* (1979). Berthé *et al.* (1979) considered S and C fabrics to form simultaneously, but other workers have described examples where the intrafolial S surfaces developed before transecting C surfaces (Vernon *et al.*, 1983; Lister & Snoke, 1984). The presence of biotite in S_4 (C surfaces) within the metapelite, but not in S_3 (S surfaces), indicates a two-stage timing for the structures discussed here. The intensity of S_4 increases with structural depth. This is consistent with a major D_4 detachment zone occurring somewhere below present outcrop levels in the Brattstrand Bluffs coastline, perhaps beneath the Ranvik Glacier.

D_5 structures are upright rather than flat lying, and reflect a different stress regime. The regional structure of the area is dominated by a large southwest-trending F_5 antiform. Brattstrand Bluffs, Hovde Island, and Steinnes Peninsula lie on the southeastern, south-dipping, shallow limb. All the Svenner Islands lie on the northwestern sub-vertical limb. Cowell Island is probably close to the F_5 hinge zone, since it is dissected by shear zones which are axial planar to the F_5 antiform and which might be expected to be most intense at the fold axis. The F_5 axis plunges shallowly southwest, but is steeper at Cowell Island and Steinnes Peninsula.

The restriction of parasitic mesoscopic and microscopic D_5 structures to outcrops around Amanda Bay could reflect their proximity either to the F_5 fold axis or the large pluton at Amanda Bay. The Amanda Bay Granite crystallized after most of the D_5 deformation, but related dykes exhibit F_5 parasitic structures. Hence the granitic intrusive activity is inferred to have been synchronous with D_5. The F_5 antiform has a profound effect on the orientation of D_4 structures: S_4 is most intense in the core of the F_5 antiform, and F_4 parasitic fold axes plunge shallowly south on the shallow limb of the F_5 antiform, and steeply north or northeast on the steep limb. Hence the apparent vergence of parasitic F_4 folds depends not only on their position with respect to major F_4 folds, but also with respect to the F_5 antiform. Localized deformation subsequent to the pervasive ductile events is attributed to D_6 and D_7, but has little affect on the regional structure.

3.5 A RELATIVE TIME FRAMEWORK OF GEOLOGICAL EVENTS

3.5.1 Introduction

This section outlines a relative time framework for the lithological and structural evolution of the Brattstrand Bluffs coastline, which is summarized in Fig. 3.9. The geological evolution is discussed in two stages: early events which pre-dated the development of the widespread S_3 fabric (Section 3.5.2), and events which were synchronous with or post-dated the development of the S_3 fabric (Section 3.5.3). Some basic inferences are made about the metamorphic conditions during this evolution (Section 3.5.4), but a quantitative assessment of the metamorphic history is left until Chapters 5 and 6.

3.5.2 Pre-S_3 evolution

The earliest features preserved are S_1 and L_1 structures in the mafic granulite. Melt veins and segregations within the mafic bodies formed during and after D_1. These mafic units were then incorporated into the composite orthogneiss, which was produced by some combination of melting of mafic granulite and injection of felsic material. This migmatite event must have post-dated the formation of the internal textures preserved in mafic units (i.e. S_1, L_1 and the melt segregations), which are truncated by the felsic material, and pre-date D_2 which affected both mafic and felsic components. At temperatures appropriate to anatexis of mafic granulite, paragneiss lithologies would also undergo significant melting, unless there were substantial contrasts in water activity between lithologies. The widespread development of syn-D_3 migmatite textures in paragneiss lithologies makes it unlikely that these units had already suffered a previous melting episode, and hence suggests that the

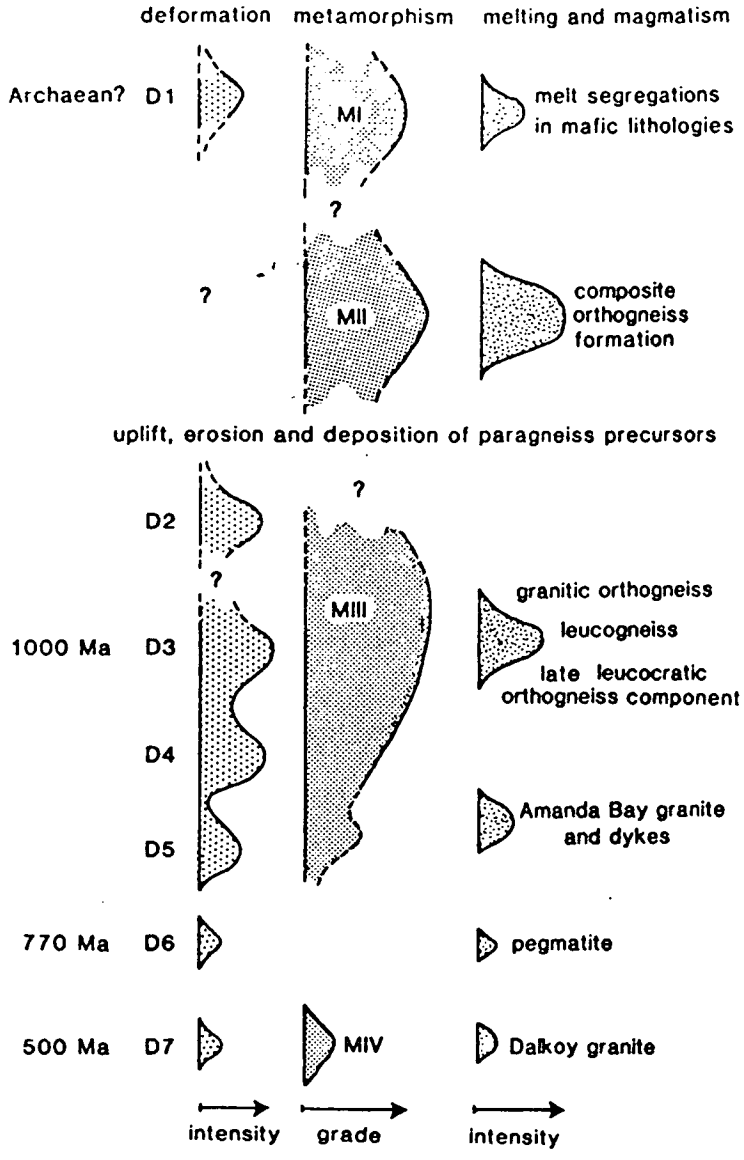

Fig. 3.9 A correlation diagram illustrating the relationships between deformation, metamorphism, melting and magmatism along the Brattstrand Bluffs coastline.

paragneiss was not at the same structural level or site as the orthogneiss during pre-D_2 migmatization.

D_2 is preserved both in the orthogneiss and paragneiss. The spatial distribution of the two associations precludes the existence of a simple boundary between them (see Section 3.2.1). Contacts between the orthogneiss and paragneiss are fabric parallel (to S_3 at Steinnes Peninsula, and S_4 at Hovde), and the simplest interpretation is that the two associations have been tectonically interleaved at their boundary. In the absence of any evidence for a deformational event between D_1 and D_2, the interleaving of orthogneiss and paragneiss sequences has been ascribed to D_2. This leaves two possibilities for the relative timing of orthogneiss migmatization, and deposition of the paragneiss precursor.

(i) The paragneiss precursor was deposited before or after orthogneiss migmatization, but in an area not affected by the migmatite event. This sequence

was then interleaved with crustal material that had experienced the migmatite event (i.e. the composite orthogneiss) during D_2. In this case, the orthogneiss and paragneiss are two distinct tectonic units.

(ii) The paragneiss precursor was deposited onto the composite orthogneiss after the migmatite event. This requires a significant time interval between migmatization and deposition of the paragneiss precursor, to allow for exhumation of the migmatized orthogneiss. In this case, the orthogneiss and paragneiss are part of a single tectonic unit comprising basement and cover sequences, which were then interleaved during D_2. This is the simplest interpretation and the one preferred here.

D_2 must have occurred at lower temperatures than those during and immediately after D_1 and during D_3, so that syn-D_2 anatexis of the paragneiss did not occur. The S_2 fabrics were folded by F_3 structures, but there is little evidence for the nature of this folding event since F_3 structures are only rarely preserved within the pervasive S_3 fabric. However, F_3 is interpreted here as an early, prograde stage of D_3, which culminated in the widespread development of S_3 fabrics at the metamorphic peak.

3.5.3 Syn- and post-S_3 evolution

All major gneissic lithologies were formed prior to S_3, which transposes F_3 and earlier structures. Syn- to post-S_3 anatexis of the paragneiss sequences produced widespread migmatitic textures and segregated sheets of partial melt. The composite orthogneiss shows little evidence of melting at this stage, since it had already experienced substantial partial melting and desiccation prior to D_2. However, the coarse-grained felsic component of the orthogneiss, which is slightly discordant to the S_3 lithological layering of the other two components, is interpreted as a result of limited melting during this event. The granitic orthogneiss at Steinnes Peninsula, with an S_3 foliation developed at its edges, is further evidence of melt production and migration at this time.

Melt-related features in the metapelitic lithologies (see Section 3.2.3) are thought to reflect a syn-S_3 metamorphic peak. Most lithologies do not record any changes during the D_3 to D_4 interval, and areas with an intense S_4 fabric exhibit the same assemblages as areas with an S_3 fabric. However, the metapelite does preserve changes in mineral assemblage, including garnet and cordierite growth associated with anatexis at the metamorphic peak and formation of post-D_3 spinel-bearing symplectites. Flat-lying D_4 structures post-date all the migmatitic textures, and are attributed to progressive, non-coaxial shearing of the area, culminating in the development of biotite-bearing S_4 zones with an intense shear fabric. Coronas around spinel and ilmenite in the metapelite post-date S_4 fabrics. D_5 folded all pre-existing

structures about a regional antiform, and produced localized mesoscopic and microscopic structures in the vicinity of Amanda Bay.

Post-S_3 biotite is common to all lithologies, but its timing with respect to D_4 and D_5 is equivocal. In metapelitic lithologies, biotite must post-date D_3 and the post-D_3 symplectites, but it pre-dates or is synchronous with the S_4 foliation. It is interpreted as a reflection of the passage of hydrous fluids along the S_4 shear zones, following crystallization of the partial melts. Late biotite also occurs in lithologies adjacent to the syn-D_5 intrusions. It is assumed that biotite in the orthogneiss and other gneissic lithologies is also syn-D_4 or syn-D_5 in age. Various localized deformational and metamorphic events overprint the relationships discussed above. Pegmatite intrusion is associated with a flexure of earlier structures (D_6), and was post-dated by D_7 mylonitic shear zones, and the intrusion of a granite pluton at Dalkoy Island.

3.5.4 Qualitative summary of the metamorphic evolution

At least four metamorphic events have been distinguished, and their relationship with melting, magmatism and deformation is shown in Fig. 3.9. Low- to medium-pressure granulite-facies conditions (MI), consistent with the stability of garnet-absent mafic granulite (Green & Ringwood, 1967), prevailed during D_1. High-grade conditions, indicated by the formation of melt segregations, continued immediately after D_1, but the subsequent evolution is unknown and could have involved significant decrease in grade. A major melting event (MII) was responsible for composite orthogneiss formation prior to D_2 tectonic interleaving of the orthogneiss and paragneiss. Preservation of S_2 helicitic sillimanite within metapelitic garnet is consistent with at least upper-amphibolite conditions during D_2, as is the continued stability of orthopyroxene-bearing orthogneiss assemblages. The post-D_2 evolution is unknown.

All S_3 assemblages are consistent with low- to medium-pressure granulite-facies conditions during peak D_3 metamorphism and melting (MIII). Most lithologies do not record any change in conditions between D_3 and D_4, but rather indicate continued granulite-facies conditions throughout this interval. Cordierite-spinel symplectites in the metapelite reflect a decrease in grade after migmatite formation, and coronas around spinel and ilmenite indicate continued retrogression after D_4, but these retrograde assemblages, which are discussed in detail in Chapter 6, are still consistent with granulite-facies conditions. Syn-D_5 metamorphic assemblages are rare, and even those outcrops with microscopic D_5 fabrics generally show no evidence of a syn-D_5 metamorphic overprint. It is difficult to identify any critical assemblages in D_5 shears, although the presence of garnet-sillimanite assemblages and leucogneiss and quartz lenses within S_5 shear zones probably imply medium- to high-grade conditions. All these features, and the stability of garnet and sillimanite and growth of biotite in

gneisses adjacent to the syn-D_5 intrusions, are consistent with at least amphibolite-facies conditions during D_5. All the assemblages developed during the D_3 to D_5 interval reflect a retrograde evolution from the MIII peak. A localized greenschist-facies overprint (MIV) is associated with D_7 mylonite.

3.5.5 Absolute age constraints

Some of the events identified in the relative time framework presented above can be correlated with absolute ages derived from elsewhere within the Proterozoic Complex. The major syn-D_3 granulite-facies metamorphism and anatexis (MIII), and the subsequent D_4 to D_5 retrograde evolution, are correlated with the 1000 Ma event identified in the Rauer Group (Tingey, 1981; Kinny & Black, 1990; see Section 2.3.9). D_6 pegmatite is correlated with the 770 Ma pegmatite event (Black *et al.*, 1987; see Sections 2.3.5 and 2.3.6). D_7 mylonite development and associated metamorphic overprint (MIV) are ascribed to the 500 Ma event (Black *et al.*, 1987; see Sections 2.3.2 and 2.3.5), as is the emplacement of the Dalkoy Granite which is correlated with the granitic intrusion at Landing Bluff (Tingey, 1981; see Section 2.3.9). Absolute ages for events prior to D_3 are less clear. Isotopic characteristics of the paragneiss are consistent with derivation from a protolith aged between 1800 and 1600 Ma (Sheraton *et al.*, 1984), but the actual erosion of this protolith could have occurred at any stage between these dates and just before the 1000 Ma event. The age of D_2 is constrained to lie between the date of erosion and the 1000 Ma event. There are almost no constraints on the age of composite orthogneiss formation (MII), except that it must pre-date D_2 and probably pre-dates erosion and deposition of the paragneiss precursor (see Section 3.5.2). It is tempting, however, to correlate MII, and the earlier MI event recorded by the mafic granulite, with the Archaean ages derived from the Rauer Group (Kinny & Black, 1990).

Chapters 5 and 6 attempt to quantify the 1000 Ma event in the Brattstrand Bluffs coastline. However, some of the events prior and subsequent to the Proterozoic metamorphism are reconsidered in Chapter 8, which integrates this study with previous work in a discussion of the geological evolution of Prydz Bay.

4. The geology and structure of the Nemesis Glacier region

4.1 INTRODUCTION

The Proterozoic outcrops of the northern Prince Charles Mountains, Mac.Robertson Land, have been the subject of various regional reconnaissance studies (Crohn, 1959; McLeod, 1964; Tingey, 1972, 1982; see Section 2.3.8), and a detailed study focused on the Radok Lake area by McKelvey and Stephenson (1990). The northern Prince Charles Mountains cover an area of some 40,000 km^2 (see Fig. 4.1), and outcrops occur in three east-west trending ranges, the Athos, Porthos and Aramis Ranges, and in a series of large isolated massifs to the south and west of Beaver Lake. This chapter describes the field and petrographic relationships of the outcrops adjacent to the Nemesis Glacier, in the eastern Aramis Range. These outcrops comprise steep-sided massifs and nunataks, associated with areas of moraine and separated by variably-crevassed blue ice. The quality of exposure is variable, and is generally best on the western or southwestern (i.e. windward) side of outcrops, but access to these areas is commonly hindered by precipitous wind scours in the adjacent ice. The following outcrop areas were visited (see Fig. 4.2): Mt Bunt, Allison Ridge, Mt Afflick, Mt Trott, Mt Butterworth, Mt Ormay, Hall Nunataks, McLean Ridge, Francey Hill, Baseline Nunataks, Mt Abbs, Thompson Massif, Saxton Ridge, White Massif and Amery Peaks Massif. Locality maps and a list of collected specimens are presented in Appendices 1 and 2 respectively.

The outcrops comprise granulite-facies gneisses, with a complex history of deformation and intrusion at high grade. The layout of this chapter is similar to Chapter 3. Section 4.2 describes the field and petrographic features of the principal gneissic lithologies, Section 4.3 describes the deformed intrusive lithologies, which preserve intrusive contacts with the gneissic lithologies but have themselves experienced pervasive deformation, and Section 4.4 describes the intrusive lithologies which show no evidence of pervasive deformation. The structure of the area is discussed in Section 4.5, and Section 4.6 outlines a relative time framework for the relationships described in the preceding sections.

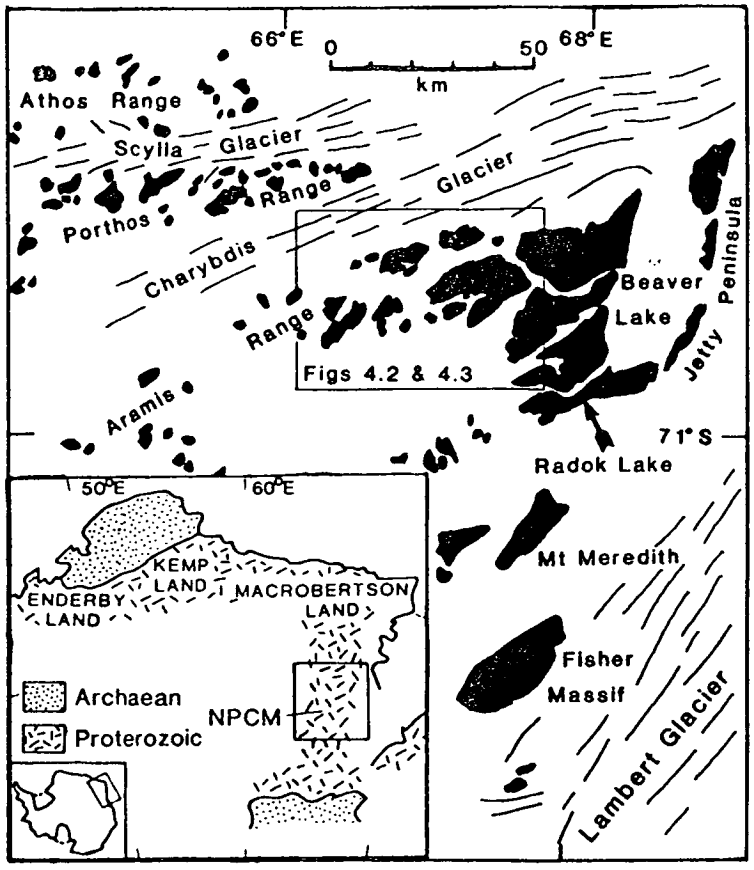

Fig. 4.1 A map of part of the northern Prince Charles Mountains in Mac.Robertson Land. The inset shows the location of this area (labelled NPCM) with respect to the Archaean and Proterozoic terrains between 50° and 70°E.

4.2 GNEISSIC LITHOLOGIES

4.2.1 Introduction

This section describes the principal gneissic lithologies, which preserve the earliest fabric identified on a regional scale (S_3; see Section 4.5.4). These lithologies account for about 85 per cent of the total outcrop (see Table 4.1), and comprise, in decreasing order of volumetric abundance, felsic gneiss, semi-pelite, mafic granulite, ultramafic rock, intermediate gneiss, amphibolite gneiss, calc-silicate and marble. No pelitic material was found in the area of study, although it has been identified elsewhere (e.g. Carter Peaks in the Athos Range; D.E. Thost *pers. comm.*, and Fitzsimons & Thost, 1991). These gneissic units are described in Sections 4.2.2 to 4.2.8, and their mineralogical features are summarized in Tables 4.2 and 4.3. The calc-silicate rocks are discussed in some detail since they preserve complex textural relationships, which are used to define the metamorphic history of the area in Chapter 7. Section 4.2.9 makes some preliminary interpretations of the origins of these lithologies.

4.2.2 Felsic gneiss

Pale-brown to yellow felsic gneiss is the most common lithology, and consists of quartz, plagioclase and microperthite with minor biotite, hornblende or

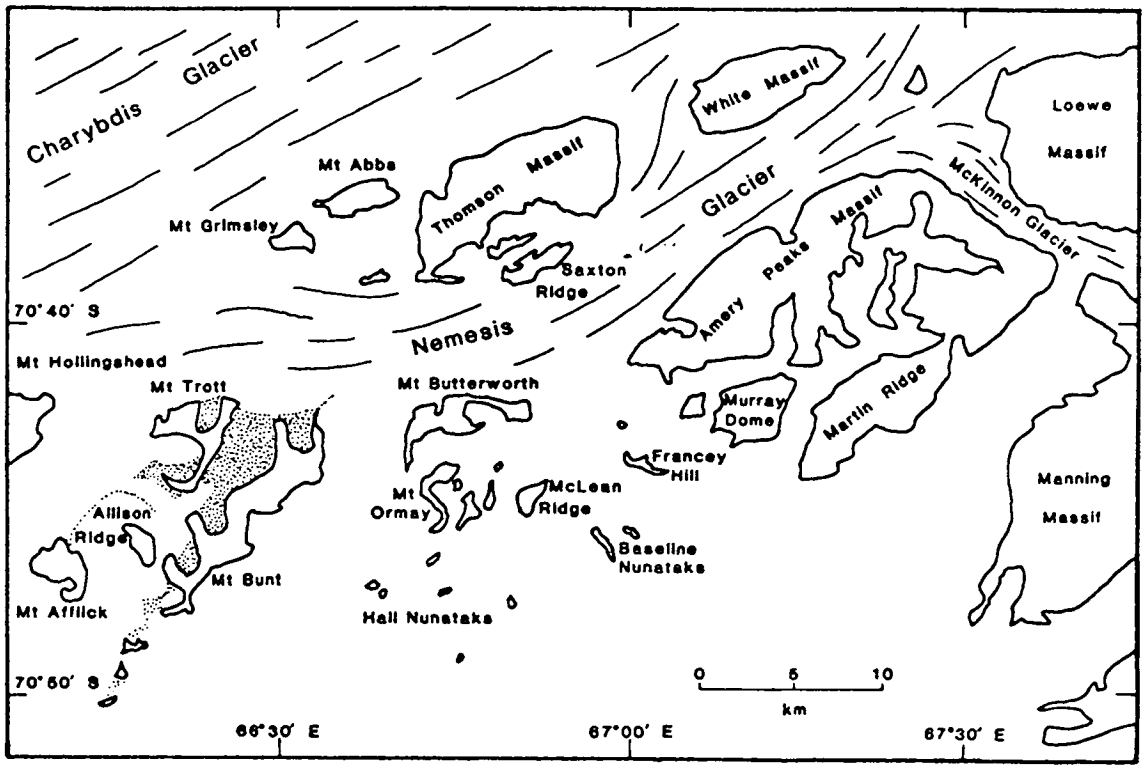

Fig. 4.2 A map of the outcrops adjacent to the Nemesis Glacier in the eastern Aramis Range, referred to here as the 'Nemesis Glacier region'.

orthopyroxene, and rare garnet (see Table 4.2). It is generally homogeneous over large areas and encloses isolated layers and boudins of mafic and ultramafic material (see Plate 4.1a,b). Locally however, felsic gneiss is intimately interlayered with other units, including semi-pelite, amphibolite and calc-silicate, on a scale of 1 to 10 m (see Plate 4.1c).

The felsic gneiss records several episodes of deformation (D_3 onwards), and its fabric varies from massive to strongly foliated or lineated. The planar and linear fabrics (S_3, or locally S_6 and L_6; see Sections 4.5.4 and 4.5.7) are defined by quartz ribbons, chains of orthopyroxene, and preferred orientation of hornblende, orthopyroxene and biotite, and are parallel to a lithological layering of enclosed boudins and interlayered gneiss. Quartz is typically blue in hand specimen, and occurs as two forms. Large xenoblastic grains up to 4 mm across have serrated grain boundaries and sub-grains, and small recrystallized blebs, less than 0.25 mm across, occur both within feldspar grains and at their interstices. Plagioclase and microperthite commonly have bent twin lamellae (D_8; see Section 4.5.9). Individual grains of orthopyroxene have ragged grain boundaries, but polygonal orthopyroxene-orthopyroxene boundaries are preserved within grain clusters. Hornblende is aligned parallel to chains of orthopyroxene, and is commonly fractured and sheared within

PLATE 4.1

Plate 4.1a
A zone of boudinaged mafic granulite bodies within homogeneous felsic gneiss at Mt Ormay. The horizontal field of view is about 10 m.

Plate 4.1b
A boudin of mafic granulite within felsic gneiss at Mt Bunt. The boudin preserves an S_1 foliation, which is truncated by the S_3 foliation of the enclosing felsic gneiss. The hammer is 0.3 m long.

Plate 4.1c
Calc-silicate and semi-pelite layers enclosed within banded felsic gneiss at Amery Peaks Massif. The foliation and boudinage are D_3 structures. The lens cap is 50 mm in diameter.

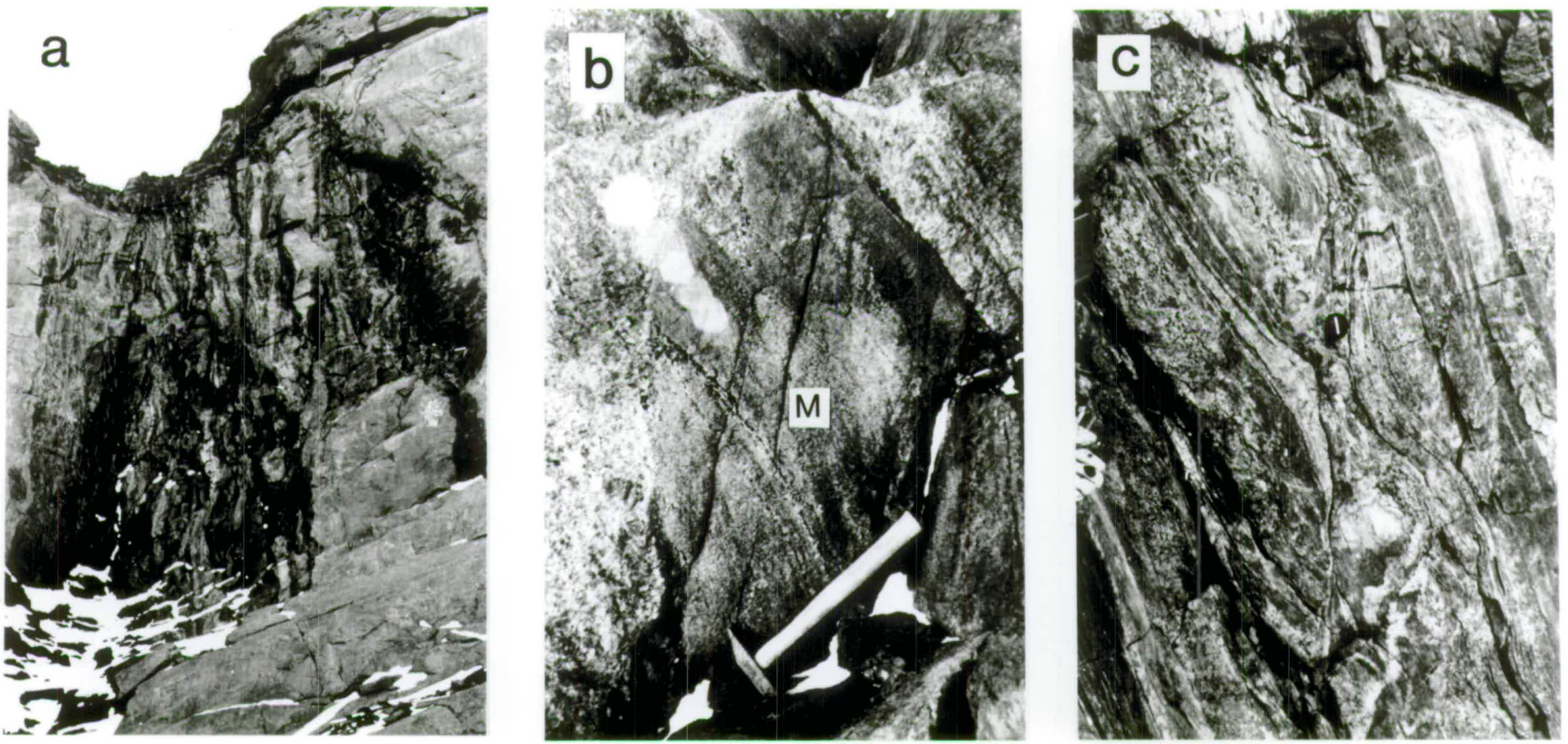
a
b
M
c

Table 4.1 The lithological constitution of the Nemesis Glacier region.

Association	Lithology		Relative abundance
Gneissic lithologies	Felsic gneiss		70%
	Mafic granulite		2%
	Ultramafic rock		1%
	Semi-pelitic gneiss	(1) garnet-biotite	10%
		(2) garnet-orthopyroxene	2%
	Banded amphibolite		Less than 1%
	Intermediate gneiss		Less than 1%
	Calc-silicate		Less than 1%
	Marble		Much less than 1%
Deformed intrusive lithologies	Leucogneiss		3%
	Charnockite		10%
	Metamorphosed mafic dykes		Much less than 1%
Undeformed intrusive lithologies	Late felsic bodies		-
	Pegmatite		-
	Late planar veins		-
	Unmetamorphosed dykes		-

Relative abundances are approximate only.

narrow mylonitic and sub-mylonitic zones. Biotite is present parallel to the foliation, and as randomly-oriented grains around orthopyroxene and hornblende. Lobate garnet grains contain inclusions of quartz, biotite and opaque phases, and accessory minerals include apatite and zircon.

4.2.3 Mafic granulite

Blocks and discontinuous layers of dark hornblende-orthopyroxene-clinopyroxene-plagioclase-ilmenite ± biotite ± quartz mafic granulite (see Table 4.2) occur within the felsic gneiss. The mafic bodies are typically 1 m across, and are boudinaged remnants of originally-continuous mafic layers. These boudinaged layers are concentrated within certain zones of the felsic gneiss (see Plate 4.1a), and are deformed along with their host by several deformational events (D_3 onwards), but also preserve early internal structures not seen in the host or other lithologies. Grain sizes are between 1 and 4 mm, and textures are polygonal granoblastic. However, a foliation of variable intensity (S_1; see Section 4.5.2 and Plate 4.1b) is defined by partial segregation of plagioclase from ferromagnesian minerals, alternation of hornblende-rich and pyroxene-rich layers, and preferred orientation of individual hornblende and pyroxene grains which also define a lineation (L_1). In some boudins, S_1 is deformed by a later folding event (F_2; see Section 4.5.3). These early fabrics are truncated by the foliation of the enclosing felsic gneisses (S_3). The mafic bodies commonly contain minor biotite and quartz. Randomly-oriented biotite occurs around

Table 4.2 Miscellaneous gneissic assemblages.

Felsic gneiss assemblages (and modal abundances):	
Prograde phases	Qtz(30-45%)-Pl(15-30%)-Kfs(20-55%)-Opx(0-5%)-Bt(0-5%)-Hbl(0-5%)-Grt(0-2%)
Retrograde phases	Bt, Bt-Pl symplectites
Accessory phases	Ilm-Ap-Zrn
Mafic granulite assemblages (and modal abundances):	
Prograde phases	Hbl(5-65)-Opx(5-35%)-Cpx(2-30%)-Pl(20-55%)-Bt(0-15)-Qtz(0-2%)-Ilm(0-5%)
Retrograde phases	Bt
Accessory phases	Ap
Ultramafic assemblages (and modal abundances):	
Prograde phases	Some combination of Opx, Cpx and Hbl
Retrograde phases	Bt
Accessory phases	Pl-Bt
Semi-pelite assemblages (and modal abundances):	
Prograde phases	(1) Grt(5-20%)-Bt(5-20%)-Pl(40-60%)-Qtz(10-40%)-Kfs(0-15%)
Retrograde phases	Bt
Accessory phases	Ilm-Ap-Zrn
Prograde phases	(2) Grt(3-15%)-Opx(3-30%)-Pl(15-50%)-Qtz(10-40%)-Kfs(10-30%)
Retrograde phases	Bt, Bt-Pl and Bt-Qtz symplectites around Opx
Accessory phases	Ap-Rt-Ilm-Zrn
Banded amphibolite assemblages (and modal abundances):	
Prograde phases	Hbl(20-50%)-Pl(20-35%)-Qtz(10-20%)-Bt(3-15%)-Opx(0-10%)-Kfs(0-20%)
Retrograde phases	Bt and opaque phases
Accessory phases	Ap-Zrn
Intermediate orthopyroxene gneiss assemblages (and modal abundances):	
Prograde phases	Opx(15-30%)-Bt(5-15%)-Pl(25-60%)-Qtz(5-35%)
Retrograde phases	Bt, Bt-Pl symplectites around Opx
Accessory phases	Ilm-Ap

Prograde phases represent S_3 and or S_6 assemblages, and retrograde phases overprint these fabrics.

hornblende and pyroxene, overprinting the polygonal fabric; but biotite also occurs aligned with the S_1 foliation and partly included by garnet. Apatite is a common accessory mineral. Rare orthopyroxene-plagioclase ± quartz segregations cut across the internal structure of the mafic bodies, but are truncated by the felsic host. The mafic bodies also exhibit rare orthopyroxene-bearing leucocratic selvages.

4.2.4 Ultramafic rock

Coarse-grained pyroxenite and amphibolite boudins are enclosed within felsic and various banded paragneisses, and commonly possess an internal foliation, sometimes folded, which is oblique to that of their host. Minor plagioclase and biotite are common.

4.2.5 Semi-pelitic gneiss

Well-layered semi-pelitic gneiss is common in the area, and two characteristic assemblages have been identified: garnet-biotite assemblages and garnet-orthopyroxene assemblages.

(i) Well-layered migmatitic garnet-biotite-quartz-plagioclase-K-feldspar gneiss has an intense foliation defined by the orientation of biotite laths (S_3, or locally S_6; see Sections 4.5.4 and 4.5.7), which is parallel to a compositional banding of quartzofeldspathic and garnet-biotite layers. Migmatitic textures include small leucocratic segregations with garnet-biotite selvages, which are typically 0.1 m across and transect the S_3 biotite foliation, and discordant leucogneiss sheets and lenses containing garnet-biotite schlieren (see Section 4.3.2).

(ii) Narrow horizons of garnet-orthopyroxene-quartz-plagioclase-K-feldspar ± biotite semi-pelite, typically less than 1 m wide, occur throughout the area. They are interlayered with garnet-biotite gneiss and orthopyroxene-bearing felsic gneiss, but are less common than these other two lithologies. A layer-parallel foliation of variable intensity is defined by chains of garnet and orthopyroxene (S_3 or locally S_6; see Sections 4.5.4 and 4.5.7). Grain sizes are up to 4 mm, and garnet and orthopyroxene preserve polygonal grain boundaries when in contact, but grain boundaries between ferromagnesian phases and the quartzofeldspathic matrix are rather irregular. Garnet contains equant inclusions of biotite, orthopyroxene, ilmenite, quartz and plagioclase, and orthopyroxene encloses garnet, quartz and plagioclase. Cross-cutting mylonite and associated micro-deformational features in quartz and feldspar reflect late deformation (D_8; see Section 4.5.9). Accessory minerals include opaque phases, rutile, apatite and zircon.

4.2.6 Banded amphibolite gneiss

Dark hornblende-plagioclase-quartz-biotite ± orthopyroxene ± K-feldspar gneiss is interlayered with semi-pelite and felsic gneiss on a metre scale, and has a well-developed layering defined by the modal abundance of hornblende. Hornblende is aligned parallel to the layering (S_3 or locally S_6; see Sections 4.5.4 and 4.5.7), and is commonly surrounded by partial coronas comprising small grains of biotite and opaque phases. Fragmentation of hornblende, deformation bands in quartz and plagioclase, bent twin lamellae in feldspar and cross-cutting mylonite and pseudotachylite are attributed to a late-stage deformation (D_8; see Section 4.5.9).

4.2.7 Intermediate orthopyroxene gneiss

Dark layers and boudins, comprising medium-grained orthopyroxene, plagioclase, biotite and quartz, are interlayered with felsic gneiss, semi-pelite and amphibolite.

Equant to elongate orthopyroxene grains are rounded, but polygonal orthopyroxene-orthopyroxene boundaries are preserved within grain clusters. A biotite foliation is parallel to a layering defined by modal abundance of orthopyroxene (S_3 or locally S_6; see Sections 4.5.4 and 4.5.7). Randomly-oriented biotite occurs around orthopyroxene and opaque phases. Deformation bands in quartz, bent plagioclase twin lamellae, fragmentation of orthopyroxene and kinked biotite are common.

4.2.8 Marble and calc-silicate gneiss

Discontinuous layers and boudins of calc-silicate are enclosed within, and interlayered with, orthopyroxene-bearing felsic gneiss and semi-pelite. Although widespread, calc-silicate rocks comprise only a small fraction of outcrop. Two types of body have been identified: complex boudins comprising interlayered marble and calc-silicate (e.g. at Saxton Ridge and Amery Peaks Massif), and relatively-homogeneous boudins with a modal zonation from core to rim (e.g. at Allison Ridge).

(i) The complex bodies are typically between 3 and 10 m wide, and comprise interlayered olivine ± clinopyroxene marble and calc-silicate (see Plate 4.2a). The calc-silicate exhibits a lithological layering on a scale of 10 to 150 mm, which is defined by bands comprising only two or three phases (see Plates 4.2b and 4.3). The boundaries between the bands are very distinct and approximately parallel to the edges of the marble units, but the bands are discontinuous on a metre scale and no consistent order of banding with respect to the marble units was identified. Both the marble and calc-silicate bands appear to be truncated by the foliation of the enclosing gneiss (S_3, or locally S_6; see Sections 4.5.4 and 4.5.7). The calc-silicate bands comprise various combinations of green clinopyroxene, dark blue or grey scapolite, white quartz, plagioclase, calcite and wollastonite and golden phlogopite (see Plate 4.3). Accessory phases include sphene and apatite. Some typical assemblages are listed in Table 4.3. Bands close to the marble units are dominated by wollastonite-clinopyroxene-scapolite-calcite layers and wollastonite-absent scapolite-quartz layers, whereas more-distant units are dominated by quartz and plagioclase.

(ii) The homogeneous calc-silicate boudins are typically less than 2 m wide and have no internal discontinuous banding, but do exhibit a continuous modal zonation from core to rim. Core assemblages are characterized by clinopyroxene, wollastonite and scapolite, and rarely garnet, whereas rim assemblages are dominated by clinopyroxene, quartz and plagioclase.

Both types of body are boudinaged parallel to the foliation of the enclosing gneiss (S_3; see Section 4.5.4), and are characterized by polygonal granoblastic textures with grain sizes between 0.25 and 3 mm (see Plate 4.4). Minerals such as scapolite,

PLATE 4.2

Plate 4.2a

Interlayered marble and calc-silicate within banded felsic gneiss at Baseline Nunataks. The horizontal field of view is about 10 m.

Plate 4.2b

Banded calc-silicate boudin within felsic gneiss at Amery Peaks Massif. The calc-silicate exhibits a lithological layering defined by modal abundance of dark clinopyroxene and scapolite, and light wollastonite and quartz. A layer of clinopyroxene occurs at the contact between the calc-silicate and the felsic gneiss. The hammer is 0.7 m long.

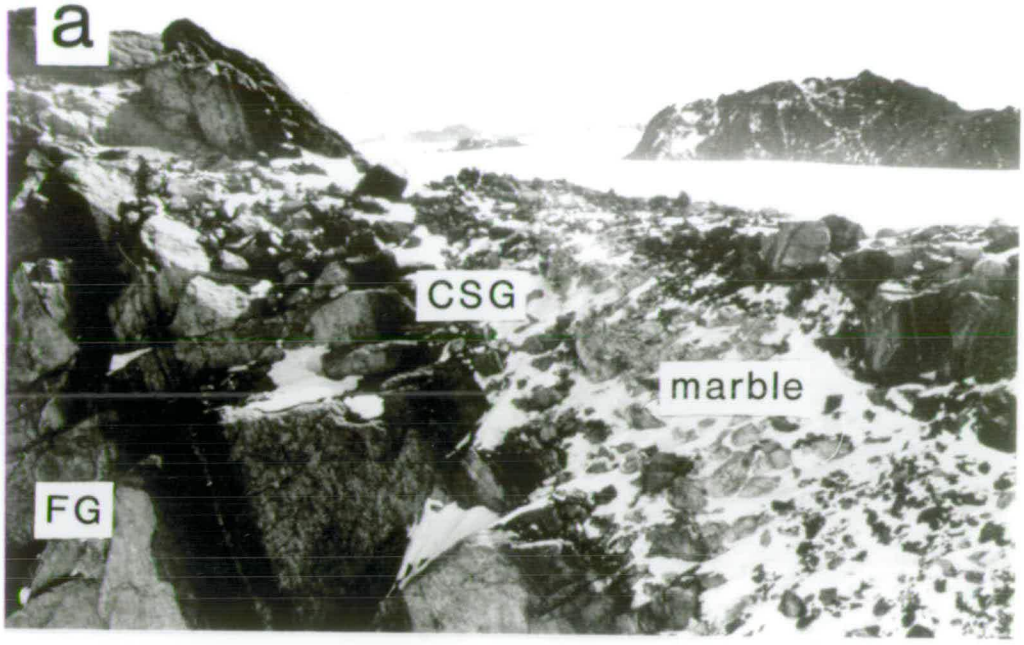
a
CSG
marble
FG


b
felsic
gneiss
calc-silicate

PLATE 4.3

Plate 4.3

Calc-silicate specimen from Amery Peaks Massif (specimen 89/334G). A foliation is defined by high-variance assemblage bands. The specimen is 14 cm high.

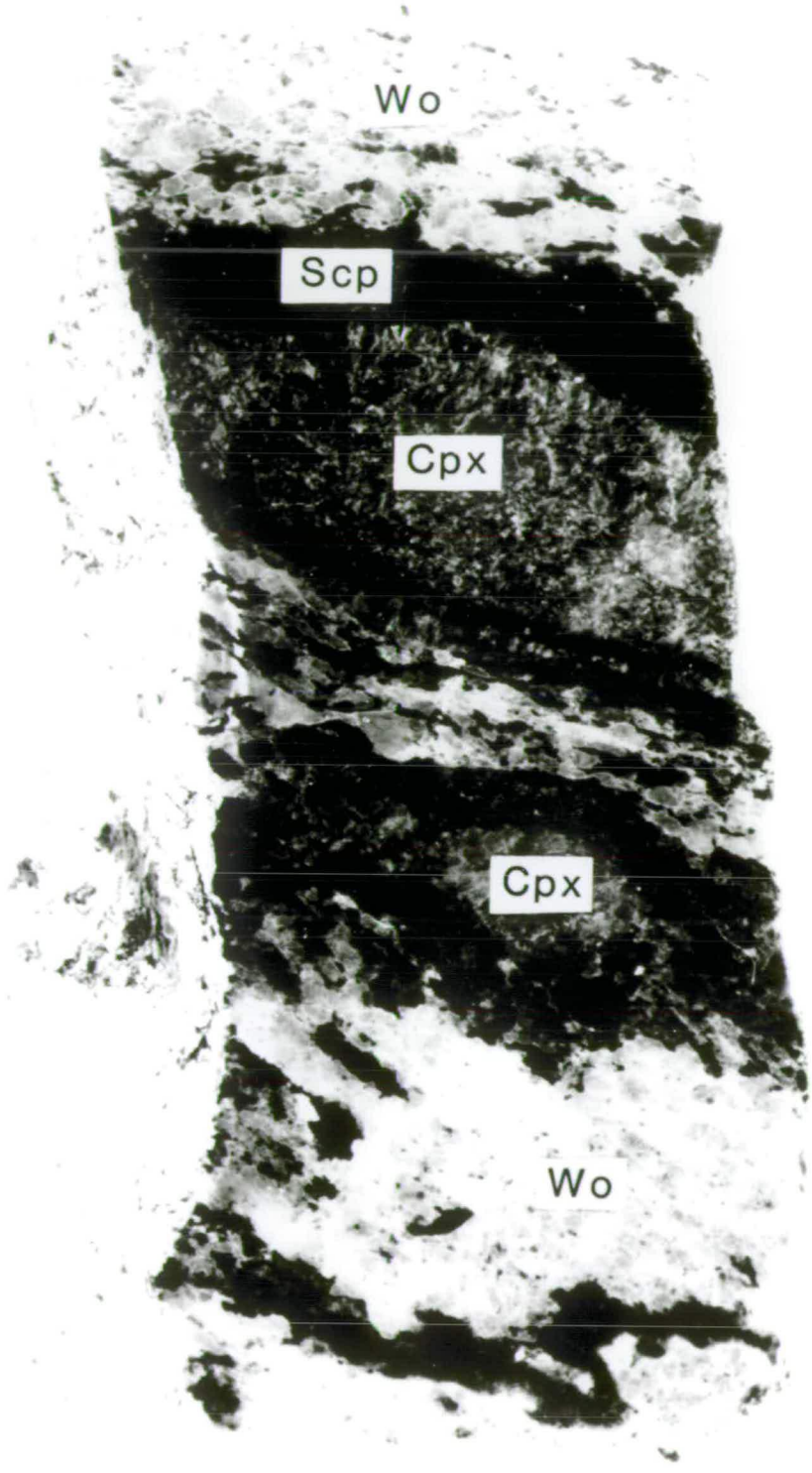
Wo
Scp
Cpx
Cpx
Wo

Table 4.3 Marble and calc-silicate assemblages.

Marble assemblage (and modal abundances):	
Prograde phases	Cal(90-98%)-Ol(2-10%)-Grt(0-5%)-Cpx(0-5%)
Retrograde phases	Serpentine after Ol
Calc-silicate assemblages:	
Typical prograde phases	Scp-Wo-Pl-Cpx
	Scp-Wo-Grt-Cpx
	Scp-Wo-Cpx-Cal
	Scp-Di-Qtz-Pl
	Di-Phl-Cal
Retrograde phases	Grt coronas and Grt-Qtz coronas in Scp-Wo assemblages
	Wo-Pl and Grt-Pl ribbed textures after Scp
	Cal-Pl symplectites after Scp
	Cal-Qtz intergrowths after Wo
	Late Tr, Czo, Prh
Accessory phases	Ap-Spn

Modal abundances are not quoted for calc-silicate assemblages because of the millimetre-scale variation in mineral assemblage. Further details of calc-silicate assemblages are given in Chapter 7.

clinopyroxene, plagioclase and quartz are equant, whereas wollastonite and phlogopite are elongate and aligned parallel to the banding. These granoblastic assemblages are commonly modified by mineral reaction textures, which occur principally in the scapolite-wollastonite assemblages of both the banded and homogeneous calc-silicate (see Table 4.3). These assemblages are characterized by one of two types of reaction texture: textures dominated by garnet coronas between scapolite and wollastonite, and textures dominated by elongate laths of plagioclase separated by ribs of garnet or wollastonite.

(i) Two types of garnet corona are developed in the coronitic calc-silicate: simple garnet coronas and composite garnet-quartz coronas. In prograde scapolite-wollastonite-plagioclase-clinopyroxene assemblages, garnet coronas occur between scapolite and clinopyroxene, and plagioclase and clinopyroxene, whereas garnet-quartz coronas occur between scapolite and wollastonite, and plagioclase and wollastonite (see Plates 4.4a,b). In prograde scapolite-wollastonite-clinopyroxene ± calcite ± garnet assemblages, composite coronas comprising garnet and a variable amount of quartz occur between scapolite and wollastonite, whereas garnet coronas occur between scapolite and calcite, and scapolite and clinopyroxene (see Plates 4.4c and 4.5). The variable quartz content of the composite coronas is discussed further in Chapter 7 (see Section 7.4.4). Both types of corona are wider at triple-grain junctions than two-phase boundaries, and range in width between 2 and 20 μm.

PLATE 4.4

Plate 4.4a

Granoblastic scapolite-wollastonite-plagioclase-clinopyroxene calc-silicate from a boudin at Allison Ridge. Garnet coronas occur between clinopyroxene and plagioclase, and clinopyroxene and scapolite, whereas garnet-quartz coronas occur between wollastonite and plagioclase, and wollastonite and scapolite. Specimen 89/55C, plane-polarized light, field of view is about 1.5 mm.

Plate 4.4b

Garnet rims between granoblastic scapolite and clinopyroxene in a calc-silicate from Allison Ridge. Specimen 89/55C, plane-polarized light, field of view is about 0.7 mm.

Plate 4.4c

Granoblastic scapolite-wollastonite calc-silicate from Amery Peaks Massif, with composite garnet-quartz coronas. A curviplanar layer of quartz occurs adjacent to wollastonite, and a high-relief layer of garnet is developed adjacent to scapolite. The garnet has a curviplanar surface adjacent to quartz and a lobate surface adjacent to scapolite. Specimen 89/334H, plane-polarized light, field of view is about 1.5 mm.

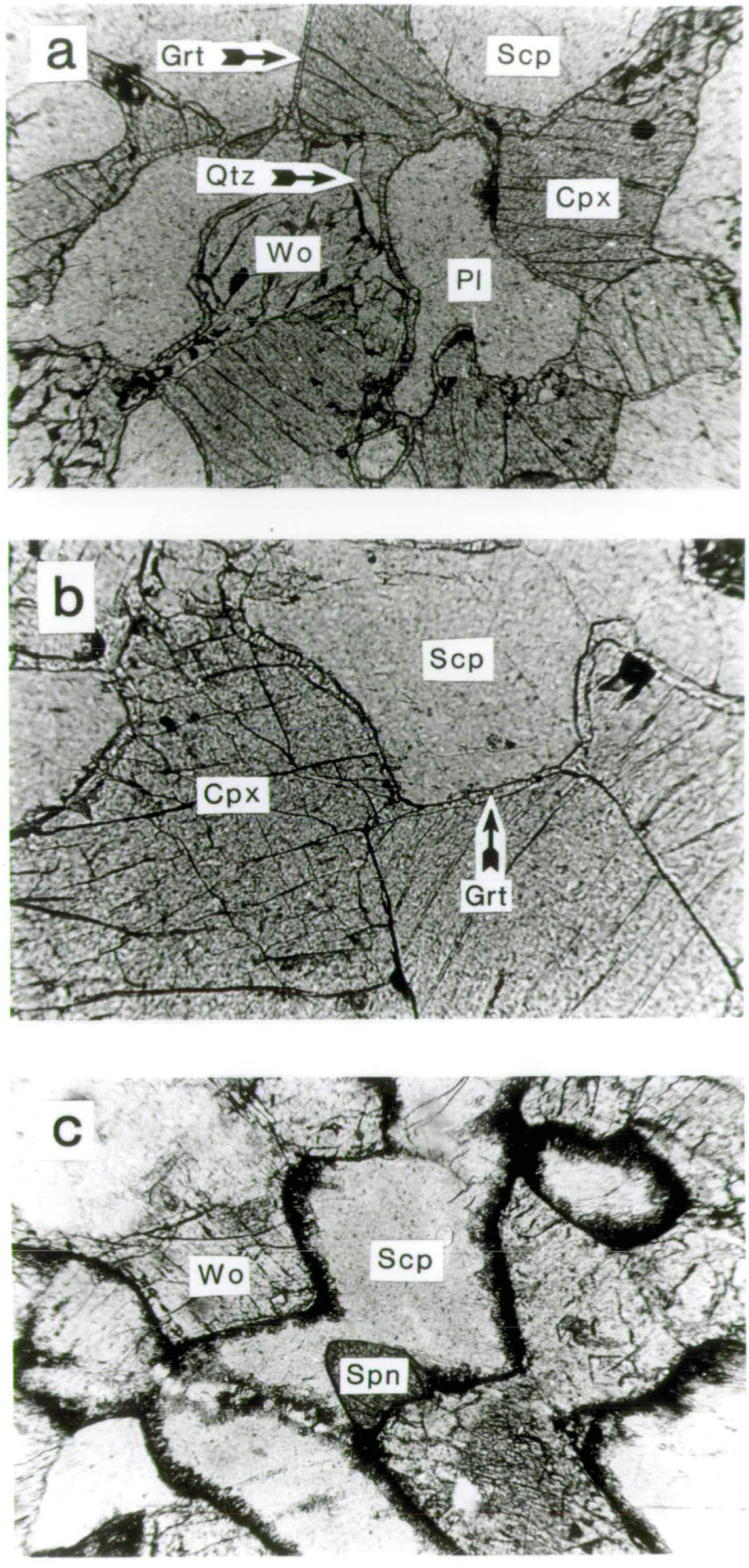
a
Grt
Scp
Qtz
Cpx
Wo
Pl
b
Scp
Cpx
Grt
c
Wo
Scp
Spn

PLATE 4.5

Plate 4.5a

A curviplanar garnet corona between scapolite and wollastonite in a calc-silicate from Allison Ridge. Isolated blebs of quartz occur locally between the continuous garnet corona and wollastonite, but not in the field of view. A relatively low-relief symplectite comprising calcite and plagioclase is developed within the scapolite, adjacent to the high-relief corona. Specimen 89/55D, plane-polarized light, field of view is about 0.4 mm.

Plate 4.5b

A composite garnet-quartz corona between scapolite and wollastonite in a calc-silicate from Amery Peaks Massif. Quartz occurs as a curviplanar layer adjacent to wollastonite, whereas the garnet is lobate and adjacent to scapolite. Specimen 89/334C, plane-polarized light, field of view is about 0.4 mm.

Plate 4.5c

A lobate garnet corona between scapolite and calcite, and a composite garnet-quartz corona between scapolite and wollastonite in a calc-silicate from Mt Trott. Specimen 89/93, plane-polarized light, field of view is about 0.7 mm.

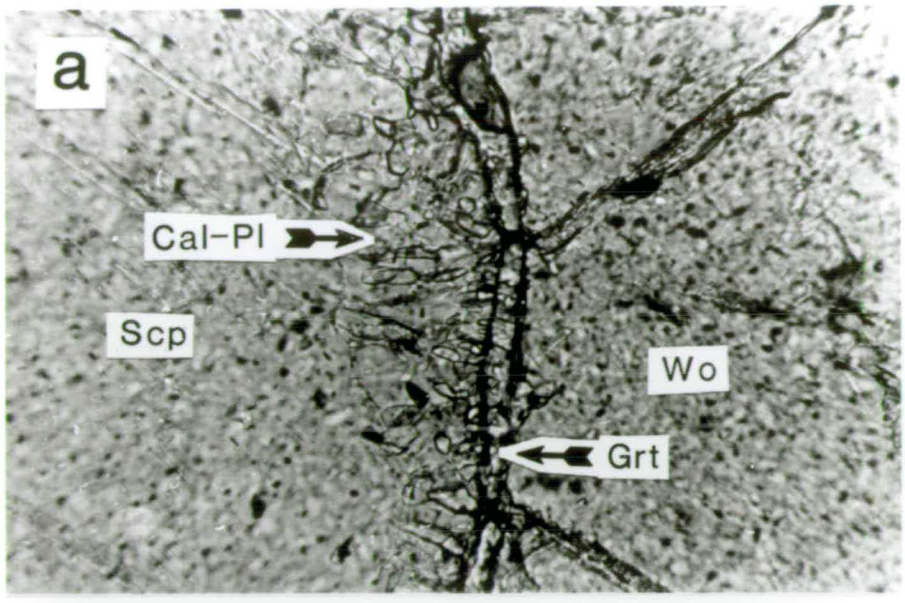
a
Cal-Pl
Scp
Wo
Grt

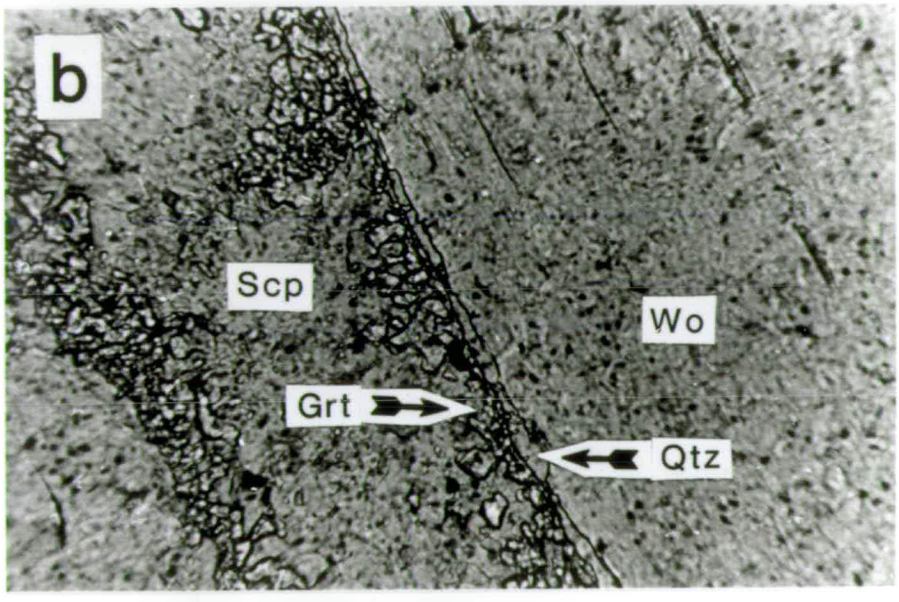
b
Scp
Wo
Grt
Qtz

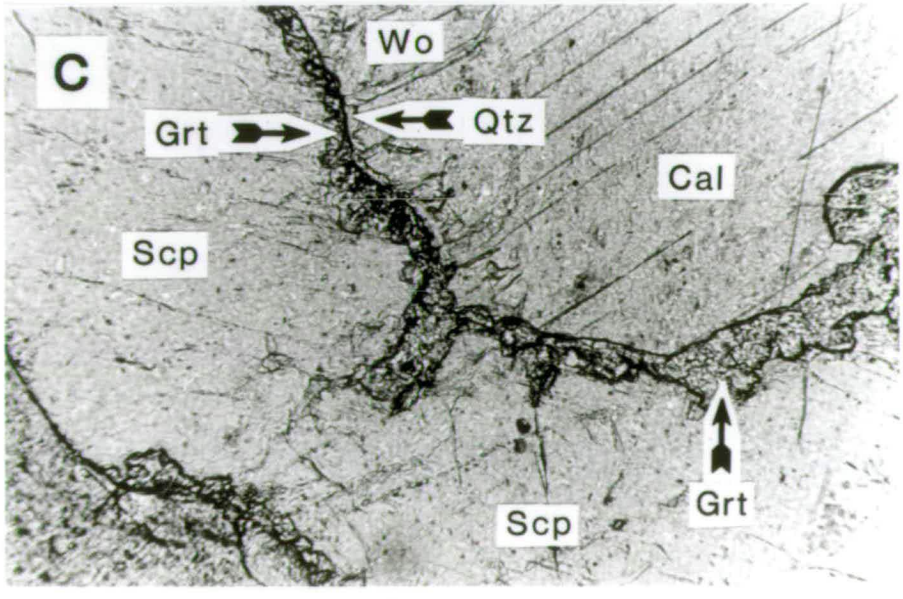
c
Wo
Grt
Qtz
Cal
Scp
Grt
Scp

The morphology of the coronas depends upon the reactant phases. Garnet coronas between scapolite and calcite comprise continuous layers of garnet, which have a lobate contact with scapolite and a curviplanar contact with calcite. The composite coronas consist of a continuous layer of garnet, and a quartz layer which may be continuous or comprise isolated blebs. The garnet and quartz display a consistent spatial distribution, with garnet adjacent to scapolite or plagioclase, and quartz adjacent to wollastonite. The boundary between garnet and quartz is generally curviplanar, as is the boundary between quartz and wollastonite, but the boundary between garnet and scapolite is commonly lobate.

Calcite-quartz intergrowths occur locally within relict wollastonite grains mantled by corona textures (see Plate 4.6a), although this texture is rarely developed to any great extent. Far more common are symplectitic textures adjacent to resorbed scapolite, which comprise plagioclase and vermiform blebs of calcite up to 50 μm across (see Plate 4.6b). Small amounts of quartz are also present in these symplectites. The degree of symplectite development is variable, but is concentrated at grain boundaries, either between two or more scapolite grains, or between scapolite and the garnet coronas. Garnet coronas in contact with unaltered scapolite are of identical appearance to coronas in contact with calcite-plagioclase symplectite, implying that the coronas pre-date symplectite development.

(ii) Other specimens display irregular and extensive reaction textures, comprising decussate plagioclase laths separated by ribs of garnet or wollastonite (see Plates 4.6c, 4.7 and 4.8). The garnet and wollastonite ribs are up to 30 μm wide, and the plagioclase laths vary from stubby grains to extremely elongate grains up to 2 mm long and only 0.1 mm wide. Areas of plagioclase with garnet ribs commonly occur adjacent to plagioclase with wollastonite ribs (see Plate 4.7a), but garnet-bearing domains and wollastonite-bearing domains are always distinct and never intergrown. Domains of decussate plagioclase are developed locally without ribs of wollastonite or garnet, but are generally associated with decussate aggregates of bladed wollastonite (see Plate 4.7c), or xenoblastic to idioblastic garnet up to 5 mm across (see Plate 4.8c), which overprint the polygonal mineral fabric. These textures are interpreted as coarse-grained equivalents of the ribbed textures. The ribbed and the coarser-grained textures commonly enclose resorbed scapolite grains (see Plate 4.6c), which themselves contain calcite-plagioclase symplectite, but it is difficult to identify any other phases involved in the reaction.

Both types of texture are locally cross-cut by veins and isolated patches of minerals such as epidote, prehnite and tremolite. The textural evolution of the calc-silicate, and

PLATE 4.6

Plate 4.6a

An intergrowth of calcite and quartz adjacent to resorbed wollastonite in a calc-silicate from Mt Trott. An isotropic garnet corona occurs between scapolite and wollastonite, and scapolite and the calcite-quartz intergrowth. Specimen 89/93, viewed under crossed polars, field of view is about 1.5 mm.

Plate 4.6b

Scapolite-wollastonite-garnet calc-silicate from Allison Ridge. Calcite-plagioclase symplectite occurs adjacent to resorbed scapolite. In addition to granular prograde garnet, an isotropic corona of retrograde garnet is developed between scapolite, or calcite-plagioclase symplectite, and wollastonite. Specimen 89/55D, viewed under crossed polars, field of view is about 1.5 mm

Plate 4.6c

Elongate plagioclase laths with multiple twins adjacent to resorbed scapolite in a calc-silicate from Saxton Ridge. Specimen 89/268E, viewed under crossed polars, field of view is about 1.5 mm.

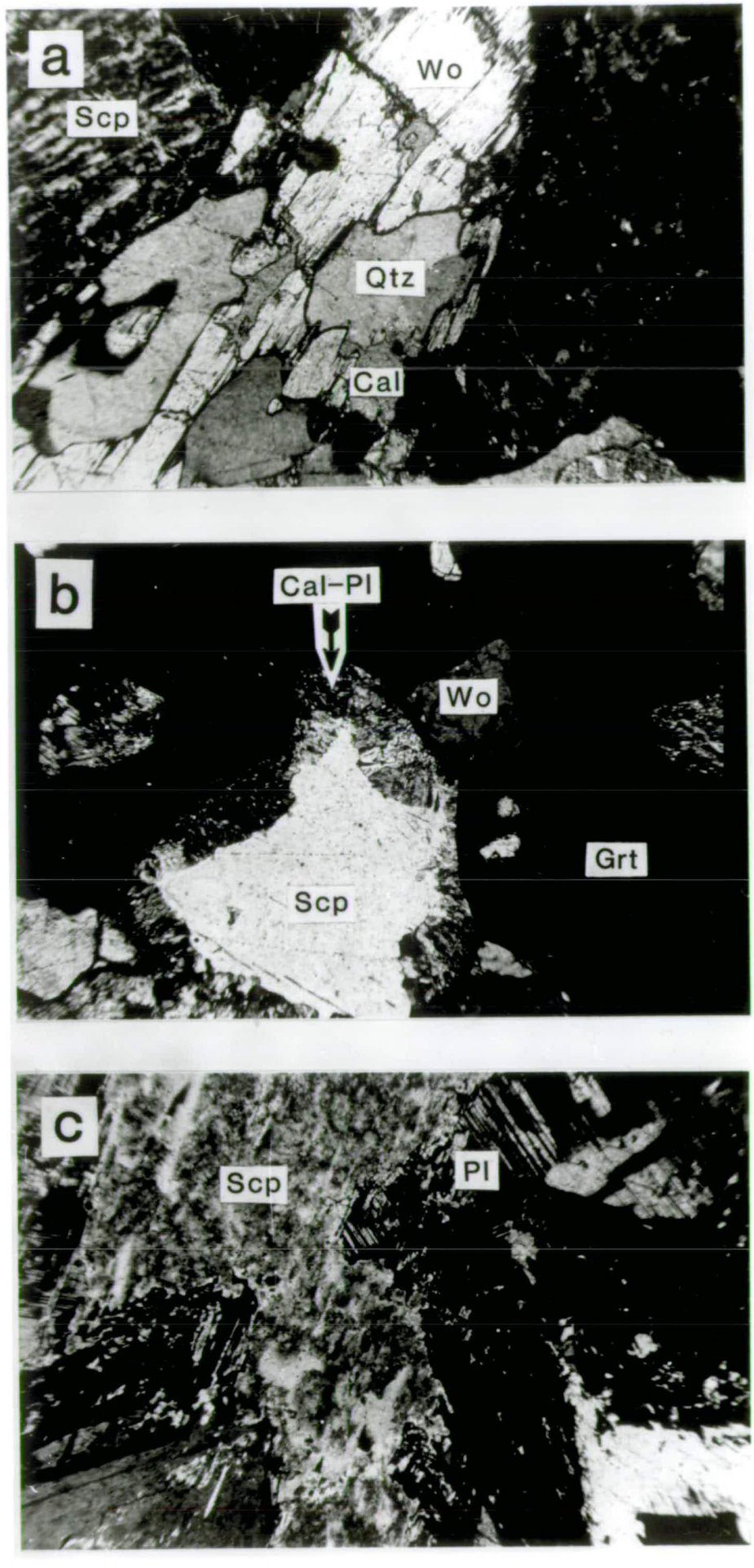
a
Wo
Scp
Qtz
Cal
b
Cal–Pl
Wo
Grt
Scp
c
Scp
Pl

PLATE 4.7

Plate 4.7a

Plagioclase laths intergrown with ribs of high-relief garnet and medium-relief wollastonite in a calc-silicate from Baseline Nunataks. Specimen 89/217B, plane-polarized light, field of view is about 0.7 mm.

Plate 4.7b

Plagioclase and ribbed wollastonite in a calc-silicate from Baseline Nunataks. Specimen 89/217B, plane-polarized light, field of view is about 1.5 mm.

Plate 4.7c

A decussate aggregate of bladed wollastonite adjacent to scapolite in a calc-silicate from Baseline Nunataks. Specimen 89/217B, plane-polarized light, field of view is about 0.7 mm.

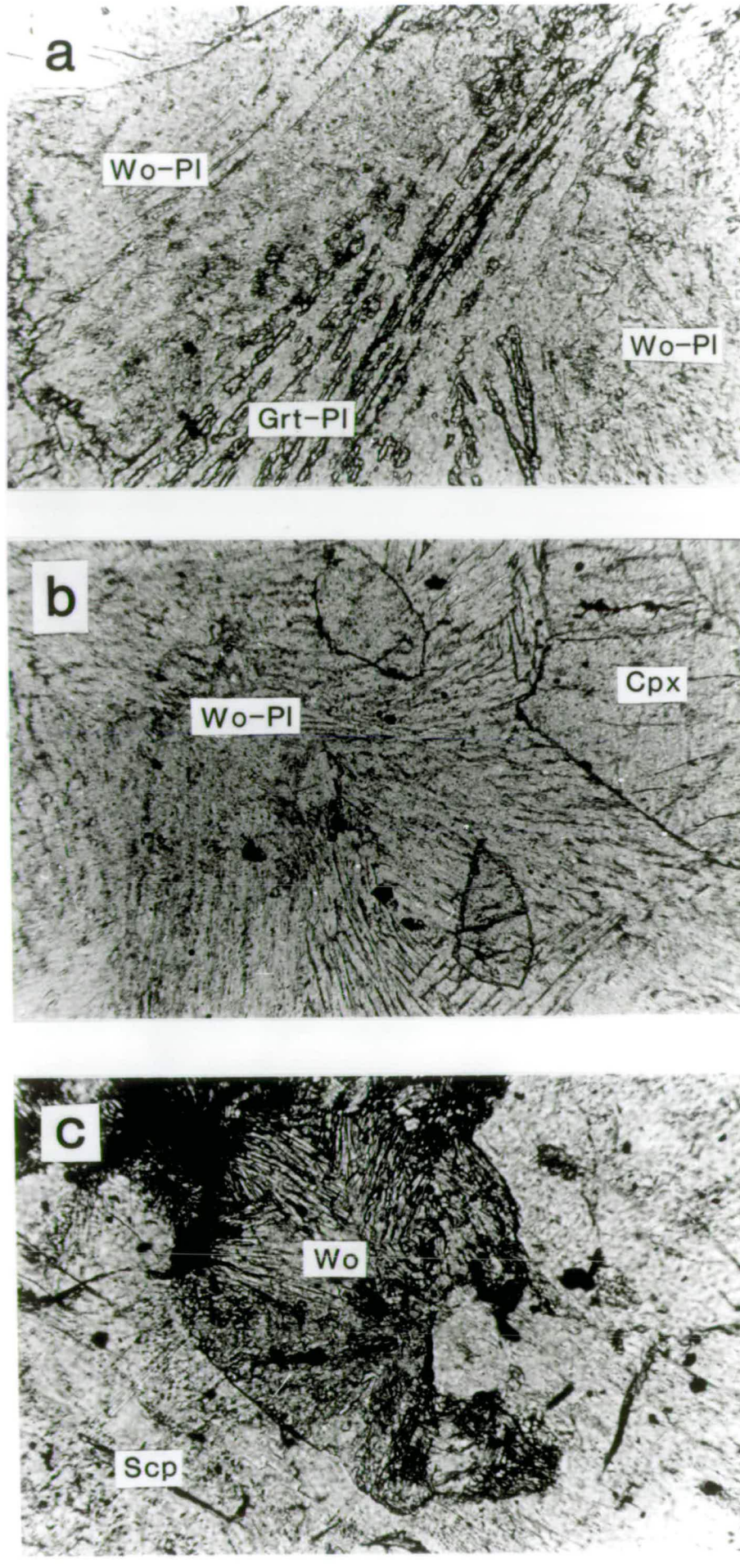
a
Wo-Pl
Wo-Pl
Grt-Pl
b
Wo-Pl
Cpx
c
Wo
Scp

PLATE 4.8

Plate 4.8a

Plagioclase laths and garnet ribs enclosing scapolite in a calc-silicate from Baseline Nunataks. Specimen 89/217B, plane-polarized light, field of view is about 1.5 mm.

Plate 4.8b

Plagioclase laths separated by garnet ribs in a calc-silicate from Baseline Nunataks. Specimen 89/217D, plane-polarized light, field of view is about 1.5 mm.

Plate 4.8c

Idioblastic garnet overgrowing wollastonite in a calc-silicate from Mt Trott. The garnet encloses linear inclusion trails of identical appearance to inclusions in the wollastonite (trending from the top to the bottom of the photograph). Specimen 89/82C, plane-polarized light, field of view is about 1.5 mm.

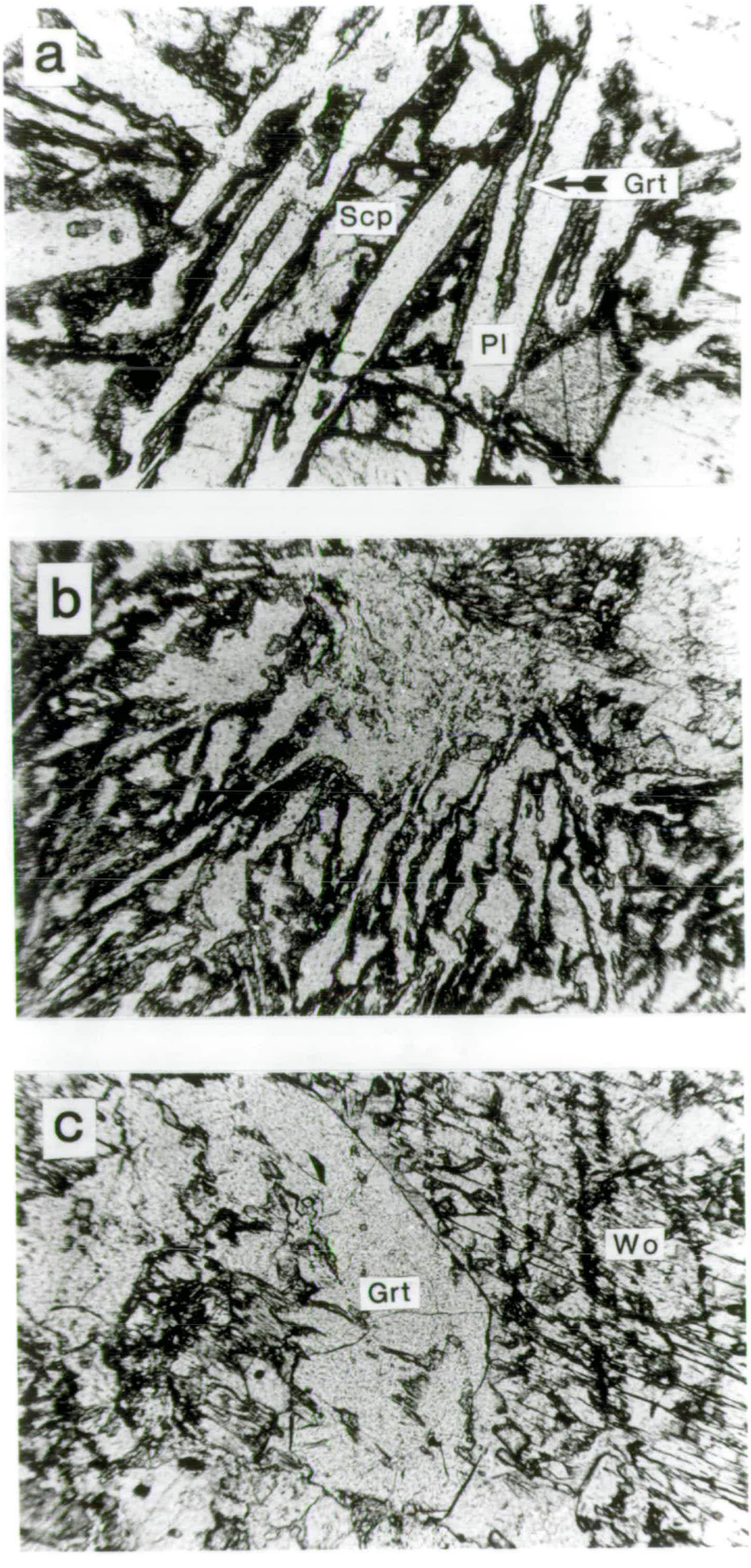
a
Grt
Scp
Pl
b
c
Wo
Grt

the constraints it imposes on the metamorphic history of the Nemesis Glacier region, are considered in more detail in Chapter 7.

4.2.9 Summary and interpretation of the gneissic lithologies

The area is dominated by felsic gneiss. The nature of the felsic gneiss precursor is uncertain, and two associations are distinguished. A sedimentary protolith is inferred for the felsic units interlayered with semi-pelite, calc-silicate and other probable paragneiss units, but most felsic gneiss is homogeneous and more consistent with an igneous protolith. The mafic and ultramafic bodies within the felsic gneiss are interpreted as transposed and boudinaged dykes or sills.

The origins of the calc-silicate are problematic. Lithological banding of high-variance assemblages is indicative of metasomatic processes, with external control of the chemical potentials of certain component species (Korzhinskii, 1959; J.B. Thompson, 1959; Brady, 1977). These processes are favoured by high fluid to rock ratios, such as those common in a contact-metamorphic environment where hydrous magmatic fluids interact with carbonate country rocks to produce skarn (Tilley, 1951; Valley, 1985), or during progressive regional metamorphism of carbonate lithologies interlayered with H_2O-rich rock such as pelite (Vidale, 1969; A.B. Thompson, 1975). Further evidence of interaction with H_2O is provided by the widespread occurrence of wollastonite. Wollastonite is a common product of high-temperature low-pressure contact metamorphism of siliceous limestone, but is only stable at low a_{CO2} under the higher pressures of regional metamorphism. Hence wollastonite cannot form during simple regional metamorphism of impure limestones, since this process is dominated by the liberation of CO_2 through decarbonation reactions, which tends to increase a_{CO2}. Wollastonite-bearing calc-silicate must develop either under H_2O-rich or fluid-absent conditions at the pressures of regional metamorphism (Valley, 1985), and the existence of metasomatic banding, which is favoured by fluid presence, implies the former. On the evidence presently available, it is uncertain whether the wollastonite-stabilizing hydrous fluids had a magmatic origin, or were derived by dehydration of H_2O-rich metasediment, but the characteristics of the host gneiss are consistent in most cases with a sedimentary precursor and hence the latter mechanism.

4.3 DEFORMED INTRUSIVE LITHOLOGIES

4.3.1 Introduction

There are a number of lithologies which, although affected by the final pervasive deformation (D_6; see Section 4.5.7), do not record the regional flat-lying foliation prominent in the gneissic lithologies discussed above (S_3; see Section 4.5.4). These

units are discordant to the gneissic lithologies, except where transposed by later deformation, and are described in Sections 4.3.2 to 4.3.4, and summarized in Section 4.3.5 and Table 4.4.

4.3.2 Leucogneiss

White, medium- to coarse-grained, quartz-K-feldspar-plagioclase-garnet ± biotite sheets and lenses range in width from 0.1 to 2 m, and enclose schlieren and larger rafts of felsic gneiss and semi-pelite. The leucogneiss sheets cross-cut the orthogneiss and paragneiss lithologies described above, and the regional flat-lying foliation (S_3; see Plates 4.9a and 4.10a and Section 4.5.4), but these discordant contacts are locally transposed within zones of upright fabric development (S_6; see Plate 4.9b,c and Section 4.5.7). More than one generation of leucogneiss have been identified. The earliest leucogneiss bodies identified are folded by flat-lying isoclines (F_4; see Plate 4.10b and Section 4.5.5). At Mt Bunt, two later generations of leucogneiss cross-cut upright symmetrical folds (F_5; see Plate 4.9a). The quartzofeldspathic matrix of the leucogneiss bodies is characterized by heterogeneous grain sizes up to 5 mm, and irregular and serrated grain boundaries. Myrmekitic plagioclase-quartz intergrowths are common, and K-feldspar is present both as microperthite and microcline. Lobate garnet porphyroblasts contain inclusions of quartz, biotite and opaque phases, and blue quartz occurs as ribbons in areas of high strain. Quartz exhibits sub-grain boundaries and deformation bands, and feldspar grains commonly have bent twin lamellae (D_8; see Section 4.5.9).

4.3.3 Charnockite

Coarse-grained quartz-microperthite-plagioclase-orthopyroxene ± hornblende ± biotite ± garnet charnockite plutons, commonly 5 km or more in diameter, occur throughout the northern Prince Charles Mountains, and comprise about 10 per cent of outcrop in the area of study. They have a distinctive dark green-brown colour and greasy lustre, and contain simply-twinned K-feldspar grains up to 30 mm across. Blocks and large schlieren of gneissic material are included within the charnockite, and discordant contacts with adjacent gneiss are reported elsewhere in the northern Prince Charles Mountains (D.E. Thost, *pers. comm.* and Fitzsimons & Thost, 1991), but contacts are concordant and somewhat gradational in the area of study. Charnockite fabric varies from weak in areas of low D_6 strain, to well lineated in areas of high D_6 strain, but none of the ductile fabrics or structures preserved by most other lithologies in low-strain zones (i.e. pre-D_6 structures) are present in the charnockite. Intense fabrics in high-strain zones are defined by quartz ribbons, aligned K-feldspar grains and chains of orthopyroxene, hornblende and garnet.

PLATE 4.9

Plate 4.9a

Two generations of leucogneiss cross-cutting garnet-biotite semi-pelite in a D_6 low-strain zone at a nunatak just south of Mt Bunt. The semi-pelite preserves a foliation (S_3) and upright symmetrical folds (F_5). The ice axe is about 0.8 m long.

Plate 4.9b

Interlayered felsic and semi-pelitic gneisses, with a layer-parallel leucogneiss, in a D_6 high-strain zone at Mt Abbs. The horizontal field of view is about 20 m.

Plate 4.9c

Banded amphibolitic gneiss and a layer-parallel leucogneiss body within a D_6 high-strain zone at Mt Bunt. Smaller leucocratic layers preserve isoclinal folds (F_5?, F_6?). Pencil for scale.

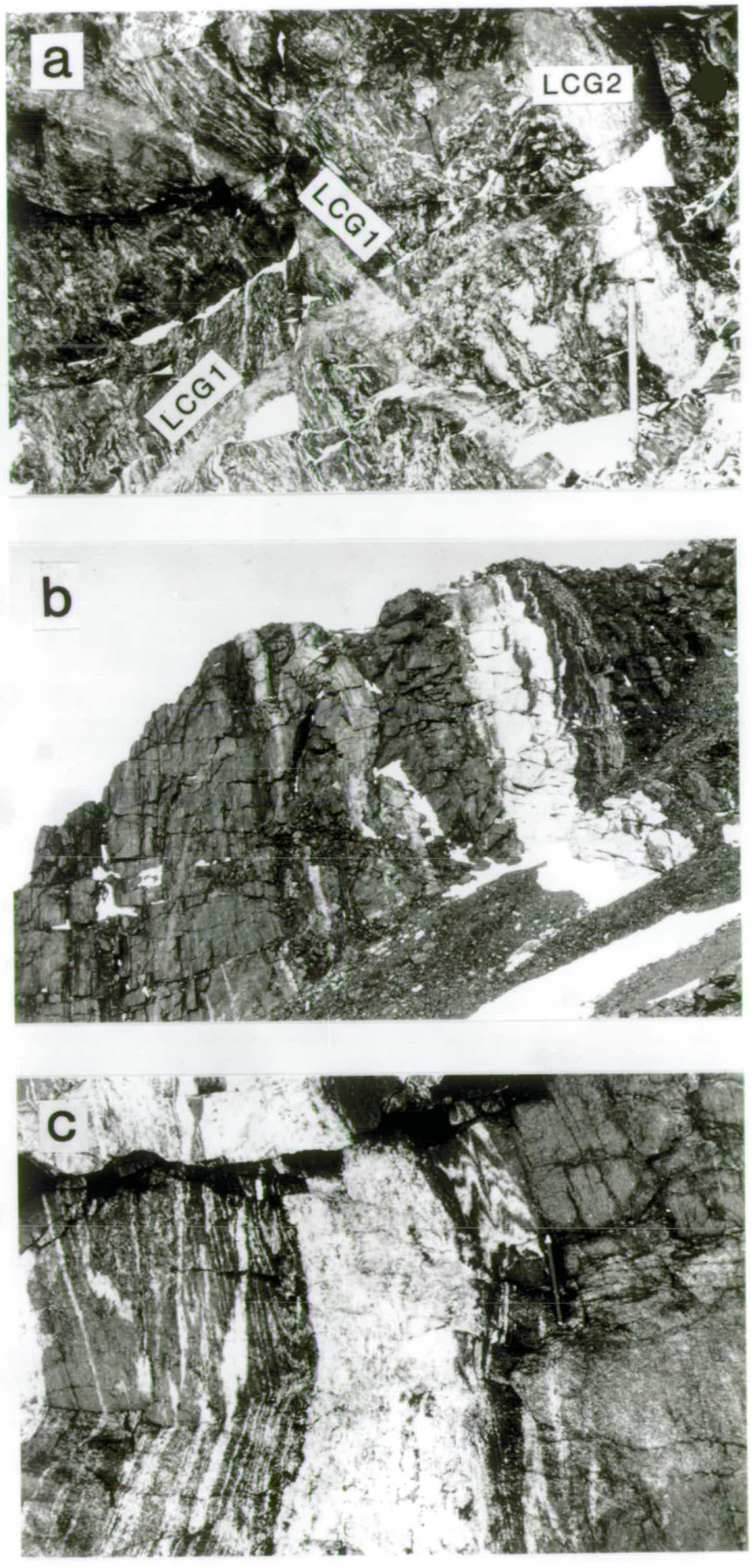
a
LCG2
LCG1
LCG1
b
c

Table 4.4 Deformed intrusive assemblages

Leucogneiss assemblage (and modal abundances):	
Prograde phases	Qtz(25-55%)-Kfs(20-55%)-Pl(10-40%)-Grt(1-5%)-Bt(0-2%)
Retrograde phases	Bt
Accessory phases	Zrn
Charnockite assemblage (and modal abundances):	
Prograde phases	Opx(5-20%)-Hbl(0-5%)-Grt(0-5%)-Qtz(20-35%)-Pl(30-45%)-Kfs(10-25%)
Retrograde phases	Bt around Opx, Cpx and Hbl
Accessory phases	Ap-Zrn and opaque phases
Metamorphosed mafic dyke assemblage (and modal abundances)	
Prograde phases	Opx(15-25%)-Cpx(5-15%)-Hbl(0-10%)-Pl(45-65%)-Qtz(0-5%)
Retrograde phases	Bt around Opx, Cpx and Hbl
Accessory phases	Ap and opaque phases

Sub-idioblastic orthopyroxene is equant to elongate, and occurs as clusters and chains in association with garnet and hornblende. Randomly-oriented biotite occurs around pyroxene and hornblende, and accessory minerals include opaque phases, apatite and zircon. Quartz is recrystallized, and antiperthitic and myrmekitic intergrowths are common, as are mylonite and pseudotachylite (D_8, see Section 4.5.9).

4.3.4 Metamorphosed mafic dykes

Fine- to medium-grained hornblende-orthopyroxene-clinopyroxene-plagioclase ± biotite ± quartz units cross-cut gneissic lithologies in areas of low strain (S_6 and L_6 weak to absent), and are interpreted as recrystallized dykes. They are generally less than 1 m wide, and commonly dismembered and boudinaged. In low strain zones they are unfoliated to weakly foliated and exhibit minor folds, but they are modified along with their host by upright fabrics in high-strain zones (S_6 and L_6; see Section 4.5.7), and discordant contacts are transposed. Cross-cutting relationships between dykes are rare, but have been identified elsewhere in the northern Prince Charles Mountains, and metamorphosed dyke bodies have been observed within charnockite (D.E. Thost *pers. comm.*, and Fitzsimons & Thost, 1991). Fabrics are granoblastic with a variable foliation defined by chains of pyroxene and hornblende. Apatite and opaque phases are common accessory minerals, and randomly-oriented biotite occurs around pyroxene and hornblende. These units are relatively free of mylonite and pseudotachylite.

4.3.5 Summary and Interpretation of the deformed intrusive lithologies

The occurrence of rafts and schlieren within leucogneiss units, and the close relationship between leucogneiss and migmatitic garnet-biotite lithologies, indicate that the leucogneiss was derived by partial melting of the gneissic lithologies. The

PLATE 4.10

Plate 4.10a
Folded (F_5) leucogneiss bodies cross-cutting mafic and felsic gneisses at a nunatak just east of Mt Ormay. Horizontal field of view is about 10 m.

Plate 4.10b
Layered paragneiss at Mt Butterworth. The gneisses preserve a sub-horizontal S_3 foliation which is locally folded by flat-lying F_4 isoclines. Horizontal field of view is about 70 m.

Plate 4.10c
A planar felsic body cross-cutting homogeneous felsic gneiss at Thomson Massif. The felsic body contains biotite schlieren. The hammer is 0.7 m long.

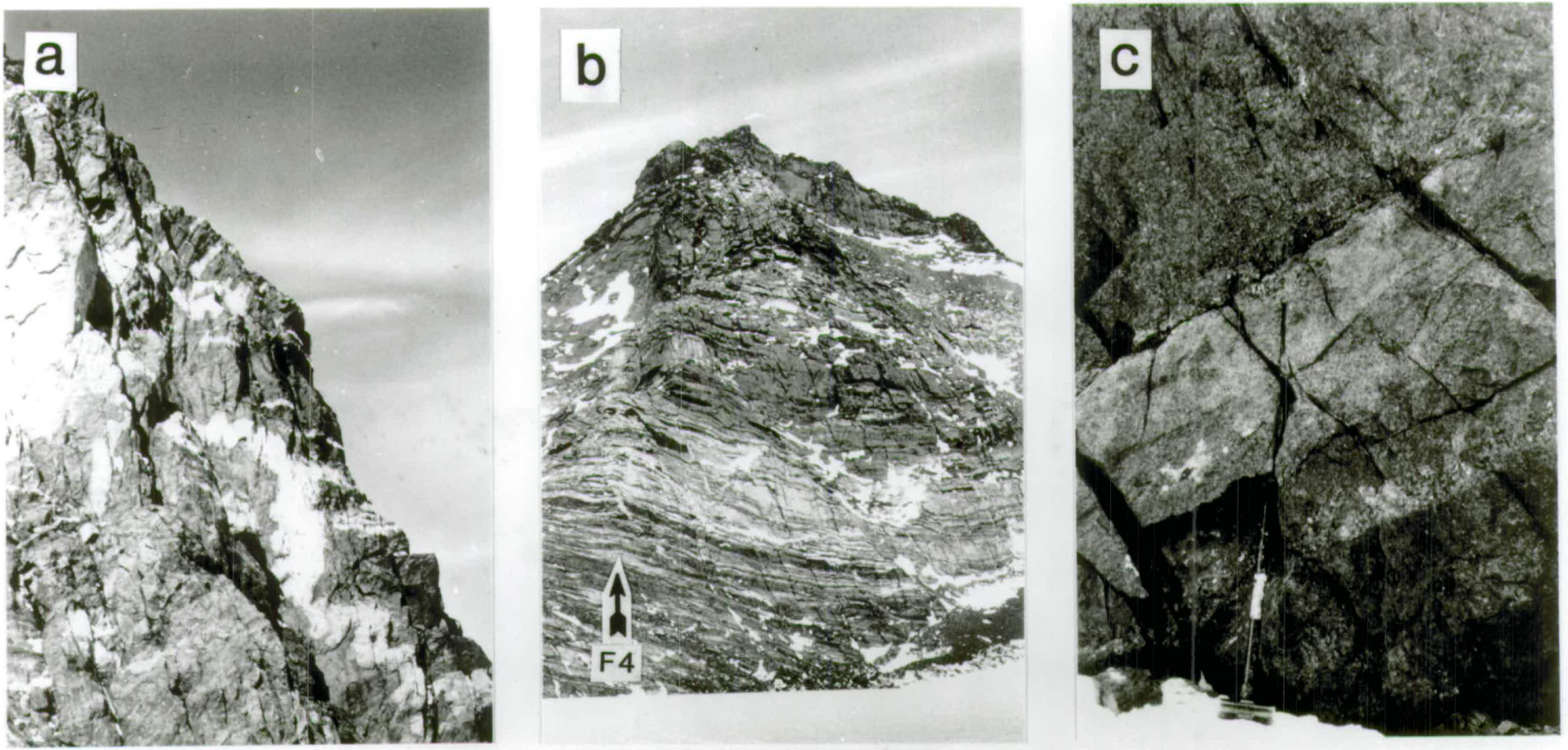
a
b
F4
c

small size of many of the leucogneiss units makes it unlikely that they have migrated any great distance from their source rock, but rather that they are locally-derived melt bodies. The charnockite units are also believed to be crystallized melts. Although intrusive contacts with the gneissic lithologies are not preserved in the area of study, enclosed blocks and schlieren of gneissic material are interpreted as xenoliths, and simply-twinned euhedral K-feldspar grains and widespread myrmekitic feldspar intergrowths are also consistent with a magmatic origin. The lack of intrusive contacts probably reflects transposition during post-emplacement deformation (D_6; see Section 4.5.7), perhaps augmented by limited chemical interaction between charnockite and country rock. In contrast, the metamorphosed mafic dykes are clearly discordant and intrusive in origin, although it is difficult to demonstrate this magmatic origin in areas of high D_6 strain.

4.4 UNDEFORMED INTRUSIVE LITHOLOGIES

4.4.1 Introduction

Some lithologies with little or no internal orientational fabric transect all the pervasive structures and fabrics in the gneissic lithologies and the deformed intrusions. These lithologies comprise only a small fraction of the outcrop area, but are relatively widespread, and are described in Sections 4.4.2 to 4.4.5 and summarized in Table 4.5.

4.4.2 Late felsic bodies

Planar dykes and irregular bodies of felsic composition are widespread in the area of study (see Plate 4.10c), and consist of quartz, K-feldspar, plagioclase and biotite, with rare orthopyroxene and garnet. These granular orange-brown units are fine to medium grained, and range in width from 30 mm to 3 m. They are generally unfoliated, although a weak foliation may be defined by biotite or orthopyroxene. The planar dykes are generally steep in orientation, and cross-cut mafic granulite, felsic gneiss, leucogneiss and charnockite. They appear to truncate the final pervasive fabric (S_6; see Section 4.5.7), although the steep attitude of both the dykes and the fabric makes it difficult to identify discordant relationships. The bodies are cut by mylonite and pseudotachylite. Accessory minerals include apatite and opaque phases, and some of the bodies contain garnet-biotite schlieren.

4.4.3 Pegmatite

Coarse-grained quartz-K-feldspar-plagioclase ± garnet ± biotite ± magnetite pegmatite bodies, typically less than 1 m wide, truncate all regional fabrics and are commonly planar although irregular bodies do occur. Their orientation varies from

Table 4.5 Undeformed intrusive assemblages.

Late felsic body assemblages (and modal abundances):	
Prograde phases	Qtz(20-35%)-Kfs(35-60%)-Pl(15-30%)-Bt(0-5%)-Grt(0-2%)-Opx(0-5%)
Retrograde phases	Bt around Grt
Accessory phases	Ap-Zrn and opaque phases
Pegmatite assemblages (and modal abundances):	
Prograde phases	Qtz(25-45%)-Kfs(20-40%)-Pl(30-45%)-Bt(0-5%)-Grt(0-3%)
Retrograde phases	Chl after Bt
Accessory phases	Zrn-Mag
Late planar vein assemblages (and modal abundances):	
Prograde phases	Qtz or Ep
Retrograde phases	cause a greenschist-facies overprint in adjacent country rocks

sub-horizontal to approximately vertical, and they locally intrude along ductile shear zones (D_7; see Section 4.5.8). Planar mylonite commonly occurs close to, and parallel with, pegmatite bodies, and mylonite has been observed within pegmatite at Mt Bunt (see Plate 4.11a).

4.4.4 Late planar veins

Near-vertical, north-south striking, planar quartz veins were noted at Mt Butterworth (see Plate 4.11b), and similar veins of an identical orientation have been identified elsewhere in the northern Prince Charles Mountains (D.E. Thost *pers. comm.*). The veins, which are less than 0.1 m wide and contain space-filling terminated quartz crystals, cross-cut pegmatite and mylonite. Epidote-rich veins of similar orientation and scale were noted at another Mt Butterworth locality (see Plate 4.11c), and gneisses adjacent to these veins have a greenschist-facies overprint. A prominent north-south trending vertical cleavage without any vein-filling material is common at many localities throughout the area (e.g. Mt Abbs), and is correlated with the veins.

4.4.5 Unmetamorphosed mafic dykes

Planar, unmetamorphosed, basaltic dykes occur throughout the northern Prince Charles Mountains, and a tholeiite has been reported at Amery Peaks Massif by Sheraton (1983), but none were identified in this study.

4.5 STRUCTURE

4.5.1 Introduction

A complex structural history is preserved in the Nemesis Glacier region. Eight deformational events have been distinguished, and are labelled D_1 to D_8. These events, and their associated structures and fabrics, are summarized in Table 4.6 and

PLATE 4.11

Plate 4.11a
A planar pegmatite body within homogeneous felsic gneiss at Mt Bunt. A mylonitic fabric is developed at the edge of, and within, the pegmatite. The sledge-hammer head is about 150 mm long.

Plate 4.11b
Planar sub-vertical quartz veins at Mt Butterworth. The ice axe is 0.8 m long.

Plate 4.11c
Planar sub-vertical epidote vein at Mt Butterworth. The lens cap is 50 mm in diameter.

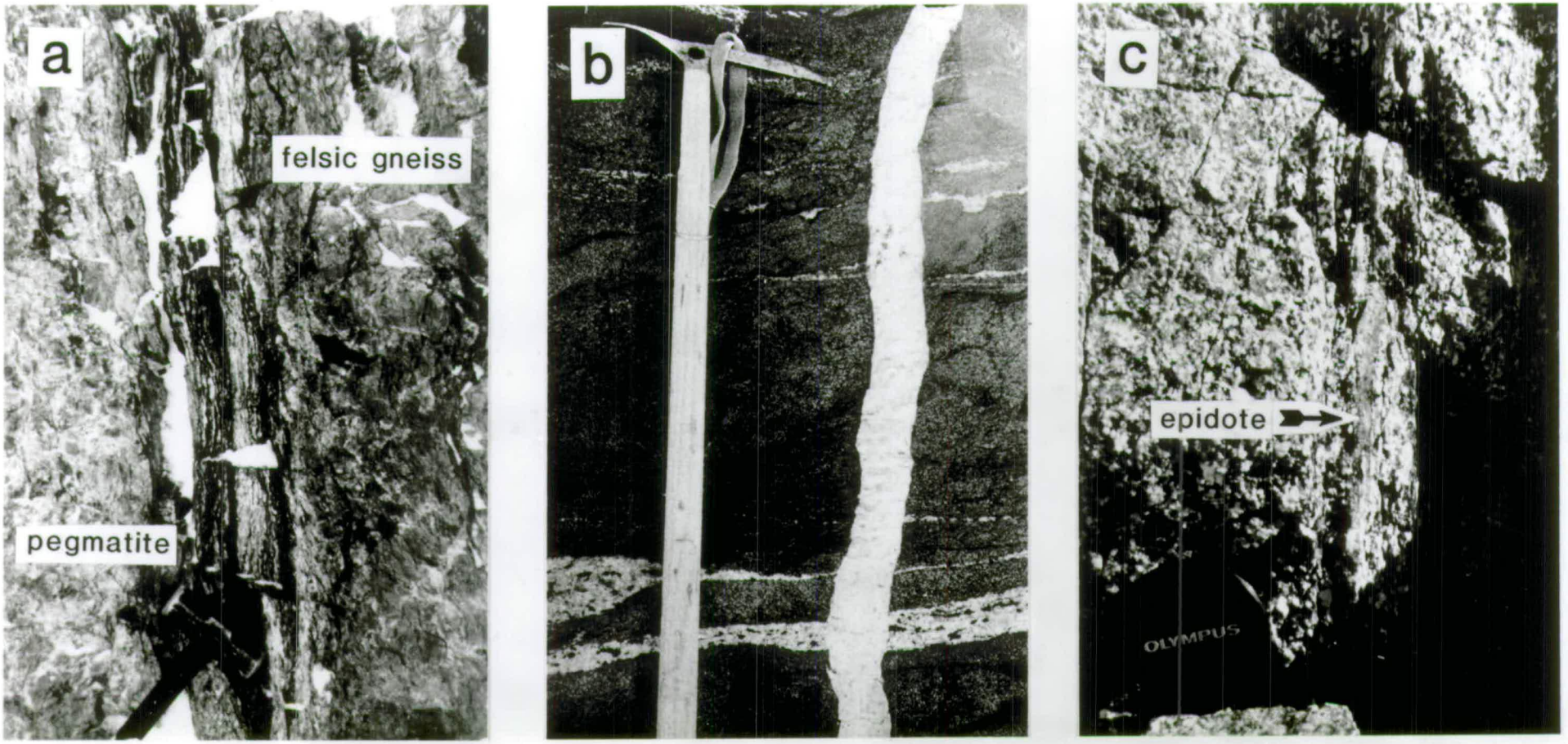
a
felsic gneiss
pegmatite
b
c
epidote
OLYMPUS

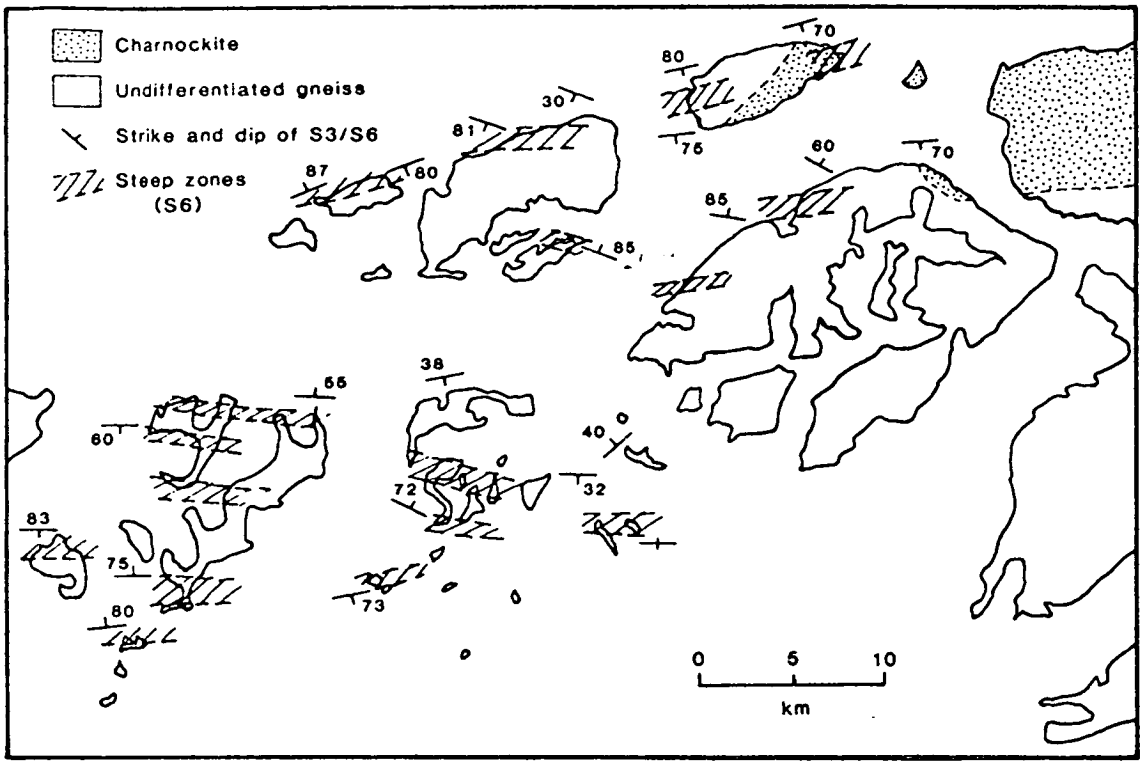

Fig. 4.3 A map of the Nemesis Glacier region depicting the outcrop extent of the charnockite and some representative strike and dip values for the gneissosity (S_3 or S_6). Also shown are east-west trending zones of steep structures (gneissosity dipping at greater than 80°), which are interpreted as zones of intense S_6 development. It is difficult to trace these high-strain zones for any great distance.

discussed below. Regional structural trends are determined principally by S_3 and S_6, and are illustrated in Fig. 4.3. Equal-area projections of structural data are presented in Fig. 4.4. A schematic illustration of the structure of the area is given in Fig. 4.5.

4.5.2 The first deformation

The oldest structures observed are a moderate to intense millimetre-scale foliation (S_1) and lineation (L_1), which are preserved in mafic and ultramafic blocks and layers (see Plate 4.1b and Sections 4.3.3 and 4.3.4). S_1 and L_1 are defined by compositional banding and mineral orientation, and are truncated by the foliation of enclosing felsic gneiss (S_3; see Section 4.5.4).

4.5.3 The second deformation

A series of low-amplitude disharmonic folds (F_2) deform S_1 structures in some of the mafic and ultramafic blocks. These folds, which do not develop an axial-planar fabric, have wavelengths less than 0.5 m and are truncated by the host foliation (S_3). F_2 structures are developed uniformly across large boudins, but smaller bodies generally display S_1 only.

Table 4.6 A summary of the geological and structural history of the Nemesis Glacier region.

Age	Event	Structures and Fabrics
?	Protolith formation	Formation of a basement composed of granitic intrusions and minor sedimentary units
?	Mafic dyke intrusion	Precursors of mafic granulite units intrude basement
?	D_1	S_1 foliation and L_1 lineation of variable intensity in mafic granulite and ultramafic rock
?	D_2	Low-amplitude disharmonic F_2 folds in mafic granulite and ultramafic rock
1000 Ma?	D_3	a) Pervasive flat-lying S_3 gneissosity in basement gneiss lithologies b) Boudinage and rotation of mafic and ultramafic units into parallelism with S_3
	Partial melting	Development of layer-parallel or discordant leucogneiss units
	D_4	Recumbent F_4 isoclines deform S_3
960 Ma	Charnockite intrusion	Coarse-grained igneous charnockite bodies intrude basement gneiss lithologies
	Mafic dyke intrusion	Two or more generations of mafic dyke intrude basement gneiss and charnockite lithologies
	D_5	Open to tight symmetrical upright F_5 folds, often associated with an L_5 east-plunging lineation
	Partial melting	Leucogneiss units intrude basement and charnockite units, and are layer parallel or discordant to S_3 and F_5
920 Ma	D_6	Regional antiformal, synformal and monoclinal structures defined by E-W trending upright high-strain zones containing an intense S_6 foliation and/or east-plunging L_6 lineation separated by flat-lying zones preserving S_3 fabrics
	Felsic intrusion	Planar or irregular felsic bodies intrude basement gneiss and charnockite units, and are discordant to S_6
	D_7	Small-scale flexures and shear zones
770 Ma	Pegmatite intrusion	Planar pegmatite bodies discordant to S_6
500 Ma	D_8	a) Mylonite, pseudotachylite, mineral fragmentation, formation of deformation bands and other microdeformational features b) Vertical N-S trending planar quartz and epidote veins associated with a greenschist-facies overprint
	Alkaline dyke intrusion	Undeformed alkali basalts and alkali mela-syenites which post-date all other lithologies and structures

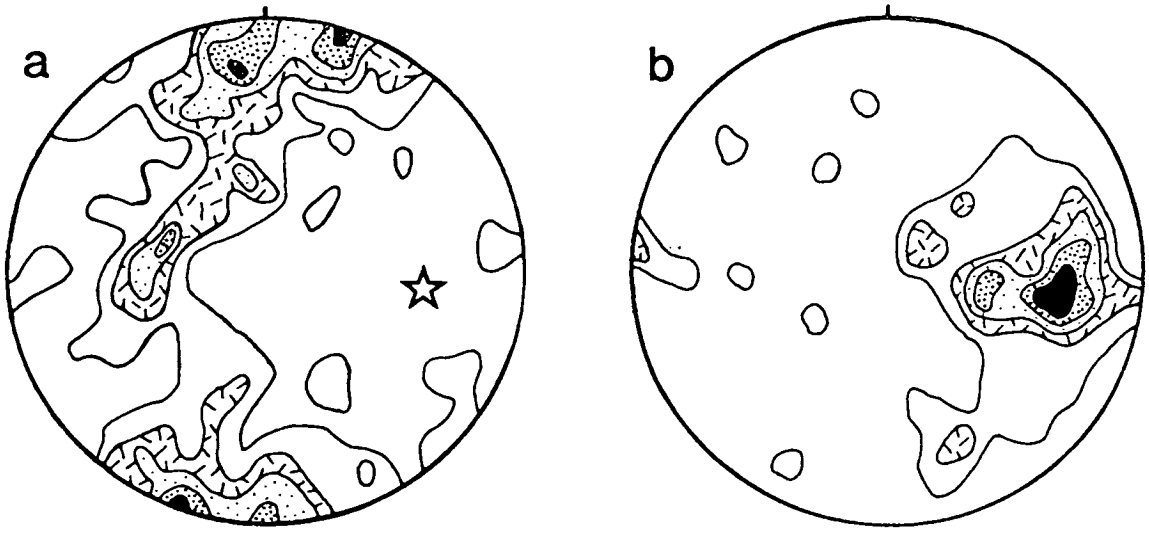

Fig. 4.4 Equal-area projections of structural data from the Nemesis Glacier region. (a) 204 poles to foliations (S_3 / S_6) contoured at 4, 6, 8 and 10% per 1% area. (b) 41 lineations and fold axes (L_5 / L_6 and F_5 / F_6) contoured at 2, 4, 6, 8 and 10% per 1% area. The star in (a) represents the pole to the best-fit girdle for the foliation data, which is approximately coincident with the lineation and fold-axis data.

4.5.4 The third deformation

The dominant regional foliation and lithological layering preserved in the felsic gneiss, semi-pelite, calc-silicate, intermediate gneiss and amphibolite in areas of low D_6 strain has been assigned to D_3 (see Plate 4.10b). The pervasive flat-lying S_3 fabric is defined both by compositional banding on a scale of 1 mm to 5 m and a layer-parallel mineral orientation. S_3 has transposed earlier structures in the gneissic lithologies, although older structures are preserved in mafic and ultramafic blocks (S_1 and F_2; see Sections 4.5.2 and 4.5.3). S_3 development was associated with boudinage of the various units enclosed within the felsic gneiss (see Plates 4.1a,c), and comparison of the internal fabrics of S_3-parallel arrays of boudinaged mafic and ultramafic bodies commonly indicates that the individual boudins have rotated.

4.5.5 The fourth deformation

In areas of low D_6 strain, S_3 fabrics are folded by rare isoclinal F_4 structures with half-wavelengths of 2 to 5 m (see Plate 4.10b). These F_4 folds are recumbent and deform a flat-lying S_3 fabric, except where reorientated by subsequent deformation. No S_4 fabric is developed.

4.5.6 The fifth deformation

Open to tight upright folds (F_5), generally with amplitudes less than 0.2 m, are preserved in areas of low D_6 strain (see Plate 4.9a). These symmetrical structures fold S_3 and plunge shallowly or moderately to the east. Equivalent folds in areas of high

D_6 strain are commonly isoclinal. An associated lineation (L_5), defined by quartz or mafic minerals, is approximately parallel to F_5 fold axes. F_5 structures were not observed in the charnockite, and some leucogneiss bodies are deformed by F_5 structures, whereas others cross-cut them. F_5 structures are coaxial with larger-scale structures developed during D_6, but the truncation of F_5 structures by leucogneiss bodies indicates an earlier origin than D_6 structures which post-date all leucogneiss bodies.

4.5.7 The sixth deformation

Regional structural trends were determined by a heterogeneous deformation (D_6), which affected all lithologies except for the late intrusive units (i.e. late felsic bodies, pegmatites, planar quartz veins and undeformed dykes). High-strain zones are distinguished by the development of an intense, upright, east-west trending S_6 foliation and an east-plunging L_6 lineation, defined by preferred mineral orientation. These pervasive fabrics generally obliterate earlier structures, and transpose originally-discordant leucogneiss, mafic dyke and charnockite (Plate 4.9b,c). The high-strain zones anastomose between outcrops, and are separated by low-strain zones preserving flat-lying to steep S_3 fabrics.

The low-strain zones define kilometre-scale F_6 folds, with a central flat-lying S_3 zone steepening towards the high-strain zones to produce regional antiformal, synformal, or monoclinal structures, with axes trending east-west (see Fig. 4.5). Such large-scale features were observed from the air at localities in the Porthos Range (D.E. Thost *pers. comm.*), but are difficult to appreciate on outcrop scale. However, a group of nunataks immediately south of Mt Bunt preserve these features on a much smaller scale: steep east-west zones of intense S_6 foliation, typically 1 to 2 m wide, are separated by monoclinal zones which are 2 to 10 m wide and preserve S_3 fabrics. Parasitic F_6 structures are common in low-strain zones, folding leucogneiss, mafic dykes, and the S_3 foliation in gneissic lithologies (see Plates 4.10a and 4.12). These asymmetric folds range from 0.1 to 10 m across, and fold-axis orientation is similar to the L_6 lineation preserved in high-strain zones, but no consistent vergence was identified.

4.5.8 The seventh deformation

Gently-dipping shear zones and minor flexures, between 10 mm and 0.5 m wide, have been assigned to D_7. In some cases, these have been later exploited by pegmatite which may show some fabric resulting from reactivation of the shear zones.

PLATE 4.12

Plate 4.12a

Felsic gneiss with biotite schlieren defining a steep foliation and rare asymmetric F_6 structures at a nunatak just east of Mt Ormay. The ice-axe head is about 0.2 m long.

Plate 4.12b

Garnet-bearing leucogneiss with biotite-rich schlieren preserving asymmetric F_6 folds at Mt Bunt. The notebook is 120 mm across.


a

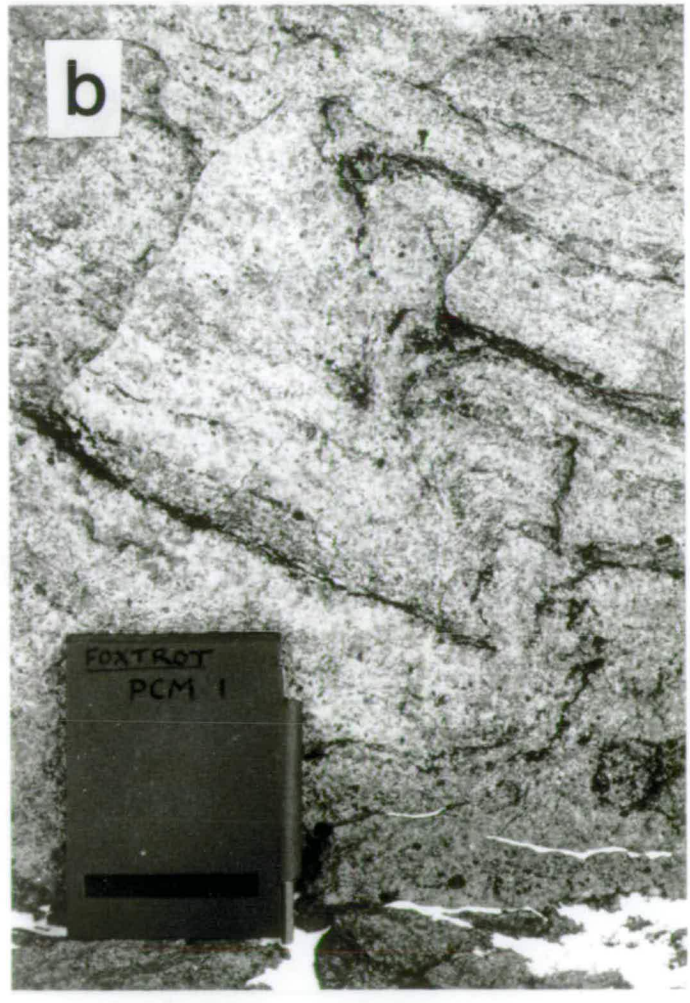
b
FOXTROT
PCM 1

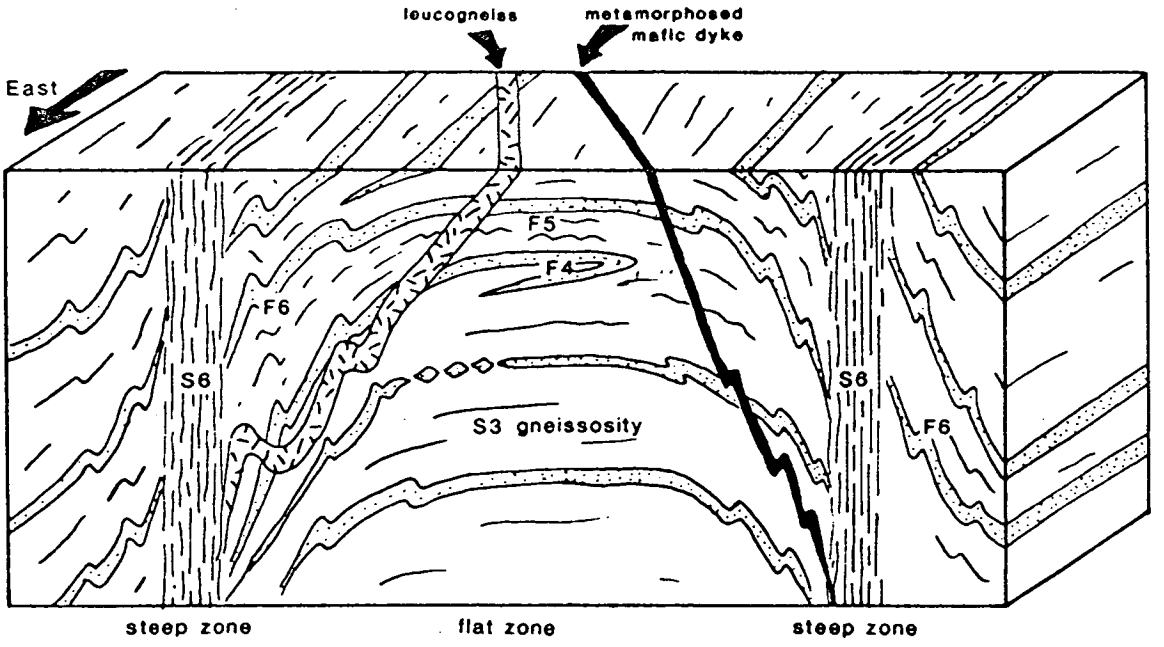

Fig. 4.5 A schematic block diagram depicting the regional F_6 folds defined by upright S_6 high-strain zones and flat-lying zones preserving S_3 and F_4 structures. The flat-lying zones are also characterized by mesoscopic F_5 and parasitic F_6 folds, which are of different style but coaxial and closely related, and discordant contacts between the gneissic lithologies and the leucogneiss and metamorphosed mafic dykes.

4.5.9 The eighth deformation

Mylonite, pseudotachylite and other microdeformational effects are common in the gneissic and deformed intrusive lithologies in the Nemesis Glacier region, but are generally not developed within mafic, ultramafic and metamorphosed dyke lithologies. The microscopic results of this deformation include bent twin lamellae in feldspar, kinked biotite, undulose extinction and deformation bands in quartz, and fragmentation of hornblende and orthopyroxene. Low- and high-angle grain boundaries in quartz reflect post-deformational recovery. Sub-horizontal to steeply-dipping planar mylonite is a ubiquitous feature of most outcrops. It typically occurs as zones less than 10 mm wide, and in a parallel orientation to nearby pegmatite, but wider mylonite zones up to 0.5 m across were also identified. The latter are commonly of a steep orientation, and were observed along the centre of a planar pegmatite at Mt Bunt (see Plate 4.11a). Mylonite cross-cuts late felsic bodies at Mt Trott and Thompson Massif. The widest mylonite zones displace rock units up to several metres, but the narrow ones show little if any displacement. Anastomosing veins and lenses of pseudotachylite commonly form network textures bounded by narrow mylonite. The north-south trending quartz and epidote veins and vertical cleavage are also attributed to this event, although no evidence of timing with respect to mylonite or pseudotachylite has been observed.

4.5.10 Summary and interpretation of structure

S_1, L_1 and F_2 are early structures which are only preserved in the competent mafic and ultramafic units; equivalent structures in the other gneissic lithologies have been transposed by the pervasive S_3 fabric. The limited extent of these early structures makes it difficult to assess the nature of the deformational regime under which they formed. It is possible that S_1 and F_2 are rotated and folded equivalents of the external S_3 foliation, but the observed discordance between S_1 and S_3, and F_2 and S_3, indicates that S_3 developed, at least in part, after the internal structures. The deformational scheme employed here reflects this temporal relationship. In addition, given that F_2 folds are developed uniformly across boudins which have behaved as coherent blocks, it is unlikely that F_2 folds are an early manifestation of the boudinage. S_3 is the only regionally-pervasive fabric, and defines a prominent, flat-lying to steep, lithological layering of the gneissic lithologies. F_4 folds are localized recumbent structures, which, like S_3, are consistent with horizontal shear, and it is possible that S_3 and F_4 are responses to an evolving progressive stress regime.

Structures developed during D_5 and D_6 are upright rather than recumbent, and clearly reflect a different stress regime. The coaxial nature of F_5 and F_6 is probably indicative of progressive deformation, but the truncation of F_5 folds by leucogneiss bodies, which are thought to pre-date D_6, suggests a two-stage timing relationship. Steeply-dipping S_6 high-strain zones divide the region into a number of relatively flat-lying belts which preserve S_3 and F_4 structures (see Fig. 4.5). Hence it is the location of the S_6 high-strain zones that is ultimately responsible for the regional structural trends of the gneissic and deformed intrusive lithologies. Localized deformation subsequent to D_6 is responsible for the development of D_7 shear zones and D_8 mylonite, pseudotachylite and microdeformation. The effects attributed to D_8 are very common in most lithologies, but are not developed to a great extent in the mafic granulite, ultramafic rocks, and deformed dykes, reflecting the competence of these granoblastic lithologies.

4.6 A RELATIVE TIME FRAMEWORK OF GEOLOGICAL EVENTS

4.6.1 Introduction

This section outlines a relative time framework for the geological and structural evolution of the Nemesis Glacier region. The events are considered in three stages: early events preserved locally in mafic and ultramafic lithologies are discussed in Section 4.6.2, events during the D_3 to D_6 time interval are discussed in Section 4.6.3, and events post-dating the pervasive ductile deformation are considered in Section 4.6.4. Some qualitative inferences are made about the metamorphic conditions during

this evolution in Section 4.6.5, but detailed discussions of the metamorphism are presented in Chapters 5 and 7. Section 4.6.6 correlates some of the events in the relative timescale with absolute age determinations from the northern Prince Charles Mountains and elsewhere within the East Antarctic Shield.

4.6.2 Pre-S_3 evolution

The pre-S_3 history of the Nemesis Glacier region is only preserved in mafic and ultramafic blocks enclosed within the felsic gneiss. Early foliations (S_1), lineations (L_1) and folds (F_2) are thought to largely pre-date the boudinage of these units, which were originally continuous and are interpreted as mafic and ultramafic dykes or sills. It is assumed that the enclosing felsic gneiss, and the interlayered felsic, semi-pelitic, amphibolitic and intermediate gneisses, were also affected by D_1 and D_2, but the early structures in these lithologies were completely transposed by the pervasive S_3 foliation. Limited post-D_1 partial melting of the mafic units before boudinage is indicated by rare orthopyroxene-bearing segregations, which transect S_1 fabrics. Their relationship with F_2 structures is uncertain.

4.6.3 S_3 to S_6 evolution

All the pervasive structures preserved on a regional scale were developed during the D_3 to D_6 time interval. D_3 was responsible for the S_3 lithological layering in all gneissic lithologies, boudinage and rotation of competent mafic lithologies, and transposition of all earlier fabrics in less-competent lithologies. Syn-D_3 partial melting is indicated by orthopyroxene-bearing leucocratic selvages around boudinaged mafic bodies, and leucocratic segregations in the semi-pelite. The localized recumbent F_4 folds are probably closely related to S_3, but the flat-lying structures ascribed to these events are quite distinct from the upright structures developed during D_5 and D_6. The D_3 to D_6 time interval was also associated with the intrusion of leucogneiss, charnockite and mafic dykes. All of these lithologies were intruded before D_6, which deformed both the gneissic basement and the intrusions to form a series of kilometre-scale antiformal, synformal and monoclinal structures (F_6) separated by zones of intense upright fabric (S_6). Leucogneiss units were derived by local partial melting of the gneissic basement at several stages of the D_3 to D_6 interval; some are deformed by F_4 folds, others overprint upright F_5 folds. The timing of F_5 with respect to the emplacement of charnockite and metamorphosed dykes is uncertain. F_5 structures were not observed in these intrusive units, but no evidence was found of the intrusions cross-cutting F_5 structures. Emplacement of the charnockite and mafic dykes between D_4 and D_5 is favoured here, since this time interval was associated with significant changes in deformational style, whereas D_5

and D_6 are inferred to have been very similar in style, with little or no time interval between them. Metamorphosed dykes locally cross-cut charnockite, and all such dykes are ascribed a post-charnockite age.

4.6.4 Post-D_6 evolution

Correlation of the retrograde assemblage development with the structural history is a problem. The timing of the calc-silicate reaction textures is difficult to assess, since both the peak metamorphic assemblage and the reaction textures have little or no preferred orientation. It is assumed here that they reflect post-D_6 retrogression after a D_3 to D_6 period of deformation and metamorphism, although they could represent an earlier period of retrogression somehow preserved from later events. Random biotite growth around pyroxene and amphibole is similarly attributed to post-D_6 evolution.

The post-D_6 evolution is characterized by localized intrusive and deformational events. Planar or irregular felsic bodies, and then planar pegmatites, were intruded into the high-grade terrain. Pegmatite emplacement post-dated or was partly synchronous with small-scale flexing and shearing (D_7). Mylonite, pseudotachylite and microdeformational effects (D_8) post-date the felsic bodies and pegmatites, as do planar quartz veins and a vertical cleavage, which are of uncertain timing with respect to D_8 but assumed to be broadly synchronous with this event. Basaltic dykes reflect igneous activity in the area over a long time period, and represent the youngest events recorded in the basement rocks of the northern Prince Charles Mountains.

4.6.5 Qualitative summary of the metamorphic evolution

Assemblage relationships impose some constraints on the nature of the metamorphic evolution of the Nemesis Glacier region. The Nemesis Glacier region preserves a complex deformational history under high-grade conditions (D_1 to D_6), but no differences in metamorphic grade have been identified between assemblages that equilibrated at different stages of this history. Syn-D_1 garnet-absent orthopyroxene-clinopyroxene-hornblende-plagioclase ± quartz mafic granulite is indicative of low- to medium-pressure granulite-facies metamorphism (Green & Ringwood, 1967). Syn-D_3 orthopyroxene-bearing assemblages in felsic gneiss, semi-pelite and intermediate gneiss indicate similar conditions. Gneissic lithologies preserving F_4 and F_5 structures show no change from syn-D_3 assemblages at fold noses or elsewhere. No contact aureoles have been recognized around the pre-D_6 charnockite intrusions, despite their large size and probable high temperature of emplacement. Rocks within S_6 high-strain zones also have orthopyroxene-bearing granulite assemblages. Granulite-facies conditions were clearly achieved at several stages of the Nemesis Glacier region evolution, but there are no data to indicate whether granulite-facies conditions were

prevalent throughout the D_1 to D_6 time interval, or whether there were periods of lower-grade conditions. The former is the simpler interpretation, and is preferred here. High-grade conditions are implied not only by diagnostic mineral assemblages, but also by localized evidence for partial melting.

The post-D_6 metamorphic evolution is partly constrained by post-D_6 assemblages. The various reaction textures in calc-silicate assemblages reflect retrograde re-equilibration following peak metamorphism. Granulite-facies conditions are implied by the orthopyroxene-bearing felsic bodies, and the pegmatite assemblages reflect at least amphibolite conditions. Mylonite zones are generally not associated with a metamorphic overprint, and appear to have been rather dry, preserving clasts of garnet and orthopyroxene within the mylonitic fabric, but the greenschist-facies overprint associated with the planar veins further defines the metamorphic history.

4.6.6 Absolute age constraints

Some of the events discussed above can be related to absolute ages derived from the northern Prince Charles Mountains and elsewhere in the Proterozoic Complex. The major granulite-facies fabric-forming time interval (D_3 to D_6) is correlated with the 1100-800 Ma ages derived from the northern Prince Charles Mountains (Arriens, 1975; Tingey, 1982; see Section 2.3.8) and the 1000 Ma event identified throughout the Proterozoic Complex. However, it is also possible that the flat-lying structures were developed significantly before the Proterozoic event. The charnockite intrusion and D_6 deformation are, however, constrained to have an age of around 1000 Ma. Charnockite is widespread in the Proterozoic Complex of Mac.Robertson Land, and dates between 1000 and 950 Ma have been derived by several workers for this intrusive event (Grew, 1978; Sheraton, 1982; Black *et al.*, 1987; Young & Ellis, 1990, 1991; Young & Black, 1991; see Section 2.3.7). Recent detailed U-Pb zircon work (Young & Ellis, 1990, 1991; Young & Black, 1991; see Section 2.3.7) has ascribed an age of 921 Ma to post-intrusion high-grade ductile deformation of the charnockite, which is correlated with D_6 in the Nemesis Glacier region.

Pegmatite in the Nemesis Glacier region is correlated with the 770 Ma pegmatite event (Black *et al*, 1987; see Section 2.3.5), and the D_8 mylonite development, microdeformation and localized greenschist overprint are correlated with the 500 Ma ages derived from the northern Prince Charles Mountains and elsewhere. The unmetamorphosed mafic dykes and lava flows in the northern Prince Charles Mountains were shown by Sheraton (1983) to have a range of Phanerozoic ages (see Section 2.3.8). However, absolute ages for events prior to D_3 are less clear. Isotopic studies suggest that the northern Prince Charles Mountains consist both of relatively-

young crustal material and older protoliths (Tingey, 1982; see Section 2.3.8), and it is possible that some of the massive felsic gneiss and boudinaged mafic granulite represent part of a reworked Archaean protolith.

Chapters 5 and 7 attempt to quantify the 1000 Ma event in the Nemesis Glacier region. Some aspects of the previous and subsequent evolution are reconsidered in Chapter 8, which integrates this study with the work of McKelvey and Stephenson (1990).

Part Three

Petrological Studies

5. Thermobarometry and mineral zonation studies

5.1 INTRODUCTION

5.1.1 Outline of study

At present, the extent of local and regional metamorphic variation within the Proterozoic Complex is virtually unknown. Quantitative knowledge of the metamorphic evolution is limited to parts of the Rayner Complex (Grew, 1978; Ellis, 1983; Harley, 1985*b*; Sandiford, 1985*b*; Black *et al.*, 1987) and the Prydz Bay coastline (Harley, 1988; Stüwe & Powell, 1989*a*; Harley & Fitzsimons, 1991; Motoyoshi *et al.*, 1991; Thost *et al.*, 1991). This chapter uses relevant thermobarometers to define the pressure-temperature conditions associated with Proterozoic metamorphism in the Brattstrand Bluffs coastline and the Nemesis Glacier region. The remainder of this introductory section discusses some aspects of thermobarometric theory and practice, and identifies the thermobarometric calibrations most suitable for granulite terrains in general and for the two areas of study in particular. Section 5.2 describes the mineral chemistry of garnet-orthopyroxene-plagioclase-quartz gneisses from both areas, and interprets compositional-zonation profiles in garnet, orthopyroxene and quartz in terms of mineral reactions. Section 5.3 presents the results of a thermobarometric study of these assemblages, and Sections 5.4 and 5.5 assess the extent to which the pressure-temperature estimates are affected by the thermodynamic basis of the calibrations used and retrograde disequilibrium respectively. Section 5.6 presents estimates of the peak metamorphic conditions in the two areas and makes tentative inferences concerning their retrograde evolution, taking into account the thermobarometric deficiencies identified in the previous sections.

5.1.2 Thermodynamic background

Thermobarometry is the characterization of metamorphic pressure and temperature conditions from preserved mineral assemblages. It is based on classical thermodynamic theory, which relates compositional variables to other intensive variables that cannot be determined directly from a rock specimen (i.e. pressure and temperature). Thermobarometry of metamorphic rocks relies on the fundamental assumption that mineral phases preserve, at least partly, compositions reflecting a state of chemical equilibrium attained at some point in time during metamorphism.

Equilibrium thermodynamics considers composition in terms of chemical potential. The chemical potential of component i (μ_i) is defined as

$$\mu_i = \left(\frac{\partial G}{\partial n_i}\right)_{P,T,nj} \quad (5.1),$$

where n_i is the number of moles of component i, n_j is the number of moles of all components other than i, and G is the Gibbs free energy of the system, which is a function of pressure, temperature and composition. The chemical potential at given pressure and temperature is commonly split into a term which refers to the chemical potential of the phase at some standard composition, called the standard chemical potential ($\mu°$), and a composition-dependent term, such that

$$\mu_{i,P,T} = \mu°_{i,P,T} + RT \ln a_{i,P,T} \quad (5.2),$$

where $\mu°_{i,P,T}$ is the chemical potential of i at pressure P, temperature T and some standard composition, and $a_{i,P,T}$ is the activity of i at P and T, which is a function of composition and commonly also pressure and temperature. The standard composition is taken as the pure end-member phase (i.e. pure i), and it follows from Equation 5.1 that $\mu°_{i,P,T}$ is equal to the Gibbs free energy of pure i at P and T ($G°_{i,P,T}$), and that

$$\mu_{i,P,T} = G°_{i,P,T} + RT \ln a_{i,P,T} \quad (5.3).$$

For any reaction at equilibrium at P and T, the sum of chemical potentials of the product phases equals that of the reactants, which can be expressed mathematically as

$$\Sigma (\upsilon_i \mu_{i,P,T}) = 0 \quad (5.4),$$

where υ_i is the stoichiometric coefficient of component i in the balanced reaction for the equilibrium, and has a positive value for products and negative for reactants. It follows from Equation 5.3 that, at equilibrium,

$$\Delta G°_{P,T} + RT \Sigma \ln (\upsilon_i a_i) = 0 \quad (5.5),$$

where $\Delta G°_{P,T}$ is the change in Gibbs free energy associated with the pure end-member reaction at P and T. An equilibrium constant K is defined such that $\ln K = \Sigma \ln (\upsilon_i a_i)$, and hence Equation 5.5 can be rewritten as

$$\Delta G°_{P,T} + RT \ln K = 0 \quad (5.6).$$

The equilibrium constant defines the composition of an equilibrium assemblage, and can be related to P and T via the fundamental relationship defining the change in Gibbs free energy of a reaction involving pure end-member phases at P and T

$$\Delta G°_{P,T} = \Delta H°_{1,T} - T\Delta S°_{1,T} + \int_1^P \Delta V°_{P,T}\, dP \quad (5.7),$$

where the first two terms on the right give the change in Gibbs free energy associated with the pure end-member reaction at 1 bar and T in terms of the enthalpy change ($\Delta H°$) and entropy change ($\Delta S°$) for pure end members at 1 bar and T, and the third

term accounts for the pressure difference between P and 1 bar in terms of the volume change ($\Delta V°$) for the pure end-member reaction. Combination of Equations 5.6 and 5.7 yields the relationship

$$\Delta H°_{1,T} - T\Delta S°_{1,T} + \int_1^P \Delta V°_{P,T}\, dP + RT \ln K = 0 \quad (5.8)$$

for any equilibrium assemblage. If all the phases in a reaction are solid, it is commonly assumed that the volume change is independent of pressure and temperature, and Equation 5.8 is simplified to

$$\Delta H°_{1,T} - T\Delta S°_{1,T} + P\Delta V° + RT \ln K = 0 \quad (5.9).$$

Values of $\Delta H°$, $\Delta S°$, $\Delta V°$ are derived by experimental study of the end-member equilibrium, or by combination of thermodynamic data derived by experimental study of related equilibria or single pure phases. The equilibrium constant for a specimen is derived by direct mineral analysis of relevant phases, and the application of solution models which relate the composition of a phase to activities of various components at relevant pressure and temperature. Activity-composition relationships are considered in terms of an activity coefficient (γ), which is defined by the equation

$$a_i = \gamma_i X_i \quad (5.10),$$

where X_i is the mole fraction of i in the phase of interest. Ideal single-site solutions have γ_i equal to unity so that activity and mole fraction are equivalent, but phases are generally non-ideal, and γ_i has some other value. Non-ideality stems from an excess free energy of mixing with respect to the individual components, which can be positive or negative. Numerous solution models of varying complexity have been proposed to quantify the mixing properties of components in mineral phases, some of which are discussed in Section 5.3.3. It follows from Equation 5.10 that the K term in Equation 5.9 can be split into activity-coefficient and composition terms to yield

$$\Delta H°_{1,T} - T\Delta S°_{1,T} + P\Delta V° + RT \ln K_\gamma + RT \ln K_X = 0 \quad (5.11),$$

where $\ln K_\gamma$ equals $\sum \ln (\upsilon_i \gamma_i)$, and $\ln K_X$ equals $\sum \ln (\upsilon_i X_i)$. Most thermobarometric calibrations are solutions to this equation, which relates pressure and temperature to mineral composition, provided that thermodynamic data and mineral solution models are available.

5.1.3 Practical considerations

The principal thermobarometric methods for estimating metamorphic conditions have been summarized by Essene (1982, 1989) and are outlined in Sections 5.1.4 to 5.1.7. All are based on mineral reactions or transformations with sufficient experimental or thermodynamic data for them to be correlated, via Equation 5.11, with a single temperature at known pressure and composition, or a single pressure at known temperature and composition. Of particular importance is the pressure-temperature

slope (dP/dT) of the equilibrium, which is related to the changes in entropy and volume by the Clausius-Clayperon equation:

$$\frac{dP}{dT} = \frac{\Delta S}{\Delta V} \qquad (5.12).$$

Good thermometers are based on reactions which are relatively independent of pressure, and hence have a large dP/dT, and generally a small ΔV. Such reactions are more sensitive if they have a large ΔS. Similarly, good barometers have a small dP/dT and are generally based on reactions with a large ΔV and small ΔS. Ideally, a number of criteria should be met for any particular thermometer or barometer to be of use to a given assemblage (Essene, 1982, 1989).

(i) All relevant phases should be present in the specimen, and be in equilibrium. Detailed textural and analytical studies should be consistent with various equilibrium criteria. The effects of disequilibrium, and in particular retrograde re-equilibration, are considered in Section 5.5.

(ii) Experimental calibrations should be reversed, and have well-characterized starting and product materials. The calibration should involve phases with the same structural states (e.g. order versus disorder) as those in the natural specimens to be studied, and the pressure-temperature conditions of the calibration should be in the same range as those of the specimens. Experimental calibrations are performed in relatively simple chemical systems, and extrapolation to natural multi-component systems (as well as any pressure-temperature extrapolation) must be modelled thermodynamically. Hence the thermodynamic models chosen must also relate to relevant structural states and preferably relevant pressures and temperatures. These problems are relatively easy to avoid for granulite assemblages, since the temperatures of granulite equilibration are similar to those used in experimental calibrations of thermobarometric equilibria.

(iii) Calibrated reactions involving end members of a solid solution should not be applied to assemblages which have these components at high dilution. Use of a calibration at high dilution increases many errors including analytical uncertainties and inaccuracies in solid-solution models.

(iv) Care should be taken when normalizing mineral formulae to derive contents of species which are not routinely detected during microanalysis, such as ferric iron, since this procedure is commonly subject to large errors.

In general, a thermobarometric calibration should only be used for a given metamorphic assemblage if it has proved successful for similar assemblages at a similar metamorphic grade. The following sections discuss the four principal types of thermobarometric method, and indicate the calibrations best suited to granulite-facies assemblages.

5.1.4 Exchange thermometry

Exchange thermometry is based on equilibrium partitioning of isovalent cations between two phases which both show solid solution. This may be represented as:

$$A(i) + B(j) = A(j) + B(i),$$

where i and j are exchanging cations and A and B are phases in equilibrium. Such reactions involve small volume changes, and are commonly good thermometers (see Equation 5.12). The equilibrium above can be represented in the form of Equation 5.11, with two K terms which, for one mole of cation exchange, are given by

$$K_\gamma = \gamma_j^A \gamma_i^B / \gamma_i^A \gamma_j^B = (\gamma_j / \gamma_i)^A / (\gamma_j / \gamma_i)^B \qquad (5.13), \quad \text{and}$$

$$K_X = X_j^A X_i^B / X_i^A X_j^B = (j / i)^A / (j / i)^B \qquad (5.14),$$

where K_X is termed the 'distribution coefficient' and usually denoted K_D. Hence Equation 5.11 can be rearranged to give

$$T = \frac{\Delta H^\circ_{1,T} + P\Delta V^\circ + RT \ln K_\gamma}{\Delta S^\circ_{1,T} - R \ln K_D} \qquad (5.15).$$

If values of ΔH°_T, ΔS°_T, ΔV° and K_γ are available for the reaction from experimental or thermodynamic data, and an independent pressure estimate can be made, K_D can be exponentially related to temperature and hence used as a thermometer.

A variety of exchange thermometers have been proposed for various mineral assemblages, and the most widely used involve exchange of magnesium and ferrous iron between two coexisting phases. Most iron-magnesium exchange thermometers involve garnet since it occurs in a wide range of bulk compositions over a wide range of metamorphic grades, and iron is preferentially fractionated into garnet over most other coexisting ferromagnesian phases. Garnet also has the advantage that it is relatively refractory and resistant to retrograde exchange. Potential thermometers for granulite assemblages include iron-magnesium exchange between garnet-biotite, garnet-hornblende, garnet-cordierite, garnet-clinopyroxene and garnet-orthopyroxene mineral pairs.

Garnet-biotite calibrations (e.g. Ferry & Spear, 1978; Pigage & Greenwood, 1982; Indares & Martignole, 1985*a*) are much used for medium-grade rocks, but give low temperatures for granulites because of retrograde re-equilibration and the high titanium and fluorine contents in biotite. It is also commonly difficult to demonstrate that biotite is part of the peak assemblage. The garnet-hornblende thermometer (Graham & Powell, 1984) is similarly plagued by re-equilibration and complex amphibole chemistry at granulite grade. Cordierite is a common ferromagnesian mineral in granulite-facies metapelites, but cordierite thermometers (e.g. A.B. Thompson, 1976; Hensen, 1977; Perchuk & Lavrent'eva, 1983; Bhattacharya *et al.*, 1988) are subject to uncertainties relating both to the structural state of cordierite, and

its volatile content. The most successful thermometers for granulites have been based on iron-magnesium partitioning between garnet and clinopyroxene (Ellis & Green, 1979; Pattison & Newton, 1989), and garnet and orthopyroxene (Harley, 1984*a*; Sen & Bhattacharya, 1984; Lee & Ganguly, 1988), but even these may suffer some retrograde re-equilibration.

5.1.5 Solvus thermometry

Solvus thermometry is based on immiscibility or compositional gaps between two solid end members, such that the compositions of the coexisting end members diverge with decreasing temperature. Although precise experimental reversals for solvi are comparatively easy to achieve, there are problems with extrapolation to natural multi-component systems, and also with use at temperatures below the 'top' of a solvus, where the high dT/dX (or 'steepness') of the solvus limbs introduces large errors. The plagioclase-K-feldspar and clinopyroxene-orthopyroxene solvi are commonly used for granulite thermometry, but the former is plagued by order-disorder transformations, changes in structural state, exsolution and non-ideality effects. Similarly, the pyroxene solvus is highly sensitive to corrections for the complex chemistry of pyroxenes, and the solvus limbs are steep at temperatures below about 850°C making the thermometer subject to large uncertainties within the temperature range of most crustal rocks and hence unreliable for most granulites.

5.1.6 Univariant equilibria

Simple univariant equilibria involving phases of fixed composition are generally well calibrated, but univariant assemblages are rarely preserved in metamorphic rocks since they are only accessible to a given composition at one pressure and temperature (reaction and assemblage variance are discussed in detail in Chapter 6). Other problems include the development of apparent univariant assemblages during retrograde disequilibrium, and the effect of solid solution which can be significant even if of very limited extent.

5.1.7 Divariant equilibria

Solid solution and the resultant increase in assemblage variance can be utilized to the advantage of thermobarometry. Divariant assemblages are preserved over a significant pressure-temperature range, and are commonly useful barometers, although they typically show temperature as well as pressure dependence. Equation 5.11 can be rearranged to express the equilibrium pressure in terms of thermodynamic variables, temperature and K terms as follows

$$P = \frac{T\Delta S^\circ_{1,T} - \Delta H^\circ_{1,T} - R \ln K_X - RT \ln K_\gamma}{\Delta V^\circ} \qquad (5.16).$$

Table 5.1 Well-calibrated end-member equilibria suitable for granulite thermobarometry.

grossularite + sillimanite + quartz = anorthite	Koziol & Newton (1988) Essene (1989)
almandine + rutile = sillimanite + ilmenite + quartz	Bohlen *et al.* (1983*a*,*b*) Essene (1989)
almandine + corundum = hercynite + sillimanite	Bohlen *et al.* (1986)
grossularite + almandine + quartz = anorthite + ferrosilite	Bohlen *et al.* (1983*a*,*b*) Essene (1989)
grossularite + pyrope + quartz = anorthite + enstatite	Perkins & Newton (1981) Newton & Perkins (1982) Perkins & Chipera (1985) Essene (1989)
grossularite + almandine + quartz = anorthite + bedenbergite	Moecher *et al.* (1988) Essene (1989)
grossularite + pyrope + quartz = anorthite + diopside	Perkins & Newton (1981) Newton & Perkins (1982) Moecher *et al.* (1988) Essene (1989)
grossularite + almandine + rutile = ilmenite + anorthite + quartz	Bohlen & Liotta (1986) Essene (1989)

For an assemblage of fixed mineral composition (i.e. fixed K_γ and K_X), Equation 5.16 can be used to define a line in pressure-temperature space, or 'isopleth', which is displaced from the position of the pure end-member reaction. The conditions under which the assemblage equilibrated lie somewhere on the isopleth, which can be used to estimate the pressure if an independent temperature estimate is available.

A number of divariant equilibria, commonly involving garnet, have been applied to granulite assemblages. For the same reasons outlined in Section 5.1.4, equilibria involving biotite, amphibole or cordierite are generally not as reliable as equilibria involving phases of less complex chemistry, and the most reliable divariant equilibria for granulite assemblages are listed in Table 5.1.

5.1.8 Suitable assemblages in the areas of study

There is a paucity of suitable thermobarometric assemblages in the two areas of study. Pyroxene-bearing mafic and felsic gneiss is garnet absent (see Sections 3.2.2, 4.2.2 and 4.2.3), and equilibria based solely on coexisting pyroxenes are unreliable for granulite assemblages. Metapelitic gneiss and migmatite at Brattstrand Bluffs have a complex history of mineral reaction (see Section 3.2.3), and although suitable assemblages (e.g. garnet-sillimanite-plagioclase-quartz, garnet-sillimanite-spinel-quartz, and less reliable cordierite assemblages) are developed during retrograde reaction, there are no peak assemblages suitable for thermobarometry. The calc-

silicate lithologies in the Nemesis Glacier region also exhibit reaction textures (see Section 4.2.8). The metamorphic histories of the metapelite and calc-silicate are investigated in Chapters 6 and 7 using a petrogenetic-grid approach, which is more suited to a complex reaction history than thermobarometric techniques.

The most suitable lithology for thermobarometric study is garnet-orthopyroxene-plagioclase-quartz ± biotite ± K-feldspar gneiss, which occurs in both areas (see Sections 3.2.5 and 4.2.5). Garnet, orthopyroxene, quartz and plagioclase appear to be in textural equilibrium in all specimens, and generally unaffected by retrograde reaction except for rare localized biotite, and biotite-plagioclase and biotite-quartz symplectites (see Sections 3.2.5 and 4.2.5). Several well-calibrated thermometers and barometers are available for garnet-orthopyroxene-plagioclase-quartz assemblages, and selected calibrations are used in this chapter to estimate peak conditions of Proterozoic metamorphism in both the Brattstrand Bluffs coastline and the Nemesis Glacier region.

5.2 MINERAL CHEMISTRY

5.2.1 Introduction

Mineral compositions of garnet, orthopyroxene and plagioclase in eight specimens from the Brattstrand Bluffs coastline and eight specimens from the Nemesis Glacier region were determined by wavelength-dispersive electron-probe microanalysis. Operating conditions and analytical precision and accuracy are described in Appendices 3.1, 3.2 and 3.7. Between 5 and 60 spot analyses of each phase were obtained from each specimen. Core and rim analyses were made in each specimen, and detailed grain traverses, comprising between 5 and 25 equally-spaced analysis points, were made across garnet, orthopyroxene and plagioclase in three specimens from each area. Normalization procedures and methods of ferric iron estimation in garnet and pyroxene are outlined in Appendix 3.3, and representative analyses are tabulated in Appendix 3.4.

5.2.2 Specimens from the Brattstrand Bluffs coastline

Garnet: Core X_{Mg}^{Grt} values vary between 0.23 and 0.39 (see Figs 5.1a and 5.2a) and commonly decrease rimwards, particularly in grains adjacent to orthopyroxene (see Fig. 5.3). The change in X_{Mg}^{Grt} associated with this zonation is only 0.01 to 0.03 units and is concentrated at grain edges. Core X_{grs}^{Grt} varies between 0.03 and 0.09 (see Fig. 5.2a), and tends to decrease rimwards (see Fig. 5.3). The extent of X_{grs}^{Grt} zonation is greatest for the most calcic garnet (specimen 88/333). Grossularite and almandine contents show a positive inter-specimen correlation for fixed plagioclase composition. X_{sps}^{Grt} varies between 0.01 and 0.06 and shows little intra-specimen variation. Site and charge balance calculations imply that ferric iron is not a significant component of the garnet.

Orthopyroxene: Core X_{Mg}^{Opx} values vary from 0.47 to 0.63 (see Figs 5.1a and 5.4a), and zone to rims richer in enstatite, especially in grains adjacent to garnet, but changes in X_{Mg}^{Opx} are only between 0.01 and 0.04 units (see Fig. 5.5). X_{Al}^{M1} varies from 0.04 to 0.17 (see Fig. 5.4a) and tends to be highest in those specimens which also have the highest X_{Mg}^{Opx}. Values of X_{Al}^{M1} generally decrease rimwards by up to 0.04 units (see Fig. 5.5). Specimens with the most aluminous and most magnesian pyroxene (88/168, 88/50, 88/118) tend to be those with the least calcic and most magnesian garnet. Charge and site balance calculations suggest that ferric iron is insignificant in most specimens, although some are ascribed a small ferric component.
Plagioclase: X_{an}^{Pl} values range from 0.39 to 0.79, and commonly increase adjacent to garnet and orthopyroxene by up to 0.06 units (see Fig. 5.6). Specimens with the highest X_{an}^{Pl} tend to be those which coexist with the most calcic garnet for a given X_{Mg}^{Grt} (see Fig. 5.2a).

5.2.3 Specimens from the Nemesis Glacier region

Garnet: Core X_{Mg}^{Grt} values vary between 0.15 and 0.32 (see Figs 5.1b and 5.2b), and grains are commonly zoned to rims richer in almandine (see Fig. 5.3). The zonation is best developed in grains adjacent to orthopyroxene and involves a decrease in X_{Mg}^{Grt} of up to 0.04 units but more typically about 0.02. Core X_{grs}^{Grt} varies between 0.02 and 0.09 (see Fig. 5.2b), and commonly increases rimwards by 0.005 to 0.015 units. The extent of X_{grs}^{Grt} zonation is greatest in those specimens with the most calcic garnet. There is a positive inter-specimen correlation between almandine and grossularite content (see Fig. 5.2b). X_{sps}^{Grt} is in the range 0.01 to 0.04 and varies by less than 0.002 in any one grain. Site and charge balance calculations indicate that ferric iron contents are negligible.
Orthopyroxene: Core X_{Mg}^{Opx} values are in the range 0.38 to 0.62 (see Figs 5.1b and 5.4b), and grains commonly show a rimward increase in enstatite content (see Fig. 5.5). The zonation is most pronounced in grains adjacent to garnet and involves an increase in X_{Mg}^{Opx} values of between 0.01 and 0.04 units. Core X_{Al}^{M1} values vary between 0.02 and 0.10 (see Fig. 5.4b), and tend to decrease rimwards by up to 0.02 units (see Fig. 5.5). The most aluminous pyroxene also tends to be the most magnesian, and coexists with the least calcic and most magnesian garnet. Site and charge balance calculations imply that ferric iron contents are insignificant for most specimens, although some are ascribed small ferric contents.
Plagioclase: X_{an}^{Pl} values are in the range 0.15 to 0.50, and can vary within a grain by up to 0.08 units (see Fig. 5.6). No consistent zonation trend was identified, but specimens with the most calcic plagioclase tend to be those with the most calcic garnet for a given X_{Mg}^{Grt} (see Fig. 5.2b).

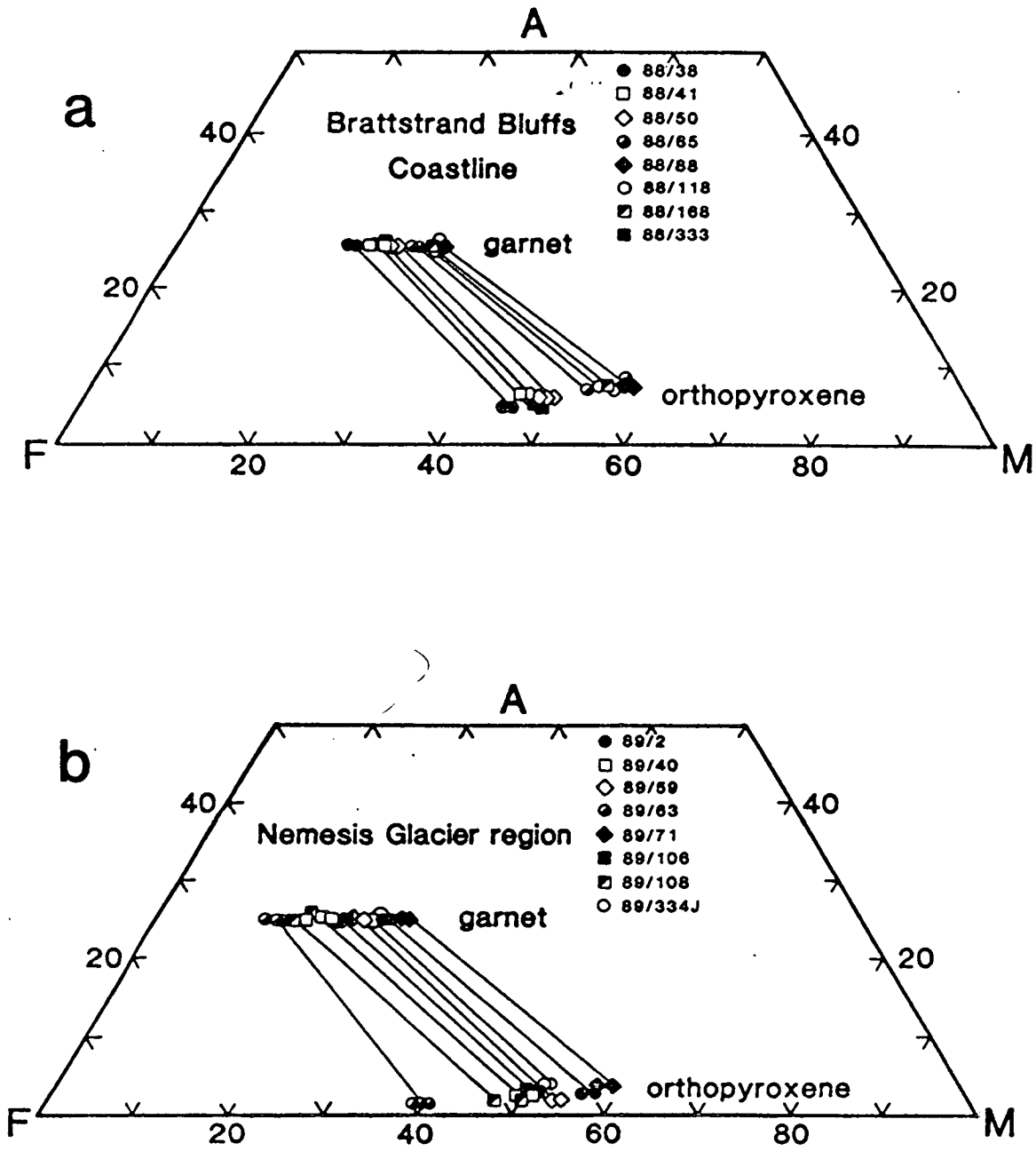

Fig. 5.1 Partial AFM (Al_2O_3-FeO-MgO) diagrams depicting the Fe-Mg distribution between garnet and orthopyroxene in specimens from (a) the Brattstrand Bluffs coastline, and (b) the Nemesis Glacier region. Only representative compositions are shown, and there is in fact more overlap between the different specimens than that indicated (see Figs 5.2 and 5.4). Orthopyroxene shows a trend of increasing aluminium content with increasing magnesium content.

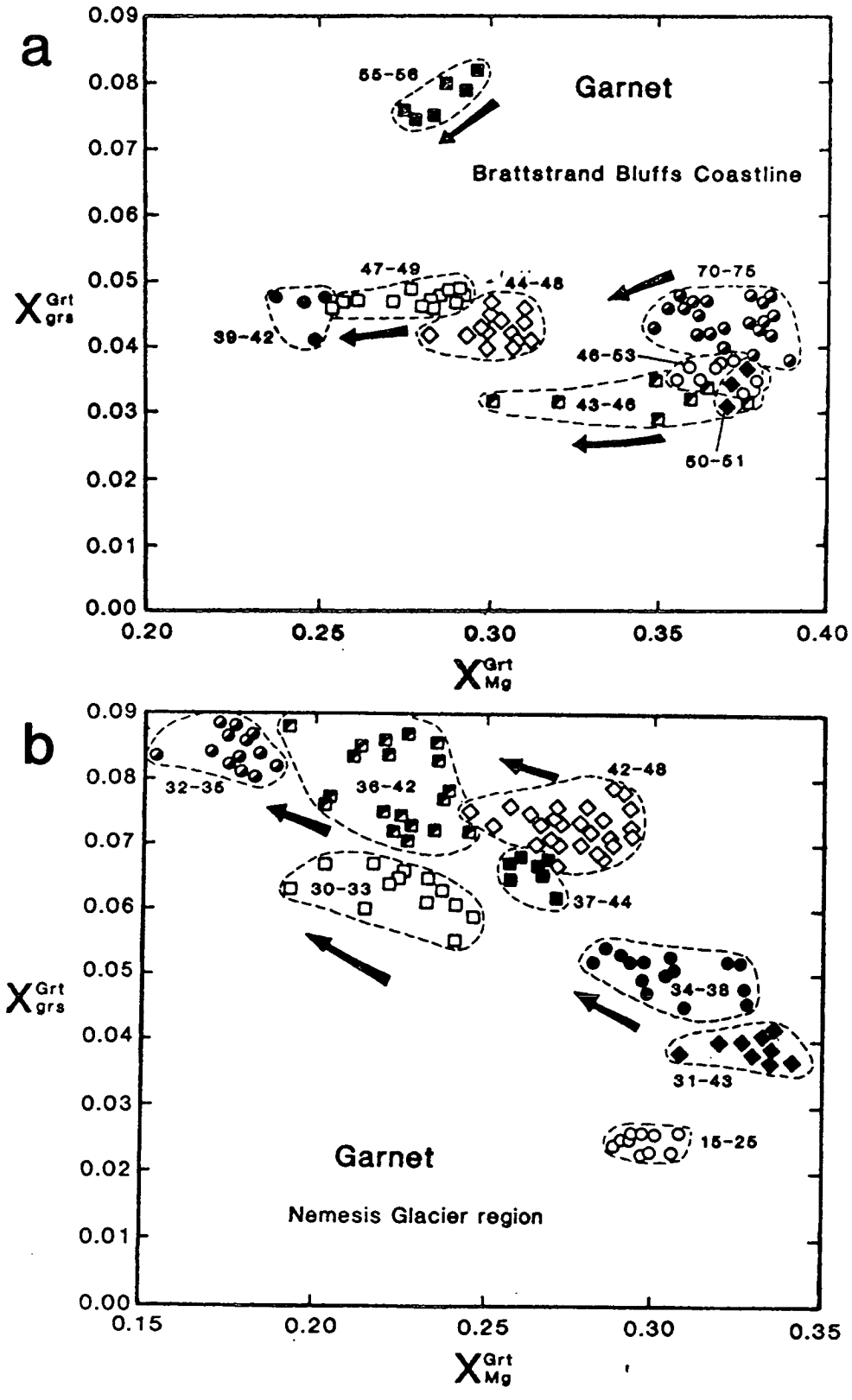

Fig. 5.2 Compositional variation in garnet from (a) Brattstrand Bluffs coastline specimens (symbols as for Fig. 5.1a), and (b) Nemesis Glacier region specimens (symbols as for Fig. 5.1b). Arrows show the direction of rimward zonation in single grains, and the numbers refer to the X_{an} compositional range of coexisting plagioclase. Note the approximate inter-specimen trends of increasing X_{grs} with decreasing X_{Mg} at fixed X_{an}, which is particularly pronounced in (b) but rather weak in (a), and increasing X_{grs} with increasing X_{an} at fixed X_{Mg} which is well developed in both diagrams. There is an intra-specimen trend of *decreasing* X_{grs} with decreasing X_{Mg} in (a), although this is only clear for specimen 88/333 which has the most calcic compositions, and *increasing* X_{grs} with decreasing X_{Mg} in (b), which is again most pronounced for the calcium-rich compositions.

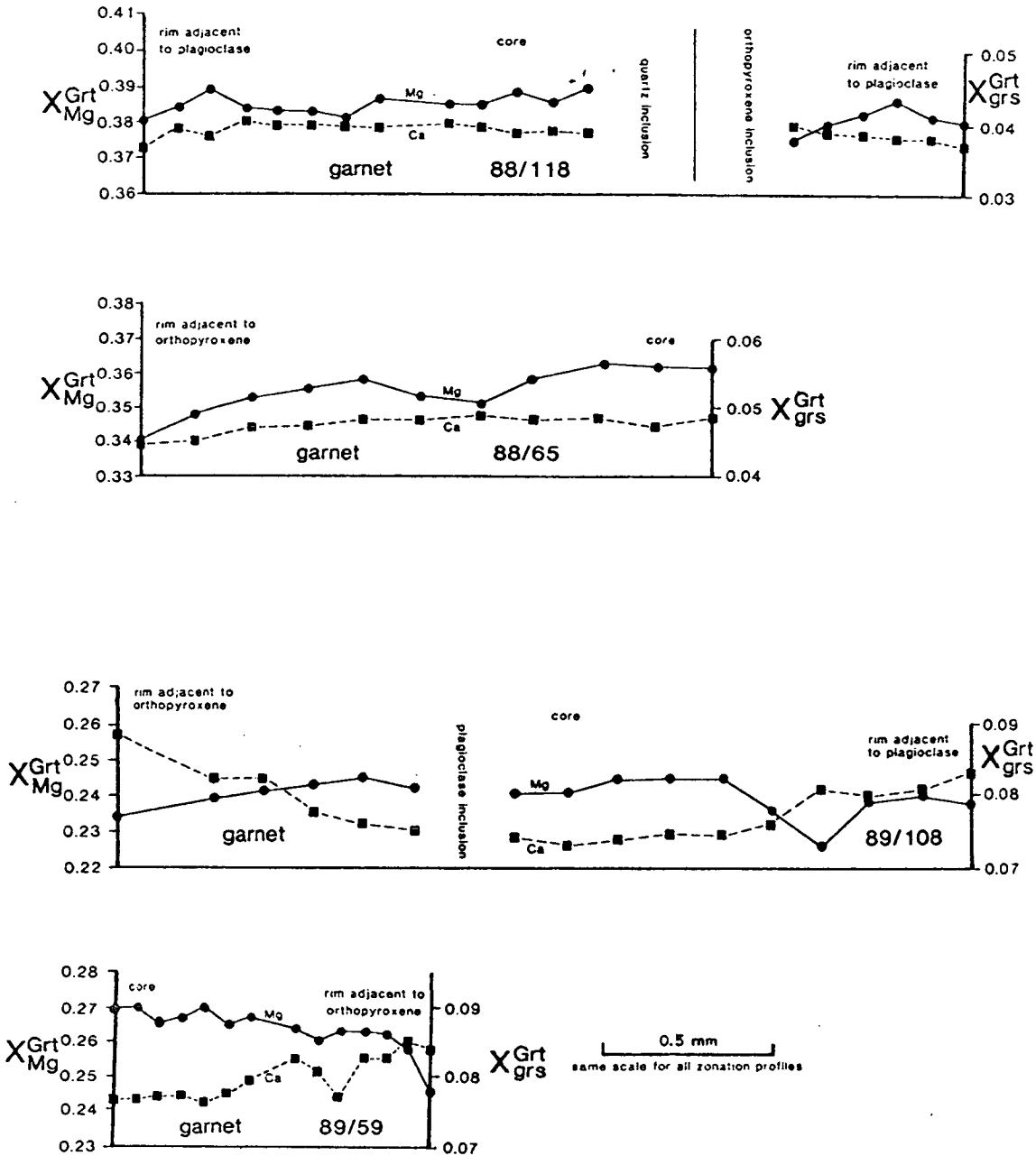

Fig. 5.3 Representative calcium and magnesium zonation profiles in garnet from the Brattstrand Bluffs coastline (specimens 88/65 and 88/118) and the Nemesis Glacier region (specimens 89/59 and 89/108). Calcium and magnesium tend to show sympathetic trends in the former but antithetic trends in the latter.

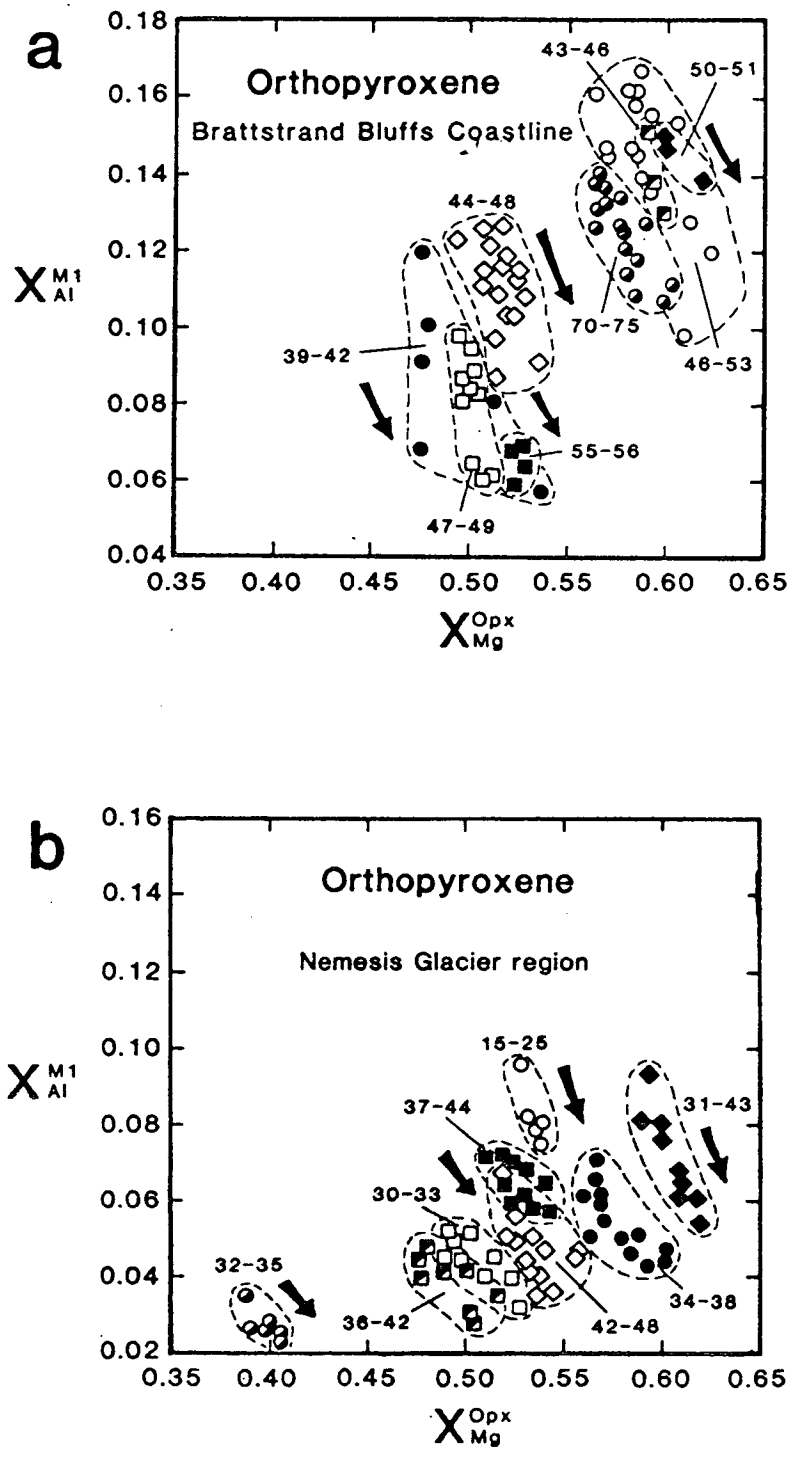

Fig. 5.4 Compositional variation in orthopyroxene from (a) Brattstrand Bluffs coastline specimens (symbols as for Fig. 5.1a), and (b) Nemesis Glacier region specimens (symbols as for Fig. 5.1b). Arrows show the direction of rimward zonation in single grains, and the numbers refer to the X_{an} compositional range of coexisting plagioclase. Note the inter-specimen trends of *increasing* X_{Al} with increasing X_{Mg} and the intra-specimen trend of *decreasing* X_{Al} with increasing X_{Mg} in both (a) and (b).

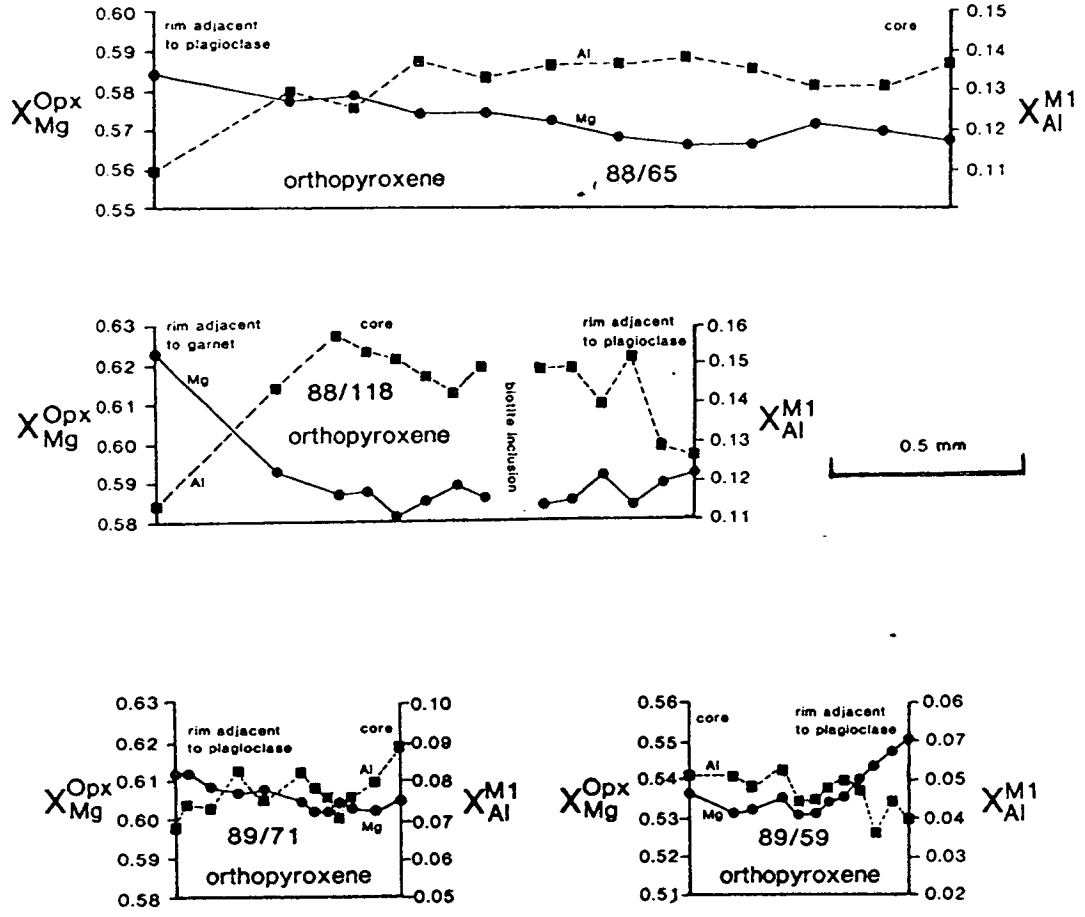

Fig. 5.5 Representative magnesium and aluminium zonation profiles in orthopyroxene from the Brattstrand Bluffs coastline (specimens 88/65 and 88/118), and the Nemesis Glacier region (specimens 89/59 and 89/71). Magnesium and aluminium show antithetic trends in both cases.

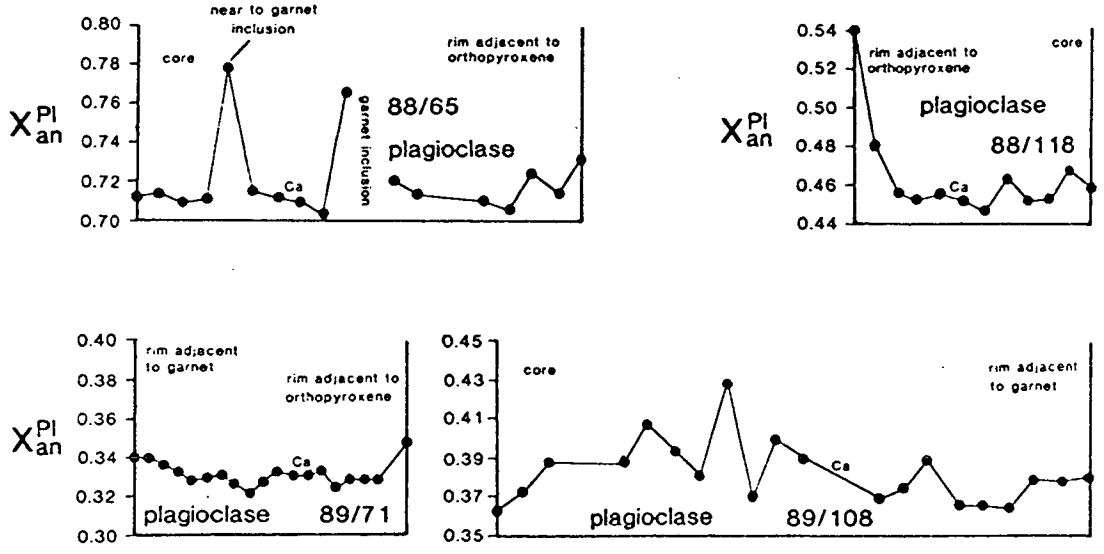

Fig. 5.6 Representative calcium zonation profiles in plagioclase from the Brattstrand Bluffs coastline (specimens 88/65 and 88/118), and the Nemesis Glacier region (specimens 89/71 and 89/108). Profiles are to the same scale as Fig.5.5 above.

5.2.4 Summary of chemical trends and reactions

Similar inter-specimen chemical variations have been identified in specimens from the Brattstrand Bluffs coastline and the Nemesis Glacier region (see Figs 5.1, 5.2 and 5.4). The most magnesian specimens, which have the most magnesian garnet and orthopyroxene, are also characterized by the most aluminous pyroxene and the least calcic garnet. The most anorthitic plagioclase coexists with garnet which has a relatively high grossularite content for a given magnesium to iron ratio.

Three important equilibria involving the phases garnet, orthopyroxene, plagioclase and quartz are the garnet-orthopyroxene iron-magnesium exchange reaction:

$$\underset{\text{pyrope}}{2Mg_3Al_2Si_3O_{12}} + \underset{\text{ferrosilite}}{3Fe_2Si_2O_6} = \underset{\text{almandine}}{2Fe_3Al_2Si_3O_{12}} + \underset{\text{enstatite}}{3Mg_2Si_2O_6} \qquad \textbf{(R5.1)},$$

the solubility of alumina in orthopyroxene coexisting with garnet:

$$\underset{\text{garnet}}{(Mg,Fe)_3Al_2Si_3O_{12}} = \underset{\text{orthopyroxene}}{(Mg,Fe)Al_2SiO_6 + (Mg,Fe)_2Si_2O_6} \qquad \textbf{(R5.2)},$$

and the reaction of garnet and quartz to form plagioclase and orthopyroxene which can be considered in terms of magnesium and iron end-member reactions:

$$\underset{\text{pyrope}}{2Mg_3Al_2Si_3O_{12}} + \underset{\text{grossularite}}{Ca_3Al_2Si_3O_{12}} + \underset{\text{quartz}}{3SiO_2} = \underset{\text{plagioclase}}{3CaAl_2Si_2O_8} + \underset{\text{enstatite}}{3Mg_2Si_2O_6} \qquad \textbf{(R5.3)},$$

$$\underset{\text{almandine}}{2Fe_3Al_2Si_3O_{12}} + \underset{\text{grossularite}}{Ca_3Al_2Si_3O_{12}} + \underset{\text{quartz}}{3SiO_2} = \underset{\text{plagioclase}}{3CaAl_2Si_2O_8} + \underset{\text{ferrosilite}}{3Fe_2Si_2O_6} \qquad \textbf{(R5.4)}.$$

Reaction R5.1 constrains the iron-magnesium distribution coefficient between garnet and orthopyroxene at fixed temperature, resulting in the specimens with the highest bulk X_{Mg} containing both the most magnesian garnet and the most magnesian orthopyroxene. Experimental studies of Reaction R5.1 (Harley, 1984*a*) indicate that an increase in X_{grs}^{Grt} at fixed pressure, temperature and bulk X_{Mg} increases the iron-magnesium distribution coefficient, causing garnet with high grossularite contents to have lower X_{Mg}^{Grt}. Similarly, experimental studies of Reaction R5.2 (Harley, 1984*b*) have shown that alumina contents of orthopyroxene increase with increasing X_{Mg}^{Opx} at constant pressure and temperature. Harley (1984*b*) also describes the effect of X_{grs}^{Grt} on the solubility of alumina in coexisting garnet and orthopyroxene. At fixed pressure, temperature and X_{Mg}^{Opx}, an increase in X_{grs}^{Grt} is associated with an increase in X_{Al}^{M1}. Reactions R5.3 and R5.4 indicate that garnet with a high grossularite content will tend to coexist with anorthite-rich plagioclase, at constant pressure and temperature. The observed inter-specimen chemical trends are consistent with the buffering of mineral compositions at different bulk composition by these reactions under a restricted pressure-temperature range for each area.

Reactions R5.1, R5.2, R5.3 and R5.4 can also be used to interpret the intra-specimen chemical variation (i.e. the zonation profiles). This variation develops at a fixed, or near-fixed, bulk composition and can therefore be considered in terms of reaction progress during pressure or temperature change, although variation in the 'reaction volume' (i.e. the scale of equilibration) during reaction progress could cause the effective bulk composition to change. Specimens from both areas exhibit a rimwards increase of X_{Mg}^{Opx} and decrease of X_{Mg}^{Grt}, reflecting progress of Reaction R5.1 from left to right which implies cooling, or possibly compression, given the steep positive slope of this reaction in pressure-temperature space (Harley, 1984*a*; see Fig. 5.7). However, the two specimen groups have contrasting grossularite zonation profiles in garnet. The rimwards increase in X_{an}^{Pl} and decrease in X_{grs}^{Grt} in specimens from the Brattstrand Bluffs coastline is consistent with progress of Reactions R5.3 and R5.4 from left to right, which implies decompression or heating given the shallow positive slope of these reactions in pressure-temperature space (Perkins & Newton, 1981; see Fig. 5.7). Given the iron-magnesium zonation profiles attributed to Reaction R5.1, decompression is the more likely of the two. The rimwards increase of X_{grs}^{Grt} in specimens from the Nemesis Glacier region is consistent with progress of Reactions R5.3 and R5.4 from right to left, which implies compression or cooling, although the plagioclase zonation is not diagnostic. Given that some component of cooling is indicated by the iron-magnesium zonation, cooling is the favoured interpretation of grossularite zonation in specimens from the Nemesis Glacier region. The rimwards decrease X_{Al}^{M1}, which occurs in many specimens from both areas, could reflect progress of Reactions R5.3 and R5.4 from left to right, which is consistent with decompression or heating (Perkins & Newton, 1981), or progress of Reaction R5.2 from right to left, which implies cooling or compression given the positive slope of this reaction in pressure-temperature space (Harley, 1984*b*; see Fig. 5.7). The evidence from garnet profiles suggests that the former is the case for the Brattstrand Bluffs coastline, whereas the latter is more likely for the Nemesis Glacier region. Hence the zonation profiles in garnet, orthopyroxene and plagioclase are consistent with retrograde decompression in the Brattstrand Bluffs coastline, with some component of cooling to account for the iron-magnesium zonation, and retrograde cooling in the Nemesis Glacier region.

Relating the zonation profiles to progress of Reactions R5.1, R5.2, R.53 and R5.4 relies on the assumption that garnet, orthopyroxene, plagioclase and quartz were in equilibrium throughout the development of the zonation profile. This is not unreasonable given the high modal abundance of all these phases, the presence of orthopyroxene, plagioclase and quartz inclusions in garnet, and garnet, plagioclase and quartz inclusions in orthopyroxene (see Sections 3.2.5 and 4.2.5), and the assumed high temperatures of granulite metamorphism. The zonation profiles, and

their implications for the metamorphic history of the Brattstrand Bluffs coastline and the Nemesis Glacier region, are considered in more detail in Sections 5.5.3 to 5.6.3.

5.3 THERMOBAROMETRY

5.3.1 Introduction

Selected core and rim analyses of garnet, orthopyroxene and plagioclase from each of the 16 specimens have been used to derive thermobarometric estimates of pressure-temperature conditions during the Proterozoic metamorphism in the Brattstrand Bluffs coastline and the Nemesis Glacier region. Core analyses were selected from the flat compositional plateau (or 'trough') at the centre of mineral grains. Rim analyses were made within 5 μm of grain edges, and, where possible, at a position of mutual contact between garnet, orthopyroxene and plagioclase. The textural setting of the chosen analysis points is considered in more detail in Section 5.6.2. All the analyses used are tabulated in Appendix 3.4, and the values of the compositional parameters (defined in Appendix 3.3) substituted into the thermobarometric expressions are listed in Table 5.2. Several calibrations of thermometer and barometer, based on Reactions R5.1, R5.2, R5.3 and R5.4 (see Section 5.2.4), have been used simultaneously to determine the pressure-temperature conditions which best fit the mineral compositions. This approach acknowledges that the compositions of coexisting garnet, orthopyroxene and plagioclase, in the presence of quartz, are buffered by all three equilibria, and also makes it unnecessary to assume a reference temperature for the barometers or reference pressure for the thermometers.

5.3.2 Thermobarometric calibrations

Reaction R5.1 has been calibrated as a thermometer by two independent experimental studies (Harley, 1984*a*; Lee & Ganguly, 1988). The thermometric equations derived in these two studies are very similar (see Section 5.4.1), although the Lee and Ganguly (1988) calibration yields temperatures between 50 and 90°C higher than the Harley (1984*a*) calibration, and Carswell and Harley (1990) have derived a 'hybrid' equation as a best fit to both data sets. Given the similarity of these three calibrations, only one calibration is used here. The Harley (1984*a*) calibration was chosen so that direct comparison can be made with its companion garnet-orthopyroxene barometer (Harley, 1984*b*), which was derived from the same experimental data. The Sen and Bhattacharya (1984) calibration of Reaction R5.1, derived by calculation from existing thermodynamic data rather than experimental study, has also been applied to the assemblages considered in this chapter.

Reaction R5.2 has been the subject of numerous experimental and thermodynamic studies, but the majority are applicable only to magnesian assemblages such as garnet lherzolites. Wood (1974) developed a barometer by

Table 5.2 Compositional parameters used for thermobarometry. Corresponding mineral analyses are tabulated in Appendix 3.4. Values marked with an asterisk were calculated from analyses corrected for ferric iron content in the orthopyroxene. Compositional parameters are defined in Appendix 3.3.

Brattstrand Bluffs coastline		X_{Mg}^{Grt}	X_{grs}^{Grt}	X_{sps}^{Grt}	X_{Mg}^{Opx}	X_{Al}^{M1}	X_{an}^{Pl}
88/38	cores	0.252	0.049	0.030	0.476	0.091	0.392
	rims	0.249	0.041	0.029	0.513	0.081	0.418
88/41	cores	0.291	0.048	0.045	0.510*	0.050*	0.480
	rims	0.277	0.048	0.045	0.510*	0.066*	0.494
88/50	cores	0.312	0.042	0.020	0.517	0.127	0.457
	rims	0.299	0.041	0.021	0.536	0.091	0.458
88/65	cores	0.382	0.048	0.025	0.566	0.136	0.712
	rims	0.348	0.044	0.025	0.584	0.109	0.733
88/88	cores	0.376	0.038	0.020	0.600	0.147	0.500
	rims	0.370	0.031	0.019	0.620	0.139	0.505
88/118	cores	0.387	0.038	0.014	0.581	0.162	0.467
	rims	0.373	0.033	0.014	0.594*	0.133*	0.526
88/168	cores	0.364	0.034	0.015	0.590	0.152	0.431
	rims	0.360	0.033	0.015	0.600*	0.128*	0.456
88/333	cores	0.296	0.080	0.018	0.502*	0.054*	0.563
	rims	0.274	0.075	0.018	0.542*	0.042*	0.568
Nemesis Glacier region		X_{Mg}^{Grt}	X_{grs}^{Grt}	X_{sps}^{Grt}	X_{Mg}^{Opx}	X_{Al}^{M1}	X_{an}^{Pl}
89/2	cores	0.328	0.047	0.015	0.560	0.061	0.354
	rims	0.305	0.054	0.015	0.603	0.047	0.369
89/40	cores	0.241	0.062	0.019	0.501*	0.037*	0.318
	rims	0.203	0.068	0.020	0.528	0.032	0.330
89/59	cores	0.280	0.070	0.028	0.520	0.067	0.435
	rims	0.245	0.076	0.030	0.545	0.036	0.444
89/63	cores	0.188	0.084	0.018	0.387	0.035	0.343
	rims	0.153	0.086	0.019	0.406	0.021	0.341
89/71	cores	0.351	0.037	0.020	0.590	0.081	0.347
	rims	0.320	0.041	0.023	0.618	0.061	0.334
89/106	cores	0.264	0.068	0.024	0.510	0.073	0.404
	rims	0.261	0.062	0.027	0.547*	0.056*	0.416
89/108	cores	0.235	0.073	0.037	0.489	0.041	0.380
	rims	0.211	0.086	0.039	0.517	0.035	0.369
89/334J	cores	0.301	0.027	0.027	0.532	0.082	0.248
	rims	0.298	0.024	0.028	0.536	0.079	0.241

integration of new experimental data in ferrous systems with magnesian data. Further experimental studies on a wider range of bulk compositions were used to produce both a semi-empirical barometer with constraints from natural rocks (Harley & Green, 1982), and a more thermodynamically-rigorous model (Harley, 1984*b*), which are the two calibrations used here.

Experimental data on Reaction R5.3 were the basis of barometers first used by Wood (1975) and Wells (1979). Newton (1978) refined earlier calibrations by considering the results of enthalpy and entropy determinations of the phases involved. Perkins and Newton (1981) and Newton and Perkins (1982) calibrated the magnesian reaction (Reaction R5.3) from available thermodynamic data and applied it to a wide range of granulite terrains. The iron end-member reaction (Reaction R5.4) was calibrated by algebraic combination of experimental data on related equilibria by Bohlen *et al.* (1983*a*,*b*). Perkins and Chipera (1985) used thermodynamic and experimental data to compare the iron and magnesium reactions, and produced mutually-consistent calibrations for both reactions. This approach has also been followed by Essene (1989), who re-calibrated both the iron and magnesium reactions with a self-consistent data base derived from the most recent experimental and thermodynamic studies. Since both calibrations involve the same phases, any discrepancy between derived pressures must stem from the calibrations themselves, incorrect temperature estimates, or disequilibrium. Four calibrations have been used here, the magnesium calibration of Newton and Perkins (1982), the iron calibration of Bohlen *et al.* (1983*a*) and the two self-consistent calibrations of Essene (1989).

Bhattacharya *et al.* (1991) have recently proposed new calibrations of the garnet-orthopyroxene thermometer (Reaction R5.1) and the garnet-orthopyroxene-plagioclase-quartz barometer (Reactions R5.3 and R5.4), but these are not considered here.

5.3.3 Solution models

Accurate solution models are a necessity for the application of thermobarometric calibrations to natural rocks. There is still no consensus on the activity-composition relationships for even the most common anhydrous minerals, including orthopyroxene, plagioclase and garnet. The approach used here is to employ the activity models recommended by the authors of each calibration.

Harley (1984*a*,*b*), Sen and Bhattacharya (1984), Newton and Perkins (1982) and Bohlen *et al.* (1983*a*) treat garnet as a ternary calcium-iron-magnesium regular solution. The activity coefficients are approximated by the following expressions (Prigogine & Defay, 1954)

$$RT \ln \gamma_{alm}^{Grt} = (X_{prp})^2 W_{FeMg} + (X_{grs})^2 W_{CaFe} + X_{prp} X_{grs}(W_{FeMg} + W_{CaFe} - W_{CaMg}) \quad (5.17),$$

$$RT \ln \gamma_{prp}^{Grt} = (X_{alm})^2 W_{FeMg} + (X_{grs})^2 W_{CaMg} + X_{alm} X_{grs}(W_{FeMg} + W_{CaMg} - W_{CaFe}) \quad (5.18),$$

$$RT \ln \gamma_{grs}^{Grt} = (X_{alm})^2 W_{CaFe} + (X_{prp})^2 W_{CaMg} + X_{alm} X_{prp}(W_{CaFe} + W_{CaMg} - W_{FeMg}) \quad (5.19).$$

W_{CaFe}, W_{CaMg} and W_{FeMg} are interaction parameters for the grossularite-almandine, grossularite-pyrope and almandine-pyrope binary joins respectively, which are related to the excess free energy derived from mixing of the components by the relationship

$$G^{ex} = X_i X_j W_{ij} \quad (5.20),$$

Table 5.3 Garnet interaction parameters used in garnet-orthopyroxene thermobarometers.

	Harley (1984*a*)	Lee & Ganguly (1988)	Sen & Bhattacharya (1984)
$W_{CaMg} - W_{CaFe}$	1400	3000	3300 - 1.5*T*
W_{FeMg}	0	0	195
	Newton & Perkins (1982)		Bohlen *et al.* (1983*a*)
W_{CaFe}	0		1050 - 1.2 *T*
W_{CaMg}	3300 - 1.5 *T*		4180 - 1.2 *T*
W_{FeMg}	0		3480 - 1.2 *T*

All the parameters are in units of cal / mol.

and hence the excess free energy of mixing is symmetrical about each binary join. Different calibrations use different values for the interaction parameters, some of which are summarized in Table 5.3. The effect of other components in garnet, principally manganese, ferric iron and chromium, have generally been ignored, although Harley (1984*a*) and Bohlen *et al.* (1983*b*) suggest approximations to allow for low manganese contents. In general, the calibrations should not be used with garnets rich in components other than calcium, ferrous iron and magnesium.

The calibrations of Lee and Ganguly (1988) and Essene (1989) treat garnet binary joins as asymmetric, and two interaction parameters are needed to define the excess free energy of mixing at each join

$$G^{ex} = X_i X_j (W_{ij} X_j + W_{ji} X_i) \quad (5.21).$$

The activity coefficients are derived from the quaternary calcium-iron-magnesium-manganese mixing model of Ganguly and Saxena (1984, p. 97), which includes ternary interaction terms as well as two binary interaction parameters for each join. Lee and Ganguly (1988) use the interaction parameters suggested by Ganguly and Saxena (1984), but Essene (1989) uses modified values of the calcium-iron mixing parameters after Anovitz and Essene (1987).

Most calibrations used in this study employ the ideal two-site iron-magnesium mixing model for orthopyroxene (Wood & Banno, 1973), which gives

$$a_{en} = X_{Mg}^{M1} X_{Mg}^{M2} \quad (5.22), \text{ and}$$
$$a_{fs} = (1 - X_{Mg}^{M1} - X_{Al}^{M1}) (1 - X_{Mg}^{M2}) \quad (5.23),$$

where M1 and M2 are the two non-tetrahedral cation sites in orthopyroxene. These expressions assume that all the aluminium is present in the M1 site and that any potential interaction effects due to aluminium solubility can be ignored. Hence the site fractions can be approximated by the following expressions

$$X_{Mg}^{M1} = X_{Mg}^{Opx} (1 - X_{Al}^{M1}) \quad (5.24) \quad \text{and}$$
$$X_{Mg}^{M2} = X_{Mg}^{Opx} \quad (5.25),$$

and the orthopyroxene activities can be expressed as

$$a_{en} = (X_{Mg}^{Opx})^2 (1 - X_{Al}^{M1}) \quad (5.26) \quad \text{and,}$$
$$a_{fs} = (1 - X_{Mg}^{Opx})^2 (1 - X_{Al}^{M1}) \quad (5.27).$$

Harley (1984*b*) treats the M2 site as a binary iron-magnesium regular solution, and the M1 site as a ternary iron-magnesium-aluminium regular solution, with reciprocal interactions across the sites, which yields more complex expressions for a_{en} and a_{fs} (see Harley, 1984*b* p. 668).

All the calibrations use the aluminium-avoidance model for anorthite activities (Newton *et al.*, 1980), which are derived as follows:

$$RT \ln \gamma_{an} = (1 - X_{an})^2 [2050 + 9392 X_{an}] \quad (5.28), \quad \text{and}$$
$$a_{an} = \frac{\gamma_{an} [X_{an} (1 + X_{an})^2]}{4} \quad (5.29).$$

5.3.4 Thermobarometric results

Calculated positions of the thermobarometric equilibria in pressure-temperature space are presented in Fig. 5.7. Each line on these diagrams represents the range of possible pressure-temperature conditions of equilibration, derived for a given thermobarometric calibration using a single composition each of garnet, orthopyroxene and plagioclase relevant for a single specimen. There are two diagrams for each specimen, one calculated using core compositions of garnet, orthopyroxene and plagioclase, and the other for rim compositions. The Harley (1984*a*) and Sen and Bhattacharya (1984) garnet-orthopyroxene exchange calibrations have a high d*P*/d*T* whereas the various garnet-orthopyroxene-plagioclase-quartz calibrations have a low d*P*/d*T*, making them particularly suitable for thermometry and barometry respectively. The Harley and Green (1982) calibration of the solubility of alumina in coexisting orthopyroxene and garnet has both a fairly strong temperature and pressure dependence, whereas the Harley (1984*b*) calibration of the same equilibrium has a relatively low d*P*/d*T*. A number of remarks can be made regarding the relative positions of the equilibria in pressure-temperature space.

(i) The Harley (1984*a*) calibration of the garnet-orthopyroxene thermometer always yields lower temperatures than the Sen and Bhattacharya (1984) calibration. The difference varies between 20 and 150°C, and is greatest in those samples which record the highest temperatures.

(ii) The Essene (1989) calibrations of the garnet-orthopyroxene-plagioclase-quartz barometer always yield higher pressures than those of Newton and Perkins (1982) and Bohlen *et al.* (1983*a*,*b*). At 800°C, the difference between the magnesium calibrations varies between 0.9 and 3.8 kbar, and the difference between the iron calibrations is between 0.9 and 1.5 kbar.

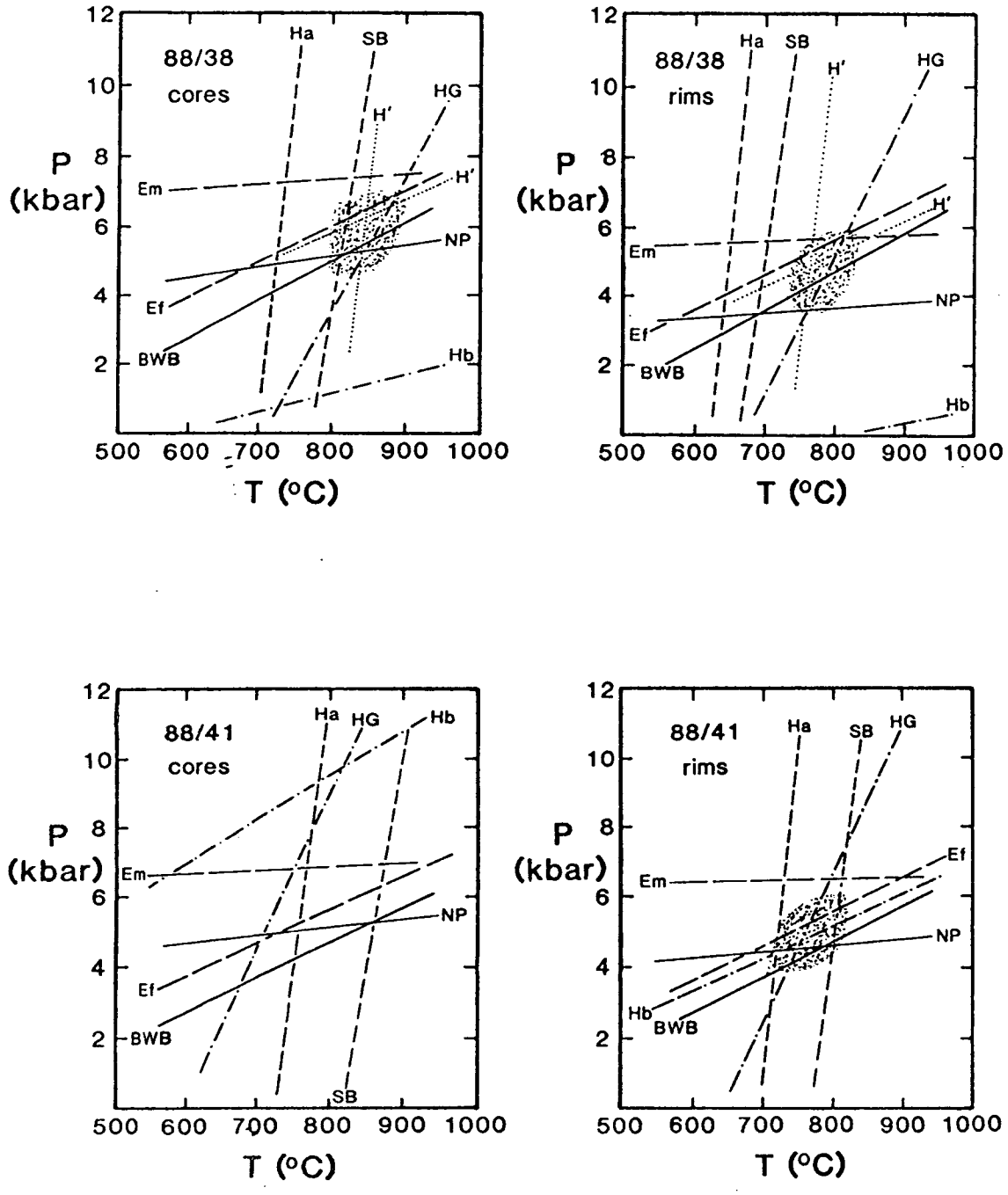

Fig. 5.7 Pressure-temperature estimates for specimens from the Brattstrand Bluffs coastline and Nemesis Glacier region, using the following calibrations for core and rim compositions: Harley, 1984*a* (Ha); Sen and Bhattacharya, 1984 (SB); Harley, 1984*b* (Hb); Harley and Green, 1982 (HG); Newton and Perkins 1982 (NP); Bohlen *et al.*, 1983*a* (BWB); the magnesium end-member calibration of Essene, 1989 (Em); and the iron end-member calibration of Essene, 1989 (Ef). The dotted lines denoted H' are the corrected positions of Ha and Hb as discussed in Section 5.6.2, and the shaded area is the favoured pressure-temperature estimate with an uncertainty of about ± 50°C, ± 1 kbar. No area is shaded on the core estimates for specimen 88/41 because of the disparate positions of the calibrations. This specimen is briefly considered in Section 5.6.2. This figure continues onto the next 7 pages.

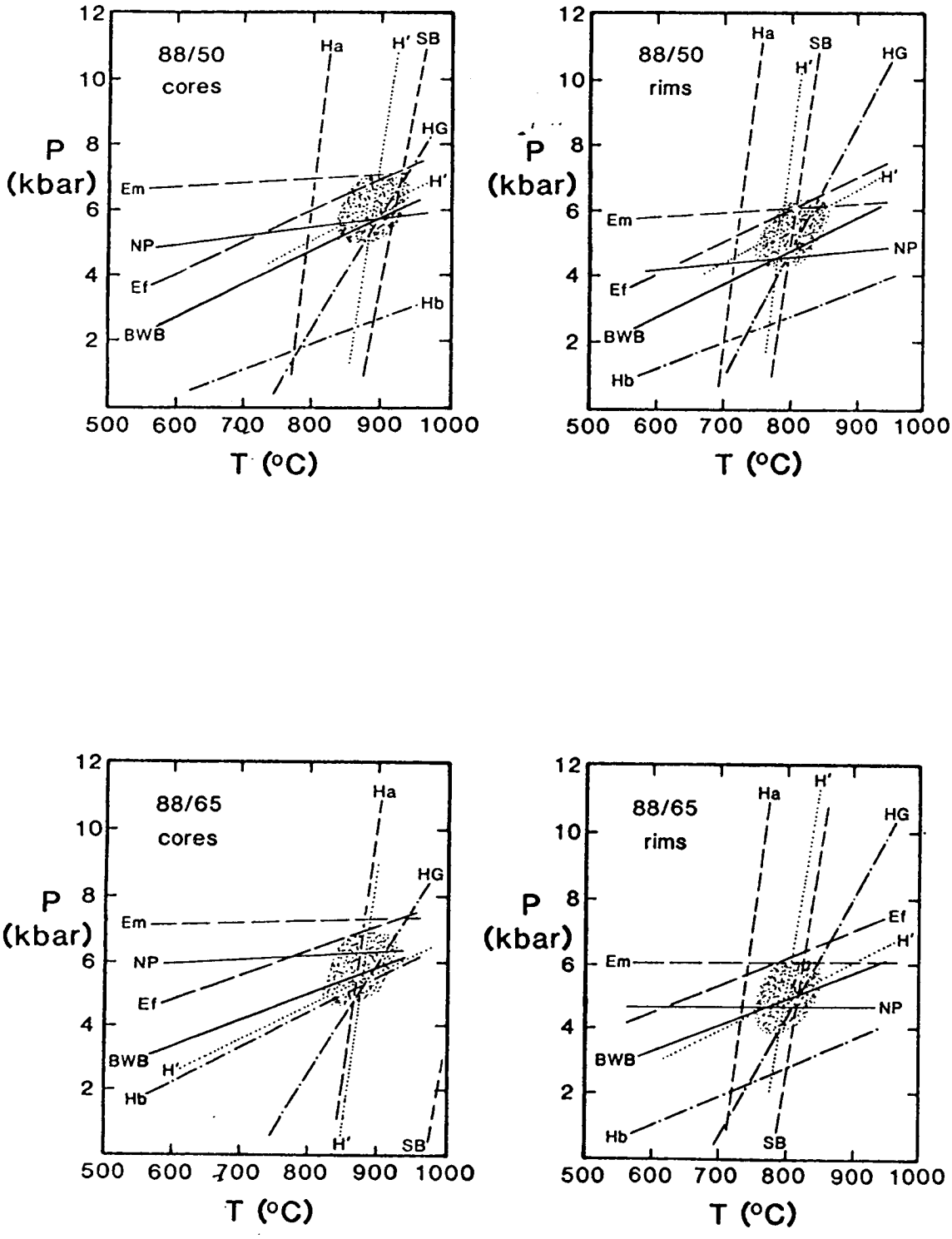

Fig. 5.7 continued.

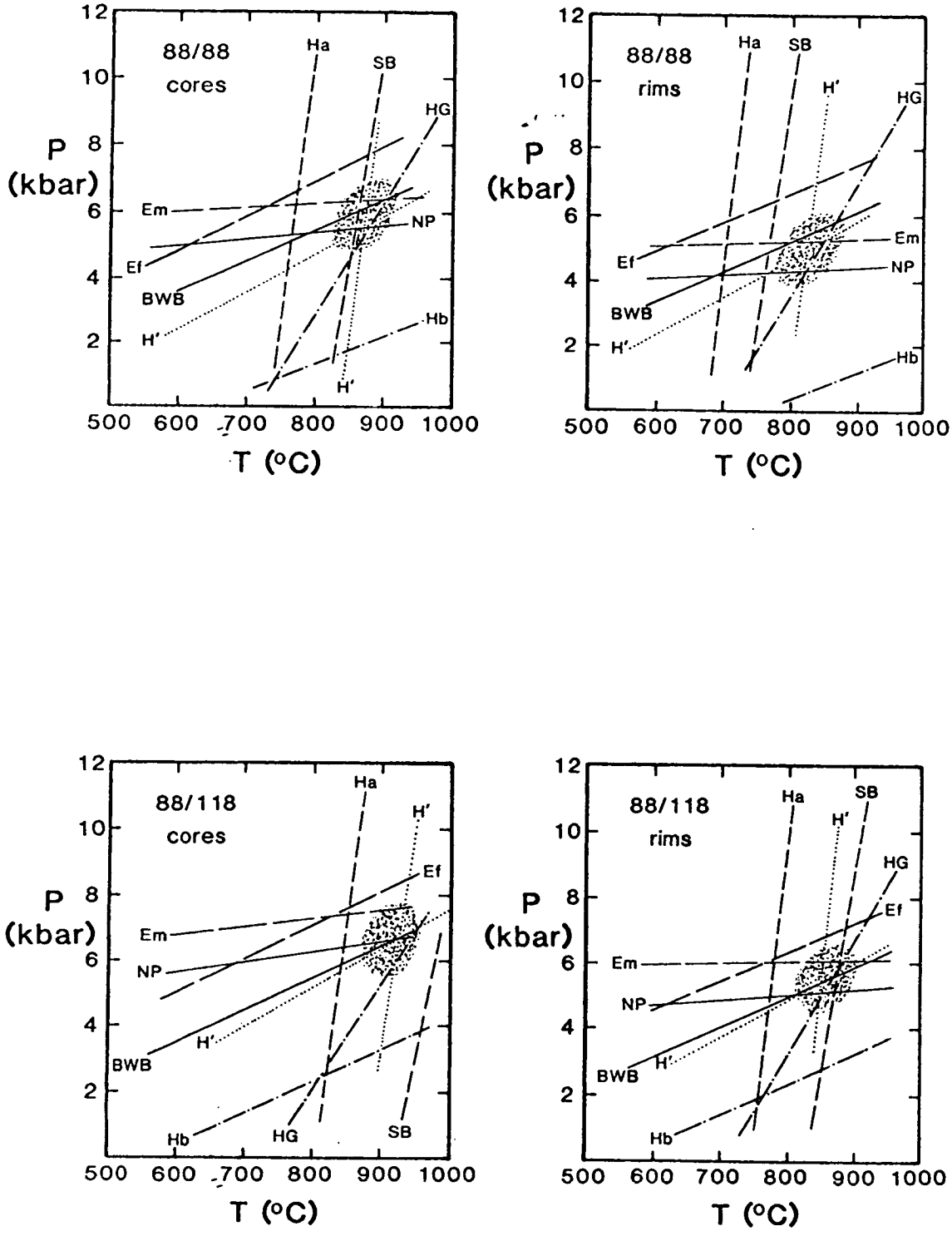

Fig. 5.7 continued.

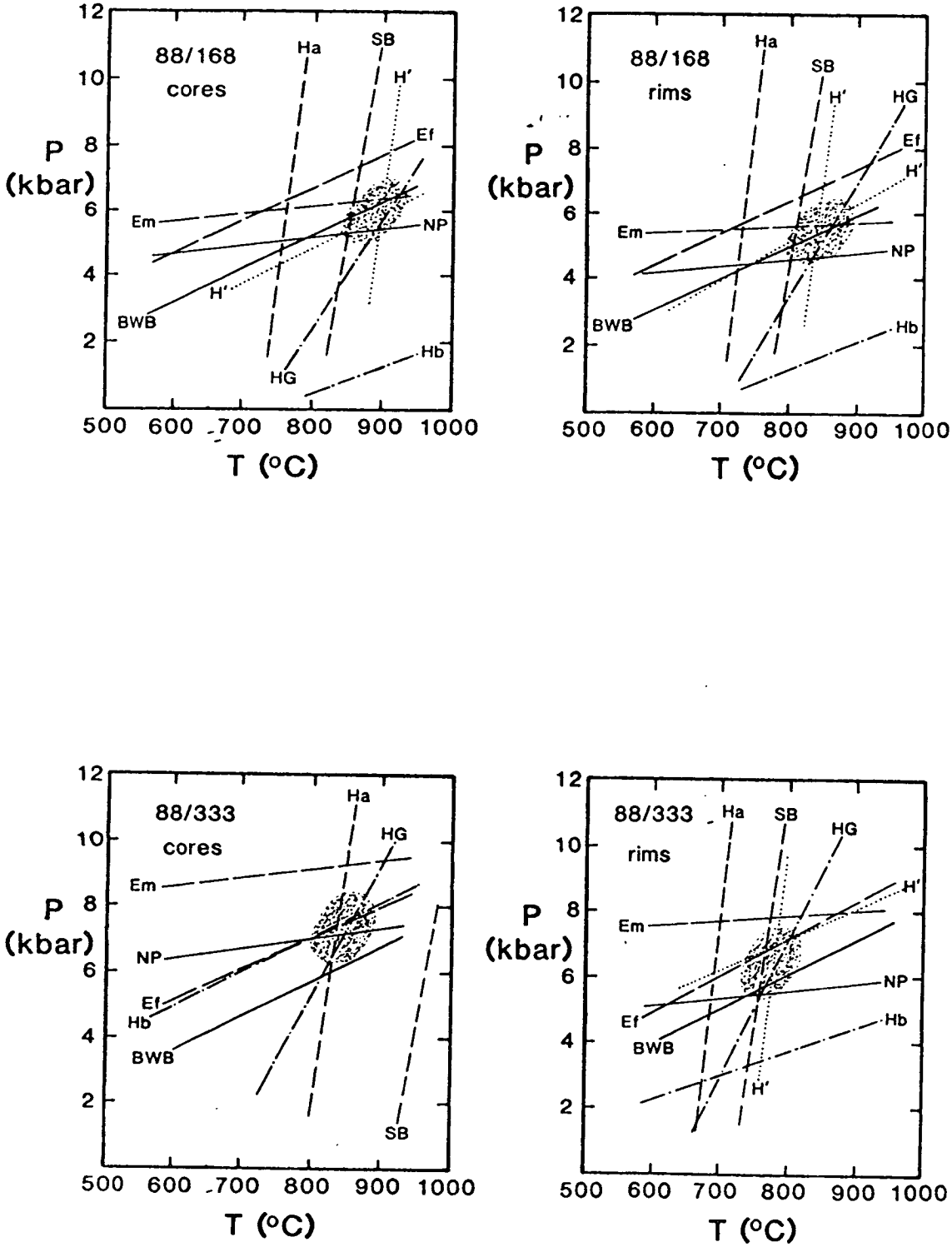

Fig. 5.7 continued.

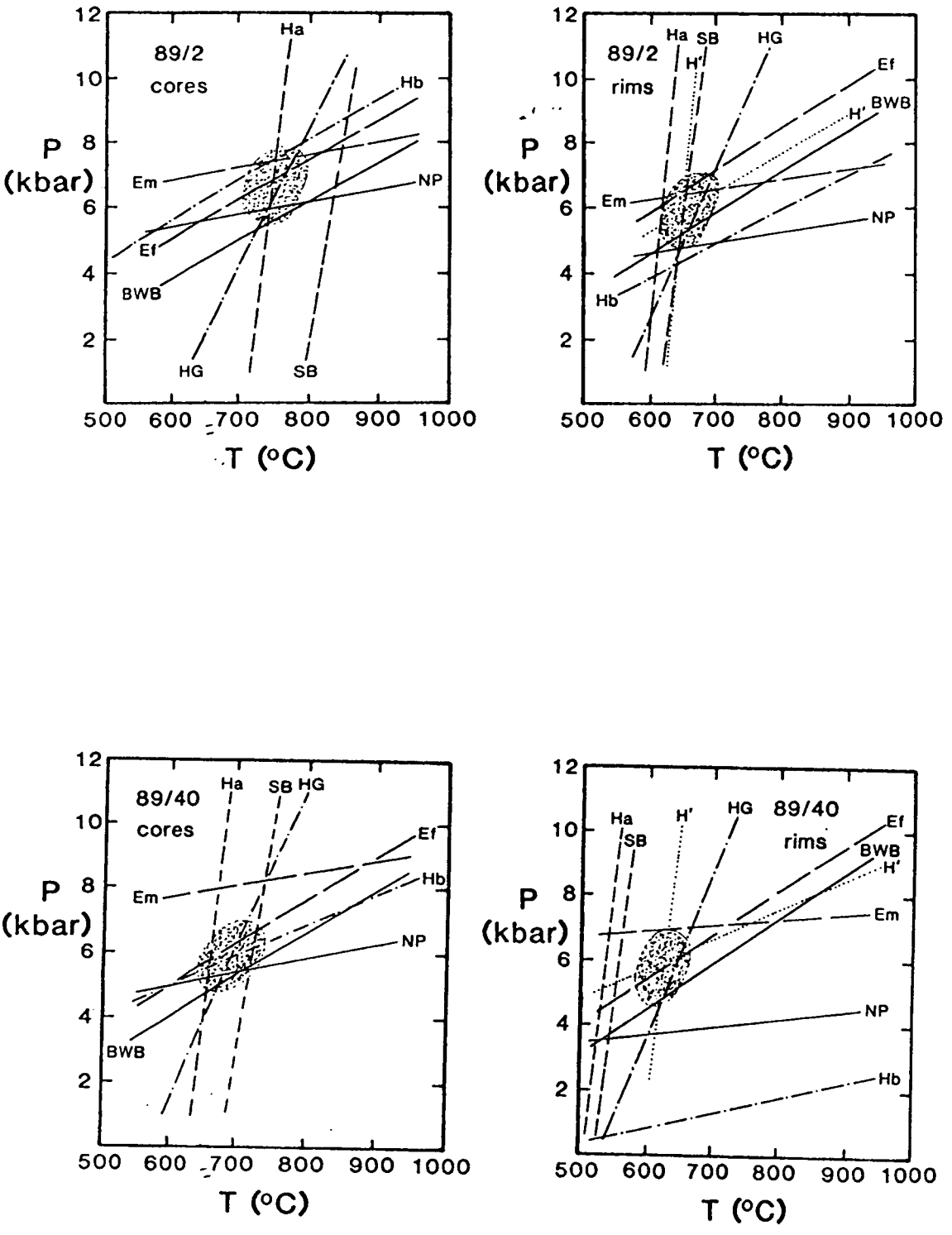

Fig. 5.7 continued.

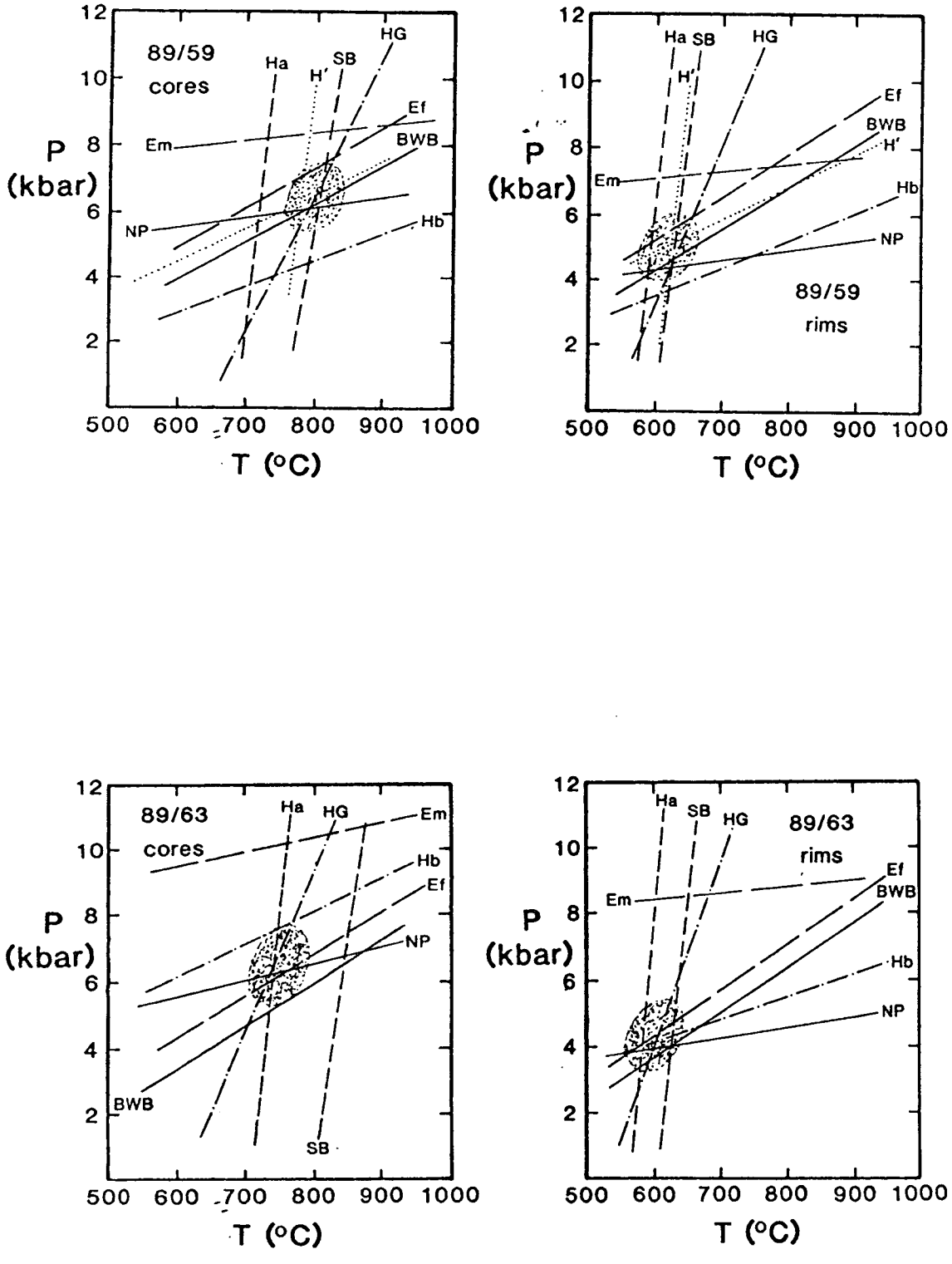

Fig. 5.7 continued.

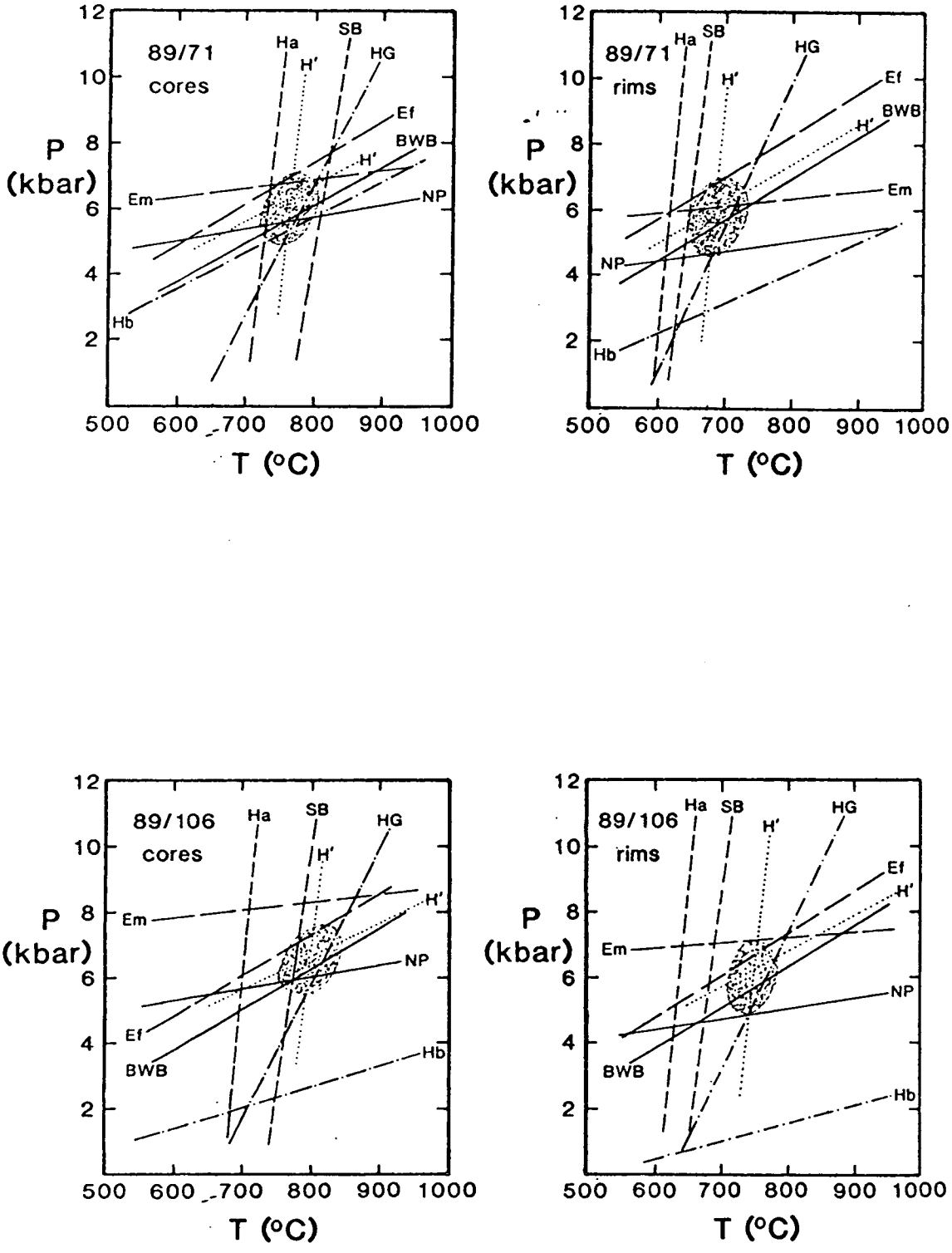

Fig. 5.7 continued.

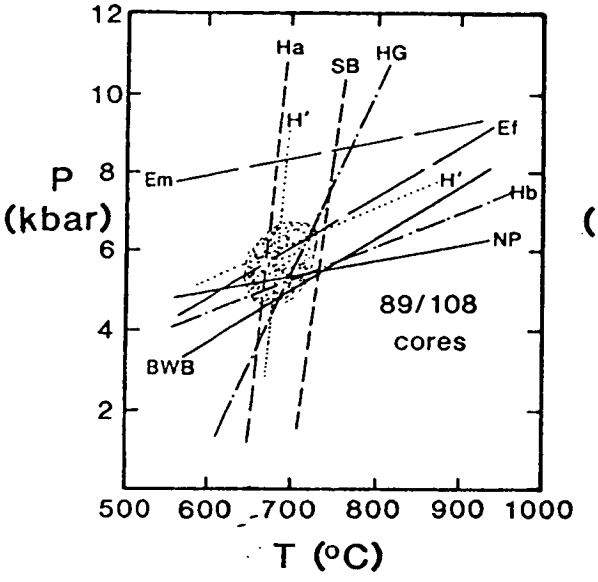

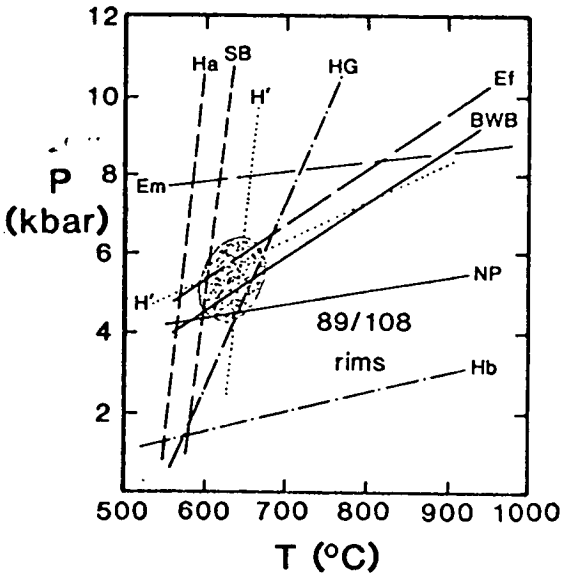

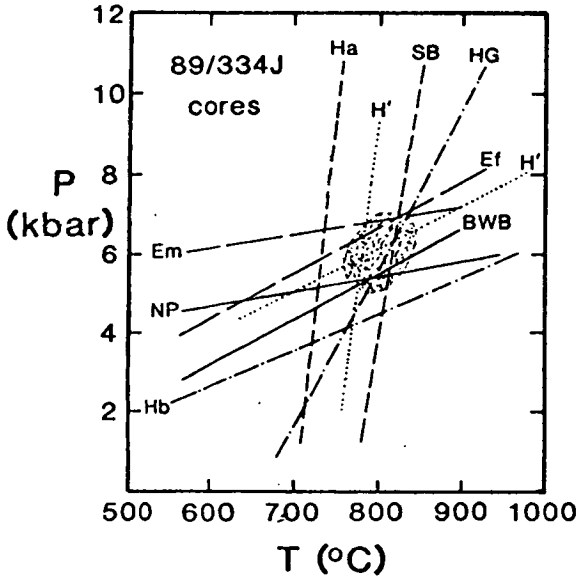

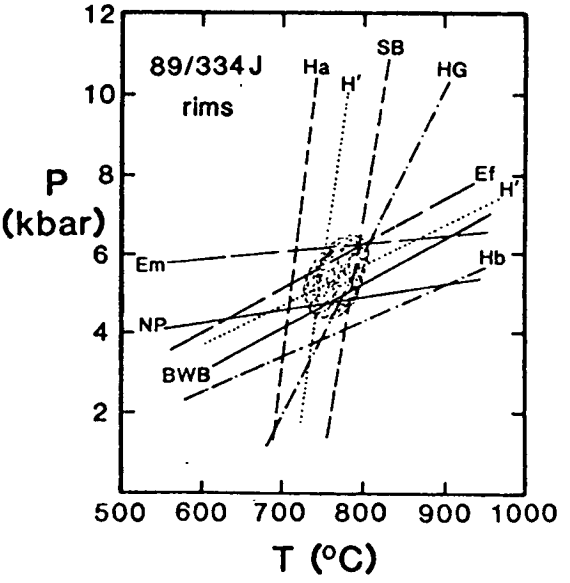

Fig. 5.7 continued.

(iii) The Harley (1984*b*) calibration of the garnet-orthopyroxene barometer exhibits variable behaviour with respect to the Harley and Green (1982) calibration. For some specimens (e.g. 88/38, 88/50, 88/168, 89/106), the Harley (1984*b*) calibration, for both core and rim compositions, is positioned at significantly lower pressures than the intersection between the Harley and Green (1982) calibration and the garnet-orthopyroxene-plagioclase-quartz barometers. In others it occurs at similar pressures for mineral cores, but lower pressures for mineral rims (e.g. 88/333, 89/40). This variation can be correlated with the behaviour of the Harley (1984*a*) thermometer. Specimens which yield low Harley (1984*b*) pressures, also yield low Harley (1984*a*) temperatures with respect to the intersection of the other calibrations, whereas specimens with Harley (1984*b*) pressures equivalent to the garnet-orthopyroxene-plagioclase-quartz barometers have Harley (1984*a*) temperatures equivalent to the Harley and Green (1982) garnet-orthopyroxene calibration in this pressure range. In the latter specimens, the Sen and Bhattacharya (1984) thermometer yields temperatures significantly higher than those indicated by all other calibrations.

(iv) Specimen 88/41 yields Harley (1984*b*) mineral core pressures which are higher than those derived from other barometers, and the Harley and Green (1982) calibration occurs at lower temperatures than the Harley (1984*a*) thermometer in the pressure range of most of the garnet-orthopyroxene-plagioclase-quartz barometers. This specimen is discussed further in Section 5.6.2.

(v) All thermobarometric calibrations yield lower temperatures and pressures for rim compositions than core compositions.

The systematic variation between core and rim calculations clearly reflects the zonation profiles discussed in Section 5.2.4, but the systematic intra-specimen variation between different calibrations requires some explanation before any pressure-temperature estimates can be made from Fig. 5.7. It is clear that the two garnet-orthopyroxene exchange calibrations cannot both be yielding peak temperature conditions from core compositions in each specimen. Similarly, all the garnet-orthopyroxene-plagioclase-quartz barometers cannot be yielding peak pressures. Of prime importance is the need to determine whether the variable positions of these equilibria reflect mineral disequilibrium or deficiencies in the thermobarometric calibrations. Disequilibrium effects are considered in Section 5.5. The next section identifies inconsistencies which are inherent to the calibrations themselves.

5.4 A COMPARISON OF THE THERMOBAROMETRIC CALIBRATIONS

5.4.1 The garnet-orthopyroxene Fe-Mg exchange thermometer

The differences in the positions of the Harley (1984*a*) and Sen and Bhattacharya (1984) thermometers in pressure-temperature space can be considered in terms of the

thermodynamic relationship they represent. These two calibrations, and that of Lee and Ganguly (1988), are solutions to Equation 5.15. All the calibrations assume that orthopyroxene is an ideal solid solution, and hence Equation 5.13 is simplified to

$$K_\gamma = (\gamma_{Fe} / \gamma_{Mg})^{Grt} \quad (5.30), \quad \text{and}$$
$$RT \ln K_\gamma = RT \ln \gamma_{Fe} - RT \ln \gamma_{Mg} \quad (5.31),$$

for one mole of cation exchange. Combination of Equation 5.31 with the regular-solution expressions for γ_{Fe} and γ_{Mg} (Equations 5.17 and 5.18) yield the relationship

$$RT \ln K_\gamma = (X_{prp} - X_{alm})\, W_{FeMg} + (W_{CaFe} - W_{CaMg})\, X_{grs} \quad (5.32).$$

This can be inserted into Equation 5.15 to produce

$$T = \frac{\Delta H^\circ_{1,T} + P\Delta V^\circ + (X_{prp} - X_{alm})\, W_{FeMg} + (W_{CaFe} - W_{CaMg})\, X_{grs}}{\Delta S^\circ_{1,T} - R \ln K_D} \quad (5.33).$$

The terms in this expression can be divided into two groups; the standard-state thermodynamic variables $\Delta H^\circ_{1,T}$, $\Delta S^\circ_{1,T}$ and ΔV°, and the interaction-parameter terms. The standard-state terms can be isolated by considering the calcium-absent FeO-MgO-Al_2O_3-SiO_2 system ($X_{grs} = 0$), and assuming that iron-magnesium mixing in garnet is ideal ($W_{FeMg} = 0$), so that Equation 5.33 can be rewritten as

$$R \ln K_D = \Delta S^\circ_{1,T} - \frac{(\Delta H^\circ_{1,T} + P\Delta V^\circ)}{T} \quad (5.34).$$

Fig. 5.8 shows the relationship between K_D and temperature in the calcium-absent system for several calibrations at pressures relevant to many granulite terrains (7.5 kbar). The positions of the lines are a function only of $\Delta H^\circ_{1,T}$, $\Delta S^\circ_{1,T}$ and ΔV°, the values of which are given in Table 5.4. The Harley (1984*a*) and Lee and Ganguly (1988) calibrations use very similar standard-state thermodynamic quantities (indeed they are within the uncertainties given in the two calibrations), but the values used by Sen and Bhattacharya (1984) are somewhat different. Table 5.4 also includes $\Delta H^\circ_{1,T}$, $\Delta S^\circ_{1,T}$ and ΔV° values calculated from the data set of Holland and Powell (1990), which comprises the most recent thermodynamic data available. Two sets of values

Table 5.4 Standard-state thermodynamic data used in the garnet-orthopyroxene exchange calibrations of Harley, 1984*a* (H); Lee and Ganguly, 1988 (L & G); Sen and Bhattacharya, 1984 (S & B); Holland and Powell, 1990, assuming that values of *H*, *S* and *V* do not vary with pressure and temperature (H & P[1]); and Holland and Powell, 1990, taking pressure-temperature dependence into account (H & P[2]).

	H	L & G	S & B	H & P[1]	H & P[2]
$\Delta H^\circ_{1,T}$ (cal / mol)	-3740	-3922	-2713	-2898	-2783
$\Delta S^\circ_{1,T}$ (cal / (mol.K))	-1.96	-1.91	-0.787	-1.081	-1.036
ΔV° (cal / kbar)	-22.86	-23.70	-22.0	24.11	-30.16

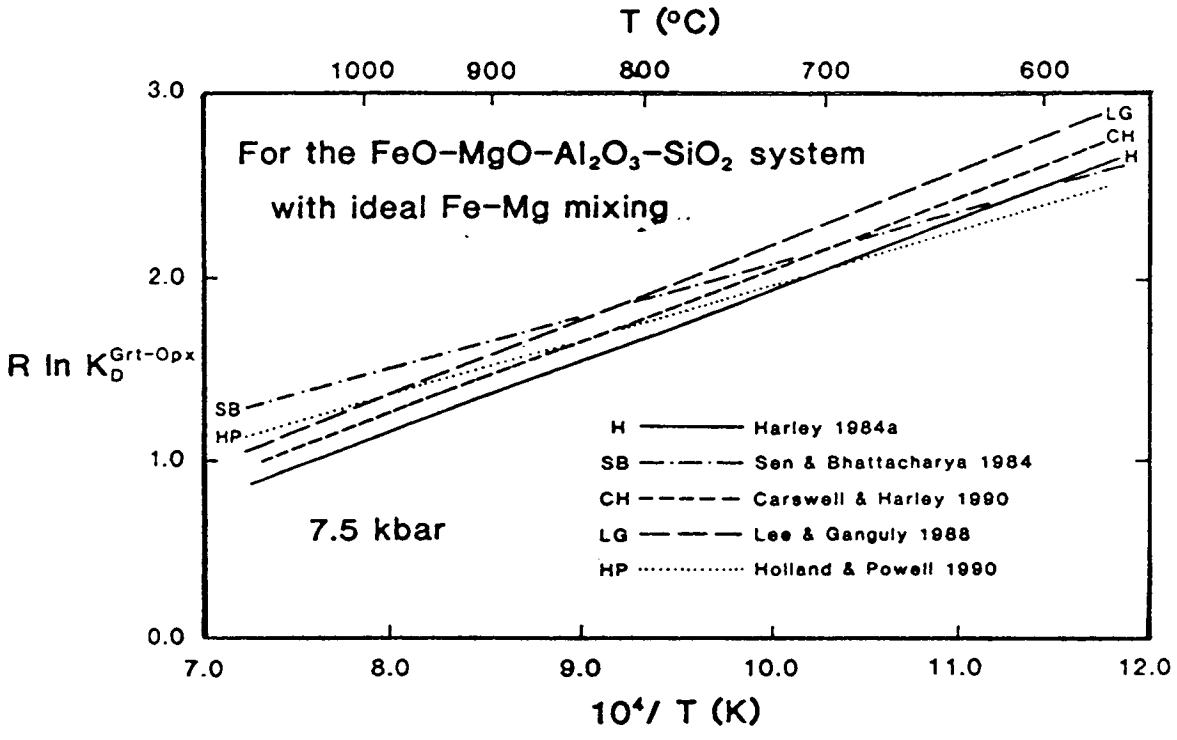

Fig. 5.8 A plot of R ln K_D versus 1 / T for various calibrations of the garnet-orthopyroxene exchange reaction at 7.5 kbar in the FMAS system with ideal Fe-Mg mixing. The positions of the reaction using the two sets of Holland and Powell (1990) data given in Table 5.4 are indistinguishable on this diagram and only one line has been drawn.

were calculated, one making the approximation that the values of $\Delta H^\circ_{1,T}$ and $\Delta S^\circ_{1,T}$ in the temperature range of Fig. 5.8 are no different from the values at 298 K, and ignoring the effect of thermal expansion and isothermal compression on ΔV°, and the other taking this pressure and temperature dependence into account. Although these calculations produced a different set of standard-state values, the combination of values for the exchange did not significantly alter the position of the Holland and Powell (1990) calibration in Fig. 5.8, indicating that ignoring pressure and temperature dependence is a valid approximation in this case.

The Holland and Powell (1990) values of $\Delta H^\circ_{1,T}$ and $\Delta S^\circ_{1,T}$ in both calculations are most consistent with the Sen and Bhattacharya (1984) calibration. As expected, the value of ΔV° ignoring the effect of thermal expansion and isothermal compression is similar to that used by all the other calibrations, but the more rigorous value is larger. In fact, the value of ΔV° is not crucial to the positioning of the lines in Fig. 5.8 since it is swamped by the value of $\Delta H^\circ_{1,T}$. The dominance of $\Delta H^\circ_{1,T}$ in determining the slope of the lines on Fig. 5.8 is indicated by the similar slopes of the Sen and Bhattacharya (1984) and Holland and Powell (1990) calibrations, and the similar slopes of the Harley (1984*a*) and Lee and Ganguly (1988) calibrations. The calibrations are also highly sensitive to the chosen value of $\Delta S^\circ_{1,T}$, which is responsible for the difference in position between the Sen and Bhattacharya (1984)

Table 5.5 A comparison of temperatures derived from the garnet-orthopyroxene exchange thermometers depicted in Fig. 5.8, using fixed K_D values equivalent to Harley (1984*a*) temperatures of 750, 800 and 850°C (for the calcium-absent system).

calibration	K_D (1)	K_D (2)	K_D (3)
Harley (1984*a*)	750	800	850
Holland & Powell (1990)	762	830	900
Carswell & Harley (1990)	782	835	885
Lee & Ganguly (1988)	820	870	925
Sen & Bhattacharya (1984)	820	890	970

and Holland and Powell (1990) calibrations, and between the Harley (1984*a*) and Lee and Ganguly (1988) calibrations. The hybrid calibration of Carswell and Harley (1990) is also plotted on Fig. 5.8, and lies between the Harley (1984*a*) and Lee and Ganguly (1988) calibrations. The effect that these differences between the calibrations has on temperature estimates at fixed K_D is indicated in Table 5.5, which gives the temperature estimates derived using various calibrations at three K_D values equivalent to Harley (1984*a*) temperatures of 750, 800 and 850°C.

It is interesting that the two experimental calibrations yield thermodynamic data which are consistent, but that differ from published collections of thermodynamic data. This could reflect effects such as aluminium solubility in orthopyroxene, which were assumed not to have an effect on K_D in the experimental studies but could cause the experimental calibrations to apparently disagree with thermodynamic data. Another important consideration is that the magnitude of the changes in enthalpy, entropy and volume associated with the exchange reaction are small compared individual values for each phase. Hence the uncertainties inherent in the standard-state thermodynamic data for each phase introduce substantial uncertainty into the differences in enthalpy, entropy and volume used to derive the temperatures via Equation 5.34.

Fig. 5.9 compares the actual difference between the Harley (1984*a*) and Sen and Bhattacharya (1984) temperatures derived from the garnet-orthopyroxene specimens with that predicted by Fig. 5.8. It is clear that most of the temperature discrepancy can be explained by the differences due to standard-state thermodynamic parameters, with only about another 20 to 30°C difference resulting from another source. This extra difference, which is less than the uncertainty quoted for the thermometers (*c.* 50°C), stems from the activity-coefficient terms (Equation 5.32) ignored in Fig. 5.8.

The interaction parameters used in calibrations for calcium-bearing systems are given in Table 5.3. The temperature difference derives from both terms on the right hand side of Equation 5.32, which are more negative for the Sen and Bhattacharya (1984) calibration than the Harley (1984*a*) calibration, and therefore the former yields higher temperatures given that ΔV° is negative. At temperatures relevant to this study

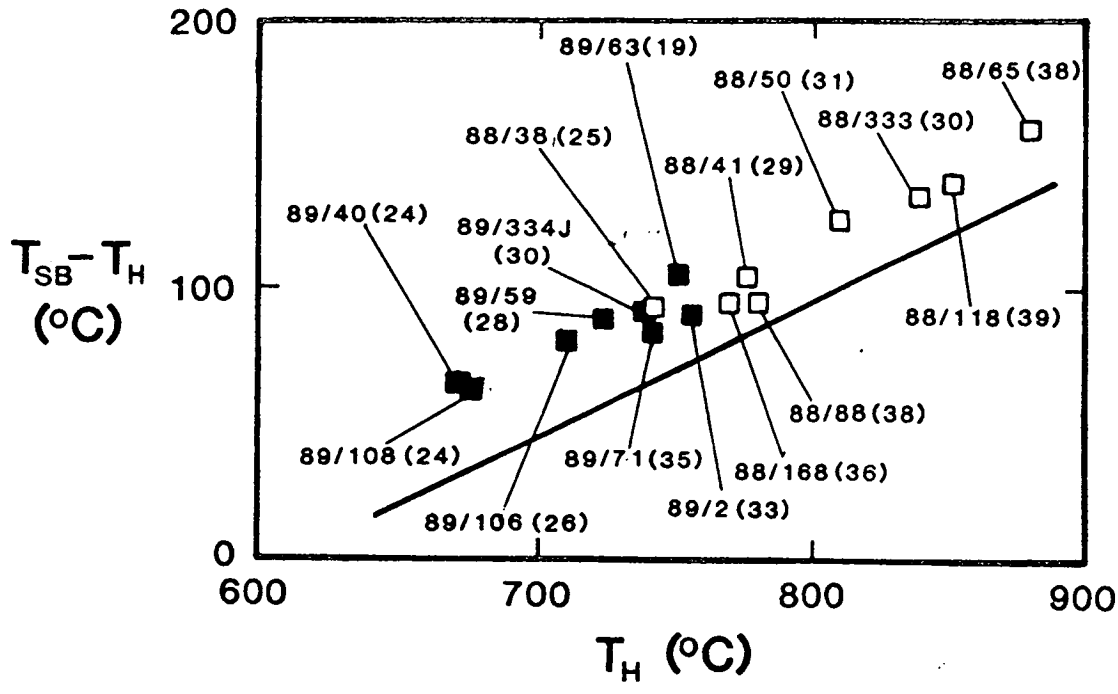

Fig. 5.9 A plot of the actual temperature difference between the Harley (1984*a*) and Sen and Bhattacharya (1984) calibrations of the garnet-orthopyroxene exchange thermometer versus the Harley (1984*a*) temperature at 7.5 kbar. Open and filled squares represent core compositions for specimens from the Brattstrand Bluffs coastline and Nemesis Glacier region respectively. The solid line is the predicted difference in temperature from Fig. 5.8 for the FMAS system with ideal Fe-Mg mixing. The discrepancy between this line and the observed difference stems from the different solution models used by the two calibrations. The numbers in parentheses beside each specimen number indicate the X_{Mg}^{Grt} value used in the calculation. Note that those specimens with the highest X_{Mg}^{Grt} plot closest to the predicted temperature difference.

(*c.* 800°C), W_{CaFe} - W_{CaMg} is 1400 cal / mol for the Harley (1984*a*) calibration and 1690 cal / mol for the Sen and Bhattacharya (1984) calibration, and Harley (1984*a*) treats iron-magnesium mixing as ideal ($W_{FeMg} = 0$) whereas Sen and Bhattacharya use a value of 195 cal / mol for W_{FeMg}. Although the difference in W_{FeMg} is slightly less than that for W_{CaMg} - W_{CaFe}, it is the more important term in Equation 5.32 since X_{prp} - X_{alm} has a substantially greater magnitude than X_{grs}. This dominance of the (X_{prp} - X_{alm}) W_{FeMg} term is indicated on Fig. 5.9, which shows that the extra temperature difference due to non-ideal mixing behaviour in garnet is greatest for the iron-rich specimens, which have the highest values of X_{grs} and therefore $|X_{prp} - X_{alm}|$ (Fig. 5.2).

The calibration of Lee and Ganguly (1988) treats iron-magnesium mixing in garnet as ideal, but has a significantly greater value for W_{CaMg} - W_{CaFe} than the Harley (1984*a*) calibration and the Sen and Bhattacharya (1984) calibration. Carswell and Harley (1990) consider the true value to be nearer the lower value of Harley (1984*a*), on the basis of natural rock data.

5.4.2 The garnet-orthopyroxene-plagioclase-quartz barometer

The discrepancies between the various calibrations of garnet-orthopyroxene-

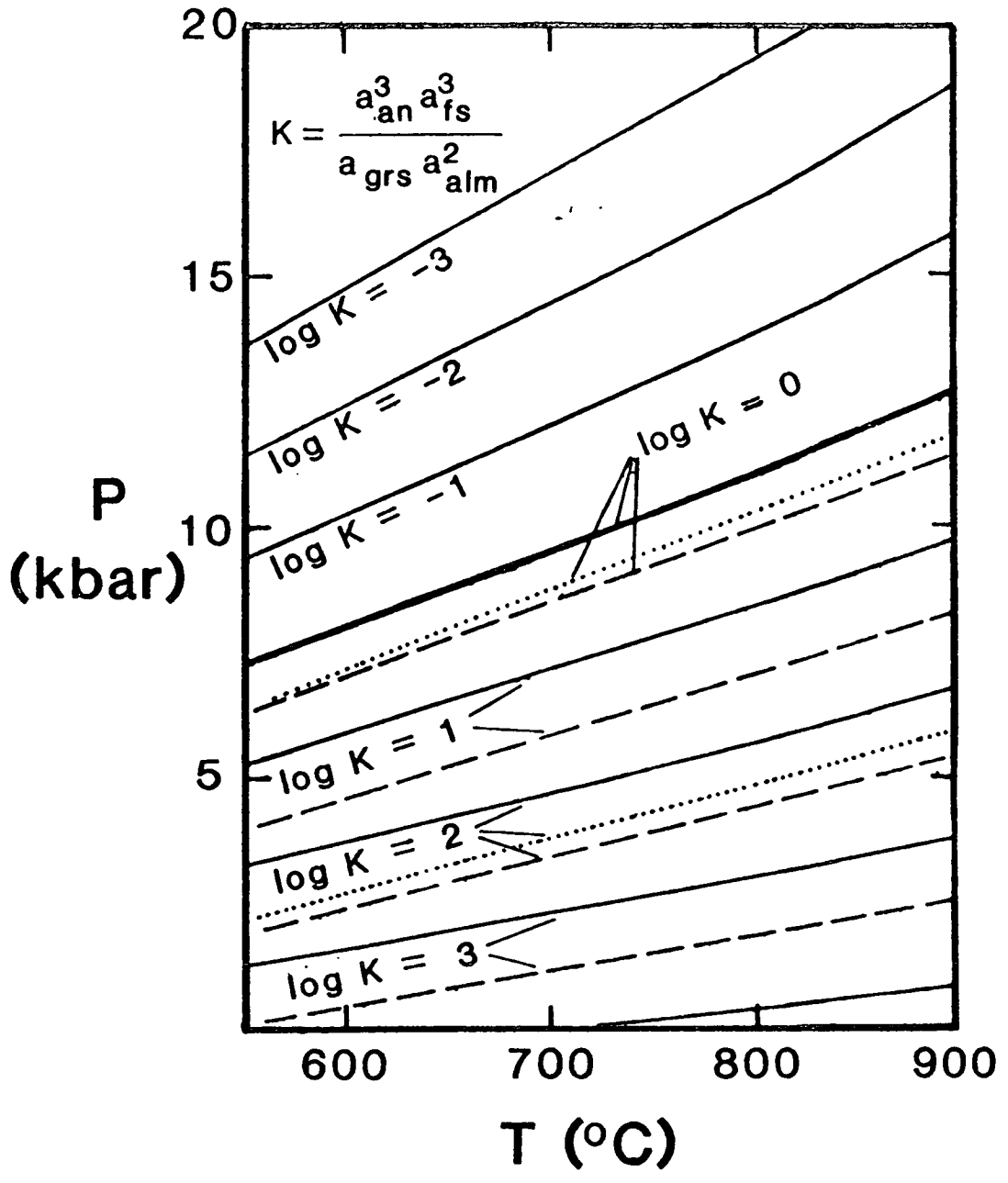

Fig. 5.10 The positions of isopleths of fixed $\log_{10} K$ displaced from the iron end-member garnet-orthopyroxene-plagioclase-quartz equilibrium (Reaction R5.4). Solid and dashed isopleths represent the calibrations of Essene (1989) and Bohlen *et al.* (1983*a*) respectively. The two dotted isopleths were calculated using the data set of Holland and Powell (1990) for $\log_{10} K$ equal to 0 and 2.

plagioclase-quartz barometer can also be divided into differences resulting from the standard-state thermodynamic variables, and differences resulting from the solution models. Differences in the thermodynamic variables are evaluated using Figs 5.10 and 5.11, which depict the position of various isopleths of fixed K (i.e. fixed K_γ and K_X) in pressure-temperature space, defined by the expression

$$P = \frac{T\Delta S^\circ_{1,T} - \Delta H^\circ_{1,T} - R \ln K}{\Delta V^\circ} \qquad (5.35).$$

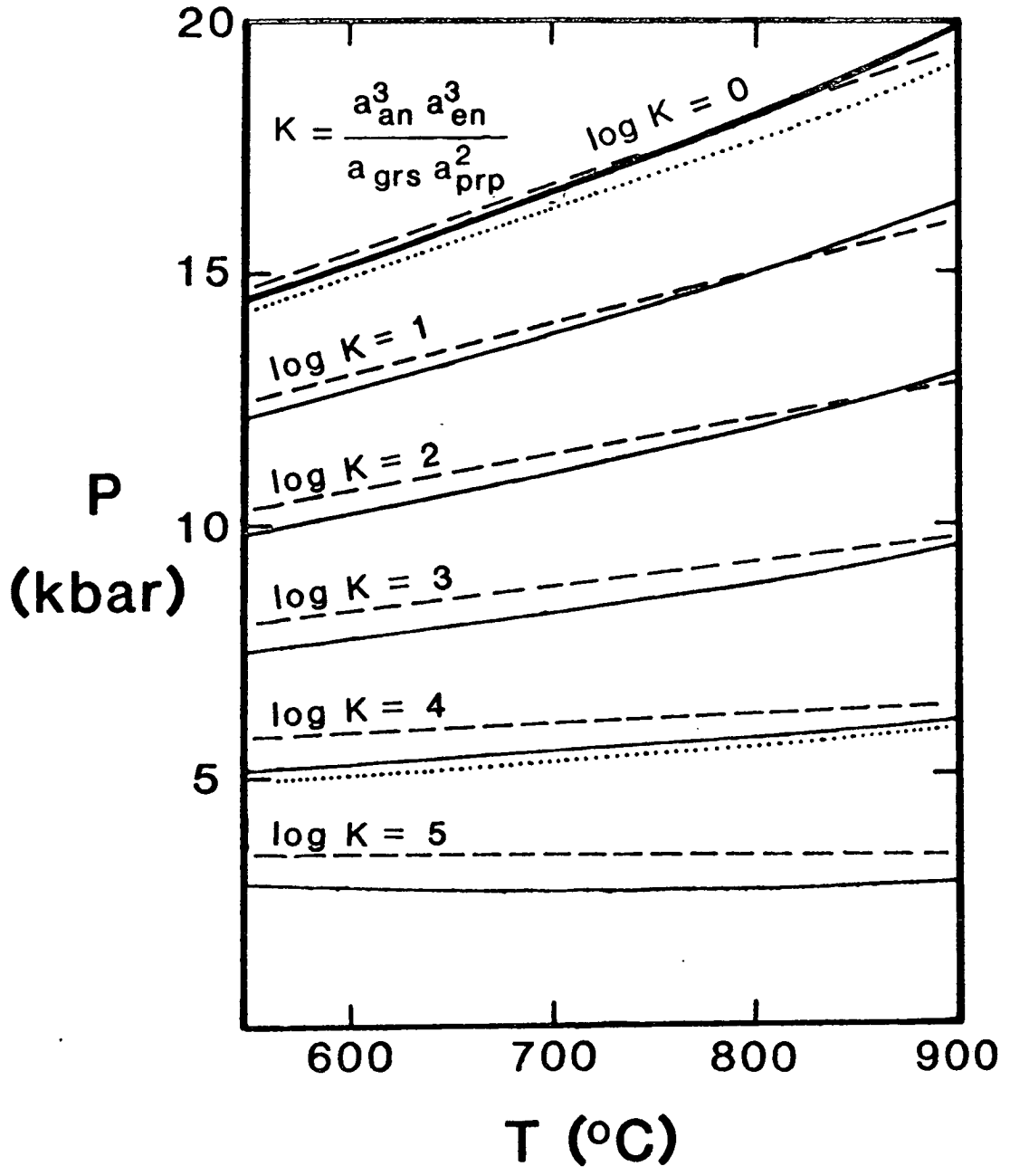

Fig. 5.11 The positions of isopleths of fixed $\log_{10} K$ displaced from the magnesium end-member garnet-orthopyroxene-plagioclase-quartz equilibrium (Reaction R5.3). Solid and dashed isopleths are the calibrations of Essene (1989) and Newton and Perkins (1982) respectively. The two dotted isopleths were calculated using the Holland and Powell (1990) data set for $\log_{10} K$ equal to 0 and 4.

Fig. 5.10 depicts isopleths for the iron end-member calibrations of Bohlen *et al.* (1983*a*) and Essene (1989). At 800°C, the Bohlen *et al.* (1983*a*) isopleths are consistently about 1.2 kbar below the equivalent Essene (1989) isopleths. This compares with a difference in the same sense of 0.9 and 1.5 kbar identified from the specimens in Section 5.3.4. Hence within the quoted uncertainties (*c.* 0.5 kbar), all the difference can be ascribed to a different choice of standard-state thermodynamic data, and any difference resulting from mixing models can be ignored. There is little

difference in slope between the calibrations, which implies that most of the discrepancy derives from the value of $\Delta H^{\circ}_{1,T}$. Isopleths calculated from the data set of Holland and Powell (1990) lie between the isopleths of the other calibrations, but closer (within 0.5 kbar) to that of Bohlen *et al.* (1983*a*).

Fig. 5.11 depicts isopleths for the magnesium end-member calibrations of Newton and Perkins (1982) and Essene (1989). The two sets of isopleths are indistinguishable near the position of the end-member reaction (*c.* 15-18 kbar), but diverge with decreasing pressure. However, even at pressures relevant to the specimens in this study (*c.* 5-8 kbar), the Newton and Perkins (1982) isopleths are positioned less than 0.5 kbar above those of Essene (1989). The consistency of the thermodynamic data is confirmed by the position of isopleths calculated using the data set of Holland and Powell (1990), which lie close to isopleths derived from the other calibrations (Fig. 5.11). This difference is within the quoted uncertainty of the calibrations. However, the final calculated pressures show much higher actual pressure discrepancies (see Section 5.3.4), with the Essene (1989) calibration yielding pressures 0.9 to 3.8 kbar higher than the Newton and Perkins (1982) version. Furthermore, this difference is in the opposite sense to that given by the standard-state thermodynamic data. This implies that the substantial discrepancy between the pressures calculated using the two calibrations is derived from the choice of solution model.

Both calibrations use the Newton *et al.* (1980) model for plagioclase, and the ideal two-site model for orthopyroxene (Wood & Banno, 1973), indicating that the differences must lie in the choice of garnet mixing model. Newton and Perkins (1982) treat garnet as a regular ternary solid solution, and use the interaction parameters given in Table 5.3. Essene (1989) uses the Ganguly and Saxena (1984) quaternary asymmetric solution model, with modified calcium-iron mixing parameters from Anovitz and Essene (1987). The K_γ term for the magnesium end-member equilibrium (Reaction R5.3) can be expressed as

$$K_\gamma = \frac{(\gamma_{an})^3 (\gamma_{en})^3}{(\gamma_{grs}) (\gamma_{prp})^2} \qquad (5.36).$$

Given that ΔV° is positive, calculated pressures will increase with decreasing K (see Equation 5.35). Hence the high pressures given by the Essene (1989) calibration indicate that γ_{grs} and/or γ_{prp} are larger than the values used in the Newton and Perkins (1982) calibration. An example of the activities calculated for a fixed garnet composition with the solution models used by Newton and Perkins (1982) and Essene (1989) is given in Table 5.6. The grossularite activities calculated by the Essene (1989) model are similar to those of the Newton and Perkins (1982) model, whereas the pyrope activities are substantially higher, indicating that the pressure difference

Table 5.6 A comparison of pyrope and grossularite activities calculated with the solution models used by Newton and Perkins (1982) and Essene (1989) for two specimens at 800°C. The pyrope activities calculated using the recent model of Berman (1990) are also tabulated.

specimen		88/168	89/63
X_{prp}		0.346	0.169
X_{alm}		0.603	0.728
X_{grs}		0.034	0.084
X_{sps}		0.015	0.018
a_{grs}	(Newton & Perkins, 1982)	0.0001	0.0009
a_{grs}	(Essene, 1989)	0.0001	0.0006
a_{prp}	(Newton & Perkins, 1982)	0.0437	0.0058
a_{prp}	(Essene, 1989)	0.0828	0.0375
a_{prp}	(Berman, 1990)	0.0494	0.0077

must stem from the values of γ_{prp}. It has been noted by other workers (Moecher *et al.*, 1988, p. 97) that the Ganguly and Saxena (1984) solution model (i.e. that used by Essene, 1989) yields much higher pyrope activity coefficients than that used by Newton and Perkins (1982). Assuming a regular-solution approximation for garnet mixing, γ_{prp} is given by Equation 5.18. Given that X_{grs} is an order of magnitude smaller than X_{alm} in the specimens discussed here, the dominant term in Equation 5.18 is the $(X_{alm})^2 W_{FeMg}$ term. This is confirmed by Fig. 5.12, which shows how the pressure difference between the Newton and Perkins (1982) and Essene (1989) calibrations varies with X_{Mg}^{Grt}. The pressure difference is clearly greatest for the most iron-rich specimens (i.e. highest X_{alm}). Hence the pressure discrepancy must stem from the pyrope-almandine mixing parameter. Newton and Perkins (1982) assumed that almandine-pyrope mixing is ideal. The Ganguly and Saxena (1984) mixing model for this join is non-ideal and asymmetric. Fig. 5.13 depicts how the Gibbs free energy of mixing varies across the almandine-pyrope join according to various mixing models. The departure of the Ganguly and Saxena (1984) model from ideality, and therefore from the Newton and Perkins (1982) model, is greatest in the X_{Mg}^{Grt} range of the specimens studied here. The latest models of garnet mixing (Berman, 1990) assume that almandine-pyrope is virtually ideal (see Fig. 5.13), and yield pyrope activities very close to those calculated using the solution models of Newton and Perkins (1982) as indicated in Table 5.6.

5.4.3 The garnet-orthopyroxene aluminium solubility thermobarometer

The different dP/dT slopes of the Harley (1984*b*) and Harley and Green (1982) calibrations reflect two different approaches to the derivation of a thermobarometric equation based on the solubility of alumina in orthopyroxene coexisting with garnet.

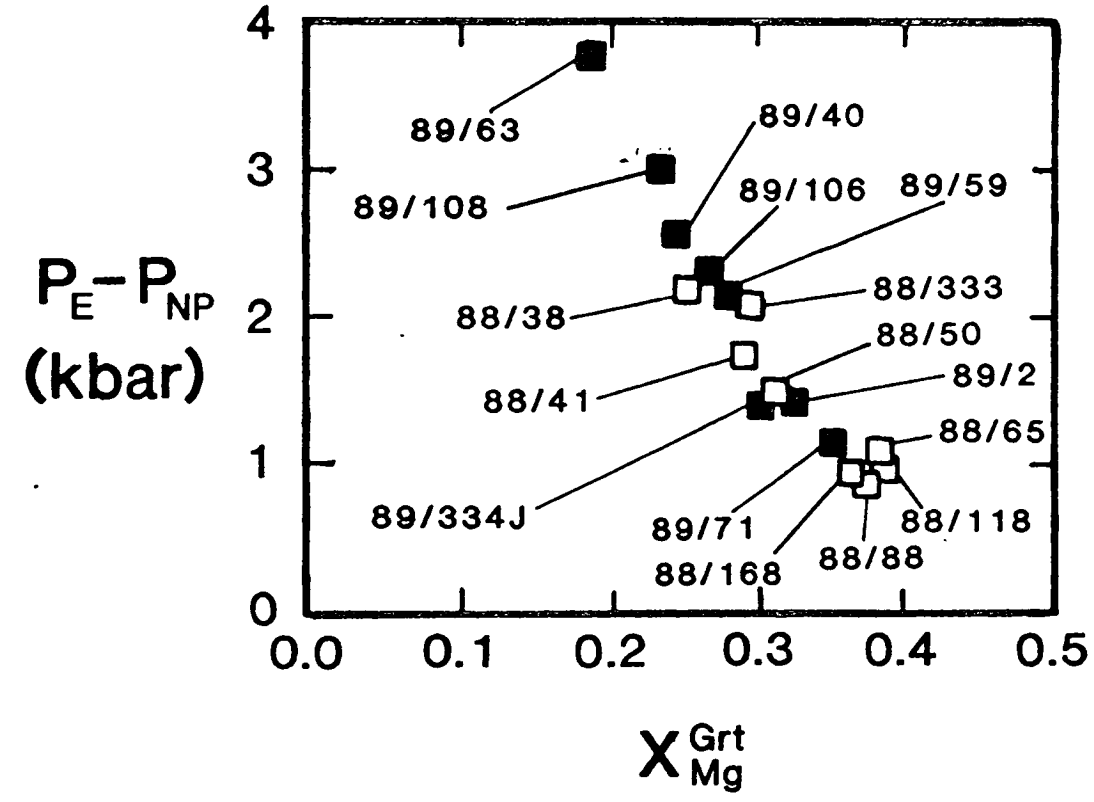

Fig. 5.12 A plot of the pressure difference between the Essene (1989) and Newton and Perkins (1982) calibrations of the garnet-orthopyroxene-plagioclase-quartz barometer versus X_{Mg}^{Grt}. Open and filled squares represent specimens from the Brattstrand Bluffs coastline and Nemesis Glacier region respectively.

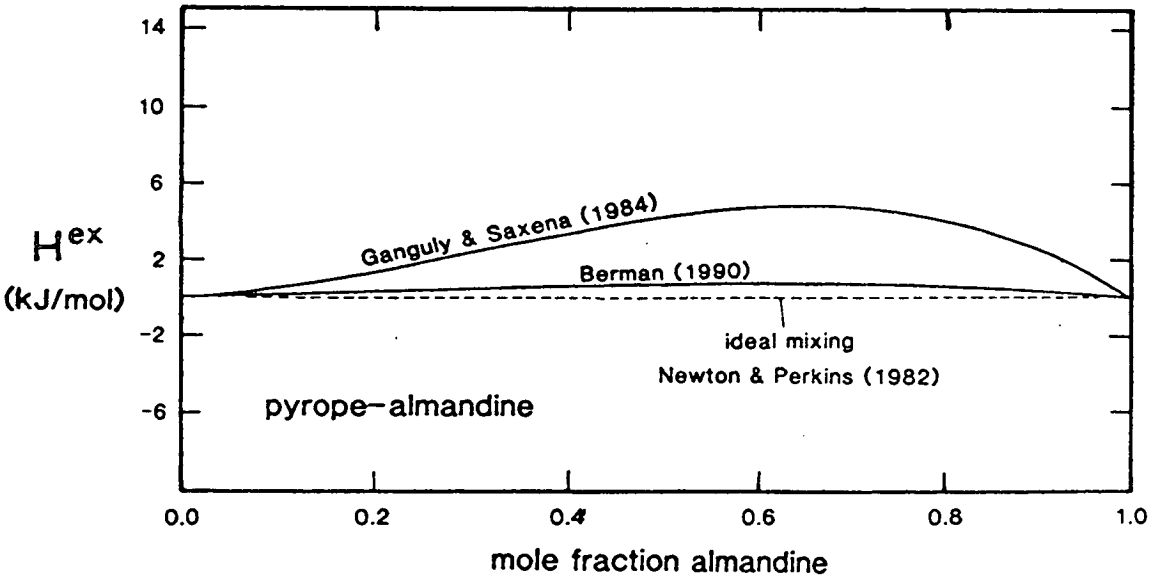

Fig. 5.13 A comparison of the excess enthalpies of mixing on the pyrope-almandine join predicted by the mixing models of Ganguly and Saxena (1984), Berman (1990) and Newton and Perkins (1982). H^{ex} is the temperature- and pressure-independent part of G^{ex}, and is much larger than the volume-dependent (V^{ex}) and temperature-dependent (S^{ex}) parts (Berman, 1990).

The calibration of Harley (1984*b*) is a rigorous solution to Equation 5.16 with

$$K_X = \frac{(X_{prp})^3}{(X_{Mg}^{Opx})^3 X_{Al}^{M1} (1 - X_{Al}^{M1})} \quad (5.37),$$

and a complex expression for K_Y (see Appendix 4.1). Hence the solutions to the thermobarometric equation are isopleths of fixed K (i.e. fixed composition of garnet and orthopyroxene). Harley and Green (1982) derived an empirical thermobarometric expression for the same equilibrium using the same experimental data, in which a small number of simple curve-fitting terms are used to account for a variety of complex mixing effects in garnet and orthopyroxene. All the effects of iron-magnesium distribution between garnet and orthopyroxene are ascribed to an empirical term which describes the variation of alumina solubility in orthopyroxene with varying X_{Mg}^{Opx}. Hence the solutions to the thermobarometric equation are isopleths of fixed alumina content in orthopyroxene for a given X_{Mg}^{Opx}, but variable X_{Mg}^{Grt}.

5.5 THE EFFECT OF DISEQUILIBRIUM

5.5.1 Introduction

If an assemblage is in complete equilibrium, all crystals are chemically homogeneous, and all crystals of a given phase have the same composition. This is rarely true for a natural metamorphic assemblage, and clearly not true for the specimens considered here. Two principal departures from equilibrium can seriously affect thermobarometry.

(i) Low rates of diffusion, reaction or heat transfer could mean that equilibrium is never attained. If so, mineral cores retain their prograde growth composition, and the cores of different phases might never have been in equilibrium.

(ii) Retrograde re-equilibration of mineral compositions during cooling, uplift or overprinting by subsequent metamorphism could destroy peak equilibrium mineral compositions. In contrast to (i), this form of disequilibrium is commonly a reflection of high rates of diffusion.

The most common expression of disequilibrium in metamorphic assemblages is mineral zonation.

5.5.2 Theoretical background to diffusion zonation

Two types of compositional zonation have been identified in metamorphic mineral grains (Tracy, 1982; Loomis, 1983). 'Growth zonation' is a result of a change in the composition of material supplied to the growing surface of a crystal. The preservation of growth zonation requires that rates of intracrystalline diffusion are low enough to retain compositional variation. 'Diffusion zonation' is a result of intracrystalline

diffusion, and is driven by reaction of the crystal's surface with other nearby phases (Lasaga *et al.*, 1977). These reactions and their associated zonation profiles commonly reflect the retrograde evolution of the rock, and are superimposed onto a pre-existing crystal which may be homogeneous or preserve growth zonation.

Diffusion is the transport of matter from one part of a system to another as a result of random atomic motions, which commonly have a direction of net transfer because of differences in concentrations or site energies. Diffusion within a rock can occur both in a crystal lattice, when it is known as 'volume diffusion', or along discontinuities such as grain boundaries (Manning, 1974; Freer, 1981). Diffusion zonation is the result of volume diffusion. The extent of diffusion is represented by the flux, which is the net flow of atoms passing through a unit area in unit time. The one-dimensional flux of component i through crystal A (J_i^A) is proportional to the concentration gradient ($\partial C_i^A/\partial x$), as defined by Fick's first law (Crank, 1975, p. 2)

$$J_i^A = -D_i^A \left(\frac{\partial C_i^A}{\partial x} \right) \quad (5.38),$$

where D_i^A is the diffusion coefficient or diffusivity for the transport of i through A at a certain temperature. If phase A is isotropic, D_i^A will have only one value at fixed temperature, but in general the value will depend on the direction of diffusion with respect to the crystal structure. The temperature dependence of the diffusion coefficient is represented by the equation

$$D_T = D_o \exp(-E_a / RT) \quad (5.39),$$

where D_T is the diffusion coefficient at the temperature of interest (T), E_a is the activation energy of diffusion and D_o is essentially the diffusion coefficient at infinite temperature. The activation energy for volume diffusion is generally somewhat larger than that for grain-boundary diffusion (typically about twice as large; Putnis & McConnell, 1980, pp. 137-138). It follows from Equation 5.39 that, at low temperature, the activation energy is an important factor in determining the relative diffusivity of volume versus grain-boundary diffusion, and the latter is dominant. At high temperature, the relative importance of activation energy decreases, and volume diffusion is the dominant process since it involves the majority of atoms in a rock.

Given that diffusion is exponentially dependent on temperature (from Equation 5.39), a cooling rock will pass through a region of transitional temperature where diffusion of a certain component in a certain phase decreases and eventually becomes negligible, even on geological time scales. The critical temperature in this transition region is known as the 'closure temperature' (T_c; see Dodson, 1973, 1979 for definition), which can be represented by the expression

$$T_c = \frac{E_a / R}{\ln [R A T_c^2 D_o / (a^2 E_a \, dT/dt)]} \quad (5.40),$$

where E_a and D_o are as defined in Equation 5.39, A is controlled by the diffusion geometry, a is a grain-size parameter, and dT/dt is the cooling rate.

Equations 5.38, 5.39 and 5.40 were all formulated for a single diffusing component, but diffusion usually affects two or more components simultaneously. This is known as 'interdiffusion', and reflects the need for a crystal to maintain the charge and mass balance imposed by stoichiometry. The simplest example is the exchange of two isovalent cations (e.g. Mg and Fe^{2+}), where the flux of the first cation in one direction must equal that of the second in the opposite direction. In this case there is a single value of the diffusion coefficient for both fluxes, the interdiffusion coefficient. When more than two species diffuse, complex diffusion coefficients with cross-coefficient terms are required (Lasaga, 1979).

5.5.3 Diffusion in the semi-pelite specimens

Garnet, orthopyroxene and plagioclase grains in the semi-pelite generally have compositionally-homogeneous cores, which imply that growth zonation has not been preserved. The homogeneous cores vary in size, but, for a grain with a diameter of 2.0 mm, the 'cores' commonly have a diameter of at least 1.5 mm. In addition, the zonation profiles are characterized by rimward increase in iron and decrease in magnesium within garnet grains, and the converse in orthopyroxene grains, which is consistent with retrograde 'reverse' zonation during cooling rather than normal growth zonation. This is confirmed by the thermobarometric calculations which yield lower-grade conditions for rim compositions than for cores (see Section 5.3.4). The lack of growth zonation is taken as evidence that mineral compositions were homogenized at the metamorphic peak (although there is evidence that cores of isolated orthopyroxene grains in specimen 88/41 were not in equilibrium with garnet cores; see Section 5.6.2). This assumption is widely held for high-grade granulite assemblages, and is consistent with studies which suggest that the compositions of garnet grains between 1 and 3 mm in diameter homogenize at temperatures of around 650°C (e.g. Yardley, 1977; Dempster, 1985).

The presence of retrograde compositional zonation in garnet, orthopyroxene and plagioclase in the semi-pelite specimens clearly indicates that retrograde re-equilibration has occurred. The zonation was interpreted in Section 5.2.4 in terms of Reactions R5.1, R5.2, R5.3, and R5.4. These reactions tend to progress in an attempt to maintain an equilibrium constant which satisfies the conditions for equilibrium (Equation 5.9) as pressure-temperature conditions evolve. The extent to which equilibrium is maintained depends on diffusion rates, since compositions can only adjust to changing metamorphic conditions if the mineral components are able to diffuse between and within phases.

Reactions R5.1, R5.2, R5.3 and R5.4 can be divided into two types. Reaction R5.1 is an 'exchange reaction', progress of which does not affect the modal

abundances of the phases involved. This contrasts with Reactions R5.2, R5.3 and R5.4, which are 'net-transfer reactions' whose progress requires the net transfer of matter from one phase, or group of phases, to another. Reaction R5.1 involves the interdiffusion of iron and magnesium between garnet and pyroxene, and Reactions R5.2, R5.3 and R5.4 involve more complex diffusion including that of calcium through garnet, and aluminium and silicon through orthopyroxene and plagioclase.

No attempt is made here to quantify the diffusive effects responsible for the zonation profiles. Values of D_o and E_a have not been determined experimentally for the diffusion and interdiffusion of all relevant components through all relevant phases; there are, for example, no suitable data on the diffusion of aluminium and silicon through orthopyroxene, and even iron-magnesium data are open to much debate. Where data do exist, there are a number of problems with their application to natural examples of diffusion, including the dependence of the diffusion coefficient on pressure, composition and direction of diffusion, and the effects of other processes, such as deformation, which may operate simultaneously with diffusion. Experimental data have generally only been applied to relatively simple examples of diffusion (e.g. planar exsolution lamellae; Sautter & Fabriès, 1990). In addition, some constraints on the cooling rate are needed before diffusion data can be used to estimate closure temperatures. However, a number of qualitative inferences concerning the preservation of diffusion profiles and the closure of various diffusive processes can be made from the semi-pelite specimens.

Equation 5.40 indicates that diffusive systems with the highest closure temperatures, and hence the most reliable systems for thermobarometry, are those with the highest activation energies and the lowest values of D_o. In addition, higher closure temperatures for any particular system are achieved in those specimens with the coarsest grain size and the fastest cooling rate. The rate of diffusion of magnesium, iron and calcium through any mineral is greater than the rate of diffusion of aluminium and silicon, since the latter process requires the destruction of silicate tetrahedra and hence has a greater activation energy. This predicted relationship has been identified in many experimental and natural examples (e.g. Carmichael, 1969; Walther & Wood, 1984; Sautter *et al.*, 1988; Sautter & Harte, 1988). This variation in diffusivity results in variable closure temperatures, such that iron and magnesium continue to re-equilibrate at lower temperatures than aluminium or silicon.

5.5.4 Implications for thermometry

The evidence that garnet, orthopyroxene and plagioclase grains were homogenized at the metamorphic peak indicates that chemical equilibrium was attained at this time, but the retrograde diffusive zonation indicates that equilibrium was locally maintained, or at least approached, during part of the retrograde evolution. This has important implications for the thermometric results detailed in Section 5.3.4.

It is generally recognized that granulites form at temperatures above the closure temperature of most iron-magnesium exchange thermometers (O'Hara, 1977; O'Hara & Yarwood, 1978), many of which are thought to have closure temperatures of 550 to 700°C (e.g. Elphick *et al.*, 1985). The existence of compositional zonation in the specimens studied here indicates that peak compositions have re-equilibrated at least at grain edges, but of more importance is whether the mineral cores have also re-equilibrated. If they have, the temperatures derived by iron-magnesium exchange thermometry will not represent peak conditions. Lasaga (1983) has shown that the shape of a diffusion profile is not indicative of the extent of diffusive re-equilibration. Even grains with broad compositionally-homogeneous core regions, and a chemical zonation limited to grain edges, may not preserve peak compositions in the core. The two principal factors which determine the shape of a compositional zonation profile are the diffusion rate in the mineral and the cooling rate of the specimen. If the cooling rate is fast relative to the diffusion rate, then interdiffusional re-equilibration is restricted to grain edges and homogeneous cores correspond to peak compositions. With decreasing cooling rate, a greater portion of the grain re-equilibrates, and if the cooling rate is relatively slow with respect to the diffusion rate, all the grain re-equilibrates. In the latter case, the mineral cores are still relatively homogeneous since fast diffusion tends to smooth out the compositional gradient developed during cooling. The slower the cooling rate the more homogeneous the re-equilibrated cores become, and there must be some knowledge of the cooling rate before core homogeneity can be used as a criterion for equilibrium (Lasaga, 1983). It should also be remembered that the compositional zonation profile in any one phase depends on the diffusivity in the other exchanging phase, since interdiffusion rates are controlled by the phase with the lower diffusivity.

The inter-specimen variation in temperatures derived using both the Harley (1984*a*) and Sen and Bhattacharya (1984) garnet-orthopyroxene thermometers reflects a wide range of K_D values, but cannot represent a real variation in peak metamorphic temperatures since many of the specimens were collected from a relatively small area. The temperatures are correlated with core closure temperatures, and the variation is ascribed to variable degrees of retrograde iron-magnesium exchange. There is, however, no means of determining whether the specimens recording the highest temperatures are revealing the peak metamorphic temperature, or merely a temperature somewhere on the cooling path corresponding to the temperature at the time when diffusion closed in mineral cores. This problem has been termed the 'granulite uncertainty principle' by Frost and Chacko (1989). If the exchange closure temperatures are retrograde, the only way to recover higher temperatures is from relict textural features such as exsolution lamellae in pyroxene or feldspar (e.g. Bohlen & Essene, 1977, 1978; Barnicoat & O'Hara, 1979; Sandiford

& Powell, 1986*b*; Harley, 1987*b*) or from relict mineral assemblages (e.g. Ellis *et al.*, 1980; Harley, 1986).

5.5.5 Implications for barometry

Reactions R5.2, R5.3 and R5.4 involve mass transfer of aluminium and silicon, which closes at higher temperatures than iron-magnesium exchange (see Section 5.5.3). Hence pressure estimates from mass-transfer reactions and temperature estimates from exchange reactions do not in general relate to the same stage of the metamorphic evolution (Fraser & Lawless, 1978; Frost & Chacko, 1989; Harley, 1989; Perkins, 1990). This problem was termed 'mismatch' by Harley (1989). Another problem, termed 'feedback' by Harley (1989), is that the positions in pressure-temperature space of the barometric equilibria used here are also sensitive to iron-magnesium exchange since they involve two ferromagnesian phases. Hence the apparent equilibrium constant for the reactions changes during iron-magnesium exchange after closure of aluminium and silicon diffusion, but never represents a true equilibrium constant for the net-transfer reaction since equilibrium is not maintained between all components. Feedback from iron-magnesium exchange into the equilibrium constant of a net-transfer reaction produces derived pressures which have no physical meaning. Clearly the granulite uncertainty principle applies to barometry as well as thermometry.

The extent to which apparent pressures derived from net-transfer equilibria continue to evolve after the net transfer itself closes depends on the sensitivity of the calibration to the iron-magnesium distribution coefficient. The position of the garnet-orthopyroxene-plagioclase-quartz equilibria (R5.3 and R5.4) shows little inter-specimen variation, except for the magnesium calibration of Essene (1989) as described in Section 5.4.2. This implies that the position of this equilibrium is not particularly sensitive to iron-magnesium exchange. In contrast, the inter-specimen variation in the position of the Harley (1984*b*) garnet-orthopyroxene 'barometer' (see Section 5.3.4) cannot be due to a difference in peak pressure or temperature conditions, but can be correlated with the position of the Harley (1984*a*) thermometer. Given that the apparent pressure decreases at fixed aluminium content of orthopyroxene with transfer of magnesium from garnet to pyroxene and iron from pyroxene to garnet (Harley 1984*b*), the position of the Harley (1984*b*) calibration depends on the extent of retrograde iron-magnesium exchange. This sensitivity derives principally from the $(X_{prp} / X_{Mg}^{Opx})^3$ term in Equation 5.37 (Harley, 1984*b*, p. 692). The position of the empirical Harley and Green (1982) thermobarometer is independent of garnet iron-magnesium composition, and is much less sensitive to retrograde iron-magnesium exchange. As a test for iron-magnesium sensitivity, the thermobarometric equations of Harley (1984*b*) and Newton and Perkins (1982) have been differentiated with respect to X_{Mg}^{Grt}, making the simplifying approximation that orthopyroxene composition is independent of X_{Mg}^{Grt}. The derived expressions for

Table 5.7 Expressions for dP/dX_{Mg}^{Grt} derived from the barometric equations of (1) Newton and Perkins (1982) and (2) Harley (1984*b*), making the simplification that orthopyroxene composition is independent of X_{Mg}^{Grt} (P in kbar, T in K).

(1) $$\frac{dP}{X_{Mg}^{Grt}} = \frac{1}{567.16}\left[\frac{2\,R\,T}{X_{Mg}^{Grt}} + (3300 - 1.5\,T)(1 - X_{grs}^{Grt})(1 - 3X_{grs}^{Grt})\right]$$

(2) $$\frac{dP}{X_{Mg}^{Grt}} = \frac{1}{206.74}\left[\frac{3\,R\,T}{X_{Mg}^{Grt}} + 5700\,X_{grs}^{Grt}(1 - X_{grs}^{Grt})\right]$$

For $X_{Mg}^{Grt} = 0.30$ and $X_{grs}^{Grt} = 0.05$ at 1073 K, (1) yields a dP/dX_{Mg}^{Grt} of about 28, and (2) yields a dP/dX_{Mg}^{Grt} of about 105.

dP/dX_{Mg}^{Grt} are given in Table 5.7, as are the values obtained from these expressions using suitable values of temperature, X_{Mg}^{Grt} and X_{grs}^{Grt}. The value of dP/dX_{Mg}^{Grt} for the Harley (1984*b*) barometer is about four times greater than that for the Newton and Perkins (1982) calibration.

5.5.6 Implications for retrograde pressure-temperature paths

Retrograde zonation profiles are commonly used to determine retrograde pressure-temperature paths for granulite terrains, by estimating two points on the path through thermobarometry of mineral core and rim compositions (e.g. Bohlen, 1987). However, the effects of pressure-temperature mismatch and feedback, which result if the entire thermobarometric assemblage does not remain in equilibrium during iron-magnesium exchange, could produce an apparent pressure-temperature path which was not followed by the rocks (Frost & Chacko, 1989; Harley, 1989; Perkins, 1990; Selverstone & Chamberlain, 1990). In fact, the apparent path is determined by the pressure sensitivity of net-transfer equilibrium constants to iron-magnesium exchange. Estimates of retrograde pressure-temperature paths are best made using textural evidence of relic phase equilibria.

5.6 CONCLUSIONS

5.6.1 An assessment of the thermobarometric calibrations

A number of conclusions can be made regarding the reliability of the various thermobarometric calibrations used in Section 5.3.4.

(i) The Harley (1984*a*) thermometer is commonly reset, even in mineral cores, down to temperatures of 600°C. In specimens which yield low Harley (1984*a*) temperatures, the Sen and Bhattacharya (1984) thermometer commonly gives reasonable temperatures for granulite metamorphism (*c.* 800°C). However, when

the Harley (1984*a*) thermometer yields reasonable temperatures, the Sen and Bhattacharya (1984) calibration gives unreasonably high temperatures (over 1000°C). In the past, many workers have considered the Sen and Bhattacharya (1984) calibration to be the more reliable of the two, and have rejected the Harley (1984*a*) thermometer. Clearly the Harley (1984*a*) thermometer, although commonly reset, behaves in a consistent manner which can be easily interpreted in terms of the extent of retrograde iron-magnesium exchange, whereas the Sen and Bhattacharya (1984) thermometer cannot, although it may fortuitously yield peak temperatures when a sufficient amount of retrograde iron-magnesium exchange has occurred.

(ii) The iron-magnesium exchange, identified by resetting of the Harley (1984*a*) thermometer, causes the Harley (1984*b*) barometer to yield low pressures. This reflects the strong dependence that the position of the Harley (1984*b*) barometer in pressure-temperature space has on the iron-magnesium distribution coefficient. For reasons outlined in (iv) below, the extent of aluminium-silicon exchange is not considered significant in mineral cores, and all the resetting of this barometer is attributed to ferromagnesian exchange. Previous thermobarometric studies have reported that the Harley (1984*b*) barometer yields erratic results. This is primarily due to a typographic error in the published barometric equation (see Appendix 4.1), and the correct version yields 'sensible' pressures which can be interpreted in terms of a variable extent of retrograde iron-magnesium exchange.

(iii) The two iron end-member calibrations of the garnet-orthopyroxene-plagioclase-quartz equilibrium give consistent and reasonable pressure estimates for low- to intermediate-pressure granulites. However, the two magnesium calibrations yield disparate results. The Essene (1989) calibration gives unreasonably high pressures for the more iron-rich specimens; for example, specimens 89/63 and 89/108 give pressures in the kyanite stability field, but all pelites reported from nearby outcrops in the northern Prince Charles Mountains are sillimanite bearing (see Section 2.3.8). In addition, recent models tend to assume that iron-magnesium mixing in garnet is near ideal (Berman, 1990), in accord with the solution model used by Newton and Perkins (1982) but in contrast to the Ganguly and Saxena (1984) mixing model used by Essene (1989). Hence the two iron equilibria and the Newton and Perkins (1982) calibration of the magnesium end member are favoured here.

(iv) The position of the garnet-orthopyroxene-plagioclase-quartz equilibrium in pressure-temperature space is much less sensitive to iron-magnesium exchange than the Harley (1984*b*) garnet-orthopyroxene barometer. Given that the closure temperatures of iron-magnesium exchange have been highly variable, the relatively constant pressures (ignoring the Essene (1989) calibration of R5.3)

derived using specimens from the Brattstrand Bluffs Coastline, and similarly the Nemesis Glacier region, implies that aluminium and silicon have not suffered substantial re-equilibration in mineral cores. Hence these calibrations are thought to provide good estimates of peak metamorphic pressures in most specimens.

Faulhaber and Raith (1991) have recently presented a critical review of garnet-orthopyroxene-plagioclase-quartz thermobarometry for specimens with a wide range of bulk X_{Mg} from Sri Lanka. Faulhaber and Raith (1991) identify an inter-specimen variation in temperatures calculated using various garnet-orthopyroxene exchange thermometers, and largely attribute this variation to a compositional dependence in the calibrations. There is some evidence of a compositional dependence in their data, which accounts for a temperature variation of about 50°C over the range of specimens studied. However, superimposed onto this compositional trend is a seemingly random variation, which can amount to a temperature difference of over 100°C, commonly between specimens of very similar composition. This variation could reflect variable extents of retrograde exchange, as proposed for the specimens discussed here. Faulhaber and Raith (1991) actually cite the small spread of temperature data for each calibration as evidence of near-isothermal equilibration of garnet and orthopyroxene across their area of study. All the calibrations used in their study exhibit a temperature spread of about 150°C, which does not seem particularly small. In fact it seems most unlikely that their field area should preserve isothermal conditions given that it extends over some 10,000 km^2, and that a regional pressure gradient of some 3 to 4 kbar has been identified. Faulhaber and Raith (1991) assumed a constant reference pressure for their specimens, and although a variation of 3 to 4 kbar only changes calculated temperatures by about 30°C, this change could significantly affect the identified compositional trends. This failure to fully account for the observed inter-specimen variation casts some doubt onto the reliability of the inferences made by Faulhaber and Raith (1991) regarding the suitability of various thermometric and barometric calibrations. However, Faulhaber and Raith (1991) do identify a strong compositional dependence in the garnet solution model of Ganguly and Saxena (1984), in agreement with this study.

5.6.2 The extent of Fe-Mg exchange: corrected temperature estimates

If retrograde aluminium and silicon diffusion has been minimal in garnet, orthopyroxene and plagioclase cores, and the three favoured calibrations of the garnet-orthopyroxene-plagioclase-quartz equilibrium record peak pressures, peak temperature estimates can be made by considering the combined effect that retrograde iron-magnesium exchange has on the Harley (1984*a*) thermometer and Harley (1984*b*) barometer. If the pressure difference between the Harley (1984*b*) barometer and the garnet-orthopyroxene-plagioclase-quartz barometers is considered to be entirely due to iron-magnesium exchange, the iron-magnesium K_D value required to

raise the Harley (1984*b*) barometer up to the others can be used to estimate the peak temperature using the Harley (1984*a*) thermometer. Clearly both garnet and orthopyroxene must change composition during the retrograde exchange, but there is no way to assess the relative amounts of X_{Mg} change in the two phases, and the procedure followed here is to accommodate all the K_D change in the garnet composition. The new garnet composition required to raise the Harley (1984*b*) barometer up to the pressures of the garnet-orthopyroxene-plagioclase-quartz barometers is then fed back into the Harley (1984*a*) thermometer, and a corrected temperature derived. This approximation is most valid for specimens with a greater modal abundance of orthopyroxene than garnet, which is commonly the case in the specimens discussed here (although the differences in modal abundance are not large), and is in effect moving the Harley (1984*b*) isopleths up pressure along the fixed alumina isopleths defined by the Harley and Green (1982) calibration.

The corrected positions of the Harley (1984*a*) and Harley (1984*b*) calibrations are depicted in Fig. 5.7. In most cases this procedure brings both calibrations into close agreement with the others, no matter how much pressure and temperature adjustment is required. This correction cannot be used for specimen 88/41, for which the Harley (1984*b*) calibration lies at higher pressures than the other barometers, and the Harley and Green (1982) calibration is positioned at temperatures below the exchange thermometers. This indicates that the assumed alumina contents of orthopyroxene are lower than those required for these calibrations to be consistent with the other thermobarometric equilibria. This discrepancy can be related to textural relationships, since the core garnet and orthopyroxene compositions chosen in 88/41 are from isolated grains, implying that the low-alumina pyroxene cores might never have been in equilibrium with garnet cores.

The extent of temperature correction required in the other specimens varies between zero and 150°C, and can also be related to textural features such as grain size and proximity of garnet and orthopyroxene grains, which are listed in Table 5.8. Analyses made on isolated garnet and pyroxene grains (88/333, 89/2, 89/63, 89/334J) generally require little or no correction to core or rim temperatures, whereas those specimens with the largest corrections are generally those for which analyses were taken from adjacent garnet and orthopyroxene grains (88/38, 88/88, 88/168, 89/106). Specimens with adjacent garnet and orthopyroxene, but coarse grain size, commonly require relatively large corrections for rim temperatures, but little correction for cores (88/65, 89/108). This is consistent with the extent of correction representing the extent of iron-magnesium exchange after the closure of aluminium and silicon diffusion, and confirms that it is invalid to assume that mineral cores retain iron-magnesium distributions which correspond to the closure temperatures of barometers.

Table 5.8 Temperature corrections (ΔT^*) for Fe-Mg exchange in mineral cores and rims, and the textural setting and grain size of analysed garnet and orthopyroxene. Isolated refers to distances of greater than 2 mm between garnet and orthopyroxene.

	ΔT^* (cores)	ΔT^* (rims)	Textural setting of Grt and Opx, and grain size
88/38	110°C	120°C	Cores and rims of adjacent grains, 1 mm
88/41	?	small	Cores and rims of isolated grains, 1 mm
88/50	90°C	65°C	Cores and rims of adjacent grains, 2 mm
88/65	5°C	65°C	Cores and rims of adjacent grains, 7 mm
88/88	105°C	120°C	Cores and rims of adjacent grains, 2 mm
88/118	75°C	75°C	Cores and rims of adjacent grains, 3 mm
88/168	135°C	110°C	Cores and rims of adjacent grains, 2 mm
88/333	0	80°C	Cores of isolated and rims of adjacent grains, 1 mm
89/2	0	30°C	Cores and rims of isolated grains, 3 mm
89/40	0	85°C	Cores and rims of adjacent grains, 1 mm
89/59	85°C	35°C	Cores and rims of adjacent grains, 3 mm
89/63	0	0	Cores and rims of isolated grains, 2 mm
89/71	30°C	65°C	Cores and rims of adjacent grains, 1 mm
89/106	95°C	110°C	Cores and rims of adjacent grains, 1 mm
89/108	15°C	70°C	Cores and rims of adjacent grains, 4 mm
89/334J	50°C	35°C	Cores and rims of isolated grains, 1 mm

5.6.3 Pressure-temperature conditions during Proterozoic metamorphism

The pressures and temperatures most consistent with the thermobarometric equilibria have been estimated from Fig. 5.7, and are illustrated in Fig. 5.14 and listed in Table 5.9. The magnesium end-member barometer of Essene (1989) and the exchange thermometer of Sen and Bhattacharya (1984) were ignored for reasons outlined above. Estimates were based principally on the positions of the garnet-orthopyroxene-plagioclase-quartz barometers of Newton and Perkins (1982), Bohlen *et al.* (1983*a*,*b*) and the iron end-member calibration of Essene (1989), the Harley and Green (1982) empirical thermobarometer, and the corrected positions of the Harley (1984*a*) thermometer and Harley (1984*b*) barometer. This assumes that there was not significant aluminium transfer after the metamorphic peak. If there was, the peak estimates are in fact estimates of the blocking conditions for aluminium diffusion.

Pressure-temperature estimates for core compositions in the Brattstrand Bluffs coastline cluster around 6 kbar and 860°C, which are the favoured peak metamorphic conditions. Specimen 88/333 was collected from Chaos Glacier, at the northern edge of the field area adjacent to the Rauer Group, which probably accounts for its high pressure. Core pressure-temperature estimates from the Nemesis Glacier region are more varied, perhaps indicating variable blocking temperatures, and the favoured peak conditions are taken as 6.5 kbar and 800°C, which are at the high pressure-temperature end of the observed trend. The correction procedure for mismatch and feedback should mean that pressure-temperature conditions derived from rim

Table 5.9. Pressure-temperature estimates derived from mineral-core and mineral-rim compositions.

Brattstrand Bluffs coastline	*P* (cores)	*T* (cores)	*P* (rims)	*T* (rims)
88/38	6.0 kbar	850°C	5.0 kbar	800°C
88/41	?	?	5.0 kbar	750°C
88/50	6.0 kbar	875°C	5.0 kbar	800°C
88/65	6.0 kbar	850°C	5.0 kbar	800°C
88/88	6.0 kbar	850°C	5.0 kbar	825°C
88/118	6.5 kbar	900°C	5.5 kbar	850°C
88/168	6.0 kbar	875°C	5.5 kbar	850°C
88/333	7.5 kbar	850°C	6.5 kbar	775°C
Nemesis Glacier region	***P*** **(cores)**	***T*** **(cores)**	***P*** **(rims)**	***T*** **(rims)**
89/2	6.5 kbar	750°C	6.0 kbar	650°C
89/40	6.0 kbar	700°C	6.0 kbar	625°C
89/59	6.5 kbar	800°C	5.0 kbar	625°C
89/63	6.5 kbar	750°C	4.5 kbar	600°C
89/71	6.0 kbar	750°C	6.0 kbar	675°C
89/106	6.5 kbar	800°C	6.0 kbar	750°C
89/108	6.0 kbar	700°C	5.5 kbar	625°C
89/334J	6.0 kbar	800°C	5.5 kbar	750°C

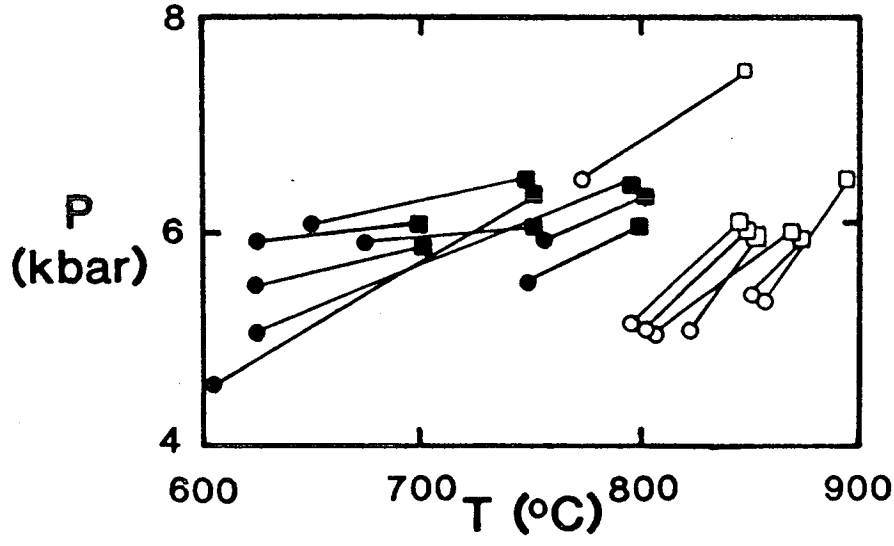

Fig. 5.14 Pressure-temperature estimates for core and rim compositions from the Brattstrand Bluffs coastline (open squares and circles) and Nemesis Glacier region (filled squares and circles).

compositions reflect a point on an actual pressure-temperature path. Fig. 5.14 indicates that rim compositions from the Brattstrand Bluffs coastline imply a greater decompressional component to the retrograde path than those from the Nemesis Glacier region, which is consistent with the zonation discussed in Section 5.2.4. The estimated pressure-temperature path gradients (i.e. d*P* / d*T*) are 17 bar / °C for the Brattstrand Bluffs coastline and 6 bar / °C for the Nemesis Glacier region. The retrograde metamorphic evolutions of these two areas are considered further in Chapters 6 and 7.

6. Metapelite phase relationships in the Brattstrand Bluffs coastline

6.1 INTRODUCTION

6.1.1 Mineral reaction textures

The previous chapter was primarily concerned with estimation of peak pressure-temperature conditions in the areas of study. The metamorphic peak represents only one instant during the evolution of a rock, and much more information regarding metamorphic and tectonic processes can be obtained if evidence is preserved of other stages of the metamorphic history. Such information is commonly presented as a pressure-temperature path. Ideally these depict both the prograde and retrograde path, but granulites rarely preserve evidence of their prograde evolution. Compositional zonation in mineral grains is one potential record of pressure-temperature evolution. However, as discussed in the previous chapter (Section 5.5.6), the effects of closure temperature, and pressure-temperature mismatch and feedback, mean that such an approach is unreliable. A better approach is to use mineral reaction textures which, in the granulite facies, typically take the form of symplectites and coronas of product phases between unstable reactants. The geometry of corona and symplectite textures implies that the 'volume of equilibration' during their formation was smaller than that during the initial equilibration of the reactant phases, which is consistent with retrograde mineral reaction. In the absence of extensive metasomatism, such textures are a record of pressure-temperature history (e.g. Ellis *et al.*, 1980; Droop & Bucher-Nurminen, 1984; Sandiford *et al.*, 1987). If the position and orientation of a given reaction in *P-T* space is well known, then the texture preserving that reaction can be related to a vector in *P-T* space. If several reactions are identified, a series of *P-T* vectors can be determined and a pressure-temperature path defined. This approach is best suited to lithologies which commonly preserve reaction textures and have well-understood phase relationships. It is difficult to satisfy both of these conditions since reaction textures are most widespread in those lithologies with complex phase relationships, and consequently those lithologies for which the phase relationships are poorly understood.

Reactions involving garnet and pyroxene in mafic and felsic granulite are relatively simple and well studied (e.g. Green & Ringwood, 1967; Perkins & Newton, 1981), but the number of potential reactions in these lithologies is limited and many granulite terrains, including those in this study, show no reaction textures in mafic or felsic lithologies. In contrast, metapelitic lithologies have complex phase relationships involving distinctive minerals, and commonly preserve reaction textures. The sensitivity of pelitic compositions to pressure and temperature change is reflected in the proportion of metamorphic studies based on metapelite compared to its volumetric abundance in metamorphic terrains. Since the pioneering work of Barrow (1893, 1912) in the Scottish Highlands, pelitic lithologies have been used as an indicator both of spatial metamorphic variation within a terrain, as in the Barrovian example, and of temporal metamorphic variation within individual specimens preserving mineral reaction textures or various generations of porphyroblast or mineral inclusion.

6.1.2 Metamorphic reactions and assemblages

Mineral reactions can be divided into 'discontinuous' and 'continuous' types. Discontinuous reactions occur at a fixed pressure for a given temperature, and are represented as lines in *P-T* space. A rock of fixed bulk composition is only stable at one point on a discontinuous reaction boundary in *P-T* space. Continuous reactions occur over a range of pressure at a given temperature, and are represented as bands in *P-T* space. A rock of fixed bulk composition is stable within the reaction band over a range of pressures and temperatures, but the compositions of at least two participating phases change as the reaction proceeds with changing pressure and temperature.

Metamorphic reactions and assemblages can also be considered in terms of their variance. Discontinuous reactions, and assemblages comprising all the participating phases in a discontinuous reaction (and no extra phases unless they consist entirely of components not present in the other phases), are referred to as 'univariant' since only one intensive variable is free to vary independently in the system. Hence, if the pressure at which a given univariant reaction occurs is fixed, the temperature and compositions of all the phases are also fixed. It follows that any phases in a univariant assemblage which exhibit solid solution vary in composition along the univariant reaction boundary in *P-T* space. Continuous reactions, and assemblages comprising all the participating phases in a continuous reaction, are 'divariant' if two of the intensive variables pressure, temperature and composition have to be fixed before the third is defined. Hence any depiction of divariant reactions in *P-T* space is only valid for one bulk composition. Rocks may also preserve 'trivariant' assemblages, which are stable over a range of pressure, temperature and composition, and 'invariant' assemblages, which are stable at a unique combination of pressure and temperature.

Trivariant and divariant assemblages are much more common than univariant assemblages, which are themselves much more common than invariant assemblages. This distribution is a simple reflection of the probability that a rock of given bulk composition attains the conditions necessary to stabilize each type of assemblage. However, despite the relative rarity of univariant reactions, an understanding of the disposition of univariant reactions, both in relative terms and in absolute *P-T* terms, is particularly useful. This is because the stability fields of divariant assemblages, which vary with bulk composition, are bracketed in *P-T* space by a fixed grid of univariant reaction lines which is applicable to all bulk compositions within the chosen chemical system. The construction of such 'petrogenetic grids' has been one of the principal aims of much recent petrological research.

6.1.3 The petrogenetic grid

The concept of a petrogenetic grid was first outlined by Bowen (1940), who visualized the dissection of pressure-temperature space by univariant mineral equilibria. Univariant equilibria intersect at points which correspond to invariant assemblages, and any divariant metamorphic assemblage can be ascribed to an area bounded by univariant equilibria, and hence to a given pressure-temperature range. Similarly, reaction textures can commonly be related to a vector in *P-T* space crossing from one divariant field to another.

Petrogenetic grids are based principally on thermodynamic constraints, and in particular on the phase rule which relates the assemblage variance (F) to the number of phases present in a stable assemblage (P) and the minimum number of chemical components required to represent all the phases of interest (C), via the expression

$$P + F = C + 2 \quad (6.1).$$

Before a grid can be constructed, the phases to be included and a suitable chemical system have to be selected. All possible univariant reactions and invariant points can then be determined, provided that the compositional or 'chemographic' relationships between the phases are known. Chemographic relationships are commonly portrayed in triangular compatibility diagrams (e.g. J.B. Thompson, 1957), which represent the phases of interest in terms of three components (i.e. C = 3). Discontinuous reactions require a change in the topology of the diagram involving four phases (i.e. P = 4): either the appearance or disappearance of a phase between three others (a terminal reaction) or the replacement of one tie line between two phases by another between two different phases (a non-terminal reaction). Continuous reactions are represented by the migration of three-phase triangles across the diagram (i.e. P = 3), and trivariant assemblages are represented by tie lines joining two phases (i.e. P = 2).

Stoichiometric coefficients of the reactants and products of univariant reactions can be calculated algebraically, and then volume and entropy changes determined for each reaction. The slope of each reaction in *P-T* space can then be calculated via the Clausius-Clayperon equation (Equation 5.12). Although molar volumes of many phases are known fairly accurately, values of molar entropy are still uncertain for a large number of minerals. However, qualitative grids can be readily constructed with the assumptions that devolatilization reactions usually proceed with increasing temperature, and that the high-pressure (i.e. high-density) side of solid-solid reactions can be determined from the volume change (J.B. Thompson, 1955; Albee, 1965).

The relative disposition of univariant reactions about invariant points can be constructed using a number of principles first outlined by F.A.H. Schreinemakers, and summarized by Niggli (1954) and Zen (1966). Application of these principles does not, however, yield a unique topological solution. In general some other information concerning the natural or experimental stability (or instability) of certain invariant points, univariant reactions, or divariant assemblages is required to determine the stable topology. If some of the equilibria have been studied experimentally, it may be possible to locate the entire topology in *P-T* space and produce a quantitative grid.

6.1.4 Metapelite grids

Interest in metapelitic phase equilibria has led to the construction of a number of petrogenetic grids applicable to pelitic compositions using experimental, natural-rock, and theoretical constraints. Fine grain size, low temperatures of equilibration which virtually preclude experimental study, and complex solid-solution behaviour have inhibited the study of low-grade rocks, but high- and medium-grade pelites have been considered in terms of two distinct groups of chemical system. The CaO-K_2O-Na_2O-Al_2O_3-SiO_2-H_2O (CKNASH) system, and various subsets of this system (e.g. KNASH, KASH, NASH), have been used to describe sub-solidus felsic mineral assemblages in rocks of pelitic composition (e.g. A.B. Thompson, 1974; J.B. Thompson & A.B. Thompson, 1976) and the relationships between these assemblages and aluminous granitic melts (e.g. A.B. Thompson & Algor, 1977; A.B. Thompson & Tracy, 1979). However, these grids ignore the relationships between ferromagnesian phases, which are commonly the most conspicuous mineralogical feature of metapelitic rocks and are typically described using grids in the K_2O-FeO-MgO-Al_2O_3-SiO_2-H_2O (KFMASH) system and various subsets (e.g. KFASH, KMASH, FMAS). These latter grids can generally be classified into one of three types:

(i) those which consider sub-solidus, water-saturated relationships in medium-grade metamorphic rocks comprising solid phases such as muscovite, chlorite, biotite, quartz, garnet, chloritoid, staurolite, cordierite and aluminosilicate polymorphs

(e.g. Albee, 1965; Hess, 1969; A.B. Thompson, 1976; Harte & Hudson, 1979; Spear & Cheney, 1989; Powell & Holland, 1990);

(ii) those which consider relationships at high grade between anhydrous phases such as cordierite, garnet, orthopyroxene, quartz (in silica-saturated assemblages), corundum (in silica-undersaturated assemblages), sapphirine, spinel and sillimanite (e.g. Hensen, 1971, 1986, 1987; Hensen & Green, 1973); and

(iii) those which consider complex relationships at conditions between those of the other two types of grid involving phases such as biotite, quartz, sillimanite, K-feldspar, garnet, cordierite, orthopyroxene, volatile fluid and silicate melt (e.g. A.B. Thompson, 1982; Grant, 1985*a*,*b*).

Type (ii) grids are considered in terms of the simple FMAS system since there are no potassic or hydrous phases, but types (i) and (iii) are generally considered in terms of the KFMASH system.

The KFMASH system is only an approximation to most pelitic compositions. Any additions to this system tend to stabilize those phases which accommodate the extra components, and produce new phases in which the extra components are essential parts. Perhaps the most-important deviations from the KFMASH system are the addition of CaO and Na_2O; K-feldspar commonly has significant Na_2O contents, and many pelitic assemblages include plagioclase feldspar which contains significant CaO and Na_2O. This has led some workers to consider the effect of extending certain reactions to the NKFMASH and CNKFMASH systems (e.g. A.B. Thompson, 1982; Grant, 1985*a*,*b*). The effects of other components can also profoundly affect the phase relationships. For example, Fe_2O_3 is an important component under oxidising conditions (i.e. high f_{O2}) which tends to expand the stability fields of those phases that readily accommodate ferric iron (such as spinel and sapphirine) with respect to those that do not. This effect has been used by Hensen (1986) to derive contrasting high-f_{O2} and low-f_{O2} grids involving spinel and sapphirine in the system FMASO (where O represents the extra oxygen component to account for Fe^{3+}) which account for apparent inconsistencies in FMAS grids. A similar effect has been described for amphibolite-facies rocks by Hudson and Harte (1985), who attributed the occurrence of almandine in a suite of aluminous metasediments to an expansion of the stability field of garnet at low f_{O2}. Some grids have included both Fe_2O_3 and TiO_2, thus enabling consideration of oxide phases which buffer the oxidation state and may play an important role in the metamorphic evolution of the rock. In particular, Powell and Sandiford (1988) have extended the FMAS and FMASO grids of Hensen (1986) into the FeO-MgO-Al_2O_3-SiO_2-TiO_2-Fe_2O_3 (FMASTO) system, and Clarke *et al.* (1989) have extended relationships in KFMASH to the related KFMASHTO system. TiO_2

also has the effect of stabilizing biotite with respect to other ferromagnesian phases. In addition, many workers have commented on the effect of MnO, which tends to stabilize garnet with respect to other phases (as does CaO). The importance of Cr_2O_3 and ZnO in stabilizing spinel has also been recognized (e.g. Vielzeuf, 1983; Montel *et al.*, 1986). Another important effect is that of variable water activity, which alters the stability of assemblages involving phases such as biotite, muscovite, silicate melt (which commonly contains dissolved water), and also cordierite which incorporates molecular water within structural channels. At medium grade, pelites are usually assumed to be saturated with a pure-water fluid (i.e. $a_{H2O} = 1$), or at least with a water-rich fluid (i.e. a_{H2O} less than one, but high and constant). At high grade, the possibility of variable and low water activity must be considered, and petrogenetic grids are visualized in terms of P-T-a_{H2O} space. Many of these effects are relevant to this study and are considered in more detail below.

6.1.5 Assemblages and reactions in the Brattstrand Bluffs metapelite

Section 3.2.3 describes the assemblages and reaction textures identified in the metapelitic gneiss and migmatite. Three components have been identified: banded mesosome consisting of intimately-interlayered aluminous and quartzofeldspathic layers, quartz-absent melanosome, and quartzofeldspathic leucosome. Several assemblages have been identified in each component, and comprise some subset of the phases quartz, K-feldspar, plagioclase, garnet, sillimanite, cordierite, spinel, biotite and ilmenite, with accessory zircon, apatite and graphite. Three generations of assemblage have been identified.

(i) An early assemblage preserved within garnet poikiloblasts (type-1 garnet), which are common in mesosome and melanosome but rare in the leucosome.

(ii) A syn- to post-S_3 matrix assemblage in the leucosome, mesosome and, less commonly, the melanosome. This assemblage is characterized by inclusion-free garnet (type-2 garnet), which is either subhedral or intergrown with quartz, and subhedral cordierite. This stage of the assemblage evolution is attributed to melting reactions at the metamorphic peak.

(iii) Retrograde assemblage development in all three migmatite components including post-S_3 spinel-bearing symplectite, pre- to syn-S_4 matrix biotite, post-S_4 coronas on spinel, and plagioclase rinds of uncertain age on garnet and sillimanite.

The rest of this chapter interprets this evolution in terms of metamorphic reactions, which are in turn related to the pressure-temperature-fluid evolution of the Brattstrand Bluffs coastline. Section 6.2 describes the mineral chemistry of the metapelite, and determines the chemographic relationships between the phases in terms of the KFMASH system. Section 6.3 derives a petrogenetic grid to describe the prograde

melting equilibria that relate assemblages (i) and (ii) above, and Section 6.4 derives grids to describe the post-melting reaction textures. Section 6.5 summarizes the metamorphic evolution, and attempts to quantify the previous sections by locating the grids in *P-T* space using suitable thermobarometric techniques.

6.2 MINERAL CHEMISTRY

6.2.1 Introduction

The composition of garnet, cordierite, spinel, ilmenite, biotite, plagioclase and K-feldspar in seventeen metapelite specimens from the Brattstrand Bluffs coastline were determined by wavelength-dispersive electron-probe microanalysis. Operating conditions and analytical precision and accuracy are described in Appendices 3.1, 3.2 and 3.7. Core and rim analyses, and continuous grain traverses, were used to identify any zonation. Normalization and site allocation procedures, and methods of ferric iron estimation, are outlined in Appendix 3.3, and representative analyses are tabulated in Appendix 3.5. Table 6.1 indicates the assemblages present in each of the analysed specimens, and Table 6.2 presents typical compositional data for each specimen.

6.2.2 Garnet

Garnet is present in all the specimens considered here, and is essentially an almandine-pyrope mixture, with X_{Mg}^{Grt} varying between 0.10 and 0.30, and generally decreasing rimwards. This zonation is most pronounced towards adjacent cordierite and biotite grains where X_{Mg}^{Grt} values change by up to 0.05 units. A similar compositional change occurs near enclosed biotite grains. Calcium contents are low: X_{grs}^{Grt} varies between 0.01 and 0.04, and shows little zonation, but may decrease rimwards by up to 0.003 units, particularly where the garnet is mantled by plagioclase. X_{sps}^{Grt} varies between 0.01 and 0.04, and shows little variation within single grains. Chromium contents are negligible, and charge and site balance calculations imply that ferric iron contents are insignificant.

No significant compositional difference was identified between the two textural types of garnet porphyroblast in any single specimen, but late garnet coronas around spinel and ilmenite have lower X_{Mg}^{Grt} values than garnet porphyroblasts in the same specimen. For example, garnet coronas in specimen 88/51 have an X_{Mg}^{Grt} of 0.10 compared with a typical value of 0.13 in the porphyroblasts.

6.2.3 Cordierite

X_{Mg}^{Crd} values vary between 0.55 and 0.80, but most are in the range 0.55 to 0.70 and commonly increase rimwards. The zonation is most pronounced towards adjacent

Table 6.1 Metapelite assemblages and textural features.

	Grt	Crd	Spl	Ilm	Bt	Sil	Qtz	Pl	Kfs	Textures
88/14B	abe	-	c	b/c	ae	abe	abc	-	b	AFGH
88/28	ab	bc	c	b/c	-	ab	abc	e	b	BCI
88/37	b	b	-	b/c	-	-	b	b	b	
88/44	ab	bce	c	b/c	a	ab	abc	e	b	BCDEI
88/51	be	-	c	b/c	de	be	bc	-	b	AFGH
88/56	abe	bce	c	b/c	ad	ab	abc	e	b	CDEFJ
88/62	be	-	c	b/c	de	be	bc	be	b	AFGHJ
88/74	ab	bce	c	b/c	ade	abe	abc	be	b	ACDEGHJ
88/102	be	bce	c	b/c	de	be	bc	-	b	A?B?C?DEFGH
88/110	be	bce	c	b/c	d	be	bc	-	b	ADEFH
88/153C	abe	ce	c	b/c	ade	ab	abc	e	b	A?DEFGJ
88/205	b	bce	c	b/c	-	be	bc	b	b	ADEH
88/273	ab	bc	c	b/c	ad	ab	abc	be	b	BDI
88/318	ab	bc	c	b/c	a	ab	abc	b	b	D
88/325	b	-	-	b/c	d	b	b	b	b	
88/328	ab	bc	c	b/c	ad	ab	abc?	b	b	BD?
88/331	ab	-	-	b/c	-	ab	b	b	b	

Textural setting of minerals: (a) type-1 garnet or inclusions in type-1 garnet, (b) syn-S_3 matrix phases or recrystallized melt, (c) symplectite and intergrowths, (d) S_4 matrix biotite and (e) post-S_4 coronas. Reaction textures: (A) Spl-Qtz intergrowths, (B) Spl-Crd symplectite, (C) Crd-Qtz intergrowth, (D) Spl-Crd-Qtz symplectite, (E) Crd coronas between Spl and Qtz, (F) Grt coronas on Spl and Ilm, (G) Bt coronas on Spl and Ilm, (H) Sil coronas on Spl and Ilm, (I) Pl overgrowths on Grt and Sil in the presence of Qtz and (J) Pl coronas between Kfs and Grt, Sil or Spl.

garnet grains, where X_{Mg}^{Crd} values increase by up to 0.05 units. Manganese contents are less than 0.02 cations per 18-oxygen formula unit. Total alkali contents are generally less than 0.03 cations per 18-oxygen formula unit, although they may be higher at grain edges. Oxide totals exceed 97 per cent, and are commonly greater than 98 per cent, implying low volatile contents.

Cordierite coronas around spinel and garnet have higher X_{Mg}^{Crd} values than cordierite porphyroblasts in the same specimens. For example, cordierite coronas in specimen 88/110 have X_{Mg}^{Crd} values of 0.66 to 0.69 compared with values of about 0.62 in the porphyroblasts.

6.2.4 Spinel

Spinel is effectively a hercynite-spinel solid solution, with X_{Mg}^{Spl} values between 0.06 and 0.24. Manganese contents are very low, less than 0.005 cations per 4-oxygen formula unit. Chromium contents, although relatively constant in any one specimen, have an inter-specimen range of 0.002 to 0.026 cations per 4-oxygen formula unit. Zinc contents are similarly variable, and range between 0.004 and 0.041 cations per

Table 6.2 A summary of mineral-chemical data for the metapelite. Core compositions are taken for garnet and cordierite. Average compositions are taken for those phases which exhibit a non-systematic variation (i.e. spinel, ilmenite, biotite and feldspar).

	garnet			cordierite	spinel				ilmenite		biotite				plagioclase	K-feldspar
	X_{Mg}	X_{grs}	X_{sps}	X_{Mg}	X_{Mg}*	X_{mag}	X_{chr}	X_{gah}	X_{ilm}	X_{hem}	X_{Mg}	TiO_2 (wt%)	F (wt%)	X_K	ab:or:an	ab:or:an
88/14B	0.24	0.02	0.02	-	0.20	0.04	0.00	0.01	0.95	0.03	0.74	2.98	3.46	0.97	-	34:64:02
88/28	0.18	0.02	0.02	0.56	0.17	0.01	0.00	0.03	0.98	0.00	-	-	-	-	70:01:29	21:76:03
88/37	0.26	0.02	0.02	0.60	-	-	-	-	0.98	0.00	-	-	-	-	76:02:22	29:67:04
88/44	0.24	0.02	0.02	0.58	0.22	0.02	0.01	0.03	0.97	0.00	0.61	3.13^{i}	1.09^{i}	0.98^{i}	69:01:30	21:77:02
88/51	0.13	0.02	0.04	-	0.11	0.01	0.00	0.01	0.99	0.00	0.67	4.03	5.32	0.96	-	39:51:10
88/56	0.26	0.02	0.02	0.65	0.22	0.01	0.01	0.02	0.97	0.00	0.74	5.66^{i} 4.18^{m}	3.93^{i} 4.74^{m}	0.92^{i} 0.96^{m}	70:01:29	29:67:04
88/62	0.15	0.02	0.03	-	0.11	0.01	0.00	0.01	1.00	0.00	0.63	4.52	4.68	0.95	78:01:21	31:63:06
88/74	0.26	0.03	0.01	0.66	0.22	0.03	0.01	na	0.99	0.00	0.73	4.77	na	0.97	61:01:38	21:76:03
88/102	0.24	0.02	0.03	0.62	0.19	0.05	0.00	0.01	0.96	0.02	0.65	4.48	4.33	0.96	-	07:80:13
88/110	0.22	0.03	0.02	0.62	0.22	0.05	0.00	0.00	0.97	0.01	0.60	5.97	3.75	0.96	-	28:72:00
88/153C	0.25	0.03	0.03	0.63	0.20	0.06	0.00	0.01	0.96	0.01	0.60	6.02	2.71	0.96	66:01:33	27:73:00
88/205	0.23	0.02	0.02	0.64	0.20	0.01	0.01	0.01	0.97	0.00	-	-	-	-	68:01:31	27:72:01
88/273	0.24	0.02	0.01	0.63	0.22	0.03	0.01	0.03	0.96	0.00	0.69	5.90^{i} 3.64^{m}	3.71^{i} 4.18^{m}	0.91^{i} 0.97^{m}	69:01:30	23:77:00
88/318	0.23	0.03	0.01	0.62	na	na	na	na	0.97	0.00	na	na	na	na	58:13:29	16:83:01
88/325	0.17	0.03	0.02	-	-	-	-	-	0.98	0.00	0.48	5.09	na	0.97	70:01:29	24:74:02
88/328	0.24	0.03	0.01	0.62	0.19	0.01	0.01	0.03	na	na	0.62	5.60^{i}	2.37^{i}	0.97^{i}	na	na
88/331	0.30	0.03	0.01	-	-	-	-	-	0.94	0.00	-	-	-	-	60:01:39	25:71:04

i = biotite inclusion in garnet, m = matrix biotite, na = not analysed, compositional parameters are as defined in Appendix 3.3.

formula unit. Site and charge balance calculations indicate the presence of a magnetite component in all specimens, with ferric iron contents up to 0.14 cations per formula unit. These calculated contents are highly variable, even within single grains, reflecting the sensitivity of the calculations to the accuracy of each analysis. Ulvöspinel is a negligible component in all specimens. No zonation trends in any of the cation contents have been identified.

6.2.5 Ilmenite

Ilmenite is the only non-aluminous iron or titanium oxide phase. Manganese contents are low, less than 0.01 cations per 3-oxygen formula unit, and magnesium contents are up to 0.07 cations per formula unit. Calculated hematite contents are also low, with X_{hem}^{Ilm} values less than 0.04 and commonly zero or just less than zero. The specimens with positive X_{hem}^{Ilm} values (88/14B, 88/102, 88/110 and 88/153C) are those with the most magnetite-rich spinels.

6.2.6 Biotite

X_{Mg}^{Bt} values vary between 0.47 and 0.81, and commonly vary by about 0.10 in a single specimen. No zonation profiles have been identified, and the intra-specimen compositional variation reflects the textural setting of individual biotite grains. The highest X_{Mg}^{Bt} values are preserved by biotite inclusions in garnet, whereas the lowest X_{Mg}^{Bt} values are preserved by biotite enclosed within quartz or feldspar, and isolated from other ferromagnesian phases. Intermediate values are preserved by pre- to syn-S_4 matrix biotite and post-S_4 biotite coronas around spinel or garnet.

Octahedral aluminium contents are variable and generally range between 0.0 and 0.5 cations per formula unit normalized to 14 octahedral and tetrahedral cations. These low values are typical of granulite-facies metapelite (Guidotti, 1984, pp. 419-423). Titanium contents vary between 0.25 and 0.80 cations per '14-cation' formula unit, and fluorine contents are also high and vary between 1.0 and 6.5 weight per cent. The most fluorine-rich biotites also tend to be the most magnesian, as identified elsewhere (e.g. Ekström, 1972), and correspond to an X_{OH} in the anion site of about 0.3. Fluorine contents in any single specimen are lowest in biotite enclosed by garnet, and highest in matrix biotite, irrespective of X_{Mg}^{Bt}.

6.2.7 Feldspar

K-feldspar occurs in all the specimens considered here. X_{an}^{Kfs} is generally less than 0.05, although it can be up to 0.15 in plagioclase-absent specimens. X_{or}^{Kfs} is typically in the range 0.50 to 0.85, and X_{ab}^{Kfs} in the range 0.10 to 0.40, although spot analyses yield variable results because of microperthitic intergrowth.

Plagioclase was identified in only about two thirds of the specimens, and in these it has a low modal abundance and occurs as narrow coronas and overgrowths on garnet, sillimanite and rarely spinel. X_{or}^{Pl} values are generally less than 0.02, and X_{an}^{Pl} and X_{ab}^{Pl} values range between 0.20 and 0.40, and 0.55 and 0.80 respectively.

6.2.8 Chemical trends and relationships

Compositions of the solid phases are depicted in Fig. 6.1, projected onto the Al_2O_3-FeO-MgO plane from quartz, K-feldspar and H_2O. A consistent relationship between X_{Mg} in each phase has been identified in all specimens: X_{Mg} increases in the order spinel, garnet, cordierite, with some overlap between spinel and garnet. X_{Mg}^{Bt} is variable, and may be less than, greater than, or show complete overlap with, X_{Mg}^{Crd}. It is clear from Fig. 6.1 that bulk X_{Mg} is an important control on the mineral assemblage, with the most iron-rich specimens (88/51, 88/62) being cordierite absent.

The iron-magnesium fractionation between garnet and spinel has been a topic of discussion for some time. Experimental and natural-rock evidence suggests that spinel can be both more magnesian (e.g. Barker, 1964; Hensen & Green, 1972; Ellis, *et al.*, 1980) and less magnesian (e.g. Hsu & Burnham, 1969; Berg, 1977*b*; Harris, 1981) than coexisting garnet. The former seems to be the case in rocks with a relatively iron-rich bulk composition, whereas the latter typifies magnesian bulk compositions, implying that there could be an inversion of the iron-magnesium distribution relationship (Hensen & Green, 1972). The specimens discussed here, in which spinel is less magnesian than coexisting garnet, have a rather iron-rich bulk composition, lending support to this theory. Such an inversion has important implications since it changes some of the univariant reactions involving garnet and spinel (Hensen, 1971; Vielzeuf, 1983), and is discussed further in Section 6.4.3.

The variation in biotite composition is a reflection of variable amounts of iron-magnesian exchange with other phases. Biotite is normally less magnesian than coexisting cordierite, but matrix biotite and biotite inclusions in garnet are commonly more magnesian than cordierite in the same specimen. In the case of matrix biotite, this could reflect the late post-cordierite origin inferred from textural relationships; in the case of the biotite inclusions it almost certainly reflects iron-magnesium exchange with surrounding garnet, which also produced a marked zonation in the garnet towards the inclusion. It is assumed here that any biotite once in equilibrium with cordierite was originally less magnesian than that in cordierite.

The choice of system for any discussion of phase relationships must be a compromise between a system that adequately describes the compositions of all the phases, and a system that is simple enough to enable clear graphical representation of the phases and the reactions between them. The remainder of this chapter considers

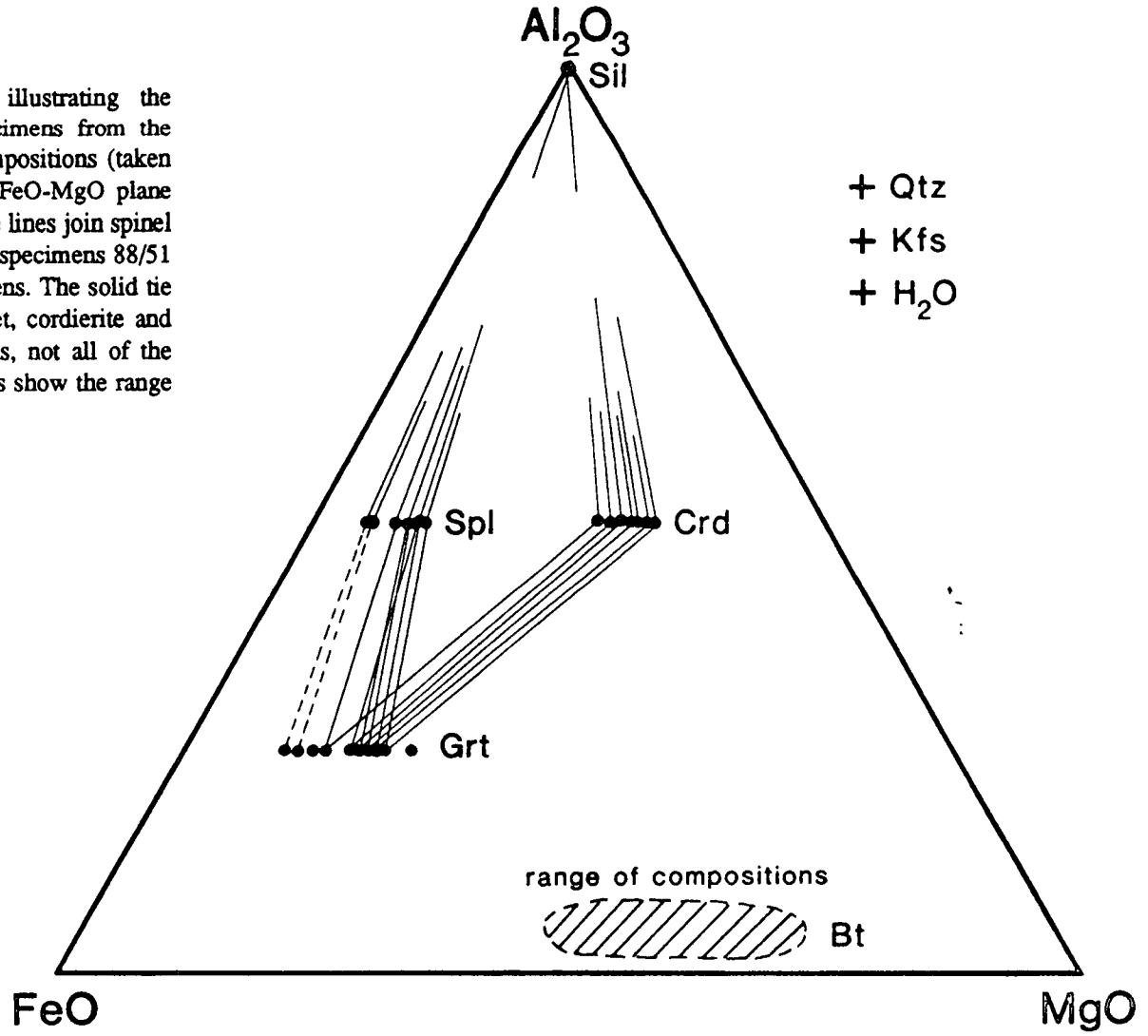

Fig. 6.1 An AFM compatibility diagram illustrating the compositions of phases in the metapelite specimens from the Brattstrand Bluffs coastline. Representative compositions (taken from Table 6.2) are projected onto the Al_2O_3-FeO-MgO plane from quartz, K-feldspar and H_2O. The dashed tie lines join spinel and garnet compositions in the cordierite-absent specimens 88/51 and 88/62, which are the most iron-rich specimens. The solid tie lines join phases in specimens containing garnet, cordierite and spinel. Given the similarity of the compositions, not all of the data in Table 6.2 are plotted, but this figure does show the range of mineral compositions in the specimens.

the metapelite phase relationships in terms of the much-used KFMASH system, which can account for many of the observed features and for which a number of theoretical grids already exist. The phases garnet, sillimanite, K-feldspar, quartz, cordierite, spinel and biotite can be adequately represented by this system. Contents of MnO, CaO, ZnO, Fe_2O_3, Cr_2O_3 and TiO_2 in these phases are small or insignificant. The only major departure from KFMASH in these phases is the sizeable but subordinate Na_2O content of K-feldspar. However, certain phases cannot be represented in KFMASH. Omission of CaO and Na_2O clearly precludes consideration of plagioclase, but this phase is of low modal abundance and does not appear to play a major role in the metamorphic evolution other than as rare, narrow overgrowths on garnet, sillimanite and spinel when adjacent to K-feldspar. In addition, the low grossularite contents of garnet suggest that CaO is not a crucial component. Similarly, omission of TiO_2 and Fe_2O_3 precludes consideration of ilmenite. Coronas around ilmenite indicate that it does participate in the retrograde evolution of the metapelite, and other workers have produced grids involving ilmenite in titanium-bearing systems (Powell & Sandiford, 1988; Clarke *et al.*, 1989, 1990; Clarke & Powell, 1991*a*,*b*). However, the absence of any other iron-titanium oxides, such as rutile or magnetite, and the minor modal importance of ilmenite, means that such complex grids provide little extra insight into the metamorphic evolution of the Brattstrand Bluffs coastline than the simpler KFMASH grids. Consideration of ilmenite is thought to be an unnecessary complication, and it is omitted from the following discussion.

6.3 PARTIAL MELTING

6.3.1 Migmatite formation and assemblage evolution

Field relationships between the mesosome, melanosome and leucosome components of paragneisses along the Brattstrand Bluffs coastline were interpreted in Chapter 3 as a reflection of syn-S_3 partial melting at the Proterozoic metamorphic peak. Syn-S_3 mineral assemblages in all three components can be related to the partial melting process, but the equilibria are best preserved in the banded mesosome where apparent melt production has been low and the reactants and products of the melting process have been retained in close proximity.

The earliest assemblage preserved in the mesosome is the biotite-sillimanite-quartz-K-feldspar inclusion suite within poikiloblastic garnet (type 1). The syn-S_3 matrix assemblage comprises cordierite, quartz, sillimanite, K-feldspar and an inclusion-free variety of garnet (type 2). Cordierite and type-2 garnet tend to be concentrated in the leucocratic layers of the stromatic mesosome, and are commonly sub-idioblastic. Garnet and, less commonly, cordierite, of identical textural

appearance to type-2 garnet and cordierite in the mesosome, occur within the quartzofeldspathic matrix of the leucosome-dominated units and segregated leucogneiss sheets. Given this close relationship, and the interpretation of the leucosome as recrystallized melt (see Section 3.2.10), it appears that the change from inclusion to matrix assemblage in the mesosome is associated with partial melting. Two types of melting reaction can account for these assemblage changes:

(i) a melting reaction consuming biotite, with garnet and cordierite crystallizing subsequently from the melt; and

(ii) an incongruent melting reaction consuming biotite and producing garnet, cordierite and melt simultaneously.

In the smaller leucosome units, the modal proportion of ferromagnesian phases to quartzofeldspathic material is high, with cordierite and type-2 garnet commonly accounting for some 30 per cent or more of the leucocratic layers and veins. Although the liquids generated by partial melting of pelitic lithologies have an excess of Al_2O_3, FeO and MgO over the simple quartz-feldspar granite system, the bulk composition of the small leucocratic veins and patches in the mesosome (i.e. garnet + cordierite + quartz + feldspar) is clearly incompatible with low-degree partial melt. However, the proportion of quartz and feldspar is too high for the veins to represent a refractory residue from which melt has been extracted. They are more likely to be a mixture of the solid and recrystallized-liquid products of an incongruent melting reaction.

Garnet-bearing segregations in metapelite or semi-pelite from central Massachusetts, USA (Tracy & Robinson, 1983), Namaqualand, South Africa (Waters & Whales, 1984; Waters, 1988), the Larsemann Hills, East Antarctica (Stüwe & Powell, 1989*b*), and Broken Hill, Australia (Powell & Downes, 1990) have been similarly interpreted as the result of incongruent melting reactions, such that garnet is a solid product of the melting process. Melt production has been low in these cases, resulting in anhydrous, biotite-absent segregations and patches of leucosome within biotite-bearing gneiss. This indicates a close association between biotite consumption and segregation formation. Although the relationship between the disappearance of biotite and the formation of garnet- and cordierite-bearing leucosome is not as unequivocal in the Brattstrand Bluffs metapelite, where melt production has been relatively high, it is likely that the same type of partial-melting process is responsible.

6.3.2 Chemographic relationships and a simple KFMASH grid in *P-T* space

In this section, the partial meting process in the Brattstrand Bluffs coastline is considered in terms of reactions between the phases garnet, cordierite, sillimanite, biotite, quartz, K-feldspar, volatile fluid and silicate melt in the KFMASH system. From Equation 6.1, it is clear that univariant equilibria in a six-component system

each comprise seven phases, and invariant assemblages comprise eight phases. Hence eight different univariant equilibria, each with one phase missing, and one invariant assemblage, can be written for the phases listed above. The nature of the univariant reactions depends on the chemographic relationships between the phases. Compositions of the solid phases are relatively straightforward: X_{Mg} increases in the order garnet, biotite and cordierite, and alumina contents of the ferromagnesian phases increase in the order biotite, garnet and cordierite. The volatile fluid is treated as a binary mixture of H_2O and CO_2 in equilibrium with hydrous phases and accessory graphite. The composition of the silicate melt is a more contentious issue.

The position of the melt composition in KFMASH space with respect to the other phases is crucial for the grid topology. The principal uncertainty lies in the position of the melt within the Al_2O_3-FeO-MgO plane when projected from quartz, K-feldspar and H_2O. The experimental data of Green (1976), Ellis (1986), Le Breton and Thompson (1988) and Vielzeuf and Holloway (1988) imply that melt is more magnesian than coexisting garnet at moderate temperatures, but that an inversion occurs at about 900°C at crustal pressures, above which melt is less magnesian than coexisting garnet. It is assumed here that the melt has an X_{Mg} intermediate between that of garnet and biotite, although other workers have taken a melt more iron-rich than all coexisting phases (e.g. A.B. Thompson, 1982). The relationship between melt composition and the garnet-cordierite tie line on the Al_2O_3-FeO-MgO plane is another matter of debate. Natural melt compositions straddle this line in a trend from aluminous compositions above the garnet-cordierite tie line, to less aluminous compositions below it. It is uncertain whether this trend of decreasing alumina represents restite unmixing (Chappell *et al.*, 1987), and hence a trend approaching true melt composition, or represents fractionation of aluminous phases such as garnet or cordierite from the melt, and hence a trend away from the true melt composition (Wall *et al.*, 1987). Given the difficulty of distinguishing between these two processes in natural specimens, the procedure followed here is to again use the composition of glasses from experimental studies of partial melting (Ellis, 1986; Le Breton & Thompson, 1988; Vielzeuf & Holloway, 1988) and assume that the melt is more aluminous than the garnet-cordierite tie line. However, it should be noted that other workers have placed melt compositions in the garnet-cordierite-biotite field (e.g. Grant, 1985*a*,*b*), and that restite is important in the Brattstrand Bluffs migmatite given the interpretation that garnet and cordierite in the leucosome are solid 'restitic' products of the melting process.

The eight possible univariant reactions between these phases of chosen composition are listed in Table 6.3. The reactions are denoted using the absent-phase

Table 6.3 Univariant reactions involving the phases garnet, sillimanite, cordierite, biotite, quartz, K-feldspar, H_2O and melt in the KFMASH system.

garnet + sillimanite + biotite + quartz + K-feldspar + H_2O = melt	(Crd)
biotite + sillimanite + quartz + K-feldspar + H_2O = cordierite + melt	(Grt)
biotite + sillimanite + quartz + H_2O = garnet + cordierite + melt	(Kfs)
biotite + sillimanite + quartz = garnet + cordierite + K-feldspar + melt	(V)
garnet + cordierite + K-feldspar + H_2O = biotite + sillimanite + melt	(Qtz)
garnet + cordierite + quartz + K-feldspar + H_2O = biotite + melt	(Sil)
garnet + sillimanite + cordierite + quartz + K-feldspar + H_2O = melt	(Bt)
biotite + sillimanite + quartz = garnet + cordierite + K-feldspar + H_2O	(L)

notation of Zen (1966) such that (i) refers to the i-absent reaction where 'i' is a phase. These univariant reactions intersect at an invariant point where all eight phases are stable, and Fig. 6.2a shows the disposition of the reactions about this point in *P-T* space. This arrangement is consistent with Schreinemakers' principles and, although only approximate, the *P-T* slopes of the reactions are drawn to be consistent with

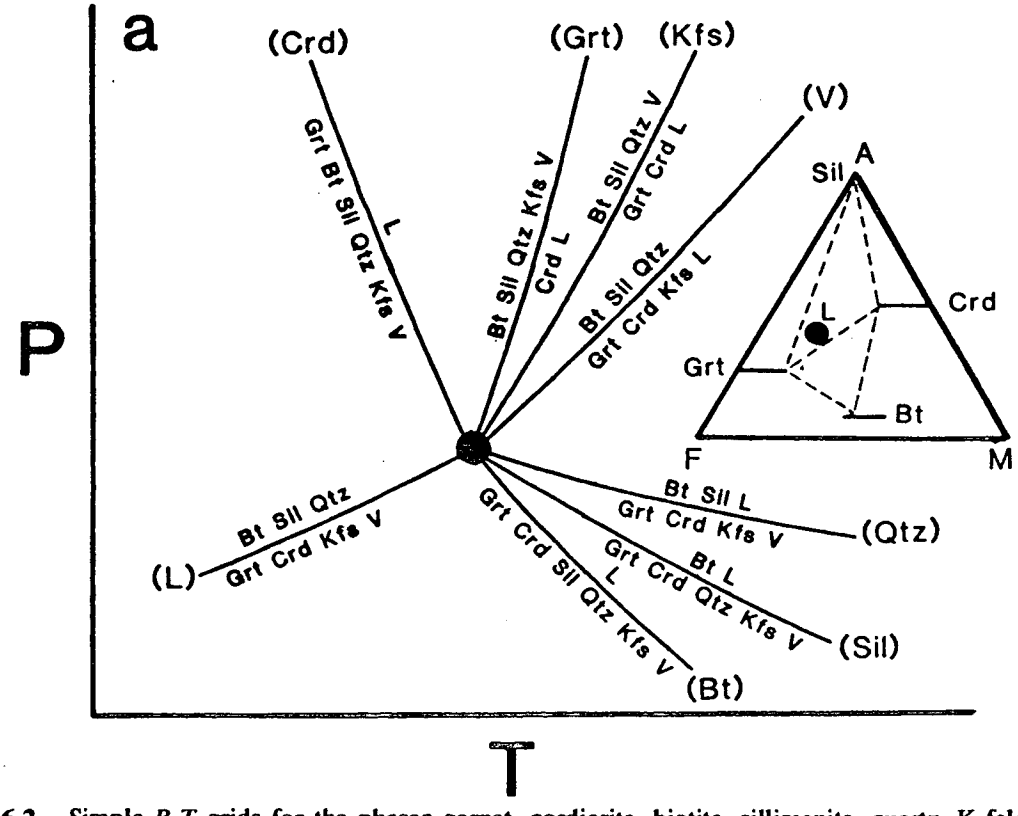

Fig. 6.2 Simple *P-T* grids for the phases garnet, cordierite, biotite, sillimanite, quartz, K-feldspar, hydrous fluid and melt in the KFMASH system, using the melt compositions of (a) Ellis (1986), (b) Thompson (1982) and (c) Grant (1985*a*, *b*). Melt compositions are depicted in AFM diagrams projected from quartz, K-feldspar and H_2O. Figs 6.2b and c are on the next page.

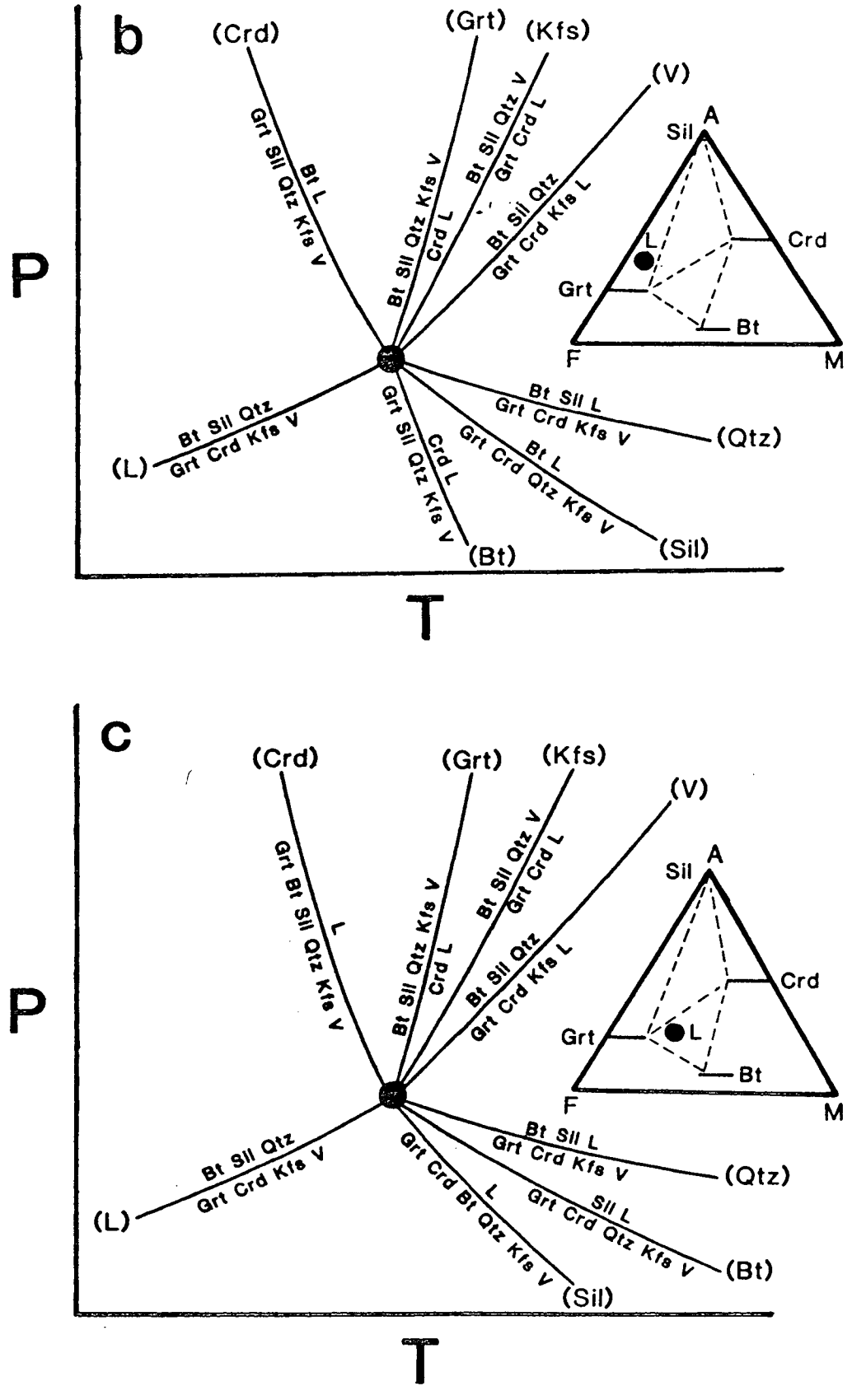

Fig. 6.2 continued. See the caption on the previous page.

other grids and experimental studies. Figs 6.2b and 6.2c show the alternative arrangements derived using the liquid compositions chosen by A.B. Thompson (1982) and Grant (1985*a*,*b*) respectively. The effect that the univariant reactions in Fig. 6.2a have on phase relationships is illustrated using various compatibility diagrams in Fig. 6.3. It is clear that the (V) reaction, which involves consumption of biotite, quartz and sillimanite, and production of garnet, cordierite, K-feldspar and melt, is consistent with the assemblage evolution described in Section 6.3.1. The assemblage must be fluid-absent for the (V) reaction to occur. Water-rich fluids are thought to be characteristic of metapelites at medium grade, and therefore some means of removing this fluid or lowering a_{H2O} is required. Clearly a_{H2O} is an important variable in the prograde evolution of the Brattstrand Bluffs metapelite, and its role is best visualized using T-a_{H2O} sections (Powell, 1983*a*).

6.3.3 The importance of water activity: a T-a_{H2O} univariant grid

Mineral equilibria involving mixed-volatile fluids are commonly depicted on isobaric T-X_{H2O} or T-X_{CO2} sections, in which the mole fractions of H_2O and CO_2 in the fluid vary antithetically across the diagram. Such diagrams are only valid if a fluid phase is present, but T-a_{H2O} or T-a_{CO2} sections have no such restrictions (Powell, 1983*a*). If H_2O-CO_2 fluids are assumed to be present under all conditions, a_{H2O} and a_{CO2} vary antithetically across the diagram in a similar manner to the T-X_{H2O} sections, although the relationship between the two is not linear but determined by activity-composition relationships. If fluid absence is considered, those parts of a T-a_{H2O} diagram where a_{H2O} equals unity still represent fluid-present conditions, with a_{CO2} equal to zero (i.e. a pure H_2O fluid). Relationships are more complex for those parts of the diagram where a_{H2O} is less than unity, since this indicates one of two types of fluid regime:

(i) fluid-present conditions with dilution of the H_2O component by CO_2 (i.e. a_{CO2} is non-zero), or

(ii) fluid-absent conditions with a_{H2O} determined by hydrous mineral phases or silicate melt.

In the latter case, a_{CO2} can be zero or non-zero depending on the absence or presence respectively of carbonate phases or dissolved CO_2 in silicate melt. For a fixed non-zero value of a_{CO2}, there is a single value of a_{H2O}, less than unity, which represents fluid-present conditions. The diagram cannot be used at higher values of a_{H2O} in this case unless a_{CO2} decreases (by H_2O influx or loss of CO_2), and a_{H2O} values less than the fluid-present value represent fluid-absent conditions unless a_{CO2} increases (by CO_2 influx or loss of H_2O). Clearly the greater the role of CO_2 in a given system, the smaller a_{H2O} has to be before fluid-absent conditions are attained. It is important to appreciate that a_{H2O} and a_{CO2} can have non-zero values under fluid-absent conditions.

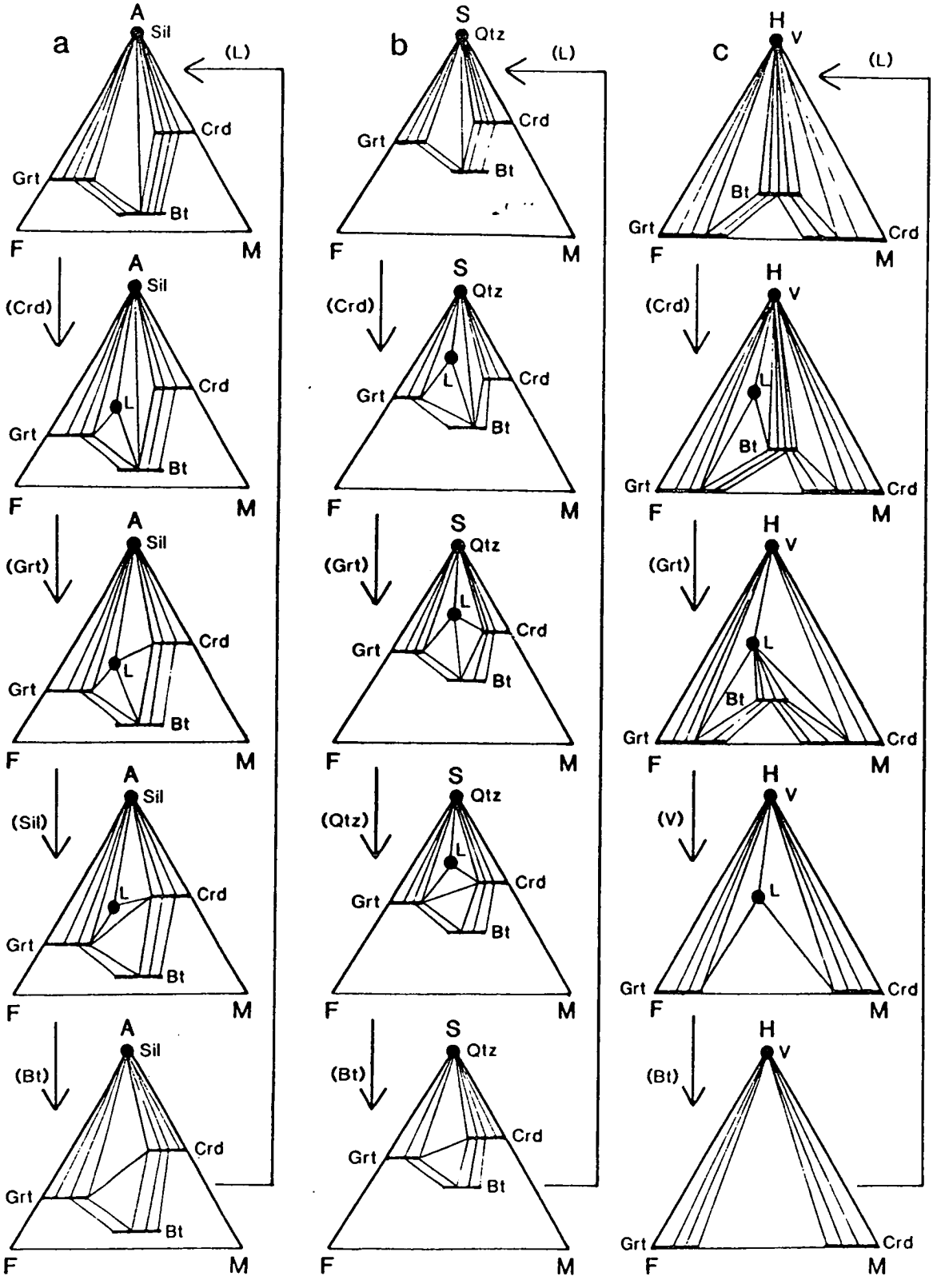

Fig. 6.3 Compatibility diagrams illustrating the metapelitic phase relationships associated with the simple *P-T* grid presented in Fig. 6.2a, projected onto (a) the Al_2O_3-FeO-MgO plane from quartz, K-feldspar and H_2O, (b) the SiO_2-FeO-MgO plane from sillimanite, K-feldspar and H_2O, and (c) the H_2O-FeO-MgO plane from sillimanite, quartz and K-feldspar. The annotated arrows indicate the reactions linking the phase relationships in each diagram.

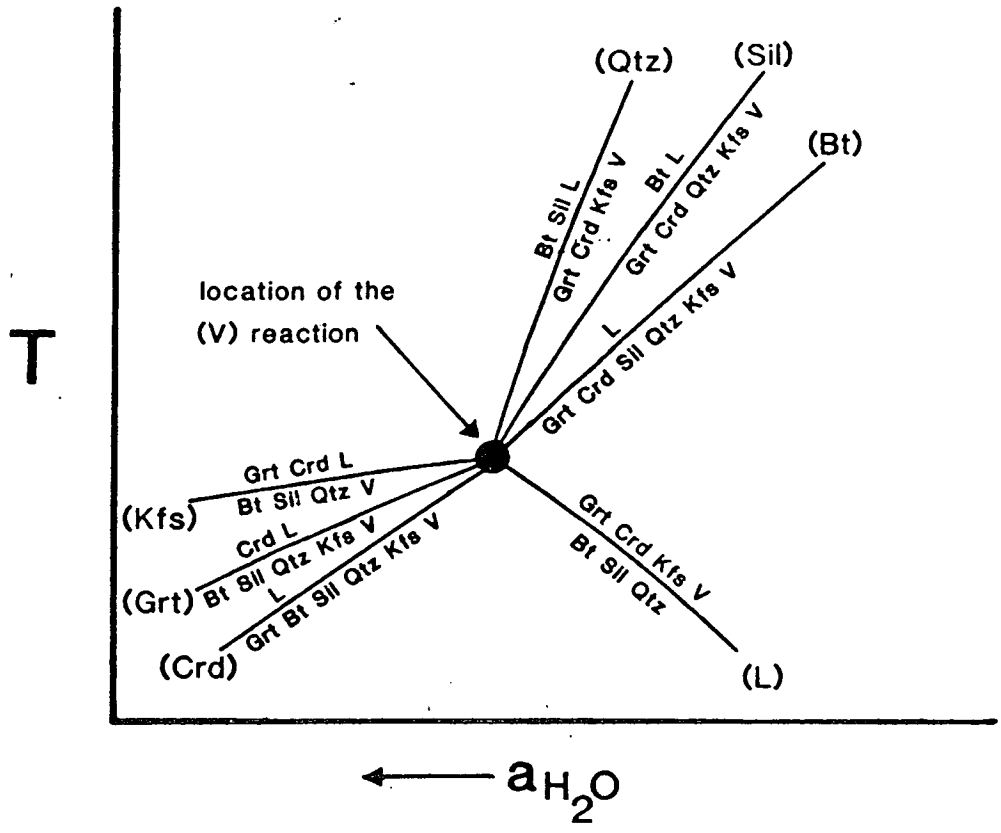

Fig. 6.4 A simple isobaric T-a_{H2O} section in KFMASH for the phases garnet, cordierite, biotite, sillimanite, quartz, K-feldspar, volatile fluid and melt. Chemographic relationships are as for Fig. 6.2a.

The simple univariant P-T grid in Fig. 6.2a can also be plotted in T-a_{H2O} space for fixed pressure (see Fig. 6.4). The sub-solidus dehydration reaction (L) has a slope such that it occurs at higher temperatures for higher a_{H2O}, whereas the melting reactions have a slope such that they occur at lower temperatures for higher a_{H2O}. Note that the (V) reaction does not appear as a line. This is because a_{H2O} varies along this reaction as drawn in Fig. 6.2a, and hence the reaction is only a point in an isobaric T-a_{H2O} section which coincides with the intersection of the other univariant equilibria. All the other equilibria in Fig. 6.2a represent constant a_{H2O} sections through reaction planesin P-T-a_{H2O} space, and hence appear as lines in Fig. 6.4. The (V) reaction on Fig. 6.2a is in fact the trace of the invariant point in P-T space as a_{H2O} decreases. At fixed pressure, the temperature and a_{H2O} of the invariant point are similarly fixed. If the pressure is fixed such that a_{H2O} at the invariant point equals unity, then conditions are fluid present at the invariant point. At any greater pressure, a_{H2O} must be less than unity, implying either the presence of CO_2 in the fluid phase or fluid absence. In the latter case, the invariant point is the fluid-absent reaction (V).

6.3.4 The role of divariant reactions

Before partial melting, the metapelite is assumed to have comprised the phases garnet (type 1), biotite, sillimanite, quartz, K-feldspar and volatile fluid. This six-phase assemblage is divariant in the KFMASH system, and represents the (Crd, L) divariant reaction. Divariant reactions have clearly been important in the evolution of the Brattstrand Bluffs metapelite. This observation is true for metamorphic rocks in general, since it is typically divariant reactions that are responsible for the assemblages developed in natural rocks, rather than univariant reactions which are rarely intersected. It follows that for a T-a_{H2O} diagram to depict the full metamorphic evolution of a rock, it should portray divariant as well as univariant equilibria.

Each KFMASH univariant reaction has a bundle of divariant equilibria associated with it. For example, the (L) univariant reaction in Fig. 6.4 has a bundle of divariant equilibria, each with silicate melt and another phase absent. This bundle comprises the (Grt, L), (Crd, L), (Bt, L), (Sil, L), (Qtz, L), (Kfs, L) and (V, L) reactions, although some of these reactions are, in general, not accessible to a particular bulk composition. For example, the (Sil, L) reaction does not occur in aluminous compositions for which sillimanite is a constituent of all possible assemblages. Divariant KFMASH equilibria are univariant equilibria in the KFASH or KMASH systems, and a divariant KFMASH reaction bundle can be considered as a bundle of K(F/M)ASH (i.e. iron or magnesium) univariant reactions around a K(F/M)ASH invariant point.

For a phase i, the K(F/M)ASH i-absent invariant point, or [i] using the phase-absent notation of Zen (1966) with square brackets to denote an invariant point, lies on the KFMASH (i) univariant reaction. Its position along that reaction is determined by the bulk composition of the rock, since each point on a univariant reaction represents a different bulk composition. Compositional change along univariant reaction boundaries, at least in KFMASH, is dominated by iron-magnesium exchange, with X_{Mg} of all coexisting ferromagnesian phases decreasing in one direction along the boundary, and increasing in the other. Hence the [i] invariant point in K(F/M)ASH can exist anywhere on the KFMASH (i) univariant reaction between the [i] invariant points for the pure KFASH and KMASH systems, and its position between the two depends on the bulk X_{Mg}, which varies along the KFMASH univariant reaction. There is one of these bundles on each of the KFMASH univariant reactions, each positioned at a point determined by the bulk X_{Mg}.

In the KFMASH system, the K(F/M)ASH univariant bundles are in fact divariant bands, whose position varies with bulk composition. The relationship between univariant, divariant and trivariant assemblages can be visualized on a P-T or T-a_{H2O}

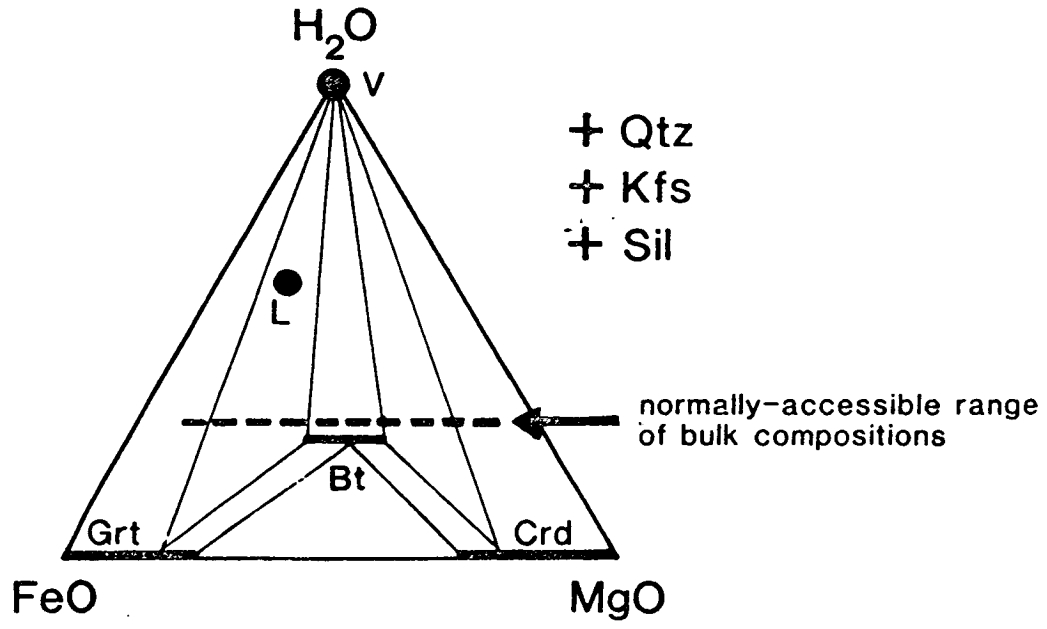

Fig. 6.5 An H_2O-FeO-MgO compatibility diagram, projected from quartz, sillimanite and K-feldspar, depicting the normally-accessible range of bulk compositions for initially fluid-present metapelite with respect to the phases garnet, cordierite, biotite, fluid and melt. After Powell and Downes (1990).

diagram drawn for a particular composition (Hensen, 1971). These diagrams have been called 'pseudosections' (e.g. Powell, 1978, pp. 219-220) and only portray those reactions and assemblages that are accessible to a given bulk composition.

KFMASH pelitic phase relationships relevant to fluid-present and fluid-absent conditions in T-a_{H2O} sections are best visualized in the H_2O-FeO-MgO compatibility diagram projected from quartz, sillimanite and K-feldspar (Thompson, 1982). There is a narrow range of normally-accessible bulk compositions for initially fluid-present pelites (Powell & Downes, 1990). These compositions, depicted on Fig. 6.5, are more water-rich than biotite in the H_2O-FeO-MgO plane since compositions below biotite in the diagram are commonly fluid absent, but much closer to biotite than the H_2O apex of the diagram since fluid-present rocks generally only have a small volume of fluid along grain boundaries. Fig. 6.6 is a schematic T-a_{H2O} pseudosection depicting trivariant assemblage fields, divariant assemblage bands and univariant reaction boundaries around the invariant point of Fig. 6.4. It has been drawn for relatively iron-rich compositions along the bulk composition band of Fig. 6.5, and it has been assumed that quartz, sillimanite and K-feldspar are present in all assemblages (and reactions with one or more of these phases absent have not been depicted).

The disposition of the trivariant and divariant fields in Fig. 6.6 can be understood in terms of the H_2O-FeO-MgO compatibility diagram. For example, low-temperature phase relationships are portrayed in Fig. 6.7 for three different water activities. For

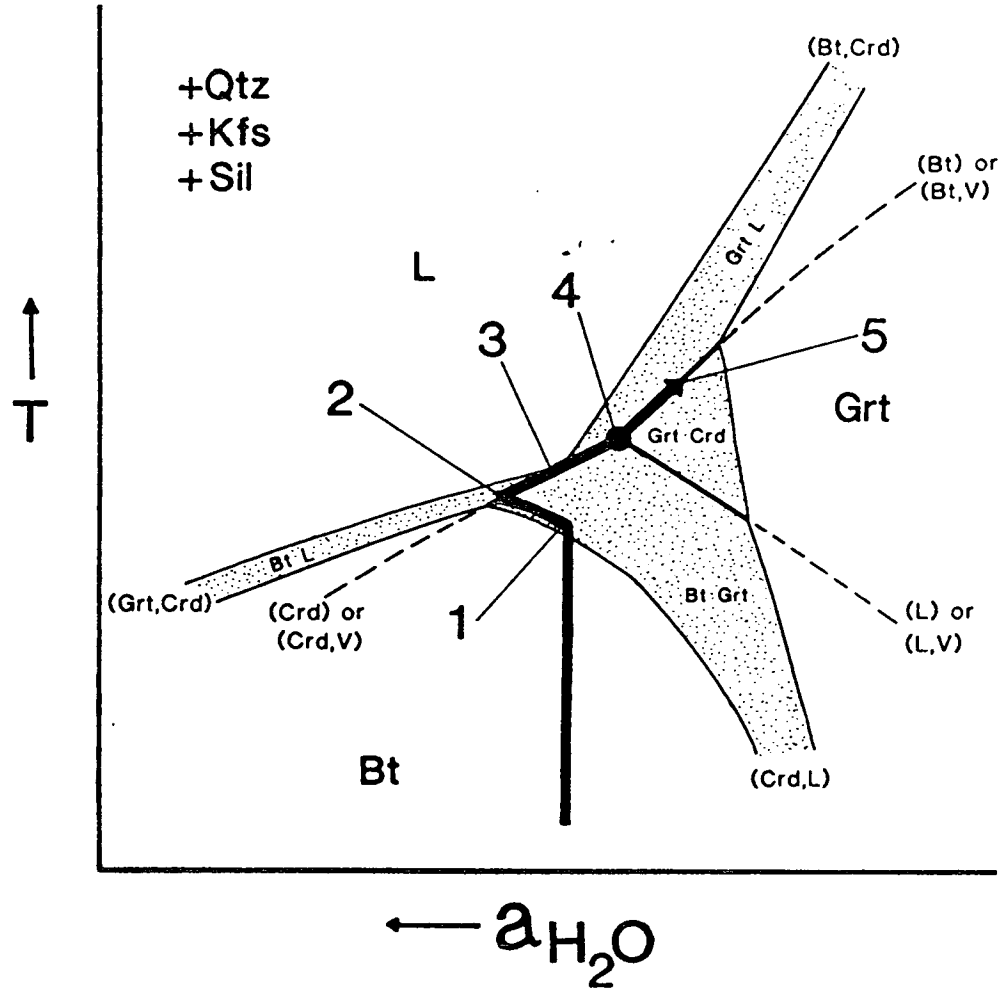

Fig. 6.6 A T-a_{H2O} pseudosection for an iron-rich bulk composition along the range of compositions illustrated in Fig. 6.5. An internal buffering path is marked for the Brattstrand Bluffs metapelite. All assemblages include quartz, K-feldspar and sillimanite, and can be fluid present or fluid absent depending on the fluid regime. The annotations on the buffering path refer to the following stages of the metamorphic evolution:

1. Type-1 garnet forms via the (Crd, L) divariant reaction, and fluid is buffered to higher a_{H2O} along this reaction.
2. The assemblage begins to melt via the (Crd) univariant reaction, and the fluid is buffered to lower a_{H2O} along this reaction as an increasing proportion of the hydrous component (both in the free fluid and the biotite) is dissolved in the melt.
3. At some point, all the fluid is consumed, and melting proceeds via the fluid-absent (Crd,V) reaction, and type-2 garnet is formed.
4. The isobaric invariant point is intersected, and cordierite forms as an additional solid product of incongruent melting via the (V) reaction.
5. When the biotite is consumed, the assemblage evolves away from the isobaric invariant point along the (Bt,V) reaction until peak temperatures are attained.

The reactions discussed above are written in full on p. 188

iron-rich bulk compositions, with water contents just greater than biotite, the relevant compatibility fields are the garnet-H_2O trivariant field, the garnet-biotite-H_2O divariant field and the biotite-H_2O trivariant field. With decreasing a_{H2O}, the biotite stability field contracts, and the garnet-biotite-H_2O divariant field translates to more

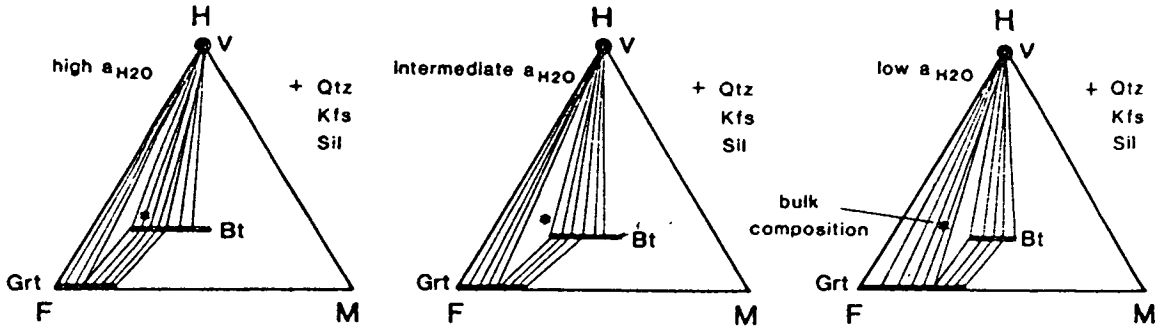

Fig. 6.7 Phase relationships for low temperatures on Fig. 6.6 at three different water activities, projected from quartz, sillimanite and K-feldspar onto the H_2O-FeO-MgO plane at (a) high a_{H2O}, (b) intermediate a_{H2O}, and (c) low a_{H2O}. The biotite stability field expands with increasing a_{H2O}.

magnesian compositions. The reverse occurs with increasing a_{H2O}. Hence a fixed bulk composition is in the biotite-H_2O trivariant field at high a_{H2O}, the garnet-biotite-H_2O divariant field at intermediate a_{H2O}, and the garnet-H_2O trivariant field at low a_{H2O}.

No fluid-absent reactions appear on Fig. 6.6 because they coincide with fluid-present equilibria. Just as the (V) univariant reaction is the locus of the KFMASH invariant point with decreasing a_{H2O}, the general divariant fluid-absent reaction (i, V) represents the locus of the univariant (i) reaction with decreasing a_{H2O}. Hence reactions such as (Crd, V) and (Bt, V) are represented as lines on an isobaric T-a_{H2O} section which coincide with the (Crd) and (Bt) univariant reactions, and the reaction boundaries on Fig. 6.6 represent fluid-present or fluid-absent reactions depending on the fluid regime. If H_2O is the only volatile species present, then the (Crd) reaction boundary represents the fluid-present univariant (Crd) reaction at $a_{H2O} = 1$ on Fig. 6.6, and the fluid-absent (Crd, V) reaction is the extension of this reaction boundary to values of a_{H2O} less than one. For CO_2-bearing fluids the situation is more complex in that a_{H2O} can be less than unity under fluid-present conditions, but the relationship between fluid-present and fluid-absent equilibria is the same. In a similar fashion, the fluid-absent (i, j, V) assemblage coincides in T-a_{H2O} space with the fluid-present divariant reaction band (i, j). The existence of fluid-absent reaction boundaries in T-a_{H2O} space means that values of a_{H2O} can change under fluid-absent conditions by the progress of these reactions. This is because a_{H2O} can be buffered in the absence of a volatile fluid by volatile-bearing phases such as biotite, cordierite and silicate melt.

6.3.5 A model for the prograde melting of the metapelite

A prograde path consistent with the observed phase relationships has been marked on Fig. 6.6. The path is based on the following interpretations of the natural rocks:

(i) conditions were fluid present before partial melting;

(ii) type-1 garnet developed before partial melting, and was in equilibrium with biotite, sillimanite, quartz and K-feldspar;

(iii) cordierite and type-2 garnet developed in equilibrium with a silicate melt; and

(iv) type-2 garnet is much more common than cordierite, reflecting progress of a cordierite-absent incongruent melting reaction in addition to the reaction that produced both garnet and cordierite.

The prograde path passes from the biotite-sillimanite-quartz-K-feldspar-fluid trivariant field into the (Crd, L) divariant field causing garnet growth via the reaction

$$\text{biotite} + \text{sillimanite} + \text{quartz} = \text{garnet} + \text{K-feldspar} + H_2O \quad \text{(Crd, L)}.$$

This garnet is correlated with type-1 garnet enclosing biotite, sillimanite, quartz and K-feldspar inclusions. Assuming that a_{H2O} is not buffered by an external fluid, it is buffered along the (Crd, L) reaction to higher values as temperature increases. Clearly the progress of dehydration reactions cannot by themselves account for fluid-absent conditions, since some means of removing the liberated fluid is required. The continuous dehydration reaction proceeds as a_{H2O} increases until the univariant (Crd) boundary is intersected. At this point the rock begins to melt via the reaction

$$\text{garnet} + \text{biotite} + \text{sillimanite} + \text{quartz} + \text{K-feldspar} + H_2O = \text{melt} \quad \text{(Crd)}.$$

This congruent melting reaction buffers a_{H2O} to lower values as temperature increases, and proceeds until one of the reactants is consumed which, in this case, is assumed to be the volatile fluid phase. At this point conditions become fluid absent and melting continues via the incongruent reaction

$$\text{biotite} + \text{sillimanite} + \text{quartz} = \text{garnet} + \text{K-feldspar} + \text{melt} \quad \text{(Crd, V)},$$

which is an extension of the (Crd) univariant reaction boundary. Progress of this reaction with increasing temperature continues to lower a_{H2O}. Garnet formed at this stage is in equilibrium with a melt, and is correlated with type-2 garnet identified in metapelite and leucogneiss specimens. This reaction proceeds until the isobaric invariant point is attained, and cordierite appears via the reaction

$$\text{biotite} + \text{sillimanite} + \text{quartz} = \text{garnet} + \text{cordierite} + \text{K-feldspar} + \text{melt} \quad \text{(V)}.$$

Provided that high-grade conditions are maintained, this reaction continues at the isobaric invariant point until one of the reactants is consumed, which is assumed in this case to be biotite given that biotite is absent from the syn-S_3 matrix assemblage. At this stage, melting proceeds via the (Bt, V) reaction

$$\text{garnet} + \text{cordierite} + \text{sillimanite} + \text{quartz} + \text{K-feldspar} = \text{melt} \quad \text{(Bt, V)},$$

buffering a_{H2O} to yet lower values. All of the phases in this equilibrium are present in

the syn-S_3 mesosome assemblage, indicating that the metamorphic peak was attained before one of the reactants was consumed. Garnet- and cordierite-bearing quartzofeldspathic leucosome in the Brattstrand Bluffs coastline is interpreted as crystallized partial melt formed by the (Crd), (Crd, V), (V) and (Bt, V) reactions. To a greater or lesser degree, the melt was segregated from the solid residue, entraining garnet and cordierite formed during the melting reactions.

This model requires a_{H2O} to have been less than unity before partial melting, so that type-1 garnet could develop via the dehydration reaction prior to partial melting. Given that sub-solidus conditions are unlikely to have been fluid absent, this model requires dilution of the H_2O component in the fluid phase with some other volatile species. CO_2 is the most likely candidate, and non-zero values of a_{CO2} are consistent with the widespread presence of accessory graphite in the metapelite.

It should be noted that this simple model is intended to be qualitative only, and the pseudosection has been constructed to be consistent with the observed phase relationships rather than rigorously calculated using thermodynamic and compositional data. Calculations are difficult in this case because of uncertainty in the compositions of melt and biotite. The model was also derived using an isobaric reaction grid. Clearly this grid is invalid if partial melting was accompanied by substantial increase or decrease in pressure. Although the retrograde evolution of the area involved substantial decompression (see Section 6.4), it is assumed that any pressure change during the partial melting interval was not sufficient to significantly alter the phase relationships depicted in Fig. 6.6.

The model is similar to that developed by Waters and Whales (1984) and Waters (1988) for melting of metapelite in Namaqualand, South Africa. Waters and Whales (1984) described garnet-bearing leucocratic segregations, which are attributed to progress of the (Crd, V) and (V) incongruent melting reactions. The importance of bulk composition in determining the metamorphic evolution is clearly illustrated in Namaqualand, where iron-rich metapelites underwent dehydration and fluid-absent melting as described above, but magnesian compositions underwent the (Grt, L) dehydration reaction rather than the (Crd, L) reaction. The magnesian compositions do not exhibit migmatite textures since the (Grt) and (Grt, V) melting reactions occur at higher temperatures than the cordierite-absent reactions accessible to iron-rich compositions. Temperatures in the Brattstrand Bluffs coastline are assumed to have been sufficient to promote melting in all pelitic compositions.

The model is also similar to that used by Powell and Downes (1990) to interpret garnet-bearing segregations at Broken Hill, Australia. Powell and Downes (1990) constructed three T-a_{H2O} pseudosections for assemblage relationships around the same

invariant point as discussed here: one for magnesian bulk compositions, one for intermediate compositions, and one for iron-rich compositions (which is identical to that depicted in Fig. 6.6).

6.3.6 A comparison with other grids

Although the KFMASH invariant point involving the phases garnet, cordierite, sillimanite, biotite, quartz, K-feldspar, volatile fluid and silicate melt is theoretically possible, it is not necessarily stable. There are two principal effects that could cause the invariant point depicted in Figs 6.2, 6.4 and 6.6 to be unstable.

(i) Phases other than those considered above are stable in pelitic compositions under suitable conditions and should be considered. Consideration of more than eight phases in a six-component system generates several possible invariant points in a 'multi-system' (Korzhinskii, 1959). If, for example, nine phases are considered there are nine possible invariant points, each with one phase absent, linked by 27 univariant reactions, each with two of the phases absent. However, it is not geometrically possible to construct a closed grid involving all these invariant points unless some of the univariant equilibria exhibit gross curvature. Since phase composition, stoichiometric reaction coefficients, and hence entropy and volume changes associated with a reaction generally change continuously along reaction boundaries, it is likely that reaction boundaries are curved. However, with a few notable exceptions (e.g. Hensen, 1987), most univariant reactions can be treated as linear or gently curved, hence precluding the stability of all possible invariant points in a multi-system. This results in a 'partially-closed' grid in which only some of the possible invariant points are stable. The other points are 'metastable', and are located outside the stability field of their respective invariant assemblages. It is necessary to use natural-rock or experimental evidence to determine which points are stable and which are metastable.

(ii) The continuous change in mineral compositions along univariant reaction boundaries can directly cause invariant points to be unstable, since univariant assemblages must lie within the stability limits of the pure end-member phases (Hensen, 1971). A KFMASH univariant reaction terminates if a point is reached where all phases in equilibrium are the iron or magnesium end members. These terminations are invariant points in the KFASH or KMASH systems respectively.

The most extensive multi-system petrogenetic grid available for partial melting of pelitic lithologies is the KFMASH grid of Grant (1985*a*,*b*). This considers all the phases listed above, plus orthopyroxene which is an important phase in the low-pressure melting of pelitic lithologies.

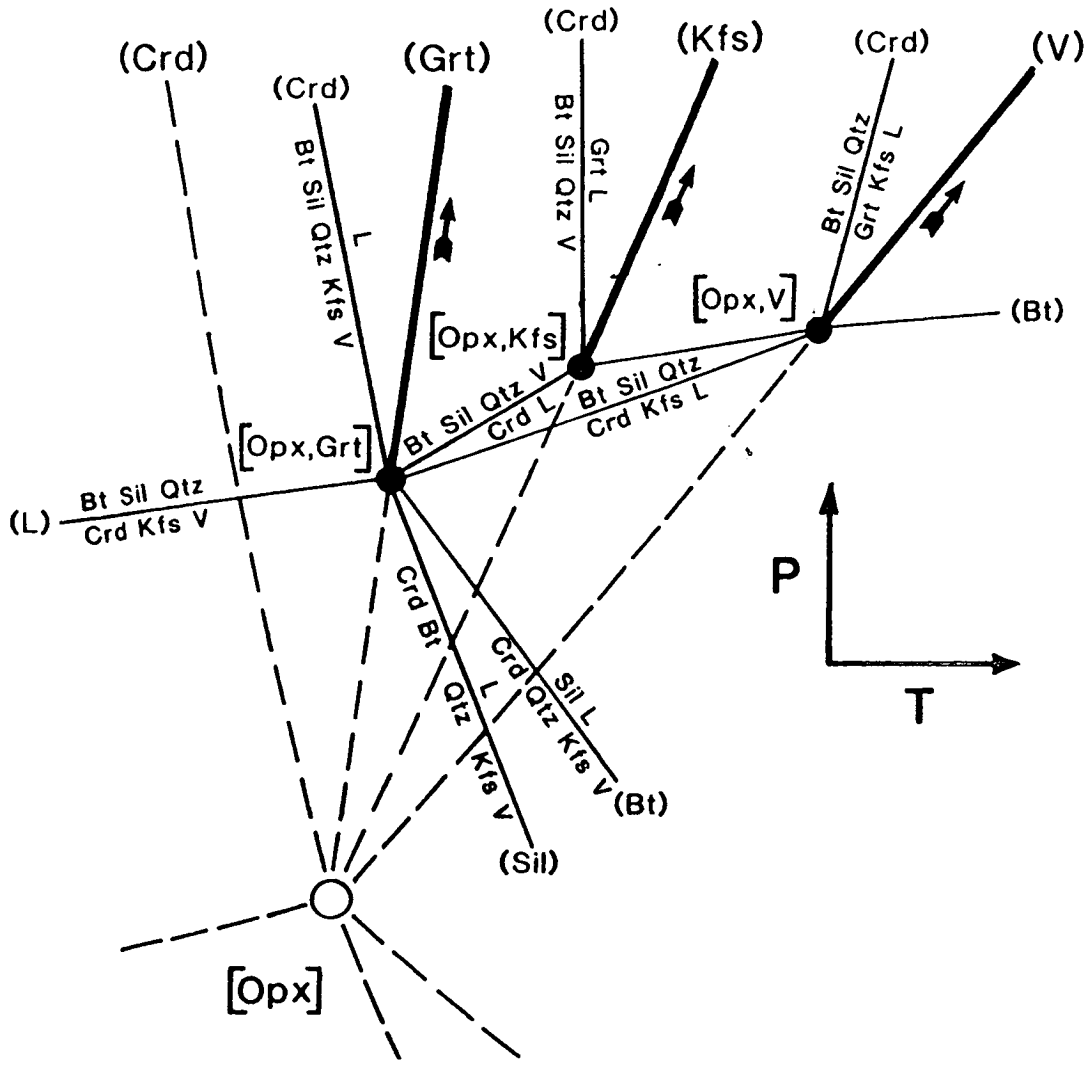

Fig. 6.8 A schematic *P-T* grid depicting univariant reactions in the KFMASH (heavy lines) and KFASH (light lines) systems, involving the phases garnet, cordierite, biotite, sillimanite, quartz, K-feldspar, fluid and melt in the vicinity of the [Opx] invariant point (for quartz-bearing assemblages with a_{H2O} equal to unity). The disposition of the KFMASH reactions is taken from Fig. 6.2a. The (Opx,Grt), (Opx,Kfs) and (Opx,V) KFMASH reactions are terminated by KFASH invariant points, and hence the (Opx,Crd), (Opx,L), (Opx,Bt) and (Opx,Sil) KFMASH reactions and the [Opx] KFMASH invariant point are unstable (dashed lines). The arrows indicate the direction of increasing X_{Mg} along the KFMASH univariant reaction boundaries. Modified from Grant (1985*a*, fig. 9).

Grant (1985*a*,*b*) used experimental and natural-rock constraints to derive a schematic grid (Grant, 1985*a*, fig. 7) involving the [Opx] and [Sil] invariant points. The invariant point depicted in Figs 6.2, 6.4 and 6.6 is equivalent to [Opx] in the Grant (1985*a*) grid, although the different choice of melt composition causes differences in the (Sil) and (Bt) reactions emanating from this point (i.e. the (Opx, Sil) and (Opx, Bt) reactions). Consideration of the orthopyroxene-absent univariant equilibria in KFASH indicates that [Opx] is not stable under water-saturated conditions (see Fig. 6.8, which is modified from Grant, 1985*a*, fig. 9). The only stable

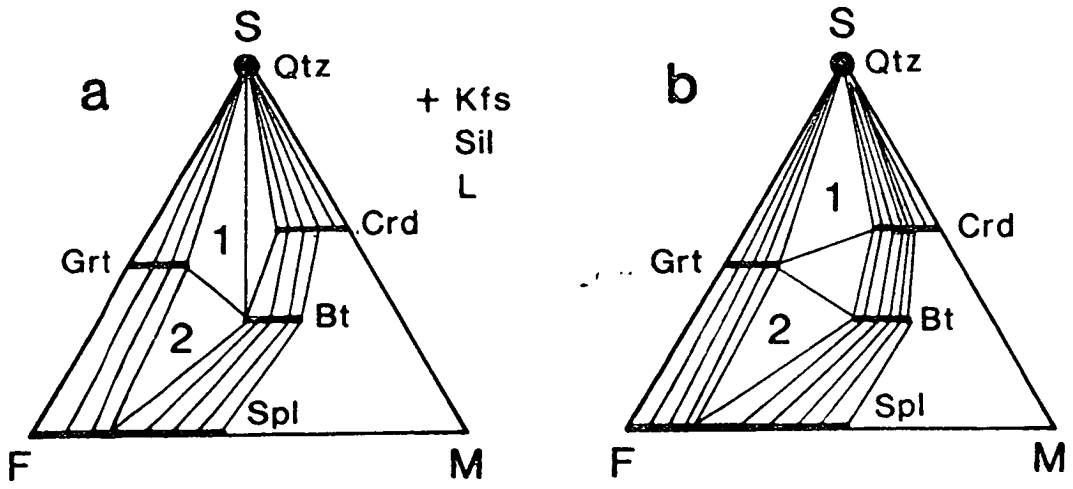

Fig. 6.9 SiO_2-FeO-MgO compatibility diagrams depicting metapelitic mesosome (1) and melanosome (2) assemblages projected from sillimanite, K-feldspar and melt (a) before the fluid-absent melting reaction and (b) after the fluid-absent melting reaction. Biotite is retained in the melanosome assemblage after this reaction, but disappears from mesosome assemblages

orthopyroxene-absent reactions for quartz-bearing assemblages are (Opx, Grt), (Opx, Kfs) and (Opx, V), and these are terminated at low pressure by the analogous KFASH invariant points [Opx, Grt], [Opx, Kfs] and [Opx, V].

The partial melting model outlined in Section 6.3.5 requires the stability of the (Crd) or rather the (Opx, Crd) reaction under fluid-present conditions. The (Opx, Crd) assemblage becomes stable in the multi-system grid if a_{H2O} is reduced, as shown by Grant (1985*a*, fig. 9 A, B and C). Given that the model outlined above requires a_{H2O} less than unity for both the fluid-present and fluid-absent parts of the metamorphic evolution, the model is not inconsistent with the multi-system grid.

6.3.7 Accounting for the melanosome assemblage

Syn-S_3 assemblages in the mesosome and leucosome are readily interpreted in terms of the dehydration and partial-melting model developed above. However, syn-S_3 assemblages in the melanosome are typified by garnet, sillimanite, spinel and biotite in the absence of quartz. This assemblage cannot be interpreted using the reaction grid of Fig. 6.6, which assumes that quartz is present in all assemblages and does not consider spinel. Comparison of quartz-present and quartz-absent pelitic assemblages is best visualized using the SiO_2-FeO-MgO compatibility diagram projected from sillimanite, K-feldspar and H_2O, or from sillimanite, K-feldspar and silicate melt if, as in this case, variation in a_{H2O} and periods of fluid absence invalidate a projection from H_2O. Fig. 6.9 depicts two such diagrams: one for assemblages developed before the discontinuous (Opx, V) melting reaction (i.e. the (V) reaction of Section 6.3.5) and the other for assemblages after this discontinuous reaction. It is clear that whereas

quartz-present assemblages cannot contain spinel, spinel is developed in quartz-absent, SiO_2-poor bulk compositions. The occurrence of spinel in quartz-absent assemblages is well-documented, and melanosome assemblages can be interpreted as rocks that were either initially SiO_2-poor or became so after the extraction of SiO_2-rich melt. Spinel-bearing assemblages are considered in more detail in Section 6.4, which discusses the post-melting retrograde development of spinel in the mesosome.

6.3.8 Problems with the fluid-absent melting model

A number of problems exist with the fluid-absent incongruent-melting model for garnet- or cordierite-bearing leucosome formation. The principal difficulties, discussed by Waters (1988) and Powell and Downes (1990), include the following.

(i) If garnet and cordierite formed as solid products of the melting process, why are they concentrated in the segregated leucosome rather than the restitic material?

(ii) If the leucosomes formed under fluid-absent conditions after dissolution of the fluid phase into the melt, why were the reactions not reversed and the garnet and cordierite dissolved when the melt crystallized and released its fluid content?

The concentration of the solid products of the melting reaction within the melt has been discussed by Powell and Downes (1990). This phenomenon is most apparent in rocks where partial melting has been limited, and large garnet porphyroblasts occur in the centre of discrete patches of leucosome enclosed by mesosome. Such textures have been described by several workers (Waters, 1988; Stüwe & Powell, 1989*b*; Powell & Downes, 1990) and were observed in sillimanite-absent semi-pelite at Steinnes Peninsula (see Section 3.2.5 and Plate 3.10b). Powell and Downes (1990) attributed the association of garnet and melt to a nucleation process, and this model can be adapted for the Brattstrand Bluffs coastline. As soon as the prograde path reaches the first incongruent melting reaction, garnet nucleates either on earlier garnet (type 1) to form composite grains or at new sites to form type-2 porphyroblasts. Each growing porphyroblast acts as a focus for the creation of reaction products, causing melt to concentrate around the garnet. If melting continues, the melt patch reaches a size when further growth of the original garnet porphyroblasts becomes kinetically unfavourable and one or more new porphyroblasts nucleate near the edge of the melt body. The melt bodies can continue to grow in this fashion and enclose numerous garnet porphyroblasts. If the melting reaction at the isobaric invariant point is encountered, cordierite begins to nucleate at the edges of the melt body. The absence of cordierite from the more extensive leucosomes is attributed to this two-stage process. The observed inverse relationship between the size of garnet porphyroblasts and the width of the leucosome (see Section 3.2.3) indicates that garnet porphyroblasts growing in narrow bodies of melt remained close enough to the

reactants for diffusion to continue, whereas growth was inhibited in the wider bodies of segregated melt.

A number of possible mechanisms have been proposed to account for the preservation of the anhydrous solid products of incongruent melting reactions after melt crystallization (Grant, 1985*b*; Waters, 1988). The occurrence of rare randomly-oriented biotite around garnet porphyroblasts in the leucosome indicates a small extent of back reaction on the release of volatiles during crystallisation, but clearly this process is far from complete and only accounts for a minor proportion of the probable water content of the melt.

A simple explanation is that the reverse reaction to hydrous assemblages is kinetically impeded. However, given that retrograde rehydration is a common feature of high-grade rocks, it seems unlikely that kinetic inhibition could account for the virtual absence of retrogression in the anhydrous leucosome. An alternative suggestion is that volatiles are lost from the system by the physical extraction of melt (Fyfe, 1973; Powell, 1983*a*; Powell & Downes, 1990). It is generally thought that rather high degrees of melting (25 to 30 per cent or more; Clemens & Vielzeuf, 1987; Wickham, 1987; Le Breton & Thompson, 1988) are required before viscous granitic melts can segregate from their source, although the effect of processes such as deformation are difficult to assess. Partial melt has clearly been extracted from its pelitic source in the Brattstrand Bluffs, as indicated by the widespread leucogneiss sheets; but they are not thought to have migrated far, and they themselves still preserve anhydrous assemblages. The high proportion of recrystallized melt along the Brattstrand Bluffs coastline, itself containing anhydrous garnet, generally precludes melt extraction as a viable means of preserving anhydrous assemblages.

Another possible mechanism is the influx of carbonic fluids into the melt before crystallization. This has been proposed to account for leucosomes in southern India (Janardhan *et al.*, 1982). Although the presence of graphite in leucosomes along the Brattstrand Bluffs coastline indicates that the melts did release CO_2 on crystallization, the modal abundance of graphite, and inferred CO_2 content of the melt, are too low to have diluted the H_2O content to a sufficient extent to inhibit rehydration. In addition, the CO_2 is assumed to have been present before melting to account for the reduced a_{H2O} required for the formation of type-1 garnet (See Section 6.3.5), whereas the CO_2-influx mechanism requires infiltration of carbonic fluids after melting but before crystallization. This narrow time interval means that this mechanism is unlikely to be applicable to migmatites in general (Waters, 1988).

Powell (1983*b*) discussed the possibility of diffusive loss of H_2O from melt into adjacent solid material, induced by chemical potential gradients resulting from a

higher a_{H2O} in the melt than the solid residue. This process would cause substantial rehydration of the material enclosing the melt bodies, and, although localized pre- to syn-S_4 biotite is common along shear zones in the Brattstrand Bluffs coastline, anhydrous assemblages are generally preserved in the mesosome as well as the leucosome. Another problem is that many of the leucosome units are too large to have lost their water contents by what is probably only a small-scale process.

Waters (1988) considered the possibility that garnet porphyroblasts are armoured by the initial solid products of melt crystallization. Garnet in leucosomes from the Brattstrand Bluffs coastline are commonly associated with, and surrounded by, quartz. Given that quartz is a reactant in the proposed melting reaction, rather than a product, it is likely to have crystallized from the melt. The evidence for a substantial amount of partial melting under fluid-absent conditions means that a high degree of melt crystallization would have occurred before the remaining melt became volatile saturated. It is also likely that garnet acted as a nucleation site for initial melt crystallization, and was therefore armoured against hydration reactions by the time the melt released its volatile content as a hydrous fluid.

The preservation of anhydrous leucosomes in the Brattstrand Bluffs coastline is attributed mainly to the last mechanism discussed above. The hydrous fluids released during melt crystallization are thought to been channellized along structural pathways through the country rock, producing only localized retrogression in the mesosome. This is discussed in more detail below.

6.4 RETROGRADE REACTION TEXTURES

6.4.1 Symplectite and corona textures in the metapelite

A number of post-S_3 reaction textures have been observed in the metapelite, and are described in Section 3.2.3. The textures occur in the mesosome, melanosome and in pelitic enclaves within the leucosome, and are assumed to post-date partial melting. The retrograde reaction textures can be divided into four groups:

(i) symplectites and intergrowths of spinel with cordierite and/or quartz after garnet and sillimanite, which post-date S_3 but pre-date S_4;

(ii) pre- to syn-S_4 biotite, which is concentrated in S_4 shear zones and correlated with channellized release of hydrous fluid by crystallizing partial melts;

(iii) syn- to post-S_4 cordierite, garnet, sillimanite or biotite coronas around spinel and ilmenite; and

(iv) narrow rinds of plagioclase around garnet, sillimanite and spinel, particularly where adjacent to K-feldspar.

Group (i) textures do not involve biotite and are best preserved in areas where S_4

shear fabrics are weak or absent. They are hence thought to pre-date crystallization of the silicate melt and to have formed under melt-present but fluid-absent conditions. In contrast, most matrix biotite, which is concentrated in S_4 shear zones, is thought to reflect interaction between solid assemblages and volatile fluid released on melt crystallization. Biotite is hence thought to have formed under fluid-present but melt-absent (i.e. sub-solidus) conditions, as are the post-S_4 coronas. Texture (iv) is not considered in this section since it is not thought to play a major role in the retrograde history and cannot be represented within the KFMASH system. Plagioclase rinds are briefly discussed in Section 6.5.7, with particular reference to their barometric implications.

The grid developed in Section 6.3 is clearly not applicable to spinel-bearing assemblages, and a new grid is required. The phases involved in the retrograde evolution are garnet, sillimanite, cordierite, spinel, biotite, quartz, K-feldspar, plagioclase, ilmenite, hydrous fluid and silicate melt, but, as above, plagioclase and ilmenite are omitted (see Section 6.2.8) and the remaining phases are considered in KFMASH. This leaves nine phases in a six-component system. At least two invariant points are required to depict the relationships between these phases, and the approach used here is to consider the evolution in terms of two separate KFMASH grids: one pertaining to fluid-absent melt-saturated conditions and the other pertaining to sub-solidus relationships. These simple grids are then compared with grids derived by other workers.

6.4.2 A simple univariant fluid-absent *P-T* grid

The phases to be considered in a fluid-absent grid relevant to the metapelite before melt crystallization are garnet, sillimanite, cordierite, spinel, quartz, K-feldspar and melt in the mesosome and leucosome, with the addition of biotite in the quartz-absent melanosome. In the KFMASH system, a maximum of one invariant [V] equilibrium and eight univariant reactions can be written involving just these phases. The phase compositions are taken to be the same as those used for the melting grids (see Section 6.3.2) with the addition of spinel which has an X_{Mg} less than that of garnet. The KFMASH univariant reactions between these phases are summarized in Table 6.4. The (Bt, V), (Kfs, V) and (L, V) reactions are 'degenerate' if cordierite is assumed to be anhydrous, since biotite and melt are the only phases that contain H_2O, and biotite, melt and K-feldspar are the only phases to contain K_2O. Hence only six different univariant reactions emanate from the invariant point, although the degenerate reaction is stable on both sides of the invariant point. Fig. 6.10 depicts the disposition of the six univariant KFMASH reactions about the [V] point in *P-T* space, in an arrangement which is consistent with Schreinemakers' principles and experimental

Table 6.4 Univariant reactions involving the phases garnet, sillimanite, cordierite, spinel, biotite, quartz, K-feldspar and melt in the KFMASH system. All reactions are fluid-absent.

biotite + spinel + quartz = garnet + sillimanite + K-feldspar + melt	(Crd,V)
biotite + sillimanite + quartz = garnet + cordierite + K-feldspar + melt	(Spl,V)
garnet + biotite + sillimanite = spinel + cordierite + K-feldspar + melt	(Qtz,V)
garnet + sillimanite = spinel + cordierite + quartz	(Bt,Kfs,L,V)
biotite + spinel + quartz = garnet + cordierite + K-feldspar + melt	(Sil,V)
biotite + sillimanite + quartz = spinel + cordierite + K-feldspar + melt	(Grt,V)

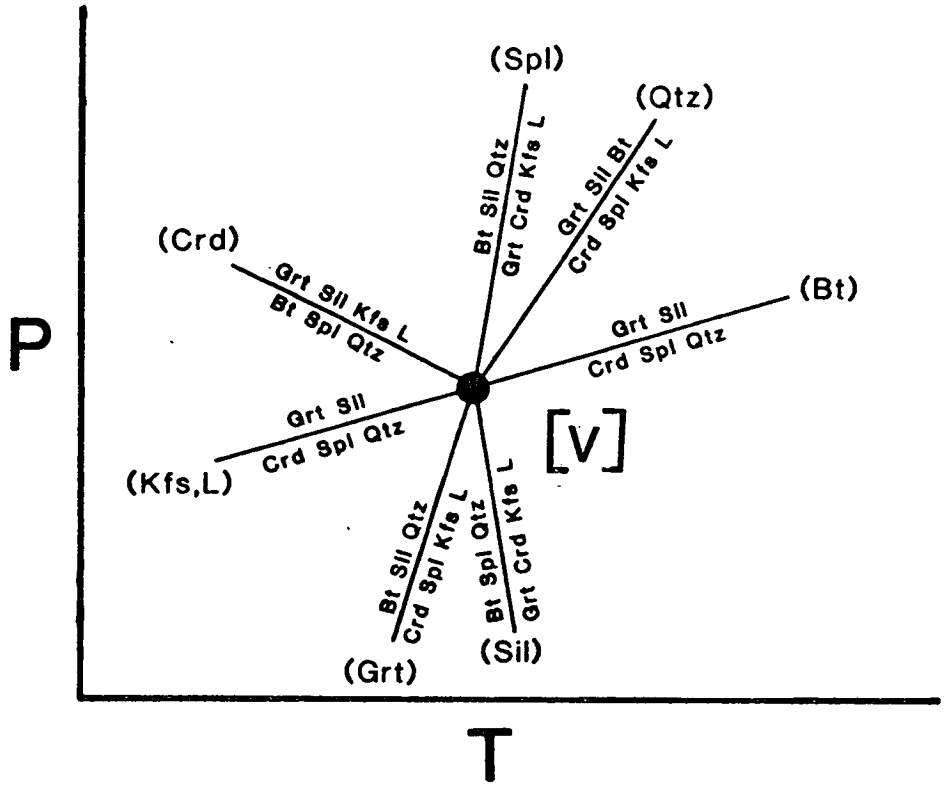

Fig. 6.10 Schematic KFMASH grid in *P-T* space depicting univariant reactions involving garnet, cordierite, biotite, spinel, sillimanite, quartz, K-feldspar and melt. All reactions are fluid-absent.

evidence. The effects of these reactions on the phase relationships are illustrated in Fig. 6.11 in terms of projections from sillimanite, K-feldspar and melt onto the SiO_2-FeO-MgO plane. This is the most suitable projection since sillimanite and K-feldspar occur in all pelitic assemblages (although K-feldspar is rare in the melanosome) and leucosome interpreted as former melt is also widespread.

6.4.3 A comparison with two multi-system grids

Two high-temperature fluid-absent grids, one for high f_{O2} and one for low f_{O2}, have been developed by Hensen (1986) for spinel-bearing assemblages. However, these

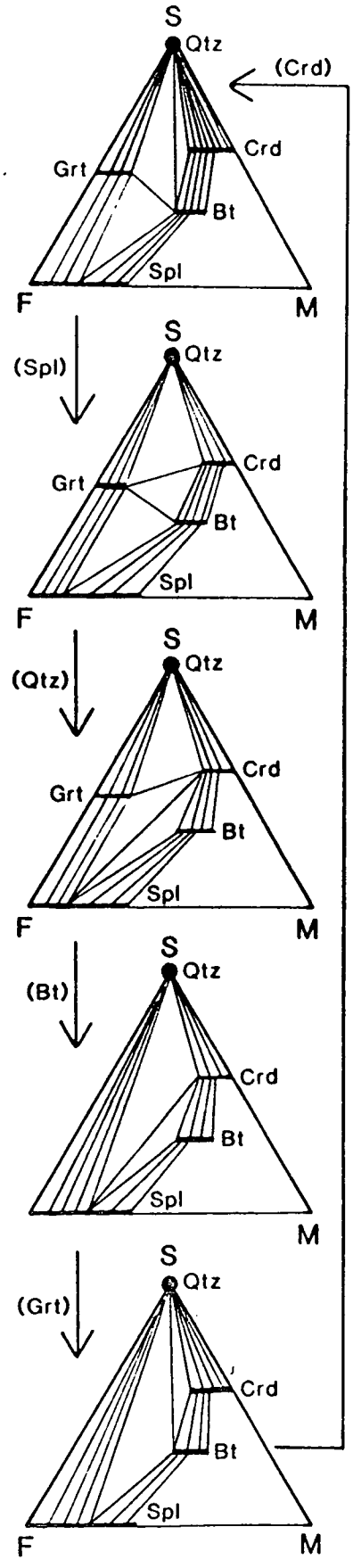

Fig. 6.11 SiO_2-FeO-MgO compatibility diagrams projected from sillimanite, K-feldspar and melt, illustrating the phase relationships associated with the reaction grid of Fig. 6.10. Annotated arrows refer to reactions in Fig. 6.10.

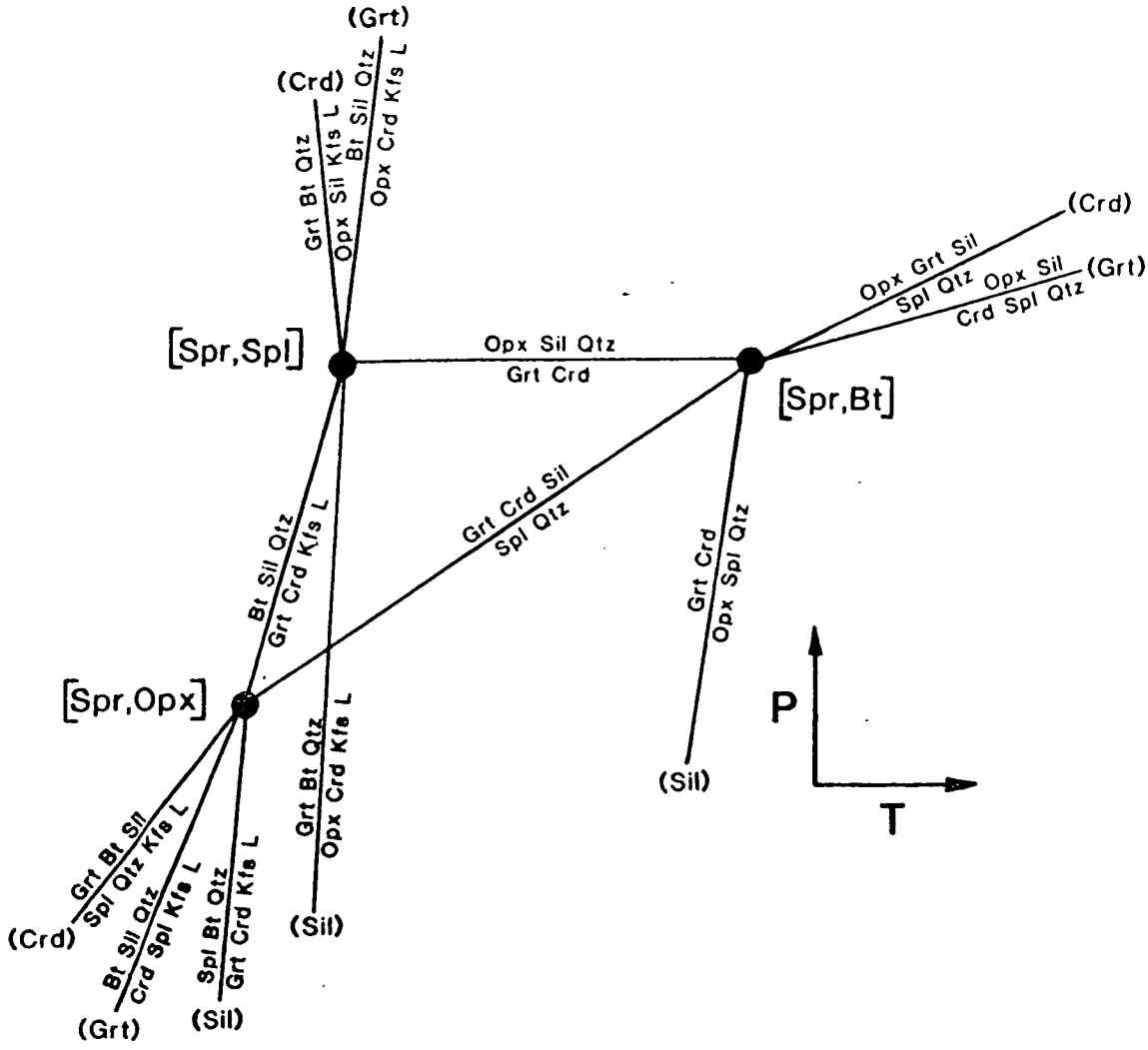

Fig. 6.12 KFMASH multi-system grid in *P-T* space for the phases garnet, cordierite, orthopyroxene, spinel, biotite and sillimanite, with quartz, K-feldspar and melt in excess. After Clarke *et al.* (1989) with X_{Mg}^{Spl} greater than X_{Mg}^{Grt}. All points and reactions are fluid absent.

were constructed for the FMAS system, and do not involve biotite. Fluid-absent, biotite-bearing KFMASH grids have been developed by Clarke *et al.* (1989) and Hensen and Harley (1990) for high-f_{O2} and low-f_{O2} conditions respectively (see Figs 6.12 and 6.13).

Clarke *et al.* (1989) derived a fluid-absent multi-system KFMASH grid by combination of part of the Grant (1985*a*,*b*) grid, involving biotite but not spinel, with part of the Hensen (1986) grid involving spinel but not biotite at high f_{O2}. This grid is depicted in Fig. 6.12. The [Spr, Opx, V] point in this grid is equivalent to the [V] point of Fig. 6.10 which did not consider orthopyroxene or sapphirine. The grid was constructed for assemblages from the Mawson coastline of East Antarctica using the assumption that X_{Mg}^{Spl} is greater than X_{Mg}^{Grt}. It is not clear why Clarke *et al.* (1989) made this assumption, since the mineral-chemical data reported in their paper indicate

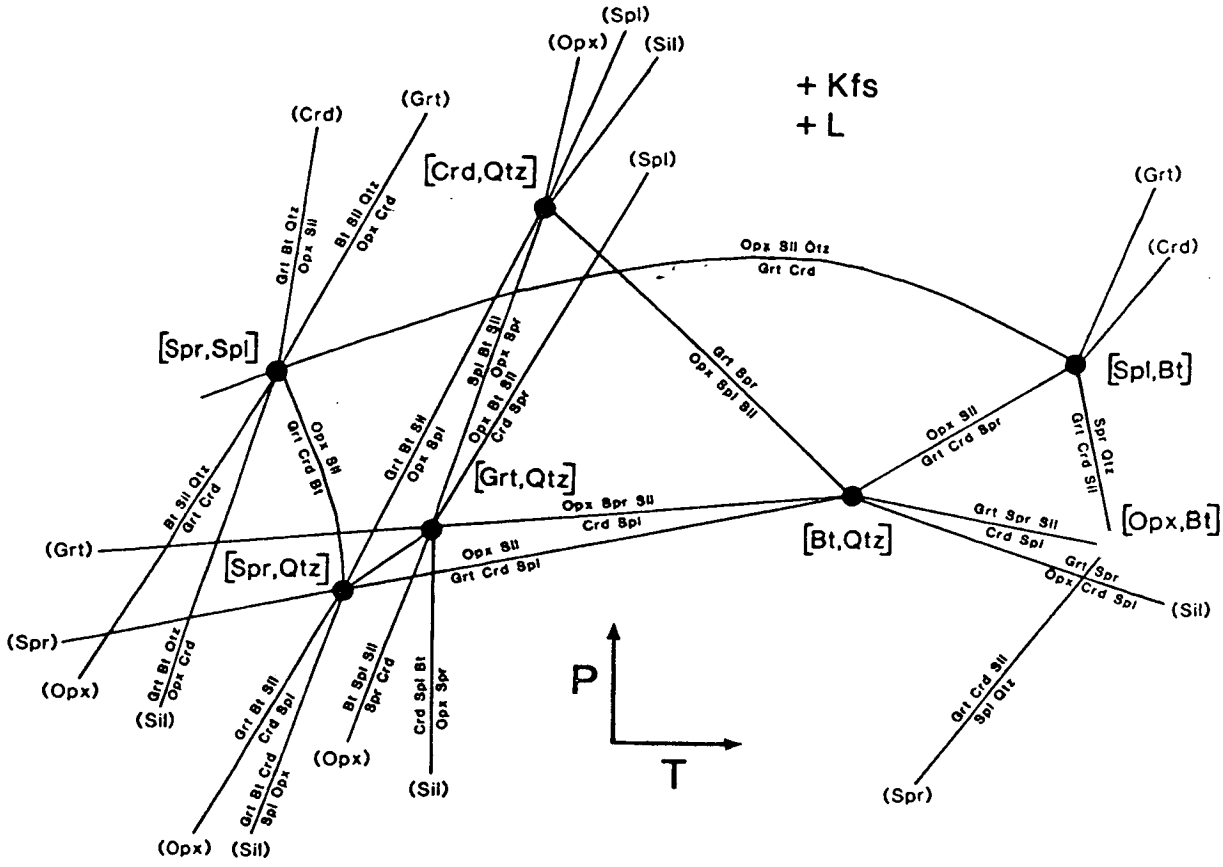

Fig. 6.13 KFMASH multi-system grid in *P-T* space for the phases garnet, cordierite, sapphirine, orthopyroxene, spinel, biotite, sillimanite and quartz, with K-feldspar and melt in excess. After Hensen and Harley (1990), with X_{Mg}^{Spl} greater than X_{Mg}^{Grt}. All points and reactions are fluid absent.

that spinel overlaps in composition with, or is more iron rich than, coexisting garnet, as is the case in this study. These compositional relationships invalidate the projection subsequently used by Clarke *et al.* (1989) to extend phase relationships into a TiO_2-Fe_2O_3-bearing KFMASHTO system. Clarke *et al.* (1989) projected all phases within the Al_2O_3-FeO-MgO compatibility diagram from garnet onto the line Al_2O_3-2FeO-MgO. As stated by Clarke *et al.* (1989), this projection is valid provided that 'the projection line lies between the projecting phase and all variable composition phases to be projected'. This is not the case if, as suggested by the analytical data from the Mawson coastline, spinel is more iron rich than coexisting garnet. However, subsequent versions of the KFMASHTO grid, applied to rocks from the Arunta Block of central Australia (Clarke *at al.*, 1990; Vernon *et al.*, 1990), avoid this problem by projecting from cordierite, which is the most magnesian phase in the pelitic assemblage. In fact, Clarke *et al.* (1990) and Vernon *et al.* (1990) noted that analytical data from their study areas in the Arunta Block indicate that X_{Mg}^{Spl} is less than X_{Mg}^{Grt}. Further use of the KFMASHTO grid by Clarke and Powell (1991*a*,*b*) has also assumed that spinel is more iron rich than garnet, and Clarke and Powell (1991*b*) have

recognized that their KFMASHTO grid is rather complex and not unequivocal. They nevertheless still use it to make inferences easily obtainable from relatively simple KFMASH grids.

Hensen and Harley (1990) extended the low-f_{O2} grid of Hensen (1986) to include biotite. This fluid-absent grid is depicted in Fig. 6.13. Since this grid also involves the phases sapphirine and orthopyroxene, the [V] point of Fig. 6.10 would be the [Spr, Opx, V] point in this grid. However, this point is not stable in the Hensen and Harley (1990) grid. The Hensen and Harley (1990) grid does, however, contain two of the crucial reactions that emanate from the [Spr, Opx, V] point: the (Spr, Opx, Spl, V) biotite-melting reaction and the (Spr, Opx, Bt, Kfs, L, V) degenerate spinel-bearing reaction. This grid, like that of Clarke *et al.* (1989), was constructed with X_{Mg}^{Spl} greater than X_{Mg}^{Grt}. As discussed above, analytical studies of granulite assemblages which equilibrated in the vicinity of the [Spr, Opx, V] point in the high-f_{O2} grid (e.g. Clarke *et al.*, 1989, 1990; Stüwe *et al.*, 1989*a*; Young *et al.*, 1989; Vernon *et al.*, 1990; Clarke & Powell, 1991*a*,*b*) suggest the opposite relationship. However, analysis of higher-grade sapphirine-bearing assemblages more relevant to the Hensen and Harley (1990) grid (e.g. Ellis *et al.*, 1980; Droop & Bucher-Nurminen, 1984; Harley, 1986; Waters, 1986; Lal *et al.*, 1987; Sandiford *et al.*, 1987; Droop, 1989; Harley *et al.*, 1990) indicate that X_{Mg}^{Spl} is greater than X_{Mg}^{Grt}. Given that the [Spr, Opx, V] point of Clarke *et al.* (1989) lies at significantly lower temperature and pressure than the sapphirine-present Hensen and Harley (1990) grid, the analytical data suggest that garnet and spinel have a compositional inversion somewhere between the [Spr, Opx, V] point of the high-f_{O2} grid (Clarke *et al.*, 1989) and the [Opx, Bt, V] point of the low-f_{O2} grid (Hensen & Harley, 1990). This can be depicted as a 'singular point' on the (Spr, Opx, Bt, Kfs, L, V) reaction in both the high-f_{O2} grid (Fig. 6.14) and the low-f_{O2} grid (Fig. 6.15). At this point, cordierite changes from one side of the reaction to the other. Singular points are not generated on the other reactions in these grids, such as (Opx, Spr, Spl, V) which occurs in both grids, and (Opx, Spr, Qtz, V) in the low-f_{O2} grid, since the chemographic relationships between the products and reactants of these reactions are not affected by an iron-magnesium inversion between garnet and spinel.

A similar explanation for the variable chemographic relationships between spinel and garnet in sapphirine-absent metapelites has recently been proposed by Sengupta *et al.* (1991), who suggested that metapelitic granulites from the Eastern Ghats, India, equilibrated at the singular point, such that X_{Mg}^{Spl} was equal to X_{Mg}^{Grt}. However, given that their assumed spinel composition is highly dependent on calculated contents of ferric iron, this equi-partitioning of iron and magnesium is not unequivocal. In contrast to the singular-point model developed above, Waters (1991) has suggested

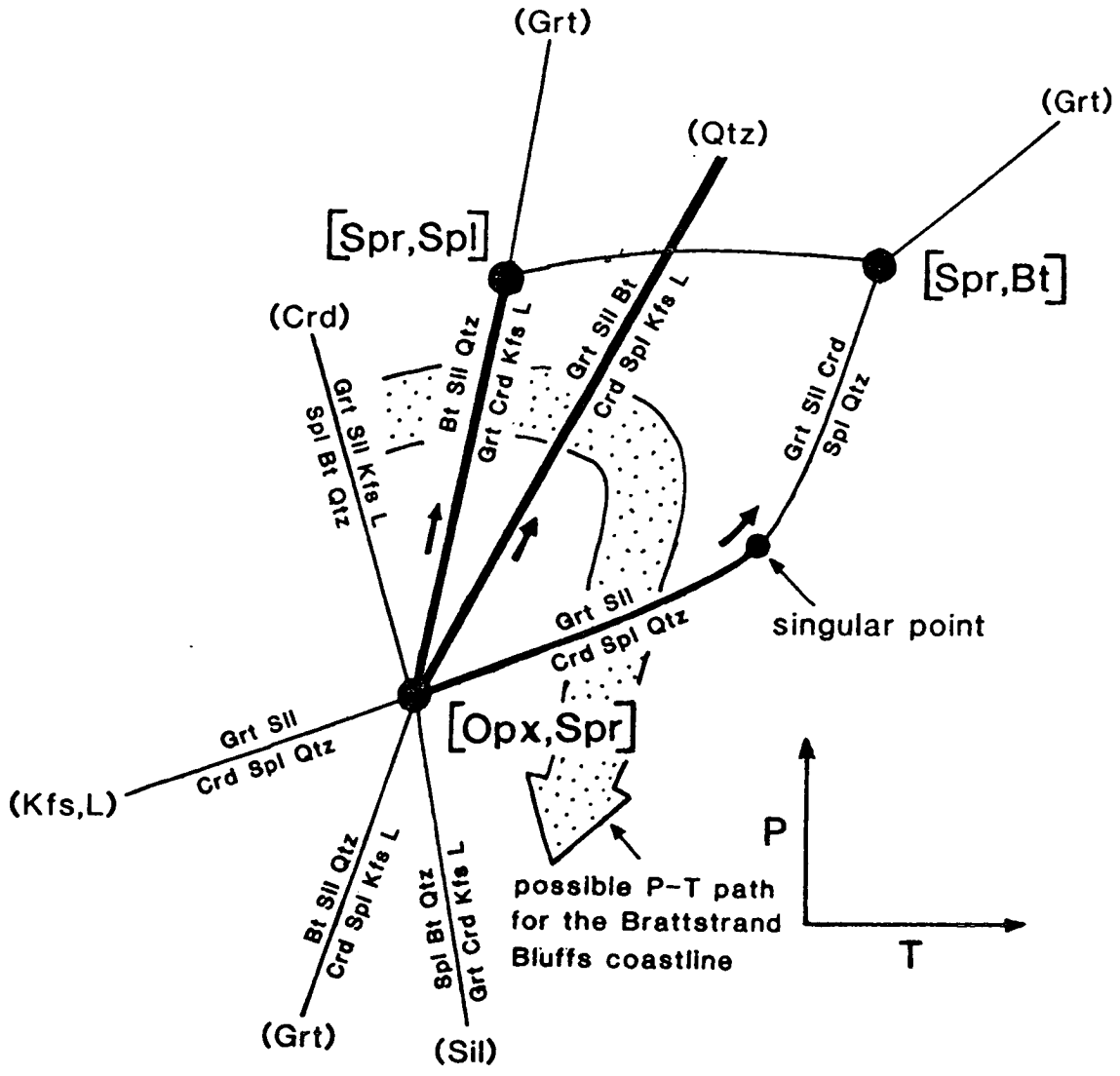

Fig. 6.14 Schematic high-f_{O2} KFMASH grid in *P-T* space adapted from Fig. 6.12 with a singular point marking a compositional inversion between garnet and spinel. Small arrows indicate the direction of increasing bulk X_{Mg} along univariant reactions. Heavy lines represent those reactions that are thought to have been intersected by the Brattstrand Bluffs metapelite. All points and reactions are fluid-absent.

that specimens which show X_{Mg}^{Grt} less than X_{Mg}^{Spl} could have suffered extensive retrograde reaction. This is certainly not the case for many pristine specimens from the Napier Complex (e.g. Ellis *et al.*, 1980).

Clearly the grids in Figs 6.14 and 6.15 are mutually exclusive and only one can apply to the Brattstrand Bluffs metapelite. The next section presents a model for the fluid-absent retrograde evolution of the metapelite, using the reactions emanating from the [Opx, Spr, V] point in the high f_{O2}-grid of Fig. 6.14. However, phase relationships attributed to fluid-absent retrogression in the Brattstrand Bluffs metapelite do not necessarily require the stability of this point and are equally

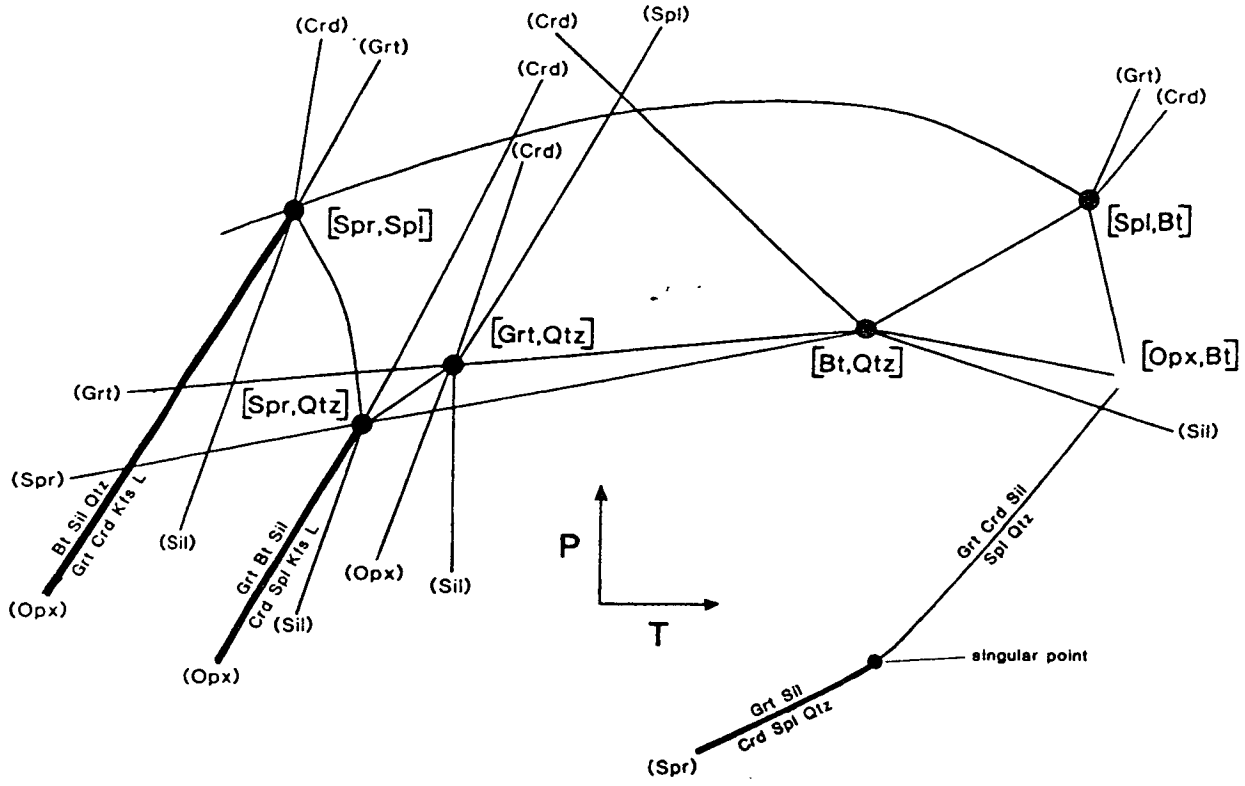

Fig. 6.15 Schematic low-f_{O2} KFMASH grid in *P-T* space, adapted from Fig. 6.13, depicting a singular point marking a compositional inversion between garnet and spinel. Heavy lines represent those reactions that are thought to have been intersected by the Brattstrand Bluffs metapelite. A similar *P-T* path to that depicted in Fig. 6.14 can be drawn crossing these reactions, despite the different topology of this grid. All points and reactions are fluid-absent.

applicable to the low-f_{O2} grid of Fig. 6.15. This is discussed further at the end of the next section. The relationship between the two grids, and further constraints on the stable topology for Brattstrand Bluffs assemblages, are discussed in Section 6.4.6.

6.4.4 A *P-T* model for the spinel symplectites and intergrowths

Fig. 6.14 can be used to interpret the textural evolution of the metapelite after fluid-absent conditions were attained during partial melting but before melt crystallization. The (Spr, Opx, Spl, V) reaction is the isobaric invariant (V) reaction discussed in Section 6.3, which produced garnet and cordierite in equilibrium with melt as the highest temperatures of metamorphism were attained. Further partial melting could have occurred in quartz-absent assemblages via the (Spr, Opx, Qtz, V) reaction

garnet + sillimanite + biotite = spinel + cordierite + K-feldspar + melt.

Some of the spinel-cordierite symplectite in melanosome units could reflect this reaction. The low abundance of K-feldspar makes it unlikely that this reaction proceeded to any great extent, although the amount of K-feldspar produced is highly dependent on the melt composition.

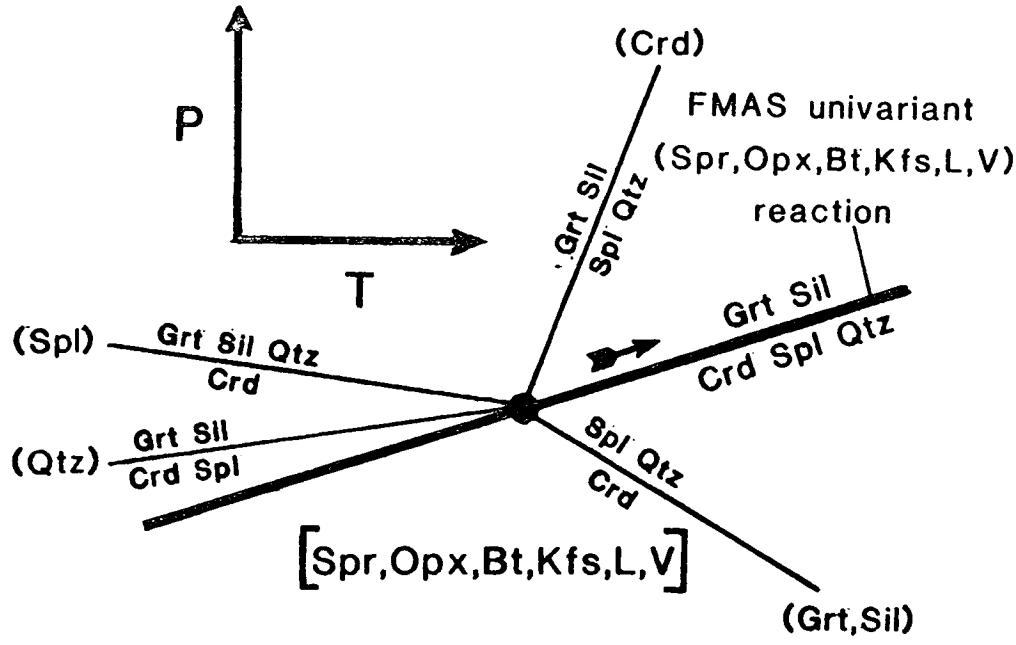

Fig. 6.16 A bundle of (F/M)AS univariant reactions (light lines) and the associated FMAS univariant reaction boundary (heavy line), involving the phases garnet, cordierite, spinel, sillimanite and quartz. The arrow represents the direction of increasing bulk X_{Mg}, and hence increasing X_{Mg} of the coexisting garnet, cordierite and spinel, along the FMAS univariant reaction boundary.

The spinel-cordierite, spinel-quartz and spinel-cordierite-quartz intergrowths after garnet-sillimanite can be interpreted in terms of the degenerate univariant (Spr, Opx, Bt, Kfs, L, V) reaction and its associated divariant reactions. The spinel-cordierite-quartz symplectites reflect progress of the univariant reaction itself

garnet + sillimanite = spinel + cordierite + quartz (Spr, Opx, Bt, Kfs, L, V),

and the cordierite-absent and quartz-absent textures can be related to the (Spr, Opx, Bt, Kfs, Crd, L, V) and (Spr, Opx, Bt, Kfs, Qtz, L, V) divariant reactions

garnet + sillimanite = spinel + quartz (Spr, Opx, Bt, Kfs, Crd, L, V) and
garnet + sillimanite = spinel + cordierite (Spr, Opx, Bt, Kfs, Qtz, L, V).

The disposition of these divariant reactions, and other closely-related divariant reactions, about the univariant (Spr, Opx, Bt, Kfs, L, V) reaction is depicted in Fig. 6.16 in terms of a bundle of (F/M)AS reactions centred on a [Spr, Opx, Bt, Kfs, L, V] (F/M)AS invariant point. This bundle of (F/M)AS reactions moves along the FMAS reaction to higher temperatures and pressures with increasing bulk X_{Mg}. Fig. 6.17 depicts three *P-T* pseudosections for quartz-bearing mesosome assemblages at different bulk compositions. All are drawn for temperatures lower than the singular point shown in Fig. 6.14, such that X_{Mg}^{Grt} is greater than X_{Mg}^{Spl}. All the observed textures are consistent with decompression, and the mineralogy of the texture is

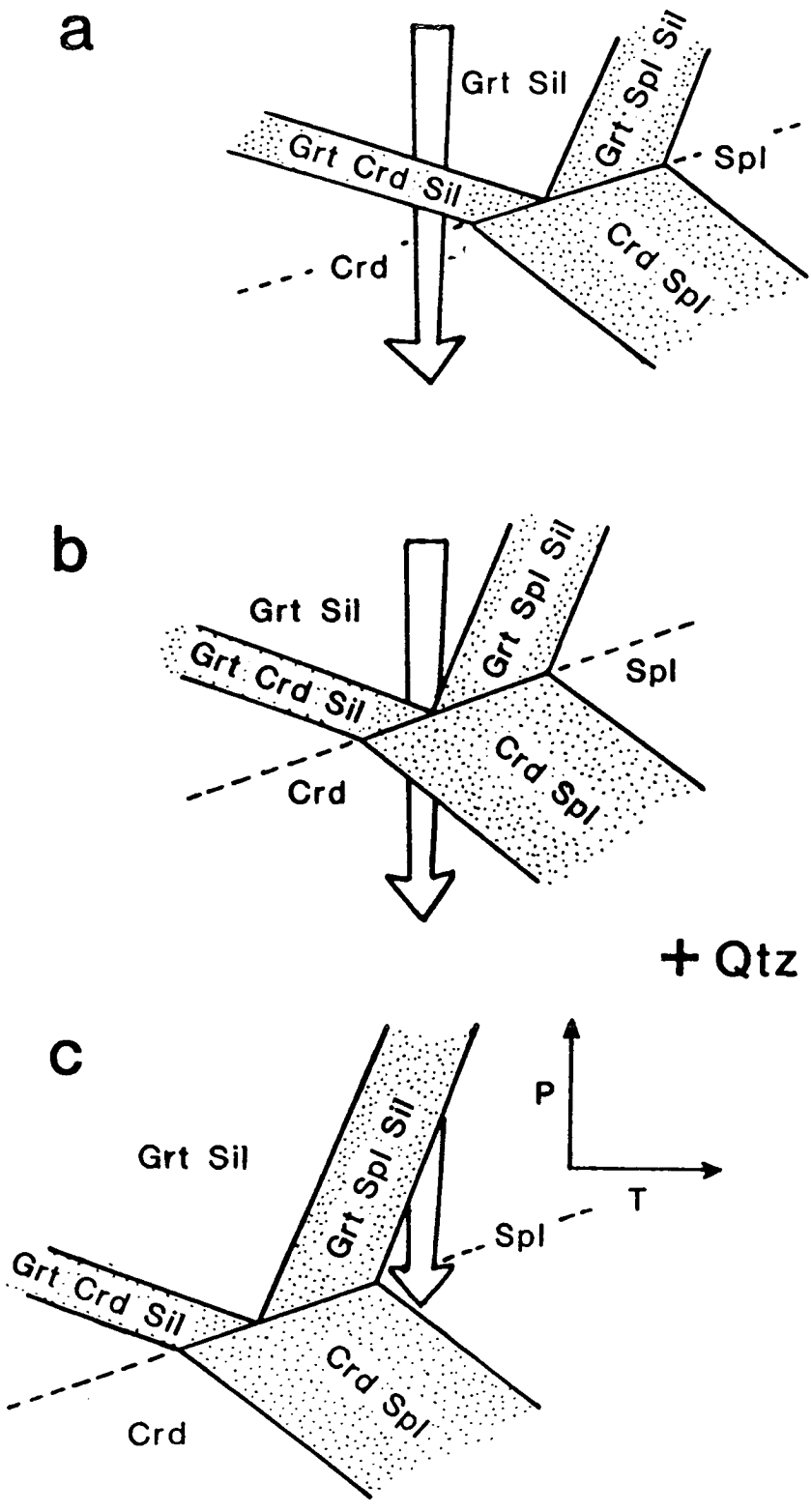

Fig. 6.17 *P-T* pseudosections for the FMAS system and the phases garnet, cordierite, spinel and sillimanite with quartz in excess, at (a) relatively high bulk X_{Mg}, (b) intermediate bulk X_{Mg} and (c) relatively low bulk X_{Mg}. Arrows indicate the different assemblages that can result from the same decompressional *P-T* path in the three different compositions.

dependent on local bulk composition. In some areas, the bulk composition is such that the KFMASH univariant reaction was intercepted and spinel-cordierite-quartz symplectite was formed. In other domains, the univariant reaction was not intercepted and the textures reflect the progress of divariant reactions. The univariant reactions at pressures less than the (Spr, Opx, Bt, Kfs, L, V) reaction in Fig. 6.14 all involve melt crystallization and the formation of biotite. The (Spr, Opx, Sil, V) reaction

garnet + cordierite + K-feldspar + melt = biotite + spinel + quartz

occurs on decompression with or without cooling, and the (Spr, Opx, Grt, V) reaction

spinel + cordierite + K-feldspar + melt = biotite + sillimanite + quartz

occurs on further cooling. The pre- to syn-S_4 biotite-sillimanite-spinel-quartz assemblage could reflect these crystallization reactions or related divariant equilibria. However, most biotite is concentrated in shear zones rather than around leucosome bodies, and biotite is thought to have formed by reaction of ferromagnesian phases with a hydrous volatile fluid, rather than a melt. Under these conditions, the fluid-absent *P-T* grid in Fig. 6.14 is invalid.

If the biotite-forming reactions were fluid- rather than melt-present, then there is no evidence for the stability of the (Spr, Opx, Sil, V) or (Spr, Opx, Grt, V) reactions, and hence the [Spr, Opx, V] invariant point in the fluid-absent grid (Fig. 6.14) need not be stable. In fact, the only reactions definitely intersected are also stable in the low-f_{O2} grid of Hensen and Harley (1990) depicted in Fig. 6.15. The only constraint, given the chemographic relationships, is that the metamorphic path must have crossed the (Spr, Opx, Bt, Kfs, L, V) reaction at temperatures below the inferred singular point. The potential stability of the [Spr, Opx, V] point is discussed in Section 6.4.6.

6.4.5 *P-T* and *T*-a_{H2O} grids for fluid-present sub-solidus conditions.

The phases to be considered in a sub-solidus grid are garnet, sillimanite, cordierite, spinel, biotite, quartz, K-feldspar and volatile fluid. Again these phases produce six univariant reactions about one invariant point in the KFMASH system, with one of these reactions being degenerate and stable on both sides of the invariant point. These univariant reactions are listed in Table 6.5, and are identical to the reactions in the fluid-absent melt-saturated grid (see Table 6.4), except that silicate melt is replaced by volatile fluid. The disposition of these reactions about the [L] invariant point, or [Spr, Opx, L] to give it its full title, in *P-T* space is depicted in Fig. 6.18. The reactions about the [Spr, Opx, L] point are directly analogous to those about the [Spr, Opx, V] point in Fig. 6.14, the only difference being that melt in the latter grid is replaced by fluid in the former causing the slopes of some of the reactions to change.

Table 6.5 Univariant reactions involving the phases garnet, sillimanite, cordierite, spinel, biotite, quartz, K-feldspar and H_2O in the KFMASH system.

biotite + spinel + quartz = garnet + sillimanite + K-feldspar + H_2O	(Crd,L)
biotite + sillimanite + quartz = garnet + cordierite + K-feldspar + H_2O	(Spl,L)
garnet + biotite + sillimanite = spinel + cordierite + K-feldspar + H_2O	(Qtz,L)
garnet + sillimanite = spinel + cordierite + quartz	(Bt,Kfs,V,L)
biotite + spinel + quartz = garnet + cordierite + K-feldspar + H_2O	(Sil,L)
biotite + sillimanite + quartz = spinel + cordierite + K-feldspar + H_2O	(Grt,L)

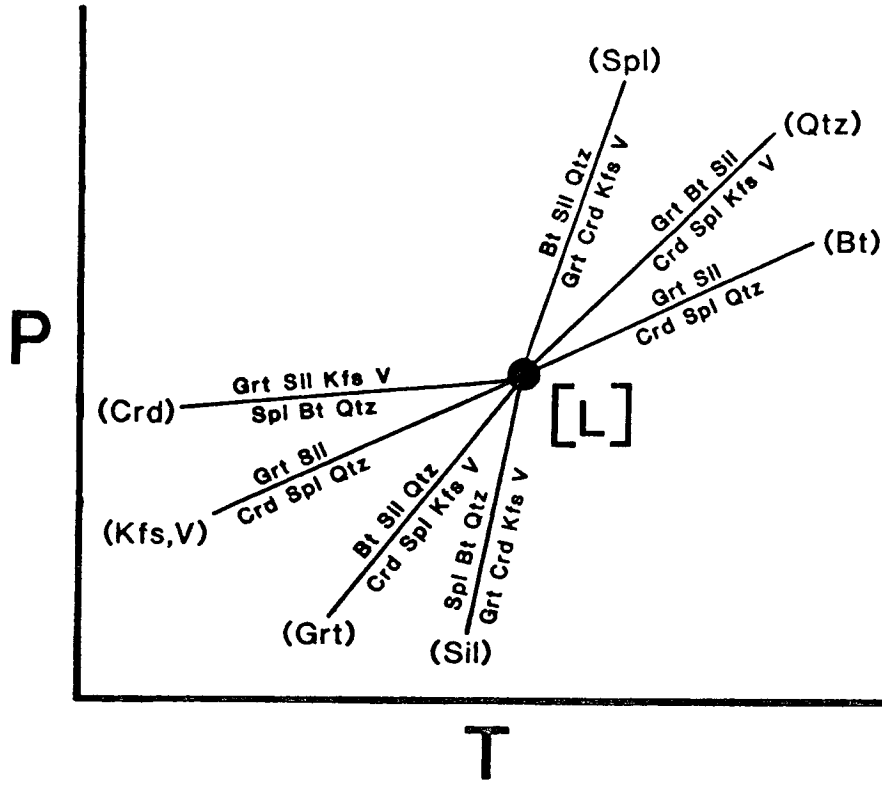

Fig. 6.18 A schematic KFMASH *P-T* grid for the phases garnet, cordierite, spinel, biotite, quartz, K-feldspar and volatile fluid at the [L], or [Spr, Opx, L], invariant point.

The [Spr, Opx, L] invariant point is located at lower pressure and temperature than the [Spr, Opx, V] point. In fact, the two points are joined by the (Spr, Opx, Bt, Kfs, L, V) reaction, which is common to both. A sub-solidus multi-system *P-T* grid for the phases garnet, sillimanite, cordierite, spinel, orthopyroxene, biotite, quartz, K-feldspar and hydrous fluid in the KFMASH system was presented by Grant and Frost (1990, fig. 12). This grid was constructed for the same chemographic relationships observed in the Brattstrand Bluffs coastline, and is reproduced in Fig. 6.19.

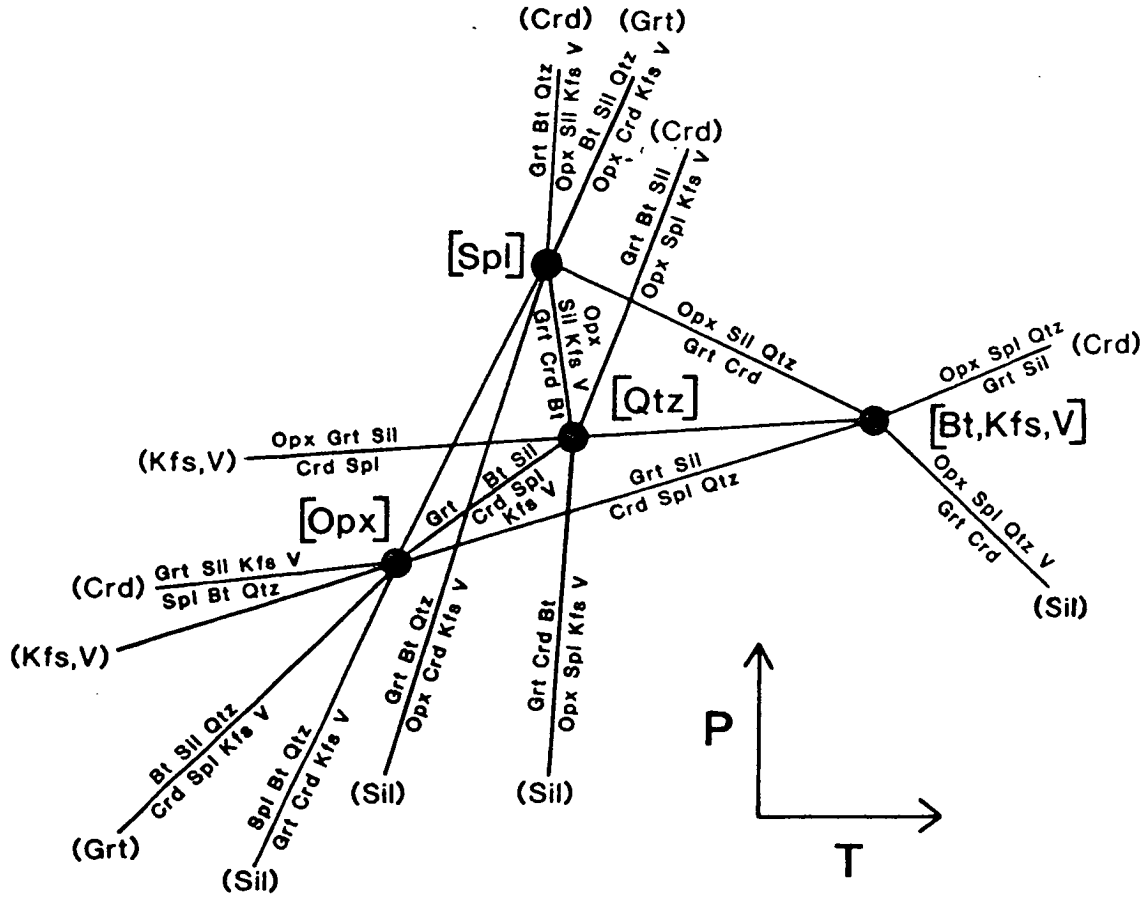

Fig. 6.19 A schematic multi-system *P-T* grid for the phases garnet, cordierite, orthopyroxene, spinel, biotite, quartz, K-feldspar and volatile fluid. Adapted from Grant and Frost (1990, fig. 12) with the additional assumption that cordierite is anhydrous. The unmarked reaction between [Opx] and [Spl] is the biotite-dehydration reaction: Bt + Sil + Qtz = Grt + Crd + Kfs + H_2O.

Given the importance of volatile fluids in the metamorphic evolution after melt crystallization, the [Spr, Opx, L] point has also been depicted in an isobaric T-a_{H2O} section (Fig. 6.20). Grant and Frost considered the [Spr, Opx, L] invariant point in a multi-system T-X_{H2O} grid (Grant & Frost, 1990, fig. 13). Although the relationships about the [Spr, Opx, L] point in this grid are identical to those in Fig. 6.20, the multi-system grid is not reproduced here since the rest of the grid contains melting reactions which are not applicable to the Brattstrand Bluffs pelite. In particular, the grid does not permit equilibria involving garnet, sillimanite and quartz above the solidus. This is because it was constructed for the metamorphic aureole of the Laramie anorthosite, which formed at pressures of about 3 kbar, and is incompatible with reaction textures in the Brattstrand Bluffs metapelite which developed at higher pressures.

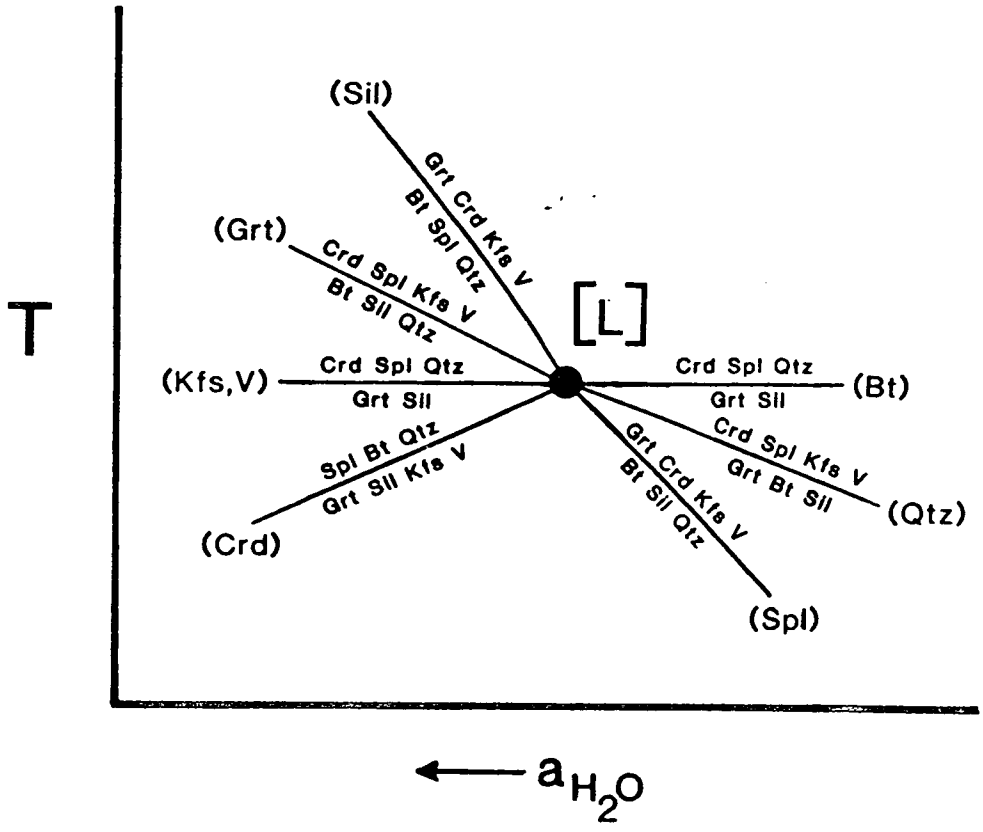

Fig. 6.20 A schematic isobaric T-a_{H2O} section for sub-solidus reactions involving the phases garnet, cordierite, spinel, biotite, sillimanite, quartz, K-feldspar and volatile fluid in the KFMASH system.

In these grids, pre- to syn-S_4 retrograde biotite growth is consistent with progress of univariant reactions including (Spr, Opx, Spl, L), (Spr, Opx, Qtz, L), (Spr, Opx, Grt, L) and (Spr, Opx, Sil, L):

K-feldspar + cordierite + garnet + H_2O = quartz + sillimanite + biotite,
K-feldspar + cordierite + spinel + H_2O = sillimanite + biotite + garnet,
K-feldspar + cordierite + spinel + H_2O = quartz + sillimanite + biotite, and
K-feldspar + cordierite + garnet + H_2O = quartz + biotite + spinel,

with a host of divariant alternatives depending on local bulk composition and assemblage. All of these reactions are consistent with cooling, water influx, or some combination of the two. Growth of garnet or sillimanite coronas around spinel is also consistent with the (Spr, Opx, Qtz, L) and (Spr, Opx, Grt, L) reactions, and with cooling or water influx, but these rather delicate structures are thought to post-date S_4 shear zone formation unlike coarse-grained matrix biotite aligned parallel to S_4. Similar coronas around spinel and ilmenite in granulites from the Mawson coastline (Clarke *et al.*, 1989) and the Arunta Block (Clarke *et al.*, 1990), comprising various

combinations of garnet, sillimanite and biotite, have been ascribed to cooling using more complex grids in the KFMASHTO system.

The cordierite coronas between spinel and quartz can be interpreted using the grid depicted in Fig. 6.16, and reflect progress of the divariant KFMASH reaction

spinel + quartz = cordierite (Spr, Opx, Bt, Kfs, Grt, Sil, L, V),

which is doubly degenerate and proceeds with cooling. The garnet and sillimanite coronas on spinel can be interpreted in terms of the KFMASH divariant reactions

spinel + quartz = garnet + sillimanite (Spr, Opx, Bt, Kfs, Crd, L, V) and
spinel + cordierite = garnet + sillimanite (Spr, Opx, Bt, Kfs, Qtz, L, V),

which, like the rehydration reactions invoked above for corona formation, proceed on cooling. These reactions (or rather the reverse reactions) were used in Section 6.4.4 to interpret reaction textures developed before melt crystallization, whereas here they are used to interpret textures attributed to sub-solidus reaction at lower temperature and pressure. These reactions only occur over a limited *P-T* range for a system of fixed bulk composition, but the occurrence of these reactions at different conditions can be readily explained in terms of 'equilibration volume'. Spinel-cordierite and spinel-quartz symplectites and intergrowths were developed during decompression as a result of mineral re-equilibration on a millimetre scale, and hence formed at *P-T* conditions relevant to a composition approaching the bulk composition of the rock specimen. The fine-scale corona textures formed via the reverse reactions on cooling at lower pressures and clearly represent a much smaller volume of re-equilibration. Hence the reactions occurred at conditions determined by the bulk composition on a sub-millimetre scale, which was different from the hand-specimen bulk composition. Given that the coronas occur around spinel, the relevant bulk composition for corona formation was more iron rich than the bulk composition of the rock, and hence the reactions were intersected at lower temperatures and pressures than they were during the high-grade decompression. The small equilibration volume during retrograde cooling also explains why garnet-absent and quartz-absent rehydration reactions were able to proceed in quartz- and garnet-bearing metapelite: the retrograde reactions operated within small-scale local domains where garnet or quartz were in fact absent.

The presence of garnet, sillimanite and biotite coronas around spinel in quartz-bearing rock requires that the [Spr, Opx, L] point was stable under the conditions of the Brattstrand Bluffs metapelite. However, like the [Spr, Opx, V] point (see Sections 6.4.3 and 6.4.4), the [Spr, Opx, L] point is thought to be stable only under certain conditions.

6.4.6 The stability of the [Spr, Opx, V] and [Spr, Opx, L] invariant points

The stability of spinel-quartz-biotite assemblages under fluid-present sub-solidus conditions, and fluid-absent melt-present conditions, requires the stability of the [Spr, Opx, L] and [Spr, Opx, V] points respectively. The degenerate KFMASH univariant (Spr, L, Opx, Bt, Kfs, V) reaction

garnet + sillimanite = spinel + cordierite + quartz,

is common to both points, and must intersect with the (Spr, L, Spl, Opx) reaction

biotite + sillimanite + quartz = garnet + cordierite + K-feldspar + fluid,

for the [Spr, Opx, L] point to be stable, and the analogous (Spr, Spl, Opx, V) reaction

sillimanite + biotite + quartz = garnet + cordierite + K-feldspar + melt,

for the [Spr, Opx, V] point to be stable. These intersections are mutually exclusive, are neither are thought to be stable in the simple KFMASH system.

The sub-solidus case has been considered by Grant (1985*b*), Montel *et al.* (1986) and Grant and Frost (1990). Grant (1985*b*, figs 3.4 and 3.5) and Grant and Frost (1990, figs 10 and 11) presented two grids, one depicting sub-solidus univariant equilibria in KFMASH and KFASH for spinel-absent assemblages, and the other for sub-solidus univariant equilibria in FMASH and FASH for biotite-absent assemblages. These two grids can be combined to produce the KFMASH grid in Fig. 6.21. This diagram has been constructed for anhydrous cordierite in keeping with the other grids in this chapter, which changes the FMASH and FASH reactions and points in the biotite-absent part of the grid into FMAS and FAS reactions and points. In this grid, the (Spr, L, Spl, Opx) and (Spr, L, Opx, Bt, Kfs, V) reactions are terminated by reactions in KFASH and FAS and do not intersect, reflecting experimental studies of the pertinent equilibria (Holdaway & Lee, 1977; Bohlen & Dollase, 1983). For these reactions to intersect, either the stability field of spinel has to expand, causing the [Spr, L, Opx, Bt, Kfs, V] FAS point to migrate towards the [Spr, L, Spl, Opx] KFASH point, or the stability field of biotite has to expand, causing the [Spr, L, Spl, Opx] KFASH point to migrate towards the [Spr, L, Opx, Bt, Kfs V] FAS point. Of course, some combination of both these effects has the same result.

Similar comments have been made concerning the stability of the [Spr, Opx, V] point in the fluid-absent KFMASH grid. In particular, Hensen and Harley (1990, fig. 2.17) have shown how translation of the (Spr, L, Opx, Bt, Kfs, V) reaction to lower temperatures causes it to intersect with the (Spr, Spl, Opx, V) biotite-melting reaction, thus stabilizing the [Spr, Opx, V] point. In addition to stabilizing the [Spr, Opx, V] point, translation of the (Spr, L, Opx, Bt, Kfs, V) reaction to lower temperatures

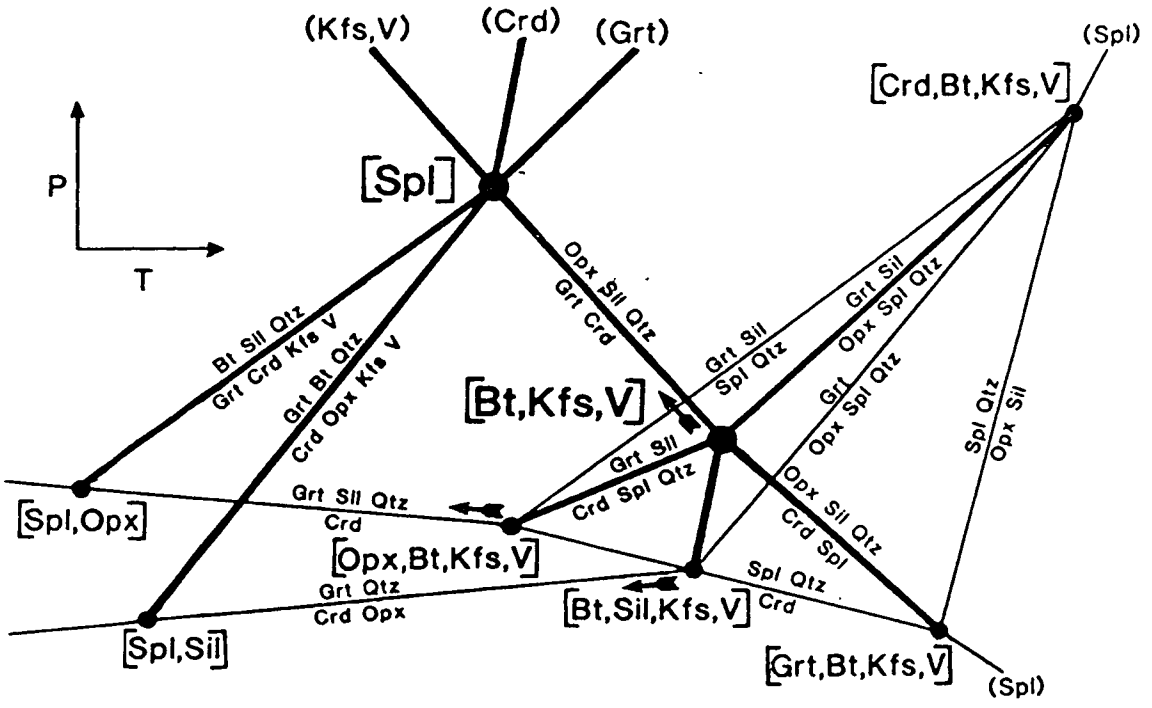

Fig. 6.21 A schematic multi-system *P-T* grid for the phases orthopyroxene, garnet, cordierite, spinel, biotite, sillimanite, K-feldspar and fluid, with quartz in excess. Heavy lines are KFMASH univariant reactions and the light lines are FAS univariant reactions. Arrows indicate the direction of movement of invariant points with increasing spinel stability. This grid has been adapted from Grant (1985*b*) with the additional restriction that cordierite is anhydrous. All assemblages are melt and sapphirine absent.

causes the [Opx, Bt, V], [Spl, Bt, V] and [Qtz, Bt, V] points to become unstable, and stabilizes the [Spr, Bt, V] point, in a manner analogous to the inversion of the FMAS grid described by Hensen (1986). This process is depicted in Fig. 6.22. The end product is identical to the grid of Clarke *et al.* (1989) shown in Fig. 6.12. As for the sub-solidus case, this transformation requires an increase in the stability fields of spinel, or biotite, or both. As discussed in Section 6.4.3, a singular point reflecting an iron-magnesium inversion between garnet and spinel should be superimposed onto the grid in Fig. 6.22 if it is to agree with analytical studies.

Given the steep slopes of the biotite-dehydration and biotite-melting reactions, and the shallow slope of the (Spr, L, Opx, Bt, Kfs, V) reaction which extends across melting and dehydration reactions, only one of the [Spr, Opx, L] and [Spr, Opx, V] points can be stable in a *P-T* grid for a fixed chemical system. Since the metapelite discussed here preserves evidence for the stability of the sub-solidus [Spr, Opx, L] point, it is assumed that the [Spr, Opx, V] point is not stable (this relationship is depicted in Fig. 6.24).

The stability of spinel-quartz-biotite-sillimanite assemblages has generally been explained in terms of various additional chemical components in spinel. Grant (1985*a*,*b*) suggested that a 5 to 10 mole per cent magnetite component in spinel could

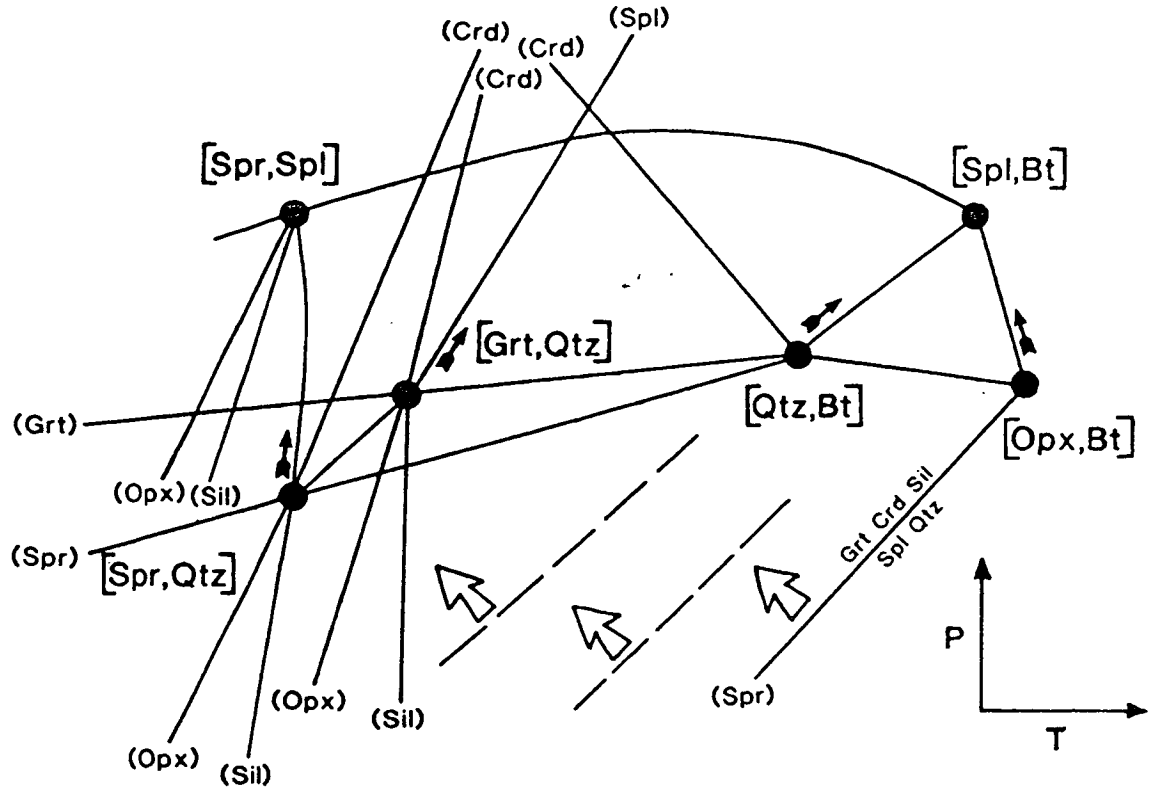

Fig. 6.22 A schematic KFMASH multi-system *P-T* grid (from Fig. 6.13) for the phases garnet, cordierite, sapphirine, orthopyroxene, spinel, biotite, sillimanite and quartz, with K-feldspar and melt in excess, illustrating the effect of increasing spinel stability. The small arrows indicate the direction of movement of the invariant points with increasing spinel stability (along the spinel-absent reactions). [Spl,Bt] and [Spr,Spl] do not migrate since they do not involve spinel. The large arrows indicate the effect that this has on the position of the (Spr, Opx, Bt, Kfs, L, V) reaction. If the invariant points migrate sufficiently, the topology becomes unstable and the three biotite-absent invariant points are replaced by [Spr, Bt] and the grid becomes identical to Fig. 6.12. All assemblages are fluid-absent.

account for the stability of quartz-spinel with biotite-sillimanite-quartz in the Laramie aureole. This indicates addition of ferric iron to the system, reflecting a high f_{O2}. An increase in f_{O2} was also used by Hensen and Harley (1990) to explain the existence of spinel and quartz in the biotite melting interval and the stabilization of [Spr, Opx, V]. Montel *et al.* (1986) attributed the stability of similar assemblages, both under sub-solidus conditions and in melting reactions, to high zinc contents in spinel. Chromium could likewise be expected to enhance spinel stability.

In this case, none of the above effects is likely to be large. The zinc contents of spinel are low, and chromium contents even lower. Accurate calculation of f_{O2} via established oxide-oxide equilibria is not possible for these rocks, given that ilmenite and hercynitic spinel are the only oxide phases present. However, the stability of graphite places a maximum constraint on f_{O2}, and the ilmenite-magnetite oxygen barometer (Buddington & Lindsley, 1964; Anderson & Lindsley, 1988) can be used to derive an approximate maximum f_{O2} value for the most oxidized specimens. The

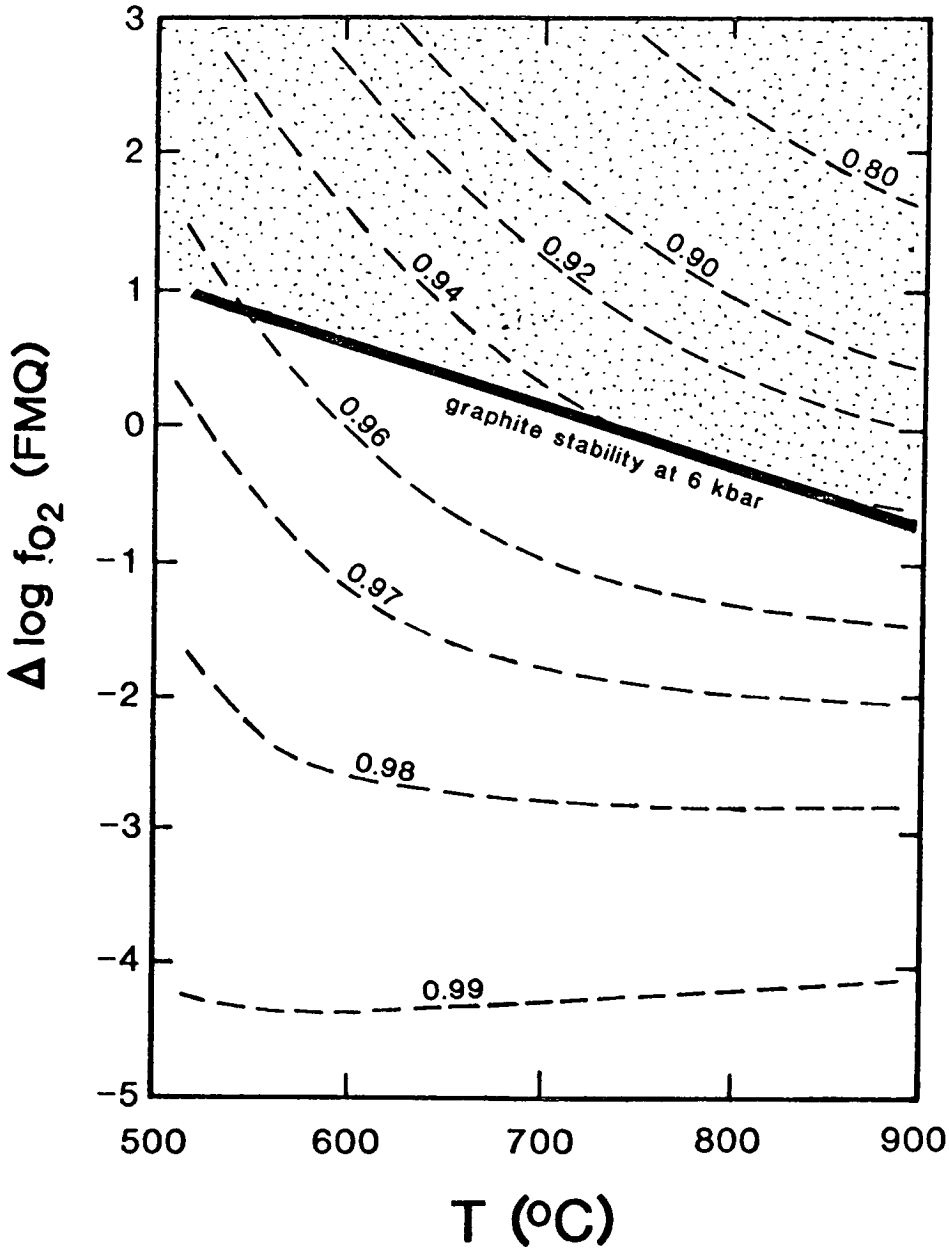

Fig. 6.23 A graph of $\Delta \log f_{O2}$ (FMQ) versus temperature for the ilmenite-composition isopleths of Anderson and Lindsley (1988) in equilibrium with magnetite. $\Delta \log f_{O2}$ (FMQ) is the difference in f_{O2} with respect to the fayalite-magnetite-quartz buffer, and the numbers beside each isopleth refer to values of X_{ilm}. Also plotted is the stability limit of graphite at 6 kbar, taken from Lamb and Valley (1985). The stippled area is outside the stability field of graphite.

magnetite component, which is contained in spinel, is so dilute that its amount is meaningless, but its presence means that the composition of the ilmenite ($X_{ilm} = 0.96$) constrains a maximum f_{O2} value. These constraints are depicted in Fig. 6.23 and indicate that f_{O2} is less than the fayalite-magnetite-quartz buffer for temperatures greater than 700°C.

Each of the effects discussed above have little individual effect on spinel stability, but the combined effect might be significant. The possibility of increased biotite stability should also be considered, particularly given the high titanium and

fluorine contents of biotite in the Brattstrand Bluffs metapelite. However, even if the spinel-quartz and biotite-sillimanite fields theoretically intersect in the absence of melt, the [Spr, Opx, L] point is in fact metastable with respect to melting reactions if a_{H2O} equals unity (Holdaway & Lee, 1977; Grant, 1985*a*,*b*; Grant & Frost, 1990). Hence spinel-quartz-biotite-sillimanite assemblages are only stable under reduced a_{H2O}. This is not a problem in the Brattstrand Bluffs coastline however, given the evidence for a carbonic component in the fluid phase.

6.5 SUMMARY OF THE *P-T*-FLUID EVOLUTION

6.5.1 Summary of the qualitative *P-T*-fluid evolution

The textural development of the metapelite reflects the following evolution:

(i) the instability of garnet-biotite-sillimanite with respect to garnet-sillimanite-melt during prograde heating;

(ii) the instability of garnet-sillimanite with respect to spinel-bearing assemblages on retrograde decompression; and

(iii) the instability of spinel-bearing assemblages with respect to biotite-garnet-sillimanite on subsequent cooling and release of hydrous fluids on melt crystallization.

The crucial univariant equilibria in this evolution have positive slopes in *P-T* space, and the circular nature of this evolution indicates that heating followed by decompression and cooling can return to the stability field of the initial assemblage.

It has been shown that the fluid evolution is also important. The metapelite was initially in equilibrium with a hydrous volatile fluid phase (with a small but significant carbonic component). The volatile components of the biotite and the fluid phase were lost into silicate melt to produce fluid-absent conditions at the metamorphic peak. These volatile species were liberated as a fluid on melt crystallization, but caused little back reaction. Retrograde biotite was developed along ductile shear zones interpreted as fluid pathways, but, even along these shear zones, back reaction was only partial and cordierite and spinel still occur. This implies that a large volume of volatile fluid escaped along the shear zones without reacting with anhydrous solid phases. The rest of this section discusses further evidence of the fluid history provided by fluorine contents in biotite and the stability of graphite, and uses thermobarometry to impose some quantitative constraints on the retrograde evolution.

6.5.2 Fluorine in biotite and implications for the metamorphic fluid

Both pre-melting and syn-S_4 matrix biotite is particularly fluorine-rich. This is not unusual for granulite-facies biotite (e.g. Guidotti, 1984, pp. 427-430) which

accommodates the fluorine released on breakdown of lower-grade phases such as muscovite. Fluorine partitions preferentially into biotite over volatile fluid by several orders of magnitude (e.g. Munoz & Ludington, 1974; Valley *et al.*, 1982), and into silicate melt over fluid by a much smaller factor unless fluorine contents are particularly high (Webster, 1990). Hence fluorine partitions into biotite over both fluid and melt by a large degree, and as biotite becomes unstable with respect to dehydration and melting reactions at high grade and decreases in modal abundance, remaining biotite becomes progressively more fluorine rich. Similarly, the first biotite to form on crystallization of a fluorine-bearing melt, or reaction of fluorine-rich fluid, is more fluorine rich than biotite formed as these processes near completion.

In those specimens with both pre-melting biotite inclusions in garnet and post-melting S_4 matrix biotite, it seems that the latter has consistently greater fluorine contents (see Section 6.2.6). This has interesting implications if it is assumed that the metapelite was a closed chemical system during the dehydration and melting interval described in Section 6.3. Before melting, only a very small fraction of the fluorine content now held by matrix biotite was in a volatile fluid phase: virtually all of it was accommodated within an early generation of biotite which is now only preserved as inclusions within garnet. At the metamorphic peak, after the consumption of the free fluid phase and the biotite, this fluorine was all dissolved in silicate melt. On melt crystallization, the fluorine was concentrated into matrix biotite. The high fluorine content of matrix biotite relative to that of the inclusion biotite implies that water must have been lost from the system so that the fluorine, which is all scavenged by the biotite, is not as diluted by water as it was before melting. Given that the matrix biotite is concentrated in S_4 shear zones, and not related to leucosome bodies, it is unlikely that biotite-producing reactions involving melt directly as a reactant were responsible for the bulk of matrix biotite growth. It is more likely that melt-derived fluids, transported along shear zones, reacted to form biotite. These fluids escaped from the area, removing a large proportion of the original water content of the metapelite from the system, presumably to higher levels of the crust, but leaving most of their fluorine content behind in biotite. The high fluorine content of the biotite imposes little useful constraint on fluorine in the fluid. Given the extreme partitioning of fluorine into biotite, relatively high fluorine contents in biotite can be readily accounted for by the typical fluorine content of shales (Valley *et al.*, 1982).

6.5.3 Graphite and implications for the metamorphic fluid

The ubiquitous presence of graphite, particularly concentrated in leucosome units, requires that any coexisting fluid phase contained some carbon component (e.g. Ohmoto & Kerrick, 1977). The abundances of the principal C-O-H fluid species can

be determined for a given temperature and pressure, if one variable such as f_{O2} is known. Accurate calculation of f_{O2} is not possible in these rocks (see Section 6.4.6), but the stability of graphite does constrain the extent of CO_2 infiltration in the area. CO_2 influx causes precipitation of graphite provided that f_{O2} remains below the maximum stability of graphite (Glassley, 1982; Lamb & Valley, 1984, 1985). Above this limit, all graphite is unstable. Hence the modal abundance of graphite can be used to estimate a maximum possible amount of CO_2 infiltration, provided that graphite is present in the rocks. This figure is only a maximum however, since graphite can also be of pre-metamorphic biogenic origin. Although locally in excess of 2 modal per cent, graphite abundance in the Brattstrand Bluffs metapelite is generally low, perhaps 0.1 modal per cent. This precludes large-scale CO_2 influx (Lamb & Valley, 1984, 1985). In addition, preliminary stable-isotopic data from the Brattstrand Bluffs (D.P. Mattey, unpublished data) indicate a biogenic origin for much of the graphite ($\delta^{13}C$ values varying between -15 and -25 per mil). The concentration of graphite within leucosome units indicates that f_{O2} was low during melt crystallization, and that the CO_2 content of the melt precipitated as graphite as it was released. Hence, in contrast to the H_2O content of the metapelite, much of which escaped to higher crustal levels during retrograde evolution, the CO_2 content was trapped within, or near to, the recrystallized melt.

6.5.4 Quantitative constraints on the metamorphic fluid

The petrological models developed above imply that water activity decreased during prograde metamorphism and melting of the metapelitic lithologies. Quantitative estimates of a_{H2O} are commonly made using low-variance mineral assemblages containing hydrous phases such as hornblende or biotite. These assemblages buffer a_{H2O} to a fixed value at a given pressure and temperature. One such equilibrium is

$$\text{biotite} + \text{sillimanite} + \text{quartz} = \text{garnet} + \text{K-feldspar} + H_2O$$

(Phillips, 1980; Powers & Bohlen, 1985; Bhattacharya & Sen, 1986; Edwards & Essene, 1988). All of these phases occur in the metapelite, although the biotite is either of early prograde origin (i.e. inclusions within garnet) or late retrograde origin (i.e. syn-S_4 biotite) and it is difficult, perhaps impossible, to demonstrate that these phases represent a single equilibrium assemblage. Despite the textural ambiguities, values of a_{H2O} have been calculated for nine of the metapelite specimens using typical compositions of biotite, garnet and K-feldspar (tabulated in Appendix 3.5) and the solution models outlined in Table 6.6. Values of a_{H2O} were calculated from the calibration curves of Edwards and Essene (1988) for the above reaction, using an equilibrium constant of 3.0, which is relevant to the metamorphic conditions of about

Table 6.6 Estimates of a_{H2O} in metapelite assemblages using the biotite-sillimanite-quartz-garnet-K-feldspar-H_2O equilibrium, as calibrated by Edwards & Essene (1988).

	biotite				Kfs			Grt			H_2O
	X_K	$X_{Fe^{vi}}$	X_{OH}	a_{ann}	X_{ab}	X_{or}	a_{or}	X_{alm}	X_{grs}	a_{alm}	a_{H2O}
88/14B	0.97	0.23	0.54	0.0035	0.31	0.66	0.71	0.76	0.02	0.54	0.027
88/44	0.98	0.32	0.86	0.0238	0.19	0.78	0.80	0.76	0.03	0.54	0.165
88/51	0.95	0.29	0.22	0.0012	0.34	0.53	0.59	0.85	0.02	0.66	0.009
88/56	0.97	0.26	0.41	0.0027	0.28	0.67	0.70	0.72	0.02	0.51	0.023
88/62	0.95	0.31	0.34	0.0034	0.33	0.62	0.68	0.84	0.02	0.65	0.023
88/102	0.95	0.33	0.49	0.0084	0.16	0.82	0.83	0.76	0.02	0.54	0.056
88/110	0.96	0.34	0.47	0.0084	0.30	0.70	0.74	0.77	0.03	0.54	0.063
88/153C	0.97	0.33	0.57	0.0109	0.36	0.65	0.76	0.76	0.03	0.53	0.087
88/273	0.91	0.23	0.49	0.0025	0.20	0.76	0.78	0.75	0.02	0.54	0.018

The values of a_{H2O} were all calculated for $K = 3.0$, where K is the equilibrium constant for the reaction $KFe_3Si_3AlO_{10}(OH)_2 + Al_2SiO_5 + 2SiO_2 = Fe_3Al_2Si_3O_{12} + KAlSi_3O_8 + H_2O$ and equal to ($a_{or}\ a_{alm}\ a_{H2O}$) / a_{ann}. Values of a_{alm} are calculated using the mixing model of Perkins and Chipera (1985), a_{or} is calculated using the activity model of Haselton *et al.* (1983) which is summarized in Appendix 4.3, and a_{ann} is taken as the product of X_K, $(X_{Fe^{vi}})^3$ and $(X_{OH})^2$ (i.e. for a biotite formula normalized to a total of seven cations in the octahedral and tetrahedral sites). N.b. For consistency with the calculations in Edwards and Essene (1988), these calculations were performed using a formula unit of biotite which is half the size of the formula unit used for this phase elsewhere in this thesis. The mineral analyses from which the activities are calculated are tabulated in Appendix 3.5, and compositional parameters are as defined in Appendix 3.3.

6 kbar and 860°C. Calculated values of a_{H2O} are summarized in Table 6.6, and are mostly less than 0.1. Although these values cannot be quoted with certainty, given the apparent lack of textural equilibrium, the small magnitude of the values does confirm that a_{H2O} was low during the Proterozoic metamorphism.

6.5.5 Quantitative constraints on the *P-T* history

A number of *P-T* constraints can be applied to the grids using experimental and natural-rock evidence, and thermobarometry. These constraints are illustrated in Fig. 6.24, which is a schematic grid comprising a few of the pertinent KFMASH univariant reactions and invariant points discussed in previous sections. These reactions and points are tentatively positioned in *P-T* space to be consistent with specimens from the Brattstrand Bluffs coastline. This grid comprises the [Spr, Opx, Spl] and [Spr, Opx, L] invariant points. The metastable [Spr, Opx, V] point (discussed in Section 6.4.6) has also been depicted at temperatures below the solidus. This figure combines all the quantitative *P-T* information described in this and the following two sections.

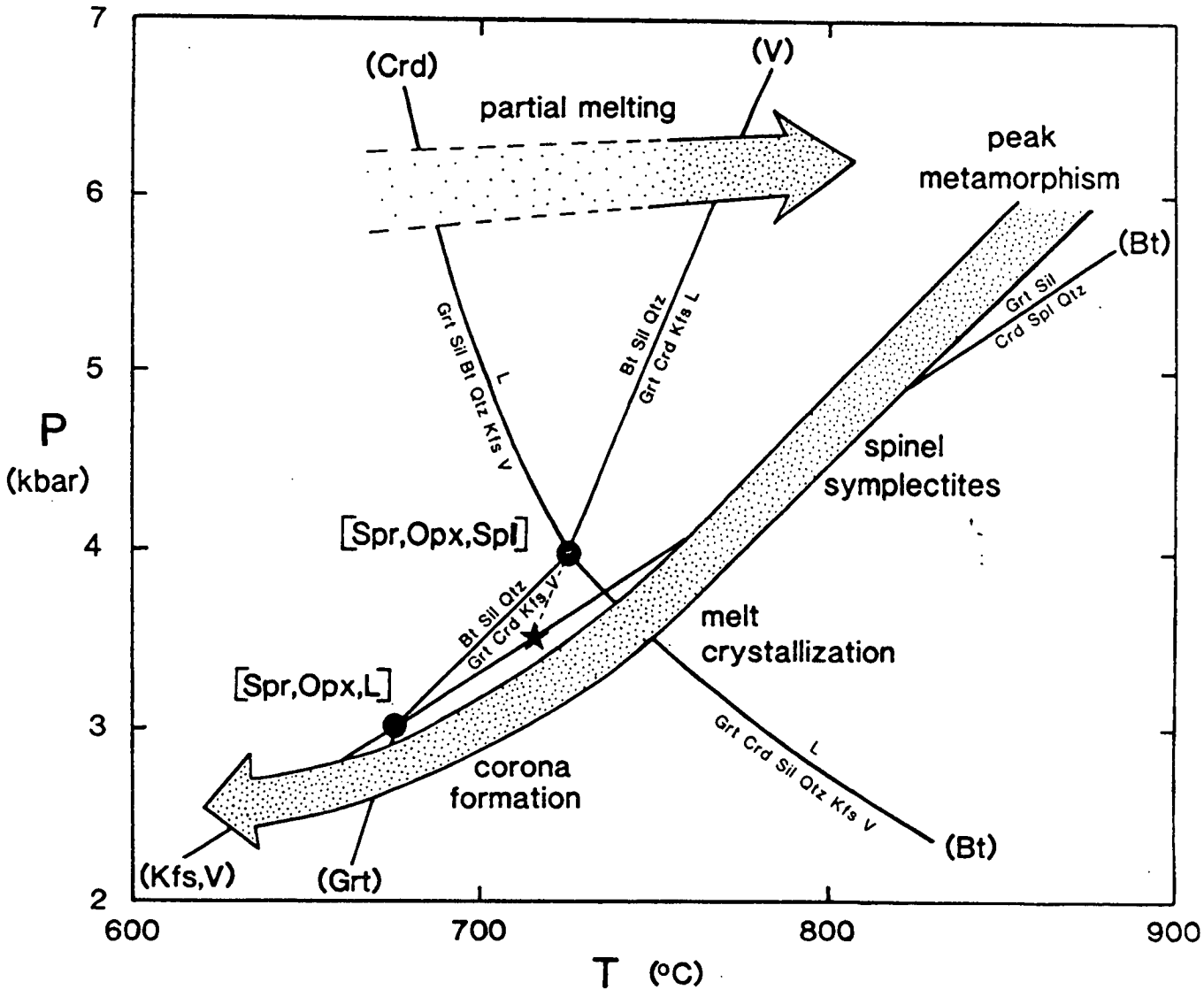

Fig. 6.24. A simple, empirical *P-T* grid for the Brattstrand Bluffs metapelite. The positions of the invariant points and univariant reactions in *P-T* space are based on various lines of evidence (see text), and are estimates only. The [Spr,Opx,V] invariant point is not stable, but would occur where the (Spr, Opx, Spl, V) reaction intersects the (Spr, Opx, Bt, Kfs, L, V) reaction and is marked on the figure by a star. The arrows indicate the favoured *P-T* path for the Brattstrand Bluffs metapelite.

The prograde melting reaction is constrained to lie between the [Spr, Opx, V] invariant point and the [Spr, Spl, V] invariant point (which is the high-pressure termination of the (V) reaction emanating from [Spr, Opx, V] and is not depicted in Fig. 6.24). The [Spr, Spl, V] point is estimated to occur at about 9 to 10 kbar and 850 to 900°C (Hensen & Harley, 1990). The [Spr, Opx, V] point is difficult to constrain experimentally, although its existence has been inferred from studies of the Laramie aureole (Grant, 1985*a*,*b*) which evolved at pressures below the point (3 kbar at about 800°C), and low-pressure granulites in the Larsemann Hills (Stüwe & Powell, 1989*a*) which evolved at pressures above the point (4.5 kbar at about 750°C). In addition, experimental studies of fluid-absent biotite melting (Le Breton & Thompson, 1988; Vielzeuf & Holloway, 1988) suggest that melting begins between 750 and 800°C, which is a maximum temperature for the [Spr, Opx, V] point. These experiments also found that melting only becomes extensive at temperatures of around 850°C. Given the fairly high extent of partial melting in the Brattstrand Bluffs coastline, possibly in excess of 20 per cent in some units, this is a reasonable peak-temperature estimate for the area and is in agreement with thermobarometry of interlayered semi-pelite lithologies (see Section 5.6.3). Peak pressures must lie between the two invariant points discussed above (i.e. between about 4 and 9 kbar), which is also consistent with the thermobarometric study.

The retrograde path involved decompression from the metamorphic peak to pressures less than the [Spr, Opx, V] point, and then cooling at pressures close to the [Spr, Opx, L] point. The latter point lies at lower temperatures and pressures than the former. Sub-solidus assemblages in the Laramie aureole are thought to have developed in the vicinity of the [Spr, Opx, L] point (Grant & Frost, 1990), which is estimated to occur at around 3 kbar and 650 to 700°C (Grant & Frost, 1990, p. 462). Retrograde growth of S_4 and corona biotite in the Brattstrand Bluffs coastline is attributed to reactions extending to lower pressures from this point, and hence occurred at around 3 kbar and temperatures less than 700°C.

The metapelite is not particularly amenable to thermobarometric study, since any one specimen commonly preserves a combination of assemblages stable at different stages of the metamorphic history. In addition, many of the preserved divariant assemblages are far from ideal for pressure-temperature estimation. A number of difficulties can be identified, including the following.

(i) Many of these assemblages include biotite which has undergone retrograde compositional change to varying extents. Even if the biotite did preserve its original composition, the effects of high titanium and fluorine contents produce large uncertainties in the activity models.

(ii) Cordierite can incorporate molecular H_2O and CO_2 in structural channels, which can strongly affect the stability of cordierite-bearing assemblages.

(iii) Spinel is another phase with compositional uncertainty, resulting in this case from exsolution relationships with other oxide phases. It is possible that some of the ilmenite in these assemblages was exsolved from the spinel, and the compositions should be reintegrated before thermobarometric study.

(iv) The coexistence of the solid phases with a silicate melt or a volatile fluid phase, or both, during the metamorphic evolution, and the resulting variation of a_{H2O} and a_{CO2}, are further complications.

However, despite these difficulties, two retrograde assemblages in the metapelite have been used to constrain the post-melting decompressional history. The garnet-sillimanite-spinel-cordierite-quartz and subset assemblages, and the garnet-sillimanite-quartz-plagioclase assemblage. Given the inherent uncertainty involved in thermobarometry with these assemblages in a texturally-complex lithology, no attempt is made here to assess the reliability of the calibrations chosen.

6.5.6 Garnet-sillimanite-spinel-cordierite-quartz thermobarometry

It was assumed in this study that the ilmenite coexisting with spinel did not exsolve from it. This seems reasonable for most specimens given that both spinel and ilmenite are relatively coarse and usually occur as separate grains, and that there are no fine-scale exsolution textures within the spinel. It is also assumed that the cordierite is anhydrous. This is consistent with preliminary analysis of cordierite volatile contents by stepped-heating mass spectrometry and ion-probe techniques (I.S. Buick, D.P. Mattey & S.L. Harley, unpublished data), and is thought to indicate that the cordierite grew in equilibrium with a fluid-undersaturated melt. The calibrations of Bhattacharya (1986) for the FAS univariant reactions

garnet + sillimanite + quartz = cordierite	(Spl),	
cordierite = spinel + quartz	(Grt, Sil)	and
garnet + sillimanite = cordierite + spinel	(Qtz)	

were used, along with a calibration for the reaction

garnet + sillimanite = spinel + quartz (Crd),

derived from the thermodynamic data used by Bhattacharya (1986) for the other reactions. These calibrations were used with the activity models suggested by Bhattacharya (1986) for garnet (Perkins & Chipera, 1985) and spinel (Fujii, 1977; Fujii & Scarfe, 1982), and an ideal two-site mixing model for cordierite (A.B. Thompson, 1976; Holdaway & Lee, 1977). Pressures for each reaction were

Table 6.7 Compositional parameters for garnet, cordierite and spinel, and pressure-temperature estimates using the garnet-sillimanite-cordierite-spinel-quartz data set of Bhattacharya (1986). Corresponding analyses for cordierite and spinel are tabulated in Appendix 3.5. The garnet analyses have not been tabulated but are similar to those used in Table 6.6.

	Grt	Grt	Crd	Spl	P_i	T_i	P_c	P_c	P_c
	X_{Fe}	X_{Ca}	X_{Mg}	X_{Mg}*	(kbar)	(°C)	(750°C)	(775°C)	(800°C)
88/14B	0.755	0.022	-	0.200	-	-	3.2	4.1	5.0
88/28	0.823	0.024	0.562	0.175	4.1	775			
88/44	0.761	0.025	0.579	0.209	4.1	770			
88/51	0.845	0.020	-	0.109	-	-	2.4	3.4	4.3
88/56	0.721	0.022	0.647	0.230	4.6	780			
88/62	0.837	0.017	-	0.112	-	-	2.5	3.4	4.3
88/74	0.717	0.027	0.621	0.218	4.4	785			
88/102	0.761	0.024	0.612	0.196	4.4	785			
88/110	0.767	0.028	0.615	0.210	4.4	780			
88/153C	0.756	0.027	0.641	0.192	4.6	795			
88/205	0.749	0.024	0.679	0.217	5.0	795			
88/273	0.752	0.023	0.642	0.217	4.6	785			
88/328	0.769	0.030	0.601	0.189	4.2	785			

P_i and T_i are the pressure and temperature at which the various FAS equilibria intersect. P_c is the pressure (in kbar) of the cordierite-absent reaction at the given reference temperature for those specimens which do not contain cordierite, and for which an intersection cannot be defined (see text for further discussion). Compositional parameters are as defined in Appendix 3.3, except for the garnet parameters X_{Fe} and X_{Ca} which are equal to Fe/(Fe+Ca+Mg) and Ca/(Fe+Ca+Mg) respectively.

calculated at three reference temperatures, and the position of the FAS invariant point defined for each specimen by the intersection of the reactions (see Table 6.7). The intersections occur between 4.0 and 5.0 kbar, and 750 and 800°C. Textural evidence implies that the retrograde path of the specimens passed very close to this invariant point, since spinel, cordierite and quartz are all involved in the reaction textures in most specimens. Hence 4.4 kbar and 775°C is a reasonable estimate for the conditions of symplectite formation in these specimens. The only exceptions are specimens 88/14B, 88/51 and 88/62, which are iron rich and do not contain cordierite. Hence *P-T* estimates can only be made using the (Crd) reaction, and an intersection cannot be defined. However, the *P-T* estimates from these specimens are consistent with the conditions derived from the cordierite-present specimens (see Table 6.7). Average pressure calculations using the data set of Holland and Powell (1990) also indicate pressures between 4 and 5 kbar at temperatures between 700 and 800°C.

Given the peak pressure-temperature estimates derived in Chapter 5, symplectite thermobarometry implies decompression of 1.5 to 2.0 kbar during a cooling interval of about 100°C. This corresponds very closely to the pressure-temperature path

gradient of 17 bar / °C calculated from mineral zonation profiles in semi-pelite from the Brattstrand Bluffs coastline (see Section 5.6.3). Hence it seems that the calibration of Bhattacharya (1986) yields *P-T* estimates in complete agreement with independent evidence of the metamorphic evolution of the Brattstrand Bluffs coastline. However, it should be noted that other calibrations, including that of Bohlen *et al.* (1986) for the (Crd) reaction and that of Waters (1989) for the (Spl) reaction, yield much higher pressures in the 700 to 800°C temperature range (up to 7 kbar), which are incompatible with other evidence from the area. In the absence of a detailed assessment of each calibration, the apparent suitability of the Bhattacharya (1986) calibration to the Brattstrand Bluffs coastline metapelite does not necessarily indicate that this is a reliable calibration for garnet-spinel-cordierite assemblages in general.

6.5.7 Garnet-sillimanite-plagioclase-quartz thermobarometry

The garnet-sillimanite-plagioclase-quartz equilibrium is one of the most reliable barometers for granulite terrains (Essene, 1989). However, its use in the Brattstrand Bluffs metapelite is associated with a large uncertainty resulting from the low grossularite content of the garnet. Even so, pressures were calculated using the calibration of Essene (1989), which is based on the experimental data of Koziol and Newton (1988). Grossularite activities were calculated using the model of Ganguly and Saxena (1984) with the modifications of Anovitz and Essene (1987), as suggested by Essene (1989), and plagioclase activities calculated with the model of Newton *et al.* (1980). There are no constraints on reference temperature for this equilibrium, but the calibration yields pressures between 2.0 and 5.0 kbar in the temperature range 700 to 800°C (see Table 6.8). The Holland and Powell (1990) data set yields very similar results with the same activity models. Like the other corona textures around spinel, the plagioclase coronas are thought to have developed synchronously with, or after, the S_4 shear foliation, when temperatures are inferred to have been about 700°C. At this temperature, garnet-sillimanite-plagioclase-quartz barometry implies pressures of 2 to 4 kbar (see Table 6.8).

The textural setting of plagioclase rinds around aluminous phases such as garnet, sillimanite and spinel implies that they did not develop directly through reaction of garnet, sillimanite and quartz. The close spatial relationship of plagioclase rinds with K-feldspar suggests that plagioclase formed due to loss of potassium from K-feldspar during reaction with aluminous phases to form biotite.

6.5.8 Summary of the quantitative *P-T* evolution

The *P-T* evolution of metapelite from the Brattstrand Bluffs coastline has been summarized in Fig. 6.24, although it should be noted that these *P-T* data are subject to

Table 6.8 Compositional parameters for garnet and plagioclase, and pressure estimates at various reference temperatures using the garnet-sillimanite-plagioclase-quartz barometer of Essene (1989). Corresponding mineral analyses are tabulated in Appendix 3.5.

	Grt X_{Mg}	Grt X_{grs}	Pl X_{an}	P (kbar) (700°C)	P (kbar) (800°C)	P (kbar) (900°C)
88/28	0.175	0.024	0.307	2.3	3.4	4.5
88/37	0.258	0.016	0.221	3.4	4.3	5.2
88/44	0.216	0.025	0.314	3.1	4.0	5.0
88/56	0.259	0.023	0.278	3.8	4.8	5.7
88/62	0.149	0.017	0.222	2.2	3.2	4.3
88/74	0.260	0.027	0.390	3.0	3.8	4.6
88/153C	0.223	0.027	0.341	3.0	4.0	4.9
88/205	0.192	0.025	0.302	2.8	3.8	4.8
88/273	0.243	0.022	0.294	3.0	4.0	4.9
88/318	0.221	0.028	0.292	4.0	5.0	5.9
88/325	0.171	0.032	0.299	4.0	5.0	5.9
88/331	0.293	0.029	0.392	3.7	4.5	5.3

Compositional parameters are as defined in Appendix 3.3.

significant uncertainty. In particular, the quantitative effects of a_{H2O} variation have only been treated empirically in the sense that the positions of the reactions are constrained by thermobarometry of Brattstrand Bluffs specimens. However, despite the inherent uncertainty, the various strands of evidence do produce a consistent grid, onto which can be drawn a *P-T* path consistent with various thermobarometric estimates. The peak metamorphic conditions are consistent with the thermobarometric study in Chapter 5 (*c.* 6 kbar, 860°C), the symplectite-forming reactions are intersected at pressures and temperatures consistent with garnet-sillimanite-spinel-cordierite-quartz thermobarometry (*c.* 4.4 kbar, 775°C; see Section 6.5.6), and the corona-forming reactions are crossed at pressures consistent with garnet-sillimanite-plagioclase-quartz barometry (*c.* 3 kbar and 650 to 700°C ; see Section 6.5.7). The pressure-temperature path defined by these constraints involves a total decompression of about 3 kbar from peak metamorphic conditions, during a cooling interval of about 175°C (see Fig. 6.24).

7. Calc-silicate phase relationships in the Nemesis Glacier region

7.1 INTRODUCTION

7.1.1 Calc-silicate as an indicator of pressure-temperature-fluid conditions

The thermobarometric study described in Chapter 5 provides estimates of the peak pressures and temperatures of metamorphism in both the Brattstrand Bluffs coastline and the Nemesis Glacier region, and consideration of mineral zonation profiles gives some insight into the retrograde evolution of these two areas. A petrological study of metapelitic lithologies, which are the most commonly-used sensor of pressure-temperature variation, has further constrained the retrograde metamorphic history of the Brattstrand Bluffs coastline (see Chapter 6). Metapelite is absent from the area of study in the Nemesis Glacier region, but calc-silicate boudins are widespread and preserve coronitic and symplectitic reaction textures. These textures reflect changes in the metamorphic conditions, and are used in this chapter to constrain the metamorphic evolution of the Nemesis Glacier region.

The sensitivity of calc-silicate assemblages to pressure-temperature conditions, and their use in the mapping of variation in metamorphic grade, have been appreciated for some time (e.g. Kennedy, 1949). Particular emphasis in the last few years has been placed on the sensitivity of calc-silicates to variation in the metamorphic fluid regime, and the use of calc-silicate assemblages as indicators of the composition of mixed-volatile fluids as well as pressure and temperature (e.g. Carmichael, 1970; Kerrick, 1974; Ferry, 1976, 1983*a*,*b*; Valley & Essene, 1980). Most of these studies have dealt with medium-grade rocks, and, although reaction textures have been identified and described in high-grade rocks of regional and contact origin (e.g. Smyth, 1897; Drever, 1939; Parras, 1958; White, 1959; Misch, 1964; Hapuarachchi, 1968; Mukherjee & Rege, 1972), only a handful of workers have attempted to interpret granulite-facies calc-silicate mineral textures in terms of a detailed pressure-temperature-fluid evolution (Schenk, 1984; Warren *et al.*, 1987; Harley, 1987*a*; Motoyoshi *et al.*, 1991).

The reluctance to use high-grade calc-silicate phase relationships as a petrological record of metamorphic evolution stems mainly from a lack of pertinent experimental and thermodynamic data. Experimental investigations have concentrated on relatively simple reactions, which involve only a small number of phases and are not directly applicable to the complex reaction textures observed in many natural specimens. For example, although there have been studies of reactions involving wollastonite, and reactions involving scapolite, there are no data for reactions involving both scapolite and wollastonite. Previous interpretations of high-grade calc-silicate reaction textures have been founded on the petrogenetic grid of D.E. Ellis (1978), which was constructed on the basis of limited experimental data. This grid has not proved entirely satisfactory (see Section 7.7.3), and recent advances in thermodynamic data sets have provided sufficient data to calculate the pressure-temperature-fluid dependence of relatively complex calc-silicate reactions on a sound thermodynamic basis, although significant uncertainties still remain for some phases, including scapolite (Holland & Powell, 1990, p. 102). The first attempt to apply a data set to a suite of high-grade calc-silicate specimens has been that of Harley and Buick (1991), who derived petrogenetic grids for calc-silicate lithologies from the Rauer Group of East Antarctica using the thermodynamic data set of Holland and Powell (1990). The study described in this chapter is complementary to the work of Harley and Buick (1991), and uses a similar approach to derive petrogenetic grids applicable to the high-grade calc-silicates of the Nemesis Glacier region, which are then used to constrain the metamorphic history of the area.

7.1.2 Phase relations in the Nemesis Glacier region calc-silicate

Section 4.2.8 describes the assemblages and reaction textures observed in the calc-silicate. Several assemblages have been identified, comprising some subset of garnet, clinopyroxene, scapolite, wollastonite, plagioclase, quartz, calcite and phlogopite (see Table 4.3). Reaction textures are most apparent in the wollastonite-scapolite assemblages which typify boudin cores, and this chapter focuses on these assemblages. Two types of texture are distinguished:

(i) textures dominated by garnet coronas, with symplectites and other mineral intergrowths within these coronas; and

(ii) rare, localized textures dominated by elongate plagioclase laths, separated by ribs of garnet and wollastonite.

The remainder of this chapter interprets these textures in terms of changes in pressure, temperature, and fluid regime. The clear spatial arrangement of product and reactant phases in the distinctive corona-dominated textures of type (i) makes them easier to interpret than the ribbed textures. The coronitic textures also impose tight constraints

Table 7.1 Prograde wollastonite-scapolite assemblages in the coronitic calc-silicate from the Nemesis Glacier region.

Specimen	Locality	Prograde assemblage	
89/55C	Allison Ridge	scapolite-wollastonite-clinopyroxene-plagioclase	(A3)
89/55D	Allison Ridge	scapolite-wollastonite-clinopyroxene-garnet	(A2)
89/93	Mt Trott	scapolite-wollastonite-clinopyroxene-calcite	(A1)
89/334C	Amery Peaks	scapolite-wollastonite-clinopyroxene	(A4)
89/334F	Amery Peaks	scapolite-wollastonite-clinopyroxene-calcite	(A1)
89/334G	Amery Peaks	scapolite-wollastonite-clinopyroxene	(A4)
89/334H	Amery Peaks	scapolite-wollastonite-clinopyroxene-calcite	(A1)

on both the pressure-temperature evolution of the area and the nature of any syn-metamorphic fluid phase, and are the principal subject of this chapter. Section 7.2 describes the prograde assemblages and reaction textures developed in seven coronitic scapolite-wollastonite specimens from the Nemesis Glacier region, and Section 7.3 describes the mineral chemistry of these specimens. Section 7.4 interprets the textures in terms of model univariant reactions in a simple chemical system, and Section 7.5 develops petrogenetic grids illustrating the disposition of the univariant equilibria in pressure-temperature-fluid space. These sections also discuss the effects of considering the assemblages in more complex chemical systems, which more closely approach the natural specimens. Section 7.6 uses the various grids to constrain the pressure-temperature-fluid evolution of the coronitic calc-silicate, and also discusses the origins of the ribbed textures. Section 7.7 assesses the general applicability of the grids by extending the results of this study to other granulite terrains, and compares the histories inferred by previous studies of these areas using the reaction grid of Ellis (1978) with those suggested by the grids developed here.

7.2 PETROGRAPHY OF THE CORONITIC CALC-SILICATE

7.2.1 Introduction

Seven coronitic specimens collected from three different localities within the field area were selected for petrographic and analytical study (see Table 7.1). Specimens 89/55C and 89/55D were collected from the core of a massive homogeneous boudin at Allison Ridge. The boudin is about 1 m across, and has no internal lithological layering, but does preserve a modal zonation from core to rim. Specimen 89/55D was

collected from the centre of the boudin, and 89/55C was collected about 0.2 m from the centre. Specimen 89/93 was collected from an interlayered sequence of calc-silicate and marble lithologies enclosed within felsic gneiss at Mt Trott. Specimens 89/334C, F, G and H were collected from four layers at the centre of a 3 m wide interlayered sequence of calc-silicate at Amery Peaks Massif. The rest of this section describes the petrographic relationships in these specimens. Many of the features described here are also discussed in Chapter 4 and are illustrated in Plates 4.4 to 4.6.

7.2.2 The prograde assemblages

The prograde assemblages of the seven specimens, which are listed in Table 7.1, all contain scapolite, wollastonite and clinopyroxene, and may also include one of the following: calcite (assemblage A1), garnet (assemblage A2), or plagioclase (assemblage A3). Some specimens appear to have none of these additional phases, and are characterized by high-variance scapolite-wollastonite-clinopyroxene assemblages (assemblage A4). Sphene is a ubiquitous accessory mineral and apatite is common. The prograde phases in all specimens exhibit polygonal, granoblastic textures (see Plate 4.4), comprising some combination of equant scapolite, clinopyroxene, garnet or plagioclase, bladed wollastonite, and small grains of calcite at the interstices of other phases. There is no prograde quartz in scapolite-wollastonite assemblages, although wollastonite-absent quartz-plagioclase-clinopyroxene-scapolite bands are interlayered with the wollastonite-scapolite bands in specimens 89/93 and 89/334C, F, G and H. The scapolite-quartz assemblages do not preserve evidence of retrograde reaction, but nevertheless impose useful constraints on the peak metamorphic conditions, and are discussed in Section 7.6.1. A foliation is defined by modal variation of clinopyroxene and scapolite, and by the orientation of wollastonite. The majority of grains are between 0.5 and 1.5 mm across. The remainder of this section describes the various mineral reaction textures, summarized in Table 7.2, which modify the granoblastic, prograde wollastonite-scapolite assemblages.

7.2.3 The retrograde coronas

Garnet coronas are a feature of all the assemblages considered here, although the nature of the coronas depends on the local prograde assemblage.

(i) Two types of garnet corona are developed in assemblage A1 (i.e. specimens 89/93, 89/334F and 89/334H). Simple garnet coronas occur between scapolite and calcite, whereas composite garnet-quartz coronas separate scapolite and wollastonite. Corona morphology is as described in Section 4.2.8: simple garnet coronas comprise continuous layers of garnet with a lobate contact to scapolite

Table 7.2 Reaction textures overprinting the four prograde scapolite-wollastonite coronitic calc-silicate assemblages (A1, A2, A3 and A4).

Prograde assemblage		Retrograde reaction textures
Assemblage A1	a	garnet coronas between scapolite and calcite
(Grs, An, Qtz)	b	garnet-quartz coronas between scapolite and wollastonite
or	c	garnet coronas between scapolite and clinopyroxene
(Grs, An, Qtz, V)	d	calcite-quartz intergrowths within wollastonite
	e	calcite-plagioclase symplectites within scapolite
Assemblage A2	a	garnet ± quartz coronas between scapolite and wollastonite
(An, Cal, Qtz)	b	garnet coronas between scapolite and clinopyroxene
or	c	calcite-quartz intergrowths within wollastonite
(An, Cal, Qtz, V)	d	calcite-plagioclase symplectites within scapolite
Assemblage A3	a	garnet ± quartz coronas between scapolite and wollastonite
(Grs, Cal, Qtz)	b	garnet-quartz coronas between plagioclase and wollastonite
or	c	garnet coronas between scapolite and clinopyroxene
(Grs, Cal, Qtz, V)	d	garnet coronas between plagioclase and clinopyroxene
	e	calcite-quartz intergrowths within wollastonite
	f	calcite-plagioclase symplectites within scapolite
Assemblage A4	a	garnet-quartz coronas between scapolite and wollastonite
(Grs, An, Cal, Qtz)	b	garnet-coronas between scapolite and clinopyroxene
or	c	calcite-quartz intergrowths within wollastonite
(Grs, An, Cal, Qtz, V)	d	calcite-plagioclase symplectites within scapolite

and a curviplanar contact to calcite; composite garnet-quartz coronas comprise a continuous curviplanar layer of quartz adjacent to wollastonite, in contact with a continuous layer of garnet with a lobate boundary to scapolite. Garnet also occurs locally between scapolite and clinopyroxene. There are no coronas between calcite and wollastonite, calcite and clinopyroxene, or between clinopyroxene and wollastonite. Single scapolite grains which have one boundary with calcite and an adjacent boundary with wollastonite, are mantled by garnet along the former and by garnet-quartz along the latter, indicating that corona development was controlled on a very local scale (see Plate 4.5c).

(ii) Composite garnet ± quartz coronas occur in assemblage A2 (specimen 89/55D) between scapolite and wollastonite. Partial garnet coronas also extend along clinopyroxene-scapolite grain boundaries. There are no coronas between wollastonite and clinopyroxene. Garnet forms a continuous curviplanar layer, whereas quartz occurs as isolated blebs. Quartz accounts for a much smaller proportion of the coronas in this assemblage than it does in the A1 coronas (see Plate 4.5a). However, garnet and quartz exhibit a similar spatial distribution to that in assemblage A1, with garnet adjacent to scapolite, and quartz blebs between garnet and wollastonite.

(iii) Composite garnet ± quartz coronas occur in assemblage A3 (specimen 89/55C) between scapolite and wollastonite, and plagioclase and wollastonite, whereas garnet coronas occur between scapolite and clinopyroxene, and plagioclase and clinopyroxene (see Plate 4.4a,b). There are no coronas between scapolite and plagioclase, nor between wollastonite and clinopyroxene. The retrograde garnet forms a continuous, curviplanar layer, and retrograde quartz is subordinate and occurs as isolated blebs between the garnet layer and the prograde wollastonite.

(iv) Assemblage A4 (specimens 89/334C and 89/334G) preserves composite garnet-quartz coronas between scapolite and wollastonite, and garnet coronas locally separate scapolite and clinopyroxene. The composite coronas comprise continuous layers of garnet and quartz (see Plate 4.5b), which are of identical appearance to the garnet-quartz coronas developed in A1 assemblages.

7.2.4 The retrograde intergrowths and symplectites

Two types of mineral intergrowth have been identified in all the scapolite-wollastonite specimens of this study:

(i) local intergrowths of calcite and quartz within and adjacent to resorbed wollastonite grains, and

(ii) widespread plagioclase-calcite ± quartz symplectites within and adjacent to resorbed scapolite.

These textures, described in Section 4.2.8 and illustrated in Plate 4.6a,b, post-date the garnet coronas since coronas of consistent appearance occur in contact with unaltered scapolite and wollastonite, and with the symplectites and intergrowths.

7.3 MINERAL CHEMISTRY

7.3.1 Introduction

The composition of garnet, scapolite, wollastonite, clinopyroxene and plagioclase in the seven selected specimens were determined by wavelength-dispersive electron-probe microanalysis. The operating conditions, and analytical precision and accuracy, are detailed in Appendices 3.1, 3.2 and 3.7. Normalization procedures, and methods of ferric iron estimation in garnet and pyroxene, are outlined in Appendix 3.3, and representative mineral analyses are tabulated in Appendix 3.6. In addition to the elements listed in Appendix 3.6, selected grains in each specimen were analysed for chromium, which was found to be negligible in all phases, and energy-dispersive spectra indicated that sulphur contents of scapolite grains in all specimens were also negligible. Between 20 and 100 analyses were made on each specimen, including individual core and rim spot analyses and traverses across grains comprising between

Table 7.3 A summary of the compositional variation shown by phases in the coronitic specimens.

specimen	89/55C	89/55D		89/93	89/334C	89/334F	89/334G	89/334H
X_{grs}^{Grt}	0.75-0.77	0.76-0.80[1]	0.81-0.82[2]	0.83-0.96	0.88-0.90	0.85-0.90	0.83-0.93	0.77-0.87
X_{adr}^{Grt}	0.14-0.17	0.14-0.18[1]	0.12-0.14[2]	0.03-0.13	0.08-0.10	0.09-0.12	0.05-0.15	0.08-0.20
X_{alm}^{Grt}	0.06-0.08	0.04-0.06[1]	0.03-0.05[2]	0.02-0.04	0.01-0.02	0.00-0.02	0.00-0.03	0.01-0.07
X_{prp}^{Grt}	0.00-0.01	0.00-0.02[1]	0.00-0.01[2]	0.00-0.01	0.00-0.01	0.00-0.01	0.00-0.01	0.00-0.01
X_{sps}^{Grt}	0.02-0.03	0.01-0.02[1]	0.01-0.02[2]	0.00-0.01	0.00-0.01	0.00-0.01	0.00-0.01	0.00-0.01
EqAn	77-80	84-90		70-73	71-78	71-75	71-76	75-82
Wo	virtually pure, with minor Fe and Mn							
Cal	pure	pure		pure	pure	pure	pure	pure
Qtz	pure	pure		pure	pure	pure	pure	pure
X_{an}^{Pl}	all between 0.94 and 0.98							
X_{Mg}^{Cpx}	0.29-0.33	0.47-0.52		0.39-0.41	0.69-0.73	0.77-0.82	0.76-0.84	0.35-0.47

The superscripts 1 and 2 for specimen 89/55D refer to compositions of prograde and retrograde garnet respectively. Garnet in all other specimens is retrograde.

5 and 10 equally-spaced analysis points. The compositional variation is summarized in Table 7.3 in terms of the main compositional parameters, and more-detailed chemical relationships are illustrated in Figs 7.1 to 7.8.

7.3.2 Garnet

Prograde garnet occurs in only one of the specimens studied (specimen 89/55D). It is a grossularite-andradite solid solution (X_{grs}^{Grt} = 0.76 to 0.80, X_{adr}^{Grt} = 0.14 to 0.18) with pyrope, almandine and spessartine components accounting for only 7 to 10 mole per cent. No significant chemical zonation from core to rim has been identified. Retrograde garnet occurs in all specimens, and is also principally a grossularite-andradite solid solution, but tends to be more calcic than the prograde garnet of 89/55D (see Fig. 7.1). Grossularite contents of retrograde garnet in all specimens range between 75 and 95 mole per cent, and andradite contents vary between 3 and 21 mole per cent.

The intra-specimen variation in grossularite and andradite contents of retrograde garnet in some specimens (89/93, 89/334F, G and H) is a similar magnitude to the inter-specimen variation. There is little intra-specimen variation in almandine content (see Fig. 7.2), but a systematic contrast exists between different specimens (X_{alm}^{Grt} ranging between 0.005 and 0.080); the most almandine-rich garnet coexists with the most hedenbergitic pyroxene and iron-rich wollastonite, indicating that ferrous-iron contents in garnet (and pyroxene and wollastonite) are controlled principally by bulk composition. Within any single specimen, almandine contents tend to show an inverse correlation with andradite, which reflects a decreasing proportion of almandine as

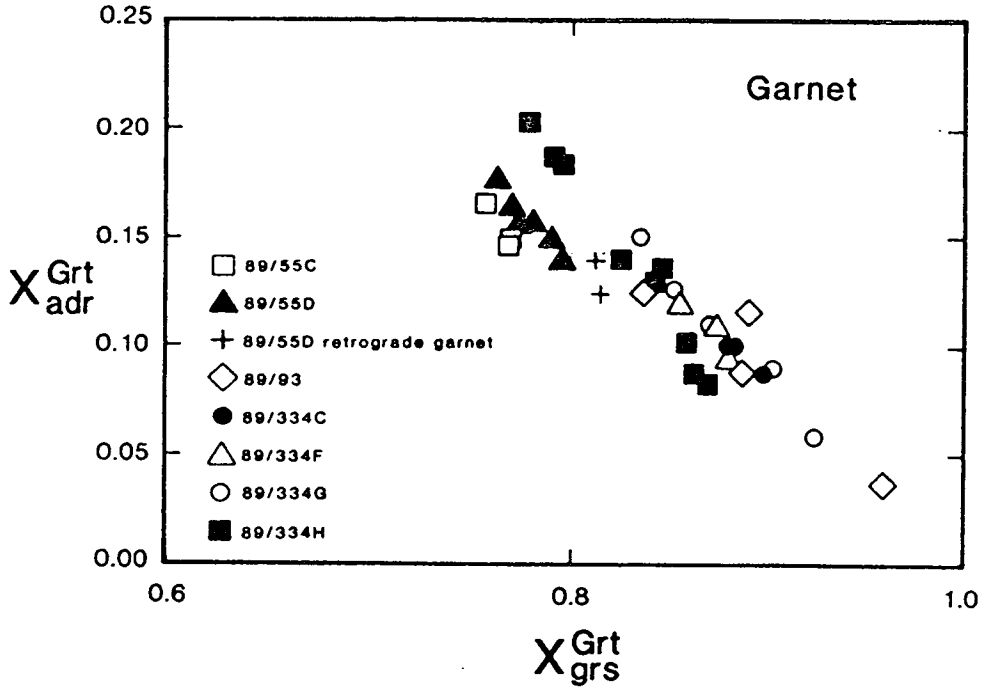

Fig. 7.1 A plot of X_{adr}^{Grt} versus X_{grs}^{Grt} for garnet in the coronitic calc-silicate. The total grossularite plus andradite contents of garnet in specimens 89/55C and 89/55D are relatively low, reflecting the relatively high contents of almandine, pyrope and spessartine, and plot just off the trend of the other specimens. There are two symbols for analyses of garnet in specimen 89/55D: one for retrograde garnet and another for prograde garnet (only one symbol is used for other phases from 89/55D in Figs 7.4 to 7.8).

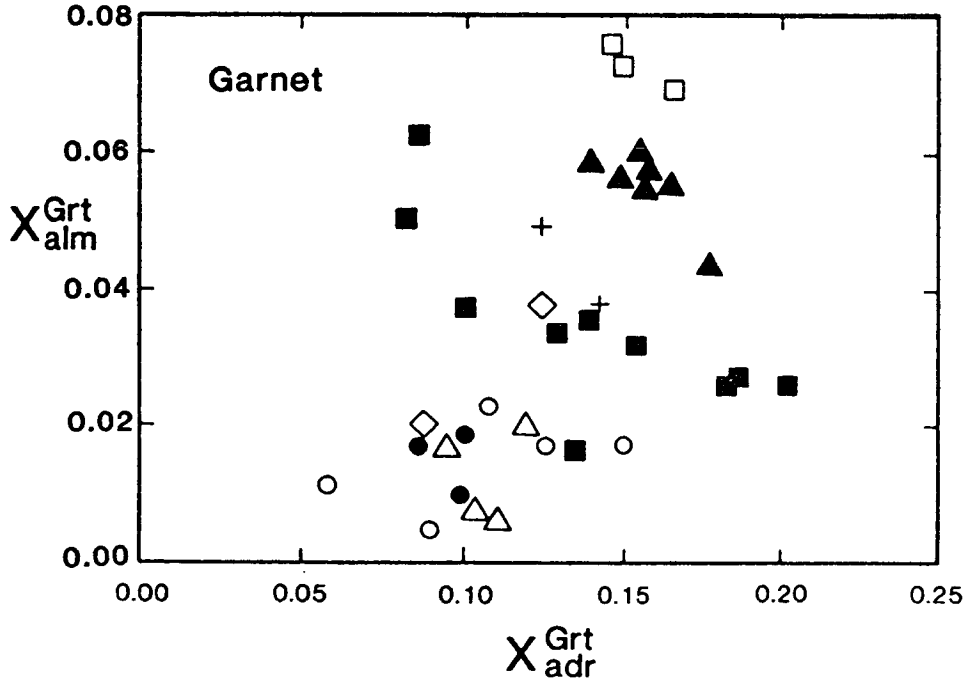

Fig. 7.2 A plot of X_{alm}^{Grt} versus X_{adr}^{Grt} for garnet in the coronitic calc-silicate (symbols as for Fig. 7.1). There is a positive inter-specimen correlation between these two components, with specimens 89/55C and 89/55D having the highest total iron content. The specimens with relatively high iron content show a negative intra-specimen correlation between ferrous and ferric iron, but no such trend is apparent in the iron-poor specimens.

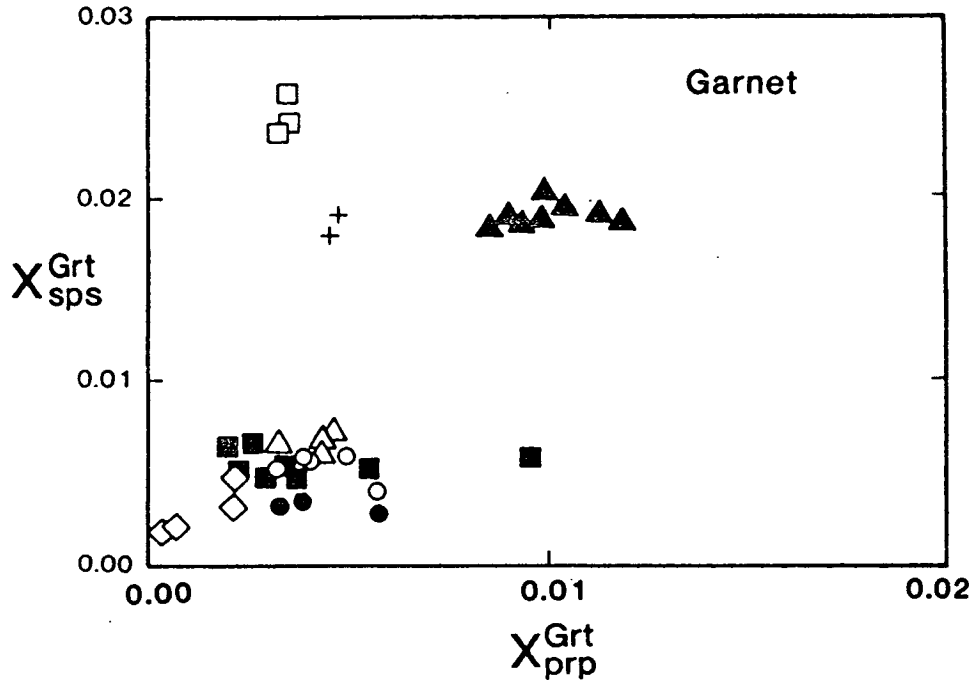

Fig. 7.3 A plot of X_{sps}^{Grt} versus X_{prp}^{Grt} for garnet in the coronitic calc-silicate (symbols as for Fig. 7.1). Most analyses cluster at very low values for both these components, whereas all garnet types in specimens 89/55C and 89/55D are relatively manganese rich. The pyrope content of prograde garnet in specimen 89/55D is also relatively high, but retrograde garnet in this specimen, and specimen 89/55C, have similar pyrope contents to the other specimens.

more andradite is incorporated into the garnet. Retrograde garnet in all specimens, including 89/55D, is less magnesian (X_{prp}^{Grt} = 0.001 to 0.010) than prograde garnet in 89/55D (see Fig. 7.3), but there is little variation in pyrope content in any one specimen. Similarly, there is little variation in spessartine content of retrograde garnet between most of the specimens (see Fig. 7.3), but specimens 89/55C and 89/55D have relatively high spessartine contents (X_{grs}^{Grt} between 0.018 and 0.026) of similar magnitude to those of the prograde garnet in 89/55D. Retrograde garnet in specimen 89/55C has higher spessartine contents than retrograde garnet in 89/55D. This is because much of the manganese in the latter specimen has been retained within the prograde garnet. Retrograde garnet in other specimens has lower spessartine contents (X_{sps}^{Grt} between 0.002 and 0.007). Uvarovite contents in both prograde and retrograde garnet analysed for chromium are negligible.

7.3.3 Scapolite

Scapolite exhibits a compositional range both between and within specimens. Compositional variation in scapolite has been represented in terms of equivalent

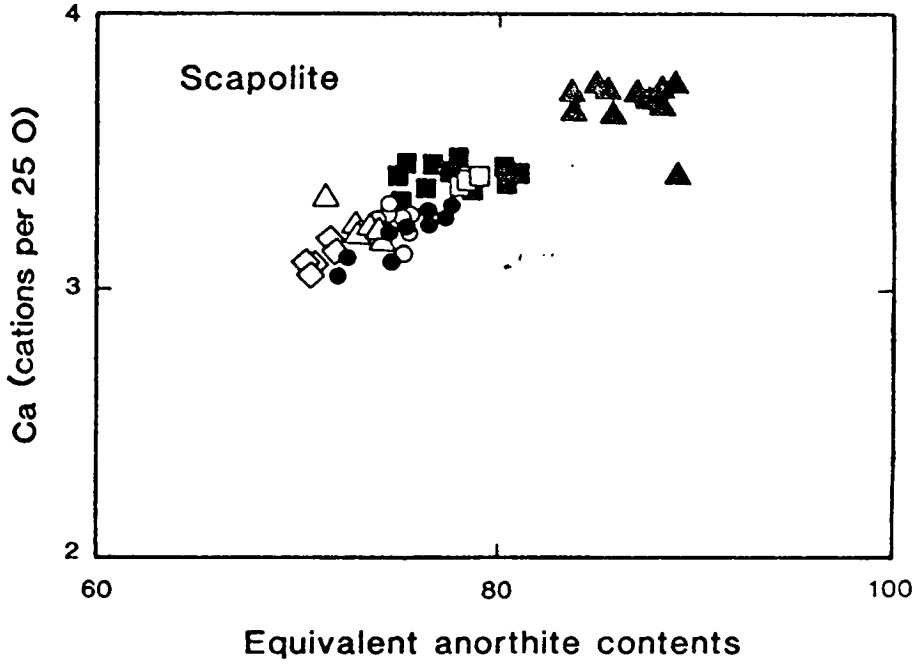

Fig. 7.4 A plot of calcium content versus equivalent anorthite values for scapolite in the coronitic calc-silicate (symbols as for Fig. 7.1).

anorthite contents[1] (EqAn values), which vary between 70 and 90 (see Fig. 7.4). Scapolite coexisting with prograde garnet in specimen 89/55D has the highest EqAn values (83 to 90), whereas EqAn values in the other specimens fall in the range 70 to 81. Although EqAn values vary within any one scapolite grain, typically by 1 to 3 units EqAn, no consistent sense of zonation has been identified: in some cases EqAn values increase rimwards, whereas in others they decrease or show no systematic variation. Scapolites with the highest EqAn values are commonly those with the most advanced and widespread development of calcite-plagioclase symplectite. Chlorine and sulphur contents are negligible.

7.3.4 Wollastonite

Wollastonite only occurs as a prograde phase, and contains minor iron (0.2 to 0.7 weight per cent) and manganese (0.1 to 0.6 weight per cent). High manganese and iron contents in specimens 89/55C and 89/55 (see Fig. 7.5) correlate positively with manganese and iron in coexisting clinopyroxene and garnet.

---

1 Equivalent anorthite contents of scapolite, or 'EqAn' values, are based on the ratio of aluminium to silicon, and are equal to 100 (Al-3) / 3, where Al is the number of aluminium cations per formula unit of scapolite which has been normalized to a total of 12 aluminium and silicon cations (Orville, 1975; Ellis, 1978). Previous workers defined scapolite composition in terms of meionite percentage (Shaw, 1960; Deer *et al.*, 1963, p. 329; Evans *et al.*, 1969), which is based on the ratio of calcium to sodium in scapolite normalized to 12 aluminium and silicon cations, and can vary independently of the aluminium to silicon ratio.

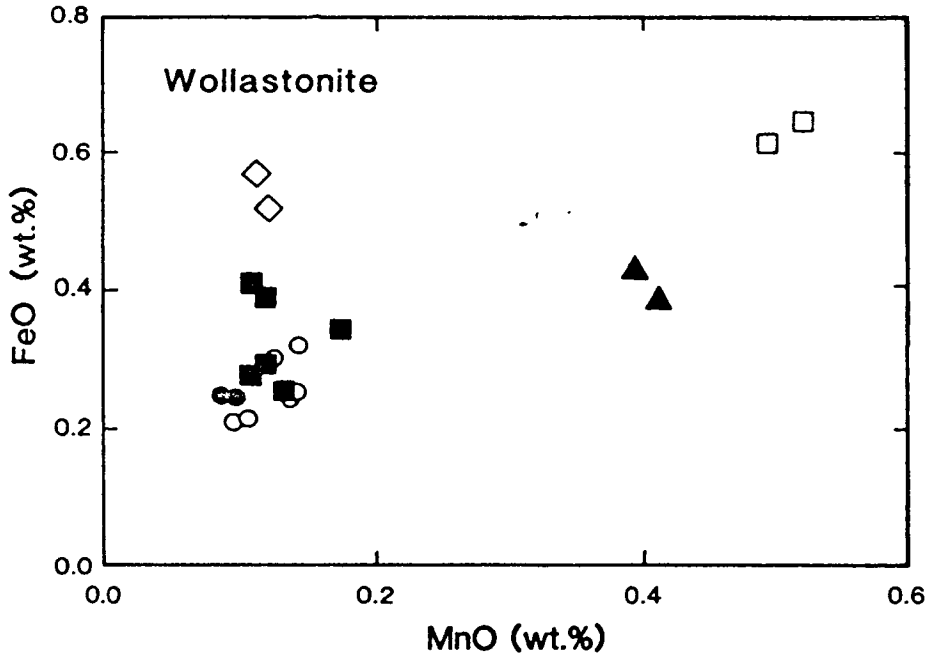

Fig. 7.5 A plot of iron content versus manganese content for wollastonite in the coronitic calc-silicate (symbols as for Fig. 7.1). Wollastonite in specimens 89/55C and 89/55D is relatively manganese rich.

7.3.5 Plagioclase

Prograde plagioclase in specimen 89/55C is anorthite rich (X_{an}^{Pl} between 0.94 and 0.96), and retrograde plagioclase in symplectites after scapolite is almost pure anorthite, with anorthite contents in the range 95 to 98 mole per cent.

7.3.6 Clinopyroxene

Clinopyroxene occurs only as a prograde phase, and is a diopside-hedenbergite solid solution with variable degrees of tschermaks ($CaAl_2SiO_6$) and ferri-tschermaks ($CaFe^{3+}AlSiO_6$) substitution (0.5 to 5.4 mole per cent and 0.0 to 4.6 mole per cent respectively). There is also minor manganese substitution, equivalent to between 2.3 and 3.8 mole per cent $CaMnSi_2O_6$ component in specimens 89/55C and 89/55D, and 0.4 and 1.2 mole per cent $CaMnSi_2O_6$ component in the other specimens (Fig. 7.6). Titanium and chromium contents are negligible. There is a large inter-specimen variation in diopside-hedenbergite proportions (X_{Mg}^{Cpx} between 0.29 and 0.85), with a positive correlation between ferrous-iron contents in clinopyroxene, and those in garnet and wollastonite. X_{Mg}^{Cpx} varies by up to 0.04 units within in any one grain, but in some specimens X_{Mg}^{Cpx} increases rimwards, whereas in others it decreases or shows no variation. There is little or no systematic zonation or variation in the tschermaks component (Fig. 7.7). In contrast, the ferri-tschermaks component always decreases rimwards in any one grain, and this variation is of similar magnitude to the

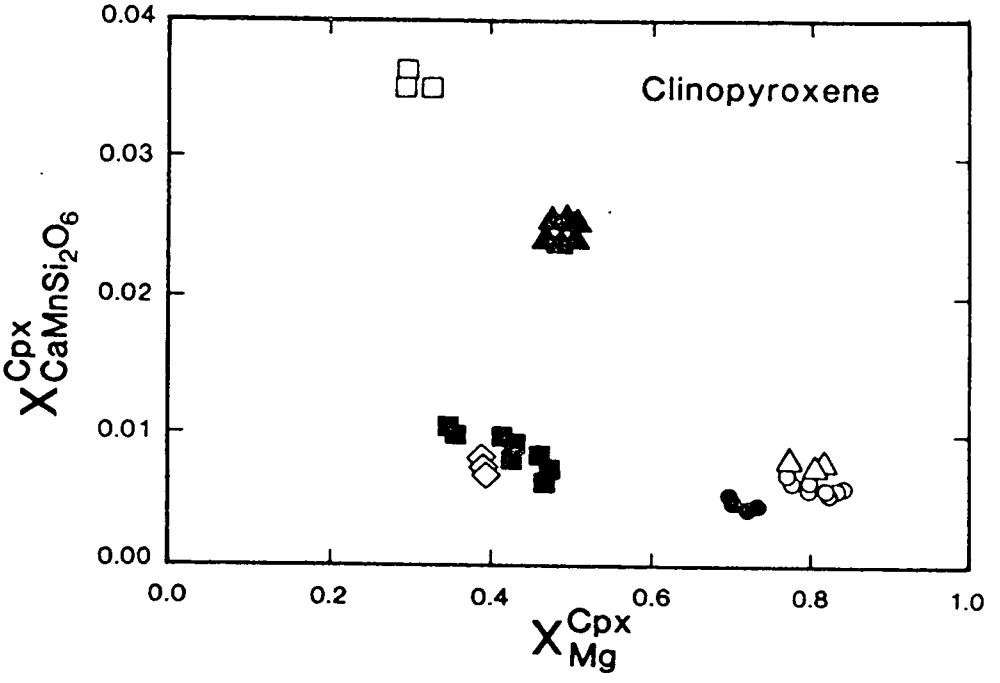

Fig. 7.6 A plot of manganese content versus X_{Mg}^{Cpx} for clinopyroxene in the coronitic calc-silicate (symbols as for Fig. 7.1). Note the wide range in X_{Mg}^{Cpx}, and the relatively high manganese contents of clinopyroxene in specimens 89/55C and 89/55D. This figure depicts core and rim compositions.

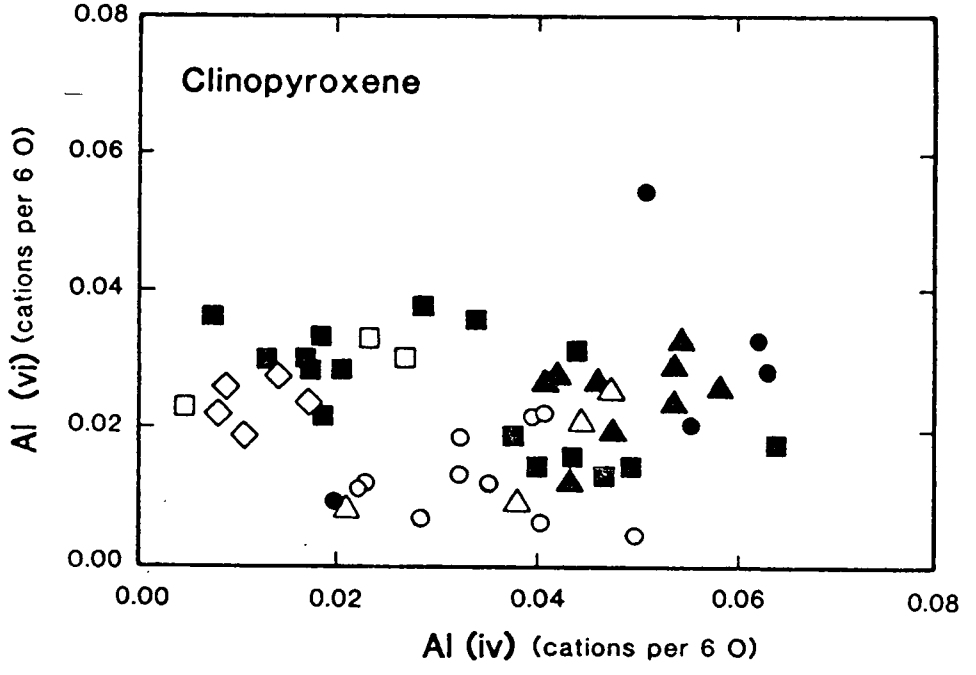

Fig. 7.7 A plot of octahedral aluminium content versus tetrahedral aluminium content for clinopyroxene in the coronitic calc-silicate (symbols as for Fig. 7.1). The allocation of aluminium between these two sites is dependent on the accuracy of each analysis.

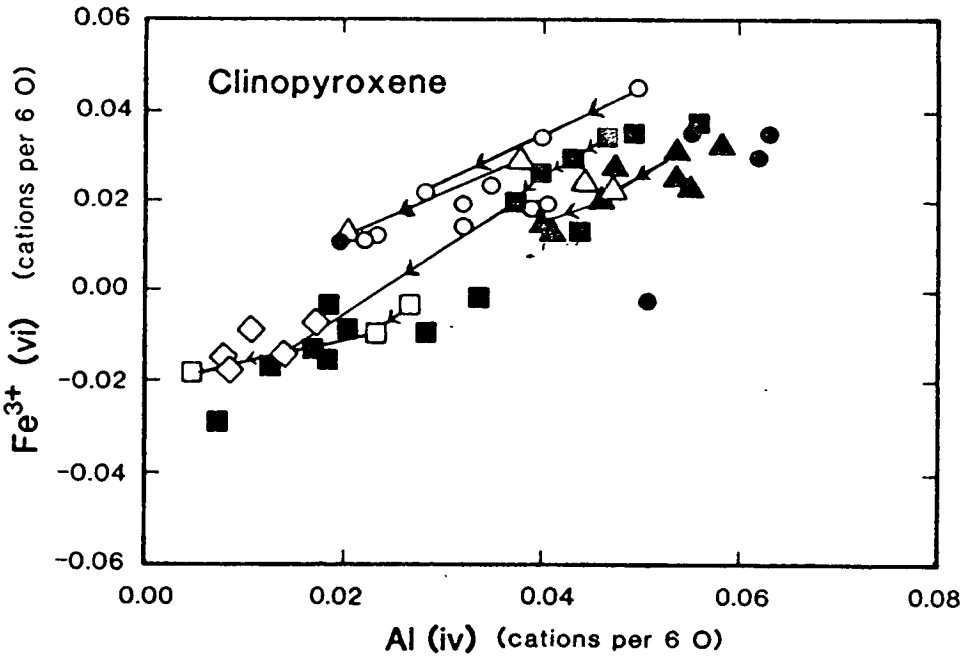

Fig. 7.8 A plot of octahedral ferric iron content versus tetrahedral aluminium content for clinopyroxene in the coronitic calc-silicate (symbols as for Fig. 7.1). The negative values reflect uncertainty in the mineral analyses (see discussion in the text). The points joined by lines are typical core to rim compositional profiles (the arrows indicate a rimwards direction).

differences in ferri-tschermaks contents between specimens (Fig. 7.8). The absolute values derived for tschermaks and ferri-tschermaks components are subject to uncertainties resulting from their method of estimation, which is highly dependent on the accuracy of each analysis and the assumption of perfect stoichiometry, as indicated by the number of negative values of ferri-tschermaks component depicted in Fig. 7.8. Tetrahedral aluminium contents, per formula unit normalized to four cations, are calculated from the silicon deficiency in the tetrahedral site (i.e. 2 - Si), octahedral aluminium contents are calculated as total aluminium minus tetrahedral aluminium, and ferric iron contents as tetrahedral aluminium minus octahedral aluminium (i.e. 4 - 2Si - Al^{total}; see Appendix 3.3). Assuming an approximate error in each silicon analysis of about ± 0.01 cations per four-cation formula unit (see Appendix 3.7), which is much larger than errors in aluminium analysis, the calculated contents of tetrahedral aluminium and ferric iron per four cations have an associated uncertainty of about 0.02 cations per formula unit. This is sufficient to raise all but one of the negative points in Fig. 7.8 above zero. The observed positive correlation between ferric iron and tetrahedral aluminium could merely reflect variation in the quality of the silicon analysis. If the analysed silicon content is high, the calculated tetrahedral aluminium and ferric iron are low. Most zonation profiles in single clinopyroxene grains are associated with a calculated change in ferric iron contents of between 0.010

and 0.025 cations per four-cation formula unit, which do not greatly exceed the analytical uncertainty. However, the same trend of decreasing ferric iron from core to rim was observed on seven out of nine analytical grain traverses, made using exactly the same operating conditions over a period of less than 24 hours. This consistent sense of zonation, and the discovery of one grain in which the difference in ferric-iron content from core to rim was about 0.055 cations per four-cation formula unit, are believed to indicate that the inferred profiles are indeed real.

7.4 TEXTURAL INTERPRETATION IN TERMS OF MODEL REACTIONS

7.4.1 A suitable chemical system

The analytical study indicates that wollastonite, plagioclase, calcite and quartz exhibit very little deviation from their pure composition, and can be adequately represented by the system CaO-Al_2O_3-SiO_2-CO_2 (CASV). This does not, however, hold for scapolite, garnet and clinopyroxene, which cannot be fully represented within this system. Scapolite has significant sodium contents, but since there are no other sodium-bearing phases (plagioclase and pyroxene have only minimal sodium contents), sodium is treated as a diluent and scapolite is represented within the CASV system with a reduced activity. Garnet contains substantial proportions of andradite and almandine components, and small amounts of pyrope and spessartine. The only other phase containing these components in significant amounts is clinopyroxene. The occurrence of garnet coronas adjacent to clinopyroxene in all specimens, at least locally, suggests that clinopyroxene was an essential reactant consumed during retrograde garnet growth, and that it provided the ferric and ferrous iron, magnesium and manganese content of the garnet. This is supported by the rimwards decrease of ferri-tschermaks component in clinopyroxene, which was identified in all specimens. Hence the non-grossularite component of retrograde garnet reflects the breakdown of prograde clinopyroxene, which is relatively rich in these components. As would be expected, given the known extent of andradite solid solution in grossularite, ferric iron has been preferentially incorporated into the retrograde garnet from prograde pyroxene, whereas magnesium, and to a lesser extent ferrous iron, have predominantly remained within the pyroxene. The large intra-specimen variation of ferri-tschermaks content in clinopyroxene, and of andradite content in some garnets, reflect the varying extent to which clinopyroxene has locally contributed to retrograde garnet growth.

Clinopyroxene is in excess in all of the assemblages considered here, and is the phase with the highest contents of the non-CASV ferromagnesian components. For the purpose of this study, all the other phases were projected into the CASV system

Table 7.4 Univariant reactions between the phases wollastonite, scapolite, grossularite, calcite, quartz, anorthite and CO_2 in the system CaO-Al_2O_3-SiO_2-CO_2.

scapolite + 3 wollastonite + 2 calcite = 3 grossularite + 3 CO_2	(An, Qtz)
scapolite + wollastonite = 3 grossularite + 2 quartz + CO_2	(An, Cal)
2 wollastonite + anorthite = grossularite + quartz	(Scp, Cal, V)
wollastonite + CO_2 = calcite + quartz	(An, Scp, Grs)
scapolite = 3 anorthite + calcite	(Wo, Qtz, Grs, V)
scapolite + wollastonite = grossularite + 2 anorthite + CO_2	(Cal, Qtz)
6 wollastonite + scapolite = 3 quartz + calcite + 3 grossularite	(An, V)
scapolite + quartz = wollastonite + 3 anorthite + CO_2	(Cal, Grs)
scapolite + 5 calcite + 3 quartz = 3 grossularite + CO_2	(Wo, An)
grossularite + 2 CO_2 = 2 calcite + anorthite + quartz	(Scp, Wo)
2 scapolite + 3 quartz = 5 anorthite + grossularite + 2 CO_2	(Cal, Wo)
wollastonite + calcite + anorthite = grossularite + CO_2	(Scp, Qtz)*

* N.b. (Scp, Qtz) is a metastable reaction in most of the grids used in this paper, but is stable in the inverted grid of Fig. 7.12).

from clinopyroxene (Fig. 7.9a,b). All the phase relationships are considered within the CASV system, and the role of clinopyroxene in the mineral reactions is ignored. The chemographic relationships between the phases grossularite, scapolite, wollastonite, calcite, anorthite and quartz are depicted in Fig. 7.9b, and all the possible univariant CASV reactions involving these phases are listed in Table 7.4. Given that there are four components, each univariant reaction involves five or less phases. There are a total of seven phases: grossularite, scapolite, wollastonite, calcite, anorthite, quartz and fluid; hence each univariant reaction must have at least two phases absent, and the maximum number of univariant reactions is 21. However, two of the possible reactions have three phases absent, and one has four phases absent. These degeneracies leave a total of 12 possible CASV reactions, which are labelled using the absent-phase notation of Zen (1966). The next sections interpret the reaction textures observed in coronitic calc-silicates from the Nemesis Glacier region in terms of these CASV reactions. The effects of clinopyroxene and non-CASV components on the equilibria are considered in Sections 7.4.4 and 7.5.4.

7.4.2 Garnet coronas

The formation of garnet rims separating scapolite from calcite in assemblage A1 is consistent with progress of the CASV model decarbonation reaction

scapolite + wollastonite + calcite = grossularite + CO_2 (An, Qtz).

Similarly, the formation of composite garnet-quartz coronas between scapolite and

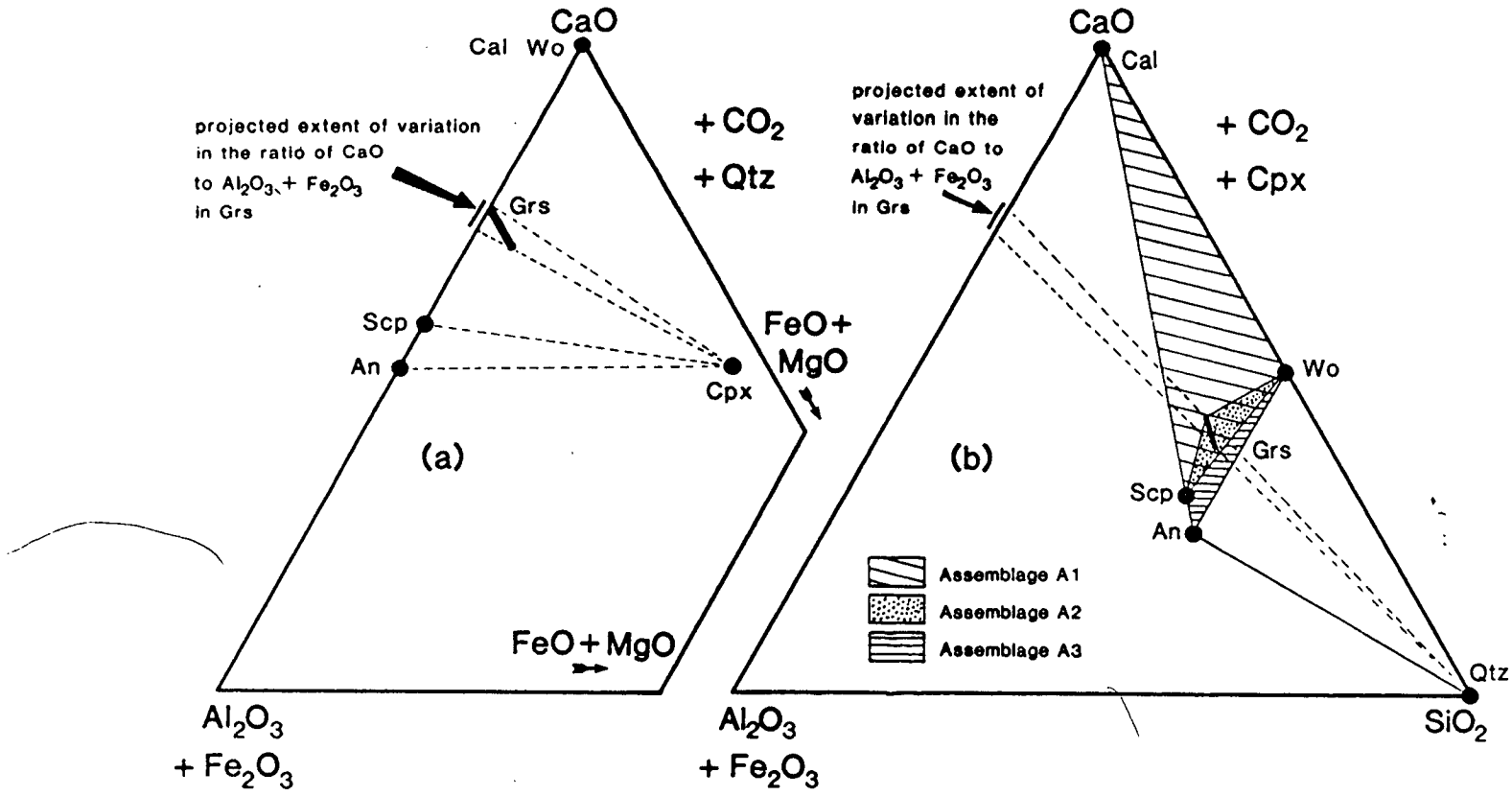

Fig. 7.9 Compatibility diagrams illustrating the chemographic relationships between calc-silicate phases projected onto (a) the CaO-(Al_2O_3+Fe_2O_3)-(FeO+MgO) plane from quartz and CO_2, and (b) the CaO-(Al_2O_3+Fe_2O_3)-SiO_2 plane from clinopyroxene and CO_2. Wollastonite, calcite, scapolite and anorthite are treated as pure CaO-Al_2O_3-SiO_2 phases, whereas clinopyroxene and grossularite exhibit some deviation from their ideal formulas. The Al_2O_3 and Fe_2O_3 content of clinopyroxene causes it to be displaced from the pure CaO-FeO-MgO-SiO_2 composition, and grossularite is plotted as a line, reflecting the variable extent of pyrope, and particularly almandine, content. The extent of variation in the ratio of CaO to (Al_2O_3+Fe_2O_3) in garnet, projected from quartz, clinopyroxene and CO_2, is depicted in both diagrams. The most almandine-rich garnet, and therefore the least calcic, plots rather close to the scapolite-wollastonite tie line in projection (b), which also depicts the chemographic relationships between assemblages A1, A2 and A3.

wollastonite in assemblages A1, A2, A3 and A4 is consistent with progress of the CASV model decarbonation reaction

scapolite + wollastonite = grossularite + quartz + CO_2 (An, Cal),

and the growth of garnet-quartz coronas between plagioclase and wollastonite in assemblage A3 is consistent with progress of the CASV model reaction

wollastonite + anorthite = grossularite + quartz (Scp, Cal, V).

The consistent spatial distribution of retrograde garnet and quartz in the composite coronas implies a strong kinetic control, which is imposed by the relatively low diffusivity of aluminium and silicon from the reactant phases to the products.

7.4.3 Mineral symplectites and intergrowths

The formation of calcite-quartz intergrowths within wollastonite grains, partially enclosed by garnet coronas, is consistent with wollastonite breakdown via the CASV model reaction

wollastonite + CO_2 = calcite + quartz (An, Scp, Grs).

This reaction must post-date the reaction of wollastonite to produce garnet coronas via the (An, Qtz), (An, Cal) or (Scp, Cal, V) reactions.

The development of calcite-anorthite symplectites within scapolite grains enclosed by garnet rims is consistent with scapolite breakdown via the CASV reaction

scapolite = anorthite + calcite (Wo, Qtz, Grs, V).

The presence of quartz within these symplectites implies an excess of silica in the scapolite with respect to plagioclase. This reflects the relatively sodic composition of scapolite, and calcic composition of plagioclase.

7.4.4 The role of clinopyroxene and non-CASV components

The involvement of clinopyroxene in the formation of garnet coronas transforms the univariant CASV equilibria responsible for the coronas into multivariant equilibria in more-complex systems such as CaO-MgO-FeO-Fe_2O_3-MnO-Al_2O_3-SiO_2-CO_2. These equilibria are of the form:

$$\text{clinopyroxene}_{(ss)} + \text{scapolite} + \text{wollastonite} + \text{calcite} = \text{garnet}_{(ss)} + CO_2,$$
$$\text{clinopyroxene}_{(ss)} + \text{scapolite} + \text{wollastonite} = \text{garnet}_{(ss)} + \text{quartz} + CO_2 \quad \text{and}$$
$$\text{clinopyroxene}_{(ss)} + \text{wollastonite} + \text{anorthite} = \text{garnet}_{(ss)} + \text{quartz},$$

where $Grt_{(ss)}$ and $Cpx_{(ss)}$ are complex solid solutions. The multivariance introduced into CASV reactions by the diopside-hedenbergite components of clinopyroxene are considered in some detail by Harley and Buick (1991). The variable proportions of

ferrous iron, magnesium and manganese incorporated into garnet cause the garnet compositions on Fig. 7.9a to plot as a line of constant aluminium and ferric iron content from the pure grossularite-andradite composition. This reflects the substitution of almandine, pyrope and spessartine for grossularite. This substitution causes the garnet composition on Fig. 7.9b to plot as a line of constant aluminium plus ferric iron to silicon ratio, extending to less calcic compositions from the pure grossularite-andradite formula. In this study, the garnets with the largest deviation from a pure grossularite-andradite solid solution (specimens 89/55C and 89/55D) plot rather close to the scapolite-wollastonite tie line. This accounts for the apparent scarcity of quartz in garnet ± quartz coronas developed between wollastonite and scapolite in these two specimens, compared with similar coronas in the other specimens in which garnet compositions more closely approach that of a pure grossularite-andradite solid solution. The closer the garnet composition plots to the scapolite-wollastonite tie line, the less quartz is required to replace wollastonite and scapolite. If the garnet composition plotted exactly on the tie line, then no quartz would be produced during progress of the reaction.

The mineral-chemical relationships outlined above imply that ferric iron is the species most easily incorporated from clinopyroxene into retrograde garnet. The loss of ferri-tschermaks component from clinopyroxene to garnet is a particularly important observation: if the andradite component of the retrograde garnet is not derived from a ferri-tschermaks component in clinopyroxene, some other source of ferric iron is required. No other phases with significant ferric iron contents have been identified in the specimens from the Nemesis Glacier region, which would mean that either some unidentified ferric phase, such as magnetite, was involved in corona formation but has since disappeared, or ferric iron was produced by oxidation of the substantial ferrous iron content of the clinopyroxene. The latter case has been inferred for calc-silicate lithologies with no apparent direct source of ferric iron (Sivaprakash, 1981, Harley & Buick, 1991).

7.5 PETROGENETIC GRIDS

7.5.1 Introduction

Various petrogenetic T-a_{CO2} (Figs 7.10, 7.11, 7.12, 7.13) and P-a_{CO2} grids (Figs 7.14, 7.15, 7.16) have been constructed for the phases grossularite, scapolite, wollastonite, calcite, quartz, anorthite and CO_2, using the computer program THERMOCALC, which is based on the internally-consistent thermodynamic data set of Holland and Powell (1990). Only the system CaO-Al_2O_3-SiO_2-CO_2 (CASV) has been considered, in effect projecting all phases from clinopyroxene and ignoring the role of

clinopyroxene in the reactions. T-a_{CO2} and P-a_{CO2} grids have been constructed rather than a P-T grid because calc-silicate reactions are very sensitive to fluid composition, and the activity of CO_2 is used, rather than mole fraction of CO_2 in a fluid phase, so that the grids remain applicable under fluid-absent conditions (Powell, 1983*a*; see Section 6.3.3). The isobaric T-a_{CO2} and isothermal P-a_{CO2} grids were calculated at pressures and temperatures in agreement with the thermobarometric estimates for peak metamorphic conditions in the Nemesis Glacier region, derived in Chapter 5. Wollastonite, calcite and quartz are taken as pure, as is anorthite since plagioclase activity models give anorthite activities very close to unity for plagioclase with greater than 95 mole per cent anorthite. Activities of grossularite in garnet, and meionite in scapolite, are calculated from typical analytical data.

7.5.2 Activity models for grossularite and scapolite

The activity-composition relationships used for garnet and scapolite are the same as used by Harley and Buick (1991) to derive CASV grids for calc-silicate rocks from the Rauer Group of East Antarctica. The grossularite-andradite activity model has been taken from Engi and Wersin (1987), who treat grossularite-andradite as an asymmetric sub-regular solution which has a strong positive deviation from ideality at grossularite-rich compositions. However, there are errors in the final activity-composition equations given in Engi and Wersin (1987), which were corrected before being used here (see Appendix 4.2). The effect of the almandine component has been approximated with the assumption that the mixing behaviour of almandine in a grossularite-andradite garnet is identical to the behaviour of almandine in a grossularite garnet, using a grossularite activity coefficient of 1.04 which is consistent with the recent work of Koziol (1990). Pyrope and spessartine have been treated as inert diluents.

Scapolite activities have been calculated using the model of Oterdoom and Gunter (1983), which assumes a high state of aluminium-silicon disorder and uses the data of Goldsmith and Newton (1977) for the positioning of the breakdown of meionite to anorthite and calcite. This model predicts a negative deviation from ideal behaviour. The recent activity models of Moecher and Essene (1990) also imply a high level of disorder, but use the alternative scapolite-breakdown data of Huckenholz and Seiberl (1990), which occurs some 75°C below the Goldsmith and Newton (1977) model. The activity model of Moecher and Essene (1990) predicts a positive deviation from ideality for scapolite at high temperatures, but yields activities greater than one for some scapolite compositions at temperatures relevant to the Nemesis Glacier region, confirming that it is unsuitable for high-temperature scapolite (Moecher & Essene, 1990, p. 1018).

7.5.3 Selected compositions and derived activities

The garnet activity model is virtually independent of temperature, but the scapolite activity model is temperature dependent and the T-a_{CO2} grids have been calculated for a variable activity of scapolite at fixed composition. All the specimens show different ranges in grossularite and meionite contents (Table 7.3), but specimens 89/93, 89/334C, 89/334F, 89/334G and 89/334H (i.e. assemblages A1 and A4) have similar ranges, and a grossularite activity of 0.95 and a meionite activity of 0.55 at 800°C (equivalent to an X_{grs} of about 0.90 and an EqAn of about 77) have been taken to represent all these specimens. A grossularite activity of 0.80 and a meionite activity of 0.60 at 800°C (X_{grs} about 0.80 and EqAn about 0.79) have been used for specimen 89/55C. A grossularite activity of 0.80 has been used for specimen 89/55D, but with a meionite activity of 0.80 at 800°C (X_{grs} about 0.80 and EqAn about 0.88). The use of other compositions within the observed compositional range, or different activity models for garnet and scapolite, change the positions of some of the reactions, but do not significantly affect their orientation or the grid topology. Similarly, alternative data sets (e.g. Berman, 1988) change the position of the grids in pressure-temperature-fluid space, but do not affect the topology or orientation of the reactions for the mineral-composition range considered here (see Harley & Buick, 1991). The following sections concentrate on the A1, A2 and A3 assemblages, since the high-variance A4 assemblage imposes no extra constraints on the metamorphic history.

7.5.4 T-a_{CO2} and P-a_{CO2} grids

Fig. 7.10 is a T-a_{CO2} grid calculated at 7 kbar for assemblage A1. This pressure is considered to be an upper limit for the peak conditions, given the thermobarometric results summarized in Section 5.6.3. The grid comprises three invariant points, the [Cal], [An] and [Wo] invariant points, following the absent-phase notation of Zen (1966). The [Cal] point is constrained to lie on the isothermal (Scp, Cal, V) reaction, the [Wo] point is constrained to lie on the isothermal scapolite-breakdown (Wo, Qtz, Grs, V) reaction, and the [An] point is constrained to lie at temperatures between these two reactions. The positions of these three points at 6 kbar are also shown, to indicate the effect of variable pressure within the pressure range indicated by the thermobarometric study of the area (see Section 5.6.3). The position of the (Wo, Qtz, Grs, V) reaction, and hence the temperature of [Wo], does not change with decreasing pressure, but both [Cal] and [An] drop in temperature causing the triangle between the three invariant points to decrease in size. The triangle continues to shrink with further pressure decrease, and at some pressure below 6 kbar the topology of Fig. 7.10 becomes unstable and the grid inverts. At this pressure, [Cal], [An] and [Wo] become metastable, and [Qtz], [Grs] and [Scp] are the stable invariant points.

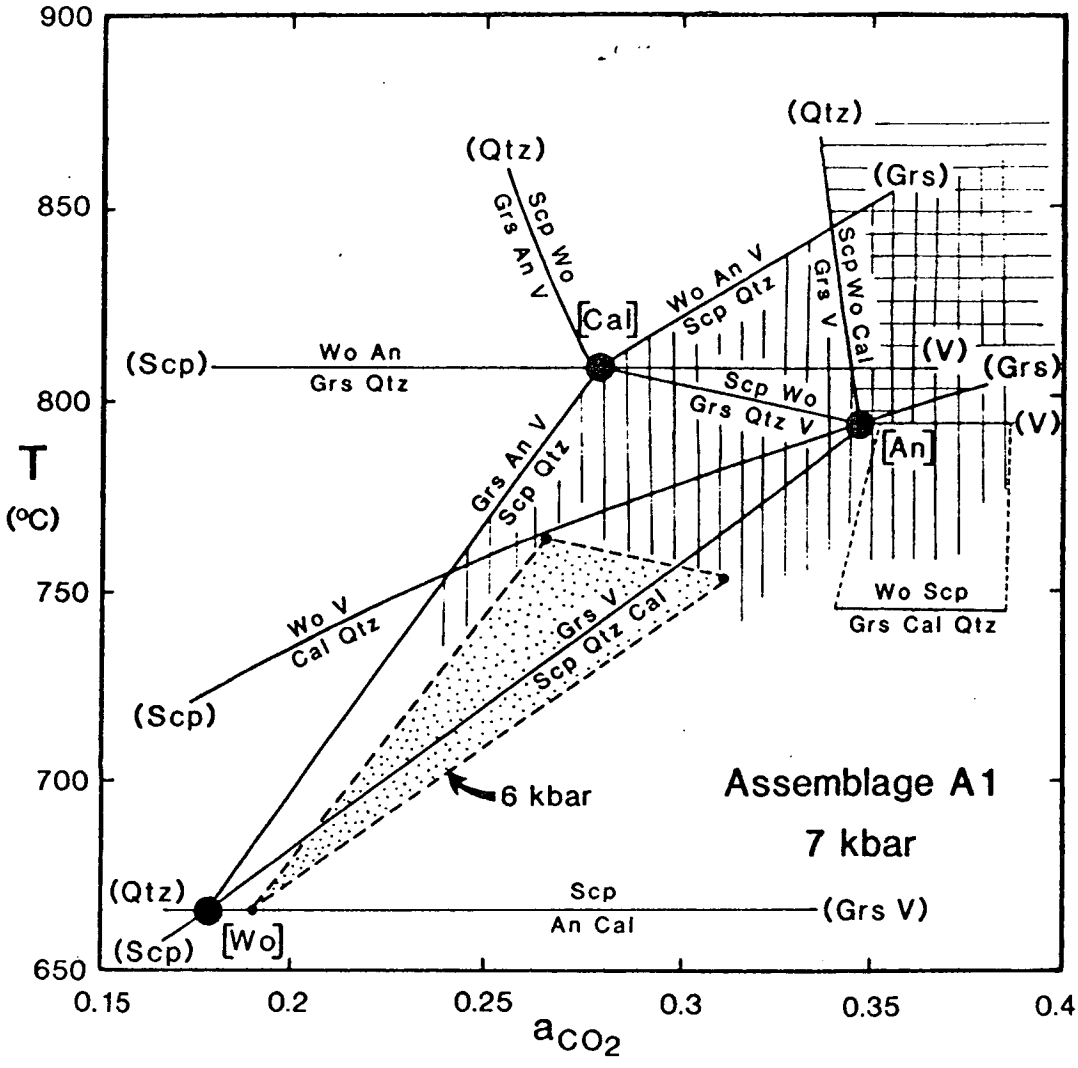

Fig. 7.10 An isobaric T-a_{CO2} reaction grid for the phases grossularite, scapolite, wollastonite, calcite, quartz, anorthite and CO_2 in the system CaO-Al_2O_3-SiO_2-CO_2, calculated at 7 kbar using reduced activities of grossularite and scapolite relevant to assemblage A1. The shaded triangle indicates the position of the three invariant points at a pressure of 6 kbar. The vertical ornament indicates the stability field of coexisting scapolite and quartz, and the horizontal ornament indicates the (An, Grs, Qtz) stability field of the prograde A1 assemblage.

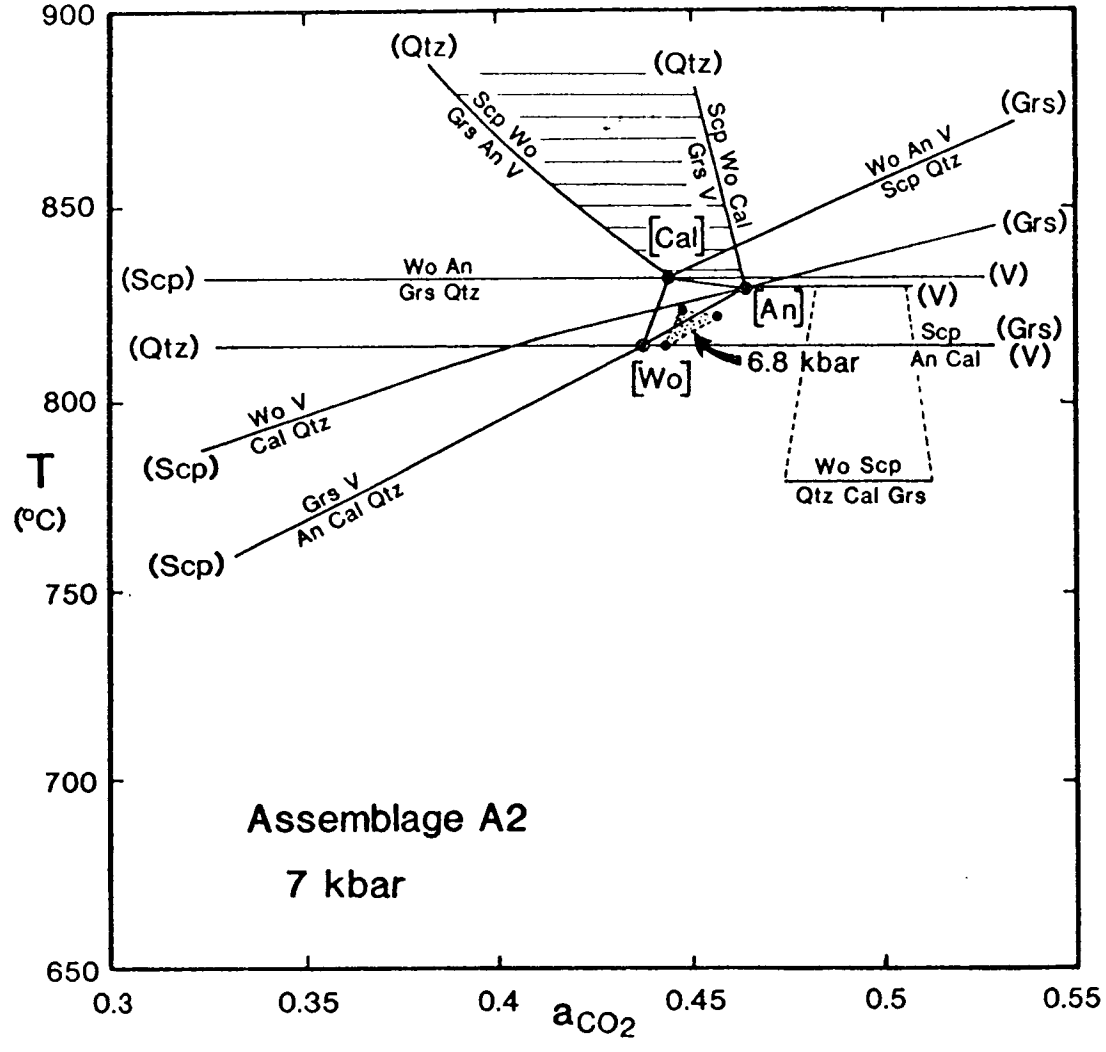

Fig. 7.11 An isobaric T-a_{CO2} reaction grid for the phases grossularite, scapolite, wollastonite, calcite, quartz, anorthite and CO_2 in the system CaO-Al_2O_3-SiO_2-CO_2, calculated at 7 kbar using reduced activities of grossularite and scapolite relevant to assemblage A2. The shaded triangle indicates the position of the three invariant points at a pressure of 6.8 kbar, and the horizontal ornament indicates the (Cal, An, Qtz) stability field of the prograde A2 assemblage.

Fig. 7.11 is a T-a_{CO2} grid calculated at 7 kbar for assemblage A2. As in the previous grid, the reactions emanate from [Cal], [An] and [Wo], which form a triangle. The topology of the two grids is identical, but in this case the (Scp, Cal, V) reaction occurs at a higher temperature on account of the lower grossularite activity, and the (Wo, Qtz, Grs, V) reaction occurs at a much higher temperature on account of

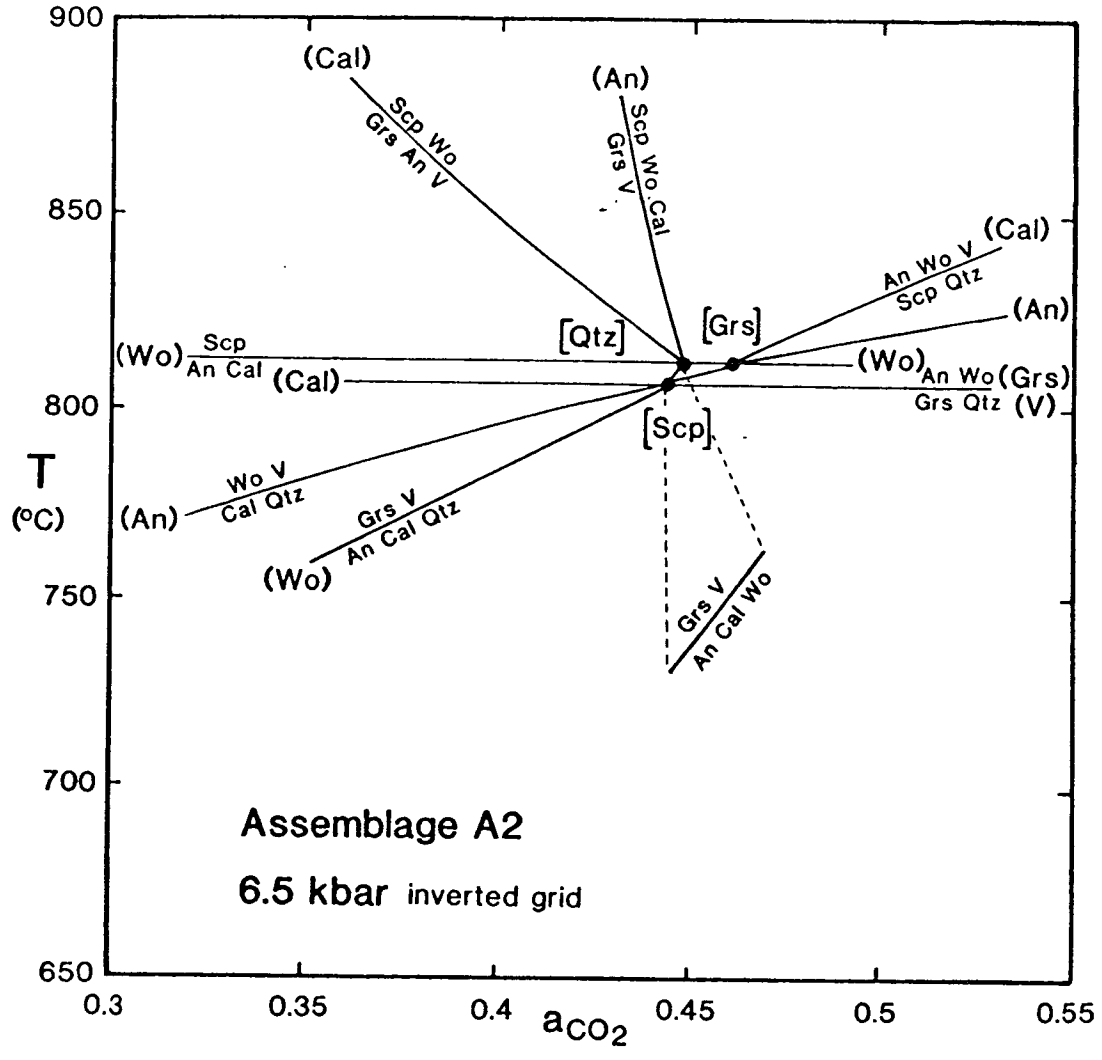

Fig. 7.12 An isobaric T-a_{CO2} reaction grid for the phases grossularite, scapolite, wollastonite, calcite, quartz, anorthite and CO_2 in the system CaO-Al_2O_3-SiO_2-CO_2, calculated with the same activity data as Fig. 7.11, but at a pressure of 6.5 kbar.

the higher meionite activity. This causes the triangle of invariant points to be much smaller at 7 kbar than in Fig. 7.10, and hence this grid inverts at a higher pressure than the grid for assemblage A1. The position of the triangle is also shown for a pressure of 6.8 kbar. At 6.5 kbar (see Fig. 7.12) the grid has inverted and [Qtz], [Grs] and [Scp] are stable. Fig. 7.13 is a T-a_{CO2} grid calculated at 7 kbar for assemblage A3. The topology is identical to the other T-a_{CO2} grids, and the relatively low meionite activity means that it is possible to decrease the pressure to 6 kbar without a grid inversion taking place.

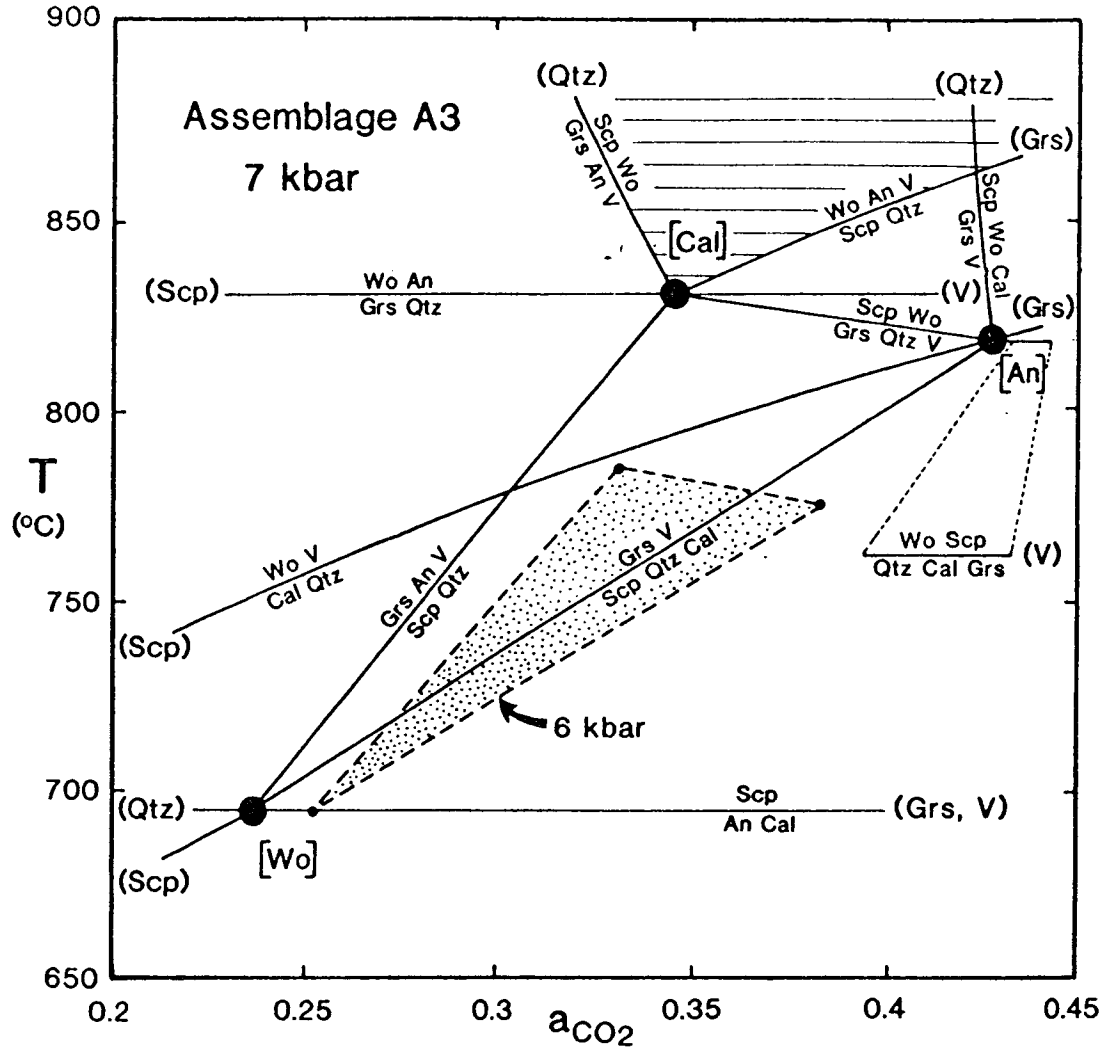

Fig. 7.13 An isobaric T-a_{CO2} reaction grid for the phases grossularite, scapolite, wollastonite, calcite, quartz, anorthite and CO_2 in the system CaO-Al_2O_3-SiO_2-CO_2, calculated at 7 kbar using reduced activities of grossularite and scapolite relevant to assemblage A3. The shaded triangle indicates the position of the three invariant points at a pressure of 6 kbar, and the horizontal ornament indicates the (Cal, Grs, Qtz) stability field of the prograde A3 assemblage.

Figs 7.14, 7.15 and 7.16 are P-a_{CO2} grids for assemblages A1, A2 and A3, calculated with the same activities as the corresponding T-a_{CO2} grids and at temperatures appropriate for the three assemblages. The temperatures used are above the scapolite-breakdown (Wo, Qtz, Grs, V) reaction, and therefore only the [Cal] and [An] invariant points are stable.

If the role of clinopyroxene in the equilibria is considered, the invariant points and univariant reactions in these grids gain one or more degrees of freedom, depending on the extra number of components considered. If just magnesium and ferrous iron are considered, which are the most abundant non-CASV components in clinopyroxene, the number of components increases to six, and univariant reactions

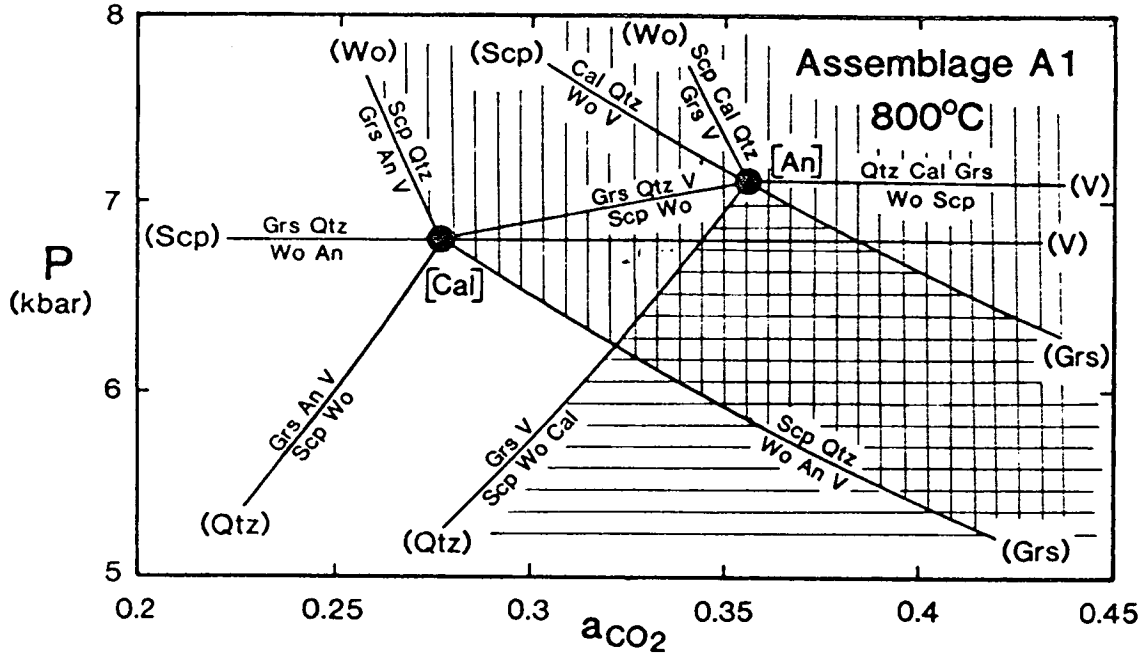

Fig. 7.14 An isothermal P-a_{CO2} reaction grid for the phases grossularite, scapolite, wollastonite, calcite, quartz, anorthite and CO_2 in the system CaO-Al_2O_3-SiO_2-CO_2, calculated at 800°C using reduced activities of grossularite and scapolite relevant to assemblage A1. The vertical ornament indicates the stability field of coexisting scapolite and quartz, and the horizontal ornament indicates the (An, Grs, Qtz) stability field of the prograde A1 assemblage.

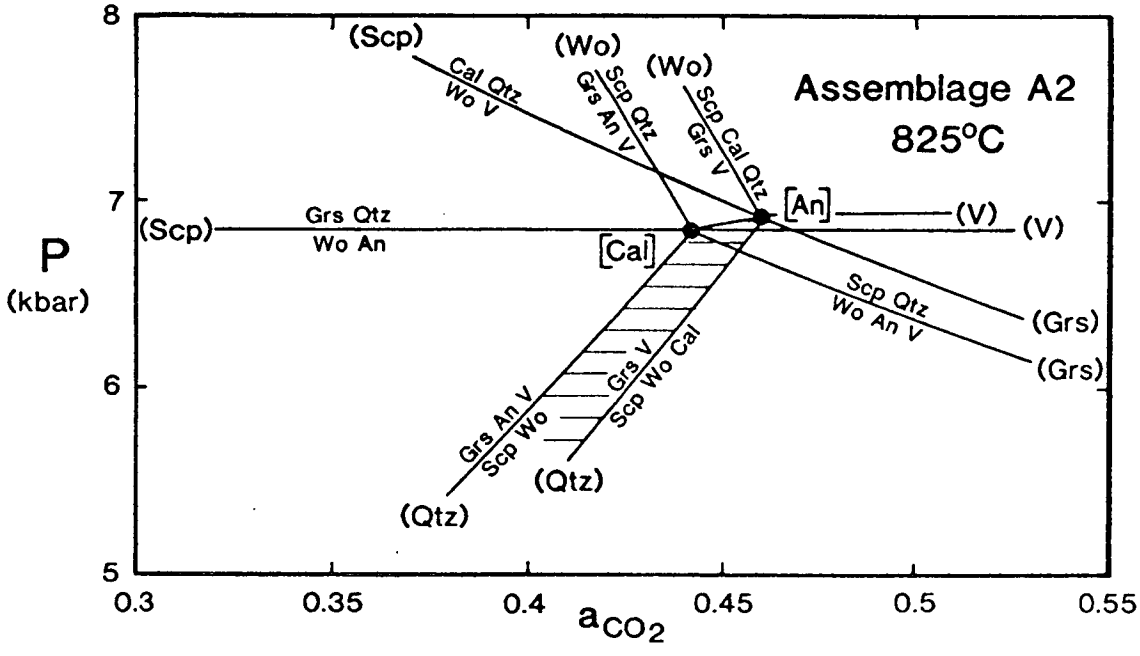

Fig. 7.15 An isothermal P-a_{CO2} reaction grid for the phases grossularite, scapolite, wollastonite, calcite, quartz, anorthite and CO_2 in the system CaO-Al_2O_3-SiO_2-CO_2, calculated at 825°C, using reduced activities of grossularite and scapolite relevant to assemblage A2. The horizontal ornament indicates the (Cal, An, Qtz) stability field of the prograde A2 assemblage.

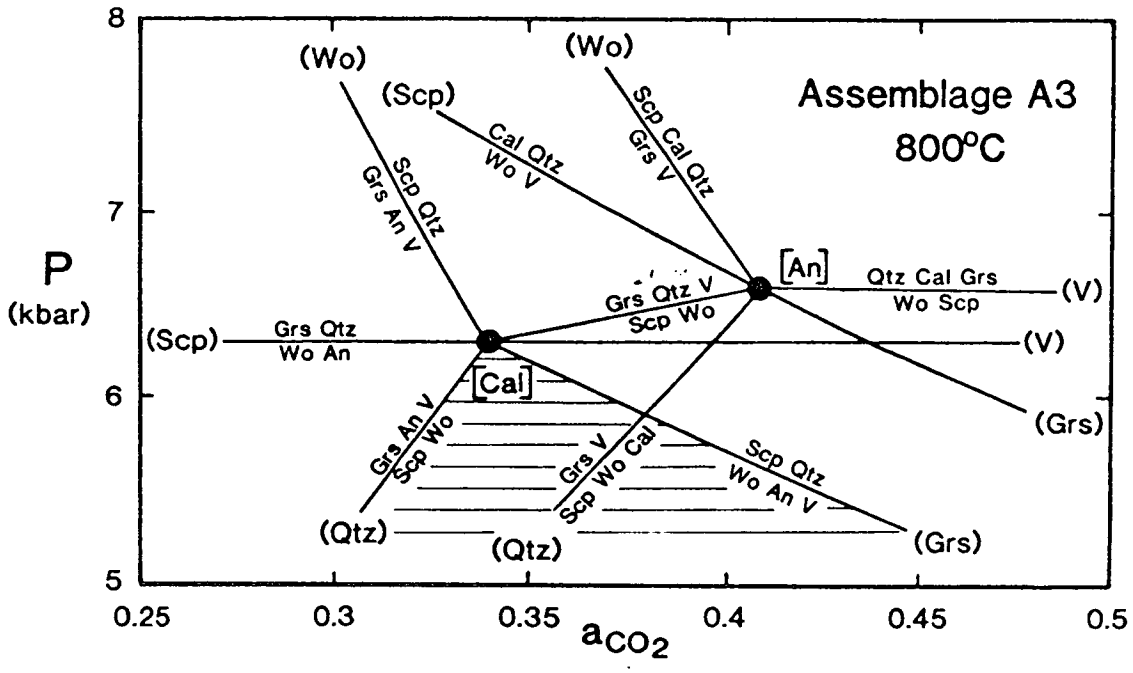

Fig. 7.16 An isothermal P-a_{CO2} reaction grid for the phases grossularite, scapolite, wollastonite, calcite, quartz, anorthite and CO_2 in the system CaO-Al_2O_3-SiO_2-CO_2, calculated at 800°C, using reduced activities of grossularite and scapolite relevant to assemblage A3. The horizontal ornament indicates the (Cal, Grs, Qtz) stability field of the prograde A3 assemblage.

comprise seven phases. Clinopyroxene-bearing analogues to the CASV univariant equilibria, such as those suggested in Section 7.4.4, comprise six phases (i.e the original five CASV phases plus clinopyroxene), and are divariant. Although magnesium and ferrous iron are the most-abundant non-CASV components in clinopyroxene, it has been shown that ferric iron is actually of more importance in the garnet-forming reactions, and hence should be included as a component. This adds another degree of freedom to all the equilibria. In a similar manner, manganese could also be considered. No matter how many extra components are considered, the invariant points and univariant reactions depicted in the petrogenetic grids are really only pseudo-invariant or pseudo-univariant respectively. This is because of the role of non-CASV components, which have been partially accommodated by using reduced activities of meionite and grossularite.

7.6 THE P-T-aCO_2 EVOLUTION OF THE CALC-SILICATE

7.6.1 Constraints on the peak metamorphic P-T-fluid conditions

The absolute P-T-a_{CO2} values indicated by the reaction grids are subject to significant uncertainties derived from the following:

(i) experimental error inherent in the thermodynamic data set,

(ii) compositional variability in the specimens

(iii) analytical error, and

(iv) errors in the activity models chosen to calculate the grid.

This chapter is primarily concerned with the change, or direction of change, in pressure, temperature and a_{CO2} during the evolution of the Nemesis Glacier region, but the absolute values do facilitate useful comparisons with the thermobarometric study described in Chapter 5.

The peak pressures experienced by specimen 89/55D (and therefore 89/55C which is from the same locality) cannot have been much less than 6.5 kbar, since the prograde assemblage and subsequent evolution is consistent with the grid in Fig. 7.11 rather than the inverted grid of Fig. 7.12. For example, the retrograde (An, Cal) reaction, which has been identified in all seven specimens, joins the [An] and [Cal] invariant points and is not stable in the low-pressure grid. Most of the specimens containing assemblages A1 and A4 were collected from Amery Peaks Massif, some 35 km from specimens 89/55D and 89/55C, but given that the independent thermobarometric studies failed to identify any systematic variation in pressure-temperature conditions across the area of study, it is inferred that peak pressures of 6.5 to 7 kbar are reasonable for all specimens.

The grids provide no other independent constraints on pressure, temperature or fluid composition, but if some value of pressure is chosen then the grids do impose constraints on the temperature and fluid composition, and similarly, if a value of temperature is chosen, constraints are imposed on the pressure and fluid composition. These constraints derive from the maximum possible stability field of coexisting wollastonite and scapolite, which is bounded by the following reactions:

scapolite + wollastonite = grossularite + quartz + CO_2 (An, Cal),

scapolite + wollastonite = grossularite + anorthite + CO_2 (Cal, Qtz), and

wollastonite + scapolite = quartz + calcite + grossularite (An, V).

In particular, for any given pressure, the T-a_{CO2} grids impose a minimum value for the peak temperature, which must have been above the [Cal] and [An] invariant points, and for a given temperature the P-a_{CO2} grids impose a maximum value of the peak pressure, which must have been below the [Cal] and [An] invariant points. Both T-a_{CO2} and P-a_{CO2} sections impose a minimum constraint on the peak a_{CO2}, which must have been higher than that of the (Cal, Qtz) reaction.

The stability fields of the prograde assemblages can be further constrained by considering the mineral assemblages in more detail. Assemblage A1 can be considered as the (Grs, An, Qtz) divariant assemblage, using the absent-phase notation of Zen (1966), and its stability field is hence constrained to lie between the

(An, Qtz) and (An, Scp, Grs) reactions on Fig. 7.10. However, it is possible that the assemblage was also fluid absent, and hence was actually the (Grs, An, Qtz, V) assemblage, in which case the maximum stability field is slightly larger and is bounded by the (An, Qtz) and (An, V) reactions. Similarly, assemblage A2 can be considered as either the (An, Cal, Qtz) assemblage or the (An, Cal, Qtz, V) assemblage, and is hence constrained to lie between the (Cal, Qtz), (Cal, An) and (An, Qtz) reactions or in the slightly-larger area bounded by the (Cal, Qtz), (Cal, An) and (An, V) reactions on Fig. 7.11. Assemblage A3 can be considered as the (Grs, Cal, Qtz) assemblage or the (Grs, Cal, Qtz, V) assemblage, and is constrained to lie between the (Cal, Qtz) and (Cal, Grs) reactions or the (Cal, Qtz) and (Cal, V) reactions on Fig. 7.13. The extent of the three fluid-present divariant assemblage fields, corresponding to A1, A2 and A3, are illustrated on Figs 7.10, 7.11 and 7.13 respectively. The equivalent fluid-absent fields have not been indicated since there is some evidence for a volatile fluid phase before the development of the retrograde textures (see Section 7.6.4).

The above reasoning implies that, at 7 kbar, peak temperatures are constrained to have been at least 800 to 830°C. These minimum peak-temperature estimates decrease for pressures of 6.5 kbar to between 750 and 810°C. Given these constraints, and the 700 to 800°C thermometric estimates derived in Chapter 5, it is inferred that peak temperatures were at least 750°C, and probably at least 800°C. Further constraints on the peak temperatures are provided by the scapolite-quartz units interlayered with assemblage A1. These constrain peak temperatures to have been below the scapolite-quartz stability limit defined by the reaction

$$\text{scapolite} + \text{quartz} = \text{wollastonite} + \text{anorthite} + CO_2 \qquad \text{(Cal, Grs)},$$

which occurs at temperatures below 900°C for reasonable values of a_{CO2}. Hence, notwithstanding the uncertainties in their pressure-temperature positioning, the grids are consistent with peak conditions in the upper range of the conditions derived by geothermobarometry (i.e. 6.5 to 7 kbar and 800°C).

Inferences can also be made about the nature of any peak metamorphic fluid. Soon after peak metamorphism, a_{CO2} is constrained to have been at a lower value than that of the [An] invariant point and a greater value than that of the [Cal] invariant point, since retrograde reactions between these points were crossed during the textural evolution. This translates to values of a_{CO2} between 0.44 and 0.46 in specimen 89/55D, 0.33 and 0.42 in specimen 89/55C, and 0.27 and 0.35 in the other specimens. Hence a_{CO2} values in all the specimens during the development of the reaction textures fall within the small a_{CO2} ranges in which the three invariant points occur. This suggests that the fluid composition was internally buffered along reaction

boundaries towards the invariant points before corona formation. This buffering could have occurred during the prograde evolution, or during the initial retrograde evolution before corona formation. The value of a_{CO2} at the metamorphic peak is unknown, although, as discussed above, the activity of CO_2 in all peak assemblages must have been greater than the (Cal, Qtz) reaction. If the internal buffering inferred above occurred before the metamorphic peak, then peak a_{CO2} is constrained to have been close to the invariant points, but if a_{CO2} was buffered towards these points after peak conditions, then peak a_{CO2} could have been significantly higher than a_{CO2} during the textural evolution. These two possibilities have important implications for the nature of the peak fluid regime.

(i) There cannot have been infiltration of a pervasive fluid phase after a_{CO2} was buffered towards the invariant points, unless the fluid was fortuitously of the correct composition to maintain a_{CO2} within the range of the invariant points. Hence, if a_{CO2} was buffered towards the invariant points during prograde evolution, fluid infiltration cannot have occurred during or immediately after the metamorphic peak.

(ii) If a_{CO2} was buffered towards the invariant points at the beginning of the retrograde evolution, before corona formation, a pervasive fluid phase could have been present during the metamorphic peak, but this fluid must have been expelled before the internal buffering. It is more likely that there was no pervasive fluid, and that conditions were fluid-absent or a fluid was present in sufficiently low amounts for its composition to be internally buffered by the local assemblage.

7.6.2 Factors controlling the prograde assemblage development.

Fig. 7.9 indicates that assemblages A2 and A3 can develop under the same pressure-temperature conditions in different bulk compositions. This is consistent with the development of A2 and A3 in a single zoned boudin. A2 developed at the calcium-rich boudin core, and A3 about 0.2 m out towards the calcium-poor rim. Comparison of the T-a_{CO2} and P-a_{CO2} grids for A2 and A3 indicates that both assemblages are stable over a similar pressure-temperature range, as expected given that the two assemblages equilibrated within a metre of each other, but that A2 is stable over a higher range of a_{CO2} than A3 which is consistent with local buffering of a_{CO2} values within a zoned boudin. However, it should be noted that if the uncertainties in the calculated values of a_{CO2} are considered (± 0.01 to 0.02), there is actually a small overlap between the inferred ranges of a_{CO2} for the two specimens. In contrast, Fig. 7.9 indicates that assemblage A1 is incompatible with assemblage A2. This implies that they developed at different pressure-temperature-fluid conditions or that there is some chemical difference of more subtle nature than gross zonation in

calcium, aluminium or silicon. Comparison of the T-a_{CO2} and P-a_{CO2} grids indicates that all the assemblages have similar pressure-temperature stability fields, although this does not rule out some variation, especially as A1 was not identified in close spatial association with A2 and A3. However, another important factor is that assemblages A2 and A3 were apparently developed in a relatively manganese-rich boudin. High manganese contents increase the stability field of garnet, and hence increase the stability of assemblage A2 with respect to A1.

7.6.3 Constraints on the retrograde *P-T* evolution

Fig. 7.17 illustrates the T-a_{CO2} reaction topology applicable to the assemblages discussed above, and summarizes the reaction textures in terms of vectors intersecting the CASV univariant reactions in T-a_{CO2} space. This 'composite grid' has been annotated with three sets of T-a_{CO2} vectors which indicate the reactions intersected by assemblages A1, A2 and A3 respectively, although it should be noted that the intersection of a single reaction boundary by more than one assemblage does not imply that this reaction is crossed at the same temperature by those assemblages. In fact the reactions are intersected at different temperatures because of the compositional variation between the assemblages. In all cases, the reactions are crossed from their high-temperature to their low-temperature side; hence all the reaction textures are consistent with cooling. The grid also predicts that the corona-forming reactions occur at higher temperatures than the wollastonite- and scapolite-breakdown reactions, which is consistent with the temporal relationships inferred from petrographic observations (see Section 4.2.8). The cooling interval recorded by the reaction textures is different in each assemblage. In all cases, the final record of the cooling history is the breakdown of scapolite to form plagioclase-calcite symplectites via the (Wo, Qtz, Grs, V) reaction, which occurs at different temperatures for each assemblage. The first reactions crossed by the A1, A2 and A3 assemblages were the (An, Qtz), (An, Cal) and (Scp, Cal, V) reactions respectively. Assuming a constant pressure of 7 kbar, Figs 7.10, 7.11 and 7.13 indicate that assemblages A1, A2 and A3 preserve cooling intervals of about 810 to 670°C, 830 to 810°C, and 830 to 690°C respectively. Fig. 7.18 depicts the P-a_{CO2} reaction topology, and indicates that progress of the (An, Qtz), (An, Cal), (Scp, Cal, V) and (An, Scp, Grs) reactions could also reflect a compressional path. However, some component of cooling is still required to account for scapolite breakdown via the (Wo, Qtz, Grs, V) reaction, which is effectively independent of pressure and a_{CO2}.

Other lithologies in the Nemesis Glacier region do not provide tight constraints on the pressure-temperature evolution. However, zonation profiles in garnet-orthopyroxene-plagioclase-quartz gneisses are consistent with an evolution dominated

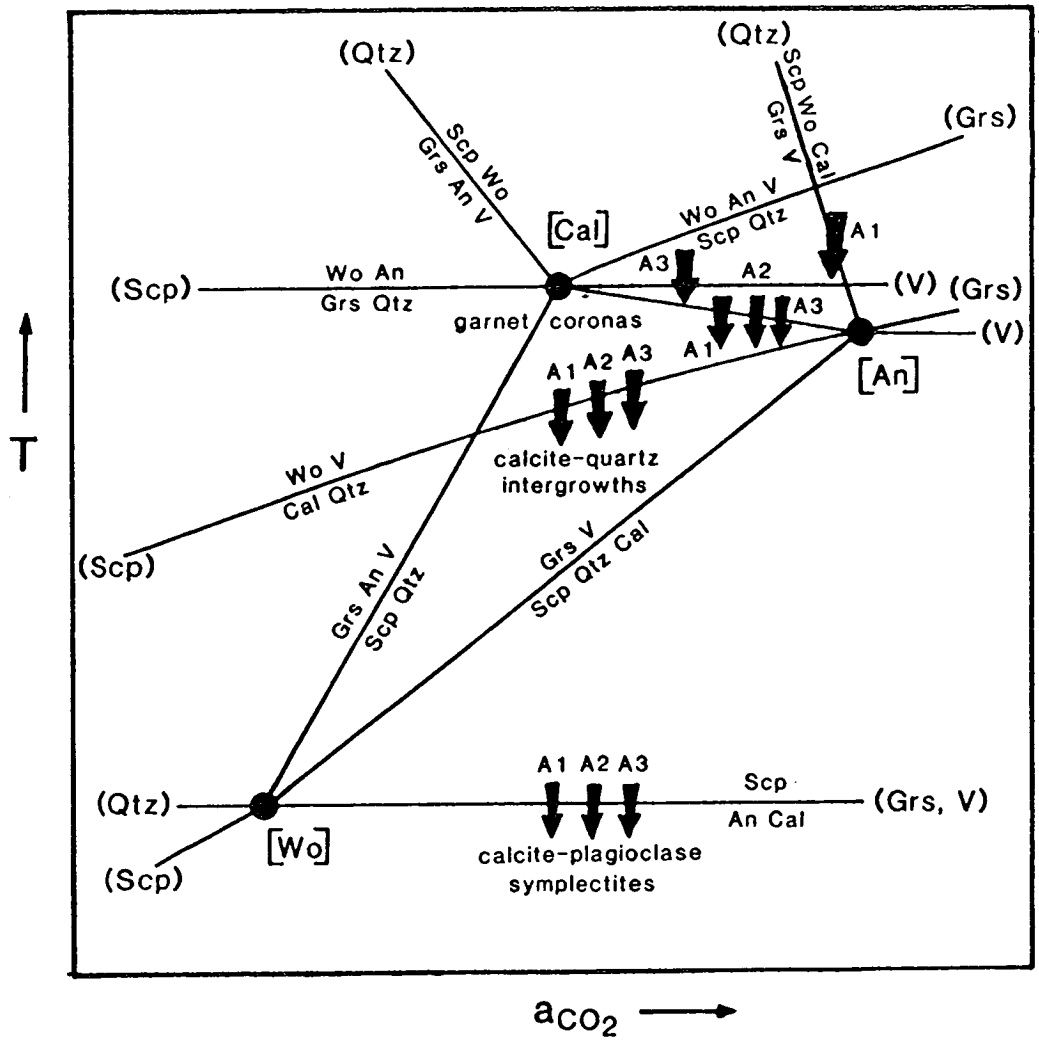

Fig. 7.17 An isobaric T-a_{CO2} grid for the phases grossularite, scapolite, wollastonite, calcite, quartz, anorthite and CO_2 in the CaO-Al_2O_3-SiO_2-CO_2 system, annotated with cooling vectors consistent with the textural evolution of calc-silicate from the Nemesis Glacier region. The disposition of the invariant points and univariant reactions is consistent with the grids calculated in this study, and the arrows represent inferred T-a_{CO2} vectors consistent with reaction textures observed in assemblages A1, A2 and A3 (n.b. the reactions occur at different T-a_{CO2} positions in different assemblages). The unlabelled reaction between [Cal] and [An] is the corona-forming reaction: Scp + Wo = Grs + Qtz + V.

by cooling (see Section 5.6.3), and cooling is the preferred origin for the observed calc-silicate textures. This does not preclude some compression during cooling, indeed, pressure-temperature paths involving a compressional component synchronous with cooling have been reported from other granulite terrains (e.g. Sandiford *et al.*, 1987; Waters, 1989; Clarke *et al.*, 1989), but all these paths are dominated by cooling. A pressure-temperature path dominated by compression would normally be associated with the prograde evolution of a metamorphic terrain, and would not be expected to accompany the cooling indicated by scapolite breakdown via the (Wo, Qtz, Grs, V) reaction, or to produce delicate corona and symplectite textures more usually associated with retrograde evolution.

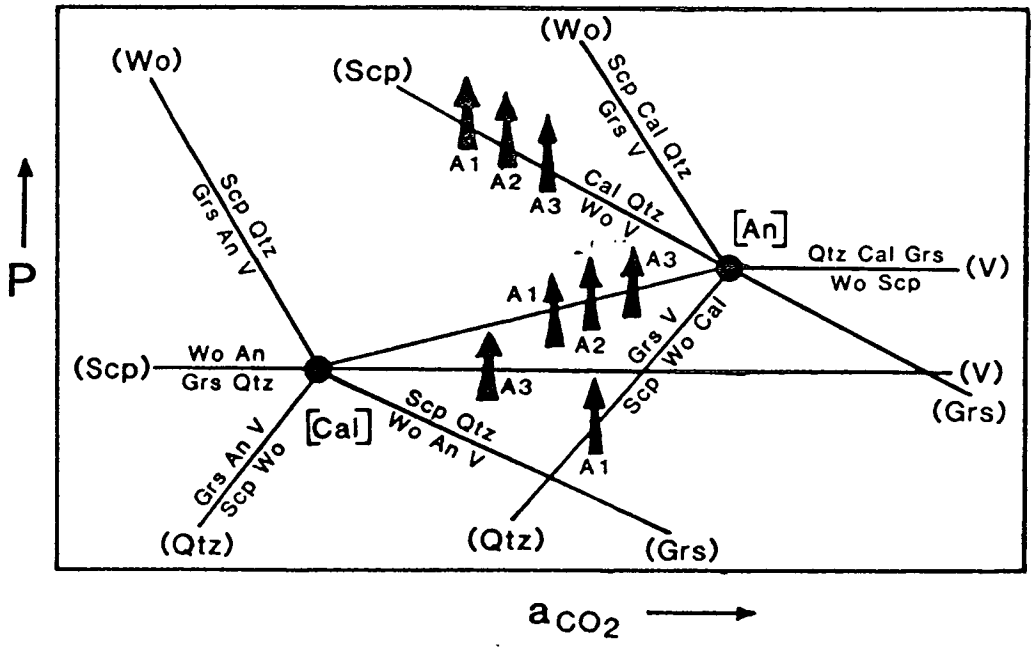

Fig. 7.18 An isothermal P-a_{CO2} grid depicting reactions between the phases grossularite, scapolite, wollastonite, calcite, quartz, anorthite and CO_2 in the system CaO-Al_2O_3-SiO_2-CO_2, annotated with compressional vectors consistent with the textural evolution of calc-silicate from the Nemesis Glacier region. The disposition of the invariant points and univariant reactions is consistent with the grids calculated in this study, and the arrows represent inferred P-a_{CO2} vectors consistent with reaction textures observed in assemblages A1, A2 and A3. As for Fig. 7.17, the reactions in this diagram occur at different positions in T-a_{CO2} space for the different assemblages. The unlabelled reaction between [Cal] and [An] is the corona-forming reaction: Scp + Wo = Grs + Qtz + V.

The textural evidence for cooling does not preclude a phase of decompression before cooling, which is a feature of many retrograde pressure-temperature paths (e.g. Schenk, 1984; Stüwe & Powell, 1989*a*), but limits on the maximum possible decompression are imposed by the P-a_{CO2} grids. The stability of wollastonite and scapolite in all prograde assemblages implies that any decompression must have commenced at pressures below the (An, V) reaction if conditions were fluid absent, or below the wollastonite-breakdown (An, Scp, Grs) reaction if a fluid was present. Further constraints exist for assemblage A1, since the stability of scapolite-quartz in adjacent layers implies that pressures are unlikely to have dropped below the (Cal, Grs) reaction. This limits any isothermal decompression to less than 1 kbar (see Fig. 7.14), if the decompression occurred at a_{CO2} values close to the [An] invariant point, which is likely given the subsequent textural development and the lack suitable reactions to buffer fluid composition towards [An] during the decompression or cooling. Hence a cooling path with little or no preceding decompression is the preferred evolution for the calc-silicate rocks from the Nemesis Glacier region.

7.6.4 Constraints on the retrograde fluid conditions

The activity of CO_2 during the retrograde textural evolution is constrained to have been between the [Cal] and [An] invariant points for each assemblage. It follows that the reactions cannot have been driven by fluid infiltration, since this range of a_{CO2} values is rather narrow and whereas the corona-forming (An, Qtz) and (An, Cal) reactions proceed with decreasing a_{CO2}, wollastonite breakdown via the (An, Scp, Grs) reaction proceeds with increasing a_{CO2}, and the corona-forming (Scp, Cal, V) reaction and scapolite-breakdown (Wo, Qtz, Grs, V) reaction are independent of fluid composition.

A remaining question is the pervasiveness of the fluid phase during textural evolution. Fluid must have been present for at least part of the evolution, since the corona-forming reactions all produce CO_2. The ubiquity of garnet coronas also indicates that there must have been a mixed-volatile fluid present before corona formation. If no species other than CO_2 were present, the liberation of CO_2 as the corona-forming reactions were intersected would have instantaneously driven a_{CO2} values away from the corona reactions to a value of unity, and garnet coronas would not have developed to any great extent. Similarly, if a volatile component other than CO_2, presumably H_2O, was present before corona formation, CO_2 must also have been present in sufficient amounts to achieve the non-zero a_{CO2} values required to intersect the corona reactions.

Evidence for the fluid regime during the textural evolution is provided by wollastonite-breakdown textures. Breakdown of wollastonite to form calcite-quartz intergrowths via the (An, Scp, Grs) reaction consumes CO_2, and the limited occurrence of this texture could reflect a limited supply of CO_2-bearing fluid phase, although it could also reflect the shielding effect of the garnet coronas. Less-equivocal evidence for a limited fluid supply comes from the complete absence of garnet breakdown via the CASV reaction

grossularite + CO_2 = scapolite + quartz + calcite (Wo, An),

which should have been intersected by all the assemblages. Unlike the breakdown of wollastonite, there are no kinetic barriers to impede the progress of this reaction, since the garnet occurs along grain boundaries where it is relatively accessible to a fluid phase. The absence of garnet breakdown via the (Wo, An) reaction is believed to indicate that the CO_2 present initially in the fluid phase, plus that CO_2 liberated by the corona-forming (An, Qtz) and (An, Cal) decarbonation reactions, was largely consumed during localized wollastonite breakdown via the (An, Scp, Grs) reaction. This would tend to decrease a_{CO2} values, and if all the CO_2 was consumed, a_{CO2} would approach zero. This would not preclude the subsequent breakdown of scapolite

via the (Wo, Qtz, Grs, V) reaction, since this reaction does not require the presence of a fluid phase, and occurs at all values of a_{CO2}. If this model is correct, and CO_2 was largely consumed by reaction with wollastonite, large volumes of fluid are precluded during the textural evolution given the limited extent of wollastonite breakdown (assuming a closed system).

Further evidence for a non-pervasive fluid comes from spatial variation in volatile activities. Figs 7.11 and 7.13 indicate that specimens 89/55C and 89/55D were in equilibrium with different values of a_{CO2} during corona formation, despite having been about 0.2 m apart. However, some overlap is possible if the uncertainty in the T-a_{CO2} positioning of the reactions is taken into account. Further evidence of volatile-activity variation comes from consideration of volatile activities in the felsic and semi-pelitic units adjacent to calc-silicate boudins. Values of a_{H2O} in the host lithologies can be calculated via the equilibrium

$$\text{biotite} + \text{quartz} = \text{orthopyroxene} + \text{K-feldspar} + H_2O$$

(Hansen *et al.*, 1984; Schreurs & Westra, 1986; Edwards & Essene, 1988). All of these phases are present in the semi-pelite specimens used for thermobarometric study in Chapter 5. Much of the biotite is inferred to be retrograde, but calculations using this assemblage still impose constraints on a_{H2O} provided that the biotite was in equilibrium with orthopyroxene, K-feldspar and quartz. Typical compositions of biotite, orthopyroxene and K-feldspar in eight semi-pelite specimens from the Nemesis Glacier region were converted into activities of annite, ferrosilite and orthoclase using the solution models detailed in Table 7.5, and values of a_{H2O} were derived from the equilibrium curves of Edwards and Essene (1988, fig. 9) using an equilibrium constant of 1.2. This value of the equilibrium constant is consistent with peak pressure-temperature conditions relevant to the Nemesis Glacier region (7 kbar, 800°C). The use of peak temperatures maximizes a_{H2O}, since the equilibrium constant is lower at lower temperatures, and the calculated value of a_{H2O} is proportional to the equilibrium constant. The calculated values of a_{H2O} are summarized in Table 7.5, and vary between 0.1 and 0.5, with most values less than 0.35. Specimen 89/334J was collected within one metre of the calc-silicate boudin from which specimens 89/334C, F, G and H were collected, and the calculated a_{H2O} value for this specimen is 0.12. Since both H_2O and CO_2 show positive departures from ideality, the sum of activities of H_2O and CO_2 for any free fluid phase should be greater than unity, provided that no species other than H_2O and CO_2 are significant. Hence the value of a_{H2O} calculated for specimen 89/334J implies that a_{CO2} in the semi-pelite must have been greater than 0.88. This is incompatible with a_{CO2} in the calc-silicate boudin, less than a metre away, which is constrained to have been between 0.27 and 0.35 for specimens

Table 7.5 Estimates of a_{H2O} in semi-pelite assemblages using the biotite-quartz-orthopyroxene-K-feldspar-H_2O equilibrium, as calibrated by Edwards and Essene (1988).

	biotite				Kfs			Opx	H_2O
	X_K	$X_{Fe^{vi}}$	X_{OH}	a_{ann}	X_{ab}	X_{or}	a_{or}	a_{fs}	a_{H2O}
89/2	0.984	0.295	0.826	0.017	0.09	0.90	0.90	0.42	0.31
89/40	0.992	0.389	0.835	0.041	0.09	0.91	0.91	0.49	0.46
89/59	0.991	0.331	0.919	0.030	0.09	0.91	0.91	0.45	0.43
89/63	0.991	0.437	0.772	0.049	0.08	0.92	0.92	0.58	0.33
89/71	0.978	0.259	0.774	0.010	0.08	0.92	0.92	0.39	0.22
89/106	0.991	0.297	0.787	0.016	0.10	0.90	0.90	0.46	0.22
89/108	0.988	0.277	0.756	0.012	0.04	0.95	0.95	0.48	0.14
89/334J	0.989	0.278	0.626	0.008	0.05	0.95	0.95	0.44	0.12

The values of a_{H2O} were all calculated for $K = 1.2$, where K is the equilibrium constant for the reaction $KFe_3Si_3AlO_{10}(OH)_2 + 3\ SiO_2 = 3\ FeSiO_3 + KAlSi_3O_8 + H_2O$ and equal to $(a_{or}\ a_{fs}^3\ a_{H2O}) / a_{ann}$. Mixing models are taken from Edwards and Essene (1988): values of a_{fs} are taken as equivalent to $X_{Fe^{vi}}$ (i.e. Fe / (cation total - Si - Al^{iv}), a_{or} is calculated using the activity model of Haselton *et al.* (1983) which is summarized in Appendix 4.3, and a_{ann} is taken as the product of X_K, $(X_{Fe^{vi}})^3$ and $(X_{OH})^2$ (i.e. for a biotite formula normalized to a total of seven cations in the octahedral and tetrahedral sites). N.b. For consistency with the calculations in Edwards and Essene (1988), these calculations were performed using formula units of orthopyroxene and biotite which are half the size of the formula units used for these phases elsewhere in this thesis. The mineral analyses from which the activities are calculated are tabulated in Appendix 3.4, and compositional parameters are as defined in Appendix 3.3.

89/334C, F, G and H, during the retrograde textural evolution. It follows that the two units cannot have been in equilibrium with a single pervasive fluid, and that volatile activities were heterogeneous on a metre scale (Valley *et al.*, 1983*a*; Valley, 1985).

The localized control of volatile activities implies that the retrograde textural evolution of the calc-silicate involved buffering of a_{CO2} along reaction boundaries. No attempt is made here to illustrate such buffering paths on a T-a_{CO2} grid, since several such paths can be drawn for each assemblage and the available textural data cannot be used to distinguish between them. In particular, it is impossible to determine whether the buffering paths intersected the pseudo-invariant points, or if progress of each reaction was terminated by kinetic barriers imposed by corona growth. Perhaps the most-likely candidate for reaction at an invariant point is assemblage A3. Cooling from the stability field of the prograde A3 assemblage requires intersection with the (Cal, Qtz) or (Cal, Grs) reaction boundaries, or the [Cal] invariant point (see Fig. 7.13). Given that there is no evidence for progress of the (Cal, Qtz) or (Cal, Grs) reactions, it might seem likely that the activity of CO_2 was fortuitously equal to that of the [Cal] invariant point. However, it is equally likely that the (Cal, Qtz) or (Cal,

Grs) reaction boundaries were intersected, to produce grossularite and anorthite, and scapolite and quartz respectively, but that the resultant textures were destroyed during subsequent reaction. Assemblage A3 does preserve textural evidence for progress of the (Cal, Scp, V) and (Cal, An) reactions, which involve consumption of anorthite and scapolite, and the formation of grossularite and quartz. It is quite possible that progress of these reactions would conceal any evidence for earlier progress of the (Cal, Qtz) and (Cal, Grs) reactions.

7.6.5 The ribbed textures

As described in Section 4.2.8, some scapolite-wollastonite specimens do not preserve garnet coronas, but rather contain areas of decussate plagioclase laths separated by ribs of garnet or wollastonite which appear to be replacing scapolite (see Plates 4.6c, 4.7 and 4.8). These textures, typified by extremely elongate grains of random orientation, imply very fast growth induced by a pronounced chemical gradient, and are markedly different from the regular coronas which reflect steady growth controlled by the solid-state diffusion rates of aluminium and silicon. Since the ribbed textures involve the same phases as the corona textures, it should be possible to interpret them using the grids derived in Section 7.5.

Mineral compositions in two specimens preserving the ribbed textures were determined by electron probe microanalysis (specimens 89/217B and 89/217D), in the same manner as the coronitic specimens (described in Section 7.3.1). Compositions were found to be very similar to those in the coronitic specimens (typical analyses from these specimens are tabulated in Appendix 3.6). Plagioclase is virtually pure anorthite ($X_{an}^{Pl} = 0.95$ to 0.98), scapolite has EqAn values in the range 75 to 85, and garnet is essentially a grossularite-andradite solid solution with X_{grs}^{Grt} in the range 0.70 to 0.90 and X_{adr}^{Grt} between 0.08 to 0.28. Wollastonite is essentially pure, and all specimens contain clinopyroxene which is inferred to have been the source of the non-grossularite components in the garnet.

Inspection of Table 7.4 indicates that the only CASV reactions consistent with the replacement of scapolite by plagioclase-wollastonite and plagioclase-garnet are

scapolite + wollastonite = grossularite + anorthite + CO_2 (Cal, Qtz),
scapolite + quartz = wollastonite + anorthite + CO_2 (Cal, Grs), and
scapolite + quartz = grossularite + anorthite + CO_2 (Wo, Cal).

The first reaction proceeds with decreasing temperature, increasing pressure, or decreasing a_{CO2}, and could hence be a further manifestation of the cooling path inferred from the corona and symplectite textures. However, the second two reactions proceed with increasing temperature, decreasing pressure, or decreasing a_{CO2}. This

implies that the ribbed textures cannot have developed in response to cooling, since the (Cal, Grs) reaction is the only means of producing the wollastonite-bearing variety. Given the localized nature of the ribbed textures, which are developed within a metre of specimens preserving coronitic textures, the favoured mechanism for their development is localized water infiltration. This is consistent with the rapid growth inferred above. Both the (Wo, Cal) and (Cal, Grs) reactions involve the consumption of quartz as well as scapolite. No relict quartz was identified in the textures, but scapolite-quartz assemblages are preserved in adjacent layers, and it is assumed that quartz has been consumed during progress of the reactions. The field setting of specimens preserving the ribbed textures are not well characterized, and potential sources of the inferred hydrous fluids have not been identified. However, the channelized release of fluids on the crystallization of magmatic bodies, such as charnockite or leucogneiss, or the passage of hydrous fluids along shear zones are possibilities.

7.7 GARNET CORONAS IN CALC-SILICATE FROM OTHER TERRAINS

7.7.1 Introduction

Garnet coronas have been reported from high-grade calc-silicates of both contact and regional origin (e.g. Smyth, 1897; Drever, 1939; Parras, 1958; White, 1959; Mukherjee & Rege, 1972; Valley *et al.*, 1983*b*; Schenk, 1984; Hiroi *et al.*, 1987; Warren *et al.*, 1987; Motoyoshi *et al.*, 1991), some of which are very similar to the garnet and garnet-quartz coronas described here. Garnet coronas appear to be a common feature of granulite-facies calc-silicate, but it is only recently that any rigorous attempt has been made to interpret these reaction textures in terms of a metamorphic evolution. In particular, Schenk (1984) has described garnet coronas around scapolite in calc-silicates from Calabria, southern Italy, and Warren *et al.* (1987) and Motoyoshi *et al.* (1991) described similar textures from the Arunta Block of central Australia and the Bolingen Islands of Prydz Bay, East Antarctica respectively. Reaction textures in all three of these terrains were interpreted using grids derived from the T-X_{CO2} section of Ellis (1978), which has some crucial differences from the grids derived here. Unlike the Nemesis Glacier region, the pressure-temperature evolution of the granulites from Calabria and the Arunta Block are constrained by phase relationships in lithologies such as metabasite and metapelite, and therefore these terrains provide a good test for the general applicability of the calc-silicate grids derived here. The metamorphic history of the Bolingen Islands is less well constrained, and is not considered here.

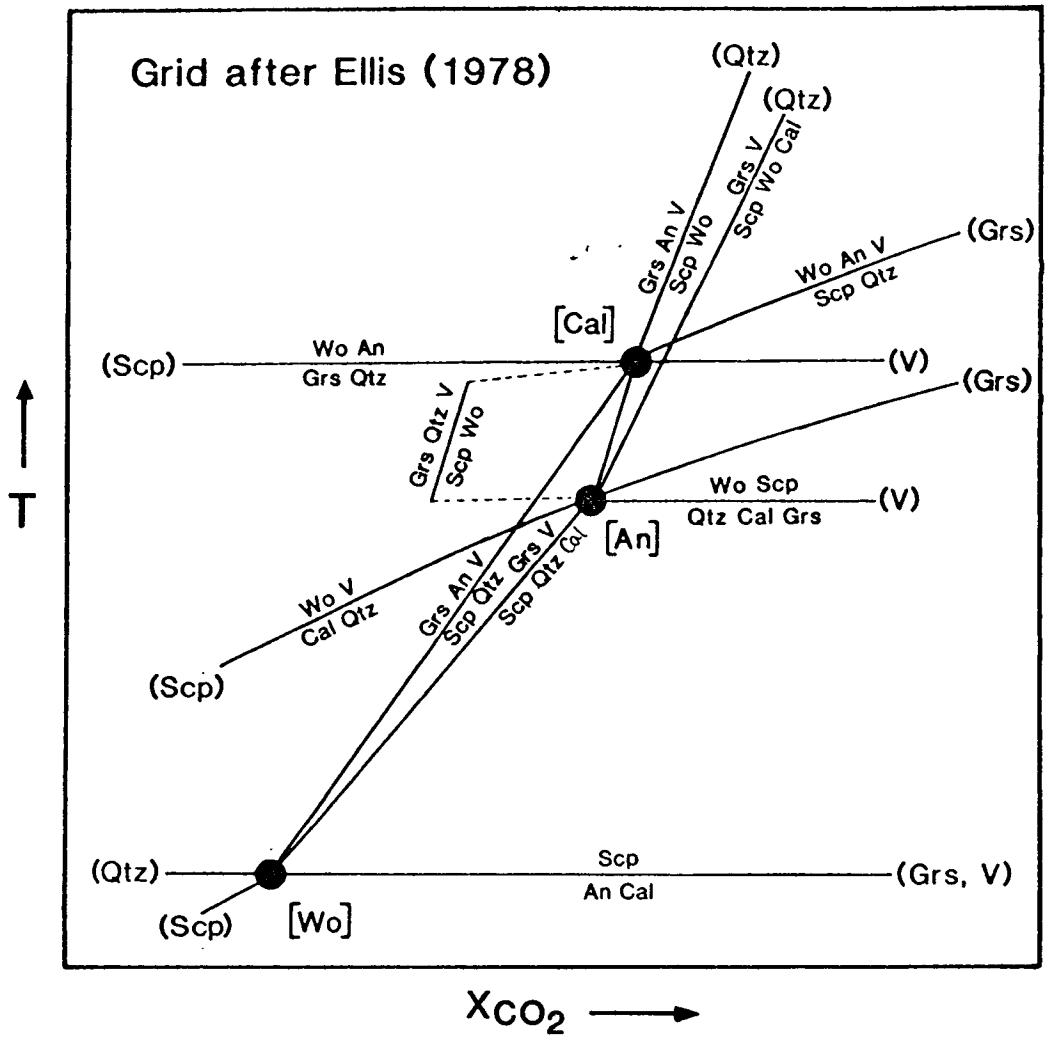

Fig. 7.19 The isobaric T-X_{CO2} grid of Ellis (1978), for the phases grossularite, scapolite, wollastonite, calcite, quartz, anorthite and CO_2 in the CaO-Al_2O_3-SiO_2-CO_2 system.

7.7.2 The reaction grid of Ellis (1978)

The high-grade calc-silicate reaction grid of Ellis (1978) is depicted in Fig. 7.19. It has many similarities with the T-a_{CO2} grid derived here and by Harley and Buick (1991), but there are some fundamental differences. Both grids hinge around the [Wo], [Cal] and [An] invariant points, and many of the reactions clustered around these points are of similar orientation in both grids. These reactions are generally those which have been studied experimentally and are relatively well calibrated:

wollastonite + CO_2 = calcite + quartz	(An, Scp, Grs),
scapolite = anorthite + calcite	(Wo, Qtz, Grs, V),
grossularite + CO_2 = calcite + anorthite + quartz	(Scp, Wo), and
wollastonite + anorthite = grossularite + quartz	(Scp, Cal, V),

which have been studied by Newton (1966), Goldsmith and Newton (1977), Gordon

and Greenwood (1971), and Greenwood (1967) and Boettcher (1970) respectively. However, there have been no experimental studies of reactions involving both scapolite and wollastonite, and it is these reactions which have different orientations in the two grids. In particular, the three scapolite-wollastonite decarbonation reactions:

scapolite + wollastonite + calcite = grossularite + CO_2 (An, Qtz),
scapolite + wollastonite = grossularite + quartz + CO_2 (An, Cal), and
scapolite + wollastonite = grossularite + anorthite + CO_2 (Cal, Qtz),

which have a negative dT/a_{CO2} or dT/dX_{CO2} in the grids derived here, have a positive dT/dX_{CO2} in the grid of Ellis (1978). Common sense predicts that decarbonation reactions should proceed with increasing temperature, and have a positive dT/dX_{CO2} as in the grid of Ellis (1978). However, from the Clausius-Clayperon equation (Equation 5.12), the orientation of any reaction in pressure-temperature space is merely a function of the entropy and volume changes associated with that reaction, and there is no *a priori* requirement that decarbonation reactions always proceed with increasing temperature. Decarbonation reactions usually proceed with increasing temperature since the entropy change of the reaction is dominated by the high entropy of CO_2, but scapolite is thought to have a high degree of aluminium-silicon disorder and hence a relatively high entropy. The entropy of scapolite can dominate the total entropy change of a decarbonation reaction, depending on the other phases and the reaction stoichiometry, since it liberates a relatively small fraction of its total formula weight as CO_2. The orientation of the scapolite-decarbonation reactions in the grids presented here is derived directly from the thermodynamic dataset of Holland and Powell (1990); their orientation in the grid of Ellis (1978) does not appear to be based on any thermodynamic or experimental data, but rather on some understandable, and incorrect, preconceptions. These decarbonation reactions produce garnet as well as CO_2, and hence their orientation in pressure-temperature-fluid space is crucial to the interpretation of many garnet-corona textures seen in granulite-facies calc-silicates.

7.7.3 Interpretation of calc-silicate reaction textures using the two grids

Schenk (1984) interprets garnet coronas around scapolite in the wollastonite-absent Calabrian calc-silicates to reflect progress of the reaction

scapolite + calcite + quartz = grossularite + CO_2 (Wo, An),

which proceeds during some combination of heating or hydration in the T-X_{CO2} grid of Ellis (1978). Given that periods of decompression and cooling have been identified in other Calabrian lithologies, Schenk (1984) invokes hydration of the calc-silicates to

explain the textures. The formation of garnet overgrowths on scapolite during water influx had previously been predicted by Aitken (1983, p. 360). The orientation of the (Wo, An) reaction in the T-a_{CO2} grid presented here is also consistent with garnet formation during heating or hydration, but Schenk did not consider the pressure dependence of this reaction. As shown in Fig. 7.18, this reaction proceeds with decompression, which is consistent with the pressure-temperature evolution recorded in other lithologies, and obviates the need to infer water influx at temperatures in excess of 750°C for which there is no apparent source (Schenk, 1984, p. 292). It is believed that the ribbed textures, described in Section 7.6.5, are far more likely to reflect water influx than garnet coronas, on the basis of their morphology as well as theoretical grid constraints. Relict wollastonite has since been identified in the Calabrian calc-silicate (V. Schenk, *pers. comm.*), suggesting that some of the garnet coronas may have formed via reaction of scapolite with wollastonite, as inferred for the textures discussed here. Hence the coronas may reflect cooling, as well as decompression, both of which are consistent with constraints from mafic granulite in the Calabrian terrain.

Warren *et al.* (1987) report retrograde garnet and garnet-quartz coronas between scapolite and wollastonite in calc-silicates from the Arunta Block of central Australia. They interpret these textures to reflect progress of the reactions:

scapolite + wollastonite + calcite = grossularite + CO_2 (An, Qtz), and
scapolite + wollastonite = grossularite + quartz + CO_2 (An, Cal).

These are the same reactions used in Section 7.4.2 to interpret the garnet coronas developed in the Nemesis Glacier region. On the Ellis (1978) T-X_{CO2} grid, these garnet-forming reactions proceed either with heating or water infiltration, and Warren *et al.* (1987) state that the reactions would also occur on decompression. The Arunta Complex has a well defined history of near-isobaric cooling following peak conditions (Warren, 1983*a*,*b*), and heating or decompression are not reasonable causes of garnet growth in the Arunta calc-silicates. This led Warren *et al.* (1987) to invoke water infiltration, on scant field evidence, as the cause of the corona textures. A shear zone within a few metres of the collected specimens was identified as a potential pathway for water-rich fluids, but no relationship was reported between the extent of corona development and distance from the shear zone. Re-evaluation of these textures using the T-a_{CO2} and P-a_{CO2} grids presented here predicts that corona formation, via the (An, Qtz) and (An, Cal) reactions, in fact proceeds with cooling, compression or water infiltration, thus enabling them to be explained by isobaric cooling. This interpretation is much more consistent with the evidence provided by other lithologies in the Arunta Block.

Hence calc-silicate reaction textures in granulites from Calabria and the Arunta Block are readily interpreted using the T-a_{CO2} and P-a_{CO2} grids developed in this chapter, and in the case of the Arunta Block this interpretation is much more consistent with other P-T data than that derived from the grid of Ellis (1978). This close agreement implies that some garnet-producing scapolite-decarbonation reactions do indeed proceed with decreasing temperature. Such a negative slope in P-T space has been recently predicted by Moecher and Essene (1990) from their theoretical treatment of thermodynamic and thermochemical data of phases in the CASV system. The Arunta Block, which preserves these decarbonation reactions in a terrain with a well documented cooling history, and presumably the Nemesis Glacier region where the metamorphic history is not as well constrained, are natural examples of decarbonation during cooling.

Part Four

Conclusions and Summary

8. Granulite stabilization in the Proterozoic Complex

8.1 INTRODUCTION

The preceding chapters have constrained the geological, structural, and metamorphic histories of the Brattstrand Bluffs coastline and the Nemesis Glacier region using a variety of observational, analytical and theoretical approaches. These histories are integrated in this final chapter, and some inferences are made about the origins of granulite metamorphism both in this high-grade terrain and in general. Section 8.2 summarizes the geological evolution of the Brattstrand Bluffs coastline, and makes comparisons with studies of other parts of Prydz Bay. Section 8.3 does likewise for the Nemesis Glacier region and other parts of the northern Prince Charles Mountains. Section 8.4 considers various tectonic models which are consistent with the pressure-temperature paths recorded in the two areas, and Section 8.5 discusses the processes responsible for the dehydration of precursor lithologies to produce anhydrous granulite assemblages. The chapter concludes with Section 8.6, which summarizes the principal results of this study, and indicates some of what are considered to be the most-promising topics for further research.

8.2 THE GEOLOGICAL HISTORY OF PRYDZ BAY

8.2.1 Introduction

The coastline of Prydz Bay is one of the most intensively-studied parts of the Proterozoic Complex of East Antarctica. Detailed structural and metamorphic studies have been published for the Larsemann Hills (Stüwe *et al.*, 1989; Stüwe & Powell, 1989*a*,*b*) and the Rauer Group (Harley, 1987*a*, 1988; Harley & Fitzsimons, 1991), which are the two largest areas of outcrop. These studies reveal a number of similarities, and it is relatively easy to correlate the geology of the Brattstrand Bluffs coastline with these other areas. This section presents a brief summary of the geological evolution of the Brattstrand Bluffs coastline, using the conclusions made in Chapters 3, 5 and 6, and then integrates this work with studies made elsewhere in Prydz Bay.

8.2.2 The evolution of the Brattstrand Bluffs coastline

The Brattstrand Bluffs coastline comprises granulite-facies gneiss and migmatite, which occur in two lithological associations. An orthogneiss association preserves high-grade structures not observed in other lithologies, but the limited occurrence of these structures, and an absence of critical mineral assemblages, preclude a quantitative investigation of these early events (MI and MII; see Section 3.5.4). A paragneiss association is interpreted as a sedimentary cover sequence deposited onto a basement consisting of the already-metamorphosed orthogneiss association. Cover and basement were tectonically interleaved and metamorphosed during a granulite-facies event at about 1000 Ma (MIII; see Section 3.5.4). Little evidence is preserved of the prograde stages of this event, but peak metamorphism was associated with partial melting and the development of a flat-lying foliation at conditions of about 6 kbar and 860°C (see Section 5.6.3). The final stages of partial melting were achieved in the absence of a volatile fluid phase. Peak metamorphism was followed by a period of decompression to pressures of about 3 kbar, with cooling to about 700°C (see Section 6.5.8). This was accompanied by the development of flat-lying folds and a penetrative flat-lying shear fabric, which are attributed to progressive non-coaxial bulk shear, and crystallization of the partial melts and release of volatile fluids (see Section 3.5.3). Subsequent evolution involved cooling and regional-scale folding, and the emplacement of a granite pluton and associated dykes. Later events are unrelated to the main Proterozoic event, and include the intrusion of planar pegmatite bodies, correlated with 770 Ma pegmatites elsewhere, and the development of mylonite zones and greenschist-facies assemblages which are attributed to localized reworking at about 500 Ma (MIV; see Section 3.5.5).

8.2.3 A correlation with other Proterozoic outcrops in Prydz Bay

This section correlates the geology of the Brattstrand Bluffs coastline with previous studies of the Larsemann Hills and the Rauer Group (see Section 2.3.9). The major correlations are illustrated in Fig. 8.1. Perhaps the most striking difference between the Rauer Group and the Larsemann Hills is that the Rauer Group is dominated by several generations of pyroxene-bearing orthogneiss (Harley, 1987*a*), whereas the Larsemann Hills are dominated by paragneiss units (Stüwe *et al.*, 1989). Two models have been proposed to account for these broad lithological differences (Sheraton & Collerson, 1983):

(i) the Rauer Group is composed of reworked Archaean material, whereas the Larsemann Hills consist entirely of Proterozoic material; and

(ii) lithologies in the Rauer Group represent an orthogneiss-dominated basement, and lithologies in the Larsemann Hills represent a cover sequence.

These models ascribe the variation in precursor composition to temporal or spatial differences respectively, and are not mutually exclusive. An Archaean component, preserving early structural and metamorphic events, has been identified in the Rauer Group (Sheraton *et al.*, 1984; Kinny & Black, 1990; see Section 2.3.9), but there is also much Proterozoic material, which, unlike the Proterozoic rocks of the Larsemann Hills, consists predominantly of orthogneiss. The paragneiss and orthogneiss associations identified in the Brattstrand Bluffs coastline are correlated with lithologies in the Larsemann Hills and the Rauer Group respectively. The favoured interpretation is that the Rauer Group consists predominantly of various basement lithologies, some of Archaean and some of Proterozoic age, and the Larsemann Hills represent a sedimentary cover sequence deposited onto the composite basement shortly before the Proterozoic metamorphic event. The Brattstrand Bluffs coastline represents the boundary zone between the basement and cover sequences, where orthogneiss and paragneiss were interleaved during the Proterozoic metamorphic event (see Section 3.5.2).

It is relatively easy to make structural correlations between the Brattstrand Bluffs coastline and the Larsemann Hills. Three deformational events have been identified in the Larsemann Hills (Stüwe *et al.*, 1989). Peak metamorphism was associated with the development of $F_{1(L)}$ folds[1] which are largely transposed by an $S_{1(L)}$ foliation. These are correlated with $F_{3(B)}$ and $S_{3(B)}$ in the Brattstrand Bluffs coastline. $S_{1(L)}$ is folded into asymmetrical, open to isoclinal, $F_{2(L)}$ folds, which are correlated with $F_{4(B)}$. An upright, southwest-plunging, regional $F_{3(L)}$ synform, which reoriented all earlier structures and fabrics, is correlated with $F_{5(B)}$. However, Stüwe *et al.* (1989) suggested that $D_{3(L)}$ and its associated metamorphic overprint were part of a 500 Ma event. The $F_{5(B)}$ antiform described in Section 3.4.6, which is of the same style, scale and orientation as $F_{3(L)}$, is cut by planar pegmatites and mylonite zones indicating an age significantly greater than 500 Ma and probably greater than 770 Ma (see Section 2.3.10). $D_{5(B)}$ and $D_{3(L)}$ are considered to have occurred relatively soon after, or during the retrograde stages of, the 1000 Ma event.

Structural correlations between the Rauer Group and outcrops further southwest are less obvious. Four ductile deformational events have been identified in the Rauer Group. $S_{1(R)}$ is a foliation in mafic granulite, which is folded by open to isoclinal $F_{2(R)}$ folds. These structures post-date orthopyroxene-bearing segregations in mafic granulite, but pre-date the formation of composite orthogneiss. $D_{1(R)}$ is similar to

---

1 In this section, the subscript (L) refers to the numbering scheme used by Stüwe *et al.* (1989) for deformational events and associated structures and fabrics in the Larsemann Hills, and (R) refers to the deformational scheme used by Harley (1987*a*) for the Rauer Group. The subscript (B) refers to the deformational scheme used in this thesis for the Brattstrand Bluffs coastline.

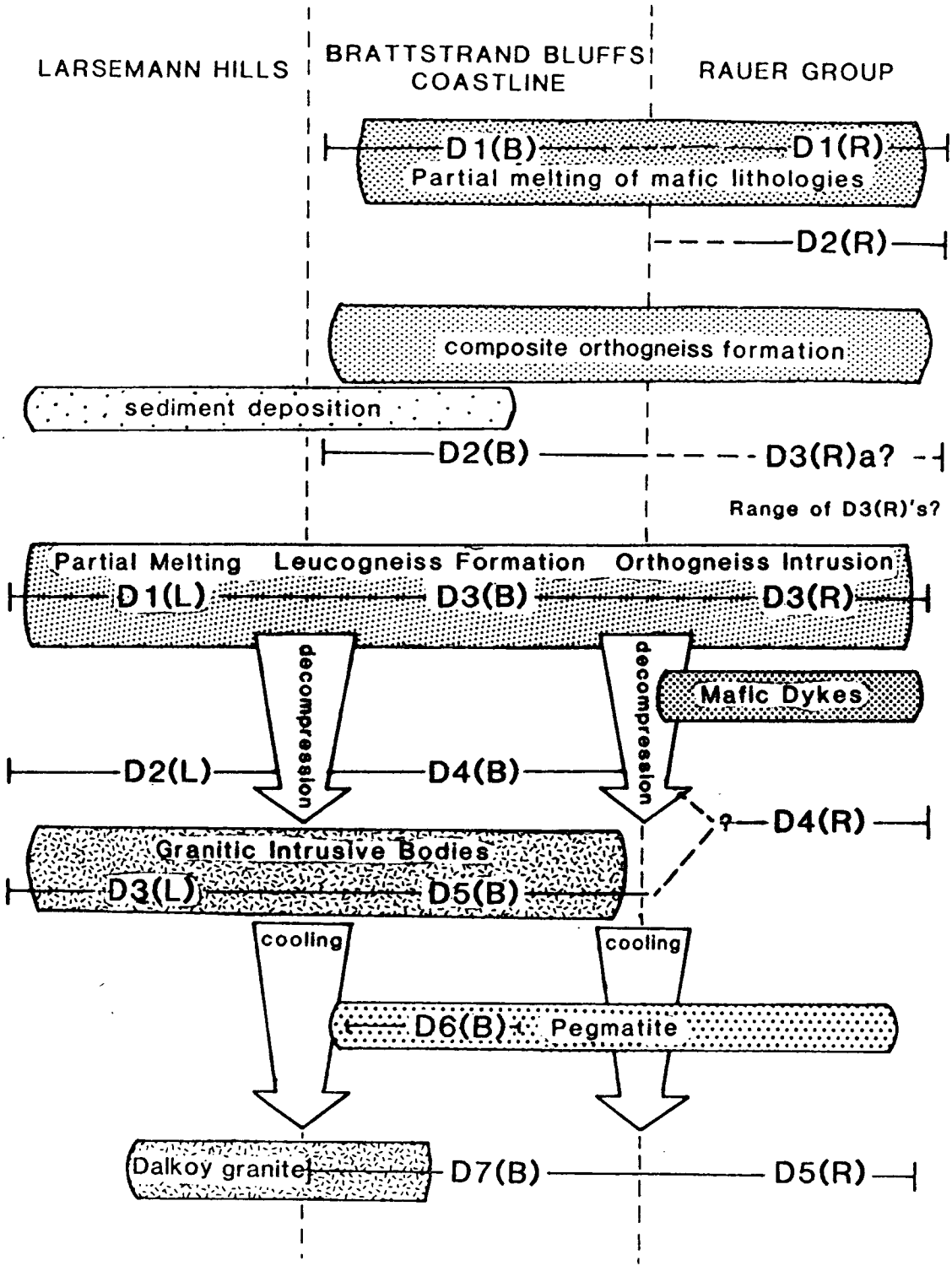

Fig. 8.1 A correlation of events identified in the Larsemann Hills (Stüwe *et al.*, 1989), the Rauer Group (Harley, 1987*a*) and the Brattstrand Bluffs coastline (this study). Pre-$D_{3(B)}$ correlations are speculative. Only the post $D_{3(R)}$ mafic dykes are shown: at least one additional dyke generation in the Rauer Group (and probably more) is thought to pre-date $D_{3(R)}$. An absolute time scale for these events is suggested in the text.

$D_{1(B)}$, but $D_{2(R)}$ cannot be correlated with $D_{2(B)}$, which pre-dates composite orthogneiss formation, unless the composite orthogneiss in the two areas are unrelated. $D_{3(R)}$ probably post-dated composite orthogneiss development and the emplacement of felsic orthogneiss, and was associated with peak Proterozoic metamorphism and the development of leucogneiss bodies. The leucogneiss bodies range from pre- to post-$D_{3(R)}$ in age, and one has been dated at 1030 Ma (Kinny & Black, 1990; see Section 2.3.9). Structures attributed to $D_{3(R)}$ include an $S_{3(R)}$ foliation in the felsic orthogneiss and metapelite, and parasitic $F_{3(R)}$ folds in older lithologies, and $D_{3(R)}$ is assumed to correspond to $D_{3(B)}$ and $D_{1(L)}$ (i.e. $D_{3(B)}$, $D_{1(L)}$ and $D_{3(R)}$ are all correlated with the 1000 Ma event). However, $D_{3(R)}$ is thought to have followed shortly after composite-orthogneiss development in the Rauer Group (Harley, 1987*a*), whereas further southwest it is $D_{2(B)}$, not $D_{3(B)}$, which follows this development. A potential solution to this problem is that it has now been recognized (Harley & Fitzsimons, 1991) that structures previously identified as $D_{3(R)}$ probably include several superposed near-coaxial deformations, which may include deformations equivalent to both $D_{2(B)}$ and $D_{3(B)}$ as defined along the Brattstrand Bluffs coastline. Even so, it should be noted that there is some difference in style between $D_{3(R)}$, dominated by isoclinal folding, steep dips and steeply-plunging lineations, and $D_{3(B)}$, dominated by an intense flat-lying foliation. $D_{4(R)}$ is represented by open to close folding in the southern Rauer Group, and by a series of ductile shear zones in the north. It is tempting to correlate $D_{4(R)}$ with $D_{4(B)}$, but again there are major differences in style between the upright folds and ductile shears of $D_{4(R)}$ and the shallowly-plunging simple shear structures of $D_{4(B)}$. Similarly there is no obvious equivalent in the Rauer Group of $D_{5(B)}$ and $D_{3(L)}$, although some late flexures have been identified which may correspond to $D_{5(B)}$ or $D_{6(B)}$. Steep mylonite zones reflect a later event ($D_{5(R)}$) correlated with $D_{7(B)}$.

The Rauer Group is also distinguished by a number of features which cross-cut the gneissic lithologies. Multiple generations of deformed mafic dykes, with granulite-facies mineral assemblages consistent with metamorphism during the Proterozoic event, are common in parts of the Rauer Group (Harley & Fitzsimons, 1991), but absent from all outcrops further southwest. The mafic dykes have been correlated with undeformed dykes in the Vestfold Hills (Sheraton & Collerson, 1983; see Sections 2.3.3 and 2.3.9) and hence used to identify crustal material which is older than the dykes, and possibly Archaean in age. Those parts of the Rauer Group characterized by multiple generations of deformed mafic dykes do generally correspond with the occurrence of rare high-temperature (*c.* 1000°C) metapelite, and Archaean zircon ages (Kinny & Black 1990; see Section 2.3.9). The absence of mafic

dykes from the paragneiss units along the Prydz Bay coastline has been used to infer that the paragneiss precursors were deposited some time after 1300 Ma (Sheraton & Collerson, 1983). However, at least one generation of mafic dykes post-dates the orthogneiss units and $D3_{(R)}$ structures ascribed to the Proterozoic metamorphic event, and hence also post-dates the paragneiss southwest of the Rauer Group. This implies that the absence of mafic dykes in the paragneiss cannot merely reflect an age difference between the paragneiss and orthogneiss. Two possible explanations are that the dykes did not extend up into the cover sequence, or that the igneous activity decreased towards the southwest. Planar pegmatite bodies, which post-date $D_{4(R)}$ in the Rauer Group, are correlated with similar pegmatite bodies along the Brattstrand Bluffs coastline, but are absent from the Larsemann Hills. Except for pegmatite bodies and rare Phanerozoic alkaline dykes, no intrusive units post-dating the main Proterozoic event have been identified in the Rauer Group. However, Stüwe *et al.* (1989) described a pink granite in the Larsemann Hills, thought to have been emplaced under high-grade conditions after the major ductile deformations. This is correlated here with the syn- to post-$D_{5(B)}$ granitic intrusive bodies in the Brattstrand Bluffs coastline (i.e. the Amanda Bay granite and associated dykes).

Peak pressure-temperature estimates for the Proterozoic metamorphic event show a systematic variation. Peak syn-$D_{1(L)}$ metamorphic conditions in the Larsemann Hills were about 4.5 kbar and 750°C (Stüwe & Powell, 1989*a*), and were associated with partial melting. These estimates were based on metapelitic lithologies, which are distinguished from those described in Chapter 6 by the stability of spinel-quartz-cordierite at the metamorphic peak rather than garnet-sillimanite. This is consistent with calculated peak pressures being about 1.5 kbar lower than those for the Brattstrand Bluffs coastline. Peak conditions were followed by near-isothermal decompression to about 3 kbar, and then cooling under stable conditions during and after $D_{2(L)}$ until exhumation, probably during the 500 Ma event (Stüwe & Powell, 1989*a*). Syn-$D_{3(R)}$ peak metamorphic conditions in the Rauer Group were 800 to 850°C at pressures of 7 to 9 kbar. The retrograde evolution involved decompression of 2 to 4 kbar, at least some of which post-dated $D_{4(R)}$, and then cooling under stable conditions at 3 to 5 kbar until exhumation, probably during the 500 Ma event (Harley, 1988; Harley & Fitzsimons, 1991). These clockwise paths are consistent with the evolution of the Brattstrand Bluffs coastline, and indicate a decreasing pressure gradient from the Rauer Group to the Larsemann Hills (see Fig. 8.2).

Stüwe *et al.* (1989) identified a late metamorphic overprint characterized by garnet and orthopyroxene segregations in the Larsemann Hills, and tentatively correlated it with $D_{3(L)}$ and the 500 Ma event. However, at least part of this overprint

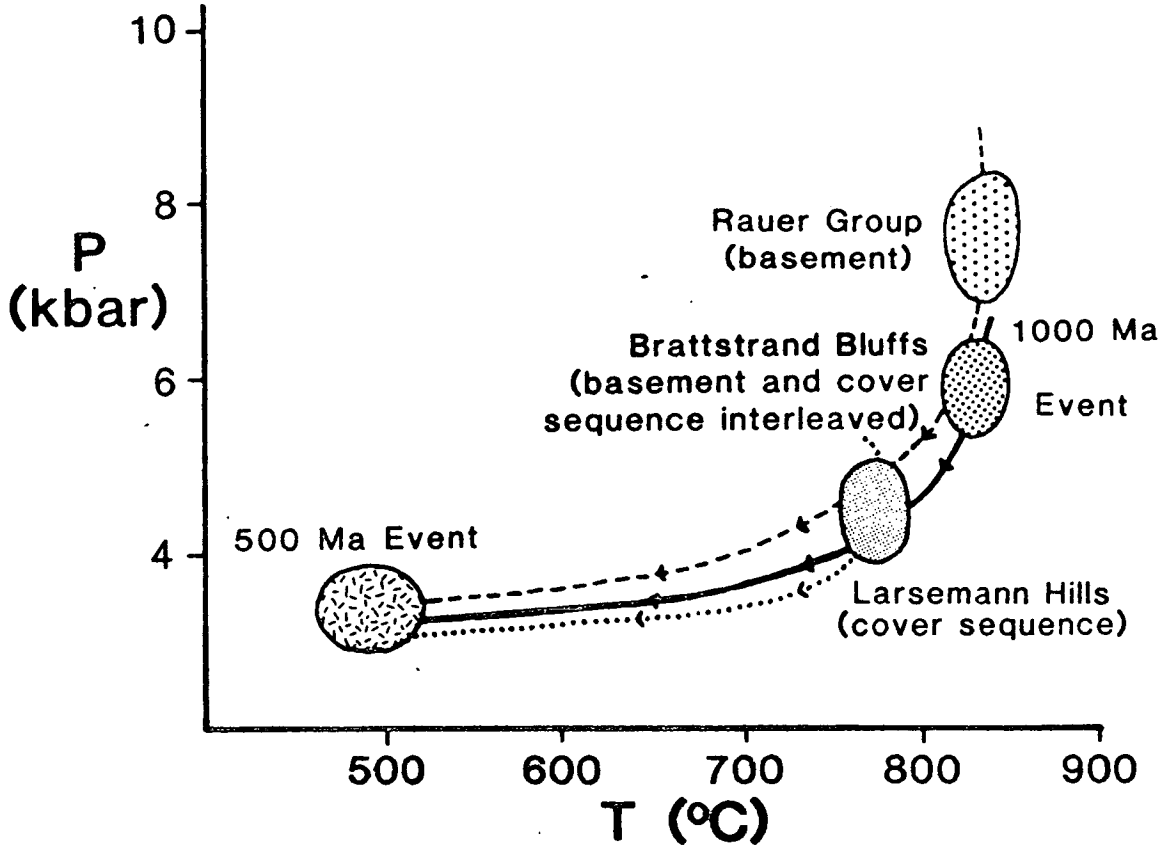

Fig. 8.2 Pressure-temperature paths for the Proterozoic outcrops of Prydz Bay. Only the retrograde paths are depicted since the prograde paths are poorly constrained. The Rauer Group path is from Harley (1987*a*, 1988) and Harley and Fitzsimons (1991), the Larsemann Hills path is from Stüwe and Powell (1989*a*), and the Brattstrand Bluffs path is from this study.

has since been ascribed by Stüwe and Powell (1989*b*) to syn-$D_{1(L)}$ peak metamorphism. It is suggested here that most or all of the features originally attributed to syn-$D_{3(L)}$ metamorphism by Stüwe *et al.* (1989) are syn-$D_{1(L)}$ relics preserved in areas of low $D_{2(L)}$ and $D_{3(L)}$ strain, and that late metamorphic mineral growth is generally a contact effect confined to gneisses adjacent to syn-$D_{5(B)}$ or $D_{3(L)}$ granitic intrusions. Rare sapphirine-bearing metapelite in the Rauer Group preserves assemblages which reflect pressure-temperature conditions far more extreme than those ascribed to the Proterozoic metamorphism (*c.* 11 kbar, 1000°C; see Section 2.3.9). These relics have been ascribed to Archaean events by Harley and Fitzsimons (1991).

Proterozoic outcrops to the southwest of the Larsemann Hills have been described in less detail. The Bolingen Islands and Sostrene Island, immediately west of the Larsemann Hills, have been described by Thost *et al.* (1988, 1991) and Motoyoshi *et al.* (1991), and are composed of paragneiss lithologies and pyroxene-bearing gneiss of similar appearance to the composite orthogneiss described from the

Rauer Group and the Brattstrand Bluffs coastline. The structure of these islands has not yet been published, although, like the Brattstrand Bluffs coastline, outcrop-scale structures are dominated by asymmetric folds and shear zones (D.E. Thost, *pers. comm.*). Pressure-temperature estimates of about 6 kbar and 775°C for the Bolingen Islands (Thost *et al.*, 1988; Motoyoshi *et al.*, 1991) are ascribed to the Proterozoic metamorphic event. The extreme pressure-temperature conditions preserved by a mafic body on Sostrene Island (*c.* 10 kbar and 980°C) are similar to those preserved by sapphirine-bearing metapelite from the Rauer Group, and are likewise possible relics of Archaean metamorphism (Thost *et al.*, 1991). Outcrops further west in the Munro Kerr Mountains have been briefly described by Stüwe and Powell (1989*a*), who noted that they are dominated by pyroxene-bearing orthogneiss, with subordinate metapelite. The structure comprises a flat-lying foliation, with shallowly-plunging isoclinal folds and shear zones parallel to the foliation. Pressure-temperature estimates of 7 to 8 kbar and 750 to 850°C have been obtained for a metapelite from the Munro Kerr Mountains (Stüwe & Powell, 1989*a*). Although not well constrained, the lithological and metamorphic characteristics of outcrops southwest of the Larsemann Hills exhibit similar trends to those outcrops northeast of the Larsemann Hills: the metamorphic pressures and the proportion of orthogneiss material both increase with distance from the Larsemann Hills. This apparent symmetry around the Larsemann Hills was noted by Stüwe and Powell (1989*a*).

8.2.4 Summary of the geological evolution

The Prydz Bay coastline comprises various outcrops metamorphosed in the granulite facies at around 1000 Ma. The outcrops can be divided into those consisting of orthogneiss-dominated basement, and those consisting of a paragneiss-dominated cover sequence. The latter crops out in the Larsemann Hills, and the former crops out both to the northeast in the Rauer Group and to the southwest in the Munro Kerr Mountains. The basement lithologies are composite in nature, comprising Proterozoic material and Archaean relics. The Archaean relics can be identified by early structural features, multiple generations of mafic dykes, distinctive mineral assemblages indicative of temperatures and pressure more extreme than those ascribed to the Proterozoic metamorphism, and isotopic dating.

The composite basement and sedimentary cover sequence were deformed and metamorphosed at around 1000 Ma, causing transposition of the basement-cover boundary to form areas of interleaved orthogneiss and paragneiss material. The metamorphic peak was associated with partial melting and widespread development of granulite-facies mineral assemblages, and was followed by a clockwise pressure-temperature path involving between 1 and 4 kbar of decompression. The peak

metamorphic pressure, and the extent of retrograde decompression, were greatest in those areas dominated by orthogneiss lithologies, and least in the paragneiss-dominated Larsemann Hills. The decompression was synchronous with the development of flat-lying fabrics and structures, which were most intense at the transposed basement-cover boundary. Regional-scale deformation folded the granulite lithologies during the cooling interval after decompression, and was accompanied by the emplacement of granitic dykes and plutons. Planar pegmatite bodies intruded the high-grade rocks, and are ascribed an age of about 770 Ma, and the area was locally affected by a structural and metamorphic overprint at around 500 Ma.

The implications that these structural and metamorphic events have for the tectonic and chemical processes responsible for Proterozoic granulite stabilization in Prydz Bay are considered in Sections 8.4 and 8.5.

8.3 THE GEOLOGICAL HISTORY OF THE NORTHERN PRINCE CHARLES MOUNTAINS

8.3.1 Introduction

The geology of the northern Prince Charles Mountains is relatively poorly known, most investigations being reconnaissance in nature (e.g. Crohn, 1959; McLeod, 1964; Tingey, 1972, 1982; see Section 2.3.8). McKelvey and Stephenson (1990) described the geology of the metamorphic basement and Permo-Triassic sedimentary units in the vicinity of Radok Lake, and provided the first integrated structural and geological history for part of the northern Prince Charles Mountains. This thesis contains the second such study, and is the first to investigate the metamorphic history in a quantitative manner. This section presents a brief summary of the geological evolution of the Nemesis Glacier region discussed in Chapters 4, 5 and 7, and then integrates this work with the conclusions of McKelvey and Stephenson (1990).

8.3.2 The evolution of the Nemesis Glacier region

The Nemesis Glacier region is composed of granulite-facies gneisses, dominated by homogeneous felsic orthogneiss enclosing transposed and boudinaged mafic and ultramafic dykes and sills. These mafic and ultramafic bodies preserve a foliation and folds which have not survived in the surrounding gneiss. A sedimentary protolith is inferred for less homogeneous felsic gneiss interlayered with semi-pelite, marble and other probable paragneiss units. Banded calc-silicate units are thought to have developed via metasomatic processes during progressive metamorphism of interlayered carbonate and water-rich units (see Section 4.2.9). High-grade metamorphism of the orthogneiss and paragneiss units was accompanied by the

development of flat-lying structures (S_3 and F_4; see Section 4.5.10) consistent with progressive horizontal shear, and then a series of upright F_5 folds culminating in the development of regional synforms, antiforms and monoclines (F_6) separated by zones of intense upright fabric (S_6). The D_3 to D_6 time interval was associated with several episodes of partial melting, which produced discordant leucogneiss bodies, and with the emplacement of mafic dykes and charnockite plutons correlated with 950 to 1000 Ma charnockite elsewhere in East Antarctica (see Section 4.6.6).

Granulite-facies conditions were achieved at several stages of this structural evolution, and on the basis of available data it is assumed that granulite conditions were prevalent throughout the D_3 to D_6 time interval. Peak metamorphic conditions of 6.5 to 7 kbar and about 800°C (see Sections 5.6.3 and 7.6.1) were followed by a period of cooling through at least 150°C, with little or no preceding decompression (see Section 7.6.3). Volatile fluid activities at the metamorphic peak, and during the initial stages of retrogression, were buffered on a scale of less than a metre by the local mineral assemblage (see Section 7.6.4). The post-D_6 evolution of the area was characterized by localized intrusive and deformational events. Planar or irregular felsic bodies were emplaced while conditions were still within the granulite facies. Planar pegmatite bodies post-dated or were partly synchronous with small-scale flexing and shearing (D_7), and are correlated with 770 Ma pegmatite elsewhere (see Section 4.6.6). Mylonite, pseudotachylite and miscellaneous microdeformational features (D_8) are assumed to be broadly synchronous with planar quartz veins, a greenschist metamorphic overprint, and a vertical cleavage, all of which are correlated with localized reworking at about 500 Ma (see Section 4.6.6).

8.3.3 A correlation with the Radok Lake area

The only other detailed geological study of the northern Prince Charles Mountains was made by McKelvey and Stephenson (1990) in the Radok Lake area, which is about 50 km southwest of the Nemesis Glacier region. There are many similarities between the two areas, and correlations are summarized in Fig. 8.3. McKelvey and Stephenson (1990) identified two lithological associations in the high-grade gneisses: one dominated by relatively homogeneous felsic gneiss, enclosing bands of mafic granulite thought to represent basaltic dykes, sills or flows, and another comprising a complex interlayered sequence of felsic and garnet-biotite ± orthopyroxene gneisses, with rare calc-silicate and metapelite. These correspond to the orthogneiss and paragneiss associations identified in the Nemesis Glacier region. No quantitative estimates of the peak metamorphic conditions or retrograde evolution have been made in the Radok Lake area, although low- to medium-pressure granulite conditions were inferred from the stability of cordierite in metapelite, and the absence of garnet from

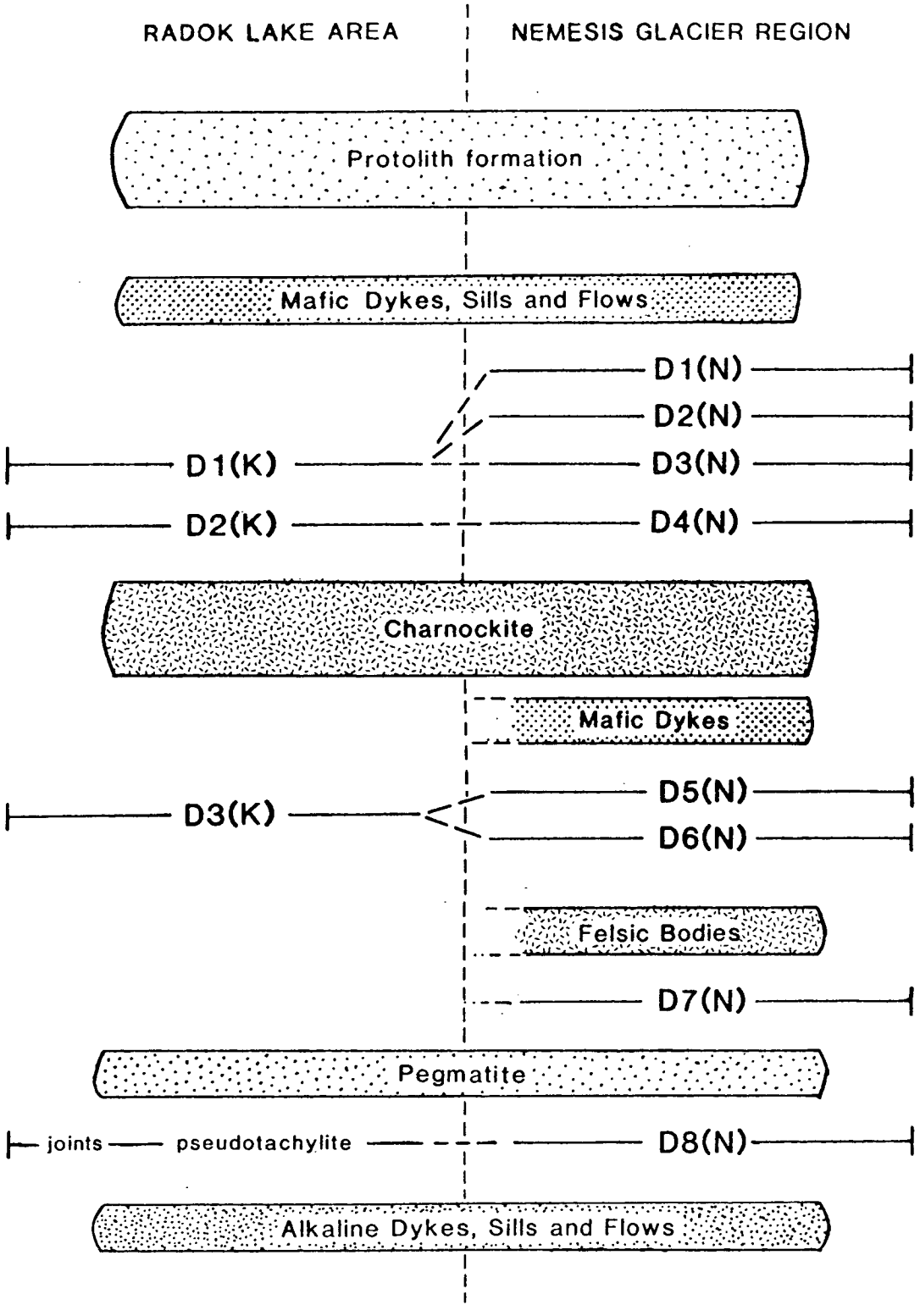

Fig. 8.3 A correlation of events identified in the Radok Lake area (McKelvey & Stephenson, 1990) and the Nemesis Glacier region (this study). Several generations of leucogneiss, not included in this diagram, have been identified in both areas. An absolute time scale for these events is suggested in the text.

mafic lithologies. Breakdown of scapolite to plagioclase, calcite and grossularite has been reported from scapolite-wollastonite-diopside calc-silicates, which could be similar to the reaction textures described in Sections 4.2.8 and 7.2.3.

McKelvey and Stephenson (1990) presented a preliminary synthesis of structural data from the Radok Lake area, which correlates quite closely with that summarized in Section 4.5.10. A steeply-dipping lithological layering in the Radok Lake area strikes east-northeast, and has been modified by a number of deformational events. An intense layer-parallel $S_{2(K)}$ foliation[2] has largely transposed earlier $F_{2(K)}$ isoclinal folds, although rare intrafolial $F_{2(K)}$ hinges preserve a relict $S_{1(K)}$ foliation. The $S_{2(K)}$ foliation is deformed into mesoscopic upright $F_{3(K)}$ folds, which plunge shallowly (*c.* 30 to 40°) to the east-northeast as does a local mineral lineation. Larger-scale folds exposed on cliff faces are of similar style and orientation to these $F_{3(K)}$ folds, and have been correlated with them by McKelvey and Stephenson (1990).

The orientation of the lithological layering in the Radok Lake area is virtually identical to that of $S_{3(N)}$ in the steeply-dipping domains of the Nemesis Glacier region, and $S_{1(K)}$, $F_{2(K)}$ and $S_{2(K)}$ are correlated with structures attributed to $D_{3(N)}$ and $D_{4(N)}$ in the Nemesis Glacier region. $S_{1(K)}$ is tentatively correlated with $S_{3(N)}$, and $F_{2(K)}$ with $F_{4(N)}$, implying that the deformation responsible for the transposition of $S_{1(K)}$ and $F_{2(K)}$ by the $S_{2(K)}$ fabric in the Radok Lake area was not as intense in the Nemesis Glacier region. $F_{3(K)}$ folds correspond very closely in terms of style, size and orientation to $F_{5(N)}$ folds in the Nemesis Glacier region. No regional folds or high- and low-strain zones corresponding to $D_{6(N)}$ were identified by McKelvey and Stephenson (1990). This could reflect a decrease in intensity of $D_{6(N)}$ to the southwest, or merely that McKelvey and Stephenson did not cover sufficient area to identify these regionally-heterogeneous structures. Similar structures to those identified in mafic and ultramafic bodies in the Nemesis Glacier region ($S_{1(N)}$ and $F_{2(N)}$) were also identified in metanorite pods in the Radok Lake area (N.C.N. Stephenson, *pers. comm.*), but were interpreted as being equivalent to the fabrics developed in the surrounding felsic gneiss rather than a reflection of earlier deformation.

McKelvey and Stephenson (1990) have described pegmatitic dykes which post-date $D_{2(K)}$, but are of unknown timing with respect to $D_{3(K)}$. It is tentatively suggested here that they correspond to the planar pegmatite bodies identified in the Nemesis Glacier region, and are likewise correlated with 770 Ma pegmatites developed elsewhere in East Antarctica. A north-northeast trending joint set, with a vertical or steep dip, has been identified in the Radok Lake area, and is correlated with the quartz

---

2 In this section, the subscript (K) refers to the numbering scheme used for deformational events and associated structures and fabrics in the Radok Lake area by McKelvey and Stephenson (1990), and (N) refers to the deformational scheme used in this thesis for the Nemesis Glacier region.

veins and cleavage of similar orientation identified in the Nemesis Glacier region. McKelvey and Stephenson (1990) also described veins of pseudotachylite, which are correlated with the $D_{8(N)}$ effects described in Section 4.5.9.

Detailed mapping has also been carried out in the Porthos Range, the results of which conform very closely to the geological history of the Nemesis Glacier region (D.E. Thost, *pers. comm.*), and some of the observations from the Porthos Range have been incorporated with due reference into the geological history inferred for the Nemesis Glacier region in Chapter 4 (a geological history for both areas has been published as Fitzsimons and Thost, 1991). Fieldwork south of Beaver Lake has revealed that rocks there are generally of lower grade than those in the Aramis and Porthos Ranges, with pyroxene-bearing assemblages being rather rare (G.T. Nichols, *pers. comm.*), but the structural and geological histories of these outcrops have yet to be published.

Given that the structural and metamorphic histories developed in Chapters 4, 5 and 7 of this thesis are far more detailed than any interpretations made for other areas of the northern Prince Charles Mountains, and that preliminary results from elsewhere in the northern Prince Charles Mountains broadly agree with those discussed here, the evolution summarized in Section 8.3.2 is taken as the best currently available for the northern Prince Charles Mountains as a whole. This will in no doubt change as the results of other studies are published.

8.4 TECTONIC PROCESSES AND GRANULITE STABILIZATION

8.4.1 Introduction

Much of the study of metamorphic rocks is based upon the fundamental assumption that the mineral assemblage in a rock reflects its pressure-temperature evolution. It follows that the spatial variation in mineral assemblage developed in a metamorphic terrain, or the 'metamorphic field gradient' (J.C. Schumacher *et al.*, 1990), is some function of the thermal gradients developed in the crust during the metamorphic event. Miyashiro (1961) suggested that the field gradients preserved in most metamorphic belts could be classified into one of three 'facies series', which reflect three different types of thermal regime characteristic of the earth's crust. The high-pressure facies series is characterized by blueschist- and greenschist-facies assemblages. The intermediate- and low-pressure series are distinguished by the aluminosilicate polymorphs developed in metapelitic lithologies. The former is characterized by a prograde transition of kyanite to sillimanite, and the latter by a prograde transition of andalusite to sillimanite, which are typical of the Barrovian and Buchan terrains in the Scottish Highlands respectively (Harte & Hudson, 1979).

The development of simple thermal models for various tectonic processes led to a preliminary correlation between metamorphic facies series and tectonic setting (e.g. Oxburgh & Turcotte, 1971, 1974; Bickle *et al.*, 1975; Richardson & Powell, 1976), and then to the more rigorous numerical modelling of England and Richardson (1977) and numerous subsequent studies (e.g. Wells, 1980; England & Thompson, 1984, 1986; Sandiford & Powell, 1986*a*; England, 1987; Loosveld & Etheridge, 1990). England and Richardson (1977) emphasized the relationship between the pressure-temperature conditions indicated by the metamorphic field gradient, and the actual pressure-temperature paths followed by the rocks. Each rock preserves a mineral assemblage developed at some point on the pressure-temperature path it followed during the metamorphic event, unless kinetic effects produce an apparent path unrelated to the actual evolution (see Section 5.5.6). This point is most probably the point of maximum entropy experienced by the rock, and is generally thought to be at, or close to, the thermal maximum of the pressure-temperature path. Hence the rocks exhibit a spatial variety of pressure-temperature conditions which, in simple one-dimensional tectonic models, depend solely on the depth at which the rock originated. The metamorphic field gradient defined by these rocks bears no relation to any one geotherm that existed during the metamorphic event, and in fact represents a diachronous array of single points from a number of geothermal gradients. Direct evidence of the pressure-temperature path followed by a rock can be derived from evidence of mineral reaction, either in terms of textural relationships between reactant and product phases (e.g. Ellis *et al.*, 1980), or mineral zonation profiles (e.g. Spear & Selverstone, 1983). However, the possibility that such features reflect an overprint by an unrelated event, rather than a continuous evolution during a single metamorphic event, must be carefully considered.

Pressure-temperature paths should be independent of variables such as the age, lithological constitution and present tectonic setting of a metamorphic rock, and merely reflect the tectonic processes operating during and immediately after metamorphism. The tectonic setting of metamorphism is commonly assessed by comparison of the actual pressure-temperature path with paths developed from theoretical models for particular tectonic settings. The remainder of this section discusses the various pressure-temperature paths identified in granulite terrains, and the tectonic models which have been proposed to explain them, and then considers the pressure-temperature paths identified in Prydz Bay and the northern Prince Charles Mountains and assesses the relevance of various tectonic processes to these areas.

8.4.2 Pressure-temperature paths and the tectonic setting of granulites

Granulites equilibrate at considerably higher temperatures than those normally

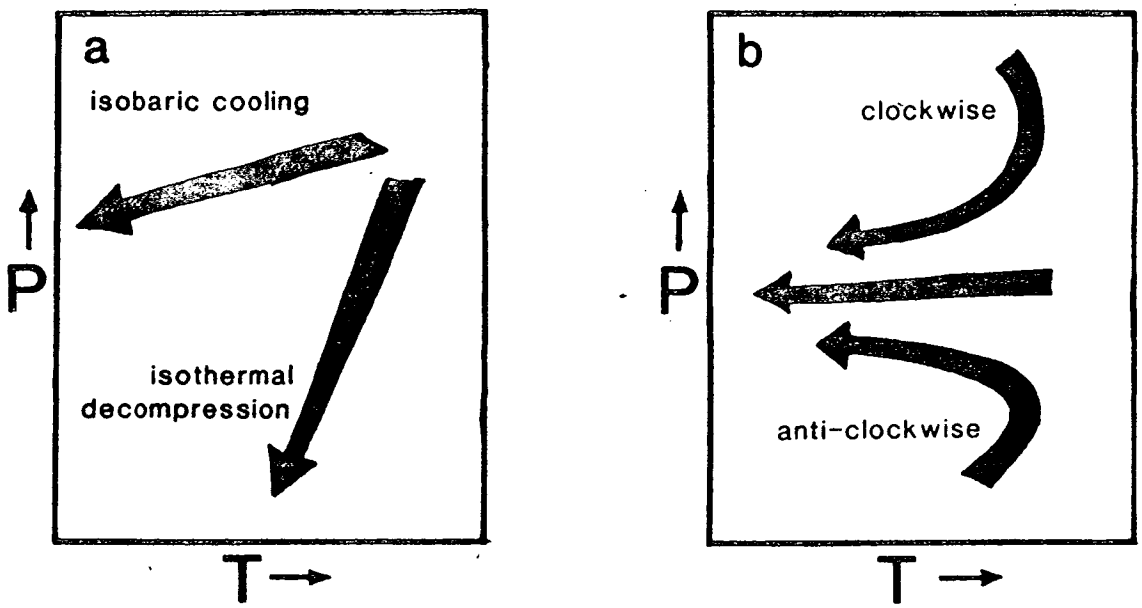

Fig. 8.4 A classification of pressure-temperature paths. Fig. 8.4a illustrates a two-fold division of retrograde paths into isobaric cooling and isothermal decompression (Harley, 1989). Fig. 8.4b illustrates a three-fold division of isobaric-cooling paths into clockwise and anti-clockwise paths preserving some evidence of pre-cooling decompressional and compressional history respectively, and simple cooling paths which preserve no evidence of an earlier history (Bohlen, 1991).

associated with the lower crust, and their formation requires some perturbation of the steady-state geothermal gradient. The tectonic processes responsible for these perturbations are particularly amenable to interpretation in terms of pressure-temperature paths because of the wealth of pertinent experimental data and the relatively common occurrence of reaction textures and mineral zonation. The high temperatures of granulite metamorphism generally preclude the preservation of the prograde pressure-temperature path which is erased by high rates of diffusion at the metamorphic peak. However, granulite terrains record a considerable diversity of retrograde paths (Harley, 1989), both in terms of their shape and their positioning in pressure-temperature space, although some workers maintain that there is a considerable bias to one particular type (Bohlen, 1987, 1991). Retrograde pressure-temperature paths are generally grouped into a small number of broad categories on the basis of path shape. Ellis (1983) and Harley (1989) have distinguished between paths dominated by near-isothermal decompression and those dominated by near-isobaric cooling (see Fig. 8.4a), but this simple division is complicated by the existence of three types of isobaric-cooling path (Harley, 1989; Bohlen, 1991; see Fig. 8.4b):

(i) 'clockwise' paths with an initial stage of decompression preceding the cooling (i.e. a path involving isothermal decompression and isobaric cooling);

(ii) 'anti-clockwise' paths in which the attainment of peak temperatures is

accompanied by compression, with a small compressional component continuing during the initial retrograde cooling; and

(iii) simple cooling paths which preserve no evidence of a precursor path, and could be a partly-preserved clockwise or anti-clockwise path, or unrelated to either.

Paths involving significant retrograde decompression are generally thought to reflect isostatic disequilibrium, and are traditionally attributed to the evolution of thickened crust in collisional zones, whereas isobaric-cooling paths have been conventionally ascribed to magmatic accretion (England & Richardson, 1977).

Tectonic thickening during continental collision is often cited as a setting for granulite formation. Evidence for crustal thickening in some granulite terrains includes high-pressure relics, such as kyanite inclusions or eclogite bodies, and the presence of syn-collisional magmatic lithologies consistent with crustal melting at depth such as orthogneiss with depleted heavy rare-earth element contents (e.g. Ellis, 1987). The clockwise nature of pressure-temperature paths produced by continental collision and subsequent erosion of the overthickened crust (see Fig. 8.5a) has been demonstrated by several studies (e.g. England & Richardson, 1977; England & Thompson, 1984, 1986), but these models can only account for granulite-facies conditions if temperatures are maximized using some combination of unrealistically-high rates of internal heat production and basal heat flux, and unrealistically-low values for the crustal thermal conductivity (Thompson & England, 1984; Harley, 1989; Bohlen, 1991). An external heat source is needed to achieve granulite conditions, such as substantial syn- to post-collisional addition to the thermal budget of the crust via mantle-derived magmas (e.g. England & Thompson, 1986; de Yoreo *et al.*, 1989).

Magmatic accretion without continental collision has also been considered a potential means of granulite formation (Wells, 1980; Bohlen, 1987). Magmatic accretion produces a transient thermal perturbation and a thickening of the crust, and models of magma accretion can produce a number of theoretical pressure-temperature paths depending principally on the thickness of the original crust and the amount and position of accretion (Wells, 1980; Harley, 1989). The addition of magma to crust of normal, or near-normal, thickness causes overthickening of the crust, and the retrograde evolution includes a period of decompression reflecting isostatic response of the thickened crust. The amount of decompression is directly dependent on the volume of magmatic accretion. Rocks beneath or within a zone of accretion experience initial compression and heating, followed by cooling and decompression, whereas rocks above the accretion zone are heated without compression, and then experience a similar cooling and decompressional retrograde history to that of the

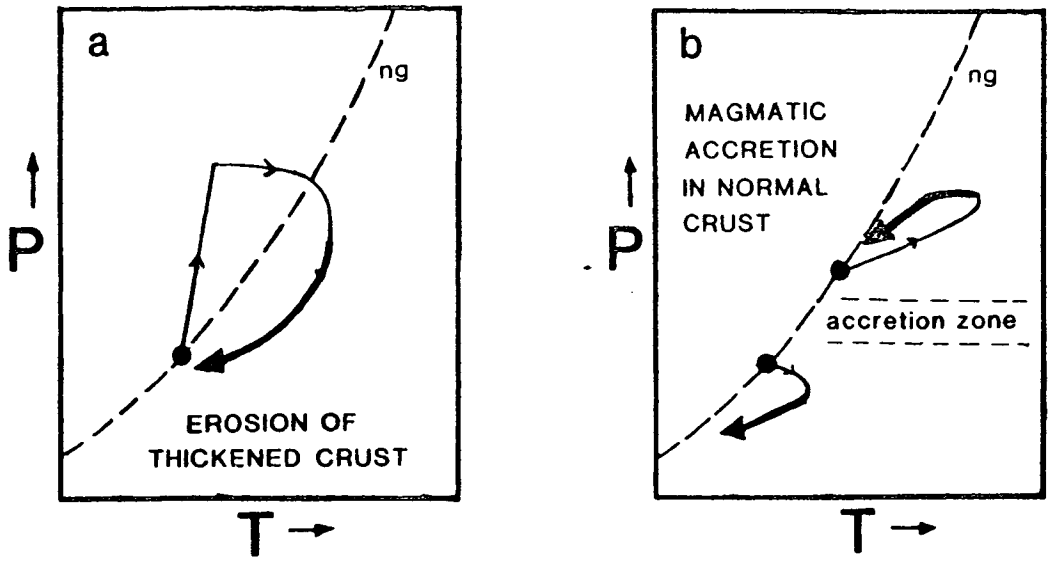

Fig. 8.5 Schematic pressure-temperature paths for a variety of tectonic settings (adapted from Harley, 1989). In all the figures, the heavy lines represent those parts of a retrograde path that are likely to be preserved, and 'ng' represents the stable geotherm for normal-thickness crust. Fig. 8.5a is a decompression-dominated clockwise path for erosion of crust thickened during continental collision (England & Richardson, 1977; England & Thompson, 1986). Fig. 8.5b depicts two paths resulting from magmatic accretion into crust of normal thickness (Wells, 1980). Rocks above the accretion zone follow a clockwise path, whereas rocks below it follow an anti-clockwise path. Both paths are dominated by cooling, with some decompressional component reflecting the isostatic response of magmatically-thickened crust. Figs 8.5c to e are on the next page.

deeper rocks. Hence rocks below the accretion zone preserve an anti-clockwise pressure-temperature path, and rocks above it preserve a clockwise path (see Fig. 8.5b). However, substantial magmatic additions to the crust could be associated with pre- or syn-magmatic extension. If magma is added to thin crust, less decompression is required to achieve isostatic equilibrium. No decompression would occur if the crust was thinned sufficiently, and rocks below and within the accretion zone would follow an anti-clockwise compression and cooling path, whereas rocks above the accretion zone would follow an isobaric heating and cooling path (see Fig. 8.5c).

Simple calculations indicate that the formation of a given volume of granulite by magmatic accretion alone requires an equivalent volume of magma (e.g. England & Thompson, 1986). Hence granulite terrains formed by magmatic accretion should have an abundance of syn-metamorphic intrusions or orthogneiss consistent with recent derivation from the mantle, a dominance of mafic compositions at the base of the crust, and a lack of evidence for substantially-overthickened crust. It has been suggested that the occurrence of similar peak temperatures over a range of depths is a reflection of the buffering effect of magma crystallization (Waters, 1986; Bohlen, 1987), and hence indicative of magmatic accretion, although extensive crustal melting, which is believed to be common at granulite conditions whatever the tectonic

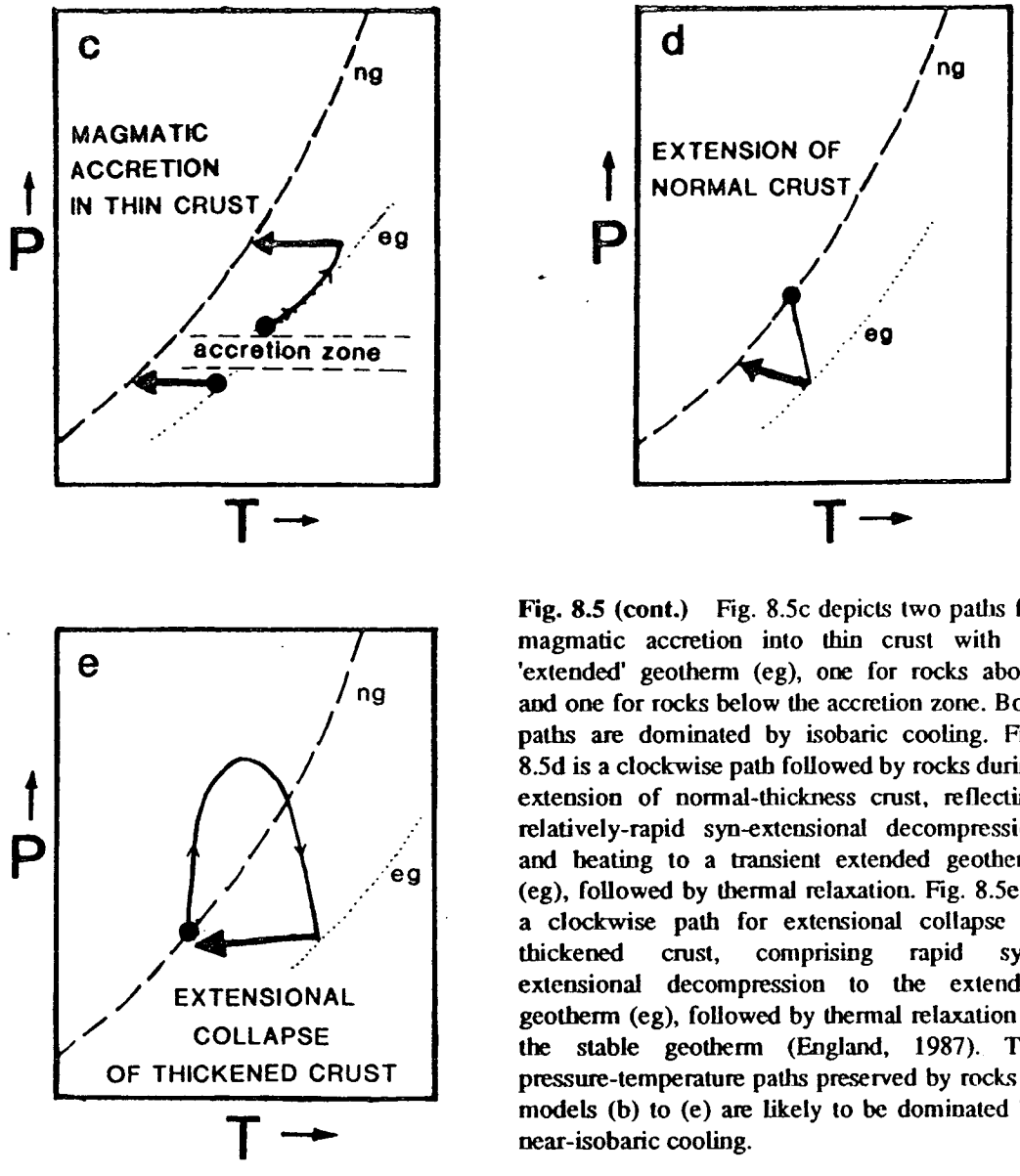

Fig. 8.5 (cont.) Fig. 8.5c depicts two paths for magmatic accretion into thin crust with an 'extended' geotherm (eg), one for rocks above and one for rocks below the accretion zone. Both paths are dominated by isobaric cooling. Fig. 8.5d is a clockwise path followed by rocks during extension of normal-thickness crust, reflecting relatively-rapid syn-extensional decompression and heating to a transient extended geotherm (eg), followed by thermal relaxation. Fig. 8.5e is a clockwise path for extensional collapse of thickened crust, comprising rapid syn-extensional decompression to the extended geotherm (eg), followed by thermal relaxation to the stable geotherm (England, 1987). The pressure-temperature paths preserved by rocks in models (b) to (e) are likely to be dominated by near-isobaric cooling.

setting (Thompson & England, 1984), would have a similar effect (Hodges *et al.*, 1988; Vielzeuf *et al.*, 1990). In addition to citing a similarity in peak temperatures as evidence for magmatic accretion, Bohlen (1987, 1991) also paradoxically claimed that an isobaric transition from amphibolite to granulite facies reflects differences in the amount of magmatic heating at similar depths and is hence indicative of magmatic accretion.

Extension of normal-thickness crust is another proposed mechanism for high-grade metamorphism, particularly at low pressures (Wickham & Oxburgh, 1985; Sandiford & Powell, 1986*a*). Crustal extension compresses the vertical thermal structure of the lithosphere, resulting in an increased heat flow which is probably enhanced by mantle-derived magmas. The resultant thermal perturbation subsequently decays as temperatures adjust to a stable geotherm. Extensional

pressure-temperature paths comprise some combination of prograde decompression and heating, followed by cooling (see Fig. 8.5d) which may be accompanied by some compression if the thermal relaxation is associated with thermal subsidence and the development of substantial sedimentary basins (McKenzie, 1978). The relationship between the extent of decompression and the maximum temperature depends on the model of extension. If extension is symmetrical, maximum temperatures are attained in the area of maximum extension and therefore maximum decompression. Heterogeneous extension models, for example extension involving crustal-scale detachments (Wernicke, 1985; Lister *et al.*, 1986), produce a maximum thermal perturbation, reflecting maximum thinning of the mantle lithosphere, which does not coincide with the area of maximum crustal extension and decompression. In the former model, pressure-temperature paths for high-grade metamorphic rocks are clockwise with prograde decompression and retrograde cooling, whereas in the latter model, the high-grade crustal rocks occur in areas of little deformation, and follow a near-isobaric heating and cooling path (Sandiford & Powell, 1986*a*). In general, rocks in all of these extensional models are likely to record near-isobaric cooling paths since any decompression precedes the metamorphic peak. However, indirect evidence of an extensional origin can be provided by syn-metamorphic flat-lying structures and syn- to post-metamorphic basic magmatism.

It has been recognized that extension can play a major role in evolution of collisional metamorphic terrains as well as being a potential cause of high-grade metamorphism by itself. The classical models of continental collision assume that thermal relaxation towards the enhanced geotherm applicable to thickened crust is terminated by erosion and uplift, but the importance of tectonic thinning in some collisional orogenic belts has been noted (e.g. Molnar & Tapponnier, 1975, 1978; Tapponnier *et al.*, 1981). This thinning occurs principally by lateral extension, driven by a potential energy contrast between the overthickened crust and its surroundings, and is more rapid than simple erosion. Extension occurs when the gravitational forces exerted by overthickened crust exceed any compressional forces by some critical amount dependent on the strength of the lithosphere (England, 1987; Sonder *et al.*, 1987), and the resultant pressure-temperature paths have been modelled by England and Thompson (1986), England (1987) and Sonder *et al.* (1987). These paths have a higher dP/dT than theoretical curves derived with an erosion model (Harley, 1989), and commonly match the shape of observed decompressional paths more closely than erosional models. Extensional collapse is thought to be particularly rapid, such that the bulk of decompression can occur before peak metamorphic temperatures are attained (see Fig. 8.5e), and the rocks only preserve the post-decompressional cooling

part of the path (e.g. Sandiford, 1989*a*; Anovitz & Chase, 1990). Hence collisional tectonics can produce isobaric-cooling paths in addition to the clockwise paths characteristic of erosion; in fact a spectrum of paths between isothermal decompression and isobaric cooling can be recorded by rocks in collisional zones (Harley, 1989) depending on the amount and rate of post-collisional extension. The possibility of extension is enhanced for particularly wide and thick collisional zones, such as the Himalayan belt, and can be initiated by removal of the compressional stresses at the cessation of convergence, or weakening of the lithosphere surrounding the elevated region. Evidence for extensional collapse of thickened crust includes the development of horizontal structures during peak and retrograde metamorphism, with associated basic magmatism as the mantle decompresses and the crust approaches normal thickness. Overthickened terrains dominated by erosion should achieve their metamorphic peaks after the pervasive deformation. Although rapid uplift by extensional collapse can produce higher temperatures at low pressure than erosional models, it is still difficult to achieve granulite conditions without extra magmatic heating unless the rocks have experienced very high initial pressures.

Neither of the thickening models discussed above can account for granulite conditions without invoking substantial additional heat input, a problem which is particularly pronounced for intermediate- and low-pressure granulites. Thermal modelling suggests that the only means of deriving sufficiently high temperatures for intermediate- or low-pressure granulite metamorphism, without invoking substantial advective heat from magmas, is to thin the mantle lithosphere (Oxburgh, 1990). Extension of normal thickness crust is one way of achieving this, but the modelling of Loosveld and Etheridge (1990) suggests that low-pressure granulites cannot form by extension alone unless the lithosphere is stretched by a factor of three or more, which is unlikely in an intracontinental setting. Lesser extensions are required if advective heating by magma is considered, or mantle plumes and hot spots are invoked, but another problem with the extensional model is that many granulite terrains preserve evidence for prograde thickening rather than extension. The metamorphic peak in extensional terrains should coincide with, or just post-date, the extension (Loosveld & Etheridge, 1990). This means that the syn-metamorphic compression indicated by many granulite terrains would have to immediately follow lithospheric extension. A more likely means of combining crustal thickening with thinning of the mantle lithosphere is 'convective thinning' at the base of thickened lithosphere in a collisional orogenic zone, causing detachment of the 'thermal boundary layer'. The thermal boundary layer comprises the lowermost part of the mantle lithosphere, and separates the asthenosphere, which is dominated by convective heat transfer, from a mechanical

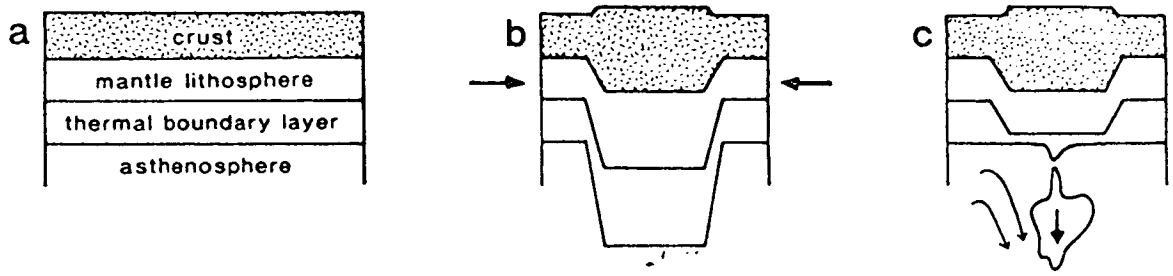

Fig. 8.6 A schematic illustration of the structure of normal-thickness and thickened continental lithosphere, adapted from Sandiford (1989*b*). Fig. 8.6a depicts thermally-stable continental lithosphere of normal thickness, with a thermal boundary layer separating the mechanical boundary layer, comprising crust and mantle lithosphere, from the asthenosphere. Fig. 8.6b depicts a homogeneous thickening of the mechanical and thermal boundary layers, and Fig. 8.6c shows how the thermal boundary layer, which forms a dense root, can be detached and replaced by hot asthenospheric mantle. The relative thicknesses of the layers are not to scale.

boundary layer which is dominated by conductive heat transfer and comprises the crust and uppermost part of the mantle lithosphere (Parsons & McKenzie, 1978). Houseman *et al.* (1981) have shown that a thermal boundary layer thickened by continental collision is colder and denser than its surroundings, and that convective instabilities can cause the detachment of this layer from the base of the lithosphere (see Fig. 8.6). Detachment of the thermal boundary layer by convective thinning has profound implications for both the thermal and tectonic evolution of the belt: hot asthenospheric mantle replaces dense lithospheric mantle, which increases the heat flow and causes a rapid increase in surface elevation promoting extensional collapse of the 'top-heavy' lithosphere (Houseman *et al.*, 1981; Sonder *et al.*, 1987; England & Houseman, 1988, 1989). Hence convective thinning can cause high temperatures of metamorphism, perhaps followed by rapid decompression.

Several recent thermal models for high-temperature low-pressure metamorphism have been based on detachment or convective thinning of the lower lithosphere (Sandiford, 1989*a*,*b*; Loosveld & Etheridge, 1990; Oxburgh, 1990; Sandiford & Powell, 1991). These models can produce anti-clockwise, clockwise, and isobaric-cooling paths, depending on the relative timing and rates of overall lithospheric shortening, mantle-lithosphere thinning, thermal relaxation of the upwelled asthenosphere, and extensional collapse. An elegant means of depicting the relationships between these various parameters has recently been described by Sandiford and Powell (1990), who represented the evolution of collisional belts in terms of the vertical strain developed in the crust and in the lithosphere as a whole. Some further consequences and applications of convective-thinning models are discussed in the next sections, which consider the relevance of these models to Proterozoic metamorphism in Prydz Bay and the northern Prince Charles Mountains.

8.4.3 Tectonic models for Prydz Bay

Harley (1988) and Stüwe and Powell (1989*a*) have presented tectonic models for Prydz Bay based on the Rauer Group and the Larsemann Hills respectively. Both models attribute the decompressional aspect of the retrograde path to thinning of overthickened lithosphere, but the two models differ in the assumed cause of prograde thickening. Harley (1988) invoked continental collision, with the necessary extra heat provided by pre- and syn-collisional magmatism, whereas Stüwe and Powell (1989*a*) suggested that the lithosphere was thickened by accretion of mantle-derived magmas. Stüwe and Powell (1989*a*) rejected the collisional model of Harley (1988) since the baric peak in the Larsemann Hills cannot have been much higher than the pressure at the thermal peak, whereas post-collisional uplift paths involve substantial decompression before peak temperatures are attained. The latter is particularly true for the extensional-collapse model invoked by Harley (1988) on the basis of path shape. To account for the relatively small amount of decompression in the Larsemann Hills, Stüwe and Powell (1989*a*) suggested that the crust under the Larsemann Hills was thinner than that under the Rauer Group. The thinning was attributed to an asthenospheric perturbation, centred under the Larsemann Hills, which was also responsible for the magmatic underplating. Stüwe and Powell (1989*a*) also noted that the location of a perturbation under the Larsemann Hills is consistent with the symmetrical distribution of rock types and metamorphic histories about the Larsemann Hills.

Neither of these models are entirely satisfactory. The temporal proximity of the thermal and baric peaks in the Larsemann Hills is inconsistent with both traditional erosion-terminated collision and extensional collapse of overthickened lithosphere. There is also a lack of evidence for particularly high pressures before the thermal peak in the Rauer Group. High-pressure relics do occur, but are attributed to a much earlier tectonothermal event. There is also no evidence for the substantial amount of magmatic under-accretion that is required by the model of Stüwe and Powell (1989*a*), and the explanation for differential uplift rates, although possible, does not consider that the site of the thinnest crust is likely to be the site of greatest magmatic under-accretion, which would tend to increase the necessary retrograde decompression. Neither Harley (1988) nor Stüwe and Powell (1989*a*) fully integrated the structural history with the pressure-temperature evolution. Harley (1988) suggested that $D_{3(R)}$ represents syn-collisional shortening, and considered $D_{4(R)}$ to be synchronous with decompression but did not suggest any cause for this deformation. Stüwe and Powell (1989*a*) suggested that the $D_{2(L)}$ folding was a compressional event post-dating the perturbation, and although they did not consider the origins of $D_{1(L)}$, they presumably

correlated it with the syn-magmatic episode of tectonic thinning. The pressure-temperature path developed in this thesis for the Brattstrand Bluffs coastline provides no extra constraints on the tectonic evolution of Prydz Bay since it is fully consistent with those published for the Rauer Group and the Larsemann Hills, but the structural history enables further evaluation of the two models.

The evidence for progressive, non-coaxial, flat-lying deformation during decompression in the Brattstrand Bluffs coastline indicates that the process responsible for retrograde thinning of the thickened crust was associated with substantial deformation. Flat-lying structures in high-grade terrains have been attributed to both compressional and extensional regimes (Sandiford, 1989*a*), but the combination of flat-lying structure and decompression is taken here as good evidence of extension. Hence at least part of the retrograde uplift is attributed to extensional thinning. Extension can also explain the regional variation of retrograde decompression: extension thins the lithosphere from within, and hence, unlike erosion, does not produce a uniform amount of decompression at all depths but rather produces the greatest decompression at the greatest depth. It follows that the areas with the highest peak pressures should exhibit the greatest retrograde decompression. This does not explain the symmetrical distribution of lithologies and metamorphic histories around the Larsemann Hills, but this is thought to reflect a later deformation. Given that the structure in the Larsemann Hills is dominated by a regional synform ($F_{3(L)}$), whereas that in the Brattstrand Bluffs coastline is dominated by a regional antiform ($F_{5(B)}$), both of which post-date decompression, it is not surprising that rocks presently exposed in the Larsemann Hills were at a higher crustal level during Proterozoic metamorphism. The exposure of deeper levels in the Rauer Group, and possibly the Munro Kerr Mountains, is likewise attributed to regional folding after or during the closing stages of Proterozoic metamorphism. However, a simple model involving extensional collapse of thickened lithosphere is still inconsistent with the temporal proximity of the baric and thermal peaks in the Larsemann Hills. In fact, the extensional collapse models of England (1987) require that rocks preserving low-pressure granulite assemblages have been decompressed rapidly through a substantial pressure interval, in order to preserve high temperatures at low pressure. Models involving convective thinning of the mantle lithosphere during continental collision can resolve these inconsistencies.

Sandiford and Powell (1990, 1991) and Loosveld and Etheridge (1990) have shown that convective thinning of the mantle lithosphere during or after convergence increases the heat flow, and can hence generate high temperatures at relatively low pressures. If convective thinning is synchronous with convergence, the thermal

maximum is achieved during convergence, and hence synchronously with the baric maximum rather than after the baric maximum as predicted by the classical collisional models. Hence convective thinning can account for the nature of the metamorphic peak along the Prydz Bay coastline: high temperatures at low pressure, and synchronicity of the thermal and baric peaks. The remaining problems relate to the retrograde evolution. The field evidence in the Brattstrand Bluffs coastline, which is not inconsistent with relationships reported in the Rauer Group and the Larsemann Hills, implies that the area returned to isostatic equilibrium via some form of extensional collapse. This collapse apparently resulted in decompression of between 1 and 4 kbar. The Tibetan Plateau, which is considered to be a present-day example of incipient extensional collapse, comprises crust which has probably doubled in thickness during the collision of India and Asia (Molnar & Tapponnier, 1975). Although the amounts of decompression recorded in Prydz Bay are minima, given that a limited amount of decompression could have preceded the thermal peak, it seems that the amount of thickening required to make the lithosphere gravitationally unstable in Prydz Bay was significantly less than that in Tibet. This discrepancy can be attributed to substantial thinning of the mantle lithosphere in Prydz Bay during collision. Sandiford and Powell (1990) have shown that the maximum possible extent of crustal thickening depends on the amount of mantle-lithosphere thinning. The greater the extent of mantle-lithosphere thinning, the smaller the amount of crustal thickening required for the potential energy of the convergent orogen to equal the compressive forces.

8.4.4 Tectonic models for the northern Prince Charles Mountains

Correlations between structure and metamorphism in the northern Prince Charles Mountains remain poorly known, and any tectonic models for the Proterozoic metamorphic event in this area are even more speculative than those proposed for Prydz Bay. The various outcrops of the Proterozoic Complex are generally associated with retrograde decompression of between 1 and 4 kbar (Harley & Hensen, 1990; Harley, 1991), and are widely held to be part of a single metamorphic belt reflecting the same tectonic event. The retrograde evolution of the northern Prince Charles Mountains is dominated by cooling rather than decompression, but this does not preclude a common tectonic origin with the decompressional granulites of Prydz Bay and the Rayner Complex. As pointed out by Loosveld and Etheridge (1990), crustal thickening and convective thinning of the lithosphere can not only produce a number of pressure-temperature paths for different metamorphic terrains, but can also produce a variety of paths for a single orogen. This variety is a result of lateral variation in the magnitude, rate, and relative timing of various thermal and tectonic processes. When

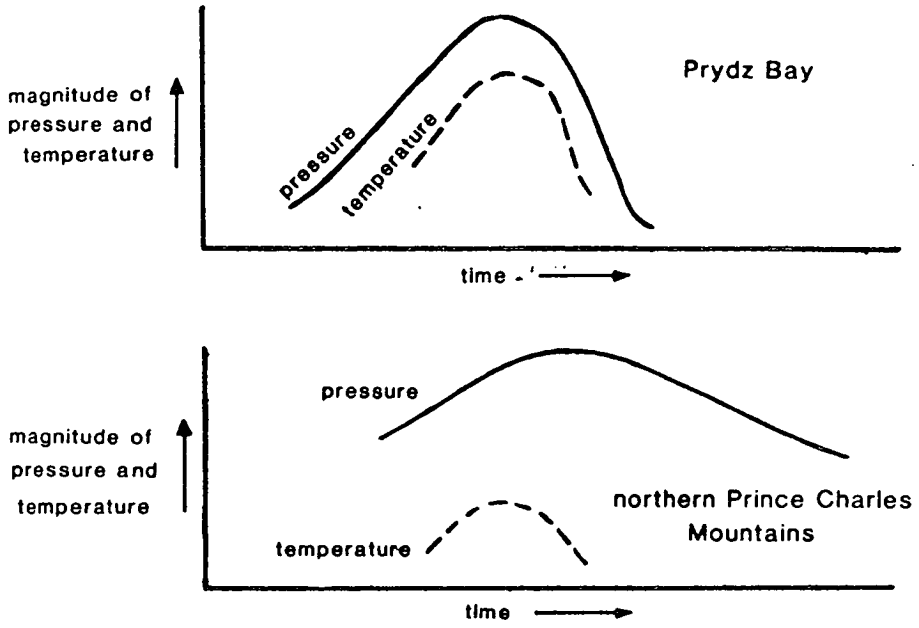

Fig. 8.7 Schematic diagrams illustrating how the magnitudes of pressure and temperature evolved with time during the Proterozoic metamorphic event in Prydz Bay and the northern Prince Charles Mountains, according to the model outlined in the text. Prydz Bay is at a relatively shallow crustal level near the centre of the orogen (i.e. relatively low pressures and high temperatures), whereas the northern Prince Charles Mountains are at relatively deep levels near the edge of the orogen (i.e. relatively high pressures and low temperatures). Crustal thickening is greatest at the centre of the orogen, where it is approximately synchronous with the thermal maximum corresponding to detachment of the thermal boundary layer, and is terminated by relatively rapid extensional collapse. The crust thickens to a lesser degree, and at a later stage in the thermal history, near the edges of the orogen, and is followed by gradual erosion and uplift.

the potential energy of the thickened lithosphere equals the compressional forces driving convergence, the orogen tends to expand and accommodate the shortening strain in previously-unthickened lithosphere. It is possible that the foreland regions are still undergoing thickening at the metamorphic peak, while the centre of the orogen is undergoing extensional collapse. Structures correlated with the closing stages of granulite metamorphism in the northern Prince Charles Mountains are upright rather than flat lying, and hence consistent with the metamorphic peak being synchronous with compressional deformation. In general, the foreland regions thicken less than the central regions and it is likely that the foreland regains isostatic equilibrium by erosion and uplift rather than extensional collapse. Erosion acts on a much longer time scale than extensional collapse, and could commence some time after the thermal peak (see Fig. 8.7). Hence granulites in the foreland regions can undergo near-isobaric cooling after the metamorphic peak. Subsequent decompression at low temperatures might not be recorded by the metamorphic assemblages. Further evidence for the northern Prince Charles Mountains being at the edge of an orogen includes the decreasing grade to amphibolite- and greenschist-facies rocks to the

south (see Section 2.3.4), and the thermal gradients implied by thermobarometry which indicate that the metamorphic peak in the Nemesis Glacier region occurred at lower temperatures and higher pressures than peak metamorphism in the Brattstrand Bluffs coastline (see Section 5.6.3).

8.4.5 Implications for the Proterozoic Complex, and some reservations

Attributing a given path to a particular tectonic setting is rarely straightforward, since a single tectonic setting can produce a variety of paths reflecting a spatial and temporal variation in the controlling parameters. Similarly, a particular path is rarely unique to a particular tectonic setting of granulite formation. It seems that, with a careful choice of thermal parameters and the option of extra heat from mantle-derived magmas, it is possible to fit an observed pressure-temperature path to any of a number of tectonic settings. This is particularly true for the models suggested here for the Proterozoic Complex. Models involving some combination of tectonic thickening and convective thinning can produce virtually any history by varying the extent and rates of convective thinning, the original thicknesses of crust and lithosphere, and the magnitude of the convergent driving forces. Although reasonable estimates can be made for the driving forces and crustal and lithospheric thicknesses, the fundamental processes behind convective thinning are poorly understood. The vigour of asthenospheric convection and the rate of convergence are thought to be important factors (Houseman *et al.*, 1981). Given that these two parameters are directly dependent on the thermal energy of the asthenosphere, which has declined with geological time (e.g. Bickle, 1978), Sandiford (1989*b*) has suggested that convective thinning of the lithosphere was more common and more rapid in Precambrian collision zones than Phanerozoic examples. Hence examples of extensional collapse and high-temperature low-pressure metamorphism should be more common in ancient terrains than recent metamorphic belts. Such variations remain, however, completely unquantified, and the extent and rate of convective thinning cannot be estimated.

It is clearly unsatisfactory to invoke a lithospheric thinning model on the basis that it produces the correct pressure-temperature path, if the only way of estimating the role of convective thinning is to work backwards from the observed paths. Until quantitative information concerning convective thinning is available, it will remain a panacea for tectonic problems, which, like most universal remedies, should be treated with caution. The relevance of such models can be tested using subsidiary information such as relict mineralogical evidence, and the nature of deformation and magmatism and their timing with respect to the pressure-temperature path; but the most powerful constraints are provided by absolute age data for deformational and thermal events (Oxburgh, 1990), since all of the processes involved operate over well-defined and

characteristic timescales. In the absence of absolute age data, the tectonic model developed here remains speculative for Prydz Bay, and even more speculative for the northern Prince Charles Mountains, but it does seem consistent with most of the structural and metamorphic evidence.

It should be noted that the northern Prince Charles Mountains are separated from the areas of extensive Proterozoic outcrop further north (i.e. the Rayner Complex and the Prydz Bay coastline) by large areas of no exposure other than a few small peaks and nunataks. At present, the correlation between the principal outcrop areas is based on similar absolute age data, which in the case of the northern Prince Charles Mountains are poorly constrained, and a similar metamorphic grade. The precise structural and metamorphic histories are different, but this does not preclude a common tectonic origin. However, the correlation will remain uncertain until more reliable age data are obtained from the northern Prince Charles Mountains. The reported decrease in grade south of the northern Prince Charles Mountains probably indicates the southern edge of the tectonic belt, but no such decrease in grade has been identified at the northern, coastal margins of the belt. If the metamorphic assemblages do reflect a former zone of continental collision, this zone, which extends for over 1500 km in an east-west direction, must be at least 500 km wide, and perhaps a lot more, and could be comparable to the Tibetan Plateau which is between 1000 and 1500 km wide. However, if convective lithospheric thinning was more active in the Precambrian, as suggested by Sandiford (1989*b*), collisional zones could have been wider than at present. The greater the convective thinning, the less thickening is required for gravitational forces to limit vertical strain, and the wider orogenic belts have to be to accommodate a given shortening strain. Hence the potential width of the Proterozoic terrain is not a problem, but not all the evidence is consistent with a simple progression from high thermal gradients and decompressional pressure-temperature paths along the coastline, to low thermal gradients and isobaric cooling further south. Reaction textures have been used to imply an isobaric-cooling path for metapelitic lithologies from the Mawson Coast of Mac.Robertson Land (Clarke *et al.*, 1989), which is located between the granulite outcrops preserving decompressional histories in Prydz Bay and the Rayner Complex. However, Clarke *et al.* (1989) note that the textures are not necessarily inconsistent with decompression before the cooling. Indeed, the textures used to infer retrograde cooling comprise coronas of garnet, sillimanite and cordierite around spinel and ilmenite, which are the same textures developed in metapelites from the Brattstrand Bluffs coastline during post-decompressional cooling (see Section 6.4.5).

8.4.5 The exposure of the Proterozoic Complex

Some granulites, such as the Gruf Complex of the Alps (Droop & Bucher-Nurminen, 1984) and the Central Gneiss Complex of British Columbia (Hollister, 1982), appear to have been exposed as a result of the same tectonic process responsible for their formation. These terrains preserve decompressional pressure-temperature paths, and were exhumed by erosion of the elevated crust produced by the granulite-forming orogenic event. In contrast, many granulite terrains reside in the lower or middle crust for substantial periods of time (e.g. Harley & Black, 1987), and are not exposed unless they are reactivated by another tectonic event (Ellis, 1987). The pressure-temperature paths for Prydz Bay indicate decompression to pressures of about 3 or 4 kbar after the Proterozoic metamorphic event, and the granulites are thought to have remained at this depth at least until the development of greenschist-facies assemblages at around 500 Ma (Harley, 1988; Stüwe & Powell, 1989*a*; Harley & Hensen, 1990). This metamorphic overprint was associated with shear zones and mylonites, and has also been identified in the northern Prince Charles Mountains and indeed much of East Antarctica. The 500 Ma event is generally thought to be responsible for the transport of the Proterozoic Complex to the upper levels of the crust and its eventual exposure (Clarke, 1988; Harley & Hensen, 1990). It has been correlated with the 'Pan-African tectonism' identified in Africa (Clifford, 1974) and other parts of Gondwana (Craddock, 1972, 1982), and was coeval with the Ross Orogeny in the Transantarctic Mountains (Elliot, 1975).

8.5 VOLATILE FLUID REGIMES AND GRANULITE STABILIZATION

8.5.1 Introduction

Granulite-facies assemblages are metastable with respect to melts at the high values of water activity commonly associated with most granulite precursors, and the transition from amphibolite to granulite assemblages must reflect not only an increase in grade, but also a decrease in water activity (a_{H2O}). It has been recognized for some time that granulites reflect relatively dry metamorphic conditions (e.g. Buddington, 1952), and this has since been quantified by calculations of a_{H2O} in granulite assemblages which generally indicate values less than 0.4, and commonly less than 0.2 (Wells, 1979; Phillips, 1980; Valley *et al.*, 1983*a*; Hansen *et al.*, 1984; Waters & Whales, 1984; Powers & Bohlen, 1985; Bhattacharya & Sen, 1986; Schreurs & Westra, 1986; Edwards & Essene, 1988). Such calculations are based on low-variance assemblages containing hydrous phases such as biotite or hornblende, which buffer a_{H2O} to a unique value at fixed pressure and temperature. There are several problems with these calculations. Firstly, they are particularly dependent on the chosen

temperature conditions, and calculated values of a_{H2O} are minima if temperature conditions are underestimated due to resetting of mineral thermometers. A more fundamental problem is that, in many cases, the existence of textural equilibrium between all the phases is rather equivocal. Many of the calculations are for biotite-bearing assemblages, and the status of biotite with respect to many peak metamorphic assemblages is uncertain (e.g. Indares & Martignole, 1985*b*; see Sections 6.5.4 and 7.6.4). It is common for there to be little or no discussion of textural relationships in papers concerned with activity calculations, and the relevance of calculated volatile activities to granulite conditions in such cases should be questioned. However, the calculations do seem to confirm that granulites do not equilibrate in the presence of a water-rich fluid. Much controversy has surrounded the causes of low water activities in granulites, and various models have been proposed to account for them. The rest of this section outlines these models, and some of the evidence for and against them, and then considers the relevance of these models to the stabilization of granulite assemblages in the Brattstrand Bluffs coastline and the Nemesis Glacier region.

8.5.2 Fluid regimes and granulite genesis

There are three principle models for the stabilization of granulite assemblages: metamorphism of fluid-absent rocks, dehydration of crustal lithologies by extraction of the hydrous component into silicate melts, and dehydration by dilution with some other volatile species.

(i) Granulite terrains certainly comprise some lithologies whose precursors, such intrusive gabbros and diorites, were originally dry. These would develop granulite assemblages at high temperatures provided that water does not diffuse inwards from hydrous country rocks. However, this model cannot account for many of the lithologies in extensive granulite terrains, which are known to have had hydrous precursors. It is possible that the precursor lithologies were dehydrated by previous unrelated metamorphic or igneous events, but this merely translates the problem of dehydration back in time. Thompson (1983) has suggested that fluid absence is a normal state for most of the middle and lower crust, with volatile fluid restricted both temporally and spatially. However, given that the onset of granulite-facies metamorphism is associated with the widespread breakdown of hydrous mineral phases, it seems that granulite metamorphism is inextricably linked to the transfer of a volatile component.

(ii) The pressure-temperature conditions of granulite metamorphism overlap with those required for partial fusion of many crustal rock types. Partial melting of granulite precursors would produce a dehydrated solid residue, since the water component of the precursor would be preferentially partitioned into the silicate

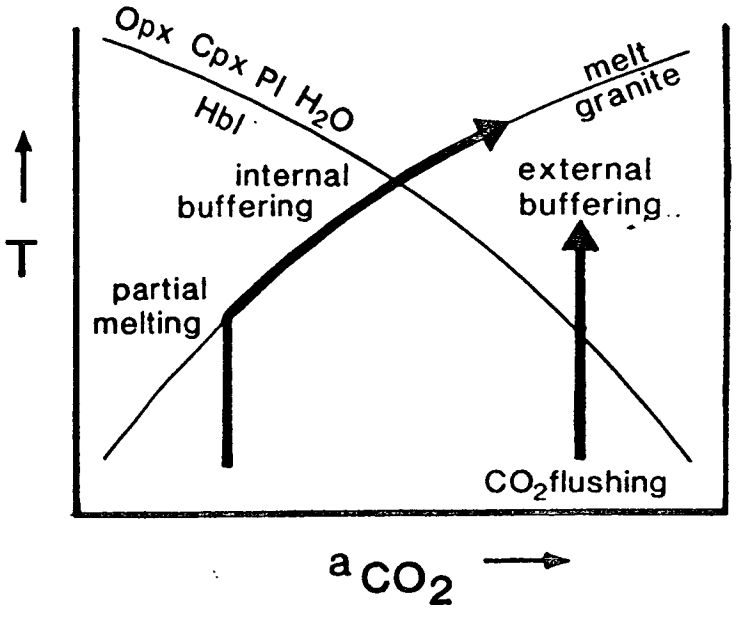

Fig. 8.8 A schematic T-a_{CO2} section depicting two methods of granulite formation. If fluid composition is buffered externally by a CO_2-rich fluid, hornblende dehydration occurs at temperatures below the solidus of crustal rocks. However, under water-rich conditions some means of lowering a_{H2O} in the fluid is required to achieve dehydration before the amphibolite precursor melts completely. This can be achieved by partial melting of less-refractory lithologies, if the fluid composition is buffered internally along the melting reaction. H_2O is partitioned into the melt rather than the fluid, increasing a_{CO2} to levels where orthopyroxene can form in basic lithologies.

melt (Fyfe, 1973). This process could also occur by the absorption of water into water-undersaturated magmas derived from deeper in the crust.

(iii) The passage of a pervasive carbonic fluid phase through the crust would dilute the hydrous component of any metamorphic fluid, thus lowering the water activity, promoting dehydration reactions, and stabilizing anhydrous assemblages (Newton *et al.*, 1980). Such carbonic fluids are usually assumed to have been derived from the mantle, but could be derived locally by decarbonation of calcareous lithologies in the crust. Although CO_2 is the prime candidate for such a process, other potential, if unlikely, diluents include N_2 and CH_4.

The first of these models is generally considered unimportant on a regional scale, except in terrains dominated by orthogneiss, but there has been much debate concerning the respective merits of the second and third mechanisms. These two mechanisms both cause a decrease in water activity, but are fundamentally different in character. One relies on the presence of silicate melt, and tends to consume volatile fluid in a trend towards fluid-absent conditions; the other requires, and indeed is driven by, a volatile fluid phase. Another distinction is that the anatectic models tend to produce local variation in volatile activities, since the dehydration is controlled internally and affected by local compositional variation, whereas dehydration via volatile flushing is controlled externally and tends to produce a uniformity in volatile activities. The two models can be considered in terms of internally-buffered and externally-buffered processes respectively (see Fig. 8.8), although the actual circumstances are generally somewhere between these two theoretical extremes.

The carbonic-infiltration model is based on the observation that the transition from amphibolite- to granulite-facies mineral assemblages in some terrains is associated with a transition from H_2O-dominated fluid inclusions to CO_2-dominated fluid inclusions (Touret, 1971*b*; Hansen *et al.*, 1984), and the development of 'charnockitization' textures (Pichamuthu, 1960; Janardhan *et al.*, 1979, 1982; Hansen *et al.*, 1987). The latter comprise veins and blebs of orthopyroxene-K-feldspar charnockite, which overprint amphibolite-facies gneiss. These veins are not related to any compositional variation in the amphibolite and are interpreted as pathways of CO_2-rich fluid. Further evidence includes the commonly-observed, but by no means general, geochemical depletion of large ion lithophile elements in granulite terrains (Heier, 1973), which is consistent with extraction by pervasive CO_2-rich fluids (Glassley, 1983; Weaver & Tarney, 1983; Lamb *et al.*, 1986).

Evidence for locally-controlled anatectic processes, rather than pervasive influx of carbonic fluids, is principally based on observation of local variations in chemical parameters such as a_{H2O} (Waters & Whales, 1984; Bhattacharya & Sen, 1986; Valley *et al.*, 1983*a*; Valley, 1985) and stable-isotope ratios (Valley & O'Neil, 1984). In addition, the recognition of low-variance assemblages capable of buffering fluid composition, and evidence of melting reactions which would tend to decrease a_{H2O} as they progress (e.g. Waters, 1988; Stüwe & Powell, 1989*b*; Powell & Downes, 1990), indicate the importance of partial melting in the development of granulites.

8.5.3 Fluid regimes in the Proterozoic Complex

Water activities in both the Brattstrand Bluffs coastline and the Nemesis Glacier region are constrained to have been low during the Proterozoic metamorphic event, and there is widespread evidence for syn-metamorphic anatexis and magmatism. In the Brattstrand Bluffs coastline, a_{H2O} values were buffered to low values by melting reactions, and there is good evidence for fluid absence at the metamorphic peak, and dissolution of volatile components in silicate melts (see Section 6.3.5). One problem with the partial-melting theory of granulite formation is that the fluids dissolved in the silicate melts must be prevented from back-reacting with the restite in order for granulite assemblages to be preserved. The simplest solution is for the melts to migrate upwards, along with their volatile contents.

Partial melting was particularly advanced in the metapelite of the Brattstrand Bluffs coastline, and leucosome units account for at least 25 per cent of the exposed rock at some outcrops (see Plate 3.3c), but there is no evidence for substantial melt migration on scales greater than 100 m. It is thought that at least 30 per cent melting is required before partial melts can efficiently segregate from their source rocks (Arzi, 1978; van der Molen & Paterson, 1979; Wickham, 1987). Hydrous fluids were

expelled into the granulite country rocks on crystallization of the partial melts in the Brattstrand Bluffs coastline, but their passage through the granulites was channellized along shear zones, and hence avoided most of the anhydrous assemblages (see Section 6.5.1). The presence of some CO_2 in the metamorphic fluid is indicated by the presence of graphite. Graphite is concentrated in the leucosome units, where it is more common than hydrous minerals. This might seem to suggest that the partial melts were associated with CO_2-rich fluids, which would account for the widespread preservation of anhydrous assemblages. However, the identification of biotite-rich shear zones, correlated with release of fluid from the crystallizing partial melts, is thought to indicate that the fluids were water rich. There is very little graphite in the shear zones, although rare carbonate has been identified. This suggests that water was released more efficiently from the crystallizing melts than CO_2, with much of the latter being trapped within the solid leucosome. This could reflect differences in the behaviour of H_2O and CO_2 fluids in the crystallized leucosome. Experimental work by Watson and Brenan (1987) suggests that H_2O should form a continuous grain-boundary film in quartz-rich rocks, whereas CO_2 should occur as isolated pockets at grain intersections which would severely limit its transport through the rock.

Partial melting was also important in the Nemesis Glacier region, but not as widespread as in the Brattstrand Bluffs coastline. However, granulite formation via pervasive carbonic flushing is precluded by the existence of substantial variation in volatile activities on a metre scale (see Section 7.6.4). Such variation could not be preserved if low values of a_{H2O} were achieved by pervasive infiltration of carbonic fluids (Valley *et al.*, 1983*a*).

Other studies of the Proterozoic Complex have also favoured fluid-absent conditions or the local buffering of a fluid phase, and a partial-melting origin for the granulite assemblages (Stüwe & Powell, 1989*b*; Harley & Buick, 1991). However, partial melting and carbonic fluids are not necessarily mutually exclusive. For example, Frost and Frost (1987) have proposed a model for granulite formation whereby magmas rising through the crust release CO_2-rich fluids and cause partial melting of the country rock. Although metamorphic fluids in both the areas of study are assumed to have had some carbonic component, this is thought to have been subordinate to the hydrous component, and the preferred method of granulite formation is via partial melting and dissolution of the hydrous fluids. Indeed, many workers now reject carbonic flushing as a major cause of granulite formation, although it may be of importance locally, and favour models involving melting and magmatism. The carbonic-flushing hypothesis is reliant on copious volumes of a transient externally-derived fluid, for which there can only ever be indirect evidence.

In contrast, the connection between granulites and partial melting is well established in the field, and the partial-melting model does not necessarily require any external input. Nevertheless, a role for CO_2 in the partial-melting process has recently been proposed following the experimental work of Peterson and Newton (1989, 1990), which has suggested that CO_2 is more soluble in magnesium-rich silicate melts than previously thought, and that melting in the presence of CO_2-rich fluids occurs at similar temperatures to melting in the presence of H_2O-rich fluids. This has led to the proposal that felsic magmas can be associated with CO_2-rich fluids (Peterson & Newton, 1989, 1990; Newton 1990) which account for the CO_2-rich fluid inclusions reported from some migmatites (Olsen, 1987; Hollister, 1988) and the preservation of phases such as orthopyroxene and garnet in leucosomes after crystallization. However, this is not accepted by other workers who maintain that CO_2 inhibits partial melting (e.g. Clemens, 1990). It seems that the role of CO_2 in granulite genesis is likely to remain a controversial issue for some time yet, even though partial melting is generally considered the prime agent of granulite formation.

8.6 SUMMARY AND FUTURE WORK

8.6.1 Summary

This thesis is a study of granulites from two areas within the Proterozoic Complex of East Antarctica. Structural and geological histories, involving polyphase metamorphic, intrusive and deformational events, have been deduced for the Brattstrand Bluffs coastline and the Nemesis Glacier region using field and petrographic observations. Both areas comprise orthogneiss and paragneiss material with granulite-facies mineral assemblages, and discordant intrusive lithologies. Partial melting at the metamorphic peak was particularly advanced in the Brattstrand Bluffs coastline, and also important in the Nemesis Glacier region. The structure of both areas is dominated by a flat-lying layer-parallel foliation. In the Brattstrand Bluffs coastline this foliation is locally overprinted by flat-lying folds and shear zones, whereas in the Nemesis Glacier region the foliation is locally overprinted by upright folds and shear zones.

Those parts of the metamorphic history ascribed to the Proterozoic event have been quantified using thermobarometry and petrogenetic-grid constraints, which imply peak conditions of about 6 kbar and 860°C followed by decompression in the Brattstrand Bluffs coastline, and 6.5 to 7 kbar and 800°C followed by cooling in the Nemesis Glacier region. There is evidence in both areas that volatile activities were buffered by local mineral assemblages, and that granulite-facies assemblages were not developed in the presence of a pervasive carbonic fluid but rather in the presence of

silicate melts. A speculative tectonic model has been proposed to explain the structural and metamorphic features of the two areas, involving crustal thickening by continental collision, convective thinning of the mantle lithosphere, and extensional collapse of the overthickened crust. The different deformational and metamorphic histories of the Brattstrand Bluffs coastline and the Nemesis Glacier region can be accounted for by a lateral variation in the relative importance and timing of these processes. The Brattstrand Bluffs coastline is located near the centre of the former collisional zone, which underwent thickening and then extensional collapse during or just after the thermal peak to produce flat-lying structures and decompressional reaction textures. The Nemesis Glacier region is located near the edge of the former collisional zone, where there was still some thickening at the thermal peak to produce upright structures. The amount of thickening was less in the Nemesis Glacier region than the Brattstrand Bluffs coastline, and the area did not undergo extensional collapse, but rather followed a near-isobaric cooling path.

In addition to evaluating the metamorphic histories of these East Antarctic granulites, this thesis has addressed some petrological problems of a more general nature. A number of commonly used thermobarometric calibrations for garnet-orthopyroxene-plagioclase-quartz assemblages have been compared, and their reliability assessed. The effects of retrograde diffusion on these calibrations has also been considered, and a method proposed to correct mineral thermometers and barometers for iron-magnesium exchange which is one of the principal causes of uncertainty in granulite thermobarometry. A number of petrogenetic grids for metapelitic rocks at granulite grade have been reviewed, and altered to account for an observed inversion in the iron to magnesium ratios of garnet and spinel, and a simple composite grid has been produced and positioned in pressure-temperature space using thermobarometric constraints for the Brattstrand Bluffs coastline. A new petrogenetic grid has also been developed for granulite-facies calc-silicates, which is far more successful at providing sensible pressure-temperature paths than previous grids.

8.6.2 Future work

Although this study has provided some constraints on the metamorphic evolution of the Proterozoic Complex of East Antarctica, there are a number of lines of research which would provide a greater understanding of this, and other, high-grade terrains. There now follows a list of what are thought to be the most important topics that follow directly from this study.

(i) More fieldwork is required in the northern Prince Charles Mountains, partly to visit areas where the detailed geology is still unknown, and partly to resolve some ambiguities remaining after this study, of which one of the most important is the

correlation between metamorphic and structural events. In particular, knowledge of the timing of the metasomatic banding and retrograde reaction textures in the calc-silicate with respect to various structural features is crucial to an understanding of the area.

(ii) The most useful addition to this study would be an absolute time framework for the various structural, metamorphic and intrusive events. Reliable age data are completely lacking from the northern Prince Charles Mountains, and a number of the events in Prydz Bay are also completely unconstrained. The resetting of isotopic systems to varying degrees in different minerals causes isotopic ages from polymetamorphic granulites to depend on both the isotopic system and the mineral used, and such ages are commonly difficult to interpret (Mezger, 1990). However, U-Pb systematics in zircon are generally considered to be the most difficult to reset completely and therefore the most likely to preserve original isotopic compositions, and in some cases zircon ages have shown previous geochronological schemes to be incorrect (e.g. Sri Lanka: Kröner *et al.*, 1987; Hölzl *et al.*, 1988). The identification of different generations of zircon growth within a single specimen, and dating of these generations using spot analysis techniques, is proving a very powerful technique for revealing the complexities of polymetamorphic rocks (e.g. granulites from the Napier Complex: Black *et al.*, 1986, 1987). A preliminary zircon dating study in Prydz Bay (Kinny & Black, 1990) has established the 1000 Ma event and confirmed the presence of Archaean relics in the Rauer Group, but much more data would confirm or disprove many of the speculative correlations and models developed in this thesis. Dates produced by other systems are also of great value, provided they are interpreted with care. For example, dating of micas and hornblende using Rb-Sr and K-Ar systems commonly gives evidence of late low-grade events, which post-date granulite metamorphism (Schenk, 1980, 1989). Detailed geochronology, and superposition of an absolute time scale onto the relative framework of events in the Proterozoic Complex would enable both a correlation of events between different areas, and a comparison between the actual time span of events and the theoretical time scales for certain tectonic and geochemical processes.

(iii) Whole-rock geochemical studies would help to confirm the nature of the protolith lithologies in the two areas of study. This is most important for the northern Prince Charles Mountains, where there are little previous data and the nature of the precursors is more ambiguous than Prydz Bay.

(iv) The metapelitic migmatites in the Brattstrand Bluffs coastline provide an excellent opportunity to study some of the detailed geochemical aspects of partial

melting. Major, minor and trace element compositions of mesosome, melanosome and leucosome could provide tight constraints on the partial melting process. The role and origins of volatile species could also be studied by analysis of the isotopic composition of graphite and the amount and composition of volatile species trapped within structural channels of cordierite.

(v) A thorough evaluation of thermobarometers involving the phases cordierite-spinel-garnet-sillimanite-quartz is needed, as there are considerable discrepancies between different calibrations involving these phases, and between these calibrations and independent estimates.

(vi) A detailed geochemical study of the gross metasomatic banding in the calc-silicates would identify chemical gradients imposed before peak metamorphism and further constrain the metamorphic and fluid regimes in the northern Prince Charles Mountains. In particular, the origin of the water-rich fluids held responsible for the banding is still unknown, but could be resolved by determination of the stable-isotopic compositions of phases such as scapolite, wollastonite and calcite.

Much of the research outlined above is already underway. Other geologists have visited the northern Prince Charles Mountains during the 1988/89, 1989/90 and 1990/91 field seasons, and the preliminary results of their work should appear in the next few years. This work included collection of specimens for whole-rock geochemistry and petrological study by numerous workers, and most importantly the collection of specimens for geochronology by P.D. Kinny. A geochemical study of the metapelitic migmatites from the Brattstrand Bluffs coastline is underway at the University of Edinburgh, and Royal Holloway and Bedford New College, London, including major, minor and trace element analysis by G.R. Watt, and a study of cordierite volatile contents by I.S. Buick, D.P. Mattey, S.L. Harley and the author.

APPENDIX I MAPS

This appendix contains locality maps of the Brattstrand Bluffs coastline and the Nemesis Glacier region, indicating the areas visited during the 1987/88 and 1988/89 field seasons. The locality maps for the Brattstrand Bluffs coastline also summarize the geology and structure of the areas. This was not possible for the Nemesis Glacier region because of the larger scale of mapping. The location of the individual localities within the Brattstrand Bluffs coastline and the Nemesis Glacier region is illustrated in Figs 3.2 and 4.2.

A locality map of Chaos Glacier is included although the geology and structure of this area, which is rather similar to parts of the Rauer Group (as described by Harley, 1987), is not considered in this thesis. This is because a specimen of garnet-orthopyroxene-plagioclase-quartz gneiss from this area was included in the thermobarometric study of Chapter 5.

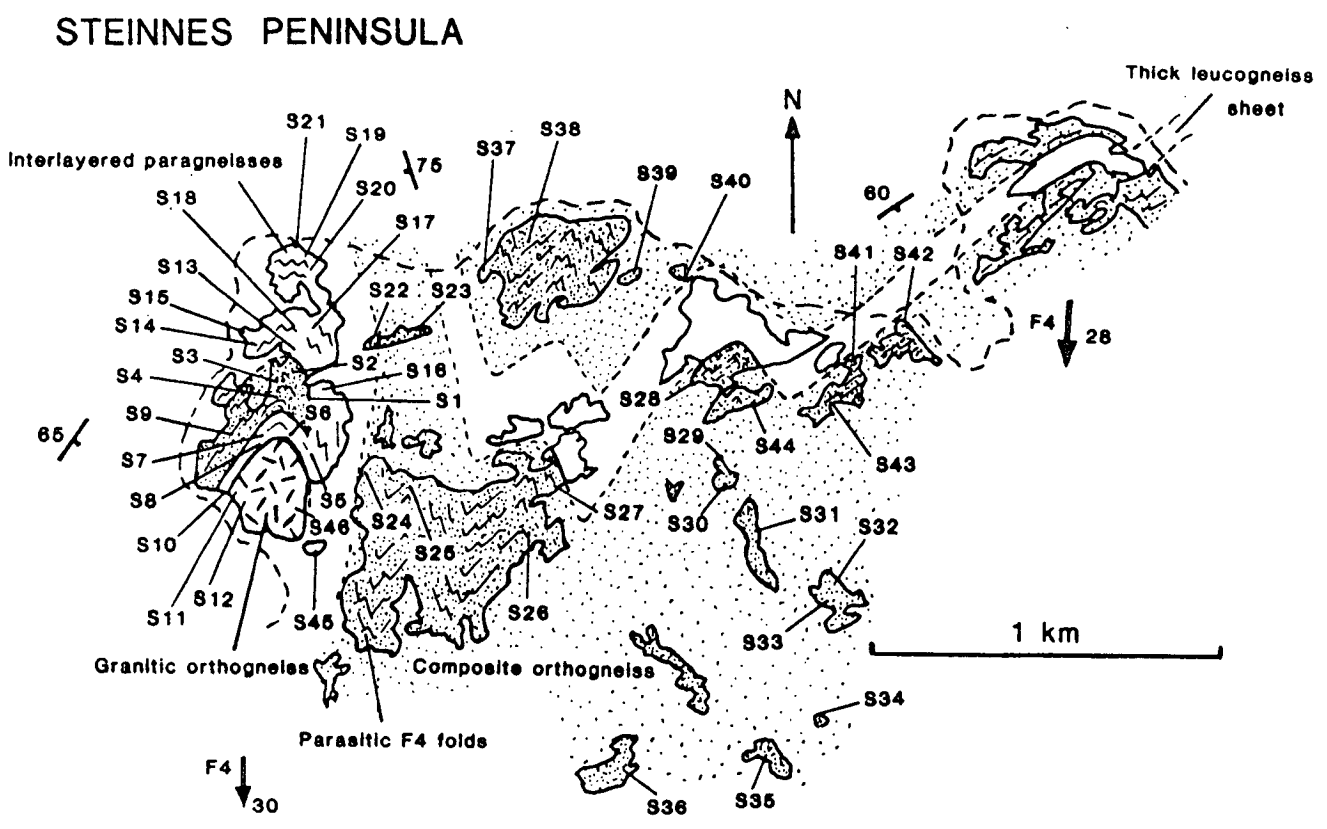

Note the refolded isoclinal fold hinge at the western margin of the peninsula. The isoclinal closure is near to the S6 locality number.

DALKOY ISLAND

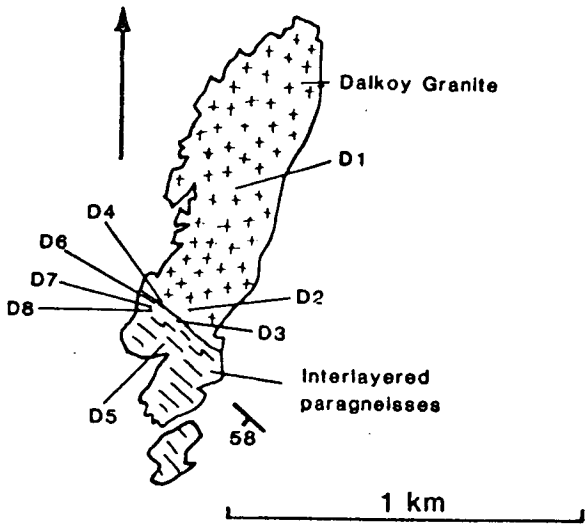

COWELL ISLAND

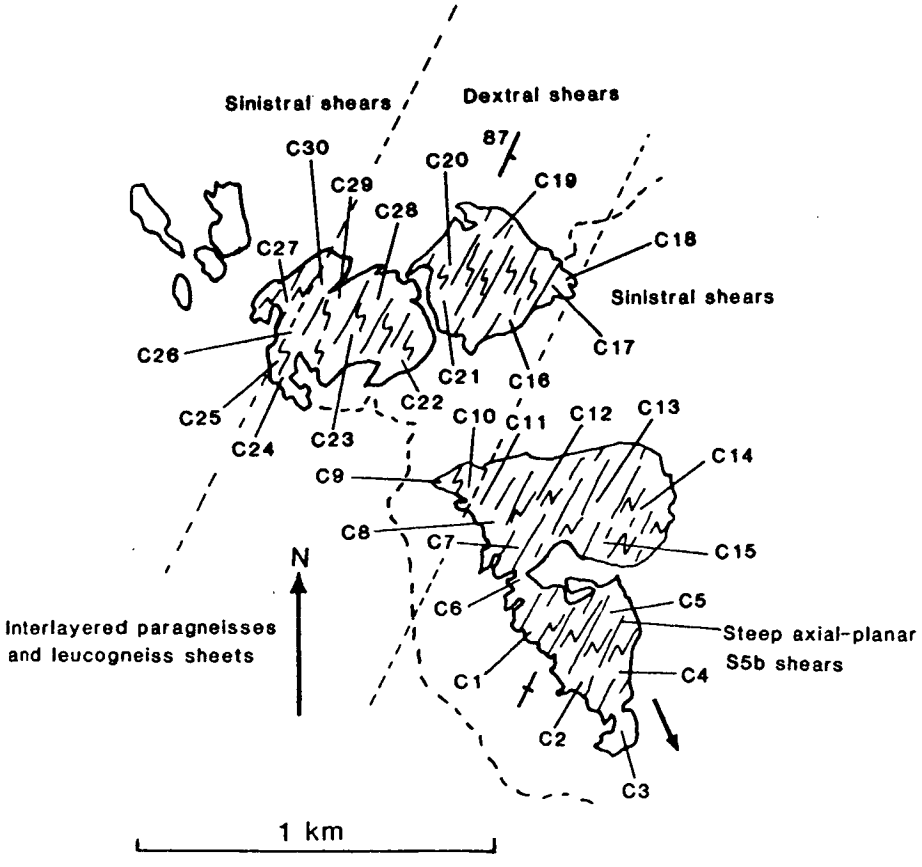

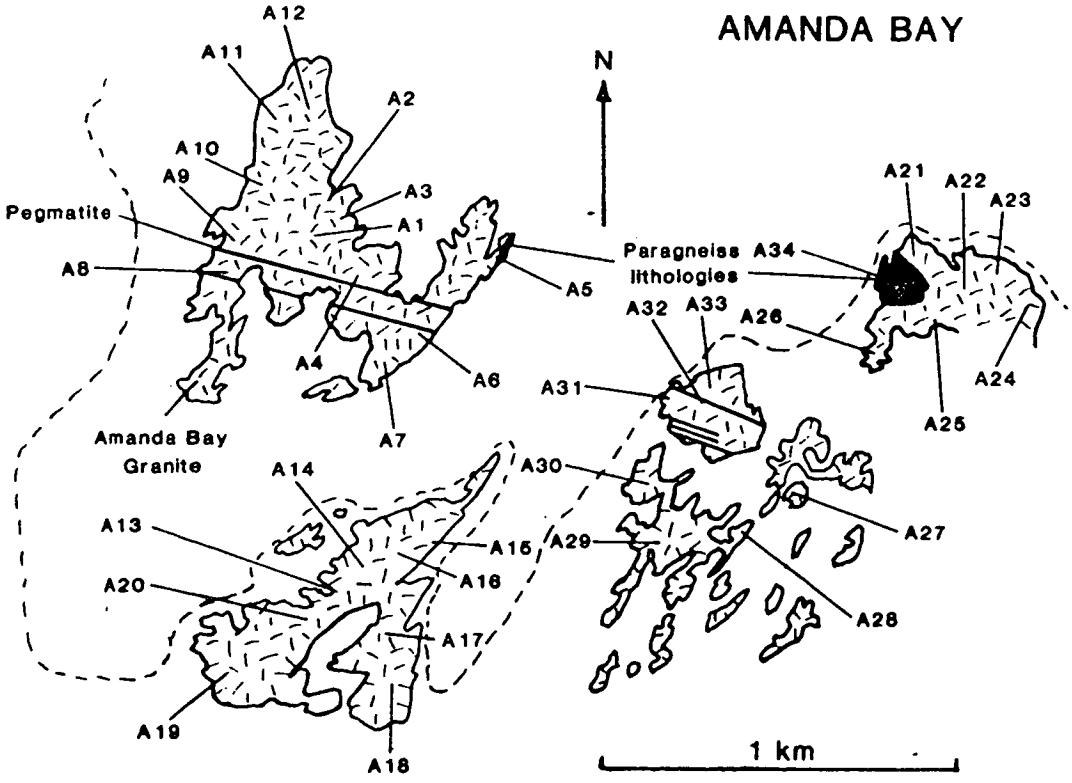
AMANDA BAY
N
A12
A11
A2
A10
A9
A3
A1
Pegmatite
A8
A5
A4
A6
A7
Amanda Bay
Granite
A14
A13
A15
A16
A20
A17
A19
A18
Paragneiss
lithologies
A34
A21
A22
A23
A32
A33
A26
A24
A31
A25
A30
A27
A29
A28
1 km

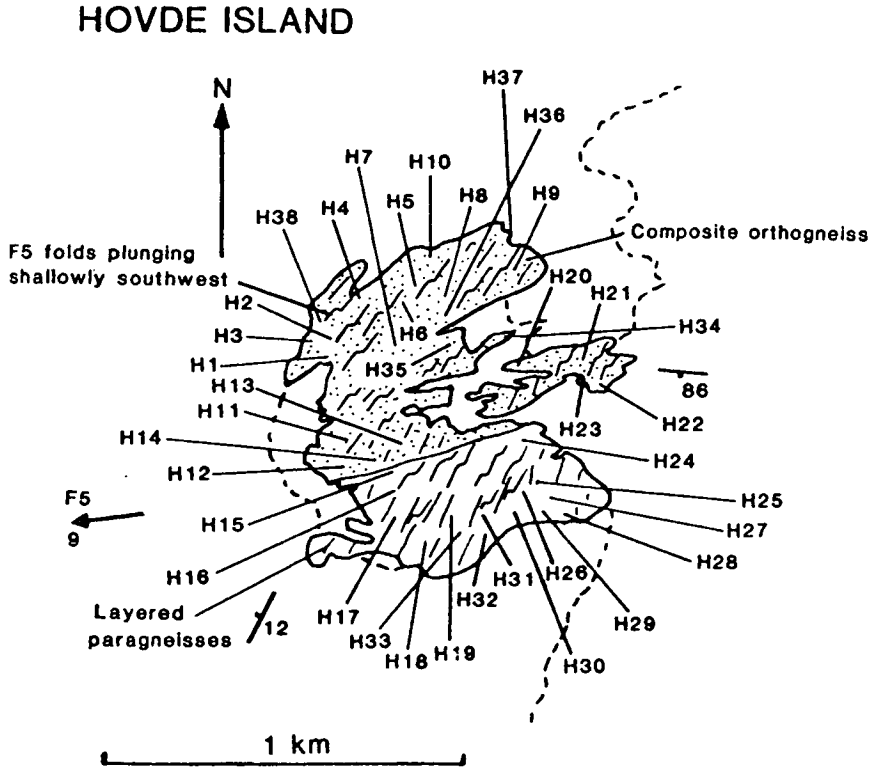
HOVDE ISLAND
N
H37
H36
H7
H10
H8
H9
H38
H4
H5
F5 folds plunging
shallowly southwest
Composite orthogneiss
H20
H2
H21
H3
H6
H34
H1
H35
86
H13
H11
H23
H22
H14
H24
H12
F5
H25
9
H15
H27
H28
H16
H31
H26
Layered
paragneisses
12
H17
H32
H29
H33
H18
H19
H30
1 km

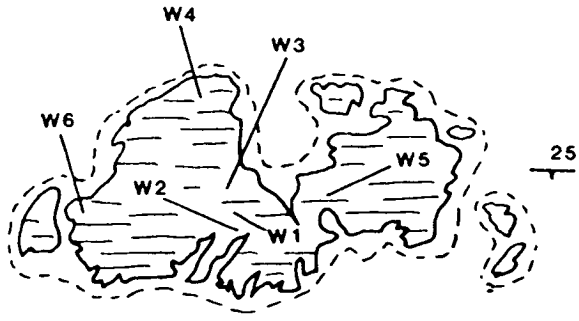

WESTERN BRATTSTRAND BLUFFS

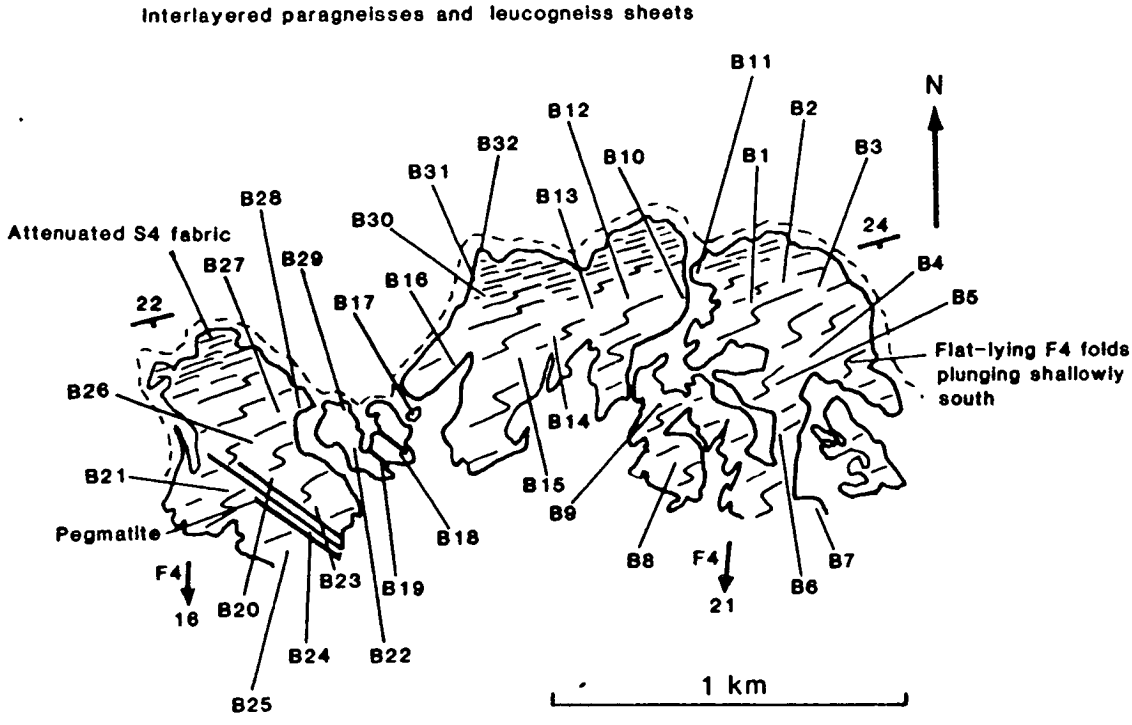

CENTRAL BRATTSTRAND BLUFFS

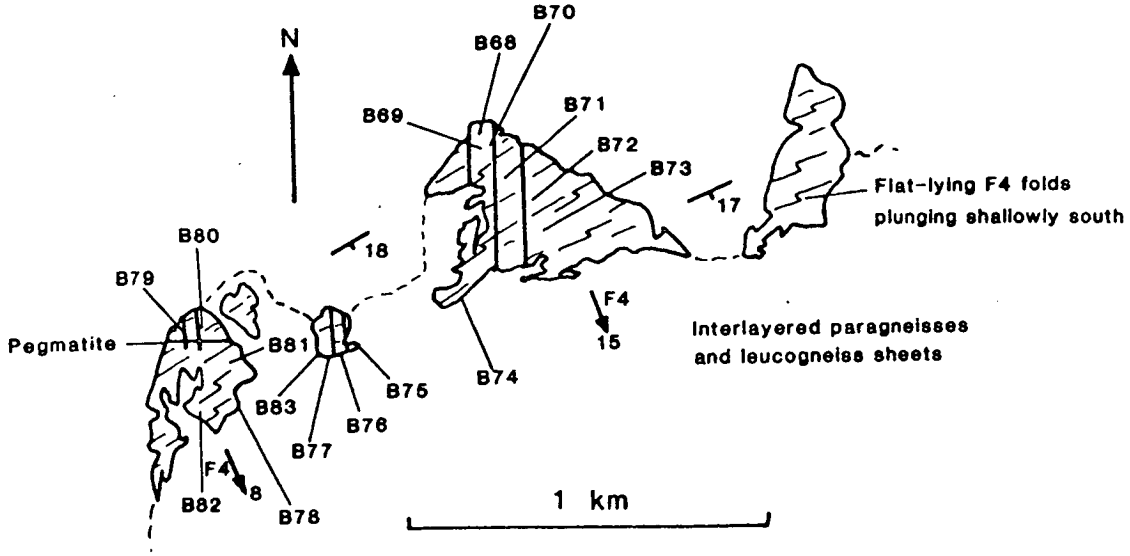

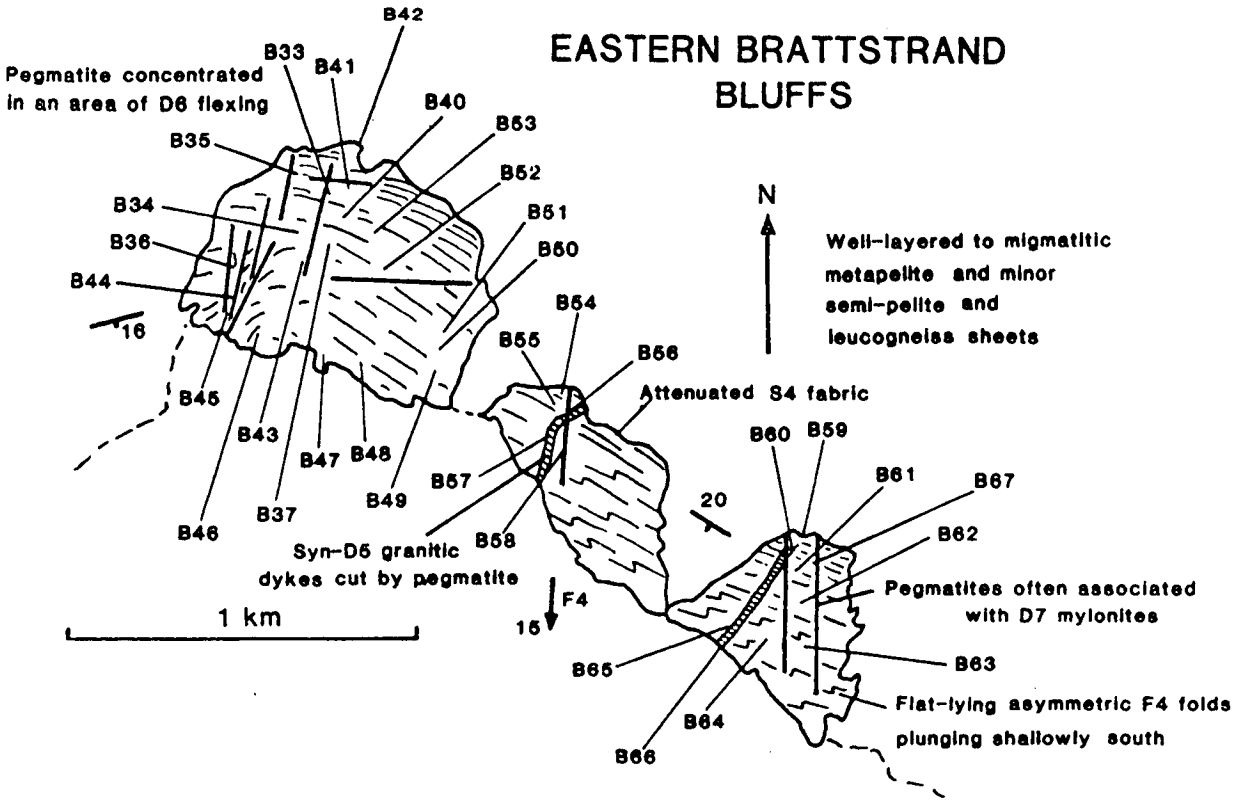
EASTERN BRATTSTRAND BLUFFS
Pegmatite concentrated in an area of D6 flexing
B42
B33
B41
B40
B63
B35
B52
B34
B51
B36
B50
B44
B54
16
B55
B56
B45
Attenuated S4 fabric
B43
B47
B48
B60
B59
B57
B61
B67
B49
20
B37
B62
B46
B58
Syn-D5 granitic dykes cut by pegmatite
F4
Pegmatites often associated with D7 mylonites
15
B65
B63
Flat-lying asymmetric F4 folds plunging shallowly south
B64
B66
1 km
N
Well-layered to migmatitic metapelite and minor semi-pelite and leucogneiss sheets

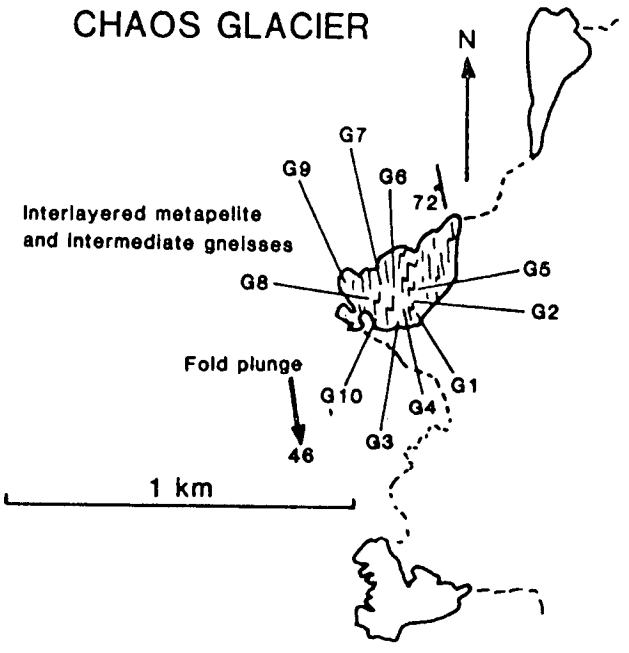
CHAOS GLACIER
N
G7
G9
G6
72
Interlayered metapelite and intermediate gneisses
G8
G5
G2
Fold plunge
G10
G1
G4
G3
46
1 km

SVENNER 1

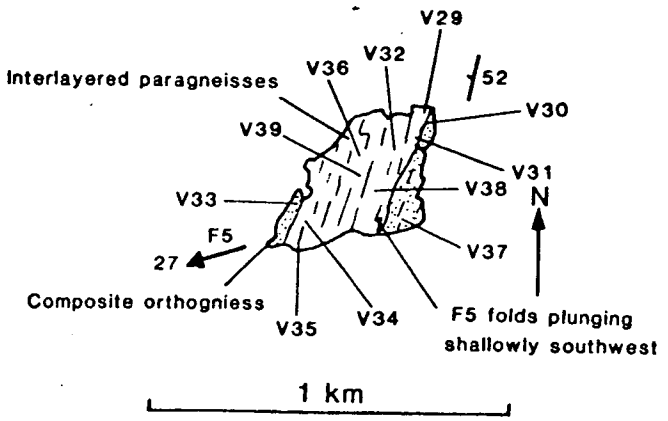

SVENNER 2

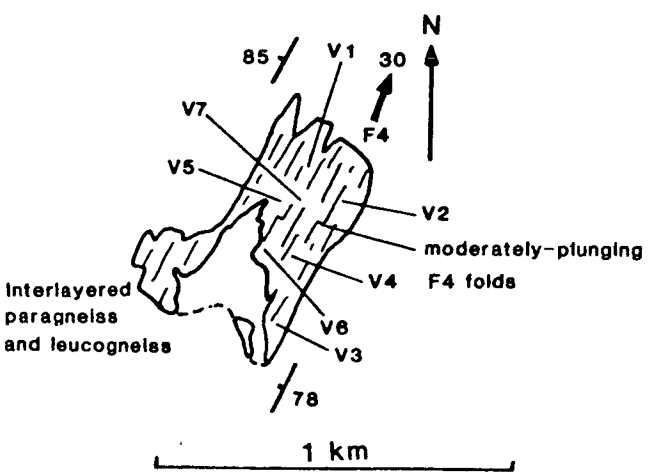

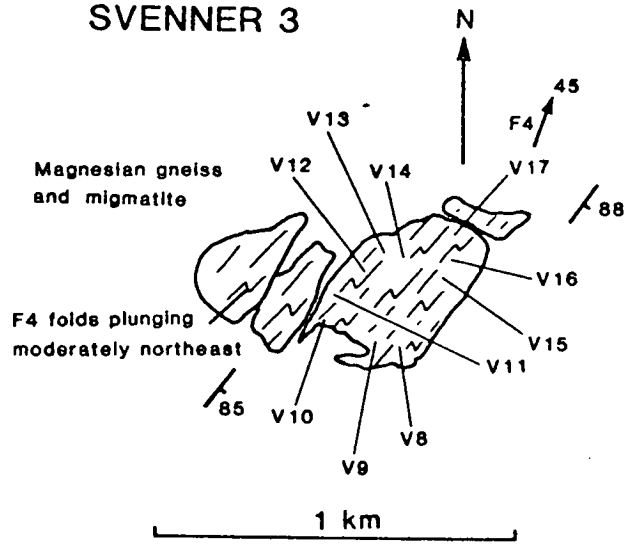
SVENNER 3
N
45
F4
V13
V12
V14
V17
Magnesian gneiss
and migmatite
88
V16
F4 folds plunging
moderately northeast
V15
V11
85
V10
V8
V9
1 km

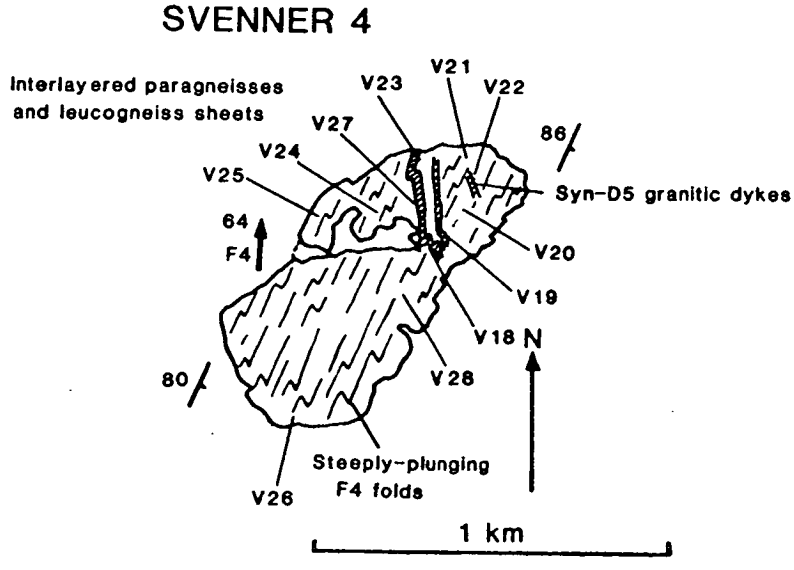
SVENNER 4
Interlayered paragneisses
and leucogneiss sheets
V21
V23
V22
V27
86
V24
V25
Syn-D5 granitic dykes
64
F4
V20
V19
V18
N
80
V28
Steeply-plunging
F4 folds
V26
1 km

Appendix 1.2 The Nemesis Glacier region

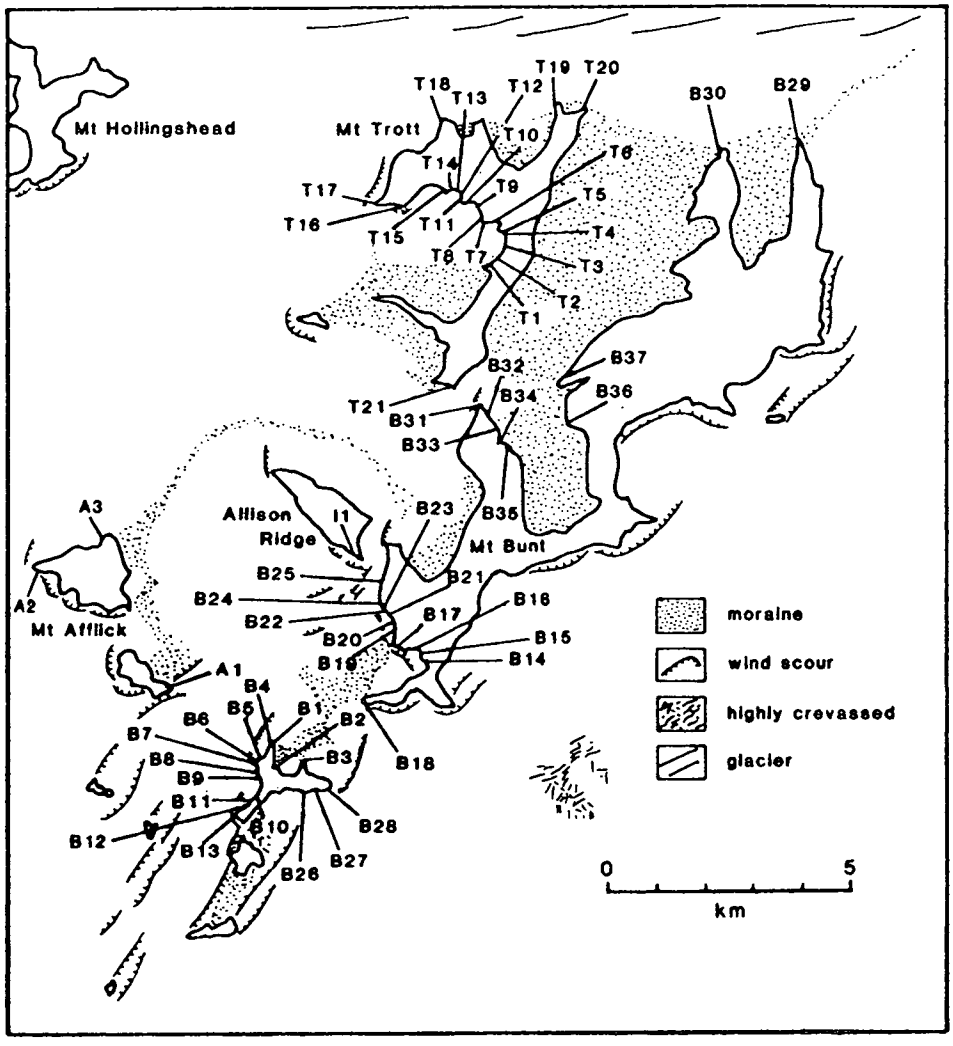

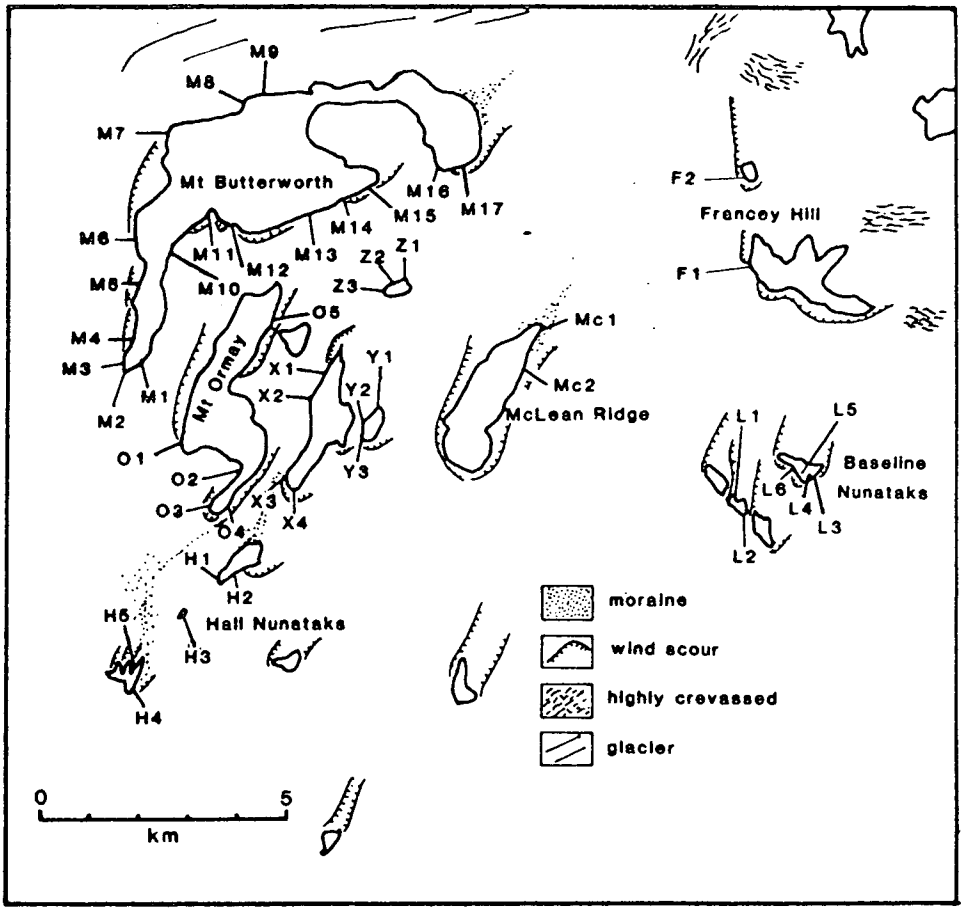
M9
M8
M7
Mt Butterworth
M16
M15
M17
M6
M14
M11
M13
Z2
Z1
M5
M12
Z3
M10
O5
M4
M3
M1
M2
Mt Ormay
X1
Y1
X2
Y2
O1
Y3
O2
O3
X3
X4
O4
H1
H2
H5
Hall Nunataks
H3
H4
F2
Francey Hill
F1
Mc1
Mc2
McLean Ridge
L1
L5
Baseline
Nunataks
L6
L4
L3
L2
moraine
wind scour
highly crevassed
glacier
0
5
km

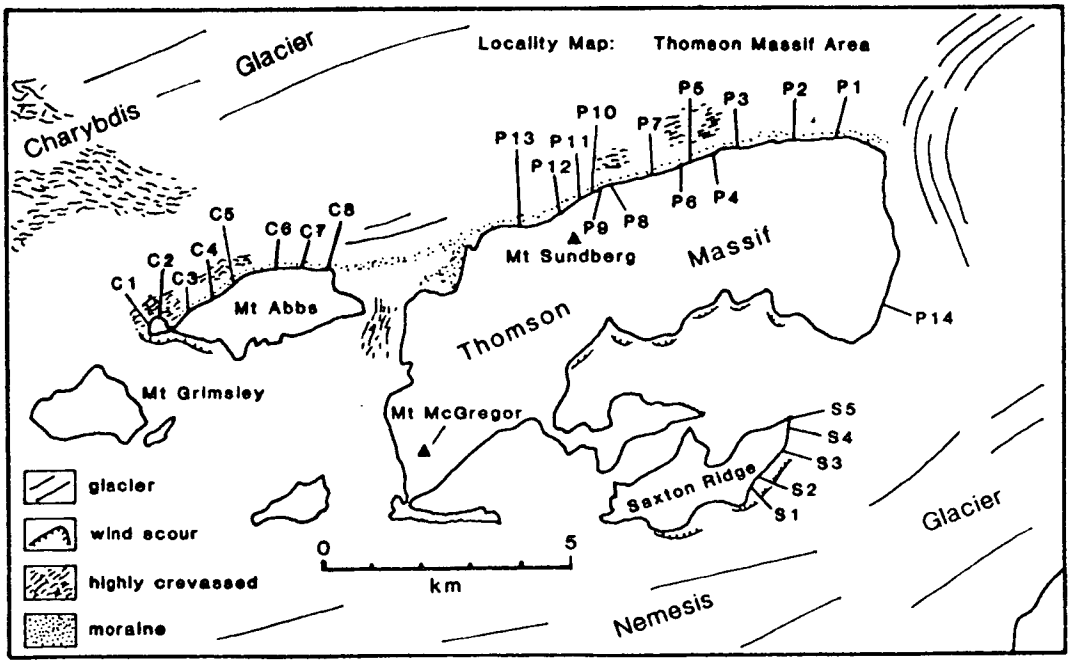
Glacier
Locality Map: Thomson Massif Area
Charybdis
P5
P3
P2
P1
P10
P7
P13
P11
P12
P6
P4
P9
P8
C5
C6
C7
C8
C2
C4
C1
C3
Mt Sundberg
Massif
Mt Abbs
Thomson
P14
Mt Grimsley
Mt McGregor
S5
S4
S3
S2
S1
Saxton Ridge
glacier
wind scour
highly crevassed
moraine
0
5
km
Glacier
Nemesis

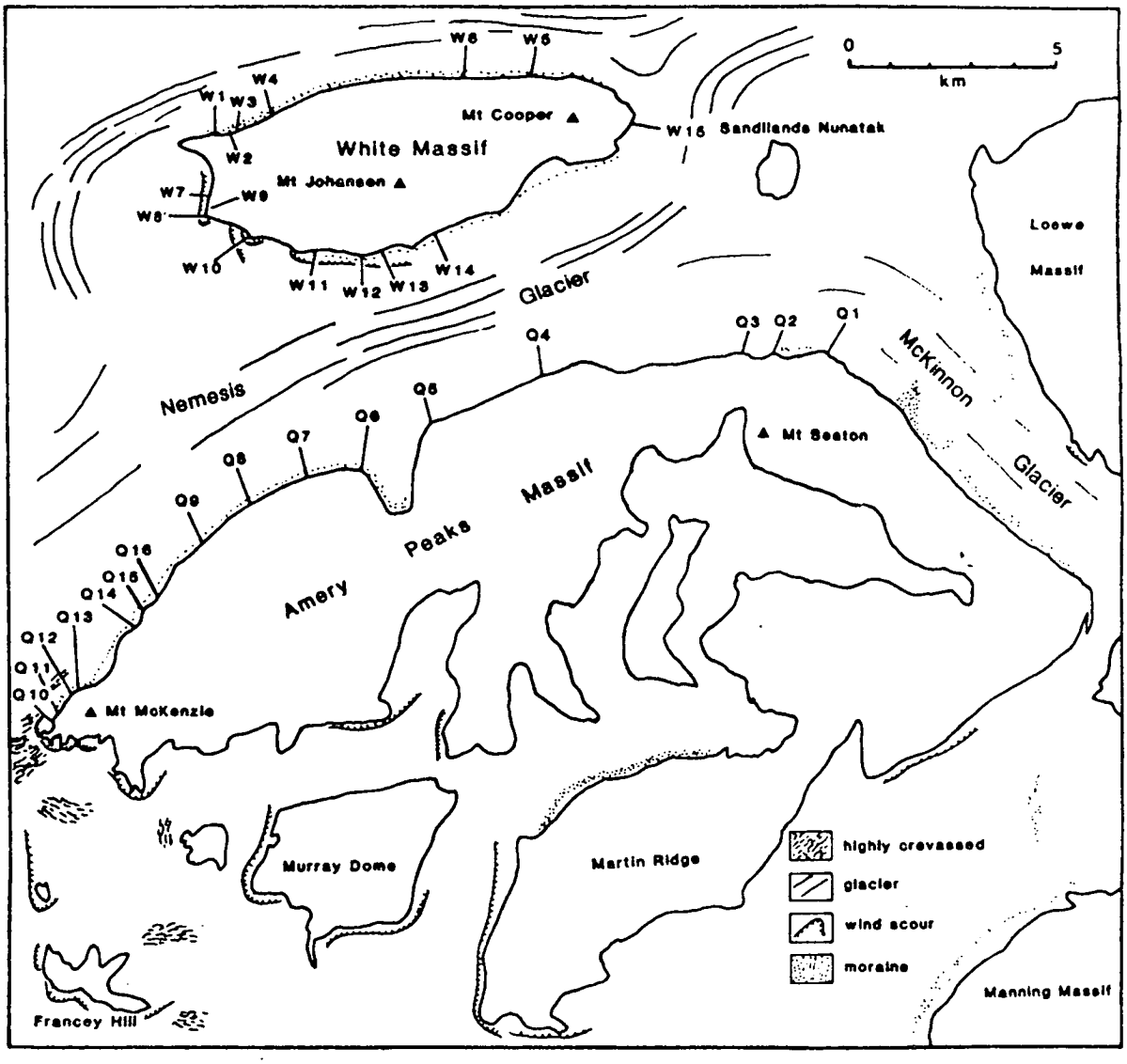
W6
W5
W4
W1
W3
W2
Mt Cooper ▲
W16 Sandllands Nunatak
White Massif
W7
W8
Mt Johansen ▲
W9
W10
W11
W12
W13
W14
Glacier
Nemesis
Q4
Q3
Q2
Q1
McKinnon
Glacier
Loewe
Massif
Q5
Q6
Q7
Q8
Q9
Mt Seaton ▲
Massif
Peaks
Amery
Q16
Q15
Q14
Q13
Q12
Q11
Q10
▲ Mt McKenzie
Murray Dome
Martin Ridge
Francey Hill
Manning Massif
0
5
km
highly crevassed
glacier
wind scour
moraine

APPENDIX 2 SPECIMENS

A large number of specimens were collected from both the Brattstrand Bluffs coastline and the northern Prince Charles Mountains during the two field seasons. These specimens are housed at the Grant Institute, Department of Geology & Geophysics, University of Edinburgh. In addition, a representative selection of duplicate specimens from the Nemesis Glacier region are housed at the Department of Geology, University of Tasmania, Hobart, Australia. This appendix comprises a list of all the specimens collected from the Brattstrand Bluffs coastline and the Nemesis Glacier region during both field seasons. Other specimens were collected from the Rauer Group, Bolingen Islands and the Larsemann Hills, but these are not considered in this thesis and are not listed. The list gives the specimen number, field locality number, approximate latitude and longitude and a brief description for each specimen. The locality numbers correspond to the annotated maps presented in Appendix 1.

Specimens collected in the 1987/88 season from the Brattstrand Bluffs coastline

IF/88/11	D2	76°30'E 69°23'S	grey biotite-bearing granite
IF/88/12	D4	76°30'E 69°23'S	biotite granite with a moderate foliation
IF/88/13	D4	76°30'E 69°23'S	biotite-bearing layered felsic gneiss
IF/88/14A	D4	76°30'E 69°23'S	foliated garnet-biotite semi-pelitic gneiss
IF/88/14B	D6	76°30'E 69°23'S	garnet-sillimanite-spinel metapelitic gneiss
IF/88/15	D7	76°30'E 69°23'S	garnet-biotite felsic gneiss
IF/88/16	D7	76°30'E 69°23'S	garnet-biotite felsic gneiss
IF/88/17	D7	76°30'E 69°23'S	weakly-foliated garnet-biotite felsic gneiss
IF/88/18	D7	76°30'E 69°23'S	garnet-biotite (altered cordierite?) gneiss
IF/88/19	D8	76°30'E 69°23'S	garnet-sillimanite leucocratic metapelite
IF/88/20	D8	76°30'E 69°23'S	garnet-sillimanite-spinel-cordierite metapelite
IF/88/21	D8	76°30'E 69°23'S	garnet-sillimanite-spinel-biotite metapelite
IF/88/22	D8	76°30'E 69°23'S	garnet (altered cordierite?) leucocratic gneiss
IF/88/23	S1	76°34'E 69°21'S	garnet-biotite felsic gneiss
IF/88/24	S4	76°34'E 69°21'S	massive mafic granulite
IF/88/25	S13	76°34'E 69°21'S	banded garnet-cordierite-biotite metapelite
IF/88/26	S15	76°34'E 69°21'S	granular intermediate orthopyroxene gneiss
IF/88/27	S21	76°34'E 69°21'S	intermediate orthopyroxene gneiss
IF/88/28	S21	76°34'E 69°21'S	garnet-sillimanite-spinel-cordierite metapelite
IF/88/29	S24	76°35'E 69°21'S	folded mafic and felsic gneisses
IF/88/30	S27	76°35'E 69°21'S	massive mafic granulite
IF/88/31	S31	76°36'E 69°21'S	massive mafic granulite
IF/88/32	S33	76°36'E 69°21'S	coarse-grained biotite-bearing felsic gneiss
IF/88/33A	S34	76°36'E 69°21'S	garnet leucogneiss
IF/88/33B	S34	76°36'E 69°21'S	massive mafic granulite
IF/88/34	S22	76°35'E 69°21'S	semi-pelite with garnet segregations
IF/88/35	S22	76°35'E 69°21'S	weakly-foliated garnet-biotite-cordierite gneiss
IF/88/36	S22	76°35'E 69°21'S	garnet leucogneiss
IF/88/37	S22	76°35'E 69°21'S	garnet (+ altered cordierite) leucogneiss
IF/88/38	S23	76°35'E 69°21'S	garnet-orthopyroxene semi-pelitic gneiss
IF/88/39	S38	76°35'E 69°21'S	garnet leucogneiss
IF/88/40	S40	76°36'E 69°21'S	massive mafic granulite

IF/88/41	S5	76°34'E 69°21'S	garnet-orthopyroxene semi-pelitic gneiss
IF/88/42	S5	76°34'E 69°21'S	folded garnet-biotite felsic gneiss
IF/88/43	S5	76°34'E 69°21'S	garnet-biotite felsic gneiss
IF/88/44	S21	76°34'E 69°21'S	garnet-spinel-sillimanite metapelitic migmatite
IF/88/45	S12	76°34'E 69°21'S	biotite-bearing orange granitic orthogneiss
IF/88/46A	B1	77°01'E 69°13'S	metapelitic melanosome
IF/88/46B	B1	77°01'E 69°13'S	leucocratic graphite-rich metapelite
IF/88/46C	B1	77°01'E 69°13'S	metapelitic migmatite with schlieren
IF/88/47A	B1	77°01'E 69°13'S	garnet (altered cordierite) leucogneiss
IF/88/47B	B1	77°01'E 69°13'S	garnet-cordierite-spinel leucocratic metapelite
IF/88/48	B2	77°01'E 69°13'S	garnet-cordierite leucocratic metapelite
IF/88/49	B2	77°01'E 69°13'S	massive intermediate orthopyroxene gneiss
IF/88/50	B3	77°01'E 69°13'S	garnet-orthopyroxene semi-pelitic gneiss
IF/88/51	B3	77°01'E 69°13'S	metapelite with an intense foliation
IF/88/52	B3	77°01'E 69°13'S	metapelite with an intense foliation
IF/88/53	B4	77°01'E 69°13'S	garnet-sillimanite-spinel-cordierite metapelite
IF/88/54	B5	77°01'E 69°13'S	foliated garnet leucogneiss
IF/88/55	B5	77°01'E 69°13'S	garnet leucogneiss
IF/88/56	B5	77°01'E 69°13'S	garnet-sillimanite-spinel-cordierite metapelite
IF/88/57	B6	77°01'E 69°13'S	metapelitic melanosome
IF/88/58	B6	77°01'E 69°13'S	metapelitic melanosome
IF/88/59	B6	77°01'E 69°13'S	massive garnet-biotite metapelite
IF/88/60	B9	77°01'E 69°13'S	garnet leucogneiss with melanosome
IF/88/61	B9	77°01'E 69°13'S	foliated garnet leucogneiss
IF/88/62	B11	77°01'E 69°13'S	metapelite with an intense foliation
IF/88/63	B18	77°00'E 69°13'S	mylonitic shear zone in metapelite
IF/88/64	B18	77°00'E 69°13'S	mylonitic shear zone in metapelite
IF/88/65	B21	76°59'E 69°13'S	coarse-grained garnet-orthopyroxene gneiss
IF/88/66	B13	77°00'E 69°13'S	semi-pelite with an intense foliation
IF/88/67	B22	77°00'E 69°13'S	garnet ± biotite foliated leucogneiss
IF/88/68	B22	77°00'E 69°13'S	garnet leucogneiss
IF/88/69	B22	77°00'E 69°13'S	banded metapelite
IF/88/70	B20	76°59'E 69°13'S	mylonitic shear zone in a leucocratic gneiss
IF/88/71	B23	76°59'E 69°13'S	metapelite with an intense foliation
IF/88/72	B24	76°59'E 69°13'S	mylonitic shear zone
IF/88/73	B24	76°59'E 69°13'S	garnet leucogneiss
IF/88/74	B25	76°59'E 69°13'S	banded metapelite
IF/88/75	B25	76°59'E 69°13'S	leucogneiss
IF/88/76	B25	76°59'E 69°13'S	garnet-biotite semi-pelitic gneiss
IF/88/77	B25	76°59'E 69°13'S	garnet-biotite semi-pelitic gneiss
IF/88/78	B25	76°59'E 69°13'S	massive intermediate orthopyroxene gneiss
IF/88/79	B26	76°59'E 69°13'S	garnet-biotite leucogneiss
IF/88/80	B28	76°59'E 69°13'S	coarse-grained garnet-biotite pegmatitic rock
IF/88/81	B28	76°59'E 69°13'S	garnet leucogneiss
IF/88/82	B28	76°59'E 69°13'S	foliated metapelitic gneiss
IF/88/83	B29	76°59'E 69°13'S	graphite-rich leucocratic metapelite
IF/88/84	B31	77°00'E 69°13'S	metapelite with an intense foliation
IF/88/85	B32	77°00'E 69°13'S	leucogneiss
IF/88/86	B32	77°00'E 69°13'S	metapelite with an intense foliation
IF/88/87	B33	77°20'E 69°11'S	banded garnet leucogneiss
IF/88/88	B33	77°20'E 69°11'S	garnet-orthopyroxene semi-pelitic gneiss
IF/88/89	B35	77°20'E 69°11'S	sheared semi-pelite next to a pegmatite
IF/88/90	B36	77°20'E 69°11'S	banded metapelitic migmatite
IF/88/91	B40	77°20'E 69°11'S	graphite-rich garnet-bearing leucocratic rock
IF/88/92	B41	77°20'E 69°11'S	leucocratic metapelitic migmatite
IF/88/93	B41	77°20'E 69°11'S	garnet (+ altered cordierite) leucogneiss

IF/88/94	B41	77°20'E 69°11'S	garnet leucogneiss adjacent to a pegmatite
IF/88/95	B41	77°20'E 69°11'S	leucogneiss
IF/88/96	B41	77°20'E 69°11'S	banded garnet-biotite semi-pelite
IF/88/97	B41	77°20'E 69°11'S	leucocratic metapelitic migmatite
IF/88/98	B41	77°20'E 69°11'S	garnet-biotite leucocratic gneiss
IF/88/99	B42	77°20'E 69°11'S	mylonite with pseudotachylite veins
IF/88/100	B42	77°20'E 69°11'S	mylonite with pseudotachylite veins
IF/88/101	B44	77°20'E 69°11'S	leucogneiss adjacent to pegmatite
IF/88/102	W1	77°00'E 69°12'S	metapelite with an intense foliation
IF/88/103	W1	77°00'E 69°12'S	foliated garnet leucogneiss
IF/88/104	W2	77°00'E 69°12'S	foliated garnet leucogneiss
IF/88/105	W3	77°00'E 69°12'S	foliated garnet leucogneiss
IF/88/106	W3	77°00'E 69°12'S	garnet-sillimanite-spinel metapelitic gneiss
IF/88/107	W4	77°00'E 69°12'S	leucogneiss
IF/88/108	W4	77°00'E 69°12'S	foliated garnet leucogneiss
IF/88/109	W4	77°00'E 69°12'S	garnet leucogneiss
IF/88/110	W4	77°00'E 69°12'S	metapelite with an intense foliation
IF/88/111	B40	77°20'E 69°11'S	leucocratic metapelite
IF/88/112	B37	77°20'E 69°11'S	pelitic schlieren in garnet leucogneiss
IF/88/113	B45	77°20'E 69°11'S	garnet-orthopyroxene semi-pelite gneiss
IF/88/114	B46	77°20'E 69°11'S	intermediate orthopyroxene gneiss
IF/88/115	B46	77°20'E 69°11'S	intermediate orthopyroxene gneiss
IF/88/116	B46	77°20'E 69°11'S	massive garnet leucogneiss
IF/88/117	B48	77°20'E 69°11'S	metapelitic migmatite
IF/88/118	B50	77°20'E 69°11'S	garnet-orthopyroxene semi-pelite
IF/88/119	B54	77°21'E 69°11'S	garnet-cordierite leucogneiss
IF/88/120	B54	77°21'E 69°11'S	banded garnet-biotite semi-pelite
IF/88/121	B54	77°21'E 69°11'S	garnet-biotite and garnet-orthopyroxene gneiss
IF/88/122	B54	77°21'E 69°11'S	leucogneiss
IF/88/123	B55	77°21'E 69°11'S	garnet-biotite-orthopyroxene semi-pelite
IF/88/124	B56	77°21'E 69°11'S	biotite-bearing foliated felsic dyke
IF/88/125	B56	77°21'E 69°11'S	biotite-bearing foliated felsic dyke
IF/88/126	B56	77°21'E 69°11'S	banded metapelitic leucosome
IF/88/127	B56	77°21'E 69°11'S	garnet-biotite leucogneiss next to pegmatite
IF/88/128	B57	77°21'E 69°11'S	massive felsic dyke
IF/88/129	B57	77°21'E 69°11'S	shear zone in a foliated felsic dyke
IF/88/130	B57	77°21'E 69°11'S	felsic gneiss
IF/88/131	B59	77°22'E 69°12'S	garnet-cordierite leucogneiss
IF/88/132	B59	77°22'E 69°12'S	intermediate orthopyroxene gneiss
IF/88/133	B59	77°22'E 69°12'S	garnet-biotite semi-pelite
IF/88/134	B59	77°22'E 69°12'S	garnet-biotite semi-pelite
IF/88/135	B60	77°22'E 69°12'S	banded garnet-biotite semi-pelite
IF/88/136	B60	77°22'E 69°12'S	massive garnet-bearing felsic dyke
IF/88/137	B61	77°22'E 69°12'S	shear zone through a felsic dyke
IF/88/138	B61	77°22'E 69°12'S	massive garnet leucogneiss
IF/88/139	B61	77°22'E 69°12'S	leucocratic metapelitic migmatite
IF/88/140	B63	77°22'E 69°12'S	leucosome with pelitic schlieren
IF/88/141	B63	77°22'E 69°12'S	foliated garnet leucogneiss
IF/88/142	B65	77°22'E 69°12'S	massive garnet-biotite felsic dyke
IF/88/143	B65	77°22'E 69°12'S	leucocratic metapelitic migmatite
IF/88/144	B65	77°22'E 69°12'S	foliated garnet-biotite semi-pelite
IF/88/145	B66	77°22'E 69°12'S	garnet-orthopyroxene semi-pelite
IF/88/146	B66	77°22'E 69°12'S	intermediate orthopyroxene gneiss
IF/88/147	B66	77°22'E 69°12'S	garnet-biotite-(altered cordierite) metapelite
IF/88/148	B66	77°22'E 69°12'S	banded metapelitic migmatite
IF/88/149	B66	77°22'E 69°12'S	leucocratic metapelitic migmatite

IF/88/150	B66	77°22'E 69°12'S	contact between metapelite and leucogneiss
IF/88/151	B66	77°22'E 69°12'S	pelitic schlieren in leucosome
IF/88/152	B66	77°22'E 69°12'S	weakly-foliated garnet leucogneiss
IF/88/153A	B65	77°22'E 69°12'S	felsic dyke
IF/88/153B	B65	77°22'E 69°12'S	contact between metapelite and felsic dyke
IF/88/153C	B65	77°22'E 69°12'S	contact between metapelite and felsic dyke
IF/88/154	B65	77°22'E 69°12'S	weakly-foliated garnet leucogneiss
IF/88/155	B65	77°22'E 69°12'S	garnet-biotite semi-pelite
IF/88/156	B65	77°22'E 69°12'S	garnet-biotite semi-pelite
IF/88/157A	B61	77°22'E 69°12'S	shear zone in metapelite adjacent to pegmatite
IF/88/157B	B61	77°22'E 69°12'S	shear zone in metapelite adjacent to pegmatite
IF/88/158	B68	77°17'E 69°12'S	leucocratic metapelitic migmatite
IF/88/159	B68	77°17'E 69°12'S	weakly-foliated garnet-biotite semi-pelite
IF/88/160	B68	77°17'E 69°12'S	banded metapelitic migmatite
IF/88/161	B68	77°17'E 69°12'S	graphite-bearing garnet leucogneiss
IF/88/162	B69	77°17'E 69°12'S	pelitic schlieren in leucosome
IF/88/163	B71	77°17'E 69°12'S	banded garnet-biotite semi-pelite
IF/88/164	B71	77°17'E 69°12'S	garnet leucogneiss
IF/88/165	B72	77°17'E 69°12'S	stromatic metapelitic migmatite
IF/88/166	B72	77°17'E 69°12'S	weakly-foliated garnet leucogneiss
IF/88/167A	B78	77°16'E 69°12'S	banded garnet leucogneiss
IF/88/167B	B78	77°16'E 69°12'S	metapelitic migmatite
IF/88/168	B80	77°16'E 69°12'S	garnet-orthopyroxene semi-pelite
IF/88/169	B81	77°16'E 69°12'S	pelitic schlieren in garnet leucosome
IF/88/170	B82	77°16'E 69°12'S	foliated garnet leucogneiss
IF/88/171	B82	77°16'E 69°12'S	contact between metapelite and leucogneiss
IF/88/172	B76	77°17'E 69°12'S	weakly-foliated garnet leucogneiss
IF/88/173	B76	77°17'E 69°12'S	metapelitic migmatite
IF/88/174	H1	76°52'E 69°15'S	orthopyroxene-bearing felsic gneiss
IF/88/175	H2	76°52'E 69°15'S	interlayered mafic and felsic orthogneiss
IF/88/176	H2	76°52'E 69°15'S	orthopyroxene-bearing felsic gneiss
IF/88/177	H2	76°52'E 69°15'S	massive mafic granulite
IF/88/178	H3	76°52'E 69°15'S	orthopyroxene-bearing felsic gneiss
IF/88/179	H4	76°52'E 69°15'S	orthopyroxene-bearing felsic gneiss
IF/88/180	H5	76°52'E 69°15'S	garnet-biotite foliated leucogneiss
IF/88/181	H8	76°52'E 69°15'S	massive orthopyroxene-bearing felsic gneiss
IF/88/182	H8	76°52'E 69°15'S	coarse-grained leucocratic vein
IF/88/183	H9	76°52'E 69°15'S	banded mafic granulite
IF/88/184	H9	76°52'E 69°15'S	orthopyroxene-bearing felsic gneiss
IF/88/185	H10	76°52'E 69°15'S	biotite-bearing leucogneiss
IF/88/186	H11	76°52'E 69°15'S	leucogneiss
IF/88/187	H11	76°52'E 69°15'S	orthopyroxene-bearing felsic gneiss
IF/88/188	H11	76°52'E 69°15'S	orthopyroxene-bearing felsic gneiss
IF/88/189	H15	76°52'E 69°15'S	garnet leucogneiss
IF/88/190	H15	76°52'E 69°15'S	metapelitic migmatite
IF/88/191	H15	76°52'E 69°15'S	metapelitic migmatite
IF/88/192	H15	76°52'E 69°15'S	metapelitic migmatite
IF/88/193	H18	76°52'E 69°15'S	garnet leucogneiss
IF/88/194	H18	76°52'E 69°15'S	garnet-biotite semi-pelite
IF/88/195	H18	76°52'E 69°15'S	metapelitic migmatite
IF/88/196	H18	76°52'E 69°15'S	metapelitic migmatite
IF/88/197	H21	76°53'E 69°15'S	orthopyroxene-bearing felsic gneiss
IF/88/198	H21	76°53'E 69°15'S	garnet-orthopyroxene semi-pelitic gneiss
IF/88/199	H21	76°53'E 69°15'S	metapelitic migmatite
IF/88/200	H23	76°53'E 69°15'S	foliated garnet leucogneiss
IF/88/201	H25	76°52'E 69°15'S	intermediate orthopyroxene gneiss

IF/88/202	H25	76°52'E 69°15'S	garnet-biotite semi-pelite
IF/88/203	H27	76°52'E 69°15'S	metapelitic migmatite
IF/88/204	H28	76°52'E 69°15'S	garnet (altered cordierite) leucogneiss
IF/88/205	H28	76°52'E 69°15'S	stromatic metapelitic migmatite
IF/88/206	H28	76°52'E 69°15'S	foliated garnet leucogneiss
IF/88/207	H28	76°52'E 69°15'S	metapelitic migmatite
IF/88/208	H28	76°52'E 69°15'S	garnet-biotite semi-pelite
IF/88/209	H32	76°52'E 69°15'S	garnet-biotite gneiss
IF/88/210	C1	76°43'E 69°16'S	leucocratic metapelite
IF/88/211	C1	76°43'E 69°16'S	garnet-biotite semi-pelite
IF/88/212	C1	76°43'E 69°16'S	shear zone in metapelite
IF/88/213	C2	76°43'E 69°16'S	massive garnet leucogneiss
IF/88/214	C3	76°43'E 69°16'S	mafic granulite
IF/88/215	C3	76°43'E 69°16'S	metapelitic migmatite
IF/88/216	C4	76°43'E 69°16'S	garnet leucogneiss
IF/88/217	C4	76°43'E 69°16'S	massive garnet-biotite semi-pelite
IF/88/218	C4	76°43'E 69°16'S	leucocratic metapelitic migmatite
IF/88/219	C7	76°43'E 69°16'S	garnet leucogneiss
IF/88/220	C11	76°43'E 69°16'S	garnet (altered cordierite) leucogneiss
IF/88/221	C11	76°43'E 69°16'S	metapelitic migmatite
IF/88/222	C14	76°43'E 69°16'S	metapelitic migmatite
IF/88/223	C14	76°43'E 69°16'S	folded garnet leucogneiss
IF/88/224	C7	76°43'E 69°16'S	ultramafic rock
IF/88/225	C18	76°43'E 69°16'S	garnet-orthopyroxene leucocratic rock
IF/88/226	C18	76°43'E 69°16'S	melanosome-rich metapelitic migmatite
IF/88/227	C19	76°43'E 69°16'S	garnet-biotite semi-pelite
IF/88/228	C20	76°43'E 69°16'S	metapelitic migmatite
IF/88/229	C21	76°43'E 69°16'S	pelitic schlieren in leucogneiss
IF/88/230	C23	76°42'E 69°16'S	leucogneiss
IF/88/231	C23	76°42'E 69°16'S	metapelitic gneiss
IF/88/232	C24	76°42'E 69°16'S	metapelitic migmatite
IF/88/233	C27	76°42'E 69°16'S	leucocratic metapelitic migmatite
IF/88/234	C30	76°42'E 69°16'S	ultramafic rock
IF/88/235	A3	76°50'E 69°17'S	grey garnet-bearing granite
IF/88/236	A3	76°50'E 69°17'S	foliated K-feldspar megacrystic granite
IF/88/237	A5	76°51'E 69°17'S	garnet-biotite gneiss
IF/88/238	A5	76°51'E 69°17'S	biotite-bearing felsic gneiss
IF/88/239	A5	76°51'E 69°17'S	garnet-biotite semi-pelite
IF/88/240	A7	76°50'E 69°17'S	garnet-biotite semi-pelitic xenolith
IF/88/241	A7	76°50'E 69°17'S	K-feldspar megacrystic granite
IF/88/242	A7	76°50'E 69°17'S	foliated K-feldspar megacrystic granite
IF/88/243	A8	76°50'E 69°17'S	K-feldspar megacrystic granite
IF/88/244	A11	76°50'E 69°17'S	K-feldspar megacrystic granite
IF/88/245	A12	76°50'E 69°17'S	garnet-biotite granite
IF/88/246	A15	76°50'E 69°17'S	graded layering in granite
IF/88/247	A17	76°50'E 69°17'S	massive K-feldspar megacrystic granite
IF/88/248	A18	76°50'E 69°17'S	massive K-feldspar megacrystic granite
IF/88/249	A19	76°50'E 69°17'S	massive K-feldspar megacrystic granite
IF/88/250	A20	76°50'E 69°17'S	foliated K-feldspar megacrystic granite
IF/88/251	A13	76°50'E 69°17'S	foliated K-feldspar megacrystic granite
IF/88/252	A13	76°50'E 69°17'S	foliated K-feldspar megacrystic granite
IF/88/253	A21	76°52'E 69°17'S	foliated K-feldspar megacrystic granite
IF/88/254	A21	76°52'E 69°17'S	garnet-biotite semi-pelitic xenolith
IF/88/255	A23	76°52'E 69°17'S	weakly-foliated K-feldspar megacrystic granite
IF/88/256	A24	76°52'E 69°17'S	garnet-biotite semi-pelitic xenolith
IF/88/257	A24	76°52'E 69°17'S	metapelitic xenolith

IF/88/258	A24	76°52'E 69°17'S	leucogneiss
IF/88/259	A24	76°52'E 69°17'S	garnet-biotite-orthopyroxene semi-pelite
IF/88/260	A24	76°52'E 69°17'S	massive biotite ± orthopyroxene semi-pelite
IF/88/261	A27	76°52'E 69°17'S	foliated K-feldspar megacrystic granite
IF/88/262	A29	76°51'E 69°17'S	foliated K-feldspar megacrystic granite
IF/88/263	A30	76°51'E 69°17'S	massive K-feldspar megacrystic granite
IF/88/264	A33	76°51'E 69°17'S	mylonite in granite near a pegmatite
IF/88/265	A34	76°52'E 69°17'S	weakly-foliated K-feldspar megacrystic granite
IF/88/266	A34	76°52'E 69°17'S	contact between granite and semi-pelite
IF/88/267	A34	76°52'E 69°17'S	garnet-biotite semi-pelite
IF/88/268	A34	76°52'E 69°17'S	garnet-biotite-orthopyroxene semi-pelite
IF/88/269	A34	76°52'E 69°17'S	intermediate orthopyroxene gneiss
IF/88/270	A34	76°52'E 69°17'S	intermediate orthopyroxene gneiss
IF/88/271	A34	76°52'E 69°17'S	intermediate orthopyroxene gneiss
IF/88/272	V1	76°44'E 69°08'S	weakly-foliated garnet leucogneiss
IF/88/273	V1	76°44'E 69°08'S	metapelitic migmatite
IF/88/274	V2	76°44'E 69°08'S	metapelite with an intense foliation
IF/88/275	V2	76°44'E 69°08'S	garnet (+ altered cordierite) leucogneiss
IF/88/276	V3	76°44'E 69°08'S	foliated garnet leucogneiss
IF/88/277	V4	76°44'E 69°08'S	metapelitic migmatite
IF/88/278	V5	76°44'E 69°08'S	garnet leucogneiss
IF/88/279	V6	76°44'E 69°08'S	garnet segregations in biotite-bearing gneiss
IF/88/280	V7	76°44'E 69°08'S	metapelitic migmatite
IF/88/281	V8	76°48'E 69°08'S	mafic granulite
IF/88/282	V8	76°48'E 69°08'S	banded cordierite-spinel magnesian gneiss
IF/88/283	V8	76°48'E 69°08'S	intermediate orthopyroxene gneiss
IF/88/284	V10	76°48'E 69°08'S	coarse-grained ultramafic rock
IF/88/285	V10	76°48'E 69°08'S	massive pink leucocratic rock
IF/88/286	V10	76°48'E 69°08'S	cordierite-spinel leucocratic magnesian gneiss
IF/88/287	V10	76°48'E 69°08'S	banded cordierite-spinel magnesian migmatite
IF/88/288	V10	76°48'E 69°08'S	banded cordierite-spinel magnesian migmatite
IF/88/289	V10	76°48'E 69°08'S	cordierite-spinel magnesian gneiss
IF/88/290	V12	76°48'E 69°08'S	cordierite-spinel magnesian migmatite
IF/88/291	V12	76°48'E 69°08'S	cordierite-spinel magnesian migmatite
IF/88/292	V12	76°48'E 69°08'S	massive mafic granulite
IF/88/293	V13	76°48'E 69°08'S	cordierite-spinel magnesian gneiss
IF/88/294	V15	76°48'E 69°08'S	weakly-foliated garnet leucogneiss
IF/88/295	V15	76°48'E 69°08'S	garnet-biotite leucogneiss
IF/88/296	V16	76°48'E 69°08'S	banded cordierite magnesian gneiss
IF/88/297	V16	76°48'E 69°08'S	garnet-cordierite-biotite magnesian gneiss
IF/88/298	V16	76°48'E 69°08'S	garnet-cordierite-biotite in leucocratic gneiss
IF/88/299	V16	76°48'E 69°08'S	cordierite-spinel-biotite magnesian gneiss
IF/88/300	V16	76°48'E 69°08'S	cordierite-spinel-biotite magnesian gneiss
IF/88/301	V16	76°48'E 69°08'S	garnet-cordierite-spinel magnesian gneiss
IF/88/302	V17	76°48'E 69°08'S	interlayered felsic gneiss and mafic granulite
IF/88/303	V17	76°48'E 69°08'S	cordierite-spinel-biotite magnesian migmatite
IF/88/304	V18	76°59'E 69°01'S	metapelitic migmatite
IF/88/305	V18	76°59'E 69°01'S	metapelitic migmatite
IF/88/306	V18	76°59'E 69°01'S	metapelitic migmatite
IF/88/307	V18	76°59'E 69°01'S	leucosome with pelitic schlieren
IF/88/308	V18	76°59'E 69°01'S	massive garnet ± biotite leucogneiss
IF/88/309	V18	76°59'E 69°01'S	massive garnet ± biotite leucogneiss
IF/88/310	V18	76°59'E 69°01'S	massive biotite-bearing felsic dyke
IF/88/311	V19	76°59'E 69°01'S	weakly-foliated metapelitic migmatite
IF/88/312	V21	76°59'E 69°01'S	metapelitic migmatite
IF/88/313	V21	76°59'E 69°01'S	massive metapelitic migmatite

IF/88/314	V21	76°59'E 69°01'S	massive metapelitic migmatite
IF/88/315	V21	76°59'E 69°01'S	massive garnet leucogneiss
IF/88/316	V21	76°59'E 69°01'S	leucosome with small pelitic schlieren
IF/88/317	V23	76°59'E 69°01'S	massive garnet-biotite felsic dyke
IF/88/318	V24	76°59'E 69°01'S	garnet leucosome with pelitic schlieren
IF/88/319	V24	76°59'E 69°01'S	metapelitic migmatite
IF/88/320	V25	76°59'E 69°01'S	banded leucosome with pelitic schlieren
IF/88/321	V25	76°59'E 69°01'S	massive garnet-biotite semi-pelite
IF/88/322	V25	76°59'E 69°01'S	massive garnet-biotite semi-pelite
IF/88/323	V27	76°59'E 69°01'S	garnet ± biotite leucogneiss
IF/88/324	V27	76°59'E 69°01'S	leucocratic metapelitic gneiss
IF/88/325	V28	76°59'E 69°01'S	massive garnet leucogneiss
IF/88/326	V28	76°59'E 69°01'S	garnet leucogneiss with sillimanite schlieren
IF/88/327	V28	76°59'E 69°01'S	pelitic melanosome within leucosome
IF/88/328	V28	76°59'E 69°01'S	pelitic melanosome within leucosome
IF/88/329	G1	77°54'E 69°01'S	intermediate orthopyroxene gneiss
IF/88/330	G1	77°54'E 69°01'S	intermediate orthopyroxene gneiss
IF/88/331	G1	77°54'E 69°01'S	garnet-sillimanite metapelitic gneiss
IF/88/332	G1	77°54'E 69°01'S	massive garnet-biotite leucogneiss
IF/88/333	G2	77°54'E 69°01'S	garnet-biotite-orthopyroxene gneiss
IF/88/334	G2	77°54'E 69°01'S	garnet-biotite-orthopyroxene gneiss
IF/88/335	G2	77°54'E 69°01'S	banded garnet-biotite semi-pelite
IF/88/336	G6	77°54'E 69°01'S	garnet leucogneiss
IF/88/337	G9	77°54'E 69°01'S	massive garnet-orthopyroxene-biotite gneiss
IF/88/338	G9	77°54'E 69°01'S	massive garnet-orthopyroxene-biotite gneiss
IF/88/339	G9	77°54'E 69°01'S	garnet-orthopyroxene-biotite gneiss
IF/88/340	G9	77°54'E 69°01'S	garnet-orthopyroxene-biotite semi-pelite
IF/88/341	G10	77°54'E 69°01'S	banded garnet-biotite semi-pelite
IF/88/342	G10	77°54'E 69°01'S	garnet-orthopyroxene-biotite semi-pelite
IF/88/343	G10	77°54'E 69°01'S	garnet-orthopyroxene-biotite semi-pelite
IF/88/344	G10	77°54'E 69°01'S	banded garnet-biotite semi-pelite
IF/88/345	G6	77°54'E 69°01'S	metapelite
IF/88/346	G6	77°54'E 69°01'S	garnet-sillimanite-biotite metapelite
IF/88/347	G6	77°54'E 69°01'S	garnet-sillimanite-biotite metapelite

Specimens collected during the 1988/89 season

(a) The Nemesis Glacier region

IF/89/1	B1	66°15'E 70°48'S	banded garnet-biotite gneiss
IF/89/2	B1	66°15'E 70°48'S	foliated garnet-orthopyroxene semi-pelite
IF/89/3	B1	66°15'E 70°48'S	banded garnet-orthopyroxene gneiss
IF/89/4	B1	66°15'E 70°48'S	massive garnet-biotite gneiss
IF/89/5	B1	66°15'E 70°48'S	garnet-bearing leucogneiss
IF/89/6	B3	66°16'E 70°48'S	banded biotite-pyroxene-hornblende gneiss
IF/89/7	B3	66°16'E 70°48'S	massive leucogneiss
IF/89/8	B3	66°16'E 70°48'S	biotite-rich banded amphibolitic gneiss
IF/89/9	B3	66°16'E 70°48'S	massive amphibolitic gneiss
IF/89/10	B7	66°15'E 70°48'S	massive garnet leucogneiss
IF/89/11	B7	66°15'E 70°48'S	massive garnet leucogneiss
IF/89/12	B7	66°15'E 70°48'S	massive garnet-biotite-pyroxene gneiss
IF/89/13	B6	66°15'E 70°48'S	orthopyroxene-plagioclase gneiss
IF/89/14	B5	66°15'E 70°48'S	garnet-orthopyroxene gneiss
IF/89/15	B5	66°15'E 70°48'S	garnet-orthopyroxene gneiss
IF/89/16	B5	66°15'E 70°48'S	banded amphibolitic gneiss
IF/89/17	B4	66°15'E 70°48'S	massive garnet leucogneiss
IF/89/18	B4	66°15'E 70°48'S	banded garnet-biotite gneiss

IF/89/19	B4	66°15'E 70°48'S	banded garnet-biotite gneiss
IF/89/20	B1	66°15'E 70°48'S	garnet leucogneiss
IF/89/21	B1	66°15'E 70°48'S	foliated garnet leucogneiss
IF/89/22	B11	66°15'E 70°49'S	banded biotite-orthopyroxene gneiss
IF/89/23	B11	66°15'E 70°49'S	orthopyroxene-hornblende-biotite gneiss
IF/89/24	B13	66°15'E 70°49'S	massive biotite-bearing felsic gneiss
IF/89/25	B13	66°15'E 70°49'S	biotite-bearing banded felsic gneiss
IF/89/26	B13	66°15'E 70°49'S	banded biotite-orthopyroxene felsic gneiss
IF/89/27	B12	66°15'E 70°49'S	banded biotite-orthopyroxene felsic gneiss
IF/89/28	B8	66°15'E 70°48'S	banded garnet-orthopyroxene felsic gneiss
IF/89/29	B14	66°21'E 70°47'S	banded garnet-biotite gneiss
IF/89/30	B14	66°21'E 70°47'S	banded garnet-biotite gneiss
IF/89/31	B14	66°21'E 70°47'S	orthopyroxene-hornblende-plagioclase gneiss
IF/89/32	B14	66°21'E 70°47'S	biotite-garnet-orthopyroxene gneiss
IF/89/33	B15	66°21'E 70°47'S	massive orthopyroxene-bearing felsic gneiss
IF/89/34	B15	66°21'E 70°47'S	banded orthopyroxene-plagioclase gneiss
IF/89/35	B15	66°21'E 70°47'S	banded orthopyroxene-plagioclase gneiss
IF/89/36	B16	66°20'E 70°47'S	foliated mafic gneiss
IF/89/37	B16	66°20'E 70°47'S	massive mafic gneiss
IF/89/38	B16	66°20'E 70°47'S	banded biotite-orthopyroxene felsic gneiss
IF/89/39	B16	66°20'E 70°47'S	contact between mafic and felsic gneiss
IF/89/40	B16	66°20'E 70°47'S	garnet-orthopyroxene gneiss
IF/89/41	B17	66°20'E 70°47'S	massive garnet leucogneiss
IF/89/42	B18	66°20'E 70°47'S	orthopyroxene-biotite banded gneiss
IF/89/43	B18	66°20'E 70°47'S	layered garnet-orthopyroxene gneiss
IF/89/44	B18	66°20'E 70°47'S	massive garnet-orthopyroxene gneiss
IF/89/45	B18	66°20'E 70°47'S	massive garnet-orthopyroxene gneiss
IF/89/46	B19	66°20'E 70°47'S	biotite-orthopyroxene-plagioclase gneiss
IF/89/47	B19	66°20'E 70°47'S	banded biotite-orthopyroxene gneiss
IF/89/48	B19	66°20'E 70°47'S	banded orthopyroxene-bearing gneiss
IF/89/49	B20	66°19'E 70°46'S	massive orthopyroxene-garnet felsic gneiss
IF/89/50	B20	66°19'E 70°46'S	massive orthopyroxene-garnet felsic gneiss
IF/89/51	B22	66°19'E 70°46'S	massive orthopyroxene-bearing felsic gneiss
IF/89/52	B23	66°19'E 70°46'S	mylonitized pegmatite with garnet augen
IF/89/53	B23	66°19'E 70°46'S	garnet-rich massive felsic gneiss
IF/89/54	B25	66°19'E 70°46'S	ultramafic rock
IF/89/55A	I1	66°17'E 70°46'S	massive felsic gneiss
IF/89/55B	I1	66°17'E 70°46'S	contact between felsic gneiss and calc-silicate
IF/89/55C	I1	66°17'E 70°46'S	massive diopside-rich calc-silicate
IF/89/55D	I1	66°17'E 70°46'S	massive diopside-grossularite calc-silicate
IF/89/55E	I1	66°17'E 70°46'S	massive diopside-grossularite calc-silicate
IF/89/56	I1	66°17'E 70°46'S	diopside-grossularite calc-silicate
IF/89/57	I1	66°17'E 70°46'S	massive orthopyroxene-bearing felsic gneiss
IF/89/58	I1	66°17'E 70°46'S	banded garnet-orthopyroxene gneiss
IF/89/59	I1	66°17'E 70°46'S	banded garnet-orthopyroxene gneiss
IF/89/60	I1	66°17'E 70°46'S	calc-silicate with folded quartz layers
IF/89/61	B28	66°17'E 70°49'S	massive garnet leucogneiss
IF/89/62	B28	66°17'E 70°49'S	massive garnet-bearing felsic gneiss
IF/89/63	B28	66°17'E 70°49'S	massive garnet-orthopyroxene felsic dyke
IF/89/64	B28	66°17'E 70°49'S	massive garnet-orthopyroxene felsic dyke
IF/89/65	T1	66°23'E 70°43'S	massive garnet leucogneiss
IF/89/66	T1	66°23'E 70°43'S	orthopyroxene-bearing felsic gneiss
IF/89/67	T2	66°23'E 70°43'S	foliated garnet-bearing leucogneiss
IF/89/68	T2	66°23'E 70°43'S	orthopyroxene-bearing foliated felsic gneiss
IF/89/69	T2	66°23'E 70°43'S	mafic granulite
IF/89/70	T2	66°23'E 70°43'S	banded garnet-orthopyroxene gneiss

IF/89/71	T2	66°23'E 70°43'S	banded garnet-orthopyroxene gneiss
IF/89/72	T3	66°23'E 70°43'S	diopside-rich calc-silicate
IF/89/73	T3	66°23'E 70°43'S	garnet-bearing banded gneiss
IF/89/74	T4	66°23'E 70°43'S	contact between banded gneiss and leucogneiss
IF/89/75	T5	66°23'E 70°43'S	contact between mafic gneiss and leucogneiss
IF/89/76	T5	66°23'E 70°43'S	foliated orthopyroxene-bearing felsic gneiss
IF/89/77	T6	66°23'E 70°43'S	orthopyroxene-biotite-plagioclase gneiss
IF/89/78	T6	66°23'E 70°43'S	orthopyroxene-biotite-plagioclase gneiss
IF/89/79	T7	66°22'E 70°43'S	orthopyroxene-bearing foliated felsic gneiss
IF/89/80	T7	66°22'E 70°43'S	orthopyroxene-biotite banded gneiss
IF/89/81	T8	66°22'E 70°43'S	massive garnet leucogneiss
IF/89/82A	T9	66°22'E 70°42'S	massive garnet leucogneiss
IF/89/82B	T9	66°22'E 70°42'S	banded green and cream calc-silicate
IF/89/82C	T9	66°22'E 70°42'S	banded green and cream calc-silicate
IF/89/82D	T9	66°22'E 70°42'S	calc-silicate and leucogneiss contact
IF/89/83	T9	66°22,E 70°42'S	massive calc-silicate
IF/89/84	T12	66°22'E 70°42'S	forsterite-calcite marble
IF/89/85	T12	66°22'E 70°42'S	foliated orthopyroxene-bearing felsic gneiss
IF/89/86	T12	66°22'E 70°42'S	contact between felsic gneiss and calc-silicate
IF/89/87A	T12	66°22'E 70°42'S	banded grey-green calc-silicate
IF/89/87B	T12	66°22'E 70°42'S	banded mica-rich calc-silicate
IF/89/87C	T12	66°22'E 70°42'S	banded mica-rich calc-silicate
IF/89/87D	T12	66°22'E 70°42'S	banded mica-rich calc-silicate
IF/89/87E	T12	66°22'E 70°42'S	banded calc-silicate
IF/89/87F	T12	66°22'E 70°42'S	banded mica-rich calc-silicate
IF/89/87G	T12	66°22'E 70°42'S	massive calc-silicate
IF/89/87H	T12	66°22'E 70°42'S	dark blue-green banded calc-silicate
IF/89/87I	T12	66°22'E 70°42'S	dark blue-green banded calc-silicate
IF/89/87J	T12	66°22'E 70°42'S	banded mica-rich calc-silicate
IF/89/87K	T12	66°22'E 70°42'S	banded green and cream calc-silicate
IF/89/87L	T12	66°22'E 70°42'S	massive calc-silicate
IF/89/88	T12	66°22'E 70°42'S	orthopyroxene-bearing banded felsic gneiss
IF/89/89	T12	66°22'E 70°42'S	foliated mafic gneiss
IF/89/90	T12	66°22'E 70°42'S	massive orthopyroxene-bearing gneiss
IF/89/91	T12	66°22'E 70°42'S	diopside-bearing calc-silicate
IF/89/92	T12	66°22'E 70°42'S	diopside-wollastonite-scapolite calc-silicate
IF/89/93	T12	66°22'E 70°42'S	diopside-wollastonite-scapolite calc-silicate
IF/89/94	T13	66°22'E 70°42'S	orthopyroxene-bearing felsic gneiss
IF/89/95	T14	66°22'E 70°42'S	clinopyroxene-rich ultramafic gneiss
IF/89/96A	T15	66°21'E 70°42'S	orthopyroxene-bearing massive felsic gneiss
IF/89/96B	T15	66°21'E 70°42'S	massive marble
IF/89/96C	T15	66°21'E 70°42'S	green calc-silicate
IF/89/97	T15	66°21'E 70°42'S	massive orthopyroxene-bearing felsic gneiss
IF/89/98	T16	66°20'E 70°42'S	foliated orthopyroxene-bearing felsic gneiss
IF/89/99	T17	66°18'E 70°42'S	garnet-biotite banded gneiss
IF/89/100	T18	66°20'E 70°41'S	massive garnet-biotite gneiss
IF/89/101	T19	66°25'E 70°41'S	massive garnet-leucogneiss
IF/89/102	T19	66°25'E 70°41'S	garnet-orthopyroxene banded gneiss
IF/89/103	T19	66°25'E 70°41'S	garnet-biotite banded gneiss
IF/89/104	T19	66°25'E 70°41'S	garnet-biotite banded gneiss
IF/89/105	T19	66°25'E 70°41'S	diopside-bearing calc-silicate
IF/89/106	T19	66°25'E 70°41'S	garnet-orthopyroxene banded gneiss
IF/89/107	B29	66°33'E 70°42'S	foliated mafic gneiss
IF/89/108	B29	66°33'E 70°42'S	massive garnet-orthopyroxene banded gneiss
IF/89/109	B30	66°30'E 70°42'S	mica-bearing grey-green calc-silicate
IF/89/110	B30	66°30'E 70°42'S	garnet-biotite banded gneiss

IF/89/111	B30	66°30'E 70°42'S	banded garnet-biotite leucocratic gneiss
IF/89/112	B30	66°30'E 70°42'S	massive garnet-biotite gneiss
IF/89/113	B30	66°30'E 70°42'S	garnet-orthopyroxene banded felsic gneiss
IF/89/114	B31	66°21'E 70°45'S	garnet-biotite banded gneiss
IF/89/115	B31	66°21'E 70°45'S	mylonite with garnet clasts
IF/89/116	B32	66°22'E 70°45'S	banded garnet-orthopyroxene felsic gneiss
IF/89/117	B32	66°22'E 70°45'S	banded orthopyroxene-biotite felsic gneiss
IF/89/118	B32	66°22'E 70°45'S	foliated garnet-orthopyroxene felsic gneiss
IF/89/119	B34	66°22'E 70°45'S	garnet-orthopyroxene banded gneiss
IF/89/120	B34	66°22'E 70°45'S	garnet-biotite banded gneiss
IF/89/121	B35	66°22'E 70°45'S	foliated mafic gneiss
IF/89/122	B36	66°25'E 70°45'S	massive orthopyroxene-bearing leucogneiss
IF/89/123	B36	66°25'E 70°45'S	massive ultramafic rock
IF/89/124	B36	66°25'E 70°45'S	banded mafic gneiss
IF/89/125	T21	66°21'E 70°44'S	massive garnet-bearing leucogneiss
IF/89/126	T21	66°21'E 70°44'S	orthopyroxene-bearing banded felsic gneiss
IF/89/127	A1	66°12'E 70°47'S	banded garnet-biotite leucocratic gneiss
IF/89/128	A1	66°12'E 70°47'S	garnet-bearing foliated felsic gneiss
IF/89/129	A1	66°12'E 70°47'S	massive orthopyroxene-bearing felsic gneiss
IF/89/130	A2	66°08'E 70°46'S	banded garnet-biotite gneiss
IF/89/131	A2	66°08'E 70°46'S	banded orthopyroxene-bearing felsic gneiss
IF/89/132	A2	66°08'E 70°46'S	banded orthopyroxene-bearing felsic gneiss
IF/89/133	A2	66°08'E 70°46'S	folded mafic and leucocratic layers
IF/89/134	A2	66°08'E 70°46'S	leucocratic gneiss with pyroxene-rich bands
IF/89/135	A2	66°08'E 70°46'S	massive garnet-orthopyroxene leucogneiss
IF/89/136	A3	66°10'E 70°45'S	foliated garnet-orthopyroxene felsic gneiss
IF/89/137	A3	66°10'E 70°45'S	foliated garnet-orthopyroxene felsic gneiss
IF/89/138	A3	66°10'E 70°45'S	massive felsic gneiss
IF/89/139	A3	66°10'E 70°45'S	foliated garnet-orthopyroxene felsic gneiss
IF/89/140	A3	66°10'E 70°45'S	foliated mafic gneiss
IF/89/141	A3	66°10'E 70°45'S	contact between mafic and felsic gneiss
IF/89/144	M1	66°41'E 70°44'S	massive mafic gneiss
IF/89/145	M1	66°41'E 70°44'S	massive garnet-orthopyroxene felsic gneiss
IF/89/146	M2	66°41'E 70°44'S	foliated garnet-orthopyroxene felsic gneiss
IF/89/147	M2	66°41'E 70°44'S	massive garnet leucogneiss
IF/89/148	M3	66°41'E 70°44'S	weakly-foliated felsic gneiss
IF/89/149	M4	66°41'E 70°44'S	banded orthopyroxene-bearing felsic gneiss
IF/89/150	M4	66°41'E 70°44'S	banded garnet-orthopyroxene felsic gneiss
IF/89/151	M6	66°41'E 70°43'S	massive orthopyroxene-bearing felsic gneiss
IF/89/152	M6	66°41'E 70°43'S	diopside-scapolite-wollastonite calc-silicate
IF/89/153	M7	66°42'E 70°42'S	foliated orthopyroxene-biotite gneiss
IF/89/154	M7	66°42'E 70°42'S	felsic gneiss with orthopyroxene-rich layers
IF/89/155	M7	66°42'E 70°42'S	felsic gneiss with orthopyroxene-rich layers
IF/89/156	M7	66°42'E 70°42'S	banded gneiss with altered pyroxene
IF/89/157	M8	66°44'E 70°42'S	foliated orthopyroxene-bearing felsic gneiss
IF/89/158	M8	66°44'E 70°42'S	massive orthopyroxene-bearing felsic gneiss
IF/89/159	M9	66°45'E 70°41'S	leucocratic gneiss with altered orthopyroxene
IF/89/160	M9	66°45'E 70°41'S	epidote vein
IF/89/161	M11	66°43'E 70°42'S	foliated orthopyroxene-bearing felsic gneiss
IF/89/162	M11	66°43'E 70°42'S	mafic gneiss cut by a planar quartz vein
IF/89/163	M12	66°44'E 70°42'S	foliated felsic gneiss
IF/89/164	M14	66°46'E 70°43'S	foliated orthopyroxene-bearing felsic gneiss
IF/89/165	O1	66°42'E 70°44'S	massive mafic gneiss
IF/89/166	O1	66°42'E 70°44'S	massive felsic gneiss
IF/89/167	O2	66°43'E 70°45'S	massive garnet leucogneiss
IF/89/168	O2	66°43'E 70°45'S	massive garnet-orthopyroxene gneiss

IF/89/169	O2	66°43'E 70°45'S	foliated garnet-orthopyroxene gneiss
IF/89/170	O2	66°43'E 70°45'S	garnet-bearing foliated intermediate gneiss
IF/89/171	O2	66°43'E 70°45'S	garnet-orthopyroxene foliated gneiss
IF/89/172	O3	66°42'E 70°45'S	weakly foliated felsic gneiss
IF/89/173	O4	66°43'E 70°45'S	massive mafic gneiss
IF/89/174	O4	66°43'E 70°45'S	massive mafic gneiss
IF/89/175	O4	66°43'E 70°45'S	orthopyroxene-bearing banded felsic gneiss
IF/89/176	O5	66°44'E 70°44'S	foliated orthopyroxene-bearing felsic gneiss
IF/89/177	M15	66°47'E 70°42'S	massive felsic gneiss
IF/89/178	M16	66°50'E 70°42'S	foliated felsic gneiss
IF/89/179	M17	66°50'E 70°42'S	foliated felsic gneiss
IF/89/180	M17	66°50'E 70°42'S	foliated orthopyroxene-bearing felsic gneiss
IF/89/181	Mc2	66°52'E 70°44'S	foliated mafic gneiss
IF/89/182	Mc1	66°52'E 70°44'S	massive ultramafic rock
IF/89/183	Mc1	66°52'E 70°44'S	foliated orthopyroxene-bearing felsic gneiss
IF/89/184	Mc1	66°52'E 70°44'S	banded orthopyroxene-bearing felsic gneiss
IF/89/185	Mc1	66°52'E 70°44'S	foliated orthopyroxene-bearing felsic gneiss
IF/89/186	Z1	66°48'E 70°43'S	lineated orthopyroxene-bearing felsic gneiss
IF/89/187	Z2	66°48'E 70°43'S	foliated orthopyroxene-bearing felsic gneiss
IF/89/188	Z2	66°48'E 70°43'S	foliated orthopyroxene-rich felsic gneiss
IF/89/189	Z2	66°48'E 70°43'S	weakly-foliated mafic gneiss
IF/89/190	Z3	66°48'E 70°43'S	massive felsic gneiss
IF/89/191	Y1	66°47'E 70°45'S	banded orthopyroxene-bearing felsic gneiss
IF/89/192	X1	66°45'E 70°45'S	weakly-foliated orthopyroxene-biotite gneiss
IF/89/193	X1	66°45'E 70°45'S	massive orthopyroxene-bearing felsic gneiss
IF/89/194	X4	66°45'E 70°45'S	mafic gneiss with quartz-bearing bands
IF/89/195	X4	66°45'E 70°45'S	weakly-foliated garnet leucogneiss
IF/89/196	X4	66°45'E 70°45'S	foliated orthopyroxene-bearing felsic gneiss
IF/89/197	X4	66°45'E 70°45'S	banded garnet-orthopyroxene gneiss
IF/89/198	X4	66°45'E 70°45'S	foliated garnet-orthopyroxene felsic gneiss
IF/89/199	X4	66°45'E 70°45'S	foliated garnet-orthopyroxene felsic gneiss
IF/89/200	H1	66°42'E 70°46'S	massive garnet leucogneiss
IF/89/201	H3	66°41'E 70°46'S	well-layered garnet-biotite gneiss
IF/89/202	H4	66°38'E 70°47'S	foliated orthopyroxene-biotite felsic gneiss
IF/89/203	H4	66°38'E 70°47'S	massive felsic gneiss
IF/89/204	H5	66°38'E 70°47'S	contact between mafic and felsic gneiss
IF/89/205	H5	66°38'E 70°47'S	interlayered felsic and mafic gneiss
IF/89/206	H5	66°38'E 70°47'S	massive mafic gneiss
IF/89/207	H5	66°38'E 70°47'S	lineated garnet-orthopyroxene felsic gneiss
IF/89/208	H5	66°38'E 70°47'S	foliated garnet-orthopyroxene felsic gneiss
IF/89/209	L1	66°58'E 70°46'S	foliated felsic gneiss
IF/89/210	L1	66°58'E 70°46'S	mafic gneiss with leucocratic layers
IF/89/211	L1	66°58'E 70°46'S	orthopyroxene-bearing banded felsic gneiss
IF/89/212	L3	67°00'E 70°46'S	massive pegmatitic plagioclase-rich rock
IF/89/213	L3	67°00'E 70°46'S	massive mafic gneiss
IF/89/214	L4	67°00'E 70°46'S	foliated orthopyroxene-bearing felsic gneiss
IF/89/215	L4	67°00'E 70°46'S	contact between mafic and felsic gneiss
IF/89/216	L4	67°00'E 70°46'S	orthopyroxene-bearing foliated felsic gneiss
IF/89/217A	L5	67°00'E 70°46'S	massive orthopyroxene-bearing felsic gneiss
IF/89/217B	L5	67°00'E 70°46'S	diopside-wollastonite-scapolite calc-silicate
IF/89/217C	L5	67°00'E 70°46'S	orthopyroxene-bearing foliated felsic gneiss
IF/89/217D	L5	67°00'E 70°46'S	scapolite-diopside-wollastonite calc-silicate
IF/89/217E	L5	67°00'E 70°46'S	contact between felsic gneiss and calc-silicate
IF/89/217F	L5	67°00'E 70°46'S	massive orthopyroxene-bearing felsic gneiss
IF/89/218	L5	67°00'E 70°46'S	interlayered garnet-biotite and felsic gneiss
IF/89/219	L5	67°00'E 70°46'S	foliated garnet leucogneiss

IF/89/220	F1	67°00'E 70°44'S	pyroxene-biotite foliated gneiss
IF/89/221	F1	67°00'E 70°44'S	pyroxene-biotite foliated gneiss
IF/89/222	C1	66°34'E 70°36'S	biotite-pyroxene-plagioclase foliated gneiss
IF/89/223	C1	66°34'E 70°36'S	massive biotite-bearing pink leucogneiss
IF/89/224	C3	66°35'E 70°35'S	foliated felsic gneiss
IF/89/225	C4	66°36'E 70°35'S	foliated mafic to ultramafic gneiss
IF/89/226	C4	66°36'E 70°35'S	weakly-foliated ultramafic rock
IF/89/227	C4	66°36'E 70°35'S	massive ultramafic rock
IF/89/228	C5	66°37'E 70°35'S	foliated orthopyroxene-bearing felsic gneiss
IF/89/229	C6	66°38'E 70°35'S	massive leucogneiss
IF/89/230	C6	66°38'E 70°35'S	weakly-foliated felsic gneiss
IF/89/231	C7	66°39'E 70°35'S	massive mafic gneiss
IF/89/232	C7	66°39'E 70°35'S	massive felsic gneiss
IF/89/233	C7	66°39'E 70°35'S	well-layered garnet-rich gneiss
IF/89/234	C7	66°39'E 70°35'S	massive felsic gneiss with rare garnet
IF/89/235	C7	66°39'E 70°35'S	contact between felsic gneiss and mafic band
IF/89/236	C9	66°40'E 70°35'S	weakly-foliated pink leucogneiss
IF/89/237	P1	66°57'E 70°33'S	massive mafic gneiss
IF/89/238	P1	66°57'E 70°33'S	massive felsic gneiss with rare orthopyroxene
IF/89/239	P1	66°57'E 70°33'S	massive mafic gneiss
IF/89/240	P1	66°57'E 70°33'S	massive mafic gneiss
IF/89/241	P2	66°56'E 70°33'S	massive pegmatitic leucogneiss
IF/89/242	P2	66°56'E 70°33'S	massive pyroxenite
IF/89/243	P2	66°56'E 70°33'S	massive pyroxenite
IF/89/244	P3	66°54'E 70°34'S	weakly-foliated pyroxene-bearing felsic gneiss
IF/89/245	P3	66°54'E 70°34'S	weakly-foliated felsic gneiss
IF/89/246	P4	66°54'E 70°34'S	garnet-pyroxene gneiss
IF/89/247	P4	66°54'E 70°34'S	banded garnet-pyroxene gneiss
IF/89/248	P4	66°54'E 70°34'S	massive garnet-orthopyroxene-biotite gneiss
IF/89/249	P5	66°53'E 70°34'S	massive felsic gneiss
IF/89/250	P5	66°53'E 70°34'S	garnet-bearing leucocratic gneiss
IF/89/251	P7	66°51'E 70°34'S	massive garnet-biotite felsic gneiss
IF/89/252	P7	66°51'E 70°34'S	biotite-bearing felsic dyke
IF/89/253	P8	66°50'E 70°34'S	garnet-bearing leucocratic pegmatite
IF/89/254	P8	66°50'E 70°34'S	weakly-foliated felsic gneiss
IF/89/255	P8	66°50'E 70°34'S	foliated garnet-bearing felsic gneiss
IF/89/256	P9	66°50'E 70°34'S	foliated felsic gneiss
IF/89/257	P10	66°50'E 70°34'S	massive felsic dyke
IF/89/258	P10	66°50'E 70°34'S	orthopyroxene-bearing felsic gneiss
IF/89/259	P10	66°50'E 70°34'S	foliated mafic granulite
IF/89/260	P11	66°49'E 70°34'S	massive garnet-biotite gneiss
IF/89/261	P12	66°49'E 70°34'S	massive garnet-bearing felsic gneiss
IF/89/262	P12	66°49'E 70°34'S	lineated mafic granulite
IF/89/263	P12	66°49'E 70°34'S	banded amphibolite gneiss
IF/89/264	P12	66°49'E 70°34'S	massive ultramafic rock
IF/89/265	S1	66°54'E 70°38'S	banded amphibolite gneiss
IF/89/266	S1	66°54'E 70°38'S	massive felsic gneiss
IF/89/267	S1	66°54'E 70°38'S	massive orthopyroxene-bearing felsic gneiss
IF/89/268A	S3	66°54'E 70°37'S	calc-silicate and felsic gneiss contact
IF/89/268B	S3	66°54'E 70°37'S	banded scapolite-wollastonite calc-silicate
IF/89/268C	S3	66°54'E 70°37'S	banded scapolite-wollastonite calc-silicate
IF/89/268D	S3	66°54'E 70°37'S	banded calc-silicate and felsic gneiss contact
IF/89/268E	S3	66°54'E 70°37'S	banded diopside-mica calc-silicate
IF/89/268F	S3	66°54'E 70°37'S	banded diopside-mica calc-silicate
IF/89/268G	S3	66°54'E 70°37'S	banded calc-silicate and felsic gneiss contact
IF/89/268H	S3	66°54'E 70°37'S	banded scapolite-wollastonite calc-silicate

IF/89/268I	S3	66°54'E 70°37'S	banded calc-silicate and felsic gneiss contact
IF/89/268J	S3	66°54'E 70°37'S	orthopyroxene-bearing felsic gneiss
IF/89/269	S4	66°55'E 70°37'S	garnet-biotite leucogneiss
IF/89/270	S4	66°55'E 70°37'S	garnet-biotite banded semi-pelitic gneiss
IF/89/271	S5	66°55'E 70°37'S	mafic granulite and felsic gneiss contact
IF/89/272	S5	66°55'E 70°37'S	lineated mafic granulite
IF/89/273	P14	66°59'E 70°36'S	banded mafic granulite
IF/89/274	P14	66°59'E 70°36'S	orthopyroxene-bearing felsic gneiss
IF/89/275	W1	67°06'E 70°32'S	banded garnet-biotite leucocratic gneiss
IF/89/276	W2	67°07'E 70°32'S	banded garnet-bearing felsic gneiss
IF/89/277	W4	67°08'E 70°32'S	massive garnet leucogneiss
IF/89/278	W5	67°16'E 70°31'S	garnet-bearing felsic gneiss
IF/89/279	W6	67°15'E 70°31'S	banded garnet-biotite semi-pelitic gneiss
IF/89/280	W6	67°15'E 70°31'S	massive garnet-biotite semi-pelitic gneiss
IF/89/281	W6	67°15'E 70°31'S	banded garnet-biotite semi-pelitic gneiss
IF/89/282	W6	67°15'E 70°31'S	weakly-foliated garnet-bearing charnockite
IF/89/283	W6	67°15'E 70°31'S	leucocratic garnet-bearing charnockite
IF/89/284	W8	67°06'E 70°33'S	orthopyroxene-bearing felsic gneiss
IF/89/285	W9	67°06'E 70°33'S	metamorphosed mafic dyke
IF/89/286	W10	67°08'E 70°34'S	massive felsic gneiss with pseudotachylite
IF/89/287	W10	67°08'E 70°34'S	orthopyroxene-bearing felsic gneiss
IF/89/288	W11	67°10'E 70°34'S	massive felsic gneiss
IF/89/289	W11	67°10'E 70°34'S	metamorphosed mafic dyke
IF/89/290	W12	67°11'E 70°34'S	orthopyroxene-bearing felsic gneiss
IF/89/291	W12	67°11'E 70°34'S	orthopyroxene-bearing felsic gneiss
IF/89/292	W13	67°12'E 70°34'S	massive charnockite
IF/89/293	W13	67°12'E 70°34'S	massive charnockite
IF/89/294	W13	67°12'E 70°34'S	felsic band within charnockite
IF/89/295	W14	67°14'E 70°33'S	felsic band within charnockite
IF/89/296	W14	67°14'E 70°33'S	massive charnockite
IF/89/297	W15	67°19'E 70°32'S	orthopyroxene-bearing felsic gneiss
IF/89/298	Q1	67°26'E 70°35'S	foliated charnockite
IF/89/299	Q2	67°21'E 70°35'S	weakly-foliated garnet-bearing felsic gneiss
IF/89/300	Q2	67°21'E 70°35'S	weakly-foliated garnet-leucogneiss
IF/89/301	Q3	67°20'E 70°35'S	massive metamorphosed mafic dyke
IF/89/302	Q3	67°20'E 70°35'S	foliated metamorphosed mafic dyke
IF/89/303	Q4	67°17'E 70°36'S	granular late felsic body
IF/89/304	Q4	67°17'E 70°36'S	granular late felsic body
IF/89/305	Q4	67°17'E 70°36'S	massive mafic granulite
IF/89/306	Q5	67°15'E 70°36'S	garnet-orthopyroxene semi-pelitic gneiss
IF/89/307	Q5	67°15'E 70°36'S	garnet-orthopyroxene semi-pelitic gneiss
IF/89/308	Q6	67°13'E 70°37'S	banded orthopyroxene-bearing gneiss
IF/89/309	Q6	67°13'E 70°37'S	orthopyroxene-bearing felsic gneiss
IF/89/310	Q7	67°12'E 70°37'S	massive garnet-orthopyroxene felsic gneiss
IF/89/311	Q9	67°07'E 70°38'S	orthopyroxene-bearing felsic gneiss
IF/89/312	Q9	67°07'E 70°38'S	mylonite
IF/89/313	Q9	67°07'E 70°38'S	mylonite
IF/89/314	Q9	67°07'E 70°38'S	mylonite
IF/89/315	Q9	67°07'E 70°38'S	massive diopside-rich calc-silicate
IF/89/316	Q9	67°07'E 70°38'S	foliated mafic granulite
IF/89/317	Q9	67°07'E 70°38'S	mica-bearing calc-silicate
IF/89/318	Q10	67°01'E 70°40'S	orthopyroxene-bearing felsic gneiss
IF/89/319	Q10	67°01'E 70°40'S	orthopyroxene-bearing gneiss
IF/89/320	Q11	67°01'E 70°40'S	quartz-rich calc-silicate
IF/89/321	Q11	67°01'E 70°40'S	quartzofeldspathic calc-silicate
IF/89/322	Q11	67°01'E 70°40'S	diopside-mica-scapolite calc-silicate

IF/89/323	Q11	67°01'E 70°40'S	massive diopside-scapolite calc-silicate
IF/89/324	Q11	67°01'E 70°40'S	mylonite
IF/89/325	Q13	67°02'E 70°40'S	sheared orthopyroxene-bearing gneiss
IF/89/326	Q13	67°02'E 70°40'S	massive orthopyroxene-bearing late felsic body
IF/89/327	Q13	67°02'E 70°40'S	massive biotite-bearing felsic gneiss
IF/89/328	Q14	67°05'E 70°38'S	sheared orthopyroxene-bearing gneiss
IF/89/329	Q14	67°05'E 70°38'S	massive orthopyroxene-bearing felsic gneiss
IF/89/330A	Q15	67°06'E 70°38'S	orthopyroxene-bearing felsic gneiss
IF/89/330B	Q15	67°06'E 70°38'S	massive dark pyroxene-rich gneiss
IF/89/330C	Q15	67°06'E 70°38'S	massive diopside-mica calc-silicate
IF/89/330D	Q15	67°06'E 70°38'S	massive mica-bearing calc-silicate
IF/89/331	Q16	67°06'E 70°38'S	massive orthopyroxene-bearing felsic gneiss
IF/89/332	Q16	67°06'E 70°38'S	foliated mafic granulite
IF/89/333A	Q12	67°02'E 70°40'S	orthopyroxene-bearing felsic gneiss
IF/89/333B	Q12	67°02'E 70°40'S	diopside-olivine calc-silicate
IF/89/333C	Q12	67°02'E 70°40'S	massive diopside-mica calc-silicate
IF/89/333D	Q12	67°02'E 70°40'S	quartzofeldspathic diopside calc-silicate
IF/89/333E	Q12	67°02'E 70°40'S	diopside-rich mica-bearing calc-silicate
IF/89/333F	Q12	67°02'E 70°40'S	orthopyroxene-bearing felsic gneiss
IF/89/333G	Q12	67°02'E 70°40'S	massive mica-bearing calc-silicate
IF/89/333H	Q12	67°02'E 70°40'S	granular marble
IF/89/333I	Q12	67°02'E 70°40'S	massive orthopyroxene-bearing mafic gneiss
IF/89/333J	Q12	67°02'E 70°40'S	orthopyroxene-bearing felsic gneiss
IF/89/333K	Q12	67°02'E 70°40'S	olivine-bearing marble
IF/89/333L	Q12	67°02'E 70°40'S	marble-felsic gneiss contact
IF/89/333M	Q12	67°02'E 70°40'S	massive mafic granulite
IF/89/333N	Q12	67°02'E 70°40'S	orthopyroxene-bearing felsic gneiss
IF/89/334A	Q5	67°15'E 70°36'S	orthopyroxene-bearing felsic gneiss
IF/89/334B	Q5	67°15'E 70°36'S	orthopyroxene-bearing felsic gneiss
IF/89/334C	Q5	67°15'E 70°36'S	foliated scapolite-wollastonite calc-silicate
IF/89/334D	Q5	67°15'E 70°36'S	banded scapolite-wollastonite calc-silicate
IF/89/334E	Q5	67°15'E 70°36'S	massive scapolite-wollastonite calc-silicate
IF/89/334F	Q5	67°15'E 70°36'S	banded scapolite-wollastonite calc-silicate
IF/89/334G	Q5	67°15'E 70°36'S	banded scapolite-wollastonite calc-silicate
IF/89/334H	Q5	67°15'E 70°36'S	felsic gneiss and banded calc-silicate contact
IF/89/334I	Q5	67°15'E 70°36'S	garnet-orthopyroxene felsic gneiss
IF/89/334J	Q5	67°15'E 70°36'S	garnet-orthopyroxene felsic gneiss
IF/89/335	Q5	67°15'E 70°36'S	diopside-mica calc-silicate
IF/89/336	Q5	67°15'E 70°36'S	banded biotite-rich felsic gneiss
IF/89/337	Q5	67°15'E 70°36'S	banded biotite-rich felsic gneiss

(b) The Brattstrand Bluffs coastline

IF/89/343	D1	76°30'E 69°23'S	grey granite
IF/89/344	H34	76°52'E 69°15'S	orthopyroxene-bearing felsic gneiss
IF/89/345	H35	76°52'E 69°15'S	mafic granulite
IF/89/346	V29	76°44'E 69°14'S	composite mafic and felsic gneiss
IF/89/347	V30	76°44'E 69°14'S	ultramafic rock
IF/89/348	V30	76°44'E 69°14'S	felsic gneiss
IF/89/349	V31	76°44'E 69°14'S	stromatic metapelitic migmatite
IF/89/350	V31	76°44'E 69°14'S	stromatic metapelitic migmatite
IF/89/351	V33	76°44'E 69°14'S	massive leucocratic gneiss

APPENDIX 3. MICROPROBE ANALYSES

Appendix 3.1 Instruments

The compositions of the various phases discussed in Chapters 5, 6 and 7 were determined by wavelength dispersive electron-probe microanalysis. Most analyses were obtained using a Cameca CAMEBAX Microbeam microprobe at the Department of Geology and Geophysics, University of Edinburgh. Additional analyses were performed using a Cambridge Instruments Microscan Mark 5 electron microprobe at Edinburgh, and a Cambridge Instruments Microscan Mark 9 electron microprobe at the Department of Earth Sciences, University of Oxford. Almost all of the analyses used in calculations in Chapters 5, 6 and 7 were obtained using the Cameca microprobe, and the following discussion refers to this machine only.

Appendix 3.2 Operating conditions and correction procedures

Analyses were performed with an accelerating potential of 20 kV, a beam current, measured at a Faraday cage, of about 20 nA, and a focused electron beam of about 1 μm in diameter. The abundance of each element at an unknown analysis point was determined by comparison of X-ray count data with data obtained from the standard material for that element, and corrected for matrix effects using an on-line ZAF correction program. Counting times at peak and background spectrometer angles were 30 and 15 seconds respectively. The standards used were as follows:

element symbol	atomic number	standard name	weight % element
F	9	magnesium fluoride	60.79
Na	11	jadeite	11.34
Mg	12	periclase	60.32
Al	13	corundum	52.91
Si	14	wollastonite	24.00
Cl	17	halite	60.62
K	19	orthoclase	12.40
Ca	20	wollastonite	34.32
Ti	22	rutile	59.95
Cr	24	chromium metal	99.99
Mn	25	manganese metal	99.99
Fe	26	iron metal	99.99
Zn	30	zinc metal	99.99

Appendix 3.3 Normalization procedures and chemical parameters

Representative microprobe analyses for the semi-pelite, metapelite and calc-silicate specimens are tabulated in Appendices 3.4, 3.5 and 3.6. The analyses are expressed both in terms of weight per cent oxide, and cations per formula unit. The latter are

generally calculated on the basis of the number of oxygens in the standard formula of each mineral (i.e. 18 for cordierite, 12 for garnet, 8 for feldspar, 6 for pyroxene and wollastonite, 4 for spinel and 3 for ilmenite). However, biotite and scapolite have been normalized on the basis of 14 octahedral and tetrahedral cations, and 12 aluminium plus silicon cations, respectively, because of unknown H_2O, CO_2 and halogen contents.

The possibility of ferric iron in feldspar, biotite, cordierite, scapolite and wollastonite has not been considered, and all iron is treated as ferrous. Ferric iron contents of garnet, pyroxene, spinel and ilmenite have been estimated using either charge or site balance calculations, after re-normalization of the cations on the basis of cation totals rather than oxygen totals (i.e. 8 for garnet, 4 for pyroxene, 3 for spinel and 2 for ilmenite). Lists of cation-normalized data for these minerals are not presented in Appendices 3.4, 3.5 and 3.6, but they can be easily derived from the oxygen-normalized data which are presented. The tables also list the various chemical parameters discussed and used in calculations in Chapters 5, 6 and 7. *If a positive ferric iron content was calculated, all the chemical parameters were calculated on the basis of cation-normalized data, taking the ferric iron into account. If the calculated ferric iron was zero or negative, all iron was assumed to be ferrous and chemical parameters were calculated using the formula units normalized on the basis of oxygen totals.* Precise details of the parameters calculated for each mineral are given below.

Garnet

Ferric iron contents were estimated using a charge balance calculation as follows:

$$Fe^{3+} = 2\,[12 - (2\,Si + 2\,Ti + 1.5\,Al + 1.5\,Cr + Fe^{total} + Mn + Mg + Ca)],$$

where Si, Ti, Al, Cr, Fe^{total}, Mn, Mg and Ca have been normalized to total of 8. Calculated ferric iron in garnet from the calc-silicate specimens is relatively large, and accounts for most of the total iron content. In the semi-pelite and metapelite however, calculated ferric iron contents are negative or zero in all except a couple of semi-pelite specimens, and in these latter specimens the values are very low compared with the total iron contents (4 per cent or less of the total iron) and have been ignored.

Mole fractions of almandine, spessartine, pyrope, grossularite, uvarovite and andradite were calculated as follows:

$$X_{alm} = (Fe^{(total)} - Fe^{3+}) / 3, \qquad X_{sps} = Mn / 3,$$

$$X_{prp} = Mg / 3, \qquad X_{grs} = (Ca / 3) - (Cr / 2) - (Fe^{3+} / 2),$$

$$X_{uvr} = Cr / 2, \text{ and} \qquad X_{adr} = Fe^{3+} / 2,$$

and then re-normalized to a total of 1. Note that this calculation scheme does not consider titanium. These mole-fraction calculations were made using cation-

normalized data if the calculated ferric iron contents were greater than zero (i.e in the calc-silicate) and oxygen-normalized data if the calculated ferric iron was assumed to be zero (i.e. in the semi-pelite and metapelite).

Orthopyroxene

Ferric iron contents were estimated using a charge balance calculation as follows:

$$Fe^{3+} = 2\,[6 - (2\,Si + 2\,Ti + 1.5\,Al + 1.5\,Cr + Fe^{total} + Mn + Mg + Ca + 0.5\,Na)],$$

where Si, Ti, Al, Cr, Fe^{total}, Mn, Mg, Ca and Na have been normalized to total of 6. The amount of aluminium in the M1 site was then calculated as follows:

$$Al(M1) = (Al^{total} - Cr - Fe^{3+} - 2\,Ti) / 2.$$

Al(M1) was calculated using cation-normalized data if calculated ferric iron was greater than zero, and oxygen-normalized data if calculated ferric iron was negative or zero (and Fe^{3+} assumed to be zero).

Clinopyroxene

Aluminium contents of clinopyroxene were divided into tetrahedral and octahedral aluminium as follows: $Al\,(iv) = 2 - Si$, and $Al\,(vi) = Al^{total} - Al\,(iv)$, after normalization of Si, Ti, Al, Fe^{total}, Mn, and Mg to a total of 4. Ferric iron contents were estimated using a site balance calculation as follows:

$$Fe^{3+} = Al\,(iv) - Al\,(vi).$$

Estimates of ferric iron were greater than zero for the majority of clinopyroxene analyses, and the negative values are of low magnitude and within the error margins of the ferric iron calculations. Hence all calculations were made on the basis of cation-normalized data. All these calculations ignore the chromium, titanium and sodium contents of the clinopyroxene, which are low in the calc-silicate.

Spinel

Ferric iron contents were estimated using a site balance calculation as follows:

$$Fe^{3+} = 2 - (Al + Cr + Ti),$$

where Ti, Al, Cr, Fe^{total}, Mn, Mg, and Zn have been normalized to a total of 3. Calculated ferric iron contents in spinel from all metapelite specimens were found to be greater than zero. Mole fractions of hercynite, galaxite, gahnite, spinel, chromite, magnetite and ulvöspinel were then calculated as follows:

$X_{hc} = Fe^{total} - 1.5\,Fe^{3+} - 2\,Ti - (Cr / 2)$, $X_{gal} = Mn$,

$X_{spl} = Mg$, $X_{gah} = Zn$,

$X_{chr} = Cr / 2$, $X_{mag} = Fe^{3+} / 2$, and

$X_{usp} = Ti$.

Ilmenite

Ferric iron contents were estimated using a site balance calculation as follows:

$$Fe^{3+} = 2\,(1 - Ti),$$

where Ti, Fe^{total}, Mn, and Mg have been normalized to a total of 2. Mole fractions of ilmenite, pyrophanite, geikielite and hematite were calculated as follows:

$$X_{ilm} = Fe^{total} - Fe^{3+}, \qquad X_{ppn} = Mn,$$

$$X_{gek} = Mg, \text{ and} \qquad X_{hem} = Fe^{3+} / 2.$$

These mole fractions were calculated with cation-normalized data if calculated ferric iron was greater than zero, and oxygen-normalized data if calculated ferric iron was negative or zero (and Fe^{3+} assumed to be zero). The mole fractions were themselves re-normalized to sum to unity.

Feldspar

Mole fractions of anorthite, albite and orthoclase were calculated as follows:

$$X_{an} = Ca / (Ca + Na + K),$$

$$X_{ab} = Na / (Ca + Na + K), \text{ and}$$

$$X_{or} = K / (Ca + Na + K),$$

where the cations have been normalized on the basis of 8 oxygens.

Scapolite

Scapolite compositions are represented in terms of equivalent anorthite contents, which are calculated using the expression:

$$EqAn = 100\,(Al - 3) / 3,$$

after the cations have been normalized on the basis of 12 aluminium plus silicon.

Biotite

Biotite formula units were normalized on the basis of 14 cations in the octahedral and tetrahedral sites, and O and OH contents calculated as follows:

$$O = 20 \times (\text{normalization factor}), \text{ and}$$

$$OH = 24 - O - F.$$

Biotite compositional parameters were then calculated as follows:

$$X_K = K / (Na + K), \quad X_{Fe^{vi}} = Fe / 6, \text{ and} \quad X_{OH} = OH / (OH + F).$$

X_{Mg} and X_{Mg}^*

In addition to all the parameters discussed above, values of X_{Mg} and X_{Mg}^* are commonly quoted for the ferromagnesian phases. These are calculated as follows:

$$X_{Mg} = Mg / (Mg + Fe^{total}), \text{ and } X_{Mg}^* = Mg / (Mg + Fe^{total} - Fe^{3+}).$$

If calculated ferric iron contents are positive, both of these parameters are calculated using cation-normalized data, whereas if ferric iron contents are assumed to be zero, X_{Mg} is calculated using oxygen-normalized data and X_{Mg}^* is not calculated since it is equivalent to X_{Mg}.

Appendix 3.4 Analyses from the semi-pelitic gneiss

Garnet analyses

specimen	88/38c	88/38r	88/41c	88/41r	88/50c	88/50r	88/65c	88/65r	88/88c	88/88r	88/118c	88/118r
SiO_2	38.13	37.93	38.67	38.53	38.74	38.56	38.92	38.85	39.13	39.11	38.86	39.31
TiO_2	0.07	0.05	.na	.na	0.09	0.05	0.07	0.07	0.09	0.05	0.05	0.05
Al_2O_3	22.10	22.25	22.05	21.91	22.59	22.57	22.72	22.66	22.48	22.72	22.82	22.75
Cr_2O_3	0.02	0.08	.na	.na	0.06	0.08	0.02	0.05	0.11	0.07	0.05	0.06
FeO	31.03	31.27	29.99	30.61	29.25	29.93	26.57	27.54	26.63	27.47	26.93	27.55
MnO	1.32	1.30	2.06	2.06	0.90	0.94	1.13	1.12	0.91	0.86	0.64	0.66
MgO	5.86	5.80	6.90	6.58	7.44	7.16	9.20	8.25	9.01	9.03	9.55	9.19
CaO	1.73	1.54	1.76	1.76	1.54	1.54	1.77	1.61	1.48	1.20	1.44	1.27
total	100.26	100.22	101.43	101.45	100.61	100.83	100.40	100.15	99.84	100.51	100.34	100.84
cations normalized for 12 oxygens												
Si	2.988	2.977	2.988	2.986	2.988	2.979	2.976	2.990	3.003	2.989	2.969	2.992
Ti	0.004	0.003	.na	.na	0.005	0.003	0.004	0.004	0.005	0.003	0.003	0.003
Al	2.042	2.058	2.008	2.001	2.054	2.055	2.048	2.055	2.034	2.047	2.055	2.041
Cr	0.001	0.005	.na	.na	0.004	0.005	0.001	0.003	0.007	0.004	0.003	0.004
Fe	2.033	2.052	1.938	1.984	1.887	1.934	1.699	1.773	1.710	1.756	1.721	1.754
Mn	0.088	0.086	0.135	0.135	0.059	0.061	0.073	0.073	0.059	0.055	0.041	0.042
Mg	0.685	0.679	0.795	0.760	0.856	0.825	1.049	0.947	1.031	1.029	1.088	1.043
Ca	0.145	0.129	0.146	0.146	0.127	0.127	0.145	0.133	0.122	0.098	0.118	0.103
total	7.986	7.989	8.010	8.012	7.980	7.989	7.995	7.978	7.971	7.981	7.998	7.982
X_{Mg}	0.252	0.249	0.291	0.277	0.312	0.299	0.382	0.348	0.376	0.370	0.387	0.373
X_{alm}	0.688	0.698	0.643	0.656	0.644	0.656	0.572	0.606	0.585	0.598	0.580	0.596
X_{sps}	0.030	0.029	0.045	0.045	0.020	0.021	0.025	0.025	0.020	0.019	0.014	0.014
X_{prp}	0.232	0.230	0.264	0.251	0.292	0.280	0.354	0.324	0.353	0.350	0.366	0.355
X_{grs}	0.049	0.041	0.048	0.048	0.042	0.041	0.048	0.044	0.038	0.031	0.038	0.033
X_{uvr}	0.001	0.002	.na	.na	0.002	0.002	0.001	0.001	0.004	0.002	0.002	0.002
X_{adr}	0.000	0.000	0.000	0.000	0.000	0.000	0.000	0.000	0.000	0.000	0.000	0.000

specimen	88/168c	88/168r	88/333c	88/333r	89/2c	89/2r	89/40c	89/40r	89/59c	89/59r	89/63c	89/63r
SiO_2	38.74	39.21	38.78	38.81	38.58	38.64	38.43	38.18	38.65	38.14	38.00	37.83
TiO_2	0.11	0.06	.na	.na	0.05	0.04	0.01	0.03	0.04	0.02	0.03	0.01
Al_2O_3	22.60	22.30	21.89	21.98	22.41	22.38	21.96	21.66	22.33	22.32	21.97	21.96
Cr_2O_3	0.06	0.05	.na	.na	0.11	0.08	0.09	0.17	0.18	0.23	0.04	0.00
FeO	28.02	28.19	30.28	30.83	28.80	29.44	31.47	32.24	29.37	30.13	32.45	33.19
MnO	0.70	0.67	0.86	0.82	0.68	0.70	0.84	0.89	1.25	1.35	0.79	0.80
MgO	9.00	8.90	7.14	6.53	7.88	7.24	5.60	4.60	6.40	5.49	4.23	3.36
CaO	1.30	1.24	2.97	2.76	1.79	1.99	2.30	2.57	2.69	2.93	2.96	2.93
total	100.53	100.62	101.92	101.73	100.30	100.51	100.70	100.34	100.91	100.61	100.47	100.08
cations normalized for 12 oxygens												
Si	2.970	3.002	2.980	2.992	2.981	2.989	3.001	3.010	2.990	2.978	2.996	3.004
Ti	0.007	0.003	.na	.na	0.003	0.002	0.001	0.001	0.002	0.001	0.002	0.001
Al	2.043	2.012	1.983	1.997	2.041	2.040	2.022	2.013	2.037	2.054	2.042	2.056
Cr	0.003	0.003	.na	.na	0.007	0.005	0.005	0.010	0.011	0.014	0.002	0.000
Fe	1.797	1.805	1.946	1.988	1.861	1.904	2.055	2.125	1.901	1.967	2.140	2.205
Mn	0.045	0.043	0.056	0.054	0.044	0.046	0.056	0.059	0.082	0.089	0.052	0.054
Mg	1.029	1.016	0.818	0.751	0.908	0.835	0.652	0.540	0.738	0.639	0.497	0.398
Ca	0.107	0.102	0.245	0.228	0.148	0.165	0.192	0.217	0.223	0.245	0.250	0.249
total	8.001	7.986	8.028	8.010	7.993	7.986	7.984	7.975	7.984	7.987	7.981	7.967
X_{Mg}	0.364	0.360	0.296	0.274	0.328	0.305	0.241	0.203	0.280	0.245	0.188	0.153
X_{alm}	0.603	0.608	0.635	0.658	0.628	0.646	0.695	0.723	0.645	0.670	0.728	0.758
X_{sps}	0.015	0.015	0.018	0.018	0.015	0.015	0.019	0.020	0.028	0.030	0.018	0.019
X_{prp}	0.346	0.342	0.267	0.249	0.307	0.283	0.221	0.184	0.251	0.217	0.169	0.137
X_{grs}	0.034	0.033	0.080	0.075	0.047	0.054	0.062	0.068	0.070	0.076	0.084	0.086
X_{uvr}	0.002	0.002	.na	.na	0.003	0.002	0.003	0.005	0.006	0.007	0.001	0.000
X_{adr}	0.000	0.000	0.000	0.000	0.000	0.000	0.000	0.000	0.000	0.000	0.000	0.000

Garnet analyses (continued)

specimen	89/71c	89/71r	89/106c	89/106r	89/108c	89/108r	89/334Jc	89/334Jr
SiO_2	39.14	38.84	38.38	38.43	38.12	38.31	38.75	38.78
TiO_2	0.04	0.04	0.05	0.01	0.01	0.06	0.03	0.02
Al_2O_3	22.47	22.57	22.26	22.23	21.92	21.92	22.42	22.41
Cr_2O_3	0.12	0.04	0.02	0.02	0.03	0.00	0.06	0.06
FeO	28.03	28.86	30.12	30.16	30.45	30.22	29.93	30.05
MnO	0.92	1.02	1.09	1.19	1.65	1.70	1.19	1.23
MgO	8.50	7.60	6.05	5.97	5.25	4.53	7.21	7.16
CaO	1.47	1.52	2.43	2.20	2.58	2.94	1.02	0.91
total	100.69	100.49	100.40	100.21	100.01	99.68	100.61	100.62
cations normalized for 12 oxygens								
Si	2.998	2.994	2.992	3.001	3.000	3.023	2.997	3.000
Ti	0.002	0.002	0.003	0.001	0.001	0.004	0.001	0.001
Al	2.029	2.051	2.045	2.046	2.033	2.039	2.044	2.043
Cr	0.007	0.003	0.001	0.001	0.002	0.000	0.004	0.004
Fe	1.796	1.861	1.964	1.969	2.004	1.994	1.936	1.944
Mn	0.060	0.066	0.072	0.079	0.110	0.114	0.078	0.081
Mg	0.971	0.874	0.703	0.695	0.616	0.532	0.832	0.826
Ca	0.120	0.125	0.203	0.184	0.218	0.249	0.084	0.075
total	7.983	7.976	7.983	7.976	7.984	7.955	7.976	7.974
X_{Mg}	0.351	0.320	0.264	0.261	0.235	0.211	0.301	0.298
X_{alm}	0.610	0.636	0.668	0.674	0.680	0.691	0.660	0.664
X_{sps}	0.020	0.023	0.024	0.027	0.037	0.039	0.027	0.028
X_{prp}	0.329	0.299	0.239	0.237	0.209	0.184	0.284	0.282
X_{grs}	0.037	0.041	0.068	0.062	0.073	0.086	0.027	0.024
X_{uvr}	0.004	0.001	0.001	0.000	0.001	0.000	0.002	0.002
X_{adr}	0.000	0.000	0.000	0.000	0.000	0.000	0.000	0.000

Orthopyroxene analyses

specimen	88/38c	88/38r	88/41c	88/41r	88/50c	88/50r	88/65c	88/65r	88/88c	88/88r	88/118c	88/118r
SiO_2	48.70	49.53	50.13	49.59	48.60	49.64	49.09	49.79	49.16	49.18	48.31	49.24
TiO_2	0.16	0.20	.na	.na	0.26	0.19	0.24	0.25	0.24	0.24	0.28	0.21
Al_2O_3	4.19	3.83	2.83	3.60	5.98	4.28	6.43	5.25	7.01	6.65	7.23	6.08
Cr_2O_3	0.05	0.05	.na	.na	0.05	0.02	0.05	0.04	0.09	0.15	0.08	0.05
FeO	30.00	28.53	29.85	29.56	27.49	27.17	25.06	24.56	23.10	21.98	24.04	23.93
MnO	0.41	0.34	0.73	0.73	0.31	0.30	0.40	0.35	0.30	0.23	0.24	0.20
MgO	15.32	16.85	16.88	16.71	16.52	17.61	18.31	19.34	19.45	20.14	18.67	19.51
CaO	0.23	0.13	0.11	0.14	0.19	0.18	0.31	0.17	0.10	0.09	0.14	0.11
Na_2O	0.03	0.02	.na	.na	0.00	0.03	0.04	0.02	0.02	0.04	0.00	0.02
total	99.09	99.48	100.53	100.33	99.40	99.42	99.93	99.77	99.47	98.70	98.99	99.35
cations normalized for 6 oxygens												
Si	1.902	1.910	1.926	1.908	1.866	1.902	1.853	1.877	1.845	1.851	1.838	1.863
Ti	0.005	0.006	.na	.na	0.008	0.006	0.007	0.007	0.007	0.007	.na	.na
Al	0.193	0.174	0.128	0.163	0.271	0.193	0.286	0.233	0.310	0.295	0.324	0.271
Cr	0.002	0.001	.na	.na	0.002	0.001	0.002	0.001	0.003	0.005	.na	.na
Fe	0.980	0.920	0.959	0.951	0.882	0.871	0.791	0.774	0.725	0.692	0.765	0.757
Mn	0.014	0.011	0.024	0.024	0.010	0.010	0.013	0.011	0.009	0.007	0.008	0.007
Mg	0.892	0.969	0.967	0.959	0.945	1.006	1.030	1.087	1.088	1.131	1.059	1.100
Ca	0.010	0.005	0.005	0.006	0.008	0.007	0.012	0.007	0.004	0.004	0.006	0.004
Na	0.003	0.001	.na	.na	0.000	0.002	0.003	0.001	0.002	0.003	.na	.na
total	4.001	3.997	4.009	4.011	3.992	3.998	3.997	3.998	3.993	3.995	4.000	4.002
Fe^{3+}			0.028	0.031								0.006
X_{Mg}	0.476	0.513	0.502	0.502	0.517	0.536	0.566	0.584	0.600	0.620	0.581	0.592
X_{Mg}*			0.510	0.510								0.594
Al (M1)	0.091	0.081	0.050	0.066	0.127	0.091	0.136	0.109	0.147	0.139	0.162	0.133

Orthopyroxene analyses (continued)

specimen	88/168c	88/168r	88/333c	88/333r	89/2c	89/2r	89/40c	89/40r	89/59c	89/59r	89/63c	89/63r
SiO_2	48.93	49.49	49.86	50.34	50.83	51.71	50.26	51.18	50.13	51.15	49.60	49.82
TiO_2	0.22	0.27	.na	.na	0.07	0.12	0.07	0.06	0.08	0.07	0.09	0.18
Al_2O_3	7.17	6.28	3.19	2.86	2.86	2.28	1.81	1.52	3.14	1.73	1.59	1.13
Cr_2O_3	0.04	0.07	.na	.na	0.07	0.04	0.05	0.03	0.14	0.10	0.00	0.03
FeO	23.70	23.73	30.55	28.76	26.43	24.01	29.91	28.51	28.06	27.18	35.15	34.44
MnO	0.21	0.19	0.28	0.24	0.19	0.17	0.27	0.23	0.42	0.37	0.31	0.29
MgO	19.11	19.81	16.64	18.13	18.83	20.45	16.77	17.87	17.06	18.22	12.46	13.18
CaO	0.16	0.12	0.22	0.21	0.16	0.14	0.16	0.17	0.28	0.22	0.27	0.21
Na_2O	0.02	0.04	.na	.na	0.03	0.05	0.00	0.00	0.01	0.05	0.03	0.04
total	99.56	100.00	100.74	100.54	99.47	98.97	99.30	99.57	99.32	99.09	99.50	99.32
cations normalized for 6 oxygens												
Si	1.840	1.853	1.915	1.921	1.937	1.956	1.954	1.968	1.932	1.966	1.975	1.981
Ti	0.006	0.008	.na	.na	0.002	0.003	0.002	0.002	0.002	0.002	0.003	0.005
Al	0.318	0.277	0.144	0.129	0.129	0.101	0.083	0.069	0.142	0.078	0.075	0.053
Cr	0.001	0.002	.na	.na	0.002	0.001	0.002	0.001	0.004	0.003	0.000	0.001
Fe	0.745	0.743	0.981	0.918	0.842	0.760	0.973	0.917	0.904	0.874	1.170	1.145
Mn	0.007	0.006	0.009	0.008	0.006	0.006	0.009	0.008	0.014	0.012	0.010	0.010
Mg	1.071	1.106	0.953	1.031	1.070	1.153	0.972	1.025	0.981	1.045	0.740	0.782
Ca	0.006	0.005	0.009	0.009	0.007	0.006	0.007	0.007	0.012	0.009	0.011	0.009
Na	0.001	0.003	.na	.na	0.003	0.004	0.000	0.000	0.001	0.003	0.002	0.003
total	3.995	4.003	4.011	4.016	3.998	3.990	4.002	3.997	3.992	3.992	3.986	3.989
Fe^{3+}		0.004	0.037	0.045			0.004					
X_{Mg}	0.590	0.598	0.493	0.529	0.560	0.603	0.500	0.528	0.520	0.545	0.387	0.406
X_{Mg}*		0.600	0.502	0.542			0.501					
Al (M1)	0.152	0.128	0.054	0.042	0.061	0.047	0.037	0.032	0.067	0.036	0.035	0.021

specimen	89/71c	89/71r	89/106c	89/106r	89/108c	89/108r	89/334Jc	89/334Jr
SiO_2	50.64	51.60	49.95	50.29	50.58	50.83	50.00	50.07
TiO_2	0.06	0.07	0.06	0.10	0.08	0.08	0.11	0.10
Al_2O_3	3.77	2.92	3.28	3.02	1.91	1.64	3.83	3.62
Cr_2O_3	0.08	0.11	0.02	0.01	0.01	0.02	0.06	0.00
FeO	24.43	23.40	28.75	27.54	29.84	28.82	27.65	27.46
MnO	0.26	0.23	0.30	0.38	0.59	0.50	0.39	0.42
MgO	19.72	21.25	16.76	18.22	16.00	17.32	17.61	17.80
CaO	0.09	0.08	0.18	0.16	0.29	0.28	0.08	0.06
Na_2O	0.00	0.02	0.04	0.04	0.00	0.00	0.03	0.01
total	99.05	99.68	99.34	99.76	99.30	99.49	99.76	99.54
cations normalized for 6 oxygens								
Si	1.920	1.933	1.930	1.924	1.967	1.963	1.913	1.918
Ti	0.002	0.002	0.002	0.003	0.002	0.002	0.003	0.003
Al	0.168	0.129	0.149	0.136	0.088	0.075	0.173	0.163
Cr	0.002	0.003	0.001	0.000	0.000	0.000	0.002	0.000
Fe	0.775	0.733	0.929	0.881	0.970	0.931	0.885	0.880
Mn	0.008	0.007	0.010	0.012	0.019	0.016	0.013	0.014
Mg	1.114	1.187	0.965	1.039	0.928	0.997	1.004	1.017
Ca	0.004	0.003	0.007	0.006	0.012	0.011	0.003	0.003
Na	0.000	0.001	0.003	0.003	0.000	0.000	0.002	0.001
total	3.993	3.998	3.996	4.004	3.986	3.995	3.998	3.999
Fe^{3+}				0.019				
X_{Mg}	0.590	0.618	0.510	0.541	0.489	0.517	0.532	0.536
X_{Mg}*				0.547				
Al (M1)	0.081	0.061	0.073	0.056	0.041	0.035	0.082	0.079

Plagioclase analyses

specimen	88/38c	88/38r	88/41c	88/41r	88/50c	88/50r	88/65c	88/65r	88/88c	88/88r	88/118c	88/118r
SiO_2	57.57	56.81	56.67	56.02	56.19	56.01	50.07	49.19	54.90	54.76	55.60	54.26
Al_2O_3	26.31	27.01	27.16	27.57	27.13	27.27	31.11	31.81	28.41	28.58	27.52	28.49
FeO	0.08	0.31	.na	.na	0.05	0.02	0.07	0.15	0.04	0.03	0.04	0.12
MgO	0.02	0.01	.na	.na	0.02	0.01	0.02	0.03	0.01	0.01	0.02	0.02
CaO	8.30	8.93	9.52	9.89	9.45	9.43	14.74	15.31	10.49	10.67	9.89	10.95
Na_2O	6.89	6.72	5.47	5.39	5.82	5.79	3.19	2.97	5.64	5.61	5.89	5.14
K_2O	0.36	0.24	0.35	0.32	0.60	0.56	0.16	0.16	0.26	0.24	0.54	0.47
total	99.53	100.03	99.17	99.19	99.26	99.09	99.36	99.62	99.75	99.90	99.50	99.45
cations normalized for 8 oxygens												
Si	2.594	2.555	2.560	2.535	2.546	2.541	2.299	2.259	2.482	2.473	2.519	2.466
Al	1.397	1.432	1.446	1.470	1.449	1.458	1.684	1.722	1.514	1.522	1.470	1.526
Fe	0.003	0.012	.na	.na	0.002	0.001	0.003	0.006	0.002	0.001	0.002	0.004
Mg	0.001	0.000	.na	.na	0.002	0.001	0.001	0.002	0.001	0.001	0.002	0.001
Ca	0.401	0.430	0.461	0.479	0.459	0.458	0.725	0.754	0.508	0.516	0.480	0.533
Na	0.602	0.586	0.479	0.473	0.511	0.509	0.284	0.265	0.494	0.491	0.518	0.453
K	0.021	0.014	0.020	0.018	0.035	0.033	0.010	0.009	0.015	0.014	0.031	0.027
total	5.019	5.029	4.966	4.975	5.004	5.001	5.006	5.017	5.016	5.018	5.022	5.010
X_{an}	0.392	0.418	0.480	0.494	0.457	0.458	0.712	0.733	0.500	0.505	0.467	0.526
X_{ab}	0.588	0.569	0.499	0.487	0.508	0.509	0.279	0.258	0.486	0.481	0.503	0.447
X_{or}	0.020	0.013	0.021	0.019	0.035	0.033	0.009	0.009	0.014	0.014	0.030	0.027

specimen	88/168c	88/168r	88/333c	88/333r	89/2c	89/2r	89/40c	89/40r	89/59c	89/59r	89/63c	89/63r
SiO_2	56.91	56.25	54.38	54.02	59.08	58.65	59.62	58.77	55.89	55.92	59.05	59.10
Al_2O_3	27.08	27.52	28.45	28.13	25.36	25.91	24.95	25.69	27.61	27.75	25.66	25.62
FeO	0.06	0.14	.na	.na	0.04	0.25	0.08	0.50	0.06	0.16	0.06	0.12
MgO	0.02	0.01	.na	.na	0.02	0.02	0.03	0.00	0.01	0.02	0.02	0.01
CaO	9.12	9.60	11.70	11.58	7.28	7.78	6.68	7.39	9.76	9.81	7.08	7.05
Na_2O	6.43	6.24	4.80	4.66	7.14	7.21	7.71	8.08	6.82	6.60	7.38	7.41
K_2O	0.35	0.14	0.33	0.30	0.28	0.18	0.33	0.30	0.27	0.28	0.17	0.17
total	99.97	99.90	99.66	98.69	99.20	100.00	99.40	100.73	100.42	100.54	99.42	99.48
cations normalized for 8 oxygens												
Si	2.558	2.532	2.465	2.471	2.656	2.624	2.675	2.622	2.513	2.511	2.648	2.649
Al	1.434	1.460	1.520	1.517	1.344	1.366	1.320	1.351	1.464	1.469	1.356	1.354
Fe	0.002	0.005	.na	.na	0.001	0.009	0.003	0.019	0.002	0.006	0.002	0.004
Mg	0.001	0.000	.na	.na	0.002	0.001	0.002	0.000	0.000	0.001	0.001	0.001
Ca	0.439	0.463	0.568	0.568	0.351	0.373	0.321	0.353	0.470	0.472	0.340	0.339
Na	0.560	0.545	0.422	0.413	0.622	0.626	0.671	0.699	0.595	0.575	0.642	0.644
K	0.020	0.008	0.019	0.018	0.016	0.010	0.019	0.017	0.015	0.016	0.010	0.010
total	5.014	5.013	4.994	4.987	4.992	5.009	5.011	5.061	5.059	5.050	4.999	5.001
X_{an}	0.431	0.456	0.563	0.568	0.354	0.369	0.318	0.330	0.435	0.444	0.343	0.341
X_{ab}	0.549	0.536	0.418	0.414	0.630	0.621	0.663	0.654	0.551	0.541	0.647	0.649
X_{or}	0.020	0.008	0.019	0.018	0.016	0.010	0.019	0.016	0.014	0.015	0.010	0.010

Plagioclase analyses (continued)

specimen	89/71c	89/71r	89/106c	89/106r	89/108c	89/108r	89/334Jc	89/334Jr
SiO_2	59.43	59.54	58.25	57.78	59.02	57.81	62.33	62.42
Al_2O_3	25.41	25.74	26.26	26.84	25.69	26.06	23.57	23.58
FeO	0.05	0.08	0.04	0.28	0.06	0.24	0.03	0.33
MgO	0.01	0.01	0.02	0.02	0.00	0.02	0.02	0.04
CaO	6.89	6.91	7.95	8.39	7.62	8.01	4.73	4.68
Na_2O	6.92	7.52	6.32	6.42	6.58	7.38	7.74	8.01
K_2O	0.37	0.17	0.26	0.14	0.42	0.30	0.24	0.17
total	99.08	99.97	99.10	99.87	99.39	99.82	98.66	99.23
cations normalized for 8 oxygens								
Si	2.668	2.654	2.621	2.588	2.648	2.600	2.784	2.778
Al	1.345	1.352	1.393	1.417	1.359	1.382	1.241	1.237
Fe	0.002	0.003	0.002	0.010	0.002	0.009	0.001	0.012
Mg	0.001	0.001	0.001	0.001	0.000	0.001	0.001	0.003
Ca	0.332	0.330	0.383	0.403	0.366	0.386	0.226	0.223
Na	0.603	0.650	0.551	0.558	0.572	0.644	0.671	0.691
K	0.021	0.010	0.015	0.008	0.024	0.017	0.014	0.009
total	4.972	5.000	4.966	4.985	4.971	5.039	4.938	4.953
X_{an}	0.347	0.334	0.404	0.416	0.380	0.369	0.248	0.241
X_{ab}	0.631	0.656	0.580	0.576	0.595	0.615	0.737	0.749
X_{or}	0.022	0.010	0.016	0.008	0.025	0.016	0.015	0.010

K-feldspar analyses

specimen	89/2	89/40	89/59	89/63	89/71	89/106	89/108	89/334J
SiO_2	64.97	63.72	63.78	63.88	63.71	64.05	63.30	63.78
Al_2O_3	18.86	18.40	18.69	18.85	18.86	18.93	18.21	18.35
FeO	0.02	0.04	0.01	0.08	0.02	0.02	0.04	0.00
MgO	0.02	0.03	0.01	0.01	0.02	0.01	0.00	0.00
CaO	0.21	0.03	0.03	0.06	0.06	0.08	0.25	0.08
Na_2O	1.08	1.15	1.06	0.96	0.97	1.21	0.51	0.56
K_2O	16.63	17.85	17.04	17.02	17.39	16.83	17.41	17.29
total	101.79	101.22	100.62	100.86	101.03	101.13	99.72	100.06
cations normalized for 8 oxygens								
Si	2.967	2.954	2.957	2.954	2.948	2.952	2.967	2.972
Al	1.015	1.005	1.021	1.027	1.028	1.028	1.006	1.008
Fe	0.001	0.002	0.000	0.003	0.001	0.001	0.002	0.000
Mg	0.001	0.002	0.001	0.001	0.001	0.001	0.000	0.000
Ca	0.010	0.001	0.002	0.003	0.003	0.004	0.013	0.004
Na	0.095	0.103	0.095	0.086	0.087	0.108	0.046	0.051
K	0.969	1.056	1.008	1.004	1.026	0.990	1.041	1.028
total	5.058	5.123	5.084	5.078	5.094	5.084	5.075	5.063
X_{an}	0.010	0.001	0.002	0.003	0.002	0.003	0.011	0.004
X_{ab}	0.089	0.089	0.086	0.079	0.078	0.098	0.042	0.047
X_{or}	0.901	0.910	0.912	0.918	0.920	0.899	0.947	0.949

Biotite analyses

specimen	89/2	89/40	89/59	89/63	89/71	89/106	89/108	89/334J
SiO_2	37.23	36.68	36.76	36.35	37.84	37.19	38.09	37.42
TiO_2	5.56	5.42	5.81	4.82	5.24	5.00	4.60	5.00
Al_2O_3	14.41	14.33	14.57	14.05	14.44	14.87	14.40	14.87
Cr_2O_3	0.18	0.12	0.21	0.04	0.17	0.04	0.01	0.17
FeO	13.71	17.94	15.36	20.01	12.15	13.86	13.13	13.06
MnO	0.10	0.01	0.05	0.03	0.04	0.03	0.02	0.00
MgO	13.87	11.55	12.83	10.75	15.16	14.05	15.45	14.76
CaO	0.01	0.00	0.00	0.00	0.19	0.00	0.01	0.00
Na_2O	0.11	0.05	0.06	0.06	0.16	0.06	0.08	0.08
K_2O	10.54	10.54	10.62	10.98	10.81	10.71	10.06	10.93
F	1.18	1.12	0.55	1.56	1.54	1.47	1.79	2.60
total	96.90	97.76	96.82	98.65	97.74	97.28	97.64	98.89
normalized to (Si+Ti+Al+Cr+Fe+Mn+Mg)=14								
Si	5.743	5.708	5.688	5.696	5.776	5.718	5.760	5.708
Ti	0.645	0.634	0.677	0.568	0.601	0.579	0.524	0.574
Al	2.619	2.629	2.656	2.595	2.597	2.693	2.568	2.673
Cr	0.022	0.014	0.026	0.005	0.021	0.004	0.001	0.021
Fe	1.769	2.334	1.988	2.623	1.551	1.782	1.662	1.666
Mn	0.012	0.002	0.006	0.003	0.005	0.004	0.003	0.000
Mg	3.190	2.679	2.959	2.510	3.449	3.220	3.482	3.358
Ca	0.001	0.000	0.000	0.000	0.032	0.000	0.002	0.000
Na	0.033	0.017	0.019	0.019	0.048	0.019	0.023	0.023
K	2.075	2.092	2.096	2.196	2.106	2.099	1.942	2.126
F	0.576	0.551	0.268	0.774	0.741	0.715	0.854	1.256
OH	2.726	2.795	3.037	2.615	2.534	2.645	2.644	2.101
O	20.698	20.654	20.695	20.611	20.725	20.640	20.502	20.643
X_{Mg}	0.643	0.534	0.598	0.489	0.690	0.644	0.677	0.668
X_K	0.984	0.992	0.991	0.991	0.978	0.991	0.988	0.989
$X_{Fe^{vi}}$	0.295	0.389	0.331	0.437	0.259	0.297	0.277	0.278
X_{OH}	0.826	0.835	0.919	0.772	0.774	0.787	0.756	0.626

N.b. The symbol 'na' indicates an element which was not analysed. The lower case letters c and r after the specimen numbers in the tables of garnet, orthopyroxene and plagioclase analyses refer to core and rim analyses used in Chapter 5.

Appendix 3.5 Analyses from the metapelitic gneiss

Garnet analyses

specimen	88/14B	88/28	88/37	88/44	88/51	88/56	88/62	88/74	88/102	88/110	88/153C	88/205
SiO_2	37.97	37.77	38.34	37.04	37.55	38.17	37.41	38.82	37.97	37.78	38.32	36.94
TiO_2	0.06	0.05	0.08	0.06	0.08	0.06	0.18	0.08	0.09	0.01	0.05	0.30
Al_2O_3	22.27	21.95	21.98	22.26	21.43	22.22	21.83	21.96	22.08	21.30	21.92	22.00
Cr_2O_3	0.04	0.05	0.02	0.04	0.02	0.04	0.02	0.04	0.04	0.03	0.02	0.00
FeO	33.35	35.08	31.85	33.30	35.77	32.21	35.64	32.88	33.02	33.74	32.77	34.53
MnO	0.83	0.67	1.04	0.76	1.59	0.80	1.32	0.54	1.21	0.98	1.26	0.86
MgO	5.51	4.18	6.21	5.16	3.17	6.30	3.50	6.48	5.22	5.06	5.28	4.60
CaO	0.78	0.90	0.59	0.90	0.72	0.86	0.60	1.01	0.85	0.97	0.95	0.88
total	100.81	100.65	100.11	99.52	100.33	100.66	100.50	101.81	100.48	99.87	100.57	100.11
cations normalized for 12 oxygens												
Si	2.976	2.990	3.005	2.950	3.006	2.980	2.983	2.999	2.989	3.004	3.009	2.943
Ti	0.003	0.003	0.005	0.003	0.005	0.004	0.011	0.005	0.005	0.000	0.003	0.018
Al	2.058	2.049	2.031	2.089	2.022	2.045	2.052	1.999	2.048	1.996	2.028	2.065
Cr	0.003	0.003	0.001	0.002	0.001	0.002	0.001	0.002	0.002	0.002	0.001	0.000
Fe	2.186	2.322	2.088	2.218	2.395	2.103	2.377	2.125	2.173	2.244	2.152	2.301
Mn	0.055	0.045	0.069	0.051	0.108	0.053	0.089	0.035	0.081	0.066	0.084	0.058
Mg	0.644	0.493	0.726	0.612	0.378	0.734	0.416	0.746	0.612	0.600	0.618	0.546
Ca	0.065	0.077	0.050	0.077	0.061	0.072	0.051	0.083	0.071	0.083	0.080	0.075
total	7.990	7.982	7.975	8.002	7.976	7.993	7.980	7.994	7.981	7.995	7.975	8.006
X_{Mg}	0.228	0.175	0.258	0.216	0.136	0.259	0.149	0.260	0.220	0.211	0.223	0.192
X_{alm}	0.741	0.791	0.712	0.750	0.814	0.710	0.810	0.711	0.740	0.749	0.733	0.773
X_{sps}	0.019	0.015	0.024	0.017	0.037	0.018	0.030	0.012	0.028	0.022	0.029	0.019
X_{prp}	0.218	0.168	0.247	0.207	0.128	0.248	0.142	0.249	0.208	0.201	0.210	0.183
X_{grs}	0.021	0.024	0.016	0.025	0.020	0.023	0.017	0.027	0.023	0.027	0.027	0.025
X_{uvr}	0.001	0.002	0.001	0.001	0.001	0.001	0.001	0.001	0.001	0.001	0.001	0.000
X_{adr}	0.000	0.000	0.000	0.000	0.000	0.000	0.000	0.000	0.000	0.000	0.000	0.000

specimen	88/273	88/318	88/325	88/328	88/331
SiO_2	37.97	37.87	37.54	37.98	39.33
TiO_2	0.08	0.06	0.06	0.06	0.04
Al_2O_3	21.61	22.32	21.04	22.14	22.03
Cr_2O_3	0.06	0.08	0.02	0.08	0.06
FeO	33.07	33.00	35.69	33.54	31.88
MnO	0.60	0.61	0.68	0.60	0.60
MgO	5.96	5.24	4.12	4.94	7.43
CaO	0.84	1.05	1.14	1.07	1.14
total	100.19	100.23	100.29	100.41	102.51
cations normalized for 12 oxygens					
Si	2.992	2.981	3.000	2.991	3.002
Ti	0.005	0.003	0.003	0.004	0.002
Al	2.007	2.071	1.981	2.055	1.982
Cr	0.004	0.005	0.001	0.005	0.003
Fe	2.179	2.173	2.385	2.209	2.035
Mn	0.040	0.040	0.046	0.040	0.039
Mg	0.700	0.615	0.491	0.580	0.845
Ca	0.071	0.089	0.097	0.090	0.093
total	7.998	7.977	8.004	7.974	8.001
X_{Mg}	0.243	0.221	0.171	0.208	0.293
X_{alm}	0.729	0.745	0.789	0.756	0.675
X_{sps}	0.013	0.014	0.015	0.014	0.013
X_{prp}	0.234	0.211	0.163	0.199	0.281
X_{grs}	0.022	0.028	0.032	0.028	0.029
X_{uvr}	0.002	0.002	0.001	0.003	0.002
X_{adr}	0.000	0.000	0.000	0.000	0.000

Cordierite analyses

specimen	88/28	88/37	88/44	88/56	88/74	88/102	88/110	88/153C	88/205	88/273	88/318	88/328
SiO_2	48.32	48.24	48.15	48.53	48.92	48.03	48.19	48.40	48.60	48.70	48.21	48.65
TiO_2	0.00	0.01	0.02	0.01	.na	0.03	0.03	0.10	0.02	0.01	0.02	0.03
Al_2O_3	32.48	32.92	33.03	33.00	33.23	33.28	31.82	32.08	33.51	31.59	33.41	33.55
FeO	10.09	9.00	9.52	7.97	8.89	8.88	8.90	8.34	7.37	8.29	8.69	8.52
MnO	0.07	0.10	0.08	0.08	.na	0.14	0.08	0.07	0.05	0.03	0.07	0.04
MgO	7.25	7.69	7.34	8.20	8.16	7.87	7.99	8.37	8.77	8.36	7.91	7.21
CaO	0.01	0.02	0.01	0.00	0.03	0.03	0.02	0.01	0.00	0.01	0.01	0.02
Na_2O	0.14	0.07	0.09	0.02	0.05	0.07	0.08	0.05	0.04	0.03	0.04	0.03
K_2O	0.03	0.02	0.00	0.00	0.02	0.06	0.05	0.02	0.01	0.02	0.01	0.01
total	98.39	98.07	98.24	97.81	99.30	98.39	97.16	97.44	98.37	97.04	98.37	98.06
cations normalized for 18 oxygens												
Si	5.012	4.994	4.987	5.008	4.995	4.959	5.037	5.028	4.976	5.075	4.967	5.014
Ti	0.000	0.001	0.001	0.001	.na	0.002	0.002	0.008	0.002	0.000	0.002	0.002
Al	3.971	4.017	4.032	4.015	3.999	4.049	3.920	3.929	4.044	3.880	4.057	4.077
Fe	0.875	0.779	0.825	0.688	0.759	0.767	0.778	0.724	0.631	0.723	0.749	0.735
Mn	0.006	0.009	0.007	0.007	.na	0.013	0.007	0.007	0.004	0.003	0.006	0.004
Mg	1.121	1.187	1.134	1.262	1.242	1.211	1.245	1.296	1.339	1.298	1.216	1.108
Ca	0.001	0.002	0.001	0.000	0.003	0.003	0.002	0.002	0.000	0.001	0.001	0.002
Na	0.027	0.015	0.018	0.004	0.010	0.015	0.017	0.010	0.008	0.006	0.009	0.007
K	0.004	0.003	0.000	0.000	0.003	0.007	0.007	0.003	0.001	0.003	0.001	0.002
total	11.017	11.007	11.005	10.985	11.011	11.026	11.015	11.007	11.005	10.989	11.008	10.951
X_{Mg}	0.562	0.604	0.579	0.647	0.621	0.612	0.615	0.641	0.679	0.642	0.619	0.601

Spinel analyses

specimen	88/14B	88/28	88/44	88/51	88/56	88/62	88/74	88/102	88/110	88/153C	88/205	88/273	88/328
SiO_2	0.05	0.00	0.04	0.01	0.02	0.04	0.31	0.04	0.04	0.07	0.02	0.01	0.02
TiO_2	0.06	0.06	0.05	0.07	0.09	0.06	0.07	0.08	0.03	0.12	0.09	0.05	0.10
Al_2O_3	57.35	59.21	58.89	59.12	59.31	58.75	58.48	57.62	56.89	56.28	59.48	57.32	58.65
Cr_2O_3	0.33	0.39	0.55	0.25	0.89	0.27	0.44	0.26	0.13	0.18	0.68	0.96	1.00
FeO	37.19	35.30	33.90	38.02	33.46	38.08	35.22	37.57	37.06	38.17	34.04	33.65	34.02
MnO	0.10	0.09	0.07	0.13	0.12	0.18	0.08	0.16	0.13	0.15	0.04	0.05	0.10
MgO	4.50	3.99	4.75	2.52	5.34	2.60	5.06	4.44	4.71	4.22	5.08	4.83	4.30
ZnO	0.47	1.34	1.21	0.29	0.86	0.24	.na	0.23	0.16	0.52	0.59	1.19	1.40
CaO	0.00	0.00	0.03	0.01	0.00	0.02	.na	0.01	0.01	0.01	0.02	0.01	0.01
total	100.05	100.38	99.49	100.42	100.09	100.24	99.66	100.41	99.16	99.72	100.04	98.07	99.60
cations normalized to 4 oxygens													
Si	0.001	0.000	0.001	0.000	0.000	0.001	0.009	0.001	0.001	0.002	0.000	0.000	0.001
Ti	0.001	0.001	0.001	0.001	0.002	0.001	0.002	0.002	0.001	0.003	0.002	0.001	0.002
Al	1.929	1.969	1.964	1.979	1.959	1.973	1.946	1.930	1.928	1.912	1.966	1.946	1.960
Cr	0.007	0.009	0.012	0.006	0.020	0.006	0.010	0.006	0.003	0.004	0.015	0.022	0.022
Fe	0.887	0.833	0.802	0.903	0.784	0.907	0.831	0.893	0.891	0.920	0.798	0.811	0.807
Mn	0.002	0.002	0.002	0.003	0.003	0.004	0.002	0.004	0.003	0.004	0.001	0.001	0.002
Mg	0.191	0.168	0.201	0.107	0.223	0.110	0.213	0.188	0.202	0.181	0.212	0.207	0.182
Zn	0.010	0.028	0.025	0.006	0.018	0.005	.na	0.005	0.003	0.011	0.012	0.025	0.029
Ca	0.000	0.000	0.001	0.000	0.000	0.001	.na	0.000	0.000	0.000	0.001	0.000	0.000
total	3.028	3.010	3.009	3.005	3.009	3.008	3.013	3.029	3.032	3.037	3.007	3.013	3.005
Fe^{3+}	0.081	0.028	0.027	0.017	0.025	0.024	0.045	0.080	0.088	0.103	0.022	0.040	0.018
X_{Mg}	0.177	0.168	0.200	0.106	0.221	0.108	0.204	0.174	0.185	0.165	0.210	0.204	0.184
X_{Mg}^*	0.200	0.175	0.209	0.109	0.230	0.112	0.218	0.196	0.210	0.192	0.217	0.217	0.189
X_{hc}	0.753	0.783	0.752	0.871	0.732	0.864	0.755	0.760	0.748	0.749	0.754	0.735	0.764
X_{gal}	0.002	0.002	0.002	0.003	0.003	0.004	0.002	0.004	0.003	0.004	0.001	0.001	0.002
X_{spl}	0.190	0.168	0.200	0.107	0.222	0.111	0.213	0.186	0.200	0.179	0.212	0.207	0.183
X_{gah}	0.010	0.028	0.025	0.006	0.018	0.005	0.000	0.005	0.003	0.011	0.012	0.025	0.029
X_{chr}	0.004	0.004	0.006	0.003	0.010	0.003	0.005	0.003	0.001	0.002	0.008	0.011	0.011
X_{mag}	0.040	0.014	0.014	0.009	0.013	0.012	0.023	0.040	0.044	0.052	0.011	0.020	0.009
X_{usp}	0.001	0.001	0.001	0.001	0.002	0.001	0.002	0.002	0.001	0.003	0.002	0.001	0.002

Ilmenite analyses

specimen	88/14B	88/28	88/37	88/44	88/51	88/56	88/62	88/74	88/102	88/110	88/153C	88/205
SiO_2	0.01	0.02	0.03	0.00	0.01	0.04	0.02	0.08	0.00	0.00	0.02	0.02
TiO_2	51.15	53.02	52.44	53.76	52.78	53.51	54.00	52.98	51.49	52.17	52.42	53.13
Al_2O_3	0.06	0.07	0.06	0.06	0.07	0.07	0.06	0.05	0.05	0.05	0.06	0.05
Cr_2O_3	0.07	0.12	0.06	0.05	0.02	0.09	0.03	0.12	0.01	0.02	0.00	0.02
FeO	47.09	46.32	45.72	44.46	46.32	43.86	45.95	44.98	46.83	46.90	46.53	46.24
MnO	0.23	0.12	1.08	0.19	0.41	0.17	0.21	0.14	0.38	0.31	0.38	0.13
MgO	0.38	0.08	0.05	1.31	0.20	1.27	0.06	0.85	0.31	0.42	0.64	0.63
total	98.99	99.75	99.44	99.83	99.81	99.01	100.33	99.20	99.07	99.87	100.05	100.22
cations normalized to 3 oxygens												
Si	0.000	0.000	0.001	0.000	0.000	0.001	0.000	0.002	0.000	0.000	0.001	0.001
Ti	0.984	1.005	1.000	1.008	1.001	1.010	1.015	1.004	0.989	0.992	0.992	1.001
Al	0.002	0.002	0.002	0.002	0.002	0.002	0.002	0.002	0.001	0.002	0.002	0.001
Cr	0.001	0.002	0.001	0.001	0.000	0.002	0.001	0.001	0.000	0.000	0.000	0.000
Fe	1.007	0.977	0.969	0.927	0.977	0.921	0.960	0.948	1.000	0.991	0.979	0.968
Mn	0.005	0.002	0.023	0.004	0.009	0.004	0.004	0.003	0.008	0.007	0.008	0.003
Mg	0.015	0.003	0.002	0.049	0.008	0.048	0.002	0.032	0.012	0.016	0.024	0.024
total	2.014	1.991	1.998	1.991	1.997	1.988	1.984	1.992	2.010	2.008	2.006	1.998
Fe^{3+}	0.043	0.000	0.000	0.000	0.000	0.000	0.000	0.000	0.031	0.022	0.019	0.000
X_{Mg}	0.014	0.003	0.002	0.050	0.008	0.049	0.002	0.033	0.012	0.016	0.024	0.024
X_{Mg}^*	0.015								0.012	0.016	0.025	
X_{ilm}	0.960	0.994	0.975	0.946	0.983	0.947	0.993	0.964	0.964	0.966	0.958	0.973
X_{ppn}	0.005	0.003	0.023	0.004	0.009	0.004	0.005	0.003	0.008	0.007	0.008	0.003
X_{gek}	0.014	0.003	0.002	0.050	0.008	0.049	0.002	0.033	0.012	0.016	0.024	0.024
X_{hem}	0.021	0.000	0.000	0.000	0.000	0.000	0.000	0.000	0.016	0.011	0.010	0.000

specimen	88/273	88/318	88/325	88/331
SiO_2	0.02	0.03	0.72	0.00
TiO_2	53.81	53.68	52.80	54.10
Al_2O_3	0.04	0.06	0.06	0.05
Cr_2O_3	0.03	0.04	0.03	0.06
FeO	45.07	45.25	44.94	45.29
MnO	0.16	0.21	1.02	0.14
MgO	0.86	0.66	0.04	1.35
total	99.99	99.93	99.61	100.99
cations normalized to 3 oxygens				
Si	0.000	0.001	0.018	0.000
Ti	1.010	1.010	0.997	1.004
Al	0.001	0.002	0.002	0.001
Cr	0.001	0.001	0.000	0.001
Fe	0.941	0.947	0.944	0.935
Mn	0.003	0.004	0.022	0.003
Mg	0.032	0.025	0.001	0.050
total	1.988	1.990	1.984	1.994
Fe^{3+}	0.000	0.000	0.000	0.000
X_{Mg}	0.033	0.025	0.002	0.050
X_{Mg}^*	0.033	0.025	0.002	0.050
X_{ilm}	0.964	0.971	0.976	0.947
X_{ppn}	0.003	0.004	0.022	0.003
X_{gek}	0.033	0.025	0.002	0.050
X_{hem}	0.000	0.000	0.000	0.000

Plagioclase analyses

specimen	88/28	88/37	88/44	88/56	88/62	88/74	88/153C	88/205	88/273	88/318	88/325	88/331
SiO_2	59.38	61.45	59.34	61.06	62.99	58.14	59.36	58.81	59.64	61.13	61.68	57.55
Al_2O_3	25.32	23.85	25.20	24.17	23.43	26.20	24.71	24.85	24.46	24.07	24.44	26.44
FeO	0.05	0.31	0.29	0.08	0.12	0.30	0.08	0.06	0.01	0.08	0.21	0.08
MgO	0.02	0.01	0.01	0.01	0.02	0.04	0.01	0.01	0.03	0.02	0.02	0.04
CaO	6.69	4.86	6.85	5.98	4.83	8.08	7.24	6.39	6.21	5.83	6.26	8.22
Na_2O	8.22	9.32	8.19	8.49	9.21	6.89	7.59	8.10	8.05	7.69	8.04	6.92
K_2O	0.18	0.23	0.13	0.15	0.27	0.15	0.20	0.09	0.25	0.17	0.11	0.20
total	99.86	100.03	100.01	99.94	100.87	99.80	99.19	98.31	98.65	98.99	100.76	99.45
cations normalized for 8 oxygens												
Si	2.656	2.735	2.654	2.719	2.772	2.608	2.672	2.667	2.693	2.736	2.721	2.592
Al	1.335	1.251	1.329	1.268	1.215	1.385	1.311	1.329	1.301	1.270	1.271	1.404
Fe	0.002	0.012	0.011	0.003	0.004	0.011	0.003	0.002	0.000	0.003	0.008	0.003
Mg	0.001	0.001	0.000	0.001	0.001	0.003	0.001	0.001	0.002	0.002	0.002	0.002
Ca	0.321	0.232	0.328	0.285	0.228	0.389	0.349	0.311	0.300	0.280	0.296	0.397
Na	0.713	0.804	0.710	0.733	0.786	0.599	0.662	0.712	0.705	0.668	0.687	0.604
K	0.010	0.013	0.007	0.008	0.015	0.009	0.011	0.005	0.014	0.010	0.006	0.011
total	5.038	5.048	5.039	5.017	5.021	5.004	5.009	5.027	5.015	4.969	4.991	5.013
X_{an}	0.307	0.221	0.314	0.278	0.222	0.390	0.341	0.302	0.294	0.292	0.299	0.392
X_{ab}	0.683	0.767	0.679	0.714	0.763	0.601	0.648	0.693	0.692	0.698	0.695	0.597
X_{or}	0.010	0.012	0.007	0.008	0.015	0.009	0.011	0.005	0.014	0.010	0.006	0.011

K-feldspar analyses

specimen	88/14B	88/28	88/37	88/44	88/51	88/56	88/62	88/102	88/110	88/153C	88/273	88/325	88/331
SiO_2	64.72	64.25	63.71	63.60	64.57	63.91	66.22	64.45	64.76	66.16	64.97	64.90	63.95
Al_2O_3	19.14	18.89	19.52	19.16	21.02	19.96	20.21	19.08	19.28	19.13	19.40	18.84	19.68
FeO	0.06	0.07	0.02	0.03	0.08	0.06	0.05	0.01	0.39	0.06	0.01	0.06	0.02
MgO	0.02	0.01	0.03	0.03	0.02	0.02	0.01	0.02	0.01	0.01	0.01	0.02	0.01
CaO	0.61	0.14	0.73	0.65	2.24	1.14	1.03	0.36	0.00	0.00	0.74	0.36	0.78
Na_2O	3.60	1.72	3.41	2.08	3.26	3.24	3.73	1.77	3.07	3.72	2.31	2.83	2.84
K_2O	11.80	14.38	11.90	13.29	7.67	11.70	10.54	13.84	10.81	10.25	13.27	12.54	12.21
total	99.95	99.46	99.32	98.84	98.86	100.03	101.79	99.53	98.32	99.33	100.71	99.55	99.49
cations normalized for 8 oxygens													
Si	2.958	2.972	2.935	2.953	2.921	2.921	2.949	2.970	2.981	3.001	2.957	2.978	2.939
Al	1.031	1.030	1.060	1.048	1.121	1.075	1.061	1.036	1.046	1.023	1.041	1.019	1.066
Fe	0.002	0.003	0.001	0.001	0.003	0.002	0.002	0.000	0.015	0.002	0.000	0.002	0.001
Mg	0.001	0.001	0.002	0.002	0.001	0.002	0.000	0.002	0.001	0.000	0.001	0.002	0.001
Ca	0.030	0.007	0.036	0.032	0.109	0.056	0.049	0.018	0.000	0.000	0.036	0.018	0.038
Na	0.319	0.154	0.304	0.187	0.286	0.287	0.322	0.158	0.275	0.327	0.203	0.252	0.253
K	0.688	0.848	0.699	0.787	0.442	0.682	0.599	0.813	0.635	0.593	0.771	0.734	0.716
total	5.029	5.015	5.037	5.010	4.883	5.025	4.982	4.997	4.953	4.946	5.009	5.005	5.014
X_{an}	0.029	0.007	0.034	0.032	0.130	0.055	0.050	0.018	0.000	0.000	0.036	0.018	0.038
X_{ab}	0.308	0.153	0.293	0.186	0.341	0.280	0.332	0.160	0.302	0.355	0.201	0.251	0.251
X_{or}	0.663	0.840	0.673	0.782	0.529	0.665	0.618	0.822	0.698	0.645	0.763	0.731	0.711

Biotite analyses

specimen	88/14B	88/44	88/51	88/56^{i}	88/56^{m}	88/62	88/102	88/110	88/153C	88/273^{i}	88/273^{m}	88/328
SiO_2	38.02	36.20	37.11	38.02	38.36	37.56	37.28	37.21	37.73	37.50	37.77	36.91
TiO_2	3.34	3.13	4.92	5.61	4.09	4.23	4.68	6.07	5.52	3.64	5.90	5.47
Al_2O_3	14.94	17.95	13.69	15.02	13.90	14.01	13.78	12.61	14.07	13.31	14.04	15.56
Cr_2O_3	0.02	0.02	0.02	0.07	0.04	0.03	0.00	0.01	0.03	0.08	0.08	0.10
FeO	11.26	15.11	13.58	9.35	12.22	14.46	15.34	15.60	15.48	13.77	10.60	14.24
MnO	0.02	0.03	0.02	0.01	0.03	0.05	0.06	0.04	0.02	0.02	0.01	0.03
MgO	17.84	13.12	14.86	16.65	16.81	14.57	14.15	13.38	14.17	15.39	15.65	13.15
ZnO	0.04	0.06	0.00	0.05	0.04	0.05	0.00	0.03	0.00	0.02	0.03	0.02
CaO	0.01	0.00	0.00	0.00	0.00	0.00	0.00	0.00	0.00	0.00	0.00	0.03
Na_2O	0.21	0.12	0.33	0.58	0.23	0.33	0.31	0.25	0.19	0.19	0.52	0.19
K_2O	8.91	9.87	9.77	9.80	10.11	9.71	9.67	8.65	8.76	8.98	8.53	9.38
F	3.91	1.09	5.86	4.03	4.66	5.01	3.90	3.86	3.34	3.50	3.71	2.59
total	98.52	96.70	100.16	99.19	100.49	100.01	99.17	97.71	99.31	96.40	96.84	97.67
normalized to (Si+Ti+Al+Cr+Fe+Mn+Mg+Zn)=14												
Si	5.650	5.509	5.742	5.744	5.764	5.768	5.725	5.808	5.706	5.800	5.807	5.680
Ti	0.373	0.358	0.573	0.637	0.462	0.488	0.541	0.712	0.627	0.423	0.683	0.632
Al	2.616	3.220	2.496	2.675	2.461	2.537	2.494	2.321	2.507	2.428	2.546	2.822
Cr	0.002	0.002	0.002	0.008	0.004	0.004	0.000	0.001	0.003	0.010	0.009	0.011
Fe	1.400	1.924	1.758	1.181	1.535	1.857	1.993	2.036	1.958	1.783	1.363	1.832
Mn	0.003	0.004	0.002	0.001	0.003	0.006	0.007	0.005	0.003	0.002	0.001	0.004
Mg	3.952	2.977	3.427	3.749	3.767	3.335	3.240	3.114	3.196	3.552	3.588	3.017
Zn	0.004	0.006	0.000	0.005	0.004	0.005	0.000	0.003	0.000	0.002	0.003	0.002
Ca	0.001	0.000	0.000	0.000	0.000	0.000	0.000	0.000	0.000	0.000	0.000	0.004
Na	0.062	0.035	0.101	0.171	0.066	0.097	0.091	0.075	0.054	0.057	0.157	0.056
K	1.690	1.917	1.929	1.888	1.938	1.902	1.896	1.721	1.691	1.772	1.672	1.841
F	1.764	0.517	2.695	1.847	2.108	2.310	1.818	1.828	1.544	1.649	1.735	1.225
OH	2.047	3.067	0.779	1.469	1.473	1.212	1.744	1.646	2.037	2.026	1.645	2.155
O	20.189	20.416	20.526	20.684	20.419	20.478	20.438	20.526	20.419	20.325	20.620	20.620
X_{Mg}	0.738	0.607	0.661	0.760	0.710	0.642	0.619	0.605	0.620	0.666	0.725	0.622
X_K	0.965	0.982	0.950	0.917	0.967	0.951	0.954	0.958	0.969	0.969	0.914	0.970
$X_{Fe^{vi}}$	0.233	0.321	0.293	0.197	0.256	0.310	0.332	0.339	0.326	0.297	0.227	0.305
X_{OH}	0.537	0.856	0.224	0.443	0.411	0.344	0.490	0.474	0.569	0.551	0.487	0.638

N.b. The symbol 'na' indicates an element which was not analysed.

Appendix 3.6 Analyses from the calc-silicate gneiss

Garnet analyses

specimens	89/55C	89/55D[1]	89/55D[2]	89/93	89/217B	89/217D	89/334C	89/334F	89/334G	89/334H
SiO_2	39.08	38.56	38.84	39.38	38.87	39.02	39.80	39.14	39.56	39.56
TiO_2	0.13	0.56	0.19	0.03	0.02	0.02	0.00	0.01	0.00	0.02
Al_2O_3	18.47	18.09	19.39	20.97	16.01	18.55	20.55	20.54	19.82	19.04
FeO	7.94	7.29	5.91	3.68	9.09	5.80	3.50	3.72	4.41	5.99
MnO	1.07	0.84	0.82	0.15	0.09	0.08	0.15	0.31	0.27	0.27
MgO	0.09	0.22	0.12	0.06	0.06	0.08	0.09	0.09	0.10	0.25
CaO	33.04	33.49	34.36	35.86	35.61	35.93	36.31	35.96	35.77	35.13
total	99.82	99.05	99.63	100.13	99.75	99.48	100.40	99.77	99.93	100.26
cations normalized for 12 oxygens										
Si	3.044	3.025	3.010	2.998	3.069	3.032	3.022	2.998	3.032	3.042
Ti	0.008	0.033	0.011	0.002	0.001	0.001	0.000	0.001	0.000	0.001
Al	1.695	1.673	1.771	1.882	1.490	1.699	1.840	1.855	1.790	1.726
Fe	0.517	0.478	0.383	0.234	0.600	0.377	0.222	0.239	0.283	0.385
Mn	0.071	0.056	0.054	0.009	0.006	0.006	0.010	0.020	0.017	0.017
Mg	0.010	0.026	0.014	0.006	0.007	0.009	0.010	0.010	0.012	0.029
Ca	2.757	2.815	2.852	2.926	3.013	2.992	2.954	2.952	2.938	2.894
total	8.102	8.106	8.095	8.057	8.186	8.116	8.058	8.075	8.072	8.094
Fe^{3+}	0.299	0.313	0.278	0.175	0.544	0.345	0.172	0.219	0.215	0.278
X_{alm}	0.070	0.053	0.034	0.019	0.014	0.009	0.016	0.006	0.022	0.034
X_{sps}	0.023	0.018	0.017	0.003	0.002	0.002	0.003	0.007	0.006	0.006
X_{prp}	0.003	0.008	0.005	0.002	0.002	0.003	0.003	0.003	0.004	0.009
X_{grs}	0.755	0.765	0.804	0.888	0.710	0.813	0.892	0.873	0.860	0.812
X_{adr}	0.149	0.156	0.140	0.088	0.272	0.173	0.086	0.111	0.108	0.139

The superscripts 1 and 2 refer to prograde and retrograde garnet respectively

Clinopyroxene analyses

specimens	89/55C	89/55D	89/93	89/217B	89/217D	89/334C	89/334F	89/334G	89/334H
SiO_2	49.36	49.84	50.33	52.87	51.83	51.61	52.67	52.71	49.88
TiO_2	0.10	0.11	0.10	0.17	0.09	0.12	0.05	0.00	0.05
Al_2O_3	1.22	1.66	0.89	1.08	1.13	2.06	1.07	1.04	1.29
FeO	19.11	14.57	17.32	6.93	9.85	9.18	6.95	7.12	17.22
MnO	1.11	0.78	0.24	0.07	0.16	0.13	0.23	0.20	0.31
MgO	4.56	7.70	6.60	13.34	11.32	11.94	13.60	13.41	6.76
CaO	23.44	24.34	23.67	25.31	24.80	24.73	25.03	25.01	23.92
Na_2O	0.19	0.08	0.10	0.15	0.15	0.18	0.16	0.16	0.17
total	99.09	99.08	99.25	99.92	99.33	99.95	99.76	99.65	99.60
cations normalized for 6 oxygens									
Si	1.974	1.951	1.982	1.971	1.971	1.944	1.968	1.973	1.960
Ti	0.003	0.003	0.003	0.005	0.003	0.003	0.001	0.000	0.002
Al	0.057	0.077	0.041	0.047	0.051	0.092	0.047	0.046	0.060
Fe	0.639	0.477	0.571	0.216	0.313	0.289	0.217	0.223	0.566
Mn	0.038	0.026	0.008	0.002	0.005	0.004	0.007	0.006	0.010
Mg	0.272	0.449	0.388	0.742	0.642	0.671	0.758	0.748	0.396
Ca	1.004	1.021	0.999	1.011	1.011	0.998	1.002	1.003	1.007
Na	0.015	0.006	0.007	0.011	0.011	0.013	0.011	0.012	0.013
total	4.002	4.010	3.999	4.005	4.007	4.014	4.011	4.011	4.014
Al (iv)	0.027	0.054	0.017	0.031	0.032	0.063	0.038	0.032	0.047
Al (vi)	0.030	0.023	0.024	0.016	0.019	0.028	0.009	0.013	0.013
Fe^{3+}		0.031		0.015	0.013	0.035	0.029	0.019	0.034
X_{Mg}	0.298	0.485	0.405	0.774	0.672	0.699	0.777	0.771	0.412
X_{Mg}^{*}		0.502		0.787	0.681	0.725	0.801	0.786	0.427

Scapolite analyses

specimens	89/55C	89/55D	89/93	89/217B	89/217D	89/334C	89/334F	89/334G	89/334H
SiO_2	43.23	40.94	45.23	42.81	42.94	43.93	44.61	44.26	43.28
TiO_2	0.02	0.00	0.00	0.07	0.02	0.04	0.00	0.00	0.00
Al_2O_3	29.42	30.56	28.88	29.87	28.72	29.09	28.96	28.84	29.56
FeO	0.19	0.12	0.18	0.13	0.04	0.05	0.08	0.08	0.26
MnO	0.00	0.01	0.02	0.02	0.02	0.01	0.01	0.00	0.02
MgO	0.02	0.06	0.11	0.03	0.01	0.05	0.11	0.09	0.05
CaO	20.64	22.38	18.96	20.74	20.47	19.79	19.76	19.72	20.64
Na_2O	1.90	1.10	2.29	1.81	2.03	2.39	2.18	2.16	1.96
K_2O	0.20	0.10	0.51	0.30	0.31	0.37	0.46	0.56	0.21
Cl	0.12	0.05	0.54	0.28	0.31	0.35	0.33	0.36	0.14
total	95.74	95.32	96.72	96.06	94.87	96.07	96.50	96.07	96.12
normalized to (Si+Al)=12									
Si	6.659	6.384	6.848	6.585	6.709	6.740	6.798	6.788	6.647
Ti	0.003	0.000	0.000	0.008	0.002	0.005	0.000	0.000	0.000
Al	5.341	5.616	5.152	5.415	5.291	5.260	5.202	5.212	5.353
Fe	0.024	0.015	0.023	0.017	0.005	0.007	0.010	0.010	0.033
Mn	0.000	0.002	0.002	0.002	0.002	0.002	0.002	0.000	0.002
Mg	0.004	0.015	0.026	0.006	0.002	0.010	0.025	0.021	0.010
Ca	3.406	3.740	3.076	3.419	3.428	3.252	3.226	3.239	3.397
Na	0.567	0.334	0.673	0.539	0.615	0.710	0.645	0.642	0.582
K	0.038	0.019	0.099	0.058	0.061	0.072	0.089	0.109	0.040
Cl	0.030	0.012	0.137	0.074	0.082	0.090	0.085	0.094	0.037
EqAn	78.031	87.203	71.748	80.514	76.353	75.345	73.400	73.753	78.411

Wollastonite analyses

specimen	89/55C	89/55D	89/217B	89/217D	89/93	89/334C	89/334F	89/334G	89/334H
SiO_2	51.15	51.24	51.06	50.98	51.58	51.69	51.42	51.58	51.21
Al_2O_3	0.02	0.02	0.01	0.03	0.03	0.03	0.02	0.03	0.01
FeO	0.65	0.44	0.36	0.34	0.57	0.25	0.21	0.32	0.39
MnO	0.52	0.40	0.08	0.06	0.12	0.10	0.10	0.15	0.12
MgO	0.03	0.06	0.03	0.03	0.02	0.04	0.02	0.03	0.01
CaO	47.02	47.94	47.86	48.30	47.42	47.85	48.06	47.76	48.25
Na_2O	0.00	0.01	0.02	0.01	0.02	0.02	0.00	0.04	0.00
K_2O	0.01	0.00	0.01	0.02	0.01	0.01	0.01	0.01	0.01
total	99.40	100.11	99.43	99.77	99.77	99.99	99.84	99.92	100.00
cations normalized to 6 oxygens									
Si	1.996	1.988	1.991	1.984	2.001	2.000	1.995	1.998	1.988
Al	0.001	0.001	0.000	0.001	0.001	0.001	0.001	0.001	0.001
Fe	0.021	0.014	0.012	0.011	0.018	0.008	0.007	0.010	0.013
Mn	0.017	0.013	0.003	0.002	0.004	0.003	0.003	0.005	0.004
Mg	0.002	0.003	0.001	0.002	0.001	0.002	0.001	0.002	0.000
Ca	1.966	1.993	2.000	2.015	1.971	1.984	1.998	1.983	2.007
Na	0.000	0.001	0.001	0.001	0.001	0.001	0.000	0.003	0.000
K	0.000	0.000	0.001	0.001	0.000	0.000	0.000	0.000	0.000
total	4.003	4.013	4.009	4.017	3.997	3.999	4.005	4.002	4.013

Plagioclase analyses

specimen	89/55C	89/55D	89/93	89/217B	89/217D	89/334C	89/334F	89/334G	89/334II
SiO_2	43.51	43.01	43.61	43.49	43.19	43.71	43.49	43.60	43.42
Al_2O_3	36.17	35.92	36.19	36.66	35.57	35.90	36.04	36.22	35.72
FeO	0.12	0.08	0.08	0.10	0.02	0.04	0.04	0.07	0.24
MgO	0.00	0.01	0.00	0.00	0.02	0.00	0.02	0.02	0.00
CaO	19.59	19.95	19.36	19.97	19.85	19.38	19.81	19.47	19.57
Na_2O	0.39	0.30	0.45	0.27	0.41	0.51	0.45	0.41	0.45
K_2O	0.01	0.01	0.00	0.02	0.01	0.01	0.04	0.05	0.01
total	99.79	99.28	99.69	100.51	99.07	99.55	99.89	99.84	99.41
cations normalized to 8 oxygens									
Si	2.018	2.009	2.023	2.005	2.021	2.031	2.018	2.021	2.024
Al	1.978	1.978	1.979	1.992	1.962	1.966	1.971	1.979	1.963
Fe	0.005	0.003	0.003	0.004	0.001	0.002	0.002	0.003	0.009
Mg	0.000	0.000	0.000	0.000	0.002	0.000	0.001	0.001	0.000
Ca	0.974	0.999	0.962	0.986	0.995	0.965	0.985	0.967	0.977
Na	0.035	0.027	0.040	0.024	0.037	0.046	0.040	0.037	0.041
K	0.001	0.001	0.000	0.001	0.000	0.001	0.002	0.003	0.000
total	5.011	5.017	5.007	5.012	5.018	5.011	5.019	5.011	5.014
X_{an}	0.964	0.973	0.960	0.975	0.964	0.953	0.959	0.960	0.960
X_{ab}	0.035	0.026	0.040	0.024	0.036	0.046	0.039	0.037	0.040
X_{or}	0.001	0.001	0.000	0.001	0.000	0.001	0.002	0.003	0.000

Appendix 3.7 Analytical precision

The statistical lower limit of detection based on 3σ error limits, and the optimum analytical precision for each element in typical analyses of each mineral, were calculated using the following expressions:

$$\text{Detection limit (wt\% element)} = \frac{6}{m}\left(\frac{R_b}{T_b}\right)^{1/2} \quad \text{and}$$

$$\text{Relative precision} = \frac{1}{T_p^{1/2}\,(R_p^{1/2} - R_b^{1/2})},$$

where m is the counts above background per second per weight per cent element (as measured on the standard material for that element), R_b and R_p are the background and peak X-ray count rates for that element at the unknown analysis point in counts per second, and T_b and T_p are the background and peak count time in seconds (see Norrish & Chappell, 1977).

Semi-pelite

garnet

cations per 12 O		2 σ	3 σ	detect. limit
Si	2.987	0.015	0.022	0.02
Ti	0.002	0.001	0.002	0.03
Al	2.040	0.013	0.019	0.02
Cr	0.000			0.04
Fe	1.980	0.015	0.023	0.05
Mn	0.070	0.004	0.006	0.04
Mg	0.707	0.010	0.016	0.02
Ca	0.202	0.004	0.006	0.03
total	7.988			

orthopyroxene

cations per 6 O		2 σ	3 σ	detect. limit
Si	1.927	0.008	0.012	0.02
Ti	0.003	0.001	0.001	0.02
Al	0.137	0.003	0.004	0.01
Cr	0.000			0.04
Fe	0.917	0.007	0.011	0.05
Mn	0.012	0.001	0.002	0.04
Mg	0.997	0.008	0.012	0.02
Ca	0.007	0.001	0.001	0.02
Na	0.001	0.002	0.003	0.03
total	4.001			

plagioclase

cations per 8 O		2 σ	3 σ	detect. limit
Si	2.582	0.010	0.015	0.02
Al	1.423	0.007	0.011	0.02
Fe	0.010	0.001	0.002	0.04
Mg	0.001	0.001	0.002	0.02
Ca	0.415	0.004	0.006	0.02
Na	0.530	0.009	0.014	0.04
K	0.016	0.001	0.002	0.03
total	4.977			

K-feldspar

cations per 8 O		2 σ	3 σ	detect. limit
Si	2.953	0.010	0.015	0.02
Al	1.027	0.006	0.009	0.02
Fe	0.003	0.001	0.002	0.04
Mg	0.001	0.001	0.002	0.02
Ca	0.003	0.001	0.001	0.02
Na	0.086	0.005	0.007	0.04
K	1.004	0.008	0.011	0.03
total	5.077			

biotite

14 (iv) + (vi) cations		2 σ	3 σ	detect. limit
Si	5.696	0.028	0.041	0.02
Ti	0.568	0.008	0.012	0.03
Al	2.595	0.020	0.030	0.02
Cr	0.005	0.004	0.006	0.04
Fe	2.623	0.025	0.037	0.05
Mn	0.003	0.004	0.006	0.04
Mg	2.510	0.025	0.038	0.02
Ca	0.000			0.03
Na	0.019	0.011	0.016	0.03
K	2.196	0.020	0.031	0.03
F	0.774	0.147	0.220	0.08

Metapelite

garnet

cations per 12 O		2 σ	3 σ	detect. limit
Si	3.005	0.015	0.022	0.02
Ti	0.004	0.001	0.002	0.03
Al	2.015	0.013	0.020	0.02
Cr	0.008	0.002	0.004	0.04
Fe	2.226	0.017	0.025	0.06
Mn	0.038	0.003	0.005	0.04
Mg	0.610	0.010	0.015	0.02
Ca	0.072	0.003	0.004	0.02
total	7.976			

cordierite

cations per 18 O		2 σ	3 σ	detect. limit
Si	5.049	0.022	0.032	0.02
Ti	0.001	0.002	0.002	0.02
Al	3.911	0.019	0.028	0.02
Fe	0.757	0.012	0.017	0.04
Mn	0.010	0.003	0.004	0.04
Mg	1.253	0.014	0.021	0.02
Ca	0.000			0.02
Na	0.007	0.005	0.007	0.03
K	0.001	0.002	0.002	0.02
total	10.996			

spinel

cations per 4 O		2 σ	3 σ	detect. limit
Si	0.000			0.02
Ti	0.002	0.000	0.001	0.03
Al	1.908	0.008	0.011	0.02
Cr	0.004	0.001	0.001	0.05
Fe	0.928	0.006	0.010	0.06
Mn	0.004	0.001	0.001	0.04
Mg	0.189	0.003	0.005	0.02
Zn	0.005	0.001	0.002	0.07
Ca	0.001	0.001	0.001	0.03
total	3.045			

ilmenite

cations per 3 O		2 σ	3 σ	detect. limit
Si	0.001	0.002	0.003	0.02
Ti	1.010	0.004	0.005	0.04
Al	0.002	0.001	0.002	0.02
Cr	0.001	0.001	0.002	0.05
Fe	0.941	0.006	0.009	0.06
Mn	0.004	0.001	0.001	0.05
Mg	0.032	0.002	0.003	0.02
total	1.990			

plagioclase

cations per 8 O		2 σ	3 σ	detect. limit
Si	2.675	0.010	0.015	0.02
Al	1.307	0.007	0.010	0.02
Fe	0.004	0.001	0.002	0.04
Mg	0.000			0.02
Ca	0.347	0.004	0.006	0.02
Na	0.662	0.010	0.015	0.04
K	0.009	0.001	0.002	0.02
total	5.004			

K-feldspar

cations per 8 O		2 σ	3 σ	detect. limit
Si	2.919	0.011	0.016	0.02
Al	1.074	0.007	0.01	0.02
Fe	0.002	0.001	0.002	0.04
Mg	0.002	0.001	0.002	0.02
Ca	0.056	0.002	0.004	0.03
Na	0.287	0.008	0.012	0.04
K	0.682	0.007	0.01	0.03
total	5.022			

biotite

14 (iv) + (vi) cations		2 σ	3 σ	detect. limit
Si	5.787	0.028	0.042	0.02
Ti	0.710	0.009	0.013	0.03
Al	2.392	0.020	0.030	0.02
Cr	0.002	0.003	0.005	0.04
Fe	2.070	0.022	0.034	0.05
Mn	0.007	0.004	0.006	0.04
Mg	3.031	0.027	0.041	0.02
Zn	0.001	0.005	0.007	0.07
Ca	0.000			0.03
Na	0.083	0.012	0.018	0.03
K	1.717	0.017	0.025	0.03
F	1.921	0.220	0.330	0.11

Calc-silicate

garnet

cations per 12 O		2 σ	3 σ	detect. limit
Si	3.038	0.014	0.021	0.02
Ti	0.003	0.003	0.004	0.05
Al	1.709	0.011	0.017	0.02
Fe	0.403	0.009	0.012	0.05
Mn	0.016	0.003	0.004	0.04
Mg	0.010	0.003	0.004	0.02
Ca	2.924	0.014	0.021	0.03
total	8.104			

scapolite

Si+Al=12		2 σ	3 σ	detect. limit
Si	6.656	0.030	0.045	0.02
Ti	0.000			0.06
Al	5.344	0.027	0.040	0.02
Fe	0.020	0.005	0.007	0.04
Mn	0.004	0.004	0.006	0.04
Mg	0.009	0.004	0.007	0.02
Ca	3.329	0.022	0.033	0.03
Na	0.560	0.021	0.031	0.03
K	0.036	0.004	0.006	0.02
Cl	0.028	0.005	0.008	0.02

clinopyroxene

cations per 6 O		2 σ	3 σ	detect. limit
Si	1.982	0.008	0.012	0.02
Ti	0.000			0.06
Al	0.046	0.002	0.003	0.02
Fe	0.494	0.006	0.009	0.05
Mn	0.008	0.001	0.002	0.04
Mg	0.446	0.006	0.009	0.02
Ca	1.013	0.006	0.009	0.03
Na	0.009	0.003	0.004	0.03
total	3.998			

wollastonite

cations per 6 O		2 σ	3 σ	detect. limit
Si	1.984	0.008	0.011	0.02
Al	0.001	0.001	0.001	0.02
Fe	0.013	0.001	0.002	0.04
Mn	0.004	0.001	0.002	0.04
Mg	0.002	0.001	0.002	0.02
Ca	2.008	0.008	0.012	0.03
Na	0.002	0.002	0.003	0.03
K	0.000			0.03
total	4.014			

plagioclase

cations per 8 O		2 σ	3 σ	detect. limit
Si	2.024	0.009	0.014	0.02
Al	1.963	0.009	0.013	0.02
Fe	0.009	0.002	0.002	0.04
Mg	0.000			0.02
Ca	0.977	0.006	0.010	0.03
Na	0.041	0.004	0.006	0.03
K	0.001	0.002	0.003	0.03
total	5.015			

N.b. The values of 2σ and 3σ in these tables represent error limits on the number of cations per normalized formula unit as tabulated in the first column, but the values given for detection limit are in units of weight per cent element and *not* the units of the cation totals.

APPENDIX 4 SOLUTION MODELS AND THERMOBAROMETERS

Appendix 4.1 The Harley (1984*b*) barometer

Although derived correctly within the text, the final barometric expression for the solubility of alumina in coexisting garnet and orthopyroxene of Harley (1984*b*) is incorrect. The correct version is as follows:

$$\begin{aligned} 206.74\,P = {} & RT \ln K_2 + T\,[0.15 + 0.001507\,(T - 970)\,] - 2467 \\ & - [2458\,(1000 / T) - 1261]\,(2(1 - X_{Mg}^{Opx})^2) \\ & - [3525\,(1000 / T) - 1667]\,[1 - 2X_{Mg}^{Opx}\,(1 - X_{Al}^{M1})]\,(1 - X_{Mg}^{Opx})\,(1 - X_{Al}^{M1}) \\ & - [4.75\,T - 6680]\,[2(1 - X_{Mg}^{Opx})^2\,(1 - X_{Al}^{M1})] \\ & + 920\,[(1 - 2X_{Al}^{M1})\,(1 - X_{Al}^{M1})\,(1 - X_{Mg}^{Opx})] \\ & + [5436 - 2.54T]\,[(1 - X_{Mg}^{Opx})[X_{Mg}^{Opx}(1 - X_{Al}^{M1}) + X_{Al}^{M1}]] \\ & + 5700\,[X_{grs}^{Grt}(X_{grs}^{Grt} + X_{alm}^{Grt})], \end{aligned}$$

where P is in kbar, T in kelvin, $K_2 = (X_{prp}^{Grt})^3 / (X_{Mg}^{Opx})^3 X_{Al}^{M1}(1 - X_{Al}^{M1})$, and the mole fraction terms are as used elsewhere in this thesis. The version of this expression in the abstract and at the end of the published paper (Harley, 1984*b*, p. 665 and p. 690) neglected to raise the $(1 - X_{Mg}^{Opx})$ term in the fourth line to the power of two.

Appendix 4.2 The Engi and Wersin (1987) solution model for calcic garnet

Engi and Wersin (1987) present a activity-composition model for grossularite-andradite based on an asymmetric or subregular solution model, but the final expressions for a_{grs} and a_{adr} are incorrect. The correct versions, which correspond to the activity-composition diagrams and calculations in Engi and Wersin are

$$a_{grs} = X_{grs}^2 \exp\,[X_{adr}^2(W_{adr} + 2X_{grs}(W_{grs} - W_{adr})) / RT], \quad \text{and}$$

$$a_{adr} = X_{adr}^2 \exp\,[X_{grs}^2(W_{grs} + 2X_{adr}(W_{adr} - W_{grs})) / RT],$$

where T is in kelvin, W_{grs} = 12.906 kJ/mol, W_{adr} = -49.910 kJ/mol, and the mole fraction terms are as used elsewhere in this thesis. In the published versions, the two terms $(W_{adr} + 2X_{grs}(W_{grs} - W_{adr}))$ and $(W_{grs} + 2X_{adr}(W_{adr} - W_{grs}))$ were swapped over.

Appendix 4.3 The Haselton *et al.* (1983) solution model for K-feldspar

Haselton *et al.* (1983) present an asymmetric (subregular solution) model for K-feldspar, and derive an expression for the activity coefficient of albite as follows:

$$RT \ln \gamma_{ab} = X_{or}^2[W_{ab}^H + 2X_{ab}(W_{or}^H - W_{ab}^H) - T\,W^S + P\,W^V].$$

where P is in bars, T in kelvin, W_{ab}^H = 18810 J/mol, W_{or}^H = 27320, W^S = 10.3 J/mol.K and W^V = 0.364 J/bar. They do not give an expression for γ_{or}, but it follows that

$$RT \ln \gamma_{or} = X_{ab}^2[W_{or}^H + 2X_{or}(W_{ab}^H - W_{or}^H) - T\,W^S + P\,W^V],$$

and this is the expression used in this thesis.

APPENDIX 5 PUBLICATIONS

A substantial part of the thesis is to be published in two papers, currently in press. The bulk of Chapter 3, and small parts of Chapters 5, 6 and 8, form the basis of Fitzsimons and Harley (1991). The bulk of Chapter 4, and parts of Chapters 5, 7 and 8, constitute a substantial part of Fitzsimons and Thost (1991).

Fitzsimons, I.C.W. & Harley, S.L., 1991. Geological relationships in high-grade gneiss of the Brattstrand Bluffs coastline, Prydz Bay, east Antarctica. *Australian Journal of Earth Sciences* (in press).

Fitzsimons, I.C.W. & Thost, D.E., 1991. Geological relationships in high-grade basement gneiss of the northern Prince Charles Mountains, east Antarctica. *Australian Journal of Earth Sciences* (in press).

BIBLIOGRAPHY

Absher, B.S. & McSween, H.Y., 1985. Granulites at Winding Stair Gap, North Carolina: the thermal axis of Paleozoic metamorphism in the southern Appalachians. *Bulletin of the Geological Society of America* **96**, 588-599.

Aitken, B.G., 1983. T-X_{CO2} stability relations and phase equilibria of a calcic carbonate scapolite. *Geochimica et Cosmochimica Acta* **47**, 351-362.

Albee, A.L., 1965. A petrogenetic grid for the Fe-Mg silicates of pelitic schists. *American Journal of Science* **263**, 512-536.

Andersen, D.J. & Lindsley, D.H., 1988. Internally consistent solution models for Fe-Mg-Mn-Ti oxides: Fe-Ti oxides. *American Mineralogist* **73**, 714-726.

Anovitz, L.M. & Chase, C.G., 1990. Implications of post-thrusting extension and underplating for P-T-t paths in granulite terranes: a Grenville example. *Geology* **18**, 466-469.

Anovitz, L.M. & Essene, E.J., 1987. Compatibility of geobarometers in the system CaO-FeO-Al_2O_3-SiO_2-TiO_2 (CFAST): implications for garnet mixing models. *Journal of Geology* **95**, 633-645.

Anovitz, L.M. & Essene, E.J., 1990. Thermobarometry and pressure-temperature paths in the Grenville Province of Ontario. *Journal of Petrology* **31**, 197-241.

Arima, M., Kerrich, R. & Thomas, A., 1986. Sapphirine-bearing paragneiss from the northern Grenville province in Labrador, Canada: protolith composition and metamorphic P-T conditions. *Geology* **14**, 844-847.

Arriens, P.A., 1975. The Precambrian geochronology of Antarctica. In: *Abstracts of the First Australian Geological Convention, Adelaide 1975*. Sydney: Geological Society of Australia, 97-98.

Arzi, A.A., 1978. Critical phenomena in the rheology of partially melted rocks. *Tectonophysics* **44**, 173-184.

Ashworth, J.R., 1985. Introduction. In: Ashworth, J.R. (ed.) *Migmatites*. Glasgow: Blackie & Son Ltd, 1-35.

Ashworth, J.R. & McLellan, E.L., 1985. Textures. In: Ashworth, J.R. (ed.) *Migmatites*. Glasgow: Blackie & Son Ltd, 180-203.

Baker, A.J. & Droop, G.T.R., 1983. Grampian metamorphic conditions deduced from mafic granulites and sillimanite-K-feldspar gneisses in the Dalradian of Glen Muick, Scotland. *Journal of the Geological Society of London* **140**, 489-497.

Barbosa, J.S.F., 1990. The granulites of the Jequié Complex and Atlantic Coast Mobile Belt, southern Bahia, Brazil - an expression of Archaean/early Proterozoic plate convergence. In: Vielzeuf, D. & Vidal, Ph. (eds) *Granulites and Crustal Evolution*. Dordrecht: Kluwer Academic Publishers, 195-221.

Bard, J.P., 1983. Metamorphism of an obducted island arc: example of the Kohistan sequence (Pakistan) in the Himalayan collided range. *Earth & Planetary Science Letters* **65**, 133-144.

Barker, F., 1964. Reaction between mafic magmas and pelitic schist, Cortlandt, New York. *American Journal of Science* **262**, 614-634.

Barnicoat, A.C., 1983. Metamorphism of the Scourian Complex, NW Scotland. *Journal of Metamorphic Geology* **1**, 163-182.

Barnicoat, A.C. & O'Hara, M.J., 1979. High-temperature pyroxenes from an ironstone at Scourie, Sutherland. *Mineralogical Magazine* **43**, 371-375.

Barrow, G., 1893. On an intrusion of muscovite-biotite gneiss in the south-eastern Highlands of Scotland, and its accompanying metamorphism. *Quarterly Journal of the Geological Society of London* **49**, 330-358.

Barrow, G., 1912. On the geology of lower Dee-side and the southern Highland Border. *Proceedings of the Geologists' Association* **23**, 274-290.

Behr, H.J., den Tex, E., de Waard, D., Mehnert, K.R., Scharbert, H.G., Sobolev, V.St., Watznauer, A., Winkler, H.G.F., Wynne-Edwards, H.R., Zoubek, V. & Zwart, H.J., 1971. Granulites - results of a discussion. *Neues Jahrbuch für Mineralogie Monatshefte* **1971**, 97-123.

Bell, T.H., 1978. Progressive deformation and reorientation of fold axes in a ductile mylonite zone: the Woodroffe thrust. *Tectonophysics* **44**, 285-320.

Bennett, A.J.R. & Taylor, G.H., 1972. Coals from the vicinity of the Prince Charles Mountains. In: Adie R.J. (ed.) *Antarctic Geology and Geophysics*. Oslo: Universitetsforlaget, 591-598.

Berg, J.H., 1977*a*. Regional geobarometry in the contact aureoles of the anorthositic Nain Complex, Labrador. *Journal of Petrology* **18**, 399-430.

Berg, J.H., 1977*b*. Dry granulite mineral assemblages in the contact aureoles of the Nain Complex, Labrador. *Contributions to Mineralogy & Petrology* **64**, 33-52.

Berman, R.G., 1988. Internally-consistent thermodynamic data for minerals in the system Na_2O-K_2O-CaO-MgO-FeO-Fe_2O_3-Al_2O_3-SiO_2-TiO_2-H_2O-CO_2. *Journal of Petrology* **29**, 445-522.

Berman, R.G., 1990. Mixing properties of Ca-Mg-Fe-Mn garnets. *American Mineralogist* **75**, 328-344.

Berthé, D. & Brun, J.P., 1980. Evolution of folds during progressive shear in the South Armorican Shear Zone, France. *Journal of Structural Geology* **2**, 127-133.

Berthé, D., Choukroune, P. & Jegouzo, P., 1979. Orthogneiss, mylonite and non coaxial deformation of granites: the example of the South Armorican Shear Zone. *Journal of Structural Geology* **1**, 31-42.

Bhattacharya, A., 1986. Some geobarometers involving cordierite in the FeO-Al_2O_3-SiO_2 ($\pm H_2O$) system: refinements, thermodynamic calibration, and applicability in granulite facies rocks. *Contributions to Mineralogy & Petrology* **94**, 387-394.

Bhattacharya, A., Krishnakumar, K.R., Raith, M. & Sen, S.K., 1991. An improved set of *a-X* parameters for Fe-Mg-Ca garnets and refinements of the orthopyroxene-garnet thermometer and the orthopyroxene-garnet-plagioclase-quartz barometer. *Journal of Petrology* **32**, 629-656.

Bhattacharya, A., Mazumdar, A.C. & Sen, S.K., 1988. Fe-Mg mixing in cordierite: constraints from natural data and implications for cordierite-garnet geothermometry in granulites. *American Mineralogist* **73**, 338-344.

Bhattacharya, A. & Sen, S.K., 1986. Granulite metamorphism, fluid buffering, and dehydration melting in the Madras charnockites and metapelites. *Journal of Petrology* **27**, 1119-1141.

Bickle, M.J., 1978. Heat loss from the earth: a constraint on Archaean tectonics from the relation between geothermal gradients and the rate of plate production. *Earth & Planetary Science Letters* **40**, 301-315.

Bickle, M.J., Hawkesworth, C.J., England, P.C. & Athey, D.R., 1975. A preliminary thermal model for regional metamorphism in the Eastern Alps. *Earth & Planetary Science Letters* **26**, 13-28.

Bingen, B., Demaiffe, D. & Delhal, J., 1988. Aluminous granulites of the Archaean craton of Kasai (Zaire): petrology and *P-T* conditions. *Journal of Petrology* **29**, 899-919.

Binns, R.A., 1964. Zones of progressive regional metamorphism in the Willyama Complex, Broken Hill district, New South Wales. *Journal of the Geological Society of Australia* **11**, 283-330.

Black, L.P., Fitzgerald, J.D. & Harley, S.L., 1984. Pb isotopic composition, colour, and microstructure of monazites from a polymetamorphic rock in Antarctica. *Contributions to Mineralogy & Petrology* **85**, 141-148.

Black, L.P., Harley, S.L., Sun, S.S. & McCulloch, M.T., 1987. The Rayner Complex of East Antarctica: complex isotopic systematics within a Proterozoic mobile belt. *Journal of Metamorphic Geology* **5**, 1-26.

Black, L.P. & James, P.R., 1983. Geological history of the Archaean Napier Complex of Enderby Land. In: Oliver, R.L., James, P.R. & Jago, J.B. (eds) *Antarctic Earth Science*. Cambridge: Cambridge University Press, 11-15.

Black, L.P., James, P.R. & Harley, S.L., 1983*a*. The geochronology, structure and metamorphism of early Archaean rocks at Fyfe Hills, Enderby Land, Antarctica. *Precambrian Research* **21**, 197-222.

Black, L.P., James, P.R. & Harley, S.L., 1983*b*. Geochronology and geological evolution of metamorphic rocks in the Field Islands area, East Antarctica. *Journal of Metamorphic Geology* **1**, 277-303.

Black, L.P., Kinny, P.D. & Sheraton, J.W., 1990. A revised chronology for the Vestfold Block based on ion-probe zircon ages. *Geological Society of Australia, Abstracts* **25**, 253.

Black, L.P., Williams, I.S. & Compston, W., 1986. Four zircon ages from one rock: the history of a 3930 Ma-old granulite from Mount Sones, Enderby Land, Antarctica. *Contributions to Mineralogy & Petrology* **94**, 427-437.

Boettcher, A.L., 1970. The system CaO-Al_2O_3-SiO_2-H_2O at high pressures and temperatures. *Journal of Petrology* **11**, 337-379.

Bohlen, S.R., 1987. Pressure-temperature-time paths and a tectonic model for the evolution of granulites. *Journal of Geology* **95**, 617-632.

Bohlen, S.R., 1991. On the formation of granulites. *Journal of Metamorphic Geology* **9**, 223-229.

Bohlen, S.R. & Dollase, W.A., 1983. Calibration of spinel-quartz stability. *Abstracts with Programs of the Geological Society of America* **15**, 529.

Bohlen, S.R., Dollase, W.A. & Wall, V.J., 1986. Calibration and applications of spinel equilibria in the system FeO-Al_2O_3-SiO_2. *Journal of Petrology* **27**, 1143-1156.

Bohlen, S.R. & Essene, E.J., 1977. Feldspar and oxide thermometry of granulites in the Adirondack Highlands. *Contributions to Mineralogy & Petrology* **62**, 153-169.

Bohlen, S.R. & Essene, E.J., 1978. Igneous pyroxenes from metamorphosed anorthosite massifs. *Contributions to Mineralogy & Petrology* **65**, 433-442.

Bohlen, S.R., & Liotta, J.J., 1986. A barometer for garnet amphibolites and garnet granulites. *Journal of Petrology* **27**, 1025-1034.

Bohlen, S.R., Valley, J.W. & Essene, E.J., 1985. Metamorphism in the Adirondacks. I. Petrology, pressure and temperature. *Journal of Petrology* **26**, 971-992.

Bohlen, S.R., Wall, V.J. & Boettcher, A.L., 1983*a*. Experimental investigation and application of garnet granulite equilibria. *Contributions to Mineralogy & Petrology* **83**, 52-61.

Bohlen, S.R., Wall, V.J. & Boettcher, A.L., 1983*b*. Geobarometry in granulites. In: Saxena, S.K. (ed.) *Kinetics and Equilibrium in Mineral Reactions*. New York: Springer-Verlag, 141-171.

Boullier, A.M. & Barbey, P., 1988. A polycyclic two-stage corona growth in the Iforas Granulitic Unit (Mali). *Journal of Metamorphic Geology* **6**, 235-253.

Bowen, N.L., 1940. Progressive metamorphism of siliceous limestone and dolomite. *Journal of Geology* **48**, 225-274.

Bradshaw, J.Y., 1989. Origin and metamorphic history of an Early Cretaceous polybaric granulite terrain, Fiordland, southwest New Zealand. *Contributions to Mineralogy & Petrology* **103**, 346-360.

Brady, J.B., 1977. Metasomatic zones in metamorphic rocks. *Geochimica et Cosmochimica Acta* **41**, 113-125.

Bridgwater, D., Watson, J. & Windley, B.F., 1973. The Archaean craton of the North Atlantic Region. *Philosophical Transactions of the Royal Society of London. Series A* **273**, 493-512.

Broch, O.A., 1946. Two contributions to Antarctic petrography. *Scientific Results of the Norwegian Antarctic Expedition* **2** (25), 1-32.

Brown, M., 1973. The definition of metatexis, diatexis and migmatite. *Proceedings of the Geologists' Association* **84**, 371-382.

Buddington, A.F., 1952. Chemical petrology of some metamorphosed Adirondack gabbroic, syenitic and quartz syenitic rocks. *American Journal of Science* **Bowen Volume**, 37-84.

Buddington, A.F., 1963. Isograds and the role of H_2O in metamorphic facies of orthogneisses of the northwest Adirondack area, New York. *Bulletin of the Geological Society of America* **74**, 1155-1181.

Buddington, A.F. & Lindsley, D.H., 1964. Iron-titanium oxide minerals and synthetic equivalents. *Journal of Petrology* **5**, 310-357.

Carmichael, D.M., 1969. On the mechanism of prograde metamorphic reactions in quartz-bearing pelitic rocks. *Contributions to Mineralogy & Petrology* **20**, 244-267.

Carmichael, D.M., 1970. Intersecting isograds in the Whetstone Lake area, Ontario. *Journal of Petrology* **11**, 147-181.

Carswell, D.A. & Harley, S.L., 1990. Mineral thermometry and barometry. In: Carswell, D.A. (ed.) *Eclogite Facies Rocks*. Glasgow: Blackie & Son Ltd, 83-110.

Chacko, T., Ravindra Kumar, G.R. & Newton, R.C., 1987. Metamorphic *P-T* conditions of the Kerala (south India) Khondalite Belt, a granulite facies supracrustal terrain. *Journal of Geology* **95**, 343-358.

Chapman, D.S., 1986. Thermal gradients in the continental crust. In: Dawson, J.B. Carswell, D.A., Hall, J. & Wedepohl, K.H. (eds) *The Nature of the Lower Continental Crust*, Geological Society of London Special Publication No. **24**, 63-70.

Chappell, B.W., White, A.J.R. & Wyborn, D., 1987. The importance of residual source material (restite) in granite petrogenesis. *Journal of Petrology* **28**, 1111-1138.

Clarke, G.L., 1987. *A comparative study of the structural and metamorphic evolution of the Olary (South Australia) and Stillwell Hills (Antarctic) Precambrian terrains*. Ph.D. thesis, University of Melbourne. (Unpublished).

Clarke, G.L., 1988. Structural constraints on the Proterozoic reworking of Archaean crust in the Rayner Complex, MacRobertson and Kemp Land Coast, East Antarctica. *Precambrian Research* **40/41**, 137-156.

Clarke, G.L., Collins, W.J. & Vernon, R.H., 1990. Successive overprinting granulite facies metamorphic events in the Anmatjira Range, central Australia. *Journal of Metamorphic Geology* **8**, 65-88.

Clarke, G.L. & Powell, R., 1991*a*. Proterozoic granulite facies metamorphism in the southeastern Reynolds Range, central Australia: geological context, *P-T* path and overprinting relationships. *Journal of Metamorphic Geology* **9**, 267-281.

Clarke, G.L. & Powell, R., 1991*b*. Decompressional coronas and symplectites in granulites of the Musgrave Complex, central Australia. *Journal of Metamorphic Geology* **9**, 441-450.

Clarke, G.L., Powell, R. & Guiraud, M., 1989. Low-pressure granulite facies metapelitic assemblages and corona textures from MacRobertson Land, east Antarctica: the importance of Fe_2O_3 and TiO_2 in accounting for spinel-bearing assemblages. *Journal of Metamorphic Geology* **7**, 323-335.

Clemens, J.D., 1990. The granulite-granite connexion. In: Vielzeuf, D. & Vidal, Ph. (eds) *Granulites and Crustal Evolution*. Dordrecht: Kluwer Academic Publishers, 25-36.

Clemens, J.D. & Vielzeuf, D., 1987. Constraints on melting and magma production in the crust. *Earth & Planetary Science Letters* **86**, 287-306.

Clifford, T.N., 1974. Review of African granulites and related rocks. *Geological Society of America Special Paper* **156**, 49 pp.

Clifford, T.N., Gronow, J., Rex, D.C. & Burger, A.J., 1975. Geochronological and petrogenetic studies of high-grade metamorphic rocks and intrusives in Namaqualand, South Africa. *Journal of Petrology* **16**, 154-188.

Cobbold, P.R. & Quinquis, H., 1980. Development of sheath folds in shear regimes. *Journal of Structural Geology* **2**, 119-126.

Collerson, K.D., Oliver, R.L. & Rutland, R.W.R., 1972. An example of structural and metamorphic relationships in the Musgrave Orogenic Belt, central Australia. *Journal of the Geological Society of Australia* **18**, 379-393.

Collerson, K.D., Reid, E., Millar, D. & McCulloch, M.T., 1983. Lithological and Sr-Nd isotopic relationships in the Vestfold Block: implications for Archaean and Proterozoic crustal evolution in the east Antarctic. In: Oliver, R.L., James, P.R. & Jago, J.B. (eds) *Antarctic Earth Science*. Cambridge: Cambridge University Press, 77-84.

Collerson, K.D. & Sheraton, J.W., 1986*a*. Bedrock geology and crustal evolution of the Vestfold Hills. In: Pickard, J. (ed.) *The Antarctic Oasis: Terrestrial Environments and History of the Vestfold Hills*. Sydney: Academic Press, 21-62.

Collerson, K.D. & Sheraton, J.W., 1986*b*. Age and geochemical characteristics of a mafic dyke swarm in the Archaean Vestfold Block, Antarctica: inferences about Proterozoic dyke emplacement in Gondwana. *Journal of Petrology* **27**, 853-886.

Coolen, J.J.M.M.M., 1980. Chemical petrology of the Furua granulite complex, southern Tanzania. *GUA Papers of Geology* (Amsterdam) **1.13**, 258 pp.

Cooray, P.G., 1962. Charnockites and their associated gneisses in the Pre-cambrian of Ceylon. *Quarterly Journal of the Geological Society of London* **118**, 239-273.

Coward, M.P. & Potts, G.J., 1983. Complex strain patterns developed at the frontal and lateral tips to shear zones and thrust zones. *Journal of Structural Geology* **5**, 383-399.

Craddock, C., 1972. Antarctic tectonics. In: Adie, R.J. (ed.) *Antarctic Geology and Geophysics*. Oslo: Universitetsforlaget, 449-455.

Craddock, C., 1982. Antarctica and Gondwanaland. In: Craddock, C. (ed.) *Antarctic Geoscience*. Madison: University of Wisconsin Press, 3-13.

Crank, J., 1975. *The Mathematics of Diffusion* (2nd edition). Oxford: Oxford University Press. 414 pp.

Crohn, P.W., 1959. A contribution to the geology and glaciology of the western part of Australian Antarctic Territory. *Bureau of Mineral Resources, Australia, Bulletin* **52**, 103 pp.

Currie, K.L. & Gittins, J., 1988. Contrasting sapphirine parageneses from Wilson Lake, Labrador and their tectonic implications. *Journal of Metamorphic Geology* **6**, 603-622.

Dallwitz, W.B., 1968. Co-existing sapphirine and quartz in granulite from Enderby Land, Antarctica. *Nature* **219**, 476-477.

Dalziel, I.W.D. & Elliot, D.H., 1982. West Antarctica: problem child of Gondwanaland. *Tectonics* **1**, 3-19.

Deer, W.A., Howie, R.A. & Zussman, J., 1963. *Rock-Forming Minerals, Volume 4 (Framework Silicates)*. London: Longmans, Green & Co. Ltd, 435 pp.

Dempster, T.J., 1985. Garnet zoning and metamorphism of the Barrovian type area, Scotland. *Contributions to Mineralogy & Petrology* **89**, 30-38.

de Waard, D., 1965*a*. The occurrence of garnet in the granulite-facies terrane of the Adirondack highlands. *Journal of Petrology* **6**, 165-191.

de Waard, D., 1965*b*. A proposed subdivision of the granulite facies. *American Journal of Science* **263**, 455-461.

de Yoreo, J.J., Lux, D.R. & Guidotti, C.V., 1989. The role of crustal anatexis and magma migration in the thermal evolution of regions of thickened continental crust. In: Daly, J.S., Cliff, R.A. & Yardley, B.W.D. (eds) *Evolution of Metamorphic Belts*, Geological Society of London Special Publication No. 43, 187-202.

Dodson, M.H., 1973. Closure temperature in cooling geochronological and petrological systems. *Contributions to Mineralogy & Petrology* **40**, 259-274.

Dodson, M.H., 1979. Theory of cooling ages. In: Jäger, E. & Hunziker, J.C. (eds) *Lectures in Isotope Geology*. Berlin: Springer-Verlag, 194-202.

Drever, H.I., 1939. A petrological study of the limestones in the Moine Series of Ardgour, Argyllshire. *Geological Magazine* **76**, 501-518.

Droop, G.T.R., 1989. Reaction history of garnet-sapphirine granulites and conditions of Archaean high-pressure granulite-facies metamorphism in the Central Limpopo Mobile Belt, Zimbabwe. *Journal of Metamorphic Geology* 7, 383-403.

Droop, G.T.R. & Bucher-Nurminen, K., 1984. Reaction textures and metamorphic evolution of sapphirine-bearing granulites from the Gruf Complex, Italian Central Alps. *Journal of Petrology* 25, 766-803.

Edwards, R.L. & Essene, E.J., 1988. Pressure, temperature and C-O-H fluid fugacities across the amphibolite-granulite transition, northwest Adirondack Mountains, New York. *Journal of Petrology* 29, 39-72.

Ekström, T.K., 1972. The distribution of fluorine among some coexisting minerals. *Contributions to Mineralogy & Petrology* 34, 192-200.

Elliot, D.H., 1975. Tectonics of Antarctica: a review. *American Journal of Science* 275-A, 45-106.

Ellis, D.E., 1978. Stability and phase equilibria of chloride and carbonate bearing scapolites at 750°C and 4000 bar. *Geochimica et Cosmochimica Acta* 42, 1271-1281.

Ellis, D.J., 1980. Osumilite-sapphirine-quartz granulites from Enderby Land, Antarctica: *P-T* conditions of metamorphism, implications for garnet-cordierite equilibria and the evolution of the deep crust. *Contributions to Mineralogy & Petrology* 74, 201-210.

Ellis, D.J., 1983. The Napier and Rayner Complexes of Enderby Land, Antarctica - contrasting styles of metamorphism and tectonism. In: Oliver, R.L., James, P.R. & Jago, J.B. (eds) *Antarctic Earth Science*. Cambridge: Cambridge University Press, 20-24.

Ellis, D.J., 1986. Garnet-liquid Fe^{2+}-Mg equilibria and implications for the beginning of melting in the crust and subduction zones. *American Journal of Science* 286, 765-791.

Ellis, D.J., 1987. Origin and evolution of granulites in normal and thickened crusts. *Geology* 15, 167-170.

Ellis, D.J. & Green, D.H., 1979. An experimental study of the effect of Ca upon garnet-clinopyroxene Fe-Mg exchange equilibria. *Contributions to Mineralogy & Petrology* 71, 13-22.

Ellis, D.J., Sheraton, J.W., England, R.N. & Dallwitz, W.B., 1980. Osumilite-sapphirine-quartz granulites from Enderby Land Antarctica - mineral assemblages and reactions. *Contributions to Mineralogy & Petrology* 72, 123-143.

Elphick, S.C., Ganguly, J. & Loomis, T.P., 1985. Experimental determination of cation diffusivities in aluminosilicate garnets. I. Experimental methods and interdiffusion data. *Contributions to Mineralogy & Petrology* 90, 36-44.

Engi, M. & Wersin, P., 1987. Derivation and application of a solution model for calcic garnet. *Schweizerische Mineralogische und Petrographische Mitteilungen* 67, 53-73.

England, P.C., 1987. Diffuse continental deformation: length scales, rates and metamorphic evolution. *Philosophical Transactions of the Royal Society of London. Series A* 321, 3-22.

England, P.C. & Houseman, G.A., 1988. The mechanics of the Tibetan Plateau. *Philosophical Transactions of the Royal Society of London. Series A* 326, 301-320.

England, P.C. & Houseman, G.A., 1989. Extension during continental convergence, with application to the Tibetan Plateau. *Journal of Geophysical Research* 94, 17561-17579.

England, P.C. & Richardson, S.W., 1977. The influence of erosion upon the mineral facies of rocks from different metamorphic environments. *Journal of the Geological Society of London* 134, 201-213.

England, P.C. & Thompson, A.B., 1984. Pressure-temperature-time paths of regional metamorphism I. Heat transfer during the evolution of regions of thickened continental crust. *Journal of Petrology* **25**, 894-928.

England, P.C. & Thompson, A.B., 1986. Some thermal and tectonic models for crustal melting in continental collision zones. In: Coward, M.P. & Ries, A.C. (eds) *Collision Tectonics*, Geological Society of London Special Publication No. **19**, 83-94.

Escher, A. & Watterson, J., 1974. Stretching fabrics, folds and crustal shortening. *Tectonophysics* **22**, 223-231.

Eskola, P., 1939. Die metamorphen Gesteine. In: Barth, T.F.W., Correns, C.W. & Eskola, P. (eds) *Die Entstehung der Gesteine*. Berlin: Julius Springer, 263-407.

Eskola, P., 1952. On the granulites of Lapland. *American Journal of Science* **Bowen Volume**, 133-171.

Essene, E.J., 1982. Geologic thermometry and barometry. In: Ferry, J.M. (ed.) *Characterization of Metamorphism through Mineral Equilibria*, Mineralogical Society of America Reviews in Mineralogy Vol. **10**, 153-206.

Essene, E.J., 1989. The current status of thermobarometry in metamorphic rocks. In: Daly, J.S., Cliff, R.A. & Yardley, B.W.D. (eds) *Evolution of Metamorphic Belts*, Geological Society of London Special Publication No. **43**, 1-44.

Evans, B.W., Shaw, D.M. & Haughton, D.R., 1969. Scapolite stoichiometry. *Contributions to Mineralogy & Petrology* **24**, 293-305.

Faulhaber, S. & Raith, M., 1991. Geothermometry and geobarometry of high-grade rocks: a case study on garnet-pyroxene granulites in southern Sri Lanka. *Mineralogical Magazine* **55**, 33-56.

Ferry, J.M., 1976. P, T, f_{CO2}, and f_{H2O} during metamorphism of calcareous sediments in the Waterville-Vassalboro area, south-central Maine. *Contributions to Mineralogy & Petrology* **57**, 119-143.

Ferry, J.M., 1983*a*. Mineral reactions and element migration during metamorphism of calcareous sediments from the Vassalboro Formation, south-central Maine. *American Mineralogist* **68**, 334-354.

Ferry, J.M., 1983*b*. Regional metamorphism of the Vassalboro Formation, south-central Maine, USA: a case study of the role of fluid in metamorphic petrogenesis. *Journal of the Geological Society of London* **140**, 551-576.

Ferry, J.M. & Spear, F.S., 1978. Experimental calibration of the partitioning of Fe and Mg between biotite and garnet. *Contributions to Mineralogy & Petrology* **66**, 113-117.

Fitzsimons, I.C.W. & Thost, D.E., 1991. Geological relationships in high-grade basement gneiss of the northern Prince Charles Mountains, east Antarctica. *Australian Journal of Earth Sciences* (in press).

Fraser D.G. & Lawless, P.J., 1978. Palaeogeotherms: implications of disequilibrium in garnet lherzolite xenoliths. *Nature* **273**, 220-222.

Freer, R., 1981. Diffusion in silicate minerals and glasses: a data digest and guide to the literature. *Contributions to Mineralogy & Petrology* **76**, 440-454.

Frost, B.R. & Chacko, T., 1989. The granulite uncertainty principle: limitations on thermobarometry in granulites. *Journal of Geology* **97**, 435-450.

Frost, B.R. & Frost, C.D., 1987. CO_2, melts and granulite metamorphism. *Nature* **327**, 503-506.

Fujii, T., 1977. Fe-Mg partitioning between olivine and spinel. *Carnegie Institution of Washington Yearbook* **76**, 563-569.

Fujii, T. & Scarfe, C.M., 1982. Equilibrium experiments on natural peridotite and basalt: a recalibration of the olivine-spinel geothermometer. *EOS* **63**, 471.

Fyfe, W.S., 1973. The granulite facies, partial melting and the Archaean crust. *Philosophical Transactions of the Royal Society of London. Series A* **273**, 457-461.

Fyfe, W.S., Turner, F.J. & Verhoogen, J., 1958. Metamorphic reactions and metamorphic facies. *Memoir of the Geological Society of America* **73**, 259 pp.

Ganguly, J. & Saxena, S.K., 1984. Mixing properties of aluminosilicate garnets: constraints from natural and experimental data, and applications to geothermobarometry. *American Mineralogist* **69**, 88-97.

Gil Ibarguchi, J.I. & Martinez, F.J., 1982. Petrology of garnet-cordierite-sillimanite gneisses from the El Tormes thermal dome, Iberian Hercynian Foldbelt (W Spain). *Contributions to Mineralogy & Petrology* **80**, 14-24.

Glassley, W.E., 1982. Fluid evolution and graphite genesis in the deep continental crust. *Nature* **295**, 229-231.

Glassley, W.E., 1983. Deep crustal carbonates as CO_2 fluid sources: evidence from metasomatic reaction zones. *Contributions to Mineralogy & Petrology* **84**, 15-24.

Goldsmith, J.R. & Newton, R.C., 1977. Scapolite-plagioclase stability relations at high pressures and temperatures in the system $NaAlSi_3O_8$-$CaAl_2Si_2O_8$-$CaCO_3$-$CaSO_4$. *American Mineralogist* **62**, 1063-1081.

Gordon, T.M. & Greenwood, H.J., 1971. The stability of grossularite in H_2O-CO_2 mixtures. *American Mineralogist* **56**, 1674-1688.

Graham, C.M. & Powell, R., 1984. A garnet-hornblende geothermometer: calibration, testing, and application to the Pelona Schist, southern California. *Journal of Metamorphic Geology* **2**, 13-31.

Grant, J.A., 1985*a*. Phase equilibria in low-pressure partial melting of pelitic rocks. *American Journal of Science* **285**, 409-435.

Grant, J.A., 1985*b*. Phase equilibria in partial melting of pelitic rocks. In: Ashworth, J.R. (ed.) *Migmatites*. Glasgow: Blackie & Son Ltd, 86-144.

Grant, J.A. & Frost, B.R., 1990. Contact metamorphism and partial melting of pelitic rocks in the aureole of the Laramie Anorthosite Complex, Morton Pass, Wyoming. *American Journal of Science* **290**, 425-472.

Grant, S.M., 1989. Tectonic implications from sapphirine-bearing lithologies, southwest Grenville Province, Canada. *Journal of Metamorphic Geology* **7**, 583-598.

Green, D.H. & Ringwood, A.E., 1967. An experimental investigation of the gabbro to eclogite transformation and its petrological applications. *Geochimica et Cosmochimica Acta* **31**, 767-833.

Green, T.H., 1976. Experimental generation of cordierite- or garnet-bearing granitic liquids from a pelitic composition. *Geology* **4**, 85-88.

Greenwood, H.J., 1967. Wollastonite: stability in H_2O-CO_2 mixtures and occurrence in a contact-metamorphic aureole near Salmo, British Columbia, Canada. *American Mineralogist* **52**, 1669-1680.

Grew, E.S., 1978. Precambrian basement at Molodezhnaya Station, East Antarctica. *Bulletin of the Geological Society of America* **89**, 801-813.

Grew, E.S., 1980. Sapphirine + quartz association from Archaean rocks in Enderby Land, Antarctica. *American Mineralogist* **65**, 821-836.

Grew, E.S., 1981. Granulite-facies metamorphism at Molodezhnaya Station, East Antarctica. *Journal of Petrology* **22**, 297-336.

Grew, E.S., 1982*a*. The Antarctic margin. In: Naim, A.E.M. & Stehli, F.G. (eds) *The Ocean Basins and Margins,* **Volume 6**. New York: Plenum Publishing Corporation, 697-755.

Grew, E.S., 1982*b*. Geology of the southern Prince Charles Mountains, East Antarctica. In: Craddock, C. (ed.) *Antarctic Geoscience*. Madison: University of Wisconsin Press, 473-478.

Grew, E.S., 1984. A review of Antarctic granulite-facies rocks. *Tectonophysics* **105**, 177-191.

Grew, E.S., 1986. Petrogenesis of Kornerupine at Waldheim (Sachsen), German Democratic Republic. *Zeitschrift der geologischen Wissenschaften* (Berlin, DDR) **14**, 525-558.

Grew, E.S., Manton, W.I. & Sandiford, M., 1982. Geochronologic studies in East Antarctica: age of pegmatites in Casey bay, Enderby land. *Antarctic Journal of the United States* **17**, 1-2.

Griffin, W.L. & O'Reilly, S.Y., 1987. The composition of the lower crust and the nature of the continental Moho - xenolith evidence. In: Nixon, P.H. (ed.) *Mantle Xenoliths*. Chichester: John Wiley & Sons, 413-430.

Grikurov, G.E., Znachko-Yavorsky, G.A., Kamenev, E.N. & Ravich, M.G., 1976. *Explanatory notes to the geological map of Antarctica* (scale 1:5000000). Leningrad: Research Institute of the Geology of the Arctic, Ministry of Geology of the USSR.

Guidotti, C.V., 1984. Micas in metamorphic rocks. In: Bailey, S.W. (ed.) *Micas*, Mineralogical Society of America Reviews in Mineralogy Vol. 13, 357-467.

Hansen, E.C., Janardhan, A.S., Newton, R.C., Prame, W.K.B.N. & Ravindra Kumar, G.R., 1987. Arrested charnockite formation in southern India and Sri Lanka. *Contributions to Mineralogy & Petrology* **96**, 225-244.

Hansen, E.C., Newton, R.C. & Janardhan, A.S., 1984. Fluid inclusions in rocks from the amphibolite-facies gneiss to charnockite progression in southern Karnataka, India: direct evidence concerning the fluids of granulite metamorphism. *Journal of Metamorphic Geology* **2**, 249-264.

Hapuarachchi, D.J.A.C., 1968. Cordierite and wollastonite-bearing rocks of south-western Ceylon. *Geological Magazine* **105**, 317-324.

Harley, S.L., 1983. Regional geobarometry-geothermometry and metamorphic evolution of Enderby Land, Antarctica. In: Oliver, R.L., James, P.R. & Jago, J.B. (eds) *Antarctic Earth Science*. Cambridge: Cambridge University Press, 25-30.

Harley, S.L., 1984*a*. An experimental study of the partitioning of Fe and Mg between garnet and orthopyroxene. *Contributions to Mineralogy & Petrology* **86**, 359-373.

Harley, S.L., 1984*b*. The solubility of alumina in orthopyroxene coexisting with garnet in FeO-MgO-Al_2O_3-SiO_2 and CaO-FeO-MgO-Al_2O_3-SiO_2. *Journal of Petrology* **25**, 665-696.

Harley, S.L., 1985*a*. Garnet-orthopyroxene bearing granulites from Enderby Land, Antarctica: metamorphic pressure-temperature-time evolution of the Archaean Napier Complex. *Journal of Petrology* **26**, 819-856.

Harley, S.L., 1985*b*. Paragenetic and mineral-chemical relationships in orthoamphibole-bearing gneisses from Enderby Land, east Antarctica: a record of Proterozoic uplift. *Journal of Metamorphic Geology* **3**, 179-200.

Harley, S.L., 1986. A sapphirine-cordierite-garnet-sillimanite granulite from Enderby Land, Antarctica: implications for FMAS petrogenetic grids in the granulite facies. *Contributions to Mineralogy & Petrology* **94**, 452-460.

Harley, S.L., 1987*a*. Precambrian geological relationships in high-grade gneisses of the Rauer Islands, East Antarctica. *Australian Journal of Earth Sciences* **34**, 175-207.

Harley, S.L., 1987*b*. A pyroxene-bearing meta-ironstone and other pyroxene-granulites from Tonagh Island, Enderby Land, Antarctica: further evidence for very high temperature (>980°C) Archaean regional metamorphism in the Napier Complex. *Journal of Metamorphic Geology* **5**, 341-356.

Harley, S.L., 1987*c*. Archaean sapphirine granulites from the Vestfold Hills. In: *Abstracts of the 5th International Symposium on Antarctic Earth Sciences, Cambridge 1987*, 150.

Harley, S.L., 1988. Proterozoic granulites from the Rauer Group, East Antarctica. I. Decompressional pressure-temperature paths deduced from mafic and felsic gneisses. *Journal of Petrology* **29**, 1059-1095.

Harley, S.L., 1989. The origins of granulites: a metamorphic perspective. *Geological Magazine* **126**, 215-247.

Harley, S.L., 1991. The crustal evolution of some East Antarctic granulites. In: Thomson, M.R.A., Crame, J.A. & Thomson, J.W. (eds) *Geological Evolution of Antarctica*. Cambridge: Cambridge University Press, 7-12.

Harley, S.L. & Black, L.P., 1987. The Archaean geological evolution of Enderby Land, Antarctica. In: Park, R.G. & Tarney, J. (eds) *Evolution of the Lewisian and Comparable Precambrian High Grade Terrains,* Geological Society of London Special Publication No. 27, 285-296.

Harley, S.L. & Buick, I.S., 1991. Wollastonite-scapolite assemblages as indicators of granulite pressure-temperature-fluid histories: application to the Rauer Group, East Antarctica and other high-grade terrains. *Journal of Petrology* (in press).

Harley, S.L. & Fitzsimons, I.C.W., 1991. Pressure-temperature evolution of metapelitic granulites in a polymetamorphic terrane: the Rauer Group, east Antarctica. *Journal of Metamorphic Geology* **9**, 231-243.

Harley, S.L. & Green, D.H., 1982. Garnet-orthopyroxene barometry for granulites and peridotites. *Nature* **300**, 697-701.

Harley, S.L. & Hensen, B.J., 1990. Archaean and Proterozoic high-grade terranes of East Antarctica (40-80°E): a case study of diversity in granulite facies metamorphism. In: Ashworth, J.R. & Brown, M. (eds) *High-temperature Metamorphism and Crustal Anatexis.* London: Unwin Hyman Ltd, 320-370.

Harley, S.L., Hensen, B.J. & Sheraton, J.W., 1990. Two-stage decompression in orthopyroxene-sillimanite granulites from Forefinger Point, Enderby Land, Antarctica: implications for the evolution of the Archaean Napier Complex. *Journal of Metamorphic Geology* **8**, 591-613.

Harris, N.B.W., 1981. The application of spinel-bearing metapelites to P/T determinations: an example from south India. *Contributions to Mineralogy & Petrology* **76**, 229-233.

Harte, B. & Hudson, N.F.C., 1979. Pelite facies series and the temperatures and pressures of Dalradian metamorphism in E Scotland. In: Harris, A.L., Holland, C.H. & Leake, B.E. (eds) *The Caledonides of the British Isles - reviewed,* Geological Society of London Special Publication No. **8**, 323-337.

Haselton, H.T., Hovis, G.L., Hemingway, B.S. & Robie, R.A., 1983. Calorimetric investigation of the excess entropy of mixing in analbite-sanidine solid solutions: lack of evidence for Na, K short-range order and implications for two-feldspar thermometry. *American Mineralogist* **68**, 398-413.

Heier, K.S., 1960. Petrology and geochemistry of high-grade metamorphic and igneous rocks on Langø, northern Norway. *Norges Geologiske Undersøkelse* **207**, 246 pp.

Heier, K.S., 1973. Geochemistry of granulite facies rocks and problems of their origin. *Philosophical Transactions of the Royal Society of London. Series A* **273**, 429-442.

Hensen, B.J., 1971. Theoretical phase relations involving cordierite and garnet in the system MgO-FeO-Al_2O_3-SiO_2. *Contributions to Mineralogy & Petrology* **33**, 191-214.

Hensen, B.J., 1977. Cordierite-garnet bearing assemblages as geothermometers and barometers in granulite facies terranes. *Tectonophysics* **43**, 73-88.

Hensen, B.J., 1986. Theoretical phase relations involving cordierite and garnet revisited: the influence of oxygen fugacity on the stability of sapphirine and spinel in the system Mg-Fe-Al-Si-O. *Contributions to Mineralogy & Petrology* **92**, 362-367.

Hensen, B.J., 1987. *P-T* grids for silica-undersaturated granulites in the systems MAS (n+4) and FMAS (n+3) - tools for the derivation of *P-T* paths of metamorphism. *Journal of Metamorphic Geology* **5**, 255-271.

Hensen, B.J. & Green, D.H., 1972. Experimental study of the stability of cordierite and garnet in pelitic compositions at high pressures and temperatures. II. Compositions without excess alumino-silicate. *Contributions to Mineralogy & Petrology* **35**, 331-354.

Hensen, B.J. & Green, D.H., 1973. Experimental study of the stability of cordierite and garnet in pelitic compositions at high pressures and temperatures. III. Synthesis of experimental data and geological applications. *Contributions to Mineralogy & Petrology* **38**, 151-166.

Hensen, B.J. & Harley, S.L., 1990. Graphical analysis of *P-T-X* relations in granulite facies metapelites. In: Ashworth, J.R. & Brown, M. (eds) *High-temperature Metamorphism and Crustal Anatexis*. London: Unwin Hyman Ltd, 19-56.

Hess, P.C., 1969. The metamorphic paragenesis of cordierite in pelitic rocks. *Contributions to Mineralogy & Petrology* **24**, 191-207.

Hiroi, Y., Shiraishi, K., Motoyoshi, Y. & Katsushima, T., 1987. Progressive metamorphism of calc-silicate rocks from the Prince Olav and Sôya Coasts, East Antarctica. *Proceedings of the National Institute of Polar Research Symposium on Antarctic Geosciences* **1**, 73-97.

Hobbs, B.E., Means, W.D. & Williams, P.F., 1976. *An Outline of Structural Geology*. New York: John Wiley & Sons, 571 pp.

Hodges, K.V., le Fort, P., Pêcher, A., 1988. Possible thermal buffering by crustal anatexis in collisional orogens: thermobarometric evidence from the Nepalese Himalaya. *Geology* **16**, 707-710.

Holdaway, M.J., 1971. Stability of andalusite and the aluminium silicate phase diagram. *American Journal of Science* **271**, 97-131.

Holdaway, M.J. & Lee, S.M., 1977. Fe-Mg cordierite stability in high-grade pelitic rocks based on experimental, theoretical, and natural observations. *Contributions to Mineralogy & Petrology* **63**, 175-198.

Holland, T.H., 1893. The petrology of Job Charnock's tombstone. *Journal of the Asiatic Society of Bengal* **62**, 162-164.

Holland, T.H., 1900. The charnockite series, a group of Archaean hypersthenic rocks in peninsular India. *Memoir of the Geological Society of India* **28**, 119-249.

Holland, T.J.B. & Powell, R., 1990. An enlarged and updated internally consistent thermodynamic dataset with uncertainties and correlations: the system K_2O-Na_2O-CaO-MgO-MnO-FeO-Fe_2O_3-Al_2O_3-TiO_2-SiO_2-C-H_2-O_2. *Journal of Metamorphic Geology* **8**, 89-124.

Hollister, L.S., 1982. Metamorphic evidence for rapid (2 mm/yr) uplift of a portion of the Central Gneiss Complex, Coast Mountains, B.C. *Canadian Mineralogist* **20**, 319-332.

Hollister, L.S., 1988. On the origin of CO_2-rich fluid inclusions in migmatites. *Journal of Metamorphic Geology* **6**, 467-474.

Hollister, L.S. & Crawford, M.L., 1986. Melt-enhanced deformation: a major tectonic process. *Geology* **14**, 558-561.

Hölzl, S., Köhler, H. & Todt, W., 1988. Datierungen an Magmatiten und Metamorphiten Sri Lankas. *Fortschritte der Mineralogie* **66**, 68.

Houseman, G.A., McKenzie, D.P. & Molnar, P., 1981. Convective instability of a thickened boundary layer and its relevance for the thermal evolution of continental convergent belts. *Journal of Geophysical Research* **86**, 6115-6132.

Howie, R.A., 1955. The geochemistry of the charnockite series of Madras, India. *Transactions of the Royal Society of Edinburgh* **62**, 725-768.

Hsu, L.C. & Burnham, C.W., 1969. Phase relationships in the system $Fe_3Al_2Si_3O_{12}$-$Mg_3Al_2Si_3O_{12}$-H_2O at 2.0 kilobars. *Bulletin of the Geological Society of America* **80**, 2393-2407.

Huang, W.L. & Wyllie, P.J., 1973. Melting relations of muscovite-granite to 35 kbar as a model for fusion of metamorphosed subducted oceanic sediments. *Contributions to Mineralogy & Petrology* **42**, 1-14.

Huckenholz, H.G. & Seiberl, W.M., 1990. Stability and phase relations of carbonate-scapolite solid solutions under the *P-T* regime of the deeper crust. *Abstracts of the Third International Symposium of Experimental Mineralogy, Petrology and Geochemistry*. Oxford: Blackwell Scientific Publications, 81.

Hudson, N.F.C. & Harte, B., 1985. K_2O-poor, aluminous assemblages from the Buchan Dalradian, and the variety of orthoamphibole assemblages in aluminous bulk compositions in the amphibolite facies. *American Journal of Science* 285, 224-266.

Indares, A. & Martignole, J., 1985*a*. Biotite-garnet geothermometry in the granulite facies: the influence of Ti and Al in biotite. *American Mineralogist* 70, 272-278.

Indares, A. & Martignole, J., 1985*b*. Biotite-garnet geothermometry in granulite-facies rocks: evaluation of equilibrium criteria. *Canadian Mineralogist* 23, 187-193.

James, P.R. & Black, L.P., 1981. A review of the structural evolution and geochronology of the Archaean Napier Complex of Enderby Land, Australian Antarctic Territory. In: Glover, J.E. & Groves, D.I. (eds) *Archaean Geology*. Special Publication of the Geological Society of Australia No. 7, 71-83.

James, P.R., Ding, P. & Rankin, L., 1991. Structural geology of the early Precambrian gneisses of northern Fold Island, Mawson Coast, East Antarctica. In: Thomson, M.R.A., Crame, J.A. & Thomson, J.W. (eds) *Geological Evolution of Antarctica*. Cambridge: Cambridge University Press, 19-23.

James, P.R. & Tingey, R.J., 1983. The Precambrian geological evolution of the East Antarctic metamorphic shield - a review. In: Oliver, R.L., James, P.R. & Jago, J.B. (eds) *Antarctic Earth Science*. Cambridge: Cambridge University Press, 5-10.

Jan, M.Q. & Howie, R.A., 1981. The mineralogy and geochemistry of the metamorphosed basic and ultrabasic rocks of the Jijal Complex, Kohistan, NW Pakistan. *Journal of Petrology* 22, 85-126.

Janardhan, A.S., Newton, R.C. & Hansen, E.C., 1982. The transformation of amphibolite facies gneiss to charnockite in southern Karnataka and northern Tamil Nadu, India. *Contributions to Mineralogy & Petrology* 79, 130-149.

Janardhan, A.S., Newton, R.C. & Smith, J.V., 1979. Ancient crustal metamorphism at low p_{H2O}: charnockite formation at Kabbaldurga, south India. *Nature* 278, 511-514.

Johannes, W. & Gupta, L.N., 1982. Origin and evolution of a migmatite. *Contributions to Mineralogy & Petrology* 79, 114-123.

Johansson, L. & Möller, C., 1986. Formation of sapphirine during retrogression of a basic high-pressure granulite, Roan, Western Gneiss Region, Norway. *Contributions to Mineralogy & Petrology* 94, 29-41.

Kars, H., Jansen, J.B.H., Tobi, A.C. & Poorter, R.P.E., 1980. The metapelitic rocks of the polymetamorphic Precambrian of Rogaland, SW Norway. Part II. Mineral relations between cordierite, hercynite and magnetite within the osumilite-in isograd. *Contributions to Mineralogy & Petrology* 74, 235-244.

Kennedy, W.Q., 1949. Zones of progressive regional metamorphism in the Moine Schists of the western highlands of Scotland. *Geological Magazine* 86, 43-56.

Kerrick, D.M., 1974. Review of metamorphic mixed-volatile (H_2O-CO_2) equilibria. *American Mineralogist* 59, 729-762.

Kinny, P.D. & Black, L.P., 1990. Zircon ages and the distribution of Archaean and Proterozoic rocks in the Rauer Islands. *Geological Society of Australia, Abstracts* 25, 251-252.

Korzhinskii, D.S., 1959. *Theory of Metasomatic Zoning*. (translated by J. Agrell and published in 1970 by the Clarendon Press, Oxford, 162 pp).

Koziol, A.M., 1990. Activity-composition relationships of binary Ca-Fe and Ca-Mn garnets determined by reversed, displaced equilibrium experiments. *American Mineralogist* 75, 319-327.

Koziol, A.M. & Newton, R.C., 1988. Redetermination of the anorthite breakdown reaction and improvement of the plagioclase-garnet-Al_2SiO_5-quartz geobarometer. *American Mineralogist* 73, 216-223.

Kretz, R., 1983. Symbols for rock-forming minerals. *American Mineralogist* 68, 277-279.

Kröner, A., Williams, I.S., Compston, W., Baur, N., Vitanage, P.W. & Perera, L.R.K., 1987. Zircon ion microprobe dating of high-grade rocks in Sri Lanka. *Journal of Geology* **95**, 775-791.

Kuehner, S.M. & Green, D.H., 1991. Uplift history of the East Antarctic Shield: constraints imposed by high-pressure experimental studies of Proterozoic mafic dykes. In: Thomson, M.R.A., Crame, J.A. & Thomson, J.W. (eds) *Geological Evolution of Antarctica*. Cambridge: Cambridge University Press, 1-6.

Lal, R.K., Ackermand, D. & Upadhyay, H., 1987. *P-T-X* relationships deduced from corona textures in sapphirine-spinel-quartz assemblages from Paderu, southern India. *Journal of Petrology* **28**, 1139-1168.

Lamb, R.C., Smalley, P.C. & Field, D., 1986. *P-T* conditions for the Arendal granulites, southern Norway: implications for the roles of *P*, *T* and CO_2 in deep crustal LILE-depletion. *Journal of Metamorphic Geology* **4**, 143-160.

Lamb, W.M. & Valley, J.W., 1984. Metamorphism of reduced granulites in low-CO_2 vapour-free environment. *Nature* **312**, 56-58.

Lamb, W.M. & Valley, J.W., 1985. C-O-H fluid calculations and granulite genesis. In: Tobi, A.C. & Touret, J.L.R. (eds) *The Deep Proterozoic Crust in the North Atlantic Provinces*. Dordrecht: Reidel, 119-131.

Lasaga, A.C., 1979. Multicomponent exchange and diffusion in silicates. *Geochimica et Cosmochimica Acta* **43**, 455-469.

Lasaga, A.C., 1983. Geospeedometry: an extension of geothermometry. In: Saxena, S.K. (ed.) *Kinetics and Equilibrium in Mineral Reactions*. New York: Springer-Verlag, 81-114.

Lasaga, A.C., Richardson, S.M. & Holland, H.D., 1977. The mathematics of cation diffusion and exchange between silicate minerals during retrograde metamorphism. In: Saxena, S.K. & Bhattacharji, S. (eds) *Energetics of Geological Processes*. New York: Springer-Verlag, 353-388.

Le Breton, N. & Thompson, A.B., 1988. Fluid-absent (dehydration) melting of biotite in metapelites in the early stages of crustal anatexis. *Contributions to Mineralogy & Petrology* **99**, 226-237.

Lee, H.Y. & Ganguly, J., 1988. Equilibrium compositions of coexisting garnet and orthopyroxene: experimental determinations in the system FeO-MgO-Al_2O_3-SiO_2 and applications. *Journal of Petrology* **29**, 93-113.

Lister, G.S., Etheridge, M.A. & Symonds, P.A., 1986. Detachment faulting and the evolution of passive continental margins. *Geology* **14**, 246-250.

Lister, G.S. & Snoke, A.W., 1984. S-C Mylonites. *Journal of Structural Geology* **6**, 617-638.

Loomis, T.P., 1983. Compositional zoning of crystals: a record of growth and reaction history. In: Saxena, S.K. (ed.) *Kinetics and Equilibrium in Mineral Reactions*. New York: Springer-Verlag, 1-60.

Loosveld, R.J.H. & Etheridge, M.A., 1990. A model for low-pressure facies metamorphism during crustal thickening. *Journal of Metamorphic Geology* **8**, 257-267.

Maboko, M.A.H., McDougall, I. & Zeitler, P.K., 1989. Metamorphic *P-T* path of granulites in the Musgrave Ranges, central Australia. In: Daly, J.S., Cliff, R.A. & Yardley, B.W.D. (eds) *Evolution of Metamorphic Belts*, Geological Society of London Special Publication No. **43**, 303-307.

Manning, J.R., 1974. Diffusion kinetics and mechanisms in simple crystals. In: Hoffman, A.W., Giletti, B.J., Yoder, H.S. & Yund, R.A. (eds) *Geochemical Transport and Kinetics*, Carnegie Institute of Washington, Publication No. **634**, 3-13.

McCarthy, W.R. & Trail, D.S., 1964. The high-grade metamorphic rocks of the MacRobertson Land and Kemp Land coast. In: Adie R.J. (ed.) *Antarctic Geology*. Amsterdam: North-Holland Publishing Company, 473-481.

McCulloch, M.T., Bradshaw, J.Y. & Taylor, S.R., 1987. Sm-Nd and Rb-Sr isotopic and geochemical systematics in Phanerozoic granulites from Fiordland, southwest New Zealand. *Contributions to Mineralogy & Petrology* **97**, 183-195.

McKelvey, B.C. & Stephenson, N.C.N., 1990. A geological reconnaissance of the Radok Lake area, Amery Oasis, Prince Charles Mountains. *Antarctic Science* **2**, 53-66.

McKenzie, D.P., 1978. Some remarks on the development of sedimentary basins. *Earth & Planetary Science Letters* **40**, 25-32.

McLellan, E.L., 1988. Migmatite structures in the Central Gneiss Complex, Boca de Quadra, Alaska. *Journal of Metamorphic Geology* **6**, 517-542.

McLellan, E.L., Linder, D. & Thomas, J., 1989. Multiple granulite-facies events in the southern Appalachians, USA. In: Daly, J.S., Cliff, R.A. & Yardley, B.W.D. (eds) *Evolution of Metamorphic Belts*, Geological Society of London Special Publication No. **43**, 309-314.

McLeod, I.R., 1959. Report on geological and glaciological work by the 1958 Australian National Antarctic Research Expedition. *Bureau of Mineral Resources, Australia, Record* **1959/131**, 75 pp. (Unpublished).

McLeod, I.R., 1964. An outline of the geology of the sector from longitude 45° to 80°E, Antarctica. In: Adie R.J. (ed.) *Antarctic Geology*. Amsterdam: North-Holland Publishing Company, 237-247.

McLeod, I.R., Trail, D.S., Cook, P.J. & Wallis, G.R., 1966. Geological work in Antarctica, January to March, 1965. *Bureau of Mineral Resources, Australia, Record* **1966/9**, 87 pp. (Unpublished).

Mehnert, K.R., 1968. *Migmatites and the Origin of Granitic Rocks*. Amsterdam: Elsevier, 393 pp.

Mehnert, K.R., 1972. Granulites - results of a discussion II. *Neues Jahrbuch für Mineralogie Monatshefte* **1972**, 139-150.

Mezger, K., 1990. Geochronology in granulites. In: Vielzeuf, D. & Vidal, Ph. (eds) *Granulites and Crustal Evolution*. Dordrecht: Kluwer Academic Publishers, 451-470.

Miyashiro, A., 1961. Evolution of metamorphic belts. *Journal of Petrology* **2**, 277-311.

Misch, P., 1964. Stable association wollastonite-anorthite and other calc-silicate assemblages in the amphibolite facies crystalline schists of Nanga Parbat, northwest Himalayas. *Beiträge zur Mineralogie und Petrographie* **10**, 315-356.

Moecher, D.P. & Essene, E.J., 1990. Phase equilibria for calcic scapolite, and implications of variable Al-Si disorder for *P-T*, T-X_{CO_2}, and *a-X* relations. *Journal of Petrology* **31**, 997-1024.

Moecher, D.P., Essene, E.J. & Anovitz, L.M., 1988. Calculation and application of clinopyroxene-garnet-plagioclase-quartz geobarometers. *Contributions to Mineralogy & Petrology* **100**, 92-106.

Molnar, P. & Tapponnier, P., 1975. Cenozoic tectonics of Asia: effects of a continental collision. *Science* **189**, 419-426.

Molnar, P. & Tapponnier, P., 1978. Active tectonics of Tibet. *Journal of Geophysical Research* **83**, 5361-5375.

Mond, A., 1972. Permian sediments of the Beaver Lake area, Prince Charles Mountains. In: Adie R.J. (ed.) *Antarctic Geology and Geophysics*. Oslo: Universitetsforlaget, 585-589.

Montel, J.M., Weber, C. & Pichavant, M., 1986. Biotite-sillimanite-spinel assemblages in high-grade metamorphic rocks: occurrences, chemographic analysis and thermobarometric interest. *Bulletin de Minéralogie* **109**, 555-573.

Motoyoshi, Y., Thost, D.E. & Hensen, B.J., 1991. Reaction textures in calc-silicate granulites from the Bolingen Islands, Prydz Bay, East Antarctica: implications for the retrograde *P-T* path. *Journal of Metamorphic Geology* **9**, 293-300.

Muhling, J.R., 1990. The Narryer Gneiss Complex of the Yilgarn Block, Western Australia: a segment of Archaean lower crust uplifted during Proterozoic orogeny. *Journal of Metamorphic Geology* **8**, 47-64.

Mukherjee, A. & Rege, S.M., 1972. Stability of wollastonite in the granulite facies: some evidences from the Eastern Ghats, India. *Neues Jahrbuch für Mineralogie Abhandlungen* **118**, 23-42.

Munoz, J.L. & Ludington, S.D., 1974. Fluoride-hydroxyl exchange in biotite. *American Journal of Science* **274**, 396-413.

Myers, J.S., 1988. Early Archaean Narryer Gneiss Complex, Yilgarn Craton, Western Australia. *Precambrian Research* **38**, 297-307.

Newton, R.C., 1966. Some calc-silicate equilibrium relations. *American Journal of Science* **264**, 204-222.

Newton, R.C., 1978. Experimental and thermodynamic evidence for the operation of high pressures in Archaean metamorphism. In: Windley, B.F. & Naqui, S.M. (eds) *Archaean Geochemistry*. Amsterdam: Elsevier, 221-240.

Newton, R.C., 1990. Fluids and melting in the Archaean deep crust of southern India. In: Ashworth, J.R. & Brown, M. (eds) *High-temperature Metamorphism and Crustal Anatexis*. London: Unwin Hyman Ltd, 149-179.

Newton, R.C., Charlu, T.V. & Kleppa, O.J., 1980. Thermochemistry of the high structure state plagioclases. *Geochimica et Cosmochimica Acta* **44**, 933-941.

Newton, R.C. & Perkins, D., 1982. Thermodynamic calibration of geobarometers based on the assemblage garnet-plagioclase-orthopyroxene (clinopyroxene)-quartz. *American Mineralogist* **67**, 203-222.

Newton, R.C., Smith, J.V. & Windley, B.F., 1980. Carbonic metamorphism, granulites and crustal growth. *Nature* **288**, 45-50.

Nicollet, C., 1990. Crustal evolution of the granulites of Madagascar. In: Vielzeuf, D. & Vidal, Ph. (eds) *Granulites and Crustal Evolution*. Dordrecht: Kluwer Academic Publishers, 291-310.

Niggli, P., 1954. *Rocks and Mineral Deposits* (translated by R.L. Parker). San Francisco: W.H. Freeman & Company, 559 pp.

Nixon, P.H., Reedman, A.J. & Burns, L.K., 1973. Sapphirine-bearing granulites from Labwor, Uganda. *Mineralogical Magazine* **39**, 420-428.

Norrish, K. & Chappell, B.W., 1977. X-ray fluorescence spectography. In: Zussman, J. (ed.) *Physical Methods in Determinative Mineralogy* (2nd edition). London: Academic Press, 201-272.

O'Hara, M.J., 1977. Thermal history of excavation of Archaean gneisses from the base of the continental crust. *Journal of the Geological Society of London* **134**, 185-200.

O'Hara, M.J. & Yarwood, G., 1978. High pressure-temperature point on an Archaean geotherm, implied magma genesis by crustal anatexis, and consequences for garnet-pyroxene thermometry and barometry. *Philosophical Transactions of the Royal Society of London. Series A* **288**, 441-456.

Ohmoto, H. & Kerrick, D., 1977. Devolatilization equilibria in graphitic systems. *American Journal of Science* **277**, 1013-1044.

Oliver, R.L., James, P.R., Collerson, K.D. & Ryan, A.B., 1982. Precambrian geologic relationships in the Vestfold Hills, Antarctica. In: Craddock, C. (ed.) *Antarctic Geoscience*. Madison: University of Wisconsin Press, 435-444.

Olsen, S.N., 1985. Mass balance in migmatites. In: Ashworth, J.R. (ed.) *Migmatites*. Glasgow: Blackie & Son Ltd, 145-179.

Olsen, S.N., 1987. The composition and role of the fluid in migmatites: a fluid inclusion study of the Front Range rocks. *Contributions to Mineralogy & Petrology* **96**, 104-120.

Orville, P.M., 1975. Stability of scapolite in the system Ab-An-NaCl-$CaCO_3$ at 4 kb and 750°C. *Geochimica et Cosmochimica Acta* **39**, 1091-1105.

Oterdoom, H. & Gunter, W.D., 1983. Activity models for plagioclase and CO_3-scapolites: an analysis of field and laboratory data. *American Journal of Science* 283-A, 255-282.

Oxburgh, E.R. & Turcotte, D.L., 1971. Origin of paired metamorphic belts and crustal dilation in island arc regions. *Journal of Geophysical Research* 76, 1315-1327.

Oxburgh, E.R. & Turcotte, D.L., 1974. Thermal gradients and regional metamorphism in overthrust terrains with special reference to the Eastern Alps. *Schweizerische Mineralogische und Petrographische Mitteilungen* 54, 641-662.

Oxburgh, E.R., 1990. Some thermal aspects of granulite history. In: Vielzeuf, D. & Vidal, Ph. (eds) *Granulites and Crustal Evolution*. Dordrecht: Kluwer Academic Publishers, 569-580.

Parras, K., 1958. On the charnockites in the light of a highly metamorphic rock complex in southwestern Finland. *Bulletin de la Commission Géologique de Finlande* **181**, 137 pp.

Parsons, B. &.McKenzie, D.P., 1978. Mantle convection and the thermal structure of the plates. *Journal of Geophysical Research* 83, 4485-4496.

Passchier, C.W., Hoek, J.D., Bekendam, R.F. & de Boorder, H., 1990. Ductile reactivation of Proterozoic brittle fault rocks; an example from the Vestfold Hills, East Antarctica. *Precambrian Research* 47, 3-16.

Paterson, S.R., Vernon, R.H. & Tobisch, O.T., 1989. A review of criteria for the identification of magmatic and tectonic foliations in granitoids. *Journal of Structural Geology* 11, 349-363.

Pattison, D.R.M. & Newton, R.C., 1989. Reversed experimental calibration of the garnet-clinopyroxene Fe-Mg exchange thermometer. *Contributions to Mineralogy & Petrology* **101**, 87-103.

Perchuk, L.L., Aranovich, L. Ya., Podlesskii, K.K., Lavrent'eva, I.V., Gerasimov, V. Yu., Fed'kin, V.V., Kitsul, V.I., Karsakov, L.P. & Berdnikov, N.V., 1985. Precambrian granulites of the Aldan Shield, eastern Siberia, USSR. *Journal of Metamorphic Geology* 3, 265-310.

Perchuk, L.L., Gerya, T.V. & Nozhkin, A.D., 1989. Petrology and retrograde *P-T* path in granulites of the Kanskaya formation, Yenisey Range, eastern Siberia. *Journal of Metamorphic Geology* 7, 599-617.

Perchuk, L.L. & Lavrent'eva, I.V., 1983. Experimental investigation of exchange equilibria in the system cordierite-garnet-biotite. In: Saxena, S.K. (ed.) *Kinetics and Equilibrium in Mineral Reactions*. New York: Springer-Verlag, 199-239.

Perkins, D., 1990. Thermometry and barometry of mafic granulites based on garnet-clinopyroxene-plagioclase-quartz assemblages. In: Vielzeuf, D. & Vidal, Ph. (eds) *Granulites and Crustal Evolution*. Dordrecht: Kluwer Academic Publishers, 435-449.

Perkins, D. & Chipera, S.J., 1985. Garnet-orthopyroxene-plagioclase-quartz barometry: refinement and application to the English River subprovince and the Minnesota River valley. *Contributions to Mineralogy & Petrology* 89, 69-80.

Perkins, D. & Newton, R.C., 1981. Charnockite geobarometers based on coexisting garnet-pyroxene-plagioclase-quartz. *Nature* 292, 144-146.

Peterson, J.W. & Newton, R.C., 1989. CO_2-enhanced melting of biotite-bearing rocks at deep-crustal pressure-temperature conditions. *Nature* 340, 378-380.

Peterson, J.W. & Newton, R.C., 1990. Experimental biotite-quartz melting in the KMASH-CO_2 system and the role of CO_2 in the petrogenesis of granites and related rocks. *American Mineralogist* 75, 1029-1042.

Petrakakis, K., 1986. Metamorphism of high-grade gneisses from the Moldanubian zone, Austria, with particular reference to the garnets. *Journal of Metamorphic Geology* 4, 323-344.

Phillips, G.N., 1980. Water activity changes across an amphibolite-granulite facies transition, Broken Hill, Australia. *Contributions to Mineralogy & Petrology* 75, 377-386.

Phillips, G.N. & Wall, V.J., 1981. Evaluation of prograde regional metamorphic conditions: their implications for the heat source and water activity during metamorphism in the Willyama Complex, Broken Hill, Australia. *Bulletin de Minéralogie* **104**, 801-810.

Pichamuthu, C.S., 1960. Charnockite in the making. *Nature* **188**, 135-136.

Pieters, P.E. & Wyborn, D., 1977. Geological work in Antarctica - 1974/75. *Bureau of Mineral Resources, Australia, Record* **1977/16**, 93 pp. (Unpublished).

Pigage, L.C. & Greenwood, H.J., 1982. Internally consistent estimates of pressure and temperature: the staurolite problem. *American Journal of Science* **282**, 943-969.

Pin, C. & Vielzeuf, D., 1983. Granulites and related rocks in Variscan median Europe: a dualistic interpretation. *Tectonophysics* **93**, 47-74.

Powell, R., 1978. *Equilibrium Thermodynamics in Petrology*. London: Harper & Row Ltd, 284 pp.

Powell, R., 1983*a*. Processes in granulite-facies metamorphism. In: Atherton, M.P. & Gribble, C.D. (eds) *Migmatites, Melting and Metamorphism*. Nantwich: Shiva Publishing Ltd, 127-139.

Powell, R., 1983*b*. Fluids and melting under upper amphibolite facies conditions. *Journal of the Geological Society of London* **140**, 629-633.

Powell, R. & Downes, J., 1990. Garnet porphyroblast-bearing leucosomes in metapelites: mechanisms, phase diagrams, and an example from Broken Hill, Australia. In: Ashworth, J.R. & Brown, M. (eds) *High-temperature Metamorphism and Crustal Anatexis*. London: Unwin Hyman Ltd, 105-123.

Powell, R. & Holland, T.J.B., 1990. Calculated mineral equilibria in the pelite system, KFMASH (K_2O-FeO-MgO-Al_2O_3-SiO_2-H_2O). *American Mineralogist* **75**, 367-380.

Powell, R. & Sandiford, M. 1988. Sapphirine and spinel phase relationships in the system FeO-MgO-Al_2O_3-SiO_2-TiO_2-O_2 in the presence of quartz and hypersthene. *Contributions to Mineralogy & Petrology* **98**, 64-71.

Powers, R.E. & Bohlen, S.R., 1985. The role of synmetamorphic igneous rocks in the metamorphism and partial melting of metasediments, northwest Adirondacks. *Contributions to Mineralogy & Petrology* **90**, 401-409.

Prigogine, L. & Defay, R., 1954. *Chemical Thermodynamics*. London: Longmans, Green & Co. 543 pp.

Putnis, A. & McConnell, J.D.C., 1980. *Principles of Mineral Behaviour*. Oxford: Blackwell Scientific Publications, 257 pp.

Raith, M. & Raase, P., 1986. High grade metamorphism in the granulite belt of Finnish Lapland. In: Dawson, J.B. Carswell, D.A., Hall, J. & Wedepohl, K.H. (eds) *The Nature of the Lower Continental Crust*, Geological Society of London Special Publication No. 24, 283-295.

Ramsay, J.G. & Graham, R.H., 1970. Strain variations in shear belts. *Canadian Journal of Earth Sciences* **7**, 786-813.

Ravich, M.G. & Kamenev, E.N., 1975. *Crystalline basement of the Antarctic platform*. New York: John Wiley & Sons, 582 pp.

Richardson, S.W. & Powell, R., 1976. Thermal causes of the Dalradian metamorphism in the central Highlands of Scotland. *Scottish Journal of Geology* **12**, 237-268.

Rollinson, H.R., 1989. Garnet-orthopyroxene thermobarometry of granulites from the north marginal zone of the Limpopo belt, Zimbabwe. In: Daly, J.S., Cliff, R.A. & Yardley, B.W.D. (eds) *Evolution of Metamorphic Belts*, Geological Society of London Special Publication No. 43, 331-335.

Ruker, R.A., 1963. Geological reconnaissance in Enderby Land and southern Prince Charles Mountains, Antarctica. *Bureau of Mineral Resources, Australia, Record* **1963/154**, 14 pp. (Unpublished).

Sacchi, R., Marques, J., Costa, M. & Casati, C., 1984. Kibaran events in the southemmost Mozambique belt. *Precambrian Research* **25**, 141-159.

Salje, E., 1986. Heat capacities and entropies of andalusite and sillimanite: the influence of fibrolitization on the phase diagram of the Al_2SiO_5 polymorphs. *American Mineralogist* **71**, 1366-1371.

Sandiford, M., 1985*a*. The metamorphic evolution of granulites at Fyfe Hills; implications for Archaean crustal thickness in Enderby Land, Antarctica. *Journal of Metamorphic Geology* **3**, 155-178.

Sandiford, M., 1985*b*. The origin of retrograde shear zones in the Napier Complex: implications for the tectonic evolution of Enderby Land, Antarctica. *Journal of Structural Geology* **7**, 477-488.

Sandiford, M., 1989*a*. Horizontal structures in granulite terrains: a record of mountain building or mountain collapse? *Geology* **17**, 449-452.

Sandiford, M., 1989*b*. Secular trends in the thermal evolution of metamorphic terrains. *Earth & Planetary Science Letters* **95**, 85-96.

Sandiford, M., Neall, F.B. & Powell, R., 1987. Metamorphic evolution of aluminous granulites from Labwor Hills, Uganda. *Contributions to Mineralogy & Petrology* **95**, 217-225.

Sandiford, M. & Powell, R., 1986*a*. Deep crustal metamorphism during continental extension: modern and ancient examples. *Earth & Planetary Science Letters* **79**, 151-158.

Sandiford, M. & Powell, R., 1986*b*. Pyroxene exsolution in granulites from Fyfe Hills, Enderby Land, Antarctica: evidence for 1000°C metamorphic temperatures in Archaean continental crust. *American Mineralogist* **71**, 946-954.

Sandiford, M. & Powell, R., 1990. Some isostatic and thermal consequences of the vertical strain geometry in convergent orogens. *Earth & Planetary Science Letters* **98**, 154-165.

Sandiford, M. & Powell, R., 1991. Some remarks on high-temperature - low-pressure metamorphism in convergent orogens. *Journal of Metamorphic Geology* **9**, 333-340.

Sandiford, M., Powell, R., Martin, S.F. & Perera, L.R.K., 1988. Thermal and baric evolution of garnet granulites from Sri Lanka. *Journal of Metamorphic Geology* **6**, 351-364.

Sandiford, M. & Wilson, C.J.L., 1983. The geology of the Fyfe Hills - Khmara Bay region, Enderby Land. In: Oliver, R.L., James, P.R. & Jago, J.B. (eds) *Antarctic Earth Science*. Cambridge: Cambridge University Press, 16-19.

Sandiford, M. & Wilson, C.J.L., 1984. The structural evolution of the Fyfe Hills - Khmara Bay region, Enderby Land, East Antarctica. *Australian Journal of Earth Sciences* **31**, 403-426.

Santosh, M., 1987. Cordierite gneisses of southern Kerala, India: petrology, fluid inclusions and implications for crustal uplift history. *Contributions to Mineralogy & Petrology* **96**, 343-356.

Sautter, V. & Fabriès, J., 1990. Cooling kinetics of garnet websterites from the Freychinède orogenic lherzolite massif, French Pyrenees. *Contributions to Mineralogy & Petrology* **105**, 533-549.

Sautter, V., Jaoul, O. & Abel, F., 1988. Aluminium diffusion in diopside using the $^{27}Al(p,\gamma)^{28}Si$ nuclear reaction: preliminary results. *Earth & Planetary Science Letters* **89**, 109-114.

Sautter, V. & Harte, B., 1988. Diffusion gradients in an eclogite xenolith from the Roberts Victor kimberlite pipe: 1. Mechanism and evolution of garnet exsolution in Al_2O_3-rich clinopyroxene. *Journal of Petrology* **29**, 1325-1352.

Scharbert, H.G. & Kurat, G., 1974. Distribution of some elements between coexisting ferromagnesian minerals in Moldanubian granulite facies rocks, lower Austria. *Tschermaks Mineralogische und Petrographische Mitteilungen* **21**, 110-134.

Schenk, V., 1980. U-Pb and Rb-Sr radiometric dates and their correlation with metamorphic events in the granulite-facies basement of the Serre, southern Calabria (Italy). *Contributions to Mineralogy & Petrology* **73**, 23-38.

Schenk, V., 1984. Petrology of felsic granulites, metapelites, metabasics, ultramafics, and metacarbonates from southern Calabria (Italy): prograde metamorphism, uplift and cooling of a former lower crust. *Journal of Petrology* **25**, 255-298.

Schenk, V., 1989. *P-T-t* path of the lower crust in the Hercynian fold belt of southern Calabria. In: Daly, J.S., Cliff, R.A. & Yardley, B.W.D. (eds) *Evolution of Metamorphic Belts*, Geological Society of London Special Publication No. **43**, 337-342.

Schreurs, J. & Westra, L., 1986. The thermotectonic evolution of a Proterozoic, low pressure, granulite dome, West Uusimaa, SW Finland. *Contributions to Mineralogy & Petrology* **93**, 236-250.

Schumacher, J.C., Hollocher, K.T., Robinson, P. & Tracy, R.J., 1990. Progressive reactions and melting in the Acadian metamorphic high of central Massachusetts and southwestern New Hampshire, USA. In: Ashworth, J.R. & Brown, M. (eds) *High-temperature Metamorphism and Crustal Anatexis*. London: Unwin Hyman Ltd, 198-234.

Schumacher, R., Schenk, V., Raase, P. & Vitanage, P.W., 1990. Granulite facies metamorphism of metabasic and intermediate rocks in the Highland Series of Sri Lanka. In: Ashworth, J.R. & Brown, M. (eds) *High-temperature Metamorphism and Crustal Anatexis*. London: Unwin Hyman Ltd, 235-271.

Sclater, J.G., Jaupart, C. & Galson, D., 1980. Heat flow through oceanic and continental crust, and heat loss of the earth. *Review of Geophysics & Space Physics* **81**, 269-312.

Selverstone, J. & Chamberlain, C.P., 1990. Apparent isobaric cooling paths from granulites: two counterexamples from British Columbia and New Hampshire. *Geology* **18**, 307-310.

Sen, S.K. & Bhattacharya, A., 1984. An orthopyroxene-garnet thermometer and its application to the Madras charnockites. *Contributions to Mineralogy & Petrology* **88**, 64-71.

Sengupta, P., Karmakar, S., Dasgupta, S. & Fukuoka, M., 1991. Petrology of spinel granulites from Araku, Eastern Ghats, India, and a petrogenetic grid for sapphirine-free rocks in the system FMAS. *Journal of Metamorphic Geology* **9**, 451-459.

Shaw, D.M., 1960. The geochemistry of scapolite. Part I. Previous work and general mineralogy. *Journal of Petrology* **1**, 218-260.

Sheraton, J.W., 1982. Origin of charnockitic rocks of MacRobertson Land. In: Craddock, C. (ed.) *Antarctic Geoscience*. Madison: University of Wisconsin Press, 489-497.

Sheraton, J.W., 1983. Geochemistry of mafic igneous rocks of the northern Prince Charles Mountains, Antarctica. *Journal of the Geological Society of Australia* **30**, 295-304.

Sheraton, J.W. & Black, L.P., 1983. Geochemistry of Precambrian gneisses: relevance for the evolution of the East Antarctic Shield. *Lithos* **16**, 273-296.

Sheraton, J.W. & Black, L.P., 1988. Chemical evolution of granitic rocks in the East Antarctic Shield, with particular reference to post-orogenic granites. *Lithos* **21**, 37-52.

Sheraton, J.W., Black, L.P. & McCulloch, M.T., 1984. Regional geochemical and isotopic characteristics of high-grade metamorphics of the Prydz Bay area: the extent of Proterozoic reworking of Archaean continental crust in East Antarctica. *Precambrian Research* **26**, 169-198.

Sheraton, J.W. & Collerson, K.D., 1983. Archaean and Proterozoic geological relationships in the Vestfold Hills - Prydz Bay area, Antarctica. *BMR Journal of Australian Geology & Geophysics* **8**, 119-128.

Sheraton, J.W. & Collerson, K.D., 1984. Geochemical evolution of Archaean granulite-facies gneisses in the Vestfold Block and comparisons with other Archaean gneiss complexes in the East Antarctic Shield. *Contributions to Mineralogy & Petrology* **87**, 51-64.

Sheraton, J.W., Ellis, D.J. & Kuehner, S.M., 1985. Rare-earth element geochemistry of Archaean orthogneisses and evolution of the East Antarctic Shield. *BMR Journal of Australian Geology & Geophysics* **9**, 207-218.

Sheraton, J.W., Offe, L.A., Tingey, R.J. & Ellis, D.J., 1980. Enderby Land, Antarctica - an unusual Precambrian high-grade metamorphic terrain. *Journal of the Geological Society of Australia* **27**, 1-18.

Sheraton, J.W., Tingey, R.J., Black, L.P., Offe, L.A. & Ellis, D.J., 1987. Geology of an unusual Precambrian high-grade metamorphic terrane - Enderby Land and western Kemp Land, Antarctica. *Bureau of Mineral Resources, Australia, Bulletin* **223**, 51 pp.

Sighinolfi, G.P., Figueredo, M.C.H., Fyfe, W.S., Kronberg, B.I. & Tanner de Oliveira, M.A.F., 1981. Geochemistry and petrology of the Jequié Granulitic Complex (Brazil): an Archaean basement complex. *Contributions to Mineralogy & Petrology* **78**, 263-271.

Sills, J.D., 1984. Granulite facies metamorphism in the Ivrea Zone, NW Italy. *Schweizerische Mineralogische und Petrographische Mitteilungen* **64**, 169-191.

Sills, J.D. & Rollinson, H.R., 1987. The metamorphic evolution of the mainland Lewisian Complex. In: Park, R.G. & Tarney, J. (eds) *Evolution of the Lewisian and Comparable Precambrian High Grade Terrains*, Geological Society of London Special Publication No. 27, 81-92.

Sills, J.D., Wang, K., Yan, Y. & Windley, B.F., 1987. The Archaean high grade gneiss terrain in E Hebei Province, NE China: geological framework and conditions of metamorphism. In: Park, R.G. & Tarney, J. (eds) *Evolution of the Lewisian and Comparable Precambrian High Grade Terrains*, Geological Society of London Special Publication No. 27, 297-305.

Sivaprakash, C., 1981. Petrology of calc-silicate rocks from Koduru, Andhra Pradesh, India. *Contributions to Mineralogy & Petrology* **77**, 121-128.

Smyth, C.H., 1897. Pseudomorphs from northern New York. *American Journal of Science* series **4 iv**, 312.

Sonder, L.J., England, P.C., Wernicke, B.P. & Christiansen, R.L., 1987. A physical model for Cenozoic extension of western North America. In: Coward, M.P., Dewey, J.F. & Hancock, P.L. (eds) *Continental Extensional Tectonics*, Geological Society of London Special Publication No. 28, 187-201.

Spear, F.S. & Cheney, J.T., 1989. A petrogenetic grid for pelitic schists in the system SiO_2-Al_2O_3-FeO-MgO-K_2O-H_2O. *Contributions to Mineralogy & Petrology* **101**, 149-164.

Spear, F.S. & Selverstone, J., 1983. Quantitative *P-T* paths from zoned minerals: theory and tectonic applications. *Contributions to Mineralogy & Petrology* **83**, 348-357.

Stähle, H.J., Raith, M., Hoernes, S. & Delfs, A., 1987. Element mobility during incipient granulite formation at Kabbaldurga, southern India. *Journal of Petrology* **28**, 803-834.

Stüwe, K., Braun, H-M. & Peer, H., 1989. Geology and structure of the Larsemann Hills area, Prydz Bay, East Antarctica. *Australian Journal of Earth Sciences* **36**, 219-241.

Stüwe, K. & Powell, R., 1989*a*. Low-pressure granulite facies metamorphism in the Larsemann Hills area, East Antarctica; petrology and tectonic implications for the evolution of the Prydz Bay area. *Journal of Metamorphic Geology* **7**, 465-483.

Stüwe, K. & Powell, R., 1989*b*. Metamorphic segregations associated with garnet and orthopyroxene porphyroblast growth: two examples from the Larsemann Hills, East Antarctica. *Contributions to Mineralogy & Petrology* **103**, 523-530.

Subramaniam, A.P., 1959. Charnockites of the type area near Madras - a reinterpretation. *American Journal of Science* **257**, 321-353.

Tait, R.E., 1989. *Local processes involved in the generation of mafic migmatites from the Rauer Islands, East Antarctica*. D.Phil. thesis, University of Oxford, 407 pp. (Unpublished).

Tait, R.E. & Harley, S.L., 1988. Local processes involved in the generation of migmatites within mafic granulites. *Transactions of the Royal Society of Edinburgh* **79**, 209-222.

Tapponnier, P., Mercier, J.L., Armijo, R., Han Tonglin & Zhou Ji, 1981. Field evidence for active normal faulting in Tibet. *Nature* **294**, 410-414.

Thompson, A.B., 1974. Calculation of muscovite-paragonite-alkali feldspar phase relations. *Contributions to Mineralogy & Petrology* **44**, 173-194.

Thompson, A.B., 1975. Calc-silicate diffusion zones between marble and pelitic schist. *Journal of Petrology* **16**, 314-346.

Thompson, A.B., 1976. Mineral reactions in pelitic rocks: II. Calculation of some *P-T-X* (Fe-Mg) phase relations. *American Journal of Science* **276**, 425-454.

Thompson, A.B., 1982. Dehydration melting of pelitic rocks and the generation of H_2O-undersaturated granitic liquids. *American Journal of Science* **282**, 1567-1595.

Thompson, A.B., 1983. Fluid-absent metamorphism. *Journal of the Geological Society of London* **140**, 533-547.

Thompson, A.B. & Algor, J.R., 1977. Model systems for anatexis of pelitic rocks: I. Theory of melting reactions in the system $KAlO_2$-$NaAlO_2$-Al_2O_3-SiO_2-H_2O. *Contributions to Mineralogy & Petrology* **63**, 247-269.

Thompson, A.B. & England, P.C., 1984. Pressure-temperature-time paths of regional metamorphism II. Their inference and interpretation using mineral assemblages in metamorphic rocks. *Journal of Petrology* **25**, 929-955.

Thompson, A.B. & Tracy, R.J., 1979. Model systems for anatexis of pelitic rocks: II. Facies series melting and reactions in the system CaO-$KAlO_2$-$NaAlO_2$-Al_2O_3-SiO_2-H_2O. *Contributions to Mineralogy & Petrology* **70**, 429-438.

Thompson, J.B., 1955. The thermodynamic basis for the mineral facies concept. *American Journal of Science* **253**, 65-103.

Thompson, J.B., 1957. The graphical analysis of mineral assemblages in pelitic schists. *American Mineralogist* **42**, 842-858.

Thompson, J.B., 1959. Local equilibrium in metasomatic processes. In: Abelson, P.H. (ed.) *Researches in Geochemistry*. New York: John Wiley & Sons, 427-457.

Thompson, J.B. & Thompson, A.B., 1976. A model system for mineral facies in pelitic schists. *Contributions to Mineralogy & Petrology* **58**, 243-277.

Thost, D.E., Hensen, B.J. & Motoyoshi, Y., 1991. Two-stage decompression in garnet-bearing mafic granulites from Sostrene Island, Prydz Bay, East Antarctica. *Journal of Metamorphic Geology* **9**, 245-256.

Thost, D.E., Motoyoshi, Y. & Hensen, B.J., 1988. Low pressure granulite metamorphism in the Bolingen Islands, East Antarctica. *Terra Cognita* **8**, 247. (Abstract).

Tilley, C.E., 1936. Enderbite, a new member of the charnockite series. *Geological Magazine* **73**, 312-316.

Tilley, C.E., 1937*a*. Rocks from Enderby Land. *Reports of the British-Australian-New Zealand Antarctic Research Expedition 1929-1931*, A **2**, 1-16.

Tilley, C.E., 1937*b*. Rocks from MacRobertson Land. *Reports of the British-Australian-New Zealand Antarctic Research Expedition 1929-1931*, A **2**, 17-25.

Tilley, C.E., 1951. The zoned contact skarns of the Broadford area, Skye: a study of boron-fluorine metasomatism in dolomites. *Mineralogical Magazine* **29**, 621-666.

Tingey, R.J., 1972. Geological work in Antarctica - 1971. *Bureau of Mineral Resources, Australia, Record* **1972/132**, 49 pp. (Unpublished).

Tingey, R.J., 1974. Australian geological mapping in the Prince Charles Mountains, 1968-73. *Polar Record* **16**, 150-153.

Tingey, R.J., 1981. Geological investigations in Antarctica 1968-1969: the Prydz Bay - Amery Ice Shelf - Prince Charles Mountains area. *Bureau of Mineral Resources, Australia, Record* **1981/34**, 72 pp. (Unpublished).

Tingey, R.J., 1982. The geologic evolution of the Prince Charles Mountains - an Antarctic Archaean cratonic block. In: Craddock, C. (ed.) *Antarctic Geoscience.* Madison: University of Wisconsin Press, 455-464.

Tingey, R.J. & England, R.N., 1973. Geological work in Antarctica - 1972. *Bureau of Mineral Resources, Australia, Record* **1973/161**, 17 pp. (Unpublished).

Tobi, A.C., 1971. The nomenclature of the charnockitic rock suite. *Neues Jahrbuch für Mineralogie Monatshefte* **1971**, 193-205.

Touret, J., 1971*a*. Le faciès granulite en Norvège méridionale. I. Les associations minéralogiques. *Lithos* **4**, 239-249.

Touret, J., 1971*b*. Le faciès granulite en Norvège méridionale. II. Les inclusions fluides. *Lithos* **4**, 423-436.

Tracy, R.J., 1982. Compositional zoning and inclusions in metamorphic minerals. In: Ferry, J.M. (ed.) *Characterization of Metamorphism through Mineral Equilibria,* Mineralogical Society of America Reviews in Mineralogy Vol. **10**, 355-397.

Tracy, R.J. & Robinson, P., 1983. Acadian migmatite types in pelitic rocks of central Massachusetts. In: Atherton, M.P. & Gribble, C.D. (eds) *Migmatites, Melting and Metamorphism.* Nantwich: Shiva Publishing Ltd, 163-173.

Trail, D.S., 1964. Schist and granite in the southern Prince Charles Mountains. In: Adie R.J. (ed.) *Antarctic Geology.* Amsterdam: North-Holland Publishing Company, 492-497.

Trail, D.S., 1970. ANARE 1961 geological traverse on the MacRobertson Land and Kemp Land coast. *Bureau of Mineral Resources, Australia, Report* **135**, 32 pp. (Unpublished).

Trail, D.S., McLeod, I.R., Cook, P.J. & Wallis, G.R., 1967. Geological investigations by the Australian National Antarctic Research Expeditions, 1965. *Bureau of Mineral Resources, Australia, Report* **118**, 48 pp. (Unpublished).

Treloar, P.J., Carney, J.N., Crow, M.J., Evans, J.A. & Barton, C.N., 1990. Pressure-temperature-time paths of granulite metamorphism and uplift, Zambesi Belt, N.E. Zimbabwe. In: Vielzeuf, D. & Vidal, Ph. (eds) *Granulites and Crustal Evolution.* Dordrecht: Kluwer Academic Publishers, 223-241.

Valley, J.W., 1985. Polymetamorphism in the Adirondacks: wollastonite at contacts of shallowly intruded anorthosite. In: Tobi, A.C. & Touret, J.L.R. (eds) *The Deep Proterozoic Crust in the North Atlantic Provinces.* Dordrecht: Reidel, 217-236.

Valley, J.W. & Essene, E.J., 1980. Calc-silicate reactions in Adirondack marbles: the role of fluids and solid solutions. *Bulletin of the Geological Society of America* **91 Part II**, 720-815.

Valley, J.W., Essene, E.J. & Peacor, D.R., 1983*b*. Fluorine-bearing garnets in Adirondack calc-silicates *American Mineralogist* **68**, 444-448.

Valley, J.W., McLelland, J.M., Essene, E.J. & Lamb, W.M., 1983*a*. Metamorphic fluids in the deep crust: evidence from the Adirondacks. *Nature* **301**, 226-228.

Valley, J.W. & O'Neil, J.R., 1984. Fluid heterogeneity during granulite facies metamorphism in the Adirondacks: stable isotope evidence. *Contributions to Mineralogy & Petrology* **85**, 158-173.

Valley, J.W., Petersen, E.U., Essene, E.J. & Bowman, J.R., 1982. Fluorphlogopite and fluortremolite in Adirondack marbles and calculated C-O-H-F fluid compositions. *American Mineralogist* **67**, 545-557.

van der Molen, I. & Paterson, M.S., 1979. Experimental deformation of partially-melted granite. *Contributions to Mineralogy & Petrology* **70**, 299-318.

Vernon, R.H., Clarke, G.L. & Collins, W.J., 1990. Local, mid-crustal granulite facies metamorphism and melting: an example in the Mount Stafford area, central Australia. In: Ashworth, J.R. & Brown, M. (eds) *High-temperature Metamorphism and Crustal Anatexis.* London: Unwin Hyman Ltd, 272-319.

Vernon, R.H. & Collins, W.J., 1988. Igneous microstructures in migmatites. *Geology* **16**, 1126-1129.

Vernon, R.H., Williams, V.A. & D'Arcy, W.F., 1983. Grain-size reduction and foliation development in a deformed granite batholith. *Tectonophysics* **92**, 123-145.

Vidale, R., 1969. Metasomatism in a chemical gradient and the formation of calc-silicate bands. *American Journal of Science* **267**, 857-874.

Vielzeuf, D., 1983. The spinel and quartz associations in high grade xenoliths from Tallante (S.E. Spain) and their potential use in geothermometry and barometry. *Contributions to Mineralogy & Petrology* **82**, 301-311.

Vielzeuf, D., Clemens, J.D., Pin, C. & Moinet, E., 1990. Granites, granulites and crustal differentiation. In: Vielzeuf, D. & Vidal, Ph. (eds) *Granulites and Crustal Evolution*. Dordrecht: Kluwer Academic Publishers, 59-85.

Vielzeuf, D. & Holloway, J.R., 1988. Experimental determination of the fluid-absent melting relations in the pelitic system. *Contributions to Mineralogy & Petrology* **98**, 257-276.

Vielzeuf, D. & Komprobst, J., 1984. Crustal splitting and the emplacement of Pyrenean lherzolites and granulites. *Earth & Planetary Science Letters* **67**, 87-96.

Vielzeuf, D. & Pin, C., 1989. Geodynamic implications of granulite rocks in the Hercynian belt. In: Daly, J.S., Cliff, R.A. & Yardley, B.W.D. (eds) *Evolution of Metamorphic Belts,* Geological Society of London Special Publication No. **43**, 343-348.

Visser, D. & Senior, A., 1990. Aluminous reaction textures in orthoamphibole-bearing rocks: the pressure-temperature evolution of the high-grade Proterozoic of the Bamble sector, south Norway. *Journal of Metamorphic Geology* **8**, 231-246.

Wall, V.J., Clemens, J.D. & Clarke, D.B., 1987. Models for granitoid evolution and source compositions. *Journal of Geology* **95**, 731-749.

Walther, J.V. & Wood, B.J., 1984. Rate and mechanism in prograde metamorphism. *Contributions to Mineralogy & Petrology* **88**, 246-259.

Warren, R.G., 1983*a*. Metamorphic and tectonic evolution of granulites, Arunta Block, central Australia. *Nature* **305**, 300-303.

Warren, R.G., 1983*b*. Prograde and retrograde sapphirine in metamorphic rocks of the central Arunta Block, central Australia. *BMR Journal of Australian Geology & Geophysics* **8**, 139-145.

Warren, R.G. & Hensen, B.J., 1989. The *P-T* evolution of the Proterozoic Arunta Block, central Australia, and implications for tectonic evolution. In: Daly, J.S., Cliff, R.A. & Yardley, B.W.D. (eds) *Evolution of Metamorphic Belts*, Geological Society of London Special Publication No. **43**, 349-355.

Warren, R.G., Hensen, B.J. & Ryburn, R.J., 1987. Wollastonite and scapolite in Precambrian calc-silicate granulites from Australia and Antarctica. *Journal of Metamorphic Geology* **5**, 213-223.

Waters, D.J., 1986. Metamorphic history of sapphirine-bearing and related magnesian gneisses from Namaqualand, South Africa. *Journal of Petrology* **27**, 541-565.

Waters, D.J., 1988. Partial melting and the formation of granulite facies assemblages in Namaqualand, South Africa. *Journal of Metamorphic Geology* **6**, 387-404.

Waters, D.J., 1989. Metamorphic evidence for the heating and cooling path of Namaqualand granulites. In: Daly, J.S., Cliff, R.A. & Yardley, B.W.D. (eds) *Evolution of Metamorphic Belts,* Geological Society of London Special Publication No. **43**, 357-363.

Waters, D.J., 1991. Hercynite-quartz granulites: phase relations, and implications for crustal processes. *European Journal of Mineralogy* **3**, 367-386.

Waters, D.J. & Whales, C.J., 1984. Dehydration melting and the granulite transition in metapelites from southern Namaqualand, S. Africa. *Contributions to Mineralogy & Petrology* **88**, 269-275.

Watson, E.B. & Brenan, J.M., 1987. Fluids in the lithosphere, 1. Experimentally-determined wetting characteristics of CO_2-H_2O fluids and their implications for fluid transport, host-rock physical properties, and fluid inclusion formation. *Earth & Planetary Science Letters* **85**, 497-515.

Weaver, B.L. & Tarney, J., 1983. Elemental depletion in Archaean granulite-facies rocks. In: Atherton, M.P. & Gribble, C.D. (eds) *Migmatites, Melting and Metamorphism*. Nantwich: Shiva Publishing Ltd, 250-263.

Webster, J.D., 1990. Partitioning of F between H_2O and CO_2 fluids and topaz rhyolite melt. *Contributions to Mineralogy & Petrology* **104**, 424-438.

Wells, P.R.A., 1979. Chemical and thermal evolution of Archaean sialic crust, southern West Greenland. *Journal of Petrology* **20**, 187-226.

Wells, P.R.A., 1980. Thermal models for the magmatic accretion and subsequent metamorphism of continental crust. *Earth & Planetary Science Letters* **46**, 253-265.

Wernicke, B., 1985. Uniform-sense normal simple shear of the continental lithosphere. *Canadian Journal of Earth Sciences* **22**, 108-125.

White, A.J.R., 1959. Scapolite-bearing marbles and calc-silicate rocks from Tungkillo and Milendella, South Australia. *Geological Magazine* **96**, 285-306.

Wickham, S.M., 1987. The segregation and emplacement of granitic magmas. *Journal of the Geological Society of London* **144**, 281-297.

Wickham, S.M. & Oxburgh, E.R., 1985. Continental rifts as a setting for regional metamorphism. *Nature* **318**, 330-333.

Windley, B.F., 1981. Phanerozoic granulites. *Journal of the Geological Society of London* **138**, 745-751.

Winkler, H.G.F. & Sen, S.K., 1973. Nomenclature of granulites and other high grade metamorphic rocks. *Neues Jahrbuch für Mineralogie Monatshefte* **1973**, 393-402.

Wood, B.J., 1974. The solubility of alumina in orthopyroxene coexisting with garnet. *Contributions to Mineralogy & Petrology* **46**, 1-15.

Wood, B.J., 1975. The influence of pressure, temperature and bulk composition on the appearance of garnet in orthogneisses - an example from South Harris, Scotland. *Earth & Planetary Science Letters* **26**, 299-311.

Wood, B.J. & Banno, S., 1973. Garnet-orthopyroxene and orthopyroxene-clinopyroxene relationships in simple and complex systems. *Contributions to Mineralogy & Petrology* **42**, 109-124.

Yardley, B.W.D., 1977. An empirical study of diffusion in garnet. *American Mineralogist* **62**, 793-800.

Yardley, B.W.D., 1978. Genesis of the Skagit Gneiss migmatites, Washington, and the distinction between possible mechanisms of migmatization. *Bulletin of the Geological Society of America* **89**, 941-951.

Yardley, B.W.D., 1989. *An Introduction to Metamorphic Petrology*. Harlow: Longman Scientific and Technical, 248 pp.

Yoder, H.S. & Tilley, C.E., 1962. Origin of basalt magmas: an experimental study of natural and synthetic rock systems. *Journal of Petrology* **3**, 342-532.

Young, D.N. & Black, L.P., 1991. U-Pb zircon dating of Proterozoic igneous charnockites from the Mawson Coast, East Antarctica. *Antarctic Science* **3**, 205-216.

Young, D.N. & Ellis, D.J., 1990. Petrology of Proterozoic igneous charnockites from Mawson, Antarctica: high-temperature, syn-orogenic granitoids produced by anatexis in thickened crust. *Geological Society of Australia, Abstracts* **25**, 261-262.

Young, D.N. & Ellis, D.J., 1991. The intrusive Mawson Charnockites: evidence for a compressional plate margin setting of the Proterozoic mobile belt of East Antarctica. In: Thomson, M.R.A., Crame, J.A. & Thomson, J.W. (eds) *Geological Evolution of Antarctica*. Cambridge: Cambridge University Press, 25-31.

Young, E.D., Anderson, J.L., Clarke, H.S. & Thomas, W.M., 1989. Petrology of biotite-cordierite-garnet gneiss of the McCullough Range, Nevada I. Evidence for Proterozoic low-pressure fluid-absent granulite-grade metamorphism in the southern Cordillera. *Journal of Petrology* **30**, 39-60.

Zen, E-an, 1966. Construction of pressure-temperature diagrams for multicomponent systems after the method of Schreinemakers - a geometric approach. *Bulletin of the US Geological Survey* **1225**, 56 pp.

Zingg, A., 1983. The Ivrea and Stona-Ceneri zones (Southern Alps, Ticino and N-Italy) - a review. *Schweizerische Mineralogische und Petrographische Mitteilungen* **63**, 361-392.